ELECTROCHEMICAL BEHAVIOUR OF PYRITE, PYRRHOTITE, PENTLANDITE AND CHALCOPYRITE

A thesis submitted for the degree of Doctor of Philosophy of the University of London

by

PAUL WILLIAM PAGE

Department of Mineral Resources Engineering
Imperial College of Science and Technology
University of London
LONDON SW7 2BP

October 1988

ACKNOWLEDGEMENTS

I wish to express my deep gratitude to Dr. G.H. Kelsall for his supervision and guidance throughout this course.

I would also like to thank British Petroleum p.l.c. for sponsoring the project, and Dr. H.L. Shergold, Dr M.N. Mahmood, Dr. D.E. Graham and Dr. L. Hazell from the BP Research Centre, Sunbury, who encouraged me throughout my studies.

Finally, to my parents, who I am particularly indebted to, for their sacrifice and support over the last eight years.

ABSTRACT

The objective of the project was to investigate the surface oxidation of pyrite (FeS_2), pyrrhotite (FeS), chalcopyrite ($CuFeS_2$) and pentlandite ($(Fe,Ni)_9S_8$), with a technological aim of achieving oxidation selectivity between one or more of the sulphides in the absence of collectors, so possibly enabling selective flotation separations to be made without surfactant addition.

Cyclic and pulse voltammetry, chronocoulometry and A.C. impedance measurements were used with the aid of E_h/pH diagrams, to characterise the oxidation and reduction processes at the four sulphide mineral/solution interfaces, as a function of electrode potential and pH. A rotating split cylinder bi-electrode (RSCBE), previously calibrated for collection efficiency, was used to detect soluble electro-active species (H_2S, Fe^{3+}, etc.) formed during mineral oxidation. The effect of S^{2-}, $S_2O_3^{2-}$, Fe^{2+}, Fe^{3+}, Cu^{2+}, and Ni^{2+} solution additions on the cyclic voltammograms of rotating mineral electrodes was also investigated. X-ray photoelectron spectroscopy was used to help identify surface phases formed during electrochemical oxidation.

To study the natural floatability of pure sulphide mineral samples, a Hallimond tube flotation cell was adapted to allow the electrode potential of mineral particles to be controlled. The influence of such factors as feeder electrode potential, conditioning time and particle size on flotation recovery were examined. The flotation results were then correlated with the mineral electrode surface characterisation studies.

The results of the mineral electrode studies broadly followed thermodynamic predictions. At pH < 1, sulphide oxidation produced S° and soluble metal ions. At higher pH, sulphate production was favoured and the oxide/sulphur ratio increased, so that $Fe(OH)_3$ became the dominant surface phase, tending to cause passivation.

The results indicated that by redox potential and pH control, it would not be possible to form an oxidation product, such as hydrophobic sulphur or hydrophilic metal oxide, on only one of a mixture of the four mineral sulphides. However, the amount of product formed and the metal oxide/sulphur ratio on each mineral were found to be different. This was confirmed by natural floatability tests in alkaline media, where chalcopyrite was rendered naturally floatable at oxidising potentials and non-floatable at reducing potentials, whereas the converse was found for pyrite. A change in the surface stoichiometry to increase the sulphide/metal and Cu^{+}/Fe^{3+} ratios in the lattice, plus the possible formation of elemental sulphur were considered to be factors making chalcopyrite floatable. The inability of pyrite to float at oxidising potentials was attributed to the presence of a hydrophilic oxide/hydroxide film, which was removed at reducing potentials rendering pyrite hydrophobic.

CONTENTS

		Page No.
ACKNOWLEDGEMENTS		(i)
ABSTRACT		(ii)
LIST OF CONTENTS		(iv)
LIST OF FIGURES		(x)
LIST OF PHOTOGRAPHIC PLATES		(xxxiii)
LIST OF TABLES		(xxxv)
NOMENCLATURE		(xxxvi)
1.	INTRODUCTION.	1
2.	LITERATURE SURVEY.	5
2.1	Physical properties.	6
2.1.1	Crystal structure.	6
2.1.1.1	Pyrite.	7
2.1.1.2	Pyrrhotite.	8
2.1.1.3	Pentlandite.	10
2.1.1.4	Chalcopyrite.	10
2.1.2	Electrical, magnetic and Mössbauer studies.	12
2.1.2.1	Pyrite.	13
2.1.2.2	Pyrrhotite.	14
2.1.2.3	Pentlandite.	15
2.1.2.4	Chalcopyrite.	16
2.2	Electrode potentials and Eh-pH diagrams.	17

		Page No.
2.3	Chemical oxidation.	28
2.3.1	Pyrite.	28
2.3.2	Pyrrhotite.	31
2.3.3	Pentlandite.	32
2.3.4	Chalcopyrite.	34
2.4	Electrochemical studies of sulphide mineral behaviour.	35
2.4.1	Anodic and cathodic reactions of sulphide minerals in aqueous solutions.	36
2.4.1.1	Pyrite.	37
2.4.1.2	Pyrrhotite.	43
2.4.1.3	Pentlandite.	44
2.4.1.4	Chalcopyrite.	45
2.4.2	Cathodic reduction of oxygen.	52
2.4.3	Non-oxidative dissolution.	55
2.4.4	Electrolytic treatment of sulphides.	59
2.4.5	Galvanic effects among sulphides.	61
3.	EXPERIMENTAL MATERIALS.	63
3.1	Origin of the Samples.	64
3.2	Characterisation of the Samples.	64
3.2.1	X-ray fluorescence analysis.	64
3.2.2	Chemical analysis.	64
3.2.3	X-ray diffraction analysis.	66
3.2.4	Optical examination of polished sections.	67
3.2.5	Energy-dispersive x-ray analysis (E.D.X.A.).	67
3.2.6	Infrared spectroscopy.	70
3.2.7	Resistivity measurements.	74
3.3	Other Chemicals.	78
4.	EXPERIMENTAL METHODS.	81

		Page No.
4.1	Preparation of deoxygenated water.	82
4.2	Electrochemical studies on sulphide mineral electrodes.	85
4.2.1	Preparation of stationary mineral electrodes.	85
4.2.2	Preparation of rotating cylinder collector electrodes.	88
4.2.3	Cell design and electrochemical instrumentation.	93
4.2.4	Cyclic voltammetric studies.	93
4.2.4.1	Experimental procedure.	95
4.2.4.2	Measurements on virgin surfaces produced by in situ polishing and first sweep voltammetric curves.	100
4.2.5	Rotating split cylinder bi-electrode studies.	100
4.2.5.1	Experimental procedure.	100
4.2.6	Pulse voltammetry.	104
4.2.6.1	Experimental procedure.	104
4.2.7	A.C. impedance measurements.	104
4.2.7.1	Experimental procedure.	105
4.3	Mineral pulp/suspension electrode studies.	107
4.3.1	Apparatus.	108
4.3.2	Experimental procedure.	110
4.3.3	Solution analysis.	113
4.3.4	Contact experiments.	115
	RESULTS AND DISCUSSION.	117
5.	THE ROTATING SPLIT CYLINDER BI-ELECTRODE (RSCBE).	118
5.1	Calibration.	118
5.2	Detection of soluble species (Fe^{2+}, Fe^{3+}, H_2S).	125
6.	ELECTROCHEMICAL STUDIES ON PYRITE ELECTRODES.	130
6.1	Thermodynamics.	131
6.2	Rest potential measurements.	133

		Page No.
6.2.1	Summary.	139
6.3	Studies on virgin pyrite surfaces.	139
6.4	Cyclic voltammetry.	144
6.4.1	Anodic and cathodic reactions at pH 1.0 (0.1 M H_2SO_4, 0.1 M $HClO_4$).	144
6.4.2	Pyrite RSCBE at pH 0 (1 M $HClO_4$).	157
6.4.3	pH 4.6 (0.5 M CH_3COOH + 0.5 M CH_3COONa).	164
6.4.3.1	Pyrite RSCBE results.	173
6.4.4	pH 7.0 (0.025 M KH_2PO_4 + 0.025 M Na_2HPO_4).	178
6.4.5	Anodic and cathodic reactions in alkaline solutions (pH > 7).	190
6.5	Pulse voltammetry on stationary pyrite electrodes.	195
6.5.1	Current-time transients at low anodic overpotentials; transition from "active" to "passive" pyrite.	195
6.5.2	Current-time transients at intermediate anodic. overpotentials; $\leq$ 200 mV positive of the critical potential.	202
6.5.3	Current time transients at high anodic overpotentials in acidic solutions.	203
6.6	Electrode impedance measurements.	206
6.7	A solid state semiconductor mechanism for pyrite oxidation.	216
6.7.1	Passive film formation.	221
6.7.2	Pyrite oxidation.	225
6.8	Relevance of these results to pyrite flotation.	229
7.	ELECTROCHEMICAL STUDIES ON PYRRHOTITE ELECTRODES.	236
7.1	Thermodynamics.	237
7.2	Studies on virgin pyrrhotite samples.	238

		Page No.
7.3	Cyclic voltammetry.	242
7.3.1	Anodic and cathodic reactions at pH 1.0 (0.1 M $HClO_4$).	242
7.3.2	Pyrrhotite RSCBE at pH 0 (1 M $HClO_4$).	248
7.3.3	pH 4.6 (0.5 M CH_3COOH + 0.5 M CH_3COONa).	249
7.3.3.1	Open-circuit decomposition of the passivating film.	253
7.3.3.2	Pyrrhotite RSCBE results.	257
7.3.4	Voltammetry in neutral and basic solutions.	257
7.4	Pulse voltammetry on stationary pyrrhotite electrodes.	262
7.4.1	pH 0 (1 M $HClO_4$).	262
7.4.2	pH 4.6 (0.5 M CH_3COOH + 0.5 M CH_3COONa) and pH 9.2 (0.05 M $Na_2B_4O_7$).	264
7.4.3	pH 13 (0.1 M NaOH).	265
7.4.4	Charge vs time measurements.	266
7.5	Impedance measurements on stationary pyrrhotite electrodes.	268
8.	ELECTROCHEMICAL STUDIES ON PENTLANDITE ELECTRODES.	274
8.1	Thermodynamics.	275
8.2	Studies on virgin pentlandite samples.	277
8.3	Cyclic voltammetry.	281
8.3.1	Anodic and cathodic reactions in acidic solutions (< pH 7).	281
8.3.1.1	Pentlandite RSCBE at pH 0 (1 M $HClO_4$).	287
8.3.2	Voltammetry in neutral and basic solutions.	288
8.4	Pulse voltammetry on stationary pentlandite electrodes.	295
8.5	Impedance measurements on stationary pentlandite electrodes.	297
9.	ELECTROCHEMICAL STUDIES ON CHALCOPYRITE ELECTRODES.	306
9.1	Thermodynamics.	307

		Page No.
9.2	Rest potential measurements.	310
9.3	Cyclic voltammetry.	310
9.3.1	Anodic and cathodic processes in acidic solutions.	310
9.3.1.1	The prewave process.	317
9.3.1.2	Chalcopyrite RSCBE at pH 0 (1 M $HClO_4$ and 1 M HCl).	321
9.3.2	Voltammetry in neutral and basic solutions.	323
9.3.2.1	pH 7 (0.025 M KH_2PO_4 + 0.025 M Na_2HPO_4).	325
9.3.2.2	pH 9.2 (0.05 M $Na_2B_4O_7$) and pH 13 (0.1 M NaOH).	329
9.4	Pulse voltammetry on stationary chalcopyrite electrodes.	330
9.4.1	pH 0 (1 M $HClO_4$).	330
9.4.2	pH 9.2 (0.05 M $Na_2B_4O_7$).	331
9.4.3	Change vs. time measurements.	332
9.5	Impedance measurements on stationary chalcopyrite electrodes.	333
10.	MINERAL PULP SUSPENSION ELECTRODE STUDIES.	338
10.1	Introduction.	339
10.2	Chalcopyrite.	339
10.3	Pyrite.	347
10.4	Contact potential measurements.	349
10.5	Effect of particle size.	352
10.6	Summary.	358
11.	CONCLUSIONS.	359
	REFERENCES	372
APPENDIX I	- Thermodynamic Equations	397
APPENDIX II	- E_h-pH and Activity-pH Diagrams	413
APPENDIX III	- Computer Programs	433

LIST OF FIGURES

		Page No.
2.1	The crystal structure of pyrite (FeS_2)[7].	7
2.2	The pyrrhotite (nickel arsenide type) structure.	9
2.3	The crystal structure of pentlandite ($(Fe,Ni)_9S_8$).	11
	(a) The cubic unit cell of the pentlandite structure. (b) The cube cluster of tetrahedrally coordinated cations occurring in the pentlandite structure. Each cation is coordinated to one $S_{(1)}$ and three $S_{(2)}$ atoms.	
2.4	The crystal structure of chalcopyrite ($CuFeS_2$)[34].	12
2.5	Electrochemical phase diagram for galena[72]. Equilibrium lines correspond to dissolved species at 10^{-4} M.	22
2.6	Electrochemical free energy profiles for a metal solution interface[74].	24
2.7	Rest potentials of PbS in $HClO_4$ solutions after cathodising then anodising for successive intervals[61].	26
3.1	X-ray diffraction of the pyrrhotite sample from Renison, Tasmania.	68
3.2	X-ray diffraction pattern of the pentlandite sample from Canada.	68
3.3	Infrared spectra of the FeS_2 sample from Spain and the $CuFeS_2$ sample from Sudbury, Canada.	73
3.4	Horizontally expanded infrared spectrum of the $CuFeS_2$ sample from Sudbury, Canada.	74

		Page No.
3.5	Electrochemical cell and equivalent circuit for controlled potential experiments on sulphide minerals.	75
3.6	Clamp arrangement to test the contact between a mineral sulphide specimen (MS) and metal.	77
3.7	Curves of current versus voltage for the contact between pyrite and metal: (a) gold (60 nm) - pyrite; (b) gold (30 nm) - pyrite; (c) brass - pyrite.	79
3.8	Curves of current versus voltage for chalcopyrite-metal pyrrhotite-metal and pentlandite-metal contacts: (Δ) pentlandite-brass; (□) pyrrhotite-brass; (o (a)) chalcopyrite-gold (60 nm); (o (b)) chalcopyrite-brass.	79
4.1	Dissolved oxygen content of water at various nitrogen flow rates.	82
4.2	Rate of deoxygenation of water.	83
4.3	Rate of re-oxygenation of water.	85
4.4	Stationary mineral electrode used in cyclic voltammetry, pulse voltammetry and A.C. impedance measurements.	86
4.5	Rotating cylinder-collector electrode.	89
4.6	Rotating split cylinder bi-electrode.	92
4.7	Electrochemical cell.	94
4.8	Electro-Hallimond tube flotation cell.	109
4.9	System used in particulate bed electrode studies to exclude oxygen.	111

Page No.

4.10 Electrochemical cell used in contact measurements and experiments on virgin sulphide surfaces. 116

5.1 Cyclic voltammograms of RSCBE pyrite working electrode in 0.1 M $K_3[Fe(CN)_6]$ + 0.1 M NaOH. (——) ω = 0 Hz; (---) ω = 10 Hz. (-.-) voltammogram in 0.1 M NaOH only, ω = 0 Hz. 119

5.2 Cyclic voltammograms of RSCBE Pt collector electrode in 0.1 M $K_3[Fe(CN)_6]$ + 0.1 M NaOH. (——) ω = 0 Hz; (---) ω = 10 Hz. (-.-) voltammogram in 0.1 M NaOH only, ω = 0 Hz. 120

5.3 0.1 M ferricyanide reduction current at a RSCBE pyrite working electrode in 0.1 M $K_3[Fe(CN)_6]$ + 0.1 M NaOH, as a function of (rotation rate, ω)$^{0.7}$. ($E_{WE(FeS_2)}$ = -0.5 V). 121

5.4 0.1 M ferricyanide reduction current at a RSCBE pyrite working electrode in 0.1 M $K_3[Fe(CN)_6]$ + 0.1 M NaOH, as a function of (rotation rate, ω)$^{0.5}$ to show low rotation rate non-linearity. ($E_{WE(FeS_2)}$ = -0.5 V). 122

5.5 Calibration of pyrite working, Pt collector, RSCBE in 0.1 M $K_3[Fe(CN)_6]$ + 0.1 M NaOH. ($E_{WE(FeS_2)}$ = -0.5 V, $E_{C(Pt)}$ = 1.0 V). 123

5.6 Collector efficiency of RSCBE in 0.1 M $K_3[Fe(CN)_6]$ + 0.1 M NaOH, as a function of ω. (⊙) mass transport controlled; (⊡) charge transfer controlled working electrode reaction. 124

5.7 Hydrodynamic flow around a RSCBE. 125

5.8 Cyclic voltammograms of RSCBE Pt collector electrode in 1M $HClO_4$ + 0.1 M Na_2S. (——) ω = 0 Hz; (---) ω = 10 Hz; (-.-) no sulphide, ω = 0 Hz. 126

Page No.

5.9 Cyclic voltammograms of RSCBE Pt collector electrode in: (——) 1 M $HClO_4$ + 0.1 M $FeSO_4$, ω = 10 Hz; (---) 1M $HClO_4$ + 0.1 M Na_2S (first three cycles), ω = 10 Hz; (-.-) 1 M $HClO_4$, ω = 10 Hz. 127

6.1 Potential-pH diagram for the S-H_2O system at 298 K with a dissolved sulphur activity of 10^{-3}[361]. 131

6.2 Potential-pH diagram for the Fe-S-H_2O system at 298 K with dissolved iron and sulphur activities of 10^{-4}. 134

6.3 The change of rest potential with pH for a pyrite electrode subject to different pretreatments. (O) no pretreatment; (●) sulphidised. 135

6.4 The change of rest potential with time (after in-situ polishing) of a pyrite electrode at pH 0 (1 M $HClO_4$). (A) commence polishing; (B) finish polishing. 140

6.5 The change of rest potential with time (after in-situ polishing) of a pyrite electrode at pH 9.2 (0.05 M $Na_2B_4O_7$). (A) commence polishing; (B) finish polishing. 140

6.6 Cyclic voltammograms of stationary pyrite electrodes in stirred solutions at pH 9.2 (0.05 M $Na_2B_4O_7$), recorded immediately after different surface pretreatments, starting from the rest potential, first cycled cathodically then anodically at 100 mV s^{-1}. (A) untreated sample; (B) fresh pyrite surface produced by in situ abrasion; (C) electrode potentiostatted at -0.2 V for 5 minutes prior to sweeping the potential; (D) potential of pyrite electrode cycled six times between -0.2 V and -0.9 V before extending the anodic potential limit to 0.8 V. 142

Page No.

6.7 Cyclic voltammograms of stationary pyrite electrodes in stirred solutions at pH 0 (1 M $HClO_4$), recorded immediately after different surface pretreatments, starting from the rest potential, first cycled cathodically then anodically at 100 mV s^{-1}. (A) untreated sample; (B) electrode potentiostatted at 0.2 V for 5 minutes prior to sweeping the potential; (C) fresh pyrite surface produced by in situ abrasion. 145

6.8 The effect of extending the anodic potential scanning limit (E_{λ_a}) on cyclic voltammograms of pyrite at pH 1 (0.1 M $HClO_4$) in stirred solution and a sweep rate of 100 mV s^{-1}. The insert shows an expanded view of the cathodic peaks at potentials < -0.6 V. 146

6.9 Cyclic voltammograms of a pyrite electrode at pH 1 (0.1 M $HClO_4$) as a function of potential sweep rate. 147

6.10 Currents for the cathodic peaks x and y plotted as a function of potential sweep rate. 148

6.11 Tafel plot for a pyrite electrode at pH 1 (0.1 M $HClO_4$). 150

6.12 Cyclic voltammogram of a pyrite electrode at pH 1 (0.1 M $HClO_4$) and a sweep rate of 50 mV s^{-1}. 151

6.13 Quantity of sulphur, sulphate, and ferric species formed on a 100 mV s^{-1} potential sweep as a function of the upper potential limit of the sweep (0.1 to 0.9 V) for a pyrite electrode at pH 1 (0.1 M $HClO_4$). 155

6.14 Quantity of sulphur, sulphate, and ferric species formed on a 100 mV s^{-1} potential sweep as a function of the upper potential limit of the sweep (0.1 to 1.4 V) for a pyrite electrode at pH 1 (0.1 M $HClO_4$). 155

Page No.

6.15 Number of monolayers of: pyrite oxidised to form sulphur (⧅); pyrite oxidised to form sulphate (Δ); total pyrite oxidised (●); sulphur formed (o), during a 100 mV s^{-1} potential sweep as a function of the upper potential limit of the sweep (0.1 to 0.9 V) for a pyrite electrode at pH 1 (0.1 M $HClO_4$). 156

6.16 Number of monolayers of: pyrite oxidised to form sulphur (⧅); pyrite oxidised to form sulphate (Δ); sulphur formed (o), during a 100 mV s^{-1} potential sweep as a function of the upper potential limit of the sweep (0.1 to 1.4 V) for a pyrite electrode at pH 1 (0.1 M $HClO_4$). 156

6.17 Cyclic voltammograms of a pyrite RSCBE in 1 M $HClO_4$ (pH 0). (—) stationary electrode; (---) rotated electrode. 158

6.18 Cyclic voltammograms of a pyrite RSCBE in 1 M $HClO_4$ + 0.1 M $FeCl_3$. (—) stationary electrode; (---) rotated electrode; (-•-•-) no ferric ions and electrode stationary. 159

6.19 Cyclic voltammograms of a pyrite RSCBE in 1 M $HClO_4$ + 0.1 M $FeSO_4$. (—) electrode stationary; (---) electrode rotated; (-•-•-) no ferrous ions and electrode stationary. 159

6.20 Cyclic voltammograms of a pyrite RSCBE in 1 M $HClO_4$ + 0.1 M Na_2S. (—) electrode stationary; (---) electrode rotated; (-•-•-) no sulphide ions and electrode stationary. 160

6.21 Cyclic voltammogram of a RSCBE in 1 M $HClO_4$ (pH 0) with the pyrite working electrode (W.E.) swept anodically from 0.0 to 1.4 V, then cathodically to -0.35 V, with the platinum collector electrode held at various potentials (E_c). 162

6.22 Cyclic voltammograms of a RSCBE platinum electrode in 1 M $HClO_4$ + 0.1 M $FeSO_4$ + 0.1 M $CuSO_4$. (—) electrode stationary; (---) electrode rotated. 163

Page No.

6.23 The effect of extending the anodic potential scanning limit (E_{λ_a}) on cyclic voltammograms of pyrite at pH 4.6 (0.5 M CH_3COOH + 0.5 M CH_3COONa) in stirred solution and a sweep rate of 100 mV s^{-1}. 165

6.24 The effect of extending the cathodic potential scanning limit (E_{λ_c}) on cyclic voltammograms of pyrite at pH 4.6 (0.5 M CH_3COOH + 0.5 M CH_3COONa) in quiescent solution and a sweep rate of 100 mV s^{-1}. 167

6.25 Effect of preconditioning at -0.1 V for various times on cyclic voltammograms of pyrite in stirred solution at pH 4.6 (0.5 M CH_3COOH + 0.5 M CH_3COONa), and a sweep rate of 100 mV s^{-1}. 169

6.26 Cyclic voltammograms of a pyrite RSCBE in 0.5 M CH_3COOH + 0.5 M CH_3COONa (pH 4.6). (—) stationary electrode; (---) rotated electrode. 174

6.27 Cyclic voltammograms of a pyrite RSCBE in 0.5 M CH_3COOH + 0.5 M CH_3COONa + 0.1 M $FeSO_4$. (—) electrode stationary; (---) electrode rotated. 175

6.28 Cyclic voltammograms of a RSCBE in 0.5 M CH_3COOH + 0.5 M CH_3COONa + 0.1 M Na_2S. (A) platinum electrode; (B) pyrite electrode; (——) electrode stationary; (---) electrode rotated; (-·-·-) stationary pyrite electrode with no sulphide ions. 176

6.29 Cyclic voltammograms of a RSCBE in 0.5 M CH_3COOH + 0.5 M CH_3COONa + 0.1 M $Na_2S_2O_3$ (A) platinum electrode; (B) pyrite electrode; (—) electrode stationary; (---) electrode rotated; (-·-·-) stationary pyrite electrode with no thiosulphate ions. 177

Page No.

6.30 The effect of extending the anodic potential scanning limit (E_{λ_a}) on cyclic voltammograms of pyrite at pH 7 (0.025 M KH_2PO_4 + 0.025 M Na_2HPO_4) in quiescent solution and a sweep rate of 100 mV s^{-1}. 179

6.31 Cyclic voltammograms of a pyrite RSCBE in 0.025 M KH_2PO_4 + 0.025 M Na_2HPO_4 (pH 7). (——) stationary electrode (---) electrode rotated. 181

6.32 The effect of extending the anodic potential scanning limit (E_{λ_a}) on cyclic voltammograms of pyrite at pH 9.2 (0.05 M $Na_2B_4O_7$) in stirred solution and a sweep rate of 100 mV s^{-1}. 191

6.33 Cyclic voltammograms of a pyrite RSCBE in alkaline solutions. (A) pH 9.2 (0.05 M $Na_2B_4O_7$); (B) pH 13 (0.1 M NaOH); (——) electrode stationary; (---) electrode rotated. 191

6.34 The effect of extending the anodic potential scanning limit (E_{λ_a}) on cyclic voltammograms of pyrite at pH 13 (0.1 M NaOH) in stirred solution and a sweep rate of 100 mV s^{-1}. 192

6.35 Cyclic voltammogram of a stationary pyrite electrode in stirred solution at pH 11 (0.025 M $NaHCO_3$ + 0.023 M NaOH), a scan rate of 50 mV s^{-1}, the anodic potential limit extended to 0.8 V. 192

6.36 Cyclic voltammogram of a RSCBE in 0.05 M $Na_2B_4O_7$ (pH 9.2) with the pyrite working electrode (W.E.) swept anodically from -0.2 to 1.0 V, then cathodically to -0.6 V, with the platinum collector held at various potentials (E_c). 194

6.37 Current-time transients for a stationary pyrite electrode pulsed anodically from an "active" rest potential (-0.055 V) in stirred 0.5 M CH_3COOH + 0.5 M CH_3COONa (pH 4.6) buffer solution. E_r, rest potential; E_{pa}, anodic pulse potential. 196

Page No.

6.38 Current-time transients for a stationary pyrite electrode pulsed anodically from an "active" rest potential (-0.135 V) in stirred 0.05 M $Na_2B_4O_7$ (pH 9.2) buffer solution. E_r, rest potential; E_{pa}, anodic pulse potential. 196

6.39 "Critical potential" for pyrite electrodes pulsed from "active" rest potentials as a function of pH. 197

6.40 Plot of i vs $t^{-1/2}$ for the falling part of the transient from t = 0 to 0.7 s for a pyrite electrode at pH 4.6 (0.5 M CH_3COOH + 0.5 M CH_3COONa), pulsed from an "active" rest potential of -0.055 V to: (1) 0.0 V; (2) 0.1 V; and (3) 0.2 V. 199

6.41 $i - i_o$ vs t plot showing the linearity in the rising part of the current-time transient from t = 0.7 to 1.0 s for a pyrite electrode at pH 4.6 (0.5 M CH_3COOH + 0.5 M CH_3COONa). i is the current; i_o is the current attributed to the falling transient (obtained by extrapolation from Figure 6.38). Electrode pulsed from an "active" rest potential of -0.055 V to: (1) 0.0 V; (2) 0.1 V; and (3) 0.2 V. 200

6.42 i vs $t^{-1/2}$ plot for the falling transient after the current maxima at ~ 1 s for a pyrite electrode at pH 4.6 (0.5 M CH_3COOH + 0.5 M CH_3COONa), pulsed from an "active" rest potential of -0.055 V to: (1) 0.0 V; (2) 0.1 V; and (3) 0.2 V. 201

6.43 Current-time transient for a pyrite electrode at pH 4.6 (0.5 M CH_3COOH + 0.5 M CH_3COONa) pulsed from an "active" rest potential of -0.055 V to 0.7 V. (---) i vs t^{-1}; R = correlation coefficient. 203

6.44 Current-time transient for a pyrite electrode at pH 13 (0.1 M NaOH) pulsed from an "active" rest potential of -0.4 V to 0.6 V. (---) i vs. $t^{-0.5}$; R = correlation efficient. 204

Page No.

6.45 Current-time transient for a pyrite electrode at pH 9.2 (0.05 M $Na_2B_4O_7$) pulsed from an "active" rest potential of -0.2 V to 1.2 V. (---) i vs. $t^{-0.5}$; R = correlation efficient. 204

6.46 Current-time transient for a pyrite electrode at pH 0 (1 M $HClO_4$) pulsed from an "active" rest potential of 0.3 V to 1.0 V. (---) i vs. t^{-1}; (-·-·-) i vs. t; R_1 = correlation coefficient for the decaying i vs. t^{-1} relationship; R_2 = correlation coefficient for the rising i vs. t relationship. 205

6.47 Current-time transients for pyrite electrodes at pH 0 (1 M $HClO_4$) pulsed from an "active" rest potential of 0.3 V to various anodic potentials. 207

6.48 Current-time transient for a pyrite electrode at pH 4.6 (0.5 M CH_3COOH + 0.5 M CH_3COONa) pulsed from an "active" rest potential of 0.0 V to 0.8 V. (---) i vs. t^{-1}; (-·-·-) i vs. t; R_1 = correlation coefficient for the decaying i vs. t^{-1} relationship; R_2 = correlation coefficient for the rising i vs. t relationship. 207

6.49 Current-time transients for pyrite electrodes at pH 4.6 (0.5 M CH_3COOH + 0.5 M CH_3COONa) pulsed from an "active" rest potential of 0.0 V to various anodic potentials. 208

6.50 Anodic charge passed after 1500 s for a pyrite electrode as a function of potential and pH. 208

6.51 Impedance spectra (0.1 Hz - 10 kHz) for a pyrite electrode in 1 M $HClO_4$ (pH 0). A) (◬) 0.5 V, (⊙) 0.9 V; (⊡) covers the whole spectrum for 1.1 V. B) (⊙) 1.1 V, (◬) 1.2 V. 209

6.52 Impedance spectra for a pyrite electrode in 1 M $HClO_4$ (pH 0) showing the high frequency branch. A) 1.1 V; B) 0.5 V. 209

Page No.

6.53 The electrode capacitance of a pyrite electrode in 1 M $HClO_4$ (pH 0) for the high frequency (C_1) and low frequency (C_2) semicircles as a function of potential. 211

6.54 Equivalent circuit (A), and complex plane impedance plot (B) for pyrite oxidation in 1 M $HClO_4$ (pH 0). R_u, solution resistance; R_s, electrode resistance; R_{ct_1}, R_{ct_2}, charge transfer resistances; R_a, adsorption resistance; C_{sc}, space charge capacitance; C_{dl}, double layer capacitance; C_a, pseudocapacitance. 212

6.55 Impedance spectrum (0.1 Hz - 10 kHz) for a pyrite electrode in 0.05 M $Na_2B_4O_7$ (pH 9.2) at 0.8 V, showing two semicircles generated by two RC networks in series (see Figure 6.56). 214

6.56 Real axis, high frequency intercept resistance (R), for pyrite at pH 0, 4.6 and 9.2, plotted as a function of potential. R_u, solution resistance; R_s, electrode resistance; R_f, electrode surface film resistance. 215

6.57 Impedance spectra (0.1 Hz - 10 kHz) for a pyrite electrode in 0.05 M $Na_2B_4O_7$ (pH 9.2). A) -0.2 to 0.6 V; B) 0.6 to 0.8 V. 216

6.58 Equivalent circuit (A) and complex impedance plot (B) for pyrite oxidation in 0.05 M $Na_2B_4O_7$ (pH 9.2). R_u, solution resistance; R_s, electrode resistance; R_{ct_1}, charge transfer resistance at pyrite oxide interface; R_f, film resistance; R_{ct_2}, charge transfer resistance at oxide/solution interface; C_g, geometric capacitance of pyrite/oxide interface; C_{d_1} differential capacitance of pyrite/oxide interface; C_{d_2}, differential capacitance of oxide solution interface. 217

6.59 Schematic representation of the solid/solution interface for a binary sulphide mineral MS (eg ZnS or PbS), showing the orientation of water molecules in the first solution layer adjacent to the mineral (IHP = Inner Helmhottz Plane). 218

Page No.

6.60 Bonding in ZnS. a) schematic molecular orbital diagram for pure ZnS; b) corresponding ZnS band model [34]. 219

6.61 Molecular orbital energy level diagram for pyrite [42]. The effect of Π bonding (if it occurs[34]) on the energy separation between non-bonding t_{2g} and antibonding e_g^* orbitals is also shown. 219

6.62 Schematic band energy model for pyrite. E_F, Fermi level; hatched bands (valence bands) are filled with electrons (modified after Bither et al[42]). 220

6.63 Position of energy bands and redox energy levels at the pyrite/electrolyte interface at pH 0. a) Equilibrium condition, no electron photoexcitation; E_F, Fermi level; hatched valence band is filled with electrons.
b) Photogeneration of electron-hole pairs results in passive film formation; E_{ss}, interbandgap surface states. 222

6.64 Fe 2p xps spectrum for pyrite oxidised in aerated triply distilled water for 1 hour. a) (——) experimental spectrum; (---) fitted curve (least squares). b) (——) fitted curve; (---) components of fitted curve. 226

6.65 Energy level diagram for pyrite oxidation. Band bending is assumed to be approximately constant (independent of the applied potential). E_F, Fermi level; E_{appl}, externally applied anodic potential. a) Small anodic bias; photocurrent ≈ dark current. b) Large anodic bias; photocurrent < dark current. 228

6.66 Flotation recovery of pyrite as a function of pH for various additions of potassium ethyl xanthate (from Fuerstenau et al [318]). (Δ) 1×10^{-5} mol dm^{-3}; (●) 2×10^{-5} mol dm^{-3}; (⊙) 2×10^{-4} mol dm^{-3}. 230

Page No.

6.67 Eh-pH diagram for the pyrite/xanthate/oxygen system showing the redox couples relevant to the flotation behaviour of pyrite at 298 K and 10^{-5} M solution species. X^-, ethyl xanthate anion; X_2, dixanthogen; Line (B), pyrite flotation recovery with 10^{-5} M potassium ethyl xanthate solution (after Fuerstenau et al[318]). Line (C), potential onset of oxygen reduction on pyrite (after Biegler et al[186]). 232

7.1 Potential-pH diagram for the Fe-S-H_2O system at 298 K for dissolved sulphur and iron activities of 10^{-4}. FeS_2 excluded. 237

7.2 The change of rest potential with time (after in situ polishing) of a pyrrhotite electrode at pH 0 (top) and pH 9.2 (bottom). (A) commence polishing; (B) finish polishing. 239

7.3 Cyclic voltammograms of a stationary pyrrhotite electrode in stirred solution at pH 0 (1 M $HClO_4$), recorded immediately after different surface pretreatments, starting from the rest potential, first cycled cathodically then anodically at 100 mVs^{-1}. (A) untreated sample; (B) fresh pyrrhotite surface produced by in situ abrasion. 241

7.4 The effect of extending the anodic potential scanning limit (E_{λ_a}) on cyclic voltammograms of pyrrhotite at pH 1 (0.1 M $HClO_4$) in stirred solution and a sweep rate of 100 mVs^{-1}. 242

7.5 The effect of electrode rotation on cyclic voltammograms of a pyrrhotite RSCBE at pH 1 (0.1 M $HClO_4$). (——) stationary electrode; (---) rotated electrode. 244

7.6 Cyclic voltammogram of a RSCBE in 1 M $HClO_4$ (pH 0), with the pyrrhotite working electrode (WE) swept anodically from 0.25 to 1.3 V, then cathodically to -0.65 V, and the platinum collector electrode held at various potentials (E_c). 248

Page No.

7.7 The effect of extending the anodic potential scanning limit (E_{λ_a}) on cyclic voltammograms of pyrrhotite at pH 4.6 (0.5 M CH_3COOH + 0.5 M CH_3COONa) in stirred solution and a sweep rate of 100 mV s^{-1}. 250

7.8 The effect of electrode rotation on cyclic voltammograms of a pyrrhotite RSCBE at pH 4.6 (0.5 M CH_3COOH + 0.5 M CH_3COONa) (——) stationary electrode; (---) rotated electrode. 252

7.9 The decay of open-circuit potential with time at pH 4.6 (0.5 M CH_3COOH + 0.5 M CH_3COONa) observed after potentiostatting a pyrrhotite electrode to 0.8 V (left) and 1.0 V (right) for 30 s then interrupting the current. 254

7.10 Cyclic voltammograms of a stationary pyrrhotite electrode in stirred solution at pH 4.6 (0.5 M CH_3COOH + 0.5 M CH_3COONa), sweeping the potential cathodically from the open-circuit potential (E_{oc}); attained after pulsing the potential anodically to 1.2 V for 10 seconds and then leaving the electrode at open-circuit for (---) 0 s, (——) 120 s, and (-·-·-) 300 s. 256

7.11 Cyclic voltammogram of a RSCBE in 0.5 M CH_3COOH + 0.5 M CH_3COONa (pH 4.6), with the pyrrhotite working electrode (WE) swept anodically from 0.0 to 1.3 V, then cathodically to -0.6 V, and the platinum collector electrode held at various potentials (E_c). 258

7.12 The effect of extending the anodic potential scanning limit (E_{λ_a}) on cyclic voltammograms of pyrrhotite at pH 7 (0.025 M KH_2PO_4 + 0.025 M Na_2HPO_4) in stirred solution and a sweep rate of 100 mV s^{-1}. 259

7.13 The effect of repetitive cycling between 1.0 and -0.7 V at 100 mV s^{-1} on the voltammetric behaviour of a stationary pyrrhotite electrode in stirred solution at pH 9.2 (0.05 M $Na_2B_4O_7$). 260

Page No.

7.14 The effect of extending the anodic potential scanning limit (E_{λ_a}) on cyclic voltammograms of pyrrhotite at pH 13 (0.1 M NaOH) in stirred solution and a sweep rate of 100 mV s^{-1}. 261

7.15 Current-time transients for a stationary pyrrhotite electrode held at various anodic potentials in stirred solution at pH 0 (1 M $HClO_4$). 262

7.16 Current-time transient for a stationary pyrrhotite electrode held at 0.9 V in stirred solution at pH 0 (1 M $HClO_4$). (---) i vs t^{-1}; (-•-•-) i vs $t^{1.5}$;
R_1 = correlation coefficient for the i vs t^{-1} relationship;
R_2 = correlation coefficient for the i vs $t^{1.5}$ relationship. 263

7.17 Current-time transients for a stationary pyrrhotite electrode held at various anodic potentials in stirred solution at pH 4.6 (0.5 M CH_3COOH + 0.5 M CH_3COONa). 265

7.18 Current-time transient for a stationary pyrrhotite electrode held at 1.1 V in stirred solution at pH 4.6 (0.5 M CH_3COOH + 0.5 M CH_3COONa). (---) i vs $t^{-0.5}$;
R = correlation coefficient. 266

7.19 Current-time transient for a stationary pyrrhotite electrode held at 0.150 V in stirred solution at pH 13 (0.1 M NaOH). (---) i vs t^{-1}; (-•-•-) i vs t;
R_1 = correlation coefficient for the i vs t^{-1} relationship;
R_2 = correlation coefficient for the i vs t relationship. 267

7.20 Current-time transient for a stationary pyrrhotite electrode held at 0.6 V in stirred solution at pH 13 (0.1 M NaOH) (---) i vs $t^{-0.5}$; R = correlation coefficient. 267

7.21 Anodic charge passed after 1500 s for a pyrrhotite electrode as a function of potential and pH. 268

Page No.

7.22 Real axis, high frequency intercept resistance, R (equivalent to the surface film resistance, R_f), for pyrrhotite at pH 0, 4.6 and 9.2, plotted as a function of potential. 270

7.23 Impedance spectra (0.1 Hz - 10 kHz) for a stationary pyrrhotite electrode in stirred solution at pH 0 (1 M $HClO_4$). A) 0.9 to 1.1 V; B) 1.1 and 1.2 V. 271

7.24 Impedance spectra (0.1 Hz - 10 kHz) for a stationary pyrrhotite electrode in stirred solution at pH 4.6 (0.5 M CH_3COOH + 0.5 M CH_3COONa). A) 0.6 to 1.4 V; B) 1.4 and 1.6 V. 272

7.25 Impedance spectra (0.1 Hz - 10 kHz) for a stationary pyrrhotite electrode in stirred solution at pH 9.2 (0.05 M $Na_2B_4O_7$). 273

8.1 Potential-pH diagram for the Fe-Ni-S-H_2O system at 298 K for dissolved sulphur, nickel and iron activities of 10^{-4}. 276

8.2 Change in the rest potential of a pentlandite electrode with time (after in situ polishing) at pH 0 (top) and pH 9.2 (bottom). (A) commence polishing; (B) finish polishing. 278

8.3 Cyclic voltammograms of a stationary pentlandite electrode in stirred solution at pH 0 (1 M $HClO_4$), recorded immediately after different surface pretreatments, starting from the rest potential, first cycled cathodically then anodically at 100 mV s^{-1}. (A) no pretreatment; (B) cathodic pretreatment at 0.15 V for 15 s; (C) cathodic pretreatment at 0.15 V for 2 min; (D) fresh pentlandite surface produced by in situ abrasion. 280

8.4 The effect of extending the anodic potential scanning limit (E_{λ_a}) on cyclic voltammograms of pentlandite at pH 1 (0.1 M $HClO_4$) in stirred solutions and a sweep rate of 100 mV s^{-1}. 281

Page No.

8.5 The effect of extending the anodic potential scanning limit (E_{λ_a}) on cyclic voltammograms of pentlandite at pH 4.6 (0.5 M CH_3COOH + 0.5 M CH_3COONa) in stirred solution and a sweep rate of 20 mV s^{-1}. 282

8.6 The effect of electrode rotation on cyclic voltammograms of a pentlandite RSCBE at pH 1 (0.1 M $HClO_4$). (——) stationary electrode; (---) rotated electrode. 284

8.7 The effect of electrode rotation on cyclic voltammograms of a pentlandite RSCBE at pH 4.6 (0.5 M CH_3COOH + 0.5 M CH_3COONa) (——) stationary electrode; (---) rotated electrode. 285

8.8 Cyclic voltammograms of pentlandite at pH 4.6 (0.5 M CH_3COOH + 0.5 M CH_3COONa) in stirred solution. (1) E_{λ_a}, 1.3 V; (2) E_{λ_a}, 1.6 V; (3) E_{λ_a} 2.0 V. 286

8.9 Cyclic voltammograms of a RSCBE in 1 M $HClO_4$ (pH 0) with the pentlandite working electrode (WE) swept anodically from 0.25 to 1.3 V, then cathodically to -0.25 V, and the platinum collector electrode held at various potentials (E_c). 287

8.10 The effect of repetitive potential cycling between 1.1 and -0.8 V at 100 mV s^{-1} on the voltammetric behaviour of a stationary pentlandite electrode in stirred solution at pH 7 (0.025 M KH_2PO_4 + 0.025 M Na_2HPO_4). 289

8.11 The effect of repetitive potential cycling between 1.0 and -0.8 V at 100 mV s^{-1} on the voltammetric behaviour of a stationary pentlandite electrode in stirred solution at pH 9.2 (0.05 M $Na_2B_4O_7$). 290

8.12 The effect of repetitive potential cycling between 0.6 and -0.9 V at 100 mV s^{-1} on the voltammetric behaviour of a stationary pentlandite electrode in stirred solution at pH 13.0 (0.1 M NaOH). 290

Page No.

8.13 The effect of electrode rotation on cyclic voltammograms of a pentlandite RSCBE at pH 4.6 (0.5 M CH_3COOH + 0.5 M CH_3COONa). (——) stationary electrode; (---) rotated electrode. 291

8.14 S 2p and Ni 2p 3/2 XPS spectra of pentlandite electrodes polarised for 10 minutes at 1.0 V in pH 4.6, 7.0 and 9.2 buffer solutions. 294

8.15 Current-time transients for a stationary pentlandite electrode held at various anodic poentials in stirred solution at pH 0 (1 M $HClO_4$). 295

8.16 Current-time transient for a stationary pentlandite electrode held at 1.0 V in stirred solution at pH 0 (1 M $HClO_4$). (A) i vs t; (B) i vs $t^{-0.5}$; R = correlation coefficient. 296

8.17 Current-time transients for a stationary pentlandite electrode held at various anodic potentials in stirred solution at pH 4.6 (0.5 M CH_3COOH + 0.5 M CH_3COONa). 298

8.18 Current-time transient for a stationary pentlandite electrode held at 0.6 V in stirred solution at pH 9.2 (0.05 M $Na_2B_4O_7$). (A) i vs t; (B) i vs t^{-1}; R = correlation coefficient. 299

8.19 Anodic charge passed after 1500 s for a pentlandite electrode as a function of potential and pH. 300

8.20 Impedance spectra (0.1 Hz - 10 kHz) for a stationary pentlandite electrode in stirred solution at pH 0 (1 M $HClO_4$). (A) 0.3 to 1.0 V; (B) 1.2 and 1.4 V. 301

8.21 Impedance spectra (0.1 Hz - 10 kHz) for a stationary pentlandite electrode in stirred solution at pH 4.6 (0.5 M CH_3COOH + 0.5 M CH_3COONa). (A) 0.3 and 0.6 V; (B) 0.8 and 1.0 V; (C) 1.0 and 1.2 V. 302

Page No.

8.22 Impedance spectra (0.1 Hz - 10 kHz) for a stationary pentlandite electrode in stirred solution at pH 9.2 (0.05 M $Na_2B_4O_7$). (A) 0.2 to 0.8 V; (B) 0.8 and 0.9 V. 303

8.23 Real axis, high frequency intercept resistance, R (equivalent to the surface film resistance, R_f), for pentlandite at pH 0, 4.6 and 9.2, plotted as a function of potential. 304

9.1 Potential-pH diagram for the Cu-Fe-S-H_2O system at 298 K for dissolved copper, iron and sulphur activities of 10^{-8}, 10^{-4} and 10^{-4}, respectively[370]. 307

9.2 Potential-pH diagrams for the Cu-S-H_2O system[376] at 298 K for dissolved sulphur and copper activities of:-

(A) 10^{-6} and 10^{-4}, respectively.
(B) 10^{-5} and 5×10^{-3}, respectively (meta-stable diagram excluding sulphur species with oxidation states > 0). 309

9.3 Change in the open-circuit potential of a chalcopyrite electrode with time after in situ polishing at pH 0 (top) and pH 9.2 (bottom). (A) commence polishing; (B) finish polishing. 311

9.4 Cyclic voltammogram of a stationary chalcopyrite in stirred solution at pH 1 (0.1 M H_2SO_4) and a sweep rate of 20 mV s^{-1}. 312

9.5 The effect of extending the anodic potential scanning limit (E_{λ_a}) on cyclic voltammograms of chalcopyrite at pH 4.6 (0.5 M CH_3COOH + 0.5 M CH_3COONa) in stirred solution and a sweep rate of 100 mV s^{-1}. 313

9.6 Cyclic voltammograms of a chalcopyrite RSCBE at pH 1 (0.1 M $HClO_4$) and a sweep rate of 100 mV s^{-1}. (A) effect of electrode rotation; (——) stationary electrode; (---) rotated electrode. (B) effect of extending the cathodic potential scanning limit (E_{λ_c}) on the anodic prewave peak height (rotated electrode). 314

		Page No.
9.7	Cyclic voltammograms of a chalcopyrite RSCBE in: (A) 1 M $HClO_4$ + 0.1 M $CuSO_4$ + 0.1 M $FeSO_4$ (B) 1 M HCl + 0.1 M $CuSO_4$ (——) stationary electrode; (---) rotated electrode.	315
9.8	Cyclic voltammograms of a RSCBE Pt collector electrode in 1 M HCl + 0.1 M $CuSO_4$ + 0.1 M $FeSO_4$ (——) stationary electrode; (---) rotated electrode.	316
9.9	Open-circuit potential versus time profiles for a chalcopyrite electrode at pH 4.6 (0.5 M CH_3COOH + 0.5 M CH_3COONa) recorded after pulsing to various anodic potentials for 20 seconds.	319
9.10	Cyclic voltammogram of a RSCBE in 1 M $HClO_4$ (pH 0) with the chalcopyrite working electrode (W.E.) swept anodically from 0.0 to 1.0 V, then cathodically to -0.35 V, and the platinum collector electrode held at various potentials (E_c).	322
9.11	The effect of extending the anodic potential scanning limit (E_{λ_a}) on cyclic voltammograms of chalcopyrite at pH 7 (0.025 M KH_2PO_4 + 0.025 M Na_2HPO_4) in stirred solution and a sweep rate of 100 mV s^{-1}.	324
9.12	The effect of extending the anodic potential scanning limit (E_{λ_a}) on cyclic voltammograms of chalcopyrite at pH 9.2 (0.05 M $Na_2B_4O_7$) in stirred solution and a sweep rate of 100 mV s^{-1}.	325
9.13	The effect of extending the anodic potential scanning limit (E_{λ_a}) on cyclic voltammograms of chalcopyrite at pH 13 (0.1 M NaOH) in stirred solution and a sweep rate of 100 mV s^{-1}.	326
9.14	Current-time transient for a stationary chalcopyrite electrode held at 1.1 V in stirred solution at pH 0 (1 M $HClO_4$). (---) i vs. $t^{-0.5}$; (-•-•-) i vs $t^{1.5}$. R_1 = correlation coefficient for the i vs. $t^{-0.5}$ relationship; R_2 = correlation coefficient for the i vs. $t^{1.5}$ relationship.	331

Page No.

9.15 Current-time transient for a stationary chalcopyrite electrode held at 1.2 V in stirred solution at pH 9.2 (0.05 M $Na_2B_4O_7$). (---) i vs t^{-1}. (-•-•-) i vs. t. R_1 = correlation coefficient for the i vs. t^{-1} relationship; R_2 = correlation coefficient for the i vs. t relationship. 332

9.16 Anodic charge passed after 1500 s for a chalcopyrite electrode as a function of potential and pH. 333

9.17 Impedance spectra (0.1 Hz - 10 kHz) for a stationary chalcopyrite electrode in stirred solution at pH 0 (1 M $HClO_4$). (A) 0.3 to 0.6 V; (B) 1.0 and 1.05 V. 334

9.18 Impedance spectra (0.1 Hz - 10 kHz) for a stationary chalcopyrite electrode in stirred solution at pH 9.2 (0.05 M $Na_2B_4O_7$). 335

9.19 Chalcopyrite electrode capacitance at pH 0 (1 M $HClO_4$) and pH 9.2 (0.05 M $Na_2B_4O_7$) as a function of potential. 336

9.20 Real axis, high frequency intercept resistance, R (equivalent to the surface film resistance, R_f) as a function of potential and pH. 336

10.1 Rate of flotation of chalcopyrite (-150 +106 μm) conditioned at different potentials in 0.025 M $NaHCO_3$ + 0.023 M NaOH + 1 M NaCl buffer solution (pH 10.5). 340

10.2 Recovery of chalcopyrite after 30 minutes flotation as a function of polarisation potential in pH 10.5 buffer solution. 341

10.3 Recovery of chalcopyrite after 30 minutes flotation as a function of polarisation potential in pH 9.0 buffer solution (0.05 M $Na_2B_4O_7$ + 1 M NaCl). 342

Page No.

10.4 Charge passed at Pt feeder electrode in pH 10.5 buffer solution as a function of polarisation potential in the absence of a mineral suspension. 343

10.5 Charge passed at Pt feeder electrode in pH 10.5 buffer solution as a function of polarisation potential with chalcopyrite particles (-150 +106 μm) in suspension. 344

10.6 Charge density for the chalcopyrite mineral suspension and flotation recovery at pH 10.5 as a function of conditioning time at 0.8 V. 345

10.7 Dissolved Cu and Fe, plus charge passed at a Pt feeder electrode in pH 10.5 buffer solution at a polarisation potential of 0.8 V with chalcopyrite particles (-150 +106 μm) in suspension, as a function of conditioning time. 346

10.8 Recovery of pyrite after 30 minutes flotation as a function of polarisation potential and polarisation time in pH 9.0 buffer solution. 347

10.9 Charge passed at Pt feeder electrode after 30 minutes polarisation in pH 9.0 buffer solution as a function of polarisation potential in the absence and presence of pyrite and chalcopyrite mineral suspensions. 349

10.10 Pt feeder - mineral and mineral feeder - mineral contact experiments for pyrite (o, □) and chalcopyrite (Δ) in pH 9.0 buffer solution. (---) immediate potential after contact; (——) potential after contact for 2 minutes. 350

10.11 Pt feeder-mineral and mineral feeder-mineral contact experiments for pyrite (o,□) and chalcopyrite (Δ) in 1 M $HClO_4$ (pH 0). (---) immediate potential after contact; (——) potential after contact for 2 minutes. 351

Page No.

10.12 Recovery-size curves for pyrite polarised for 30 minutes in pH 9.0 buffer solution prior to flotation. Flotation carried out in the absence/presence of amyl alcohol. 353

10.13 Recovery-size curves for chalcopyrite polarised for 30 minutes in pH 9.0 buffer solution prior to flotation. Flotation carried out in the absence/presence of amyl alcohol. 354

10.14 Recovery-size curves for oxidised chalcopyrite (0.6 V, 30 min polarisation, 30 min flotation) corrected for entrainment. 355

10.15 Recovery-size curves for reduced pyrite (-0.6 V, 30 min polarisation, 30 min flotation) corrected for entrainment. 356

LIST OF PLATES

		Page No.
3.1	Reflected light microscope photograph of pentlandite (Pe) showing the finely disseminated norite (N) and grey exsolved quartz grains (Q).	69
3.2	Reflected light microscope photograph of pyrite (Py) showing an inclusion of covellite (Co).	69
3.3	(top left) and 3.4 (top right). Typical secondary X-ray emission spectra of chalcopyrite obtained from different points on the mineral surface.	71
3.5	(bottom left) and 3.6 (bottom right). Typical secondary X-ray spectra of pentlandite obtained from different points on the mineral surface.	71
4.1	Stationary mineral sulphide electrodes used in cyclic voltammetry, pulse voltammetry and a.c. impedance measurements.	86
4.2	Stationary mineral sulphide electrode used in pulse voltammetric experiments subsequently analysed by ESCA.	87
4.3	Rotating cylinder-collector electrode.	90
4.4	Rotating split cylinder bi-electrode.	92
4.5	Stationary mineral sulphide electrode and electrochemical cell used in cyclic voltammetry, pulse voltammetry and a.c. impedance measurements.	96
4.6	Nicolet (Explorer I) digital storage oscilloscope recording a cyclic voltammogran of platinum in 0.05 M $Na_2B_4O_7$.	97

Page No.

4.7 The modular potentiostat units used in a bi-potentiostat mode for rotating split cylinder bi-electrode studies. 101

4.8 Apparatus used in rotating split cylinder bi-electrode studies.

1 - rotating split cylinder bi-electrode
2 - Oxford Electrode motor.
3 - electrochemical cell. 102

4.9 Apparatus and electrochemical instrumentation used in rotating split cylinder bi-electrode studies. 103

4.10 Solartron 1174 frequency response analyser and Schlumberger electrochemical interface. 105

4.11 Apparatus and electrochemical instrumentation used in a.c. impedance measurements. 107

4.12 Conditioning of agitated mineral sulphide particles in the electro-Hallimond tube flotation cell. 113

4.13 The electro-Hallimond tube flotation cell and electrochemical instrumentation used to control the Pt feeder electrode potential during the conditioning stage. 114

4.14 The electro-Hallimond tube flotation cell showing the flotation of mineral sulphide particles with purified nitrogen after conditioning. 114

7.1 Optical photomicrograph of a pyrrhotite electrode after oxidation at 1.1 V (vs. S.H.E.) for 1500 s in 1 M $HClO_4$. 264

LIST OF TABLES

		Page No.
Table 2.1	Crystal Structure of Sulphides[6].	6
Table 2.2	Physical and Electrical Properties of the Four Sulphide Minerals.	19
Table 3.1	XRF Analyses for Each Sulphide Mineral.	65
Table 3.2	Chemical Analysis of Sulphide Minerals.	65
Table 3.3	Electrical Properties of Mineral Specimens.	80
Table 4.1	Instrumentation Used During Electrochemical Experiments.	95
Table 4.2	The Composition of Buffer Electrolytes.	97
Table 6.1	Quantity of Pyrite Oxidised via Reactions (e) and (f) at pH 1 (0.1 M $HClO_4$) on a 100 mV s^{-1} Potential Sweep from the Rest Potential (E_r) to Different Values of the Anodic Potential Scanning Limit (E_{λ_a}).	153
Table 6.2	Quantity of Products Formed when Pyrite is Oxidised at pH 1 (0.1 M $HClO_4$) on a 100 mV s^{-1} Potential Sweep as a Function of Anodic Potential Scanning Limit (E_{λ_a}).	154
Table 6.3	Effect of Temperature and Preconditioning Time at -0.1 V on the Charge (q_A) Measured Under the Anodic Peak at 0.4 V and the Combined Charges (q_c) Under the Cathodic Peaks at ~ 0.4 V and ~ 0.2 V.	171
Table 6.4	Quantity of Pyrite Oxidised via Reactions (s_1) and (t_1) at pH 7 (0.025 M Na_2HPO_4 + 0.025 M KH_2PO_4) on a 100 mV s^{-1} Potential Sweep from the Rest Potential (E_r) to Different Values of the Anodic Potential Scanning Limit (E_{λ_a}) in Quiescent Solution.	184
Table 6.5	Quantity of Pyrite Oxidised to Sulphur and a Sulphur-Oxygen Anion at pH 7 (0.025 M Na_2HPO_4 + 0.025 M KH_2PO_4) on a 100 mVs^{-1} Sweep from the Rest Potential (E_r) to Different Values of the Anodic Potential Scanning Limit (E_{λ_a}) in Quiescent Solution.	186
Table 7.1	Molar $H^+/Fe(OH)_3$ Ratio for Sulphur and Sulphate Formation on Pyrrhotite, Pyrite and Pentlandite.	253
Table 8.1	Volume Changes Associated with Sulphide Mineral Oxidation Reactions.	292
Table 10.1	The Point of Zero Charge of Some Metal Sulphide and Metal Hydroxide Compounds.	358

NOMENCLATURE

A = Electrode area (cm^2)

A = Avogadro number

a_j = Activity of species j

C_j = Concentration of species j (mol dm^{-3}, mol cm^{-3})

C_o = Bulk concentration of species j (mol dm^{-3}, mol cm^{-3})

C = Capacitance (F, $\mu F\ cm^{-2}$)

C_a = Pseudocapacitance (F, $\mu F\ cm^{-2}$)

C_{dj} = Differential capacitance of interface j (F, $\mu F\ cm^{-2}$)

C_{dl} = Double layer capacitance (F, $\mu F\ cm^{-2}$)

C_g = Geometrical capacitance (F, $\mu F\ cm^{-2}$)

D = Diffusion coefficient ($cm^2\ s^{-1}$)

E = Electrode potential, all quoted values

E_{eq} = Equilibrium potential (V) versus S.H.E.

E^o = Standard potential of an electrode

E_{oc} = Open-circuit potential (V)

E_{appl} = Externally applied dc component of potential (V, mV)

E_F = Fermi level (eV)

E_{fb} = Flat-band potential (V)

E_G = Band-gap of a semiconductor (eV)

E_{oc} = Open-circuit potential (V)

E_p = Peak potential in cyclic voltammetry (V)

E_{pa} = (a) Anodic peak potential in cyclic voltammetry (V)
(b) Anodic potential in pulse voltammetry (V, mV)

E_{pc} = Cathodic peak potential in cyclic voltammetry (V)

E_r = (a) Reversible potential (V)
(b) Rest potential (V)

E_h = Potential versus S.H.E. (V)

E_{ss} = Interbandgap surface states

$E_{\lambda a}$ = Anodic potential scanning limit in cyclic voltammetry (V)

$E_{\lambda c}$ = Cathodic potential scanning limit in cyclic voltammetry (V)

F = Faraday constant, charge on one mole of electrons (96, 485 C mol^{-1}).

f = F/RT (V^{-1})

G = Gibbs free energy (kJ mol^{-1})

ΔG° = Standard Gibbs free energy change (kJ mol^{-1})

H = Enthalpy (kJ mol^{-1})

ΔH° = Standard ethalpy change (kJ mol^{-1})

i = Current (A, mA)

i_a = Anodic component current (A, mA)

i_c = (a) Cathodic component current (A, mA)
(b) Collector current (mA, μA)

i_L = Limiting current (A, mA)

i_{WE} = Working electrode current (A, mA)

I_p = Peak current (A, mA)

I_{pa} = Anodic peak current (A, mA)

I_{pc} = Cathodic peak current (A, mA)

j = Current density (mA cm^{-2}, μA cm^{-2})

K = Equilibrium constant

k° = Standard heterogeneous rate constant (m s^{-1})

K_{mj}, m_j = Mass transfer coefficient of species j (cm s^{-1})

N = Collector efficiency at RCCE and RSCBE

Z, n = Electrons per molecule oxidised or reduced, Faradays per mole of substance electrolysed.

n_α = Number of electrons involved in rate determining step

Q = Charge passed in electrolysis (C)

Q_A, q_A = Anodic charge (mC cm^{-2})

Q_c, q_c = Cathodic charge (mC cm^{-2})

R = (a) Universal gas constant (8.314 J mol^{-1} K^{-1})
(b) Resistance (Ω)
(c) Correlation coefficient

R_Ω = Ohmic solution resistance (Ω cm^2)

R_a = Adsorption resistance (Ω cm^2)

R_{ct} = Charge transfer resistance (Ω cm^2)

R_f = Electrode surface film resistance (Ω cm^2)

R_i = Resistance of insulating film (Ω cm^2)

R_u = Uncompensated resistance (Ω cm^2)

R_s = Series resistance in an equivalent circuit (Ω)
= Electrode resistance (Ω cm^2)

R_e = Reynolds number ($dv\nu^{-1}$)

r = Characteristic radius of RCCE or RSCBE (cm)

ΔS = Entropy change in a chemical process (kJ mol^{-1})

$\Delta S°$ = Standard entropy change in a chemical process (kJ mol^{-1})

Sh = Sherwood number ($K_m r\ D^{-1}$)

S_c = Schmidt number ($\nu\ D^{-1}$)

t = Time (h,s)

T = Absolute temperature (K)

v = Linear velocity of rotating cylinder surface, ($r\omega$, cm s^{-1})

Z = Impedance (Ω)

ZI = Imaginary part of impedance (Ω cm^2)

ZR = Real part of impedance (Ω cm^2)

α = Transfer coefficient

ε_r = Relative permittivity ($C^2N^{-1}\ m^{-2}$)

ε_o = Permittivity of free space ($C^2N^{-1}\ m^{-2}$)

= Chemical potenital of species j (kJ mol^{-1})

ρ = Resistivity (Ω m, Ω cm)

δ = Diffusion layer thickness at an electrode fed by convective transfer (cm).

ν = (a) Linear potential scan rate (V s^{-1}, mV s^{-1})
(b) Kinematic viscosity ($cm^2\ s^{-1}$)

ω = (a) Rotation rate (rad s^{-1})
(b) Angular frequency (rad s^{-1})

ω_{max} = Angular frequency at maximum of charge transfer semicircle (rad s^{-1}).

AAS = Atomic absorption spectrophotometry

CV = Cyclic voltammetry

EDAX = Energy-dispersive X-ray Analysis

IHP = Inner Helmholtz plane

OHP = Outer Helmholtz plane

RDE = Rotating disc electrode

RRDE = Rotating ring disc electrode

RCCE = Rotating cylinder-collector electrode

RSCBE = Rotating split cylinder bi-electrode

SCE = Saturated calomel electrode

SHE = Standard hydrogen electrode

XPS = X-ray photoelectron spectroscopy

XRD = X-ray diffraction

XRF = X-ray fluorescence spectroscopy

zpc = Zero point of charge

CHAPTER ONE

INTRODUCTION

CHAPTER ONE : INTRODUCTION

In the production of base metals from their sulphide ores, froth flotation is used to separate the sulphide minerals from associated gangue and from each other, to produce a sulphide concentrate feed for a subsequent extractive metallurgical process.

Many approaches have been used to study sulphide mineral flotation phenomena. Bubble contact and the measurement of contact angles on polished sections of sulphide minerals in various surfactant solutions, have provided knowledge of the limits of flotation due to collector concentration and pH. Hallimond tube and batch flotation tests have indicated the regions of good dynamic flotation as opposed to the static bubble adhesion studies. These techniques demonstrate whether flotation is possible or not without giving any clear understanding of the surface phases or the adsorbed species formed at the mineral/solution interface.

Quantitative and kinetic measurements of the adsorption of surfactants on the flotation behaviour of metal sulphides has contributed to the knowledge of the mechanism of collector attachment. However, variations in experimental conditions due to a lack of preventative measures in controlling mineral sulphide oxidation both before, and/or during experiments, and a disregard for proper sample characterisation when natural minerals have been used, have only produced many conflicting results in the literature.

More recently, electrochemical investigations, mostly on galena (PbS), chalcopyrite ($CuFeS_2$) and pyrite (FeS_2), have provided detailed information on mineral sulphide/collector systems and have helped to identify the surface species responsible for rendering sulphide minerals hydrophobic. These investigations have shown that the flotation of sulphide minerals involves oxidation, usually by dissolved oxygen, of either/both the mineral and a surfactant, which is added to adsorb and render the sulphide(s) selectively hydrophobic/floatable. The surfactants used are commonly thio-type

collectors, such as ethyl xanthate (dithiocarbonate), which in most cases do not impart sufficient hydrophobicity for flotation to occur, and must be oxidatively coupled to give dixanthogen, which chemisorbs on the sulphide surface before a floatable material is obtained. Selective flotation between sulphides is achieved principally by pH control which determines the relative ease of oxidation of the mineral and surfactant. However, the electrochemical investigations have drawn attention to the importance of the electrochemical, or redox potential (E_h) at the mineral sulphide/solution interface in determining the rate of mineral/surfactant oxidation at a fixed pH value. It is now becoming increasingly common for the redox potential of the flotation pulp to be monitored in sulphide flotation circuits. In practice, the rate of oxidation of the sulphide(s)/surfactant could be controlled by adjusting the redox potential electrochemically, or chemically by the addition of oxidising (Fe^{3+}, O_2) reducing (SO_2, $S_2O_4^{2-}$) agents. Excessive mineral oxidation in the neutral/alkaline pH range produces strongly hydrophilic oxide/hydroxide surfaces, which inhibit mineral particles adhering to air bubbles and being buoyed to the surface. However, small amounts of oxidation render galena and chalcopyrite floatable even in the absence of surfactants. This behaviour has been attributed to the formation of hydrophobic adsorbed sulphur product layers.

Thus to obtain selective flotation in complex sulphide ores, it is necessary to adjust the redox potential and pH, either:-

(a) to control the type of product formed e.g. hydrophobic sulphur or hydrophilic metal oxide, chemisorbed xanthate or dixanthogen etc. on each mineral, or

(b) to control the kinetics of the reactions and thereby the amount of product formed on each mineral.

Unfortunately, most electrochemical investigations have been concerned with sulphide/xanthate systems and only a few attempts have been made to study the "natural" floatability of sulphides over a range of E_h/pH

values. Thus although dixanthogen, sulphur and in some cases chemisorbed xanthate are all hydrophobic species, it is difficult to say what importance each plays in rendering a sulphide hydrophobic under given E_h/pH conditions. For example, there are many reports in the literature of mineral sulphide flotation with xanthate being promoted by trace amounts of metal ions. It is not clear whether the effect of the metal ions is merely to make the mineral naturally floatable or whether it encourages the adsorption of xanthate.

Clearly there is a need to make a systematic study of the causes of "natural" floatability. The objectives of this investigation were to study the surface oxidation of pyrite, pyrrhotite (FeS), chalcopyrite and pentlandite ($(Fe,Ni)_9S_8$) over a wide range of E_h/pH conditions, with a technological aim of achieving selective oxidation between one or more of the sulphides in the absence of collectors, so possibly enabling selective flotation separations to be made without surfactant addition. Electrochemical techniques were chosen to study and characterise the sulphide mienral oxidation reaction kinetics and mechanisms.

CHAPTER TWO

LITERATURE SURVEY

CHAPTER 2 : LITERATURE SURVEY

2.1 Physical Properties

To achieve oxidation selectively between one or more of the sulphides, differences in the surface properties of the various solid phases must be exploited. The surface characteristics are primarily determined by the atomic or molecular structure of the solid and the types of bonding involved. Therefore, some of the physical properties of the four sulphides are summarised below.

2.1.1 Crystal Structure

Hitherto, there has been a lack of experimental techniques for studying the surface chemical and structural changes that occur at a sulphide/electrolyte interface, and few attempts have been made to link the complex crystal structures of sulphides with their electrochemical behaviour.

Many attempts have been made to classify known sulphide mineral structures into major structural types. The classification is usually based on the packing of sulphur atoms[1,2,5], or on the mode of linkage of atoms in space[3,4,6]. The classification by Bray and Claringbull[6] is shown below in Table 2.1.

Table 2.1 Crystal Structure of Sulphides[6]

	Structure Type	Compound
Isometric	Rock salt Ni-As Pyrite and marcasite Zincblende and wustite	PbS, MgS, CaS, SrS, MnS, EuS, PuS Pyrrhotite, CoS FeS_2, CoS_2, NiS_2, MnS_2, OsS_2, RuS_2 $CuFeS_2$, HgS
Layer structures	PbI_2 Molybdenite	TiS_2, ZnS_2, SnS_3, PtS_2 MoS_2, WS_2
Chain structures	Stibnite SiS_2	SbS_3, Bi_2S_3 SiS_2

Unfortunately, because the crystal chemistry of sulphides is extremely complex, an overall classification of mineral sulphide structures still awaits formulation.

2.1.1.1 Pyrite

The precise compositional range of pyrite is unknown, though it is certainly less than 1 at. %. Smith[39] reported the S/Fe ratio to lie in the range 1.94 - 2.01. However, Kullerud and Yoder[8] considered this was due to analysis errors, and the ratio was undistinguishable from 2.00.

Pyrite crystallises in the cubic system with iron atoms at the corners and face centres of the cube and the sulphur atoms arranged in pairs (as S_2 molecules) between them (Figure 2.1). Each S atom is coordinated to three Fe and one S atom (the other half of the S_2 molecule) in a distorted tetrahedral configuration. Each Fe is at the centre of an octahedron of S atoms. Although all six Fe-S distances

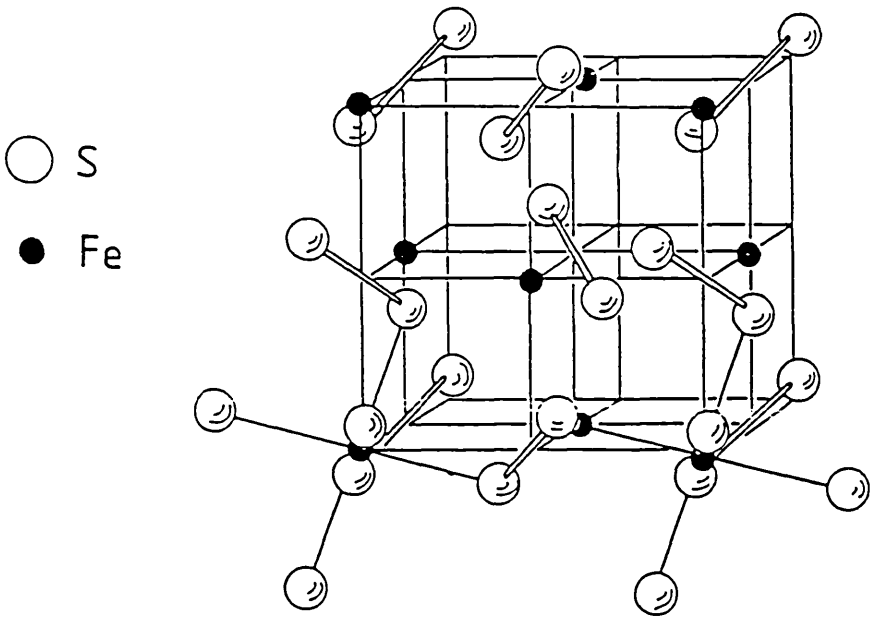


Fig 2.1 The crystal structure of pyrite (FeS_2)[7].

are equal, the octahedron is slightly compressed along one axis. The internuclear distance of the S_2 molecule is 0.218 nm, the Fe-S distance 0.226 nm, and the edge of the cubic lattice 0.542 nm[7]. Although the structure of pyrite cannot be classified as close packed, it is densely packed compared with the other sulphides. Marcasite is the orthorhombic polymorph of pyrite, though pyrite is the stable form up to 400 °C[8], and an X-ray study has shown that grinding provides the energy necessary to convert marcasite to pyrite[9]. Therefore, in mineral processing operations, FeS_2 is usually in the pyrite form.

2.1.1.2 Pyrrhotite

The composition of pyrrhotite is bounded by FeS and Fe_7S_8. Carpenter and Desborough[10] regarded pyrrhotite as having three distinct phases: troilite, hexagonal pyrrhotite, and monoclinic pyrrhotite. Monoclinic pyrrhotite has the formula Fe_7S_8, although there are reports that it tolerates variations in iron deficiency of ± 0.2 at. % from the stoichiometric composition of 46.67 at. % Fe[11,12]. Troilite is FeS, with no detectable departure from stoichiometry; it occurs primarily in meteorites. The phase relations of hexagonal pyrrhotite are complex and not known completely. The formula for hexagonal pyrrhotite can be written as $Fe_{1-x}S$ where x represents the fraction of vacant cation sites in the structure. At room temperature its compositional limits are narrow and range from 47.2 to 47.9 at. % Fe[14]. Morimoto et al[15] argued that hexagonal pyrrhotite was not one solid solution field, but three very narrow (0.03 at. %) fields centered at Fe_9S_{10}, $Fe_{10}S_{11}$ and $Fe_{11}S_{12}$, which correspond to 47.37, 47.62 and 47.83 at. % Fe. Arnold[13] studied the phases present in 82 natural terrestrial pyrrhotites and found that 60 samples (73 %) consisted of two-phase intergrowths of hexagonal with monoclinic pyrrhotite.

The crystal structure of pyrrhotite is of the nickel arsenide type consisting of sulphur atoms hexagonally close packed with iron atoms in octahedral interstices. The metal atoms of the Ni-As structure are in triangular layers between the sulphur layers (Figure 2.2).

However, in FeS the lattice is distorted by displacement of S atoms

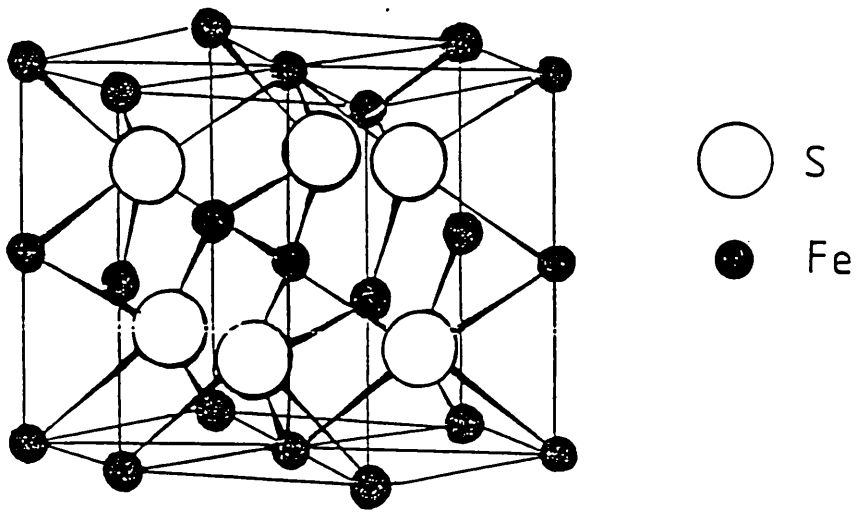


Fig 2.2 The pyrrhotite (nickel arsenide type) structure.

along the c-axis. Alternative metal triangles are contracted and expanded with sulphur atoms displaced away from contracted triangles and towards the dilated triangles along the c-axis[16]. In hexagonal pyrrhotite ($Fe_{1-x}S$), the vacancies on the Fe sites are ordered. Bertaut[17] found monoclinic pyrrhotite (Fe_7S_8) to have an ordered defect structure related to the Ni-As type. One vacancy exists in every four metal positions, confined to alternate metal planes. He postulated that charge balance is maintained by Fe^{3+} ions in the same layers as the vacancies. Tokonami et al[18] have confirmed Bertaut's model although with iron and sulphur atoms collapsed towards the vacancy. The vacancy ordering has also been observed by high-resolution electron microscopy[19].

The only iron-rich non-stoichiometric sulphide is MacKinawite (FeS_{1-x}, where $0.057 \leq x \leq 0.064$[20]). It has a tetragonal crystalline structure[21] and its non-stoichiometry results from sulphur deficiency rather than excess metal atoms in the structure.

2.1.1.3 Pentlandite

The first X-ray diffraction study of pentlandite was performed by Alsen[22]. He identified the structure as cubic but wrongly assumed the formula to be (Fe,Ni)S. Lindqvist et al[23] showed that pentlandite was isomorphic with synthetic Co_9S_8 and that the formula should be $(Fe,Ni)_9S_8$. The pentlandite crystal lattice can be described as a face centred cubic lattice of 32 sulphur atoms and 36 metal atoms; 32 metal atoms are in tetrahedral sites and 4 are octahedrally coordinated. The sulphur atoms are arranged so that 8 show four-fold and 24 five-fold coordination to the metal atoms. Ramjamani and Prewitt[24] refined the structures of two naturally occurring pentlandites and showed that the metal atoms in tetrahedral sites are surrounded by distorted tetrahedra, one of the sulphurs being closer than the other three ($S_{(1)}$, Figure 2.3B). They also showed that there are three metal-metal bonds extending from each tetrahedral cation forming isolated "cubic clusters" of tetrahedral cations (Figure 2.3). The metal-metal distance in the cluster is 0.2531 nm, a value similar to the distance between nickel atoms in metallic nickel. The tetrahedrally coordinated sulphur atoms are associated with tetrahedral metal atoms, while the five-fold coordinated sulphur atoms are associated with four tetrahedral metal atoms and one octahedral atom in a square pyramid.

2.1.1.4 Chalcopyrite

The crystal structure of chalcopyrite was first described by Burdick and Ellis in 1917[25]. The currently accepted structure for chalcopyrite was first reported by Pauling and Brockway[26] and then by Donnay et al[27]. Ignoring the difference between Cu and Fe atoms the structure is that of sphalerite (ZnS). However, to accommodate the difference, the tetragonal unit cell of chalcopyrite is twice the volume of the unit cell of sphalerite. In each half of the chalcopyrite unit cell the four zinc atoms of sphalerite are replaced by two Cu and two Fe atoms, so that Cu and Fe occupy alternate positions along the c-axis (Figure 2.4). Hall and Stewart[28] have

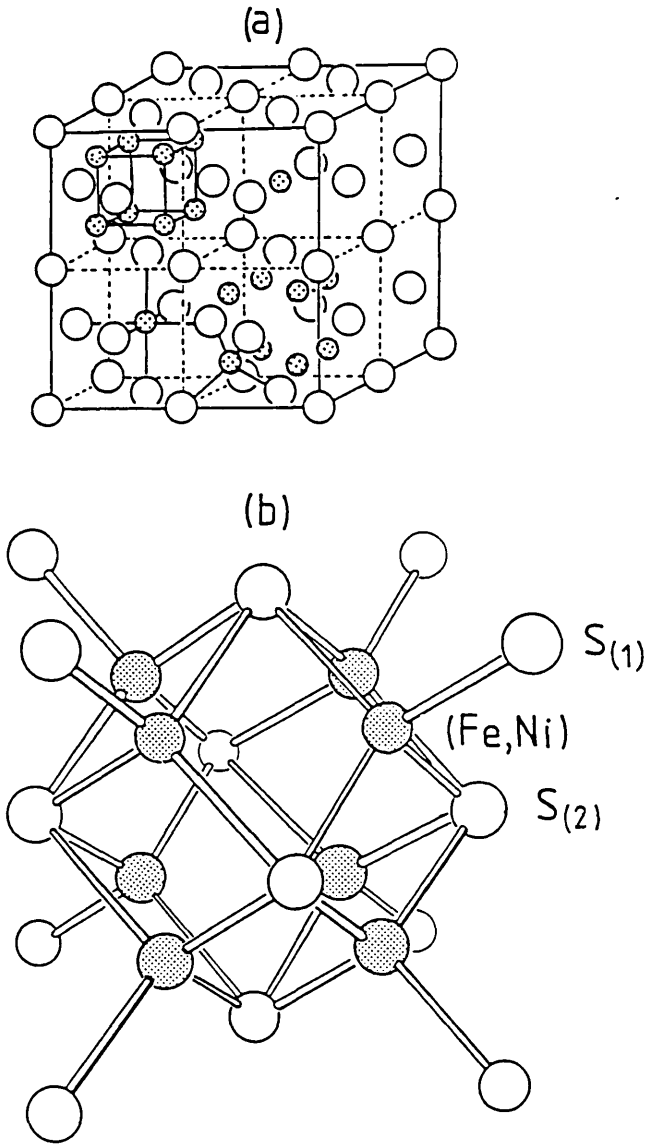


Fig 2.3 The crystal structure of pentlandite ($(Fe,Ni)_9S_8$).
(a) The cubic unit cell of the pentlandite structure.
(b) The cube cluster of tetrahedrally coordinated cations occurring in the pentlandite structure. Each cation is coordinated to one $S_{(1)}$ and three $S_{(2)}$ atoms.

shown that within each metal tetrahedron the sulphur atom is displaced away from Cu and towards Fe, resulting in an axial compression of the tetragonal unit cell. Other chalcopyrite-like minerals have been identified viz, mooihoekite ($Cu_9Fe_9S_{16}$), talnakite ($Cu_9Fe_8S_{16}$), and haycockite ($Cu_4Fe_5S_8$)[29,30]. All three minerals have structures

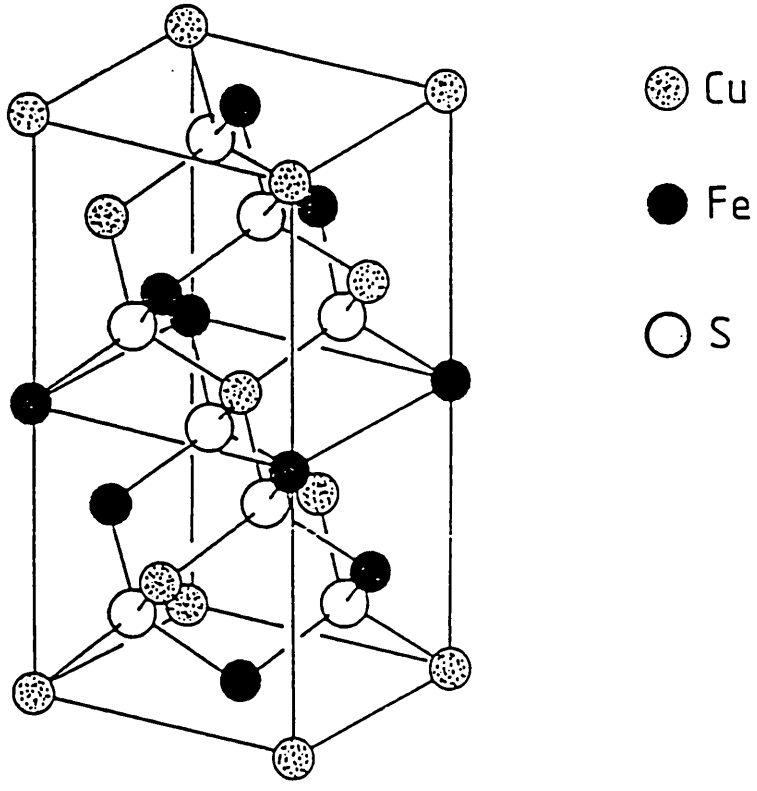


Fig 2.4 The crystal structure of chalcopyrite ($CuFeS_2$)[34].

based on chalcopyrite with the excess metal atoms filling unoccupied tetrahedral sites in the cubic close-packed sulphur lattice[31].

2.1.2 Electrical, Magnetic and Mössbauer Studies

The electric and magnetic properties of metal sulphides are so diverse that they constitute the basis of separation techniques for mineral processing. However, minute concentrations of impurities may effect electrical properties so that selective separations of natural mineral samples may be inefficient.

The resistivities of most sulphides lie between those of metals (10^{-7} to 10^{-8} Ω m at room temperature) and semiconductors (10^{-4} to 10^{7} Ω m at room temperature)[32] so they can be described as "pseudo-

semiconductors". Their semiconductor behaviour derives from free charge carriers (holes or electrons) arising from non-stoichiometry, trace element impurities, and thermal excitation across the energy gap[33]. The semiconduction is termed n-type or p-type according to whether electrons or holes are the dominant charge carriers.

The electrical and magnetic properties of sulphides have been extensively reviewed by Vaughan and Craig[34] and Shuey[35]. Some of the more salient properties are summarised below.

2.1.2.1 Pyrite

Magnetic susceptibility measurements on pyrite show it to have no magnetic moment[36,37]. The conclusion drawn from this is that iron in pyrite is present as Fe^{2+}. Its six d electrons are paired and completely fill the t_{2g} ground state orbitals. Sulphur is present as S_2^{2-} with its twelve electrons completely filling the bonding P_σ, P_π and antibonding P_{π^*} orbitals. The pairing of electrons both in Fe^{2+} and S_2^{2-} explains the absence of a magnetic moment. The Mössbauer spectrum of iron in pyrite also supports these conclusions[38]. The FeS internuclear distance of 0.226 nm, which is much less than the sum of the ionic radii (0.260 nm), suggests that there is some covalent bonding between iron and sulphur.

Electrical resistivity measurements show pyrite to occur in both n- and p-type semiconductor modes; p-type samples having a higher resistivity than n-type samples. Using data collected from 123 different pyrite samples, Pridmore and Shuey[33] reported a modal resistivity of 1×10^{-3} Ω m for n-type and 3×10^{-2} Ω m for p-type. There have also been reports of type differences within a single crystal[39,40]. For p-type material, the resistivity decreases with temperature, but for n-type it increases[39,41]. Resistivity is proportional to the product of carrier density and mobility[35]. Therefore where deviations from stoichiometry and/or purity are known, the carrier density can be calculated, the resistivity measured and then the mobility calculated. For a given mineral, semiconductor

type, and temperature, there is a definite upper limit to the mobility, due to lattice vibrations. At room temperature these limits are approximately 250 $cm^2\ V^{-1}\ s^{-1}$ for n-type pyrite (electron mobility)[42], and 2 $cm^2\ V^{-1}\ s^{-1}$ for p-type (hole mobility)[43]. Mobility may also be reduced by scattering due to point defects, dislocations, and grain boundaries. For pyrite, there is no statistical difference in carrier density between n- and p-type, hence differences in resistivity are due entirely to the differences in mobility of electrons and holes. The data of Horita[43] on Hall constant and resistivity in the region of intrinsic semiconduction implies that the intrinsic carrier concentration at room temperature is about $2 \times 10^{14}\ cm^{-3}$. The important donor impurities found in natural pyrite samples are Co, Ni, Cu, whereas As is the only acceptor impurity[33,44].

Bither et al[42] have studied the optical reflectivity spectrum of synthetic pyrite and inferred a band gap of 0.9 ± 0.1 eV. Marinace[41] reported a value of 1.2 eV, while Horita[43] found an average of 0.77 eV for a collection of natural crystals.

2.1.2.2 Pyrrhotite

The Mössbauer spectrum of monoclinic pyrrhotite (Fe_7S_8) has been studied by Levinson and Treves[45] and Vaughan and Ridout[38]. Neither found evidence to support the presence of Fe^{3+}, postulated in the bonding scheme of Bertaut[17], who proposed an ionic formula $Fe_5^{2+}Fe_2^{3+}S_8^{2-}$. Levinson and Treves[45] suggested a valence model of the type $Fe_7^{2.286+}S_8^{2-}$ from the reduced isomer shift values (relative to FeS), which were attributed to a greater covalency in the Fe-S bond.

Pyrrhotite is a good electronic conductor with resistivities in the range 10^{-4} to $10^{-6}\ \Omega\ m$[46,47]. Parasnis[46] found the resistivity of troilite not to differ significantly from other pyrrhotites. Hihara[48] found no evidence for electrical anisotropy in hexagonal and monoclinic pyrrhotite although synthetic single-crystals of

troilite had a high resistivity (10^{-3} Ω m) along the c-axis at room temperature. Theodossiou[47] made resistivity and Hall effect measurements on natural pyrrhotite samples and found them all to be p-type at room temperature with carrier concentrations over 10^{20} cm^{-3}. It is usually assumed that the charge carriers in pyrrhotite are holes (Fe^{3+}) associated with iron vacancies. Thus, the carrier concentration should be proportional to the iron deficiency relative to FeS. However, there is no evidence for this; troilite has been found to be as conducting as hexagonal and monoclinic pyrrhotite. Kaplan and Worrell[49], in a study of synthetic hexagonal pyrrhotite over the compositional range $Fe_{0.901}$ - $Fe_{0.923}S$ and temperature range 943 - 1173 K, found the conductivity to increase with increasing iron deficiency, but much less than proportionately. They reported conductivity increasing as the (1/30) power of sulphur pressure compared with the predicted value of (1/6) power. They also indicate all $Fe_{1-x}S$ phases should be regarded as metallic with the electronic states delocalised (except along the c-axis in FeS).

2.1.2.3 Pentlandite

The low resistivity of pentlandite (10^{-5} to 10^{-6} Ω m) means that it can be regarded as a metallic conductor[52].

Mössbauer studies by Vaughan and Ridout[38] show that the tetrahedral site iron atoms are low-spin with a formal oxidation state less than +2 because of the metal-metal bonding. The iron atoms in natural pentlandites show a slight preference for the octahedral sites[24], where they probably occur as high spin divalent iron[50].

Rosenqvist[51] suggested that pentlandite was stabilised by a specific electron/atom ratio like many alloys. Since Co_9S_8 and $Fe_{4.5}Ni_{4.5}S_8$ appeared to be the most stable compositions, Ramjamani and Prewitt[24] assumed the most stable configuration was 7 electrons. Pentlandite compositions where the nickel content increased above 4.5 atoms resulted in nickel being ordered into octahedral sites creating vacancies in tetrahedral sites, while if the iron content was

increased, the excess iron entered unoccupied tetrahedral sites. Thus, the structural formula for pentlandite can be written as:-

$$(Fe_uNi_v)^{6fold}\ (Fe_xNi_y\Delta_z)_8{}^{4fold}\ S_8$$

6 fold and 4 fold refer to the metal coordination, Δ indicates metal vacancies. The electron configuration of iron is $(3d)^6$, and for nickel it is $(3d)^8$. Thus, the number of metal vacancies (z) is given by:-

$$z = [(x.6 + y.8)-7]/7$$

$$\text{and metal/sulphur} = (9 - 8.z)/8 = (1.125 - z)$$

2.1.2.4 Chalcopyrite

Both Wyckoff[53] and Hall and Stewart[28] have suggested that chalcopyrite exists in a strong covalently bonded configuration with an effective ionic state between:-

$$Cu^+Fe^{3+}(S^{2-})_2 \text{ and } Cu^{2+}Fe^{2+}(S^{2-})_2$$

However, the lack of a magnetic moment on the copper atom, observed in neutron diffraction experiments[27], supports the Cu^+ state, and the small isomer shift and absence of quadrupole splitting in the Mössbauer spectrum[54] is consistent with high-spin Fe^{3+} in the tetrahedral sites. Hence, the spectroscopic data supports the scheme $Cu^+Fe^{3+}(S^{2-})_2$.

The resistivity of natural chalcopyrite samples falls within a narrow range centred near 10^{-3} Ω m[33,55]. All the published determinations on natural chalcopyrite show n-type conduction, although p-type natural samples can occur[56]. Teranishi[57] found the conductivity along the tetragonal axis to be 1.3 to 2.6 times greater than that in a perpendicular direction. For a natural single crystal he reported a carrier concentration of 8×10^{18} cm^{-3} and an electron mobility of 18

$cm^2\ V^{-1}\ s^{-1}$ at room temperature when limited only by lattice vibrations. Austin et al[56] reported a value of hole mobility of 32 $cm^2\ V^{-1}\ s^{-1}$. Optical absorption studies indicate a band gap of about 0.6 eV[56,57].

The characteristic n-type conduction is a consequence of a slight metal excess[59]. A typical carrier concentration of 10^{19} cm^{-3} corresponds to a metal excess of the order 0.1 per cent. There is no indication that impurities have an important effect on the resistivity and type of chalcopyrite. Assuming the ionic configuration $Cu^+Fe^{3+}(S^{2-})_2$, copper substituting for iron produces acceptors, which compensate some of the donors, decreasing the carrier concentration, so increasing the resistivity. Conversely, Fe substituting for Cu increases the numbers of donors and decreases resistivity. This effect was observed by Pridmore and Shuey[33] and Harvey[60], who noted that chalcopyrite samples from copper-rich environments are systematically higher in resistivity than those from iron-rich environments.

A summary of the physical and electrical properties of the four sulphide minerals is presented in Table 2.2.

2.2 Electrode Potentials and E_h-pH Diagrams

Iron and copper sulphides have very small solubility products ($CuFeS_2$, 10^{-62}[267]; CuS, 10^{-36}[267]; FeS_2, 10^{-29}[268]; FeS, 10^{-18}[268]), and in the solid state, large electronic conductivities. Therefore, as with metals, they can be used as electrodes in aqueous solution. However, metal sulphide electrodes differ from pure metal electrodes in two respects:-

(a) They possess several components (sulphur and at least one metal).

(b) Most sulphides are semiconductors, which gives them characteristic electronic properties (band structure etc.), which distinguishes them from metals[61,62].

A lack of appreciation of these two points has meant that observed electrode potentials rarely show satisfactory agreement with the values thermodynamically calculated. To explain these discrepancies Sato[62] proposed a thermodynamic model in which the half-cell potential of a semiconductive simple binary sulphide in aqueous solution is not only a function of ionic activities in the solution, but also a function of the activities of the component elements in the compound phase. Thus, if a semiconductor with a formula M_iS_j dissociates by the reaction:-

$$M_iX_j = iM^{j+}_{(aq)} + jX^{i-}_{(aq)}$$

the half-cell potential is described by the following equation:-

$$E_{M_iX_j} = E^\circ_{M_iX_j} + \frac{RT}{2ijF} \ln\left[\frac{(a_{M^{j+}})^i_{(aq)} \; (a_X)^j_{M_iX_j}}{(a_{X^{i-}})^j_{(aq)} \; (a_M)^i_{M_iX_j}}\right]$$

where $E^\circ_{M_iX_j} = 1/2 \left[E^\circ_{M,M^{j+}} + E^\circ_{X^{i-},X}\right]$

Hence, even though the composition of the aqueous solution is fixed, the electrode potential is not defined uniquely; it will vary within a range as the exact composition of the sulphide varies. Using aqueous solution of known ionic activities, the half-cell potential of a binary sulphide may be used as a means of studying the non-stoichiometric properties of the sulphide.

Peters[61] proposed a model similar to Sato's and argued that the electrode potential of a metal sulphide can be written in the

Table 2.2 Physical and Electrical Properties of the Four Sulphide Minerals

Mineral	Theoretical Composition	Relative Molar Mass (g)	At-% Composition				Density ($g\ cm^{-3}$)	Crystal System	Resistivity Ω m	Conductor Type	Carrier Concentration at room temp. (cm^{-3})	Mobility ($cm^2\ v^{-1}\ s^{-1}$)		Energy Gap (eV)
			Cu	Fe	Ni	S						Electrons	Holes	
Pyrite	FeS_2	119.96		33.33		66.67	4.8–5.1	Cubic	1–100 x 10^{-3} [33]	n- and p-semiconductor	2 x 10^{14} [43]	250 [42]	2 [43]	0.9 [42]
Pyrrhotite	Fe_7S_8	647.36		46.67		53.33	4.4–4.65	Monoclinic	1–100 x 10^{-6} [46,47]	p-metallic	1 x 10^{21} [47]	6 [35]		
Pentlandite	$Fe_{4.5}N_{4.5}S_8$	771.91		26.47	26.47	47.05	4.6–5.0	Cubic	1–10 x 10^{-6} [52]	n-metallic				
Chalcopyrite	$CuFeS_2$	183.50	25.0	25.0		50.0	4.1–4.3	Tetragonal	1–100 x 10^{-4}	n-semiconductor	8 x 10^{18} [57]	18 [57]	32 [56]	0.6 [56,57]

same way as that of a pure metal, but an extra Nernst term is needed to take into account the chemical potential of the metal in the form of a sulphide, viz.:-

$$M^{i+}_{(aq)} + ne = M^{\circ}_{(MS)}$$

$$E = E_1^{\circ} - \frac{2.3\ RT}{nF} \log a_{M^{\circ}} + \frac{2.3\ RT}{nF} \log a_{M^{i+}} \qquad (2.1)$$

where a_x is the activity of x with respect to the standard state (which for a metal is the pure metal).

It can also be written in terms of an appropriate electrochemical reaction for sulphur:-

$$S_{(MS)} + 2H^+ + 2e^- = H_2S_{(g)}$$

$$E = E^{\circ}_2 - \frac{2.3\ RT}{2F} \log f_{H_2S} + \frac{2.3\ RT}{2F} \log a_{S^{\circ}} - \frac{2.3\ RT}{F}\ pH \qquad (2.2)$$

where f_{H_2S} is the fugacity of H_2S gas and $a_{S^{\circ}}$ is the activity of elemental sulphur in the solid sulphide phase. Because of the thermodynamic link between $a_{S^{\circ}}$ and $a_{M^{\circ}}$ in the solid and between f_{H_2S} and $a_M{}^{i+}$ in the aqueous phase, the potential of equation (2.2) is the same as that of equation (2.1).

The stability or instability of a sulphide mineral in contact with the aqueous solutions of selected composition may be represented in the form of a potential-pH diagram or electrochemical phase diagram. Presenting thermodynamic data in this way was first devised by Pourbaix[63] for metal systems and extended to mineral systems by Garrels and Christ[64]. It allows regimes of stability to be defined beyond which the system is thermodynamically unstable. It also identifies any solid or gaseous product phases which should form during such decomposition. It does not indicate the rate of decomposition of an unstable mineral; this can vary from rates so fast that they are controlled by mass transfer limitations, to rates so slow

that geological time periods are required for the evidence to be directly observed. Also, it cannot predict whether meta-stable species may occur along a reaction pathway. For example, meta-stable species such as thiosulphate ($S_2O_3^{2-}$), trithionate ($S_3O_6^{2-}$) and tetrathionate ($S_4O_6^{2-}$) are known to persist over many hours during the ammonia pressure leaching of pentlandite[75].

Four different kinds of solution in which a sulphide mineral might decompose can be identified[65]:-

1. Oxidising solutions, leading to (a) elemental sulphur, or (b) sulphate ions in solution, depending on the oxidising potential and the selected pH.

2. Strong acid solutions, leading to H_2S evolution and dissolved copper and/or iron - "non-oxidative dissolution".

3. Reducing solutions, leading to H_2S evolution or hydrosulphide/sulphide ion formation and lower valence sulphide or metal phase.

4. Strong alkali solutions, leading to sulphide ions in solution and metal oxides (or lower sulphides).

The above four systems are generally applicable to all metal sulphides, although the strong acid and strong alkali limits are sometimes beyond the strengths available for real aqueous systems. The oxidising (1) and reducing (3) systems can be further subdivided into acid and alkali systems. Peters has presented E_h-pH diagrams for the systems Pb-S-H_2O[61,65], Fe-S-H_2O[61,65,66], Cu-Fe-S-H_2O[61,65,67], Ni-S-H_2O, Zn-S-H_2O, Mo-S-H_2O and S-H_2O[65]. E_h-pH diagrams for the Fe-Ni-S-H_2O system have also been reported[68,69,70,71].

An E_h-pH diagram shows that at least two reactions may occur for the simplest sulphide system. From the simplified E_h-pH diagram for PbS

(Figure 2.5) it is clear that at an acidic pH PbS can coexist with

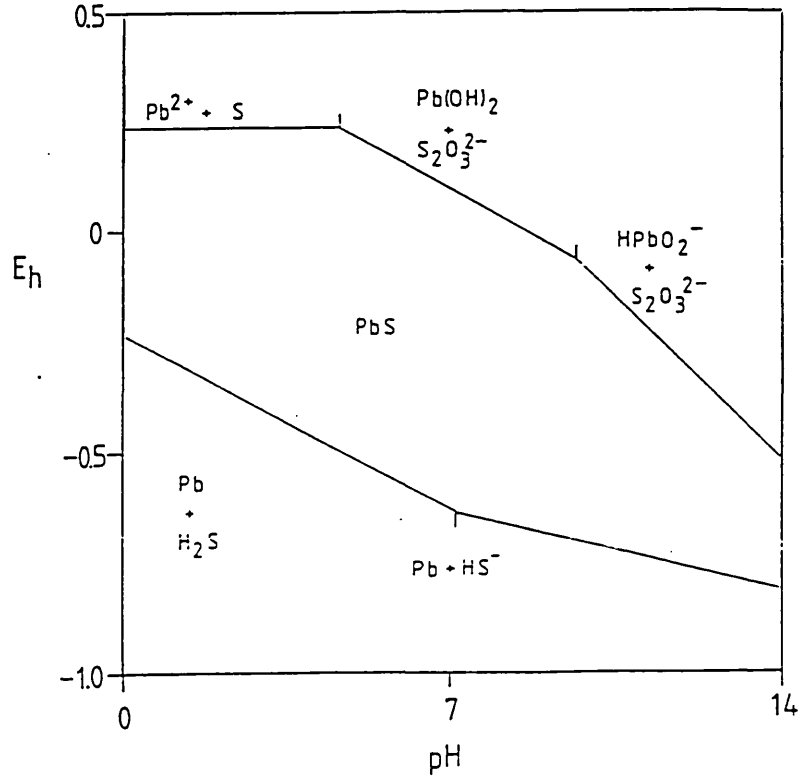


Fig 2.5 Electrochemical phase diagram for galena[72]. Equilibrium lines correspond to dissolved species at 10^{-4} M.

either sulphur or lead according to the equations:-

$$PbS_{(s)} = Pb^{2+}{}_{(aq)} + S_{(s)} + 2e \qquad (2.3)$$

$$\text{or } PbS_{(s)} + 2H^+ + 2e = Pb_{(s)} + H_2S_{(aq)} \qquad (2.4)$$

The concept of surface reactions proceeding by separate, simultaneous anodic and cathodic electrochemical steps at a solid-solution interface is well established in many fields, e.g. metal corrosion, where anodic dissolution and the formation of passive layers are

driven by some cathodic reduction process, such as hydrogen evolution or oxygen reduction. The open-circuit, or rest, potential of a sulphide mineral in solution is the electrode potential observed when the net current density at the mineral/solution interface is zero. The rest potential may be either an equilibrium potential or a mixed potential.

An equilibrium potential may be defined as the potential measured when a single anodic/cathodic reaction occurs between electrode and electrolyte. The forward and reverse current densities are then equal, and there is no net reaction. In this case the electrode potential E_h is related to the activities of reactants and products by the Nernst equation.

A mixed potential is measured when two different reactions occur at separate but adjacent anodic and cathodic sites on the electrode surface at equal rates[73]. For example, in the PbS region the anodic current from reaction (2.3) equals the cathodic current from reaction (2.4) so that the net current is zero. This mechanism is known as the Wagner-Traud mixed potential mechanism[114] and was derived for an ideal homogeneous surface that allows the anodic and cathodic reactions to occur simultaneously over the entire surface. In reality variations in electrode composition results in a heterogeneous composite of anodic and cathodic sites. Localised anodic and cathodic areas on galena have been observed by Plaksin et al[115,116]. A mixed potential is not an equilibrium potential for either reactions (2.3) or (2.4), but provides an overvoltage for both the anodic and cathodic reactions. When an open-circuit electrode potential is measured, it is not possible, a priori, to distinguish between equilibrium and mixed potentials.

A fundamental property of electrode processes such as (2.3) and (2.4) is that the free energy changes with potential across the solid solution interface. Thus at the electrode-solution interface, thermal energy will cause ions to collide continuously with the electrode surface. Any ion with sufficient energy may surmount the energy hump (activation energy) in releasing or acquiring electrons at the electrode (Figure 2.6[74]).

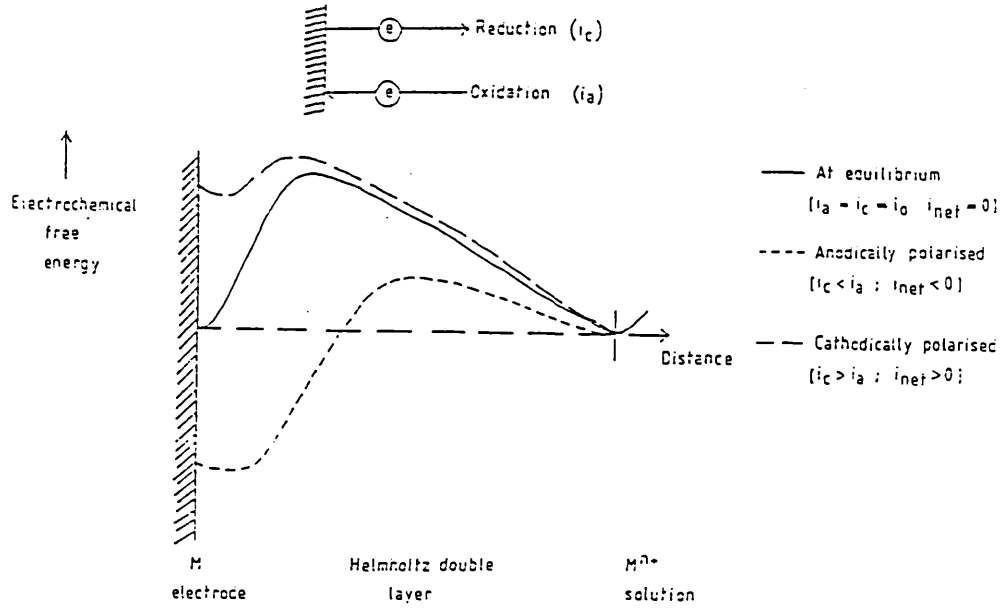


Fig 2.6 Electrochemical free energy profiles for a metal solution interface[74].

The Gibbs phase rule states that:-

$$P + F = C + 2$$

where P = Number of phases
F = Number of degrees of freedom
C = Number of components

thus in the single solid phase region for PbS

P = 2 (solid and aqueous phases)
C = 3 (Pb_xS_y, $Pb^{2+}_{(aq)}$, $S^{2-}_{(aq)}$)

Hence $2 + F = 3 + 2$

i.e. the number of degrees of freedom, $F = 3$

Therefore, at constant temperature and pressure a simple sulphide mineral, such as PbS, will have one degree of freedom, which can be identified with the chemical potential of the metal in the metal sulphide lattice, i.e.:-

$$\mu_{Pb(PbS)} = -RT \ln a_{Pb}$$

The chemical potential is the partial Gibbs free energy which is in turn linked to the electrode potential. Thus, the rest potential of a sulphide mineral lies within a range defined by an upper and lower limit. The upper limit corresponds to the potential of the two phase potential sulphur/sulphide couple (PbS/S°) and the lower limit corresponds to the potential of the pure metal electrode (Pb/PbS). However, the actual value of the rest potential is determined by the activity of the metal (Pb) in the solid sulphide, i.e. the stoichiometry or M/S ratio in the solid phase, and will vary within this range as the composition of the sulphide varies. Thus, a fixed electrode potential is not obtained (c.f. Sato's equation for a half cell potential[62].

However, once a second phase is formed, either the pure metal or sulphur, the Gibbs phase rule becomes:-

$$3 + F = 3 + 2$$

$$\Rightarrow F = 2$$

Thus, at constant temperature and pressure, the electrochemical potential becomes invariant and a fixed electrode potential is obtained. Sato[62] has also shown that for an invariant potential to be achieved two solid phases must coexist.

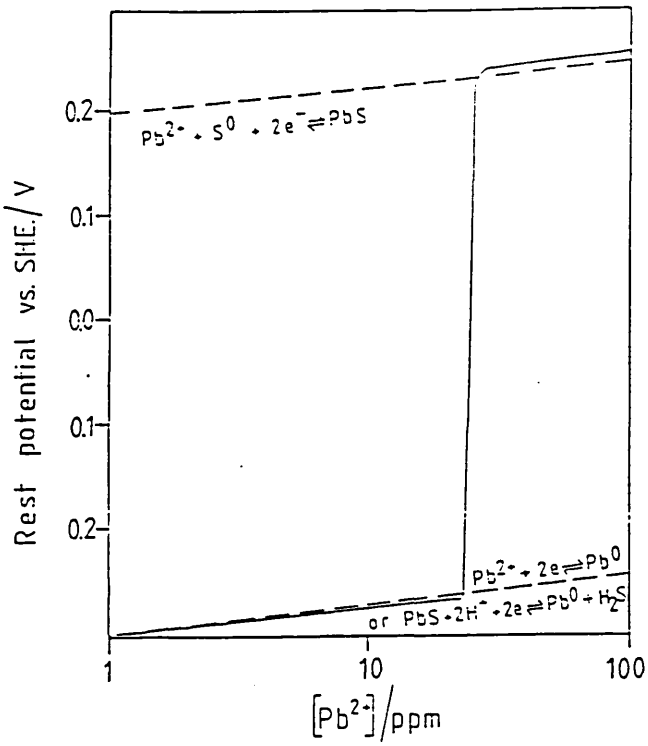


Fig 2.7 Rest potentials of PbS in $HClO_4$ solutions after cathodising then anodising for successive intervals[61].

Peters[61] presented data that showed that under certain conditions of polarisation, the single-phase PbS range is very narrow. Although the region extended for about half a volt, the rest potential within this region could be altered by very small currents (Figure 2.7).

At equilibrium the phenomenon of oxidation and reduction may be visualised as two equal and opposite electric currents (i_a and i_c) and their magnitude for a given reaction defines the exchange current density (i_o). It also follows that i_o is related to the activation energy for the electrode reaction and depends on the concentration of electroactive species. If the electrode is made more positive or negative than the equilibrium potential by an external current, either i_a or i_c predominates and current (i_{net}) flows through the electrode.

Thus, in the single solid phase region for PbS the dissociation reaction:-

$$PbS_{(s)} = Pb^{2+}{}_{(aq)} + S^{2-}{}_{(aq)}$$

can be considered to be taking place where the activities of the lead and sulphide species are linked by the solubility product for PbS:-

$$\text{Solubility product } K_{sp} \text{ (PbS)} = a_{Pb2+} \cdot a_{S2-}$$

In considering the stoichiometry or composition range of a sulphide it is useful to write the formula in terms of variable metal in relation to a stoichiometric sulphide compound i.e. pyrrhotite can be written as $Fe_{1-x}S$, where the composition range at room temperature is $0 \leq x \leq 0.14$[61]. For galena at room temperature the composition range is very small. Thus, even a minute change in the stoichiometry of PbS will cause a significant change to the rest potential in solution.

Peters[61] pointed out that the variation in rest potential of galena could also be due to the nucleation and growth of a second phase on the surface (i.e. sulphur or lead). This would be kinetically faster that the solid state diffusion of lead or sulphur in PbS necessary to alter the stoichiometric range to a significant depth from the surface. Thus, the smaller the allowed stoichiometric range for a sulphide mineral, the greater is the instability of the single phase sulphide region and rest potentials will tend towards either the two phase M/MS potential or the two phase MS/S° potential. For a sulphide with a large compositional range, the rest potential will not be so sensitive to a change in stoichiometry and the single phase sulphide region should be more stable.

For a ternary system such as Cu-Fe-S, there are three components and therefore one more degree of freedom. Thus, for a three component sulphide system to become invariant in electrochemical potential, three non-aqueous phases must be in equilibrium with each other. Similarly, the link between a_{M}° and a_{S}° for equations written in the form of equations (2.1) and (2.2) must now include the third component and hence involve a three component Gibbs-Duhem relationship[61].

The main problem of using E_h-pH diagrams to interpret the possible reactions taking place at the rest or mixed potential at a given pH lies in the fact that the diagrams are constructed from data that refers to bulk species, whereas flotation generally involves only sub-monolayer quantities. The thermodynamics of such layers can differ significantly from those of the bulk phases; in essence they can be classified as "non-thermodynamic" phases.

2.3 Chemical Oxidation

Traditionally, sulphide minerals have been treated by pyrometallurgical extractive metallurgical processes. However, due to the emission of SO_2 gas these methods have become unacceptable to modern society, unless the gas can be adsorbed into the production of fertilisers, or sulphuric acid, which in many cases is uneconomic. Thus hydrometallurgical processes, involving the use of leaching agents, have been sought as alternative methods for treating sulphide minerals with the possibility of recovering elemental sulphur, iron and non-ferrous metals.

The advent of direct acid pressure leaching of sulphide concentrates has led to investigations of the kinetics and mechanism of sulphide oxidation in aqueous media. These studies are relevant to the electrochemical oxidation of sulphides because of the similar reactions involved in both chemical and electrochemical oxidation.

2.3.1 Pyrite

Allen and co-workers[76,77] proposed that the aqueous oxidation of pyrite by molecular oxygen could be represented by the equation:-

$$2FeS_2 + 7O_2 + 2H_2O = 2FeSO_4 + 2H_2SO_4 \qquad (2.5)$$

Sulphur has been observed as a product in some investigations[66,78-82]. However, the yield is usually low which has lead to many reports claiming that pyrite is oxidised exclusively to

sulphate, with iron passing into solution in the ferrous or ferric state, depending on the operating conditions[83-87]. Stenhouse and Armstrong[84] investigated the aqueous oxidation of pyrite suspensions in caustic solutions and found the pyrite particles became coated with an amorphous layer of sulphur and oxygen compounds that also contained Fe_2O_3 and Fe_3O_4. Their experiments indicated that mass transfer through the layer determined the rate of the reaction. During alkali pressure leaching Burkin and Edwards[91] were not able to detect Fe_3O_4 or mixed hydroxy-sulphur compounds, but $Fe(OH)_2$ and FeOOH. Kim and Choi[79] found that the pressure leaching rate of pyrite was independent of pH at elevated temperatures and pressures in strong acid solutions. McKay and Halpern[88] studied the system in more detail at various acidities and oxygen pressures at temperatures between 100 - 130 °C. They found that the formation of elemental sulphur was favoured by high acidities and low temperatures. Low acidities and high temperatures favoured the formation of sulphuric acid. They found a first-order dependence of the overall rate of oxidation on oxygen partial pressure and proposed an oxygen adsorption mechanism followed by a chemical reaction. The mechanism required a rapid chemisorption of oxygen on the pyrite surface, which became covered by a monolayer of oxygen, comprising one O_2 molecule at each FeS_2 site, i.e.:-

$$FeS_2 + O_{2(aq)} \xrightarrow{\text{fast}} FeS_2.O_2 \qquad (2.6)$$

Oxidation occurred through the attack of a second O_2 molecule on an O_2-covered site; this was considered the rate-determining step:-

$$FeS_2.O_2 + O_{2(aq)} \xrightarrow{\text{slow}} FeS_2.2O_2 \rightarrow FeSO_4 + S^\circ \qquad (2.7)$$

Ferric sulphate may be formed in the reaction scheme by the subsequent oxidation of ferrous sulphate and by the oxidation of elemental sulphur i.e.:-

$$8FeSO_4 + 2O_2 + 2H_2SO_4 \rightarrow 8Fe_2(SO_4)_3 + 4H_2O \qquad (2.8)$$

and

$$2S + 3O_2 + 2H_2O \rightarrow 2H_2SO_4 \qquad (2.9)$$

An alternative mechanism, recognised by McKay and Halpern[88], is one in which elemental sulphur is not an intermediate in the formation of sulphate, but elemental sulphur and sulphate are produced by simultaneously competing reactions with a common intermediate:-

$$FeS_2 + O_2 \xrightarrow{\text{slow}} FeS_2.O_2 \qquad (2.10)$$

$$FeS_2.O_2 \rightarrow FeSO_4 + S \qquad (2.11)$$

$$FeS_2.O_2 \rightarrow FeSO_4 + H_2SO_4 \qquad (2.12)$$

Initially, this adsorption mechanism requires a 50:50 distribution of elemental sulphur and sulphate as products. This was observed experimentally only at approximately 120 °C.

Bailey and Peters[89] proposed an electrochemical mechanism with separate anodic and cathodic reactions:-

$$\text{anodic} \quad FeS_2 + 8H_2O = Fe^{3+} + 2SO_4^{2-} + 16H^+ + 15e \qquad (2.13)$$

$$FeS_2 = Fe^{2+} + S^\circ + 2e \qquad (2.14)$$

$$\text{cathodic} \quad O_2 + 4H^+ + 4e = H_2O \qquad (2.15)$$

The main difference in the two approaches is that, in the electrochemical mechanism, the oxygen in the products is derived from water, whereas in the adsorption mechanism, it is derived from molecular oxygen. Also in the electrochemical mechanism, elemental sulphur and sulphate are formed through separate independent reactions with different reaction kinetics. The formation of a common intermediate is not required.

Bailey and Peters[89] suggested that the production of elemental sulphur is self-inhibitive owing to the formation of a passive sulphur film. Pyrite is one of the few sulphide minerals with a molar volume smaller than its sulphur content when the sulphur is in elemental form (24 cm^3 mol^{-1} FeS_2 → S^o volume of 32.7 cm^3[65]. Thus, elemental sulphur protects pyrite from oxidation under conditions in which the sulphur does not oxidise.

Investigations of the kinetics and mechanism of pyrite oxidation by ferric ion are sparse and contradictory. Thomas and Whalley[90] studied the leaching of pyrite by ferric sulphate solutions at 90°C. The reaction rate was reported to be faster than the oxidation of pyrite to ferric sulphate in air. The following reaction stoichiometry was proposed:-

$$FeS_2 + 7Fe_2(SO_4)_3 + 8H_2O = 15FeSO_4 + 8H_2SO_4 \qquad (2.16)$$

McKay and Halpern[88] made a brief study of the oxidation of pyrite by ferric ion in 0.075 M sulphuric acid at 110 °C and concluded that ferric ion was a poor oxidant compared with molecular oxygen. However, the experimental procedure and conditions were not compared with those used by Thomas and Whalley[90].

2.3.2 Pyrrhotite

Downes and Bruce[85] studied the oxidative pressure leaching of pyrrhotite and found that iron oxide, elemental sulphur and sulphate were produced. The yield of elemental sulphur was found to be up to 80 % under 150 psi air pressure at 110 °C after 1.5 hours. The remainder of the sulphur in pyrrhotite was oxidised to sulphate. Gerlach et al[92] studied the kinetics of the pressure leaching of oxygen at 30 to 80 °C. From their results they proposed the following reaction sequence:-

$$FeS + 2H^+ = Fe^{2+} + H_2S \quad (2.17)$$

$$2H_2S + O_2 = 2S^\circ + 2H_2O \quad (2.18)$$

$$H_2S + 2O_2 = SO_4^{2-} + 2H^+ \quad (2.19)$$

$$H_2S + 2Fe^{3+} = S^\circ + 2Fe^{2+} + 2H^+ \quad (2.20)$$

$$H_2S + 8Fe^{3+} + 4H_2O = SO_4^{2-} + 8Fe^{2+} + 10H^+ \quad (2.21)$$

$$2S^\circ + 3O_2 + 2H_2O = 2SO_4^{2-} + 4H^+ \quad (2.22)$$

Reaction steps (2.20) and (2.21) were considered insignificant because oxidation of ferrous to ferric proceeds slowly in sulphuric acid media[269]. 30 % of the total sulphur product occurred as sulphate and was attributed to reactions (2.19) and (2.22). Kunda et al[93] carried out oxidative leaching experiments on pyrrhotite formed by the thermal decomposition of pyrite. They proposed a flowsheet whereby elemental sulphur and iron metal were eventually recovered. Oxidative leaching experiments were carried out on a pilot plant scale by Thornhill[94] in an autoclave at 110 °C and 100 psi air pressure. The pyrrhotite was oxidised to Fe_2O_3 and sulphur with a 60 % recovery of the latter. Leaching of pyrrhotite in nitric acid was investigated by Habashi[95]. The sulphur recovery was 65 % using 30 % HNO_3 in an open vessel.

2.3.3 Pentlandite

Studies of the oxidation of pentlandite have concentrated on natural weathering in the geological environment[96-100]. However, Dutrizac and MacDonald[101] studied the ferric oxidation of pentlandite, and Forward et al[75], the ammonia pressure leaching of Ni concentrates.

Sandefur[96] reported that the supergene alteration of pentlandite produced violarite ($FeNi_2S_4$), a more nickel-rich sulphide. Subsequently, this oxidised completely to basic nickel sulphates.

Michener and Yates[97] found that violarite was formed rapidly on pentlandite when the latter was exposed to the atmosphere. The violarite was then leached to limonite ($Fe_2O_3.H_2O$), or under certain conditions to millerite (NiS) with the loss of iron. Nickel et al[98] proposed an electrochemical mechanism for the supergene alteration of nickel sulphide ores, with the anodic reaction:-

$$(Fe,Ni)_9S_8 = 2FeNi_2S_4 + 2Fe^{2+} + Ni^{2+} + 6e^- \qquad (2.23)$$

coupled to the cathodic reduction of oxygen (reaction (2.15)).

Dutrizac and MacDonald[101] investigated the leaching of low grade pentlandite ores with ferric sulphate at temperatures between 24 °C and 60 °C. In the absence of bacteria, all the sulphide was converted to elemental sulphur. The introduction of bacteria into the system helped to catalyse the direct oxidation of sulphide to sulphate with the regeneration of ferric ion, though only 30 % of the sulphide was oxidised to sulphate. The following reactions were suggested:-

$$(Fe,Ni)_9S_8 + 18Fe^{3+} = 22.5Fe^{2+} + 4.5Ni^{2+} + 8S^\circ \qquad (2.24)$$

and in the presence of bacteria:-

$$(Fe,Ni)_9S_8 + 17.625O_2 + 3.5H_2SO_4 = 2.25Fe_2(SO_4)_3 + 3.5H_2O + 4.5NiS \qquad (2.25)$$

From X-ray diffraction studies of pentlandite leach residues and chemical analysis of the final solution, Kelt[102] concluded that oxidation of pentlandite by ferric chloride occurred by the dissolution of iron and nickel with the formation of orthorhombic sulphur.

Forward and MacKiw[75] studied the ammonia pressure leaching of nickel sulphide concentrates and concluded that the iron present in pentlandite particles was converted directly to hydrated iron oxide, pseudomorphic with the original mineral. Leached particles consisted

of a sulphide core surrounded by an iron oxide layer, through which nickel and sulphur ions diffused to react with oxygen to form thiosulphate. Oxidation of thiosulphate to thionate and eventually sulphate occurred homogeneously in solution, but no analytical detail was given[75].

2.3.4 Chalcopyrite

Although oxygen pressure leaching has been studied[169,172-174], most attention has been given to the use of ferric ion as an oxidant. There is general agreement that acid ferric leaching of chalcopyrite can be represented by the following equation[103-111]:-

$$CuFeS_2 + 4Fe^{3+} = Cu^{2+} + 5Fe^{2+} + 2S^\circ \qquad (2.26)$$

However, there is little consensus as the reaction rate law and mechanism. The oxidation kinetics of chalcopyrite for similar experimental conditions at low pH have been reported as both (i) linear[106,111], i.e. copper dissolved (Cu_d)α time (t), and (ii) parabolic[105,106-110], $Cu_d \alpha\ t^{1/2}$. These results have been interpreted in terms of rate control by the oxidant due to respectively, (i) chemisorption at the mineral surface, and (ii) diffusion through a porous sulphur layer formed during the reaction. Linge[108] found the parabolic dissolution kinetics were much slower than the rate of diffusion of oxidant through a porous layer and interpreted the results in terms of a solid state diffusion step within the crystal lattice. Chen and Harvey[165] have measured the self-diffusion coefficients of copper and iron in chalcopyrite and estimated the fastest rates of chemical leaching reactions that might be sustained by the solid-state diffusion of metal atoms to the chalcopyrite/solution interface.

Although reaction (2.26) predicts a dissolved Fe^{2+}/Cu^{2+} ratio of 5, the ratio is very much greater than 5 during the initial stages of the reaction[146,147,158]. A similar phenomena has been observed when dissolved oxygen is used as an oxidising agent[153,154,158,168].

Munoz et al[109] presented a mechanism based on the Wagner theory of oxidation which implies that a protective sulphur layer is formed during the oxidation of chalcopyrite at 90 °C with the rate limited by the transport of electrons through the insulating layer.

These mechanisms do not explain the greater leaching reactivity of ferric chloride over ferric sulphate[111], which implies that the complexing ability of chloride ions for cuprous species may be the important factor.

Kruesi et al[111,112] patented a process, called the "Cymet Process", for the treatment of chalcopyrite concentrates in chloride media. It combines leaching with an anodic dissolution stage followed by the electrolytic recovery of Cu and Fe. The reaction scheme is as follows:-

Leaching: $CuFeS_2 + HCl + 3FeCl_3 = CuCl_2^- + 4FeCl_2 + H^+ + 2S$ (2.27)

Anodic dissolution: $CuFeS_2 + 4HCl = CuCl_2^- + FeCl_2 + 4H^+ + 2S + 3e^-$ (2.28)

Cathodic reaction: $CuCl_2^- + e^- = Cu + 2Cl^-$ (2.29)

Ferrous chloride solution is electrolysed in a separate cell to recover metallic iron and to regenerate the leaching agent, $FeCl_3$.

Cathodic reaction: $FeCl_2 + 2e^- = Fe + 2Cl^-$ (2.30)

Anodic reaction: $FeCl_2 + Cl^- = FeCl_3 + e^-$ (2.31)

2.4 Electrochemical Studies of Sulphide Mineral Behaviour

A chemical reaction may be defined as one in which anodic and cathodic reactions take place at the same site and electron transfer takes

place within one or two molecular distances only. A reaction is defined as electrochemical when the anodic reaction occurs remotely (i.e. in a different location) from the cathodic reaction and requires the transport of electrons through a conductor. This necessarily restricts electrochemical reactions to conductors and semiconductors. As sulphide minerals are semiconductors, their acid leaching reactions can be considered to occur by an electrochemical mechanism[104], with the reduction of oxygen occurring at cathodic sites by the reaction:-

$$1/2O_2 + 2H^+ + 2e = H_2O \qquad (2.33)$$

and the oxidation of the metal sulphide at anodic sites by the reaction:-

$$MS = M^{2+} + S^\circ + 2e^- \qquad (2.34)$$

As early as 1830, Fox[117] showed that sulphide minerals, and particularly pyrite, can exhibit a potential difference of up to 1 volt with the surrounding country rock; this is known as a self-potential. The phenomenon has been used as a geophysical prospecting technique and was reviewed by Sato and Mooney[118]. Gottschalk and Buhler[122] proposed an electrochemical mechanism for the secondary enrichment of sulphide ore deposits. However, Kamienski[119,120] was the first person to make an electrochemical study of a sulphide mineral, when he investigated the effect of pH on the equilibrium potentials of galena. The application of electrochemical techniques to flotation research was introduced by Salamy and Nixon[121] and an electrochemical mechanism for the hydrometallurgical treatment of sulphides was proposed by Woodcock[104]. Since that time, numerous electrochemical studies on sulphide minerals have been reported.

2.4.1 Anodic and Cathodic Reactions of Sulphide Minerals in Aqueous Solutions

2.4.1.1 Pyrite

Using potentiostatic control, the anodic polarisation behaviour of pyrite has been investigated in $HClO_4$[66,78,123,124], HCl[78,124,125] and H_2SO_4[78,124,126] at ambient temperature, and in $HClO_4$ at temperatures > 100 °C[82] and H_2SO_4 at 100 °C[82]. There appears to be no influence of pyrite's semiconducting properties on the kinetics of the anodic process[78,123,124]. Springer[124] and Peters et al[66] found no differences in the anodic polarisation curves for pyrite obtained in $HClO_4$, HCl, H_2SO_4 and HNO_3. A Tafel slope of 120 mV per decade in 1 M acid was reported. Meyer[126] reported that the Tafel slope falls in the range 80 - 110 mV per decade, whereas Biegler and Swift[78] reported a narrower range of 90 - 105 mV per decade and a slope that was independent of the anion in solution. However, these values are dubious since current values are time-dependent over the potential range investigated due to changes in the surface composition of pyrite. The main anodic reaction of pyrite in solutions of pH < 2 has the following stoichiometry:-

$$FeS_2 + 8H_2O = Fe^{3+} + 2HSO_4^- + 14H^+ + 15e \qquad (2.35)$$

There are conflicting reports as to whether sulphur is formed at all[78,89,106]. If it is formed the anodic reaction is either:-

$$FeS_2 = Fe^{2+} + 2S^\circ + 2e \qquad (2.36)$$

or

$$FeS_2 = Fe^{3+} + 2S^\circ + 3e \qquad (2.37)$$

Peters and Majima[66] anodically polarised a pyrite specimen at a constant current of 1 mA cm^{-2} in 1 M $HClO_4$ under helium for 6 days. The potential averaged 0.81 V versus the standard hydrogen electrode (S.H.E.) without significant variations. They analysed the final solution for total iron, Fe^{2+}, and SO_4^{2-}, but only detected Fe^{3+} and SO_4^{2-}. Biegler and Swift[78] noted that anodic polarisation causes

the surface to darken. Klein and Shuey[123] attempted to identify the product by anodising a sample at 1.16 V (SHE) at pH 0 for 4 hours. At the end of this time the electrode surface was completely converted to a black material which, when scraped from the electrode, was found to be highly magnetic. The material could not be positively identified but it was suggested that it could be a spinel iron oxide, either magnetite (Fe_3O_4), or maghemite (α-Fe_2O_3). A subsequent experiment with magnetite indicated that the surface tarnish was not magnetite but more likely to have been maghemite or some other iron oxide.

Biegler and Swift[78] reported coulometric experiments at pH 0 where the final solution was analysed for total iron and sulphur, the latter being obtained by CS_2 extraction. The results were interpreted in terms of a combination of reactions (2.35) and (2.37) to give an overall reaction:-

$$FeS_2 + 8xH_2O = Fe^{3+} + 2xSO_4^{2-} + 2(1-x)S + 16xH^+ + (12x + 3)e \qquad (2.38)$$

where x is the fraction of pyrite reacting via reaction 2.35 i.e. the % yield of sulphate. Their results, expressed as Faradays per mole of iron dissolved, gave values of 12x + 3, from which sulphate yields were calculated for given experimental potentials. A linear dependence of sulphate yield on potential was observed, ranging from approximately 80 % at 0.9 V to 100 % at 1.4 V vs. S.H.E.. Meyer[126] carried out solution analyses after constant current experiments on pyrite electrodes in 1 M $HClO_4$ and detected only Fe^{3+} with varying percentages of sulphate. Analyses for lower oxidation states of sulphur were not carried out because Fe^{3+} in solution would probably have oxidised them to sulphate if they were present. Although sulphur was not determined, Meyer concluded that sulphur is probably produced either in colloidal form in solution or as a retained phase on the mineral surface. Koch[52] reported that the reaction product is entirely sulphate at 0.81 V vs. S.H.E.. Peters and Majima[66] reported that oxygen evolution occurred if the potential was raised to 1.57 V vs. S.H.E.. Neither Klein and Shuey[123], nor Springer[124],

was able to observe oxygen evolution at 1.2 V vs. S.H.E. and 10 mA cm^{-2}, but this was due to the potential being below the reversible potential for oxygen evolution of 1.229 V vs. S.H.E.. Following polarisation to high current densities the specimens were always deeply pitted[78,126]. Nagai and Kuichi[82] carried out anodic polarisation experiments on pyrite at temperatures up to 175 °C in the absence of oxygen and found mostly ferrous ion with little ferric in solution together with elemental sulphur and sulphate. At a given anodic current density in the Tafel region, the electrode potential decreases with increasing pH due to the anodic wave shifting to more negative potentials with increasing pH. The pH dependence was reported to be -30 to -40 mV per pH unit over the pH range 0 to 5[123,126]. Tafel slopes for the electrochemical behaviour of pyrite in alkali media have been reported by Yashina et al[127].

In alkaline solution, investigation of the oxidation mechanism is complicated, except at very high pH, by the insolubility of iron hydroxides which makes solution analysis of iron impossible. Janetski et al[129] and Hamilton et al[134] observed current peaks on cyclic voltammograms of pyrite electrodes in basic solutions and assigned them to the $Fe(OH)_2/Fe(OH)_3$ redox couple. Michell and Woods[128] analysed the surface of pyrite by X-ray emission spectroscopy, after oxidising the surface electrochemically in pH 9.2 buffer solution. The results indicated the presence of an oxygen containing layer, interpreted as being hydrated ferric oxide. Under similar experimental conditions, X-ray diffraction studies by Meyer[126] showed that iron appears in the film as iron (II), i.e. FeO; no iron (III) compounds were detected. However, the film was reddish-brown in colour so it was suggested that iron (III) is probably present in amorphous forms.

Various authors have measured the open circuit or rest potential of pyrite over the entire pH range. The rest potential decreases linearly with pH over the pH range 2 to 12 in perchlorate[123,130,131] and nitrate media[132,133], but becomes independent of pH below pH 2[130,131], adopting a value of approximately 0.62 V vs. S.H.E..

Several authors have noted that this is about 0.3 V higher than the thermodynamic reversible potential for the upper stability limit of pyrite described by reaction (2.36)[61,78,123,126]. Since the mineral does not decompose at an appreciable rate on standing in acid solutions, this has generally been interpreted as evidence for the formation of a passive film (Section 1.3.1). Sato[131] suggested that the oxidation reaction for pyrite which gives the closest fit to the observed potential at pH values < 2, is:-

$$FeS_2 = Fe^{2+} + S_2 + 2e$$

$$E = 0.757 + 0.0295 \log [Fe^{2+}] \qquad (2.39)$$

The sulphur is not in the crystalline state, but in a diatomic molecular form. Its standard free energy of formation was given as 80.35 kJ mol^{-1}.

For pH values > 2, the rest potential of pyrite decreased by approximately 0.059 V/pH unit, which Sato[131] attributed to the hydrolysis of iron by the reaction:-

$$FeS_2 + 3H_2O = Fe(OH)_3 + S_2 + 3H^+ + 3e$$

$$E = 0.857 - 0.591 \text{ pH} \qquad (2.40)$$

This mechanism is not unreasonable from the standpoint of crystal structure (Section 2.1.1.1), since in the pyrite structure two sulphur atoms exist close together, forming -Fe-S_2-Fe- type bonds. Therefore, during oxidation, these bonds may be broken liberating S_2 molecules, either into solution, or as a product retained on the surface. The S_2 molecule is extremely unstable and would oxidise to sulphate or decompose to yield sulphur. Peters and Majima[66] performed experiments in which pyrite samples were subjected to a series of cathodic potentials. After each "pre-treatment potential", the current was turned off for 10 minutes and the rest potential determined. Their results showed that the rest potential could decrease to between 0.2 and 0.3 V vs. S.H.E. by such treatment.

The mechanism of the anodic process is still unclear. Bailey and Peters[89] concluded that sulphate and sulphur formation proceed by two independent paths. Biegler and Swift[78] discounted elemental sulphur in the formation of sulphate, since in the leaching of sulphides, the product once formed is stable even at elevated temperatures[106]. In addition, sulphur is a very stable product of the anodic oxidation of H_2S in 0.1 M H_2SO_4 in the potential range 1.2 - 1.7 V vs. S.H.E.[137-139]. High sulphate yields are obtained for the anodic polarisation of pyrite in this potential region. Meyer[126] proposed a two layer anodic process. One layer is associated with the oxidation of Fe^{2+} to Fe^{3+}, which occurs in a thin surface layer within the solid phase:-

$$Fe^{2+} = Fe^{3+} + e \qquad (2.41)$$

The other layer involves oxidation of S_2^{2-} through intermediates such as $S_2O_2^{2-}$, $S_2O_3^{2-}$, to SO_4^{2-}. The initial step was postulated to lead to the formation of the intermediate $S_2(OH)_2$ (thiosulphurous acid), as yet unknown in the free state, by the reaction:-

$$S_2^{2-} + 2H_2O = S_2(OH)_2 + 2H^+ + 4e \qquad (2.42)$$

Sulphur may be produced by decomposition of the acid form of these intermediates, which are known to be unstable in acid solutions. Using cyclic voltammetry, Conway et al[135] observed two almost reversible monolayer surface processes occurring on the pyrite surface in the potential range -0.2 to +0.45 V vs. S.H.E. at pH 1. The following surface process at FeS_2 was postulated:-

$$2e + S_2^{2-}{}_{(lattice)} = 2S^{2-}{}_{(lattice)} \qquad (2.43)$$

When the potential was increased above 0.5 V, they proposed that other anodic processes occurred, producing the species SO_3^{2-}, $S_2O_3^{2-}$, SO_4^{2-} and Fe^{2+}[135].

Biegler and Swift[78] postulated a mechanism involving adsorbed oxygen-containing intermediates. The initial step involved adsorption of oxygen onto the pyrite surface by adsorption and deprotonation of water molecules:-

$$FeS_2 + H_2O = FeS_2(OH)_{ads} + H^+ + e \qquad (2.44)$$

$$FeS_2(OH)_{ads} = FeS_2(O)_{ads} + H^+ + e \qquad (2.45)$$

reaction (2.45) being rate-determining. If the Tafel constants α and β are assumed to be 0.5, the mechanism predicts a Tafel slope of 59 mV per decade, which is low compared with the observed experimental values of approximately 100 mV per decade.

Investigations of pyrite reduction at pH 0[66,123] have shown that at potentials less than -0.3 V vs. S.H.E., pyrite decomposes according to the equation:-

$$FeS_2 + 4H^+ + 2e = Fe^{2+}_{(aq)} + 2H_2S_{(g)} \qquad (2.46)$$

However, the current efficiency for this reaction is low[66]; hydrogen is simultaneously discharged at potentials in the range -0.2 to -0.5 V vs. S.H.E. at a current efficiency of 65 to 80 %. This value is high compared with minerals like chalcopyrite and galena which will generate 100 % H_2S under these conditions. Peters and Majima[66] showed the hydrogen evolution reaction rate to be a linear function of $[H^+]$, while H_2S evolution was slightly higher than first order. Having observed that the potential at which the hydrogen evolution reaction begins is very sensitive to pH, Klein and Shuey[123], using the data of Peters and Majima[66], calculated the derivative of potential with respect to pH at constant cathodic currents, for both H_2S and H_2. They quoted values of -0.09 V per pH unit for the H_2 component and -0.13 V per pH unit for the H_2S component. Their calculations predicted that at pH values greater than zero the H_2 component will dominate the H_2S component with pyrite functioning as an inert electrode. The hydrogen overvoltage on pyrite at pH 0 is

very low, about 0.26 V at 1 mA cm^{-2} of hydrogen discharge current[66,140]. This value is below that for metals such as silver, nickel, iron and copper, but above that for platinum, and gold.

In a recent review of the chemistry and physics of pyrite, Lowson[136] concluded that the following questions remained to be answered: is the Fe^{2+} ion oxidised to Fe^{3+} before dissolution from the pyrite lattice? What is the oxidation path for S_2^{2-} to SO_4^{2-}? What are the controlling factors for the production of elemental sulphur?

2.4.1.2 Pyrrhotite

There are few reports of the electrochemical behaviour of pyrrhotite. Potential measurements made on synthetic FeS electrodes in solutions of various Fe^{2+} ion concentrations, have shown the electrode potential of FeS to be independent of Fe^{2+} ion concentration, i.e. it does not obey the Nernst relationship[141]. Hamilton and Woods[134] investigated the surface oxidation of pyrrhotite by cyclic voltammetry using a natural pyrrhotite sample of stoichiometry $FeS_{1.13}$ (or $Fe_{0.885}S$) from Mount Isa, Queensland. Analysis of the products of anodic oxidation were made entirely from the characteristics of their reduction on a subsequent reverse potential scan. No analysis of the solution was made for Fe^{2+}, Fe^{3+} or SO_4^{2-}. The following anodic reactions were proposed:-

$$FeS_{1.13} = Fe^{2+} + 1.13S + 2e \qquad (2.47)$$

$$FeS_{1.13} = Fe^{3+} + 1.13S + 3e \qquad (2.48)$$

$$FeS_{1.13} + 4.52H_2O = Fe^{2+} + 1.13SO_4^{2-} + 9.04H^+ + 8.78e \qquad (2.49)$$

$$FeS_{1.13} + 4.52H_2O = Fe^{3+} + 1.13SO_4^{2-} + 9.04H^+ + 9.78e \qquad (2.50)$$

They concluded that sulphur is the major product of pyrrhotite oxidation at pH 4.6, 9.2 and 13. Sulphate is also formed in significant quantities, particularly in alkaline solutions. At pH 9.2

and 13, production of surface ferric oxide strongly inhibited further oxidation of pyrrhotite. Conway et al[135] also used cyclic voltammetry to study the surface redox reactions of pyrrhotite and comparisons were made with pyrite also. Their results indicated that FeS behaves much less reversibly than FeS_2 with three or four distinguishable electrochemical surface processes occurring over the potential range -0.4 to 0.2 V vs. S.H.E. at pH 1.

Henry et al[142] studied the electrochemical reduction of synthetic iron sulphides ($Fe_{1-x}S$) in chloride media at pH 0.2. By measuring the amount of charge corresponding to the reduction of Fe^{3+} in the solid and by evaluating the Fe^{2+} concentration in solution after electroreduction, the stoichiometry of a range of iron sulphides was determined. In a study of the non-oxidative leaching of metal sulphides, Scott et al[143] investigated the dissolution of hexagonal pyrrhotite (Fe_9S_{10}) at various applied cathodic potentials. They found that the ratio of the dissolution rate to the faradaic current necessary to sustain it, was consistent with the reduction of pyrrhotite to troilite (FeS) by the reaction:-

$$Fe_9S_{10} + 2H^+ + 2e = 9FeS + H_2S \qquad (2.51)$$

followed by the dissolution of troilite (see section 2.4.3).

$$FeS + 2H^+ = Fe^{2+} + H_2S \qquad (2.52)$$

2.4.1.3 Pentlandite

The only investigation of the electrochemical behaviour of pentlandite was carried out by Thornber[70]. Cyclic voltammetry and intermittent galvanostatic polarisation were carried out on pentlandite and violarite at pH values of 0, 2, 4, 6 and 8. The results indicated that the mineral/solution interfaces of both minerals behave similarly. Below pH 4, anodic dissolution favoured sulphur formation (reaction 2.53), and above pH 4, sulphate formation (reaction 2.54). Cathodic dissolution favoured H_2S formation over H_2 evolution at low pH values (reaction 2.55).

$$Fe_{4.5}Ni_{4.5}S_8 = 4.5Fe(II) + 4.5Ni(II) + 8S + 18e \qquad (2.53)$$

$$Fe_{4.5}Ni_{4.5}S_8 + 32H_2O = 4.5Fe(II) + 4.5Ni(II) + 8SO_4^{2-} + 16H^+ + 66e \qquad (2.54)$$

$$16e + Fe_{4.5}Ni_{4.5}S_8 + 16H^+ = 4.5Ni + 4.5Fe + 8H_2S \qquad (2.55)$$

It was argued that although complex adsorption and hydrolysis reactions take place within the solution as the interface reacts, the above reactions best represent the overall reactions of the mineral components at the interface. The variation in pH of the solution during cyclic voltammetric experiments was monitored by means of a pH electrode. A decrease in pH during an anodic potential sweep was indicative of the sulphate acid producing reaction predominating (reaction 2.54). However, little confidence can be put in this interpretation for two reasons: firstly, no attempt was made to measure the interfacial pH changes[144], and secondly, the pH was monitored under close-circuit conditions where the applied field between working and counter electrodes will effect the potential difference monitored at the pH electrode.

2.4.1.4 Chalcopyrite

A number of studies have been published [145 - 150, 152, 159 -164, 166, 167, 170, 171, 175] on the electrochemical behaviour of chalcopyrite under conditions comparable to those encountered during chemical leaching, i.e. in 1 M H_2SO_4, or 1 M HCl. The ferric leaching reaction (2.26; Section 2.3.4) can be represented in electrochemical terms by two half-cell reactions:-

Anodic: $$CuFeS_2 = Cu^{2+} + Fe^{2+} + 2S^\circ + 4e \qquad (2.56)$$

Cathodic: $$4Fe^{3+} + 4e = 4Fe^{2+} \qquad (2.57)$$

The corrosion of chalcopyrite, at low anodic potentials (0.4 to 0.8 V vs. S.H.E.) and ambient temperature, is complicated by the formation of varying film thicknesses of sulphur and other compact solid oxidation products that passivate the chalcopyrite surface. The oxidation products may be resistive (e.g. CuCl, Fe_2O_3[156,157], or sulphur), or p- and/or n-type semiconductors[108,152,170,171], such as p-type covellite (CuS), or metal-deficient polysulphides[148-150,160,161,164]. Moreover, the oxidation products may slow the transfer of electrons and transport of ions between the oxidising chalcopyrite and the species at the solid-liquid interface, limiting the rate of oxidation.

(a) Processes at Low Anodic Potentials (0.4 to 0.8 V vs. S.H.E.)

Biegler and Swift[167] studied the anodic behaviour of chalcopyrite in 1 M H_2SO_4 and 1 M HCl and found that from the rest potential of around 0.4 V to 0.85 V vs. S.H.E., there was a broad prewave in which current passed through a peak or a plateau depending on the conditions used. On potential cycling, the prewave was absent on the second and subsequent sweeps. Delays of more than one minute between surface preparation and start of the first sweep tended to decrease the definition of the prewave and the charge passed in the prewave region.

Parker et al[160,161] observed that between 0.4 and 0.7 V vs. S.H.E. the current density was < 1 mA cm^{-2}, and that the passive nature of the films formed diminished as the potential was increased. Constant potential pulse experiments in this potential region have shown that the current always decays with time[145-150,167]. This has been interpreted as evidence for chalcopyrite dissolution being retarded by diffusion of products through a slowly thickening film[160,161]. Parker et al[160,161] proposed that the main oxidation products over this potential range were Fe^{2+}, Cu^{2+} ($CuCl_2^-$ in chloride media) and S°, although no analysis of the mineral surface or solution was carried out. More recently, they concluded that the passivating layer consisted of a copper polysulphide, Cu_yS (where $y < 1$)[176,177].

Baur et al[158] and others[145-147,152-154,167,168,170,171] have reported the initial preferential release of iron from the chalcopyrite lattice, during anodic dissolution. Warren et al[148-150] interpreted this as being consistent with the reaction:-

$$CuFeS_2 = Cu_{1-x}Fe_{1-y}S_{2-z} + xCu^{2+} + yFe^{2+} + zS^{\circ} + 2(x+y)e \quad (2.58)$$

(where $y > x$). The metal-deficient compound $Cu_{1-x}Fe_{1-y}S_{2-z}$ is an intermediate product phase which, mixed with sulphur, forms an electron conducting passive layer on the mineral surface, termed film S_1. Parker[161,176] referred to the intermediate as a polysulphide having semiconducting properties that differed from those of chalcopyrite. However, their results were inconclusive. Jones et al[145-147] and Gardner et al[175] proposed that covellite (CuS) is the phase formed in the low current region during the anodic dissolution of chalcopyrite.

Ammou-Chokroum et al[152,170,171], who studied the electro-oxidation of chalcopyrite in acid chloride solution, also proposed a mechanism involving the formation of CuS to explain the decrease in electro-dissolution rate. Its formation was thought to be responsible for the superficial enrichment of the solid surface in copper, as well as for the retardation of the Fe^{2+} solubilisation rate. They argued that CuS covers the chalcopyrite/electrolyte interface by accumulating in the porous sulphur network, which forms a gradually thickening layer at the surface. The CuS gradually blocks the sulphur pores, causing a decrease in the reaction area and hence in the dissolution rate[152]. From their results, they proposed the following reaction scheme for the formation of CuS:-

$$Cu^{+}Fe^{3+}S_2^{2-} + 4H^{+} = Cu^{+} + Fe^{3+} + 2H_2S\uparrow \quad (2.59)$$

$$Cu^{+} + Fe^{3+} = Cu^{2+} + Fe^{2+} \quad (2.60)$$

Part of the Cu^{2+} is precipitated by H_2S through a secondary reaction taking place on the surface of chalcopyrite:-

$$Cu^{2+} + H_2S = CuS\downarrow + 2H^+ \qquad (2.61)$$

The overall equation for the double reaction of "acid-precipitation"[152] resulting from these reactions is therefore:-

$$CuFeS_2 + 2H^+ = CuS\downarrow + Fe^{2+} + H_2S\uparrow \qquad (2.62)$$

Oxidation of $CuFeS_2$ and CuS takes place according to the reactions:-

$$CuFeS_2 = Cu^{2+} + Fe^{2+} + 2S^\circ\downarrow + 4e \qquad (2.63)$$

$$CuS = Cu^{2+} + S^\circ\downarrow + 2e \qquad (2.64)$$

Warren et al[148-150] proposed an alternative mechanism for the formation of CuS whereby their postulated initial intermediate sulphide phase, S_1 (formed by reaction 2.58), oxidised to from a second intermediate non-stoichiometric product phase, S_2, by the reaction:-

$$Cu_{1-x}Fe_{1-y}S_{2-z} = (2-z)CuS(n-s) + (1-y)Cu^{2+} + (1-y)Fe^{2+} + 2(1-y)e \qquad (2.65)$$

Reaction (2.65) is consistent with the results of Bauer et al[158] who demonstrated that after 8 minutes at 27 °C the rates of copper and iron release were approximately equal. The corrosion or dissolution of the S_2 layer would occur at low potentials by the reaction:-

$$CuS(n-s) = Cu^{2+} + S^\circ + 2e \qquad (2.66)$$

They suggested that the two intermediate product phases, S_1 and S_2, are bornite and covellite respectively, as could be predicted from the potential versus pH diagram for the Cu-Fe-S-H_2O system[61,64,65].

The nature of the product layer has been further investigated by studying the rate of electron transfer from various redox couples

(I_3^-/I^-, Fe^{3+}/Fe^{2+}, Cu^{2+}/Cu^+) to the surface layer[160,161,164]. Parker et al[160,161] showed the Fe^{3+}/Fe^{2+} couple (especially in sulphate media) to be much less reversible on corroding chalcopyrite than on pyrite or platinum. The couples Cu^{2+}/Cu^+, I_3^-/I^- and $Fe(CN)_6^{3-}/Fe(CN)_6^{4-}$ were more reversible than Fe^{3+}/Fe^{2+}, but all couples were much less reversible on chalcopyrite than on pyrite. MacKinnon et al[164] used cyclic voltammetry to compare electron transfer from redox couples to Pt, n- and p-type chalcopyrite. They obtained similar results to Parker et al[160,161] and found no differences in the results between n- and p-type samples with one notable exception. They found that Fe^{3+}/Fe^{2+} species passivated the surface of p-type chalcopyrite in the potential region where electron transfer readily occurs to the I_3^-/I^- and Cu^{2+}/Cu^+ redox couples. Passivation did not occur on n-type chalcopyrite.

(b) Processes at High Anodic Potentials (> 0.9 V vs. S.H.E.)

At higher potentials (> 0.9 V vs. S.H.E.) the low anodic potential processes still occur, but the amount of product formed is negligible compared with the amount of $CuFeS_2$ oxidised completely to Cu^{2+} and Fe^{3+}. In the high potential region the reactions are strongly pH sensitive, the anodic current increasing with increasing pH[149]. The main reactions are:-

$$CuFeS_2 = Cu^{2+} + Fe^{3+} + 2S^\circ + 5e \qquad (2.67)$$

$$\text{and } CuFeS_2 + 8H_2O = Cu^{2+} + Fe^{3+} + 2SO_4^{2-} + 16H^+ + 17e \qquad (2.68)$$

If x is the fraction of chalcopyrite oxidised according to reaction (2.67), the composite equation for the total process is[167]:-

$$CuFeS_2 + 8xH_2O = Cu^{2+} + Fe^{3+} + 2xSO_4^{2-} + 2(1-x)S^\circ + 16H^+ + (12x + 5)e \qquad (2.69)$$

By measuring the charge passed per mole of dissolved iron or copper, the current efficiency for the formation of sulphur (reaction 2.67), or sulphate (reaction 2.68), can be calculated. Warren et al[148-150] calculated the average amount of sulphur formed for all experiments run in H_2SO_4 electrolytes to be 90 %, and 88 % for both H_2SO_4 and $HClO_4$. This compares with the value of 88 % predicted by Biegler and Swift[167] and 90 % calculated by Jones[145-147] for acid chloride media. Warren et al[148-150] proposed that the intermediate product layer, S_2 (CuS(n-S)), corrodes at the higher anodic potentials by the reaction:-

$$CuS(n\text{-}s) + H_2O = Cu^{2+} + 1/4SO_4^{2-} + 3/4S^\circ + 2H^+ + 7/2e \quad (2.70)$$

Biegler et al[167] and Hillrichs et al[159] suggested that breakdown of the passive film occurs during electrochemical polarisation when a critical potential is reached, which activates the nucleation and growth of pits.

In alkaline solutions, Gardner and Woods[175] proposed the formation of ferric hydroxide and covellite at low anodic potentials:-

$$CuFeS_2 + 3H_2O = CuS + Fe(OH)_3 + S + 3H^+ + 3e \quad (2.71)$$

followed by the further oxidation of covellite at higher potentials to yield sulphur and cupric hydroxide:-

$$CuS + H_2O = Cu(OH)_2 + S + 2H^+ + 2e \quad (2.72)$$

Springer[124] briefly considered the semiconducting properties of chalcopyrite. For an n-type semiconductor one would expect to find a limiting current on anodic polarisation if minority carriers (holes) were determining the oxidation rate, however, he could find no saturation current on anodically polarising chalcopyrite samples with currents up to 10 mA cm^{-2}. Biegler and Swift[167] observed that there were no differences in cyclic voltammograms obtained in the dark and with illumination. However, Zevgolis[162,163] has reported a

saturation current (in 1 M H_2SO_4) of approximately 50 mA cm^{-2} at potentials above 2.5 V vs. S.H.E.. Unfortunately, the anomously high potentials quoted (0 - 14 V) suggests that there was a large IR potential drop, or contact resistance, across the experimental specimens. Also, illumination of the rear rather than the working surface of the electrode, limits the confidence with which one can interpret the results.

The cathodic dissolution of chalcopyrite has been studied almost exclusively by Biegler and co-workers[179-182]. E_h-pH diagrams for chalcopyrite[61,64,65] predict that in solutions of about zero pH, the copper-containing solid phases found at equilibrium at progressively decreasing potentials are chalcopyrite, bornite (Cu_5FeS_4), chalcocite (Cu_2S) and elemental copper, in that order. The possible cathodic reactions are [178]:-

$$5CuFeS_2 + 12H^+ + 4e = Cu_5FeS_4 + 6H_2S + 4Fe^{2+} \qquad (2.73)$$

$$2CuFeS_2 + 6H^+ + 2e = Cu_2S + 3H_2S + 2Fe^{2+} \qquad (2.74)$$

$$CuFeS_2 + 4H^+ + 2e = Cu + Fe^{2+} + 2H_2S \qquad (2.75)$$

Biegler and Swift[179] cathodically reduced chalcopyrite electrodes in several acidic electrolytes and found that at current densities below 10 mA cm^{-2} the product is generally the grey copper sulphide, chalcocite (Cu_2S), though in some runs the closely related sulphide djurleite ($Cu_{1.97}S$), distinguishable only by X-ray diffraction, was found. At higher current densities elemental copper is formed and becomes the major component of the product above 50 mA cm^{-2}. Experimentally, copper was observed to appear when the potential reached about -0.4 V vs. S.H.E.. Examination of the electrodes in section showed that copper formed at the solution side of the chalcocite layer, indicating that chalcocite is an intermediate in the reduction to copper (reaction 2.76)[179].

$$Cu_2S + 2H^+ + 2e = 2Cu^\circ + H_2S \qquad (2.76)$$

Bornite was not detected in any of the products of galvanostatic electrolysis.

Macleod and Muir[183] studied the reduction of chalcopyrite in copper (I) solutions and found that polished sections of the product revealed distinct reaction zones. Electron microprobe X-ray analysis confirmed that the outer layer consisted mainly of Cu_2S, followed by an inner layer of Cu_5FeS_4, then copper enriched $CuFeS_2$, and finally a core of unreacted $CuFeS_2$. Biegler[182] observed that the first cathodic linear sweep voltammogram of a freshly polished chalcopyrite electrode exhibited a prewave between -0.05 and -0.2 V vs. S.H.E., preceding the main voltammetric wave for reduction to chalcocite (Cu_2S). It was suggested that the prewave represented the formation of an intermediate product phase(s) in the overall reduction to chalcocite. A general electrode reaction was proposed to represent the cathodic prewave process[182]:-

$$CuFeS_2 + (4-2z)H^+ + (2x+2y-2z)e = Cu_xFe_6S_z + (1-x)Cu^{2+} + (1-y)Fe^{2+} + (2-z)H_2S \qquad (2.77)$$

where $x+y > z$. Possible products that fulfil this condition include bornite (Cu_5FeS_4), haycockite ($Cu_4Fe_5S_8$), mooihoekite ($Cu_9Fe_9S_{16}$), idaite (Cu_3FeS_4), fukuchilite (Cu_3FeS_8), djurleite ($Cu_{1.97}S$) and digenite ($Cu_{1.8}S$)[179,182,184].

2.4.2 Cathodic Reduction of Oxygen

The electrochemical mechanisms that underlie the weathering of sulphides in nature[98,118,130,131], leaching of sulphides in hydrometallurgical systems[189] and the production of mineral sulphide concentrates by froth flotation[72,190] all involve corrosion-like processes consisting of coupled anodic and cathodic reactions. The reduction of dissolved oxygen is the most important cathodic process in these systems. Although it has been shown that oxygen is reduced on galena[191] and pyrite[66,192], an analysis of the kinetics and mechanism of the reaction has been carried out only by Biegler, Rand

and Woods[185-188]. Firstly, they studied oxygen reduction at a rotating pyrite electrode[186] and demonstrated that the overall reaction involves four electrons. In acid solution the reaction is:-

$$O_2 + 4H^+ + 4e = 2H_2O$$

$$E = 1.229 - 0.0592\ pH + 0.0148 \log P_{O2} \qquad (2.78)$$

and in alkali media:-

$$O_2 + 2H_2O + 4e = 4OH^- \qquad (2.79)$$

Experiments indicated that the reaction proceeded via the formation of hydrogen peroxide, which was detected in solution[186]:-

$$O_2 + 2H^+ + 2e = H_2O_2$$

$$E = 0.695 - 0.0592\ pH + 0.0296 \log \frac{P_{O2}}{[H_2O_2]} \qquad (2.80)$$

$$H_2O_2 + 2H^+ + 2e = 2H_2O$$

$$E = 1.763 - 0.0592\ pH + 0.296 \log [H_2O_2] \qquad (2.81)$$

In acid solution, a Tafel slope of 120 mV per decade was observed indicating that the first electron transfer step:-

$$O_2 + e = O_2^- \qquad (2.82)$$

was rate-determining. At higher pH values the Tafel slope decreased, consistent with the subsequent reaction step:-

$$O_2^- + 2H^+ + e = H_2O_2 \qquad (2.83)$$

becoming important. The following stage, hydrogen peroxide reduction, gave a Tafel slope of 245 mV per decade.

No correlation between electrochemical behaviour and semiconductor-type for oxygen reduction on pyrite could be established[187]. Rand[188] presented current-potential curves for a range of sulphide electrodes which showed that pyrite and pentlandite are only slightly less active for oxygen reduction than gold. At pH 9.06, the activity for oxygen reduction increased in the order galena < pyrrhotite < arsenopyrite < bornite < covellite < chalcopyrite < pentlandite < chalcocite < pyrite. With the exception of galena, this is the reverse of the order for oxygen requirement in flotation with xanthate collectors as reported by Plaksin and Bessonov[193]; galena requires the least amount of oxygen. The anomaly can be explained by the different constitution of its hydrophobic surface; galena being rendered hydrophobic by a chemisorbed xanthate layer, whereas dixanthogen is the important hydrophobic rendering species for the other sulphides[72]. Thus, Rand[188] suggested that the activity of the sulphide surfaces for xanthate oxidation is similar and that differences in the rate of formation of dixanthogen and hence flotation are determined by differences in the activity for oxygen reduction.

Behnet et al[194] studied the oxygen reduction activity of thiospinels and sulphides of transition metals. They found that the metals cobalt, iron and nickel showed the highest activity in sulphur compounds; other transition metals decreased the activity. An interpretation of the results in terms of the geometric and electrostatic properties of the structures was presented.

Tributsch[195-197] used metal sulphide electrodes for the reduction of hydrogen peroxide, an intermediate in the reduction of oxygen. On copper (I)-containing sulphides (viz Cu_5FeS_4, $CuFeS_2$ and Cu_2S) high amplitude and frequency current oscillations were observed under potentiostatic conditions. It was concluded that monovalent Cu^+ ions were the essential sites for the proposed autocatalytic decomposition mechanism.

2.4.3 Non-Oxidative Dissolution

The dissolution of a sulphide mineral may also occur by a non-oxidative process. This may be defined as dissolution resulting in the oxidation state of the solute species being identical in both the solution and solid state[205]. For a sulphide mineral, the process involves liberation of hydrogen sulphide according to the reaction:-

$$MS + 2H^+ = M^{2+} + H_2S \qquad (2.84)$$

Non-oxidative dissolution has been extensively reviewed by several authors[199,200,209-211] and has been proposed as a means of leaching metals from sulphide ores[198]. Indeed, the non-oxidative dissolution of copper-nickel-iron mattes, which contain metal sulphide phases, is operated industrially on a large scale[207,208].

Under non-oxidising conditions, chalcopyrite, pyrite and pentlandite respond very slowly to attack by acids. Jibicki[200] reported that pentlandite dissolves 60 times slower than pyrrhotite under the same acid leaching conditions. Nothing has been published on the non-oxidative dissolution of pyrite and chalcopyrite, except on "activation processes" that create acid leachable mineral phases on the surfaces of these minerals, thereby enhancing the overall dissolution rate[103].

Peters[65] proposed four acid decomposition reactions for chalcopyrite on the basis of thermodynamic considerations, although in practice none of the proposed reactions have been observed. The most probable of these reactions was:-

$$CuFeS_2 + 2H^+ = CuS + Fe^{2+} + H_2S \qquad (2.85)$$

because, unlike the other reactions, it did not require the nucleation of pyrite or excessively low pH values. An acid decomposition reaction for pyrite was also proposed[65]:-

$$FeS_2 + 2H^+ = Fe^{2+} + H_2S + S^\circ \qquad (2.86)$$

The initial step involves the release of disulphide ion S_2^{2-} into solution followed by its disproportionation to yield H_2S and S°. Therefore, the overall reaction (2.86) is not a non-oxidative process in the true sense, as the formal oxidation of the sulphur species in the solid and solution phases is different.

The kinetics and mechanism of the non-oxidative dissolution of iron sulphides has been studied by a number of workers[200-205]. Ingraham et al[201] measured the dissolution rate of non-stoichiometric pyrrhotite under non-oxidising conditions in aqueous solutions containing hydrochloric acid. The amount of elemental sulphur formed was found to be directly proportional to the non-stoichiometry of the pyrrhotites, suggesting the dissolution reaction:-

$$FeS_x + 2H^+ = Fe^{2+} + H_2S + (x-1)S^\circ \qquad (2.87)$$

(where $1 \leq x \leq 1.143$). Van Weert et al[202] investigated the kinetics of the dissolution of pyrrhotite concentrates in 6 to 8 M HCl at temperatures between 60 and 90 °C. They observed that rapid dissolution with the evolution of H_2S was preceded by an "induction period", during which no H_2S was evolved, although some iron dissolved slowly. The length of the induction period decreased at higher acid concentrations and at higher temperatures. It was attributed to the effect of an inhibiting layer of sulphur formed by H_2S oxidation at the pyrrhotite surface, effected by ferric ions released into solution by the preferential dissolution of the 8 to 10 % magnetite (Fe_3O_4) contained in the samples. However, no sulphur was detected on the surfaces of the pyrrhotite particles and the results could equally well be explained by assuming that only magnetite dissolved during the induction period[205].

An induction period prior to pyrrhotite dissolution has been observed by other workers[200,201,204], and also prior to the dissolution of nickel sulphide concentrates[205]. Some reports favour the formation

of an inhibiting sulphur layer as being responsible for the induction period[201,202,205], whereas others[200,204] suggest surface oxidation, forming a relatively insoluble film, to be the cause.

Yazawa and Eguichi[204] found a correlation between the length of the induction period and the amount of oxygen consumed on the pyrrhotite surface during oxidation. Oxygen consumption was measured by weighing the amount of H_2O formed during hydrogen reduction of the partially oxidised pyrrhotite. Jibiki[200] found that the dissolution rate of various iron and nickel sulphides was strongly dependent on the electrochemical potential of the sulphides.

Similar results were obtained by Nicol and Scott[143,205,210,211]. They found that for synthetic electrodes of troilite (FeS) and hexagonal pyrrhotite (Fe_9S_{10}) the dissolution rate in 0.1 M HCl at 25 °C increased rapidly with decreasing potential to a maximum value at about -0.3 to -0.4 V vs. S.C.E, below which it decreased slowly with decreasing potential. Over the range of potentials in which non-oxidative dissolution occurs, small steady-state cathodic currents were observed. A direct proportionality between the measured dissolution rates and the cathodic currents was found, the ratio of which was consistent with the following reactions[211]:-

$$Fe_{1-x}S + 2xH^+ + 2xe = (1-x)FeS + xH_2S \qquad (2.88)$$

$$(1-x)FeS + 2(1-x)H^+ = (1-x)Fe^{2+} + (1-x)H_2S \qquad (2.89)$$

They suggested that only an FeS compound that was exactly stoichiometric would dissolve in acid solutions by the transfer of Fe^{2+} and S^{2-} ions across the interphase[205]. The rapid increase in dissolution of all sulphur-rich sulphides at potentials between -0.1 V and -0.2 V vs. S.C.E. was determined by the potential dependence of the rate of reduction to the stoichiometric compound, in accordance with reaction (2.88). At potentials between -0.2 and -0.35 V the rate was governed by both the reduction and the rate of the ionic-charge transfer reaction (equation 2.89). Finally, at potentials < -0.35 V,

the rate of dissolution was controlled by the rate of ionic charge transfer alone.

The small dependence of this rate on potential, and its approximately half-order dependence on the acidity[211], is consistent with that predicted for ion transfer across the solid-liquid interface by Vermilyea's theory[212], in which the rate of anion transfer is first-order with respect to H^+. This implies that HS^- is the species transferred across the interface, as was originally suggested by Tewari and Campbell[203]. It reacts rapidly with further H^+ to form H_2S (at pH values < 7). The results of Nicol and Scott[205,211] indicate that some cathodic process is a prerequisite for the dissolution of apparently stoichiometric troilite (FeS). In an earlier paper, this was interpreted in terms of the reduction troilite to form a non-stoichiometric iron-rich surface intermediate, viz mackinawite
(FeS_{1-x} where $0.7 \geq x \geq 0.4$), by the reaction:-

$$FeS + 2xH^+ + 2xe = FeS_{1-x} + xH_2S \qquad (2.90)$$

followed by non-oxidative dissolution[143]. However, in recent work[205,210], it is proposed that the synthetically prepared troilite is a slightly non-stoichiometric iron-deficient compound at the solid/solution interface, i.e. $Fe_{1-x}S$, where x is very small. The reaction mechanism is therefore the same as for hexagonal pyrrhotite i.e. reactions (2.88) and (2.89).

It is apparent from these reports that much still remains to be resolved in terms of the mechanisms of these apparently simple reactions. There is no doubt that an induction period involving a cathodic process is a prerequisite for dissolution. However, the nature of the process is still in doubt. The induction period may remove an inhibiting sulphur layer[201,202,205], an insoluble oxide layer[200,204], or it may reduce the non-stoichiometry of the sulphide to produce an exactly stoichiometric compound at the surface which then dissolves by the mechanism of ionic charge transfer[143,205,210,211].

2.4.4 Electrolytic Treatment of Sulphides

The direct electrolysis of sulphide mattes or concentrates to produce electrowon metal and elemental sulphur and/or hydrogen sulphide, as a commercial hydrometallurgical process, have been reviewed by several authors[213-216]. The electrochemical mechanism in acidic electrolyte, when the sulphide is made the anode, may be represented by the reaction:-

$$\text{Anode:} \quad MS = M^{2+} + S^{\circ} + 2e \qquad (2.91)$$

Elemental sulphur remains adhering to the anode and the metal ions in solution deposit at the cathode (reaction 2.92).

$$\text{Cathode:} \quad M^{2+} + 2e = M \qquad (2.92)$$

When the metal sulphide is made the cathode, metal forms at the cathode according to [213]:-

$$MS + 2e = M + S^{2-} \qquad (2.93)$$

$$S^{2-} + 2H^{+} = H_2S \qquad (2.94)$$

Much less attention has been given to the cathodic dissolution route.

The processing of metal matte anodes has been successfully used on an industrial scale by I.N.C.O. in Manitoba, Canada[217,281,222], Shimura Nickel Company in Tokyo, Japan[219], Norilsk Mining and Metallurgical Combine in USSR[220], and Englehard Minerals and Chemical Corporation in Newark, New Jersey, USA[221]. Numerous attempts have been made to apply the technique to compacted sulphide anodes other than nickel, especially to copper sulphides[166,223-232]. However, efficient operation of matte dissolution processes are restricted by the brittle nature of the matte anodes, the relatively small surface area of the anodes per unit cell volume, the large amounts of anode residues produced, and the high cost of excessive polarisation at the anode, due to the formation of a non-conducting sulphur layer[216].

Studies of the electrochemical dissolution of chalcocite and covellite anodes have shown that after a period of uniform electrolysis, the cell voltage rises sharply. Etienne[228] proposed a mechanism whereby diffusing copper ions crystallise in fissures and cracks deep in the oxidising anode. This creates a large resistance to the flow of ionic current between the faradaic surfaces at the bottom of the fissures and the aqueous electrolyte; hence the rise in anodic potential.

Results showed that the time at which the cell voltage rose sharply and the current efficiency, increased with decreasing current density[223-232]. It was found that current densities less than 1 mA cm^{-2} were needed to avoid the increase in cell voltage. Compared with typical commercial electrorefining current densities of 20 to 40 mA cm^{-2}, the length of time needed to complete oxidation would prove uneconomic[232] at a current density less than 1 mA cm^{-2}.

An alternative approach is the direct electrochemical dissolution of metals from sulphide suspensions. This bypasses the problem of casting sulphide anodes and the large surface area to unit volume of the slurry means that low current density processes become economic. The anodic dissolution of chalcocite and covellite slurries has been studied by MacKinnon[233,234] and Cole[235]. Chalcocite dissolution was inhibited after about 50 % copper extraction by the evolution of oxygen gas at the feeder electrode[233] and covellite dissolution was accompanied by oxygen evolution except at unrealistically low applied currents[234]. However, the electrolytic production of chemical oxidants (Cl_2, Br_2) in situ at the feeder electrode resulted in the anodic dissolution of covellite proceeding at an acceptable current density.

The anodic dissolution of chalcopyrite in sulphuric acid by slurry electrolysis, was investigated by Oki and Ono[237]. A current efficiency for copper (II) dissolution of 80 - 90 % was reported. Illangovan et al[236] added a chemical oxidant ($FeCl_3$) to a sulphuric acid electrolyte to complement direct electrochemical dissolution. The "Cymet process"[112,113], described in Section (2.3.4), utilises a similar process route.

As mentioned earlier, little attention has been given to the cathodic process route, probably because any process route would have to deal with the treatment of the cathodic gases, hydrogen sulphide and hydrogen, and in hydrochloric acid, the anodic gas chlorine. However, Biegler and Constable[180,181] have studied the cathodic electrolysis of a chalcopyrite slurry and reported that 95 % of the chalcopyrite was reduced to chalcocite at a current efficiency of about 50 %. More recently, House[353] studied the alteration of chalcopyrite when contacted with electrogenerated reductants, such as Cr(II) solution. He also found that chalcopyrite was reduced mainly to chalcocite.

2.4.5 Galvanic Effects Among Sulphides

The relatively high electronic conductivity of sulphide minerals suggests the possibility of galvanic action between different sulphide particles, similar to galvanic corrosion between metals. The conditions for a galvanic interaction requires that the conducting minerals of different rest potentials be in electronic contact. When in contact, the material with the lower rest potential will react anodically, imposing cathodic behaviour on the material with the more noble rest potential.

The rest potentials of sulphide minerals at pH 0 and pH 4, gathered from various sources, have been presented by Majima[189,238]. In the presence of oxygen, pyrite has been observed to have the noble rest potential of all sulphides, and acts as a cathode for the reduction of oxygen, increasing the corrosion of mineral sulphides in galvanic contact with it. Gottschalk and Buehler[122] found that galena, sphalerite and covellite oxidise 8 to 20 times faster when pyrite is present. These results were confirmed by Peters and Majima[241]. Berry et al[240] have reported that galvanic contact between chalcopyrite and pyrite enhanced the leaching of chalcopyrite during the bacterial leaching of low-grade waste. Galvanic conversion of chalcopyrite to chalcocite by the interaction with copper metal has also been investigated[239].

An important consequence of galvanic interaction in the selective flotation of complex sulphide ores, was mentioned by Majima[238]. He argued that difficulties in selective flotation of such ores in acidic media containing some pyrite, may be partly due to the accelerated formation of hydrophobic sulphur on the sulphide particles, due to their galvanic interaction with pyrite.

CHAPTER THREE

EXPERIMENTAL MATERIALS

CHAPTER THREE : EXPERIMENTAL MATERIALS

3.1 Origin of the Samples

The pyrite sample was of Spanish origin and obtained from Gregory Bottley Limited, UK. Falconbridge Nickel Mines Limited supplied samples of high grade pentlandite and chalcopyrite from their Strathcona mine on the north run of the Sudbury basin, Canada. High purity pyrrhotite from Renison, Tasmania, was obtained from the Mineral Chemistry Division of CSIRO, Port Melbourne, Australia.

All the mineral samples were received in the form of large irregularly shaped nodules. Several pieces, considered by visual examination to be representative of each mineral, were selected for characterisation. In the case of the pentlandite sample, large blocks of the host rock were attached to the pentlandite mineral. These were cut away using a diamond saw before selecting samples for mineral characterisation.

3.2 Characterisation of the Samples

3.2.1 X-ray Fluorescence Analysis

A sample of each mineral sulphide was analysed semi-quantitatively by X-ray fluorescence spectroscopy for heavy and light elements to determine the main impurities in each sample. The results are shown in Table 3.1.

3.2.2 Chemical Analysis

A sample of each sulphide mineral was digested in concentrated nitric acid[242] and the resulting solution analysed by atomic absorption spectroscopy for quantitative determination of metal impurities. Because of the larger number of possible stoichiometries for pyrrhotite (FeS, Fe_9S_{10}, $Fe_{10}S_{11}$, $Fe_{11}S_{12}$ and Fe_7S_8) and the high impurity levels in pentlandite, the major elemental components were also determined so that the exact stoichiometry of each sample could

Table 3.1 - XRF Analyses for Each Sulphide Mineral

Pyrite		Pyrrhotite		Pentlandite		Chalcopyrite	
Impurity	% in Sample	Impurity	% in Sample	Impurity	% in Sample	Impurity	% in Sample
Cu,As	0.5-5.0			Si,Cu	0.5-5.0	Ni	< 1.0
Sb,Si	0.05-0.5	Cu,Si,Ca Sn, Ba	0.05-0.5	Ca,K,Zn	0.05-0.5	Si,Ca,Zn	0.05-0.5
Ca,K,Ti,Zn	< 0.05	Ni,K,Mn	< 0.05	Ti, Mn	< 0.05	K	< 0.05

Table 3.2 Chemical Analysis of Sulphide Minerals

Element	Wt % in Sample			
	Pyrite	Pyrrhotite	Pentlandite	Chalcopyrite
Cu	1.79 ± 0.05	0.35 ± 0.01	1.22 ± 0.10	*
As	0.55 ± 0.03	*	*	*
Fe	*	56.51 ± 0.15	31.47 ± 0.06	*
S	*	35.87 ± 0.15	26.24 ± 0.05	*
Ni	*	*	28.98 ± 0.05	0.75 ± 0.01

* Not analysed for

be obtained. The results of chemical analyses on each sulphide mineral with the 95 % confidence limits are given in Table 3.2.

The ratio of iron to sulphur gave a non-stoichiometric value of the pyrrhotite sample of $Fe_{0.905}S$, assuming that all the iron and sulphur was in the pyrrhotite phase. Similarly, the pentlandite content of the sample was 84.43 % assuming all the nickel was present in the pentlandite phase, and that its stoichiometry was $(Fe_{4.5},Ni_{4.5})S_8$.

3.2.3 X-ray Diffraction Analysis

X-ray powder diffractometry[243] was employed to identify the main mineral phases present in each sample. The sensitivity of the X-ray powder method to the detection of small amounts of a particular mineral in a mixture depends on the minerals concerned. A well crystallised mineral with strong reflections (e.g. quartz or calcite) can often be detected at concentrations below 1 %, whereas large concentrations of poorly crystallised mineral may be undetected. Diffraction patterns were identified using the powder diffraction reference files of the Joint Committee on Powder Diffraction Standards[244].

The X-ray diffraction patterns for pyrite, pyrrhotite and chalcopyrite, did not reveal the presence of any impurity mineral phases, because the level of contamination in these minerals was below the lower detection limit of X-ray diffraction. The powder pattern for pyrrhotite exhibited only a single (102) reflection at a 2θ value for Cu K radiation of 39.8°, which was characteristic of hexagonal pyrrhotite (see Figure 3.1). Monoclinic pyrrhotite would have exhibited a doublet centred at the same 2θ value [34]. Nevertheless, a small peak at 65.5° 2θ, which was characteristic of monoclinic pyrrhotite, indicated that small amounts of monoclinic pyrrhotite may have been intergrown with the hexagonal phase (See section 2.1.1.2 and [13]).

The diffraction pattern for the pentlandite sample was identical to that of the file pattern for a pentlandite sample taken from the Frood

mine, Sudbury, Canada [244] file No. 30-657). Anomalous peaks that were not characteristic of pentlandite were attributed to a "double-chain" calcium nickel silicate ($CaNiSi_4O_{10}$), which belongs to the amphibole group (Figure 3.2).

3.2.4 Optical Examination of Polished Sections

Polished mineral sections of each sulphide were prepared and examined under reflected light. No impurity mineral phases were detected in the pyrrhotite and chalcopyrite samples.

Hewins[245] and Abel et al[246] identified the host rock of the Strathcona Cu-Ni sulphide ore body as a dark norite breccia, which is a calcic alkaline igneous rock. It was found to consist of 40% euhedral hypersthene, 15% clinopyroxene with interstitial subhedral plagioclase and minor amounts of potash feldspar, quartz and apatite[245]. Visual inspection of the Strathcona pentlandite sample revealed a sharp boundary between the grey to black medium grained host rock and pentlandite. However, examination of polished sections showed that norite was finely disseminated throughout the sample with some of the norite containing grey exsolved quartz grains (Plate 3.1, see section 3.2.5).

Polished sections of pyrite revealed no other phases except for one sample which contained a few small inclusions of ex-solved covellite (CuS): identified by their characteristic blue colour and pleochroism in reflected light[247] (Plate 3.2). This suggested that the relatively large impurity level of copper revealed by XRF and chemical analysis was due to contamination by a separate mineral phase, viz covellite, rather than by solid solution in the pyrite lattice.

3.2.5 Energy-Dispersive X-ray Analysis (EDAX)

Electron-probe X-ray microanalysis[248] provides a means of determining the chemical composition of very small areas (1 μm in diameter) at the surface of polished petrological sections.

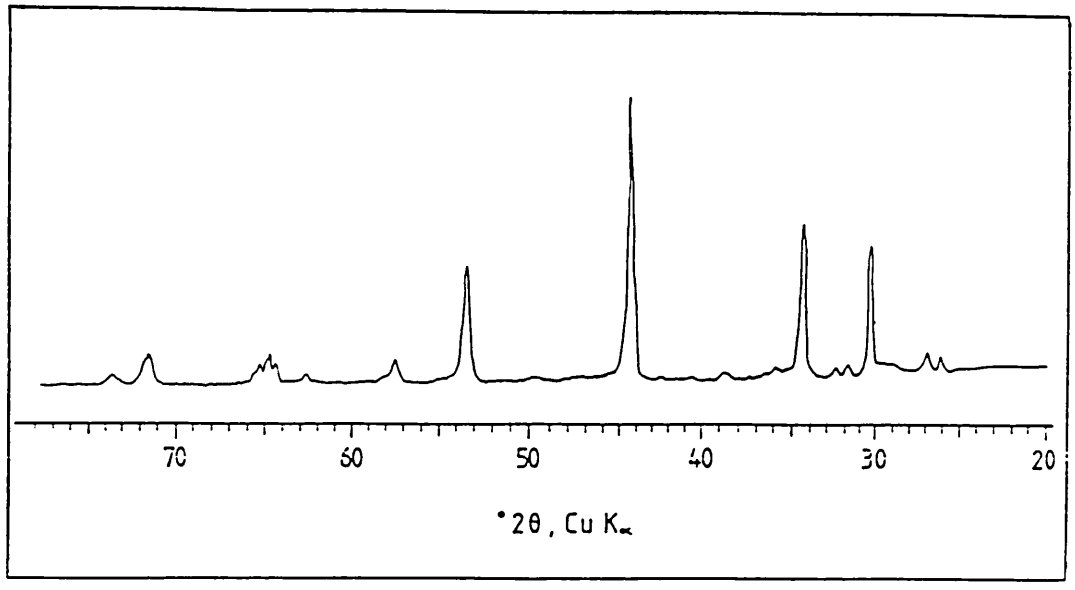


Fig 3.1 X-ray diffraction of the pyrrhotite sample from Renison, Tasmania.

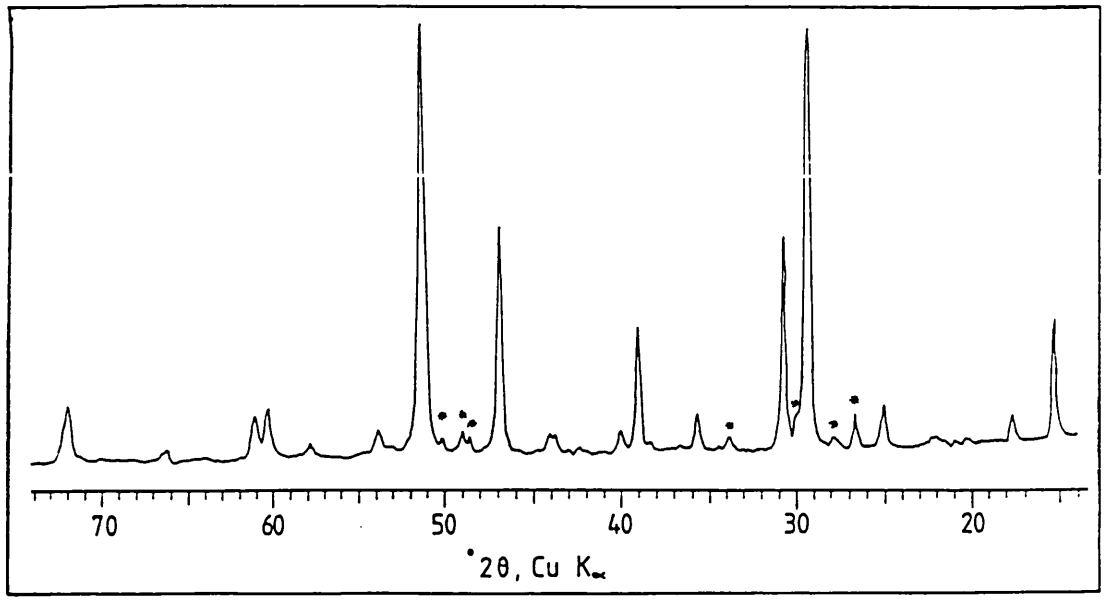


Fig 3.2 X-ray diffraction pattern of the pentlandite sample from Canada.

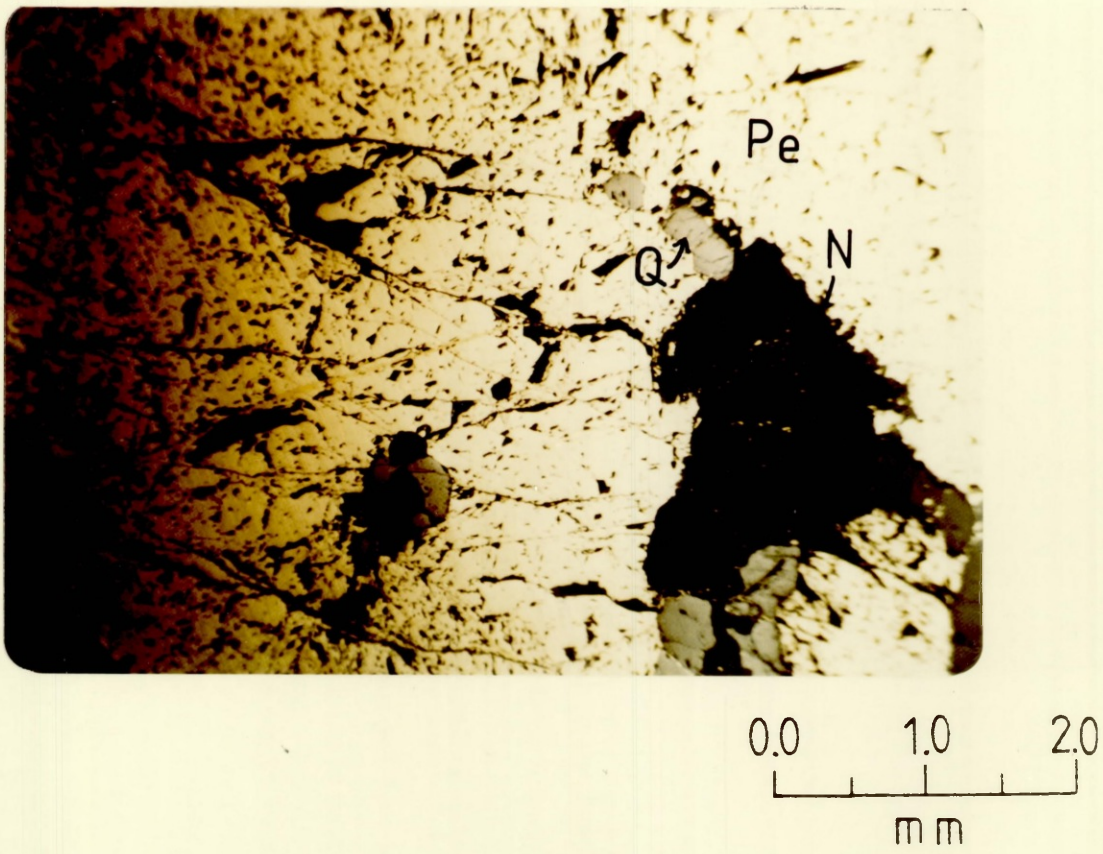


Plate 3.1 Reflected light microscope photograph of pentlandite (Pe) showing the finely disseminated norite (N) and grey exsolved quartz grains (Q).

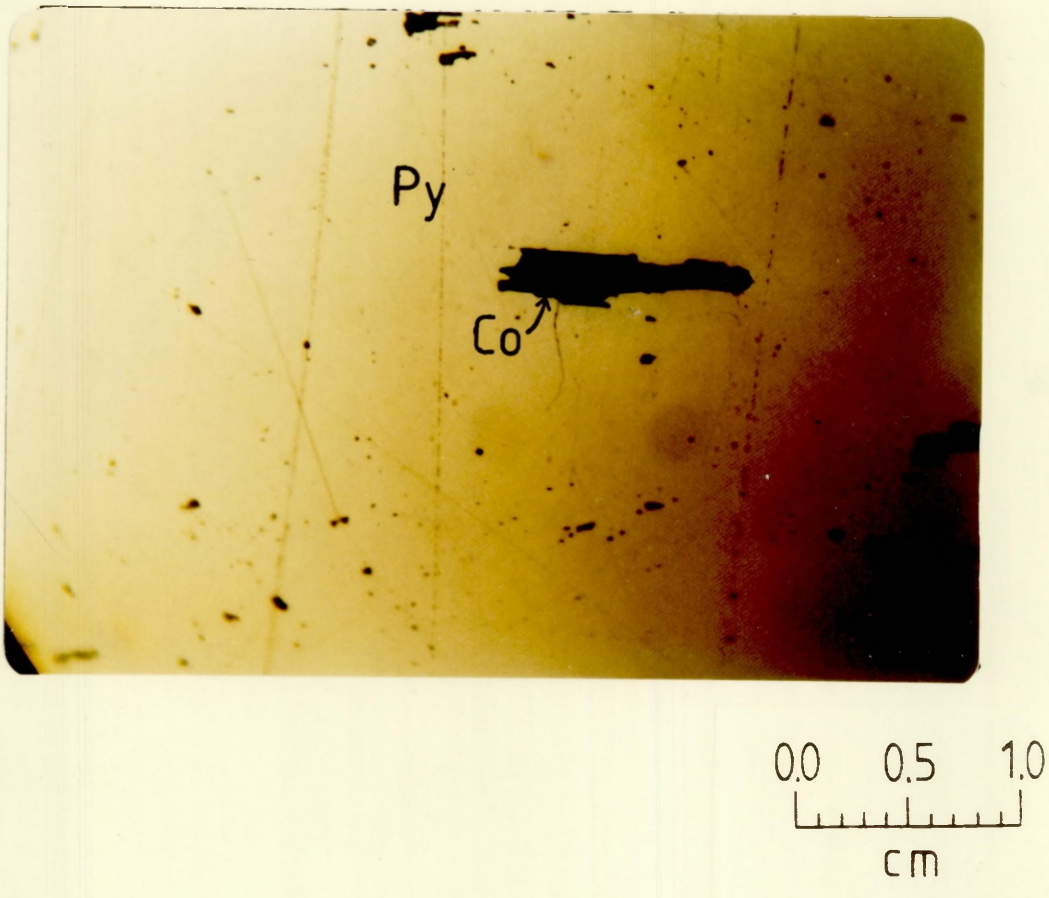


Plate 3.2 Reflected light microscope photograph of pyrite (Py) showing an inclusion of covellite (Co).

A polished section of each sulphide mineral was mounted on a stage and subjected to electron microprobe semi-quantitative analyses at constant traverse increments across the sample. A beam accelerating voltage of 20 kV, and energy dispersive analysis of X-rays (EDAX) was employed. At each traverse point the number of secondary X-rays emitted from a 6400 μm^2 area of the sample, and the energy of each X-ray was monitored over a 10 second period to produce a secondary X-ray emission spectrum. Plates 3.3 to 3.6 show typical spectra obtained from chalcopyrite and pentlandite samples at different traverse points. The emission lines characteristic of a particular element are labelled in the plates, and in the top left-hand corner the total number of X-ray counts measured during the 10 second period is shown (labelled "FS").

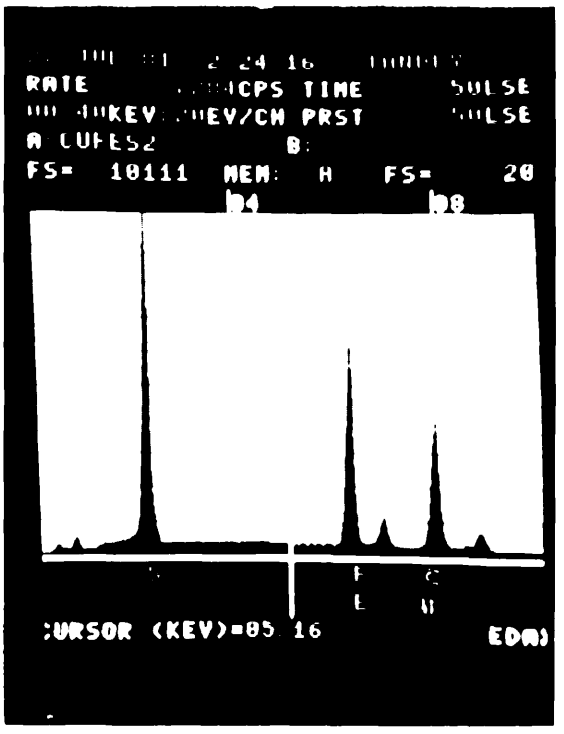
Although the height of the emission lines is proportional to elemental concentration, the measurement is only semi-quantitative, as the concentration sensitivity for each element depends on its atomic number. However, by comparing the relative peak heights the spectra did show that the metal to sulphur ratio, and for chalcopyrite and pentlandite, the metal to metal ratio, was uniform over the surface of each sulphide sample investigated.

Electron-probe X-ray microanalysis also confirmed that the grey inclusions associated with norite in the pentlandite sample, shown in Plate 3.1 (section 3.2.4), were composed entirely of pure silica.

3.2.6 Infrared Spectroscopy

The energy of most molecular vibrations corresponds to that of the infrared region of the electromagnetic spectrum. Spectra characteristic of particular structural groups are produced as a result of stretching, twisting, or bending motions induced by the incident radiation.

The use of infrared spectroscopy in mineral and inorganic compound studies has been widely discussed[249]. However, relative to other



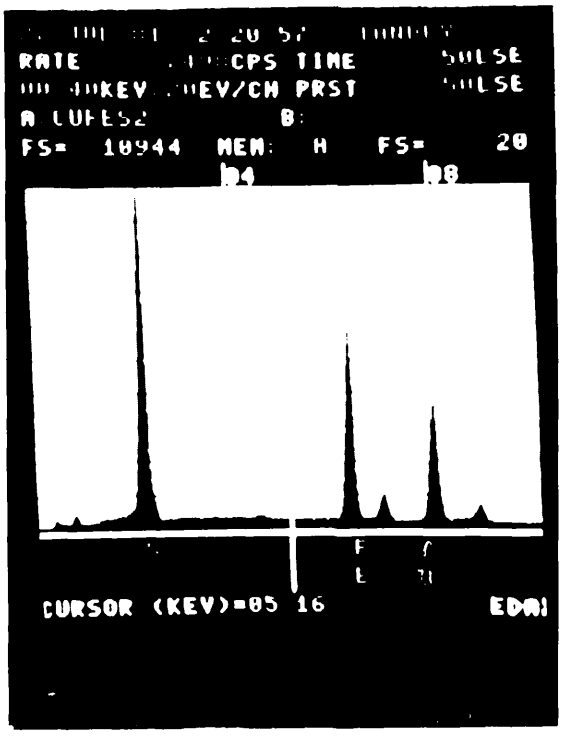
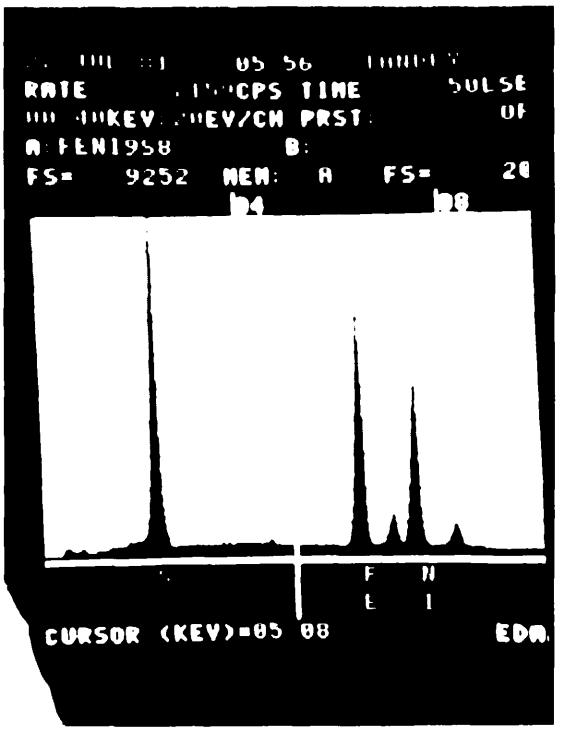


Plate 3.3 (top left) and 3.4 (top right). Typical secondary X-ray emission spectra of chalcopyrite obtained from different points on the mineral surface.



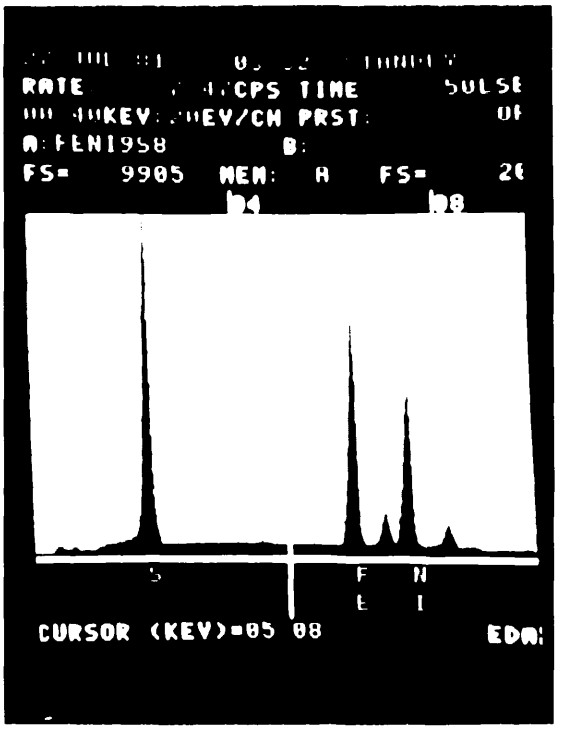


Plate 3.5 (bottom left) and 3.6 (bottom right). Typical secondary X-ray spectra of pentlandite obtained from different points on the mineral surface.

mineral groups, eg oxides and silicates, there has been little infrared absorption work on sulphide minerals[249-254]. Sulphide minerals with ionic and metallic bonding, eg pyrrhotite and pentlandite, have no fundamental vibrational absorption bands. However, minerals with some degree of covalent bonding, eg pyrite and chalcopyrite, do exhibit fairly intense infrared absorption bands. These arise from internal vibrations within a covalent group (< 450 cm^{-1}), e.g. the S_2^{2-} group in pyrite, or from external (lattice) vibrations (< 300 cm^{-1}).

If a mineral sulphide absorbs in the infrared region, infrared spectroscopy may be useful in three areas:-

1) The semiconductor band gap for a mineral sulphide can be accurately determined. Poling and Leja[255] studied the photoconductive properties of n-type PbS films using infrared spectroscopy. An absorption edge in the infrared spectrum was observed at a frequency of about 3500 cm^{-1} corresponding to the band gap of PbS (0.4 eV). Above this frequency the infrared light was strongly absorbed by excitation of electrons into the conduction band. Below the absorption edge light was absorbed by promoting electron transitions within the conduction band and by processes involving the presence of impurities in the crystals[255].

2) Sulphide minerals are frequently polymorphic, i.e. exist in more than one structural form. Structural variations are accompanied by changes in infrared spectra which are useful in characterisation. For example, cubic pyrite, which exhibits strong, moderate and weak absorption bands at frequencies of 411, 345 and 289 cm^{-1} respectively, is easily distinguished from its orthorhombic form marcasite, which displays two strong absorption bands at 418 and 396 cm^{-1} and two moderate bands at 352 and 325 cm^{-1}[254].

3) Changes in non-stoichiometry may be monitored by infrared spectroscopy. For example, stoichiometric chalcopyrite exhibits three absorption bands in the infrared, viz. a shoulder at 370 cm^{-1}, a strong absorption at 358 cm^{-1} and a moderate band at 316 cm^{-1}. However, as

the Cu content in chalcopyrite increases, the frequency of the shoulder decreases, whereas that of the strong absorption band increases[254].

Samples were prepared according to the potassium bromide method of Liese[254]. This involved mixing 0.5 mg of the fine particulate sulphide sample with 175 mg of potassium bromide and pressing the homogeneous mixture into a disc, 10 mm in diameter and 1 mm in thickness, care being taken to minimise water absorption from the atmosphere. The disc was then analysed in comparison with a blank potassium bromide disc employing a Perkin Elmer 599B infrared spectrometer.

The infrared spectra of the FeS_2 and $CuFeS_2$ samples are shown in Figures 3.3 and 3.4. The spectra confirmed that the FeS_2 sample was

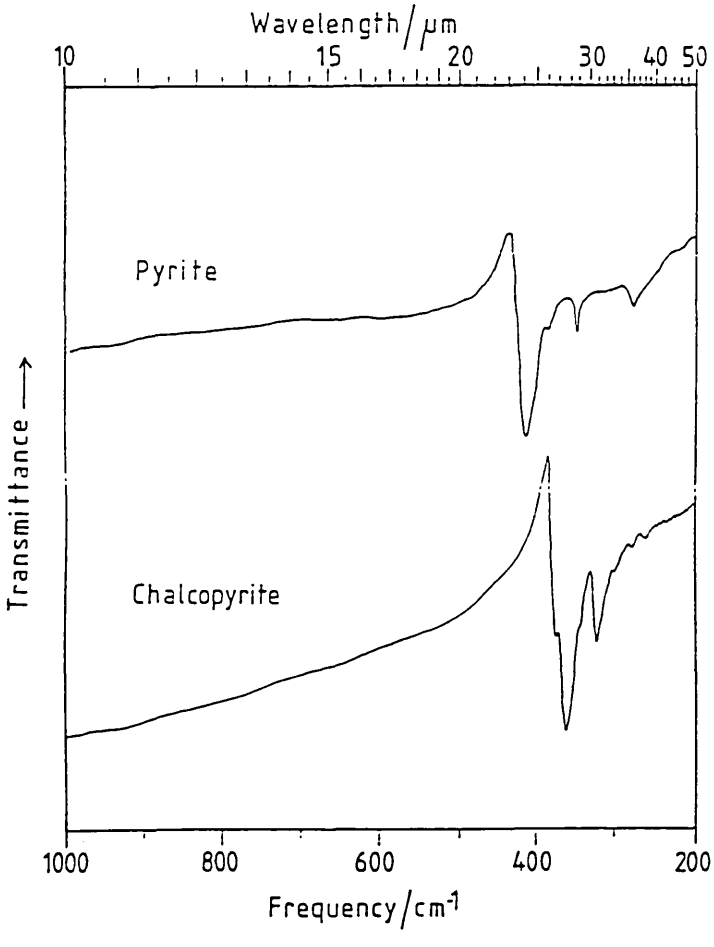


Fig 3.3 Infrared spectra of the FeS_2 sample from Spain and the $CuFeS_2$ sample from Sudbury, Canada.

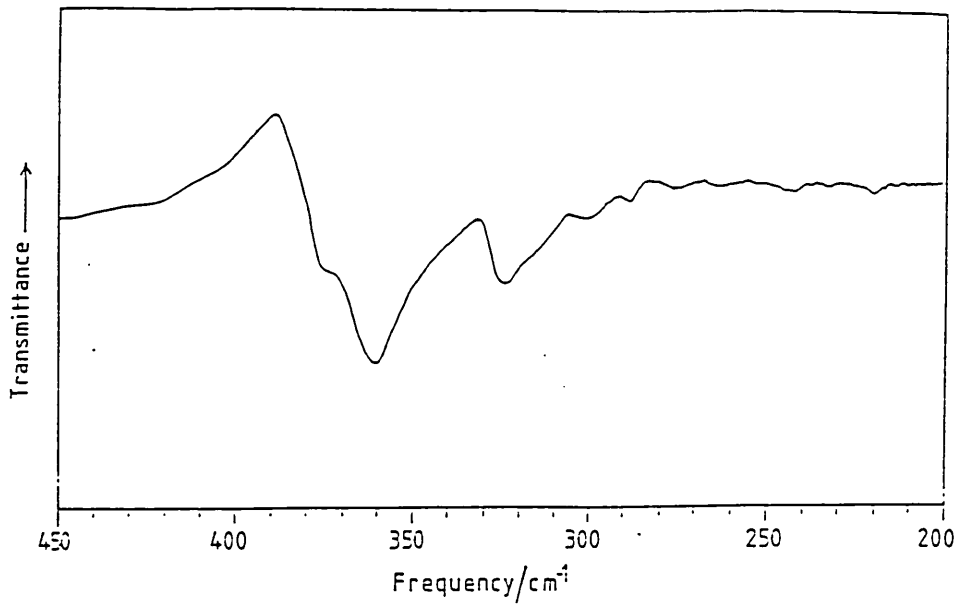


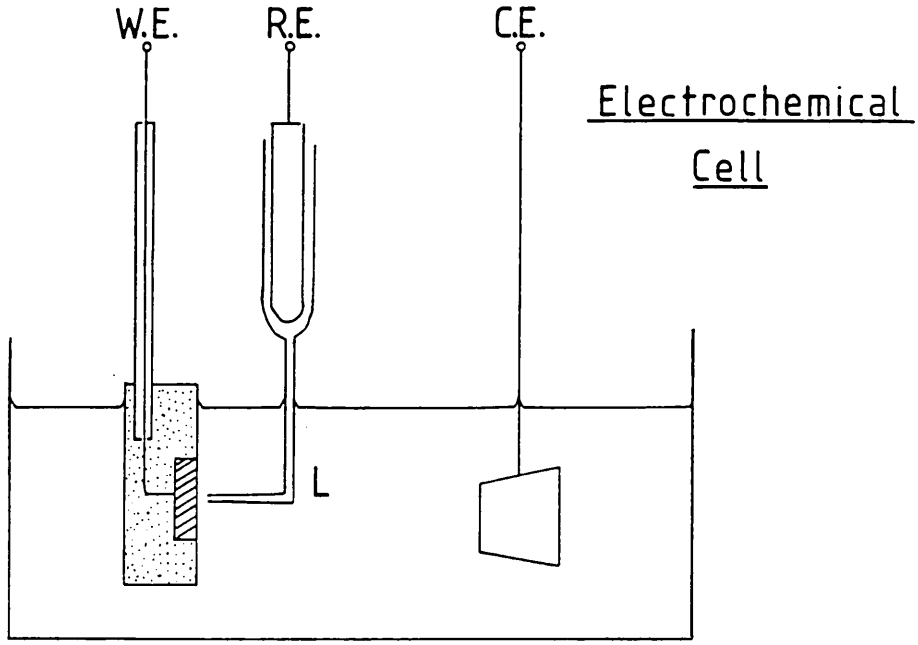
Fig 3.4 Horizontally expanded infrared spectrum of the $CuFeS_2$ sample from Sudbury, Canada

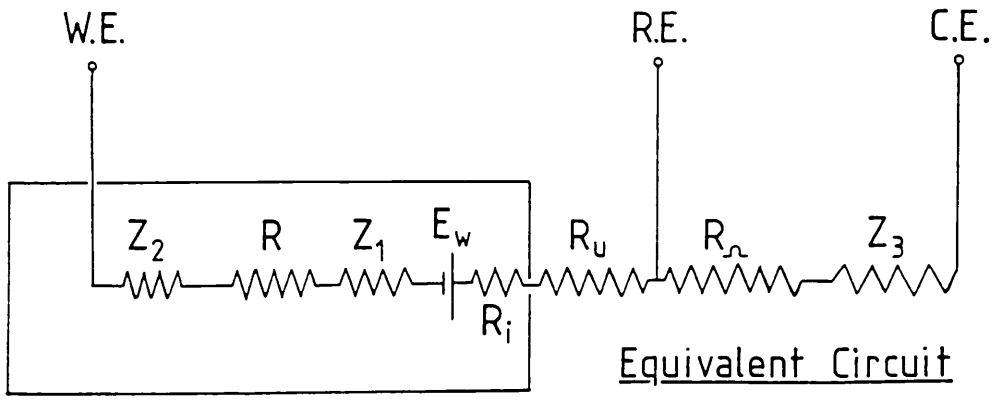
in the cubic pyrite form and that there was no copper excess in chalcopyrite.

3.2.7 Resistivity Measurements

Some sulphide minerals have low electrical conductivities, i.e. they behave as semiconductors. Therefore during potential controlled electrochemical experiments the IR potential drop across an experimental specimen may be appreciable[61]. Furthermore, non-ohmic junctions with either the current supplying electrical lead, or the electrolyte-mineral interface, may be formed[61,256,257].

Figure 3.5 shows the equivalent electrical circuit for the electrochemical cell during controlled potential experiments on sulphide minerals. Peters[61] argued that measuring the potential difference between a sulphide working electrode and a reference electrode incorporates the IR potential drops across Z_2-R-Z_1-R_i-R_u.





W.E. - Working electrode
R.E. - Reference electrode
C.E. - Counter electrode
$R_{\sim}$ - Ohmic solution resistance
R_u - Uncompensated solution resistance
R_i - Resistance of insulating film
R - Resistance of electrode
E_w - Potential of working electrode
Z_1 - Impedance of working electrode - electrolyte interface.
Z_2 - Impedance of semiconductor - metal connection with circuit.
Z_3 - Impedance of counter electrode - electrolyte interface.

Fig 3.5 Electrochemical cell and equivalent circuit for controlled potential experiments on sulphide minerals

Thus, to accurately determine the current versus voltage (I vs E) properties of the E_w-R_i-Z_1 combination, R_u, R and Z_2 should be as small as possible, or characterised as a function of current so that corrections to the I vs E measurements can be made.

The value of R_u is very small if a high concentration of background electrolyte is used and the Luggin capillary is positioned close to the working electrode. R can be reduced by thinning the electrode. Z_2 can be thought of as a non-ohmic "contact resistance", for which Berger[257] proposed two explanations.

1) In a thin surface layer of the semiconductor beneath the contact metal, the charge carrier density differs from that of the semiconductor bulk due to differences in the work functions of the metal and semiconductor, or due to surface states at the semiconductor/metal interface.

2) Layers of foreign matter (e.g. oxide layers) may sometimes impede contact of metal and semiconductor.

In cases where Z_2 is large and non-ohmic its elimination presents the greatest difficulty.

Characterisation of each mineral sulphide specimen used in electrode preparation included the experimental determination of their electrical conductivity and semiconductor-type.

Preparation involved cutting hand-picked specimens into rectangular prisms with an area between 0.4 and 1.0 cm^2 and grinding to a thickness of approximately 3 mm. The faces of each specimen were ground on successively finer grades of silicon carbide paper, down to 800 grade, taking care to avoid cracks and voids. The resistance across each specimen was obtained by clamping the sample between two brass contacts and plotting I vs E curves. An arrangement similar to that used by Lowe[256] (Figure 3.6) was employed with a Thurlby PL 320 power supply incorporating a built-in voltmeter and ammeter. From the

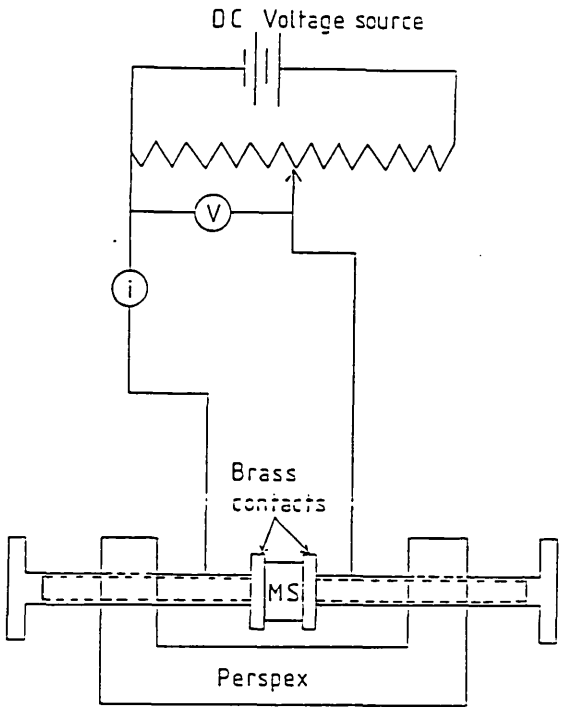


Fig 3.6 Clamp arrangement to test the contact between a mineral sulphide specimen (MS) and metal.

shape of the plots it was possible to ascertain whether a linear ohmic contact with the sample had been made, though ideally a "four point probe" method is to be preferred.

Figure 3.7 shows the typical I vs E response observed for a pyrite sample contacted to brass. The sample exhibited a non-ohmic I vs E curve with an average resistance of approximately 250 Ω between faces. This fell to about 120 Ω when the opposite faces of pyrite were vacuum sputtered with a 30 nm layer of gold, care being taken to polish off any gold deposited around the circumference. Although the contact was still non-ohmic, clearly the resistance across the pyrite sample contacted to brass was mainly due to a large contact resistance Z_2. By coating the opposite faces of pyrite with an intimate layer of gold the area of contact was increased and the contact resistance reduced.

After increasing the gold thickness to 60 nm the resistance of the sample was further reduced to about 80 Ω and an ohmic linear I vs E response observed (Figure 3.7). Further experiments showed that increasing the gold coating to thicknesses greater than 60 nm did not decrease the pyrite resistance further. Similar results were found for other pyrite and chalcopyrite samples (Figure 3.8).

Pyrrhotite and pentlandite samples behaved as metals, exhibiting high conductivities and ohmic I vs E plots (Figure 3.8). For these minerals Z_2 was negligible and gold sputtering the samples produced no measurable increase in apparent conductivity.

The type of semiconductivity of each mineral specimen was determined qualitatively using the hot-probe method[265] based on measuring the thermoelectric or Seebeck voltage. Two copper wires were placed on different areas of the sample. One of the wires was heated with a soldering iron creating a temperature gradient and the potential difference between the wires was measured (Seebeck voltage). The polarity of the thermoelectric voltage was used to determine the sign of majority carriers since electrons give rise to negative Seebeck voltages, whereas holes result in a positive potential. Details of the resistivity and type of semiconductivity are given in Table 3.3.

3.3 Other Chemicals

High purity conductivity water was used throughout the work. This was prepared by passing distilled water through a mixed bed of ion-exchange resins and then through a column of activated charcoal followed by redistillation. The conductivity of the water was less than 4.0×10^{-4} ohm^{-1} m^{-1} and bubble persistence tests[258] indicated that there were no surface active impurities present.

Nitrogen gas was supplied by the British Oxygen Company and was of their "white spot" grade (< 10 ppm oxygen). This was further purified by passing over charcoal and soda asbestos to remove organic impurities and CO_2 respectively. It was then passed through two

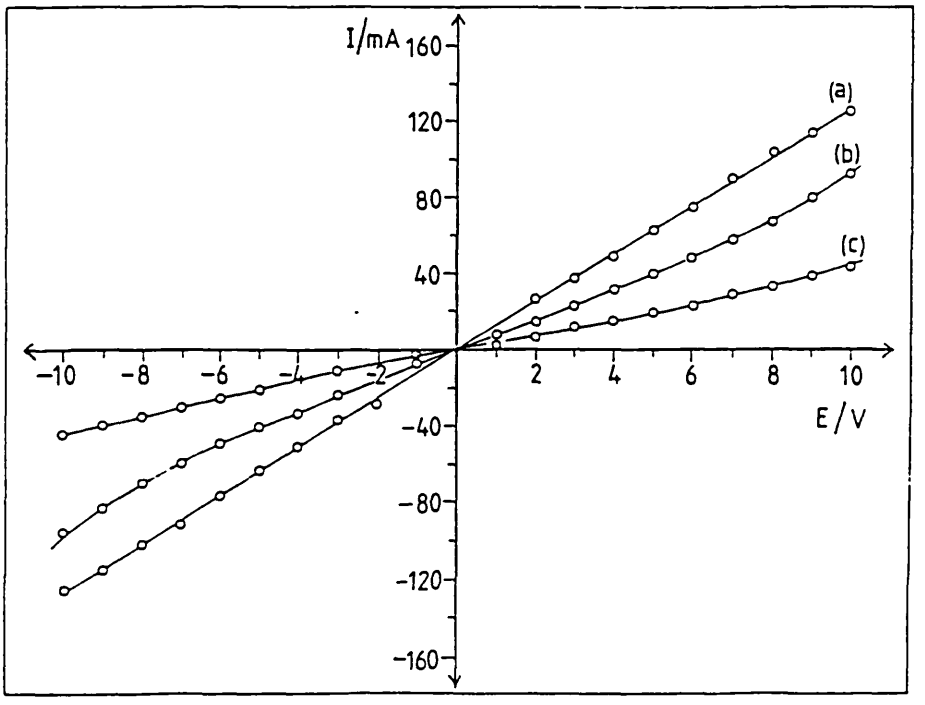


Fig 3.7 Curves of current versus voltage for the contact between pyrite and metal: (a) gold (60 nm) - pyrite; (b) gold (30 nm) - pyrite; (c) brass - pyrite.

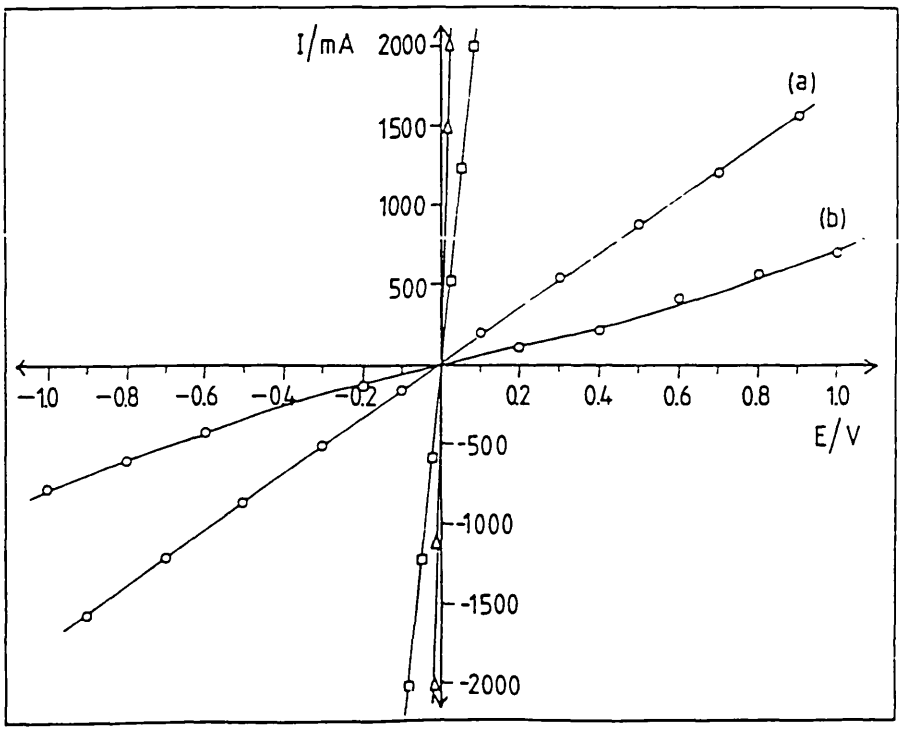


Fig 3.8 Curves of current versus voltage for chalcopyrite-metal pyrrhotite-metal and pentlandite-metal contacts: (Δ) pentlandite-brass; (□) pyrrhotite-brass; (o (a)) chalcopyrite-gold (60 nm); (o (b)) chalcopyrite-brass.

Table 3.3 Electrical Properties of Mineral Specimens

Mineral	Formula	Origin	Semiconductor Type	Resistivity (Ω m)		No of Samples
				Low	High	
Pyrite	FeS_2	Spain	All n-type	2.1×10^{-1}	2.06	14
Chalcopyrite	$CuFeS_2$	Sudbury, Canada	All n-type	1.7×10^{-3}	3.7×10	10
Pyrrhotite	$Fe_{1-x}S$	Renison, Tasmania	All p-type	1.75×10^{-4}	3.2×10	6
Pentlandite	$(Fe,Ni)_9S_8$	Sudbury Canada	All n-type	all $< 10^{-5}$		14

flasks of acidified hypovanadous (V^{2+}) solution which had been prepared by dissolving 0.5 moles of vanadium pentoxide in 0.05 M sulphuric acid followed by reduction with zinc amalgam[259]. Oxygen removal was accomplished by the following reaction:-

$$2V^{2+} + O_{2(aq)} = 2VO^{2+} \qquad (3.1)$$

The vanadyl ion, VO^{2+} then being reduced back to V^{2+} by reduction with zinc metal.

$$VO^{2+} + Zn + 2H^{+} = V^{2+} + Zn^{2+} + H_2O \qquad (3.2)$$

Finally, the nitrogen was passed over copper turnings heated to 900 °C in a tube furnace to remove any remaining traces of oxygen[259].

All the chemical reagents were of BDH Analar grade.

Glassware was cleaned with chromic or nitric acid. After washing with distilled water, conductivity water was used for rinsing.

CHAPTER FOUR

EXPERIMENTAL METHODS

CHAPTER FOUR : EXPERIMENTAL METHODS

4.1 Preparation of Deoxygenated Water

Deoxygenated distilled water was used to prepare all solutions used. The most common method applied for removing dissolved oxygen involves lowering the oxygen partial pressure above the water by bubbling nitrogen gas through it. However, most authors have made no attempt to determine the degree of deoxygenation. The concentration of residual oxygen remaining in "deoxygenated water" is determined by the level of oxygen that contaminates the nitrogen and on the leakage of oxygen into the preparation vessel.

Nitrogen purified by the method described in section 3.3 was dispersed through a sintered glass disc into a 150 cm^3 sample of air saturated distilled water, contained in the three compartment electrochemical cell (see section 4.2.3). The dissolved oxygen content of the water at 293 K was monitored continuously with a Philips PW 9600 Dissolved Oxygen transmitter connected to a Sinclair Digital Voltmeter and a PL4 J.J. Lloyd XY/t chart recorder. Figure 4.1 shows the decrease in

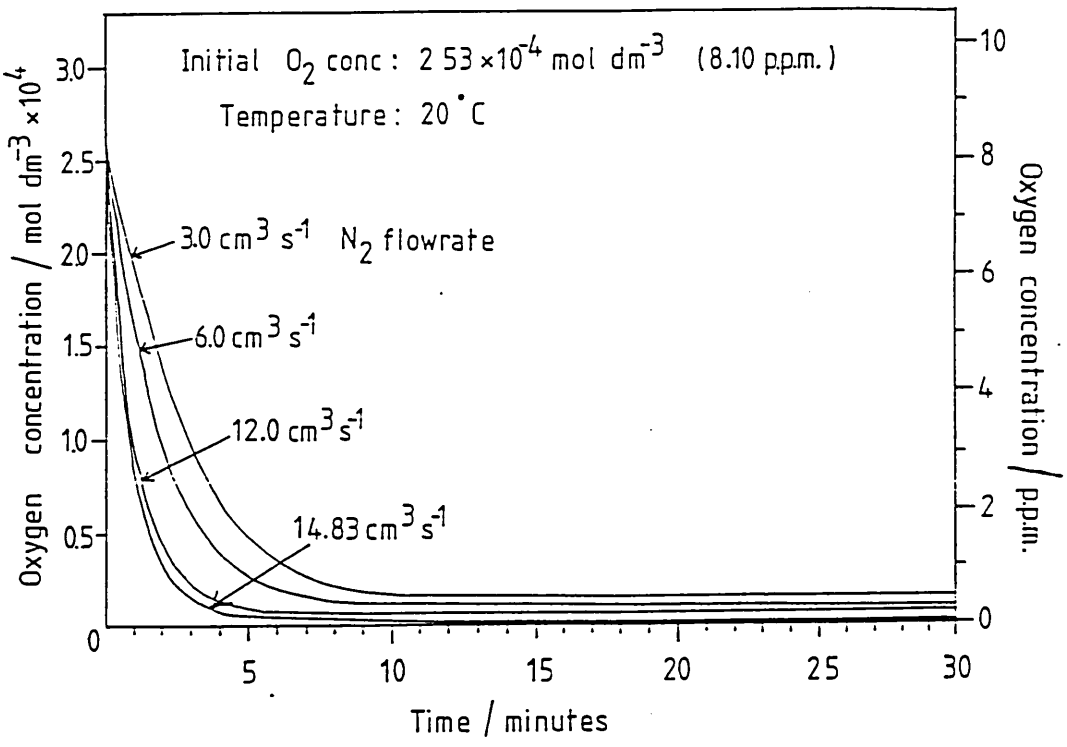


Fig 4.1 Dissolved oxygen content of water at various nitrogen flow rates.

dissolved oxygen with time, for various nitrogen flowrates according to the meter. The lowest attainable oxygen concentration was 1.56×10^{-6} mol dm^{-3} (50 p.p.b.). However, this represented the lower detection limit of the oxygen meter rather than the actual concentration obtained.

If C_i represents the initial concentration of dissolved oxygen at 293 K, and C, the concentration at time t, then for the various flowrates of nitrogen tested, plots of log C_i/C against time, were found initially be be linear (Figure 4.2), demonstrating that the deoxygenation process was first order with respect to oxygen concentration.

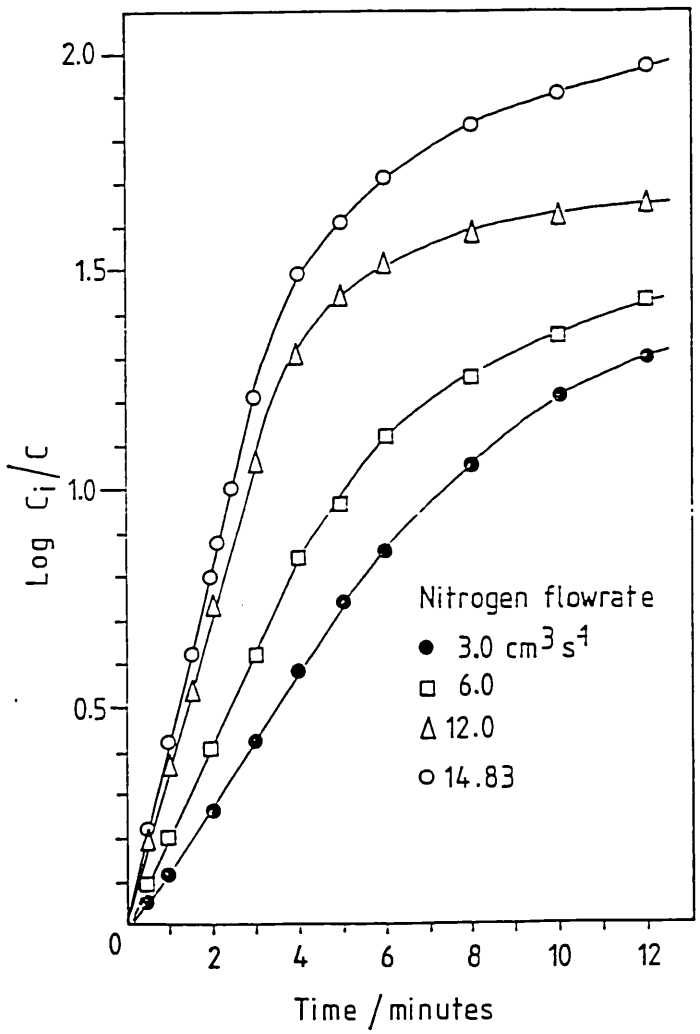


Fig 4.2 Rate of deoxygenation of water.

The Winkler reaction[260] provides a titrimetric method of determining quantities of dissolved oxygen in water down to 1.56×10^{-8} mol dm^{-3} (0.5 p.p.b.). The method lacks great accuracy due to the exposure of "oxygen-free" water to air during sampling and chemical determination, and entrainment of air in the processing reagents[261]. However, Potter and White[262,263], after designing a sophisticated sampling vessel and methods to prevent oxygen entrainment in the processing reagents, reported an analytical precision of 0.0006 mg l^{-1} (0.6 p.p.b.), for a single determination of dissolved oxygen in the concentration range 0.0007 - 0.0544 mg dm^{-3}. Gilroy and Mayne[264] used the methods devised by Potter and White to assess the efficiency of deoxygenation of aqueous solutions. They found that after one hour the residual oxygen content of a solution could be decreased to 9.375×10^{-8} mol dm^{-3} (3 ± 1 p.p.b.) using "white spot" nitrogen, and to 1.56×10^{-8} mol dm^{-3} (0.5 p.p.b.) using purified nitrogen, which was about the detection limit of the analytical method.

Using a value for the Van der Waals radius of oxygen of 0.152 nm[266] gives a molecular area of 1.45×10^{-19} m^2 for each O_2 molecule. Assuming a residual oxygen concentration of 1.56×10^{-6} - 1.56×10^{-8} mol dm^{-3} (50 - 0.5 p.p.b.) in 150 cm^3 of deoxygenated water, then the theoretical area coverage for oxygen is 2 – 200 cm^2. In subsequent electrochemical experiments mineral electrodes with areas of 0.4 - 1.0 cm^2 were used, so that theoretically, there would still be enough oxygen in solution to provide far more than monolayer coverage.

In practice, deoxygenated water was prepared by bubbling oxygen-free nitrogen through purified water for at least six hours before use in a clean glass container. Solutions used in electrochemical experiments were deoxygenated in the electrochemical cell for thirty minutes before any experiments were performed.

Figure 4.3 shows the rate of re-oxygenation of 150 cm^3 of water in the electrochemical cell after purging with nitrogen was terminated and the cell lid removed.

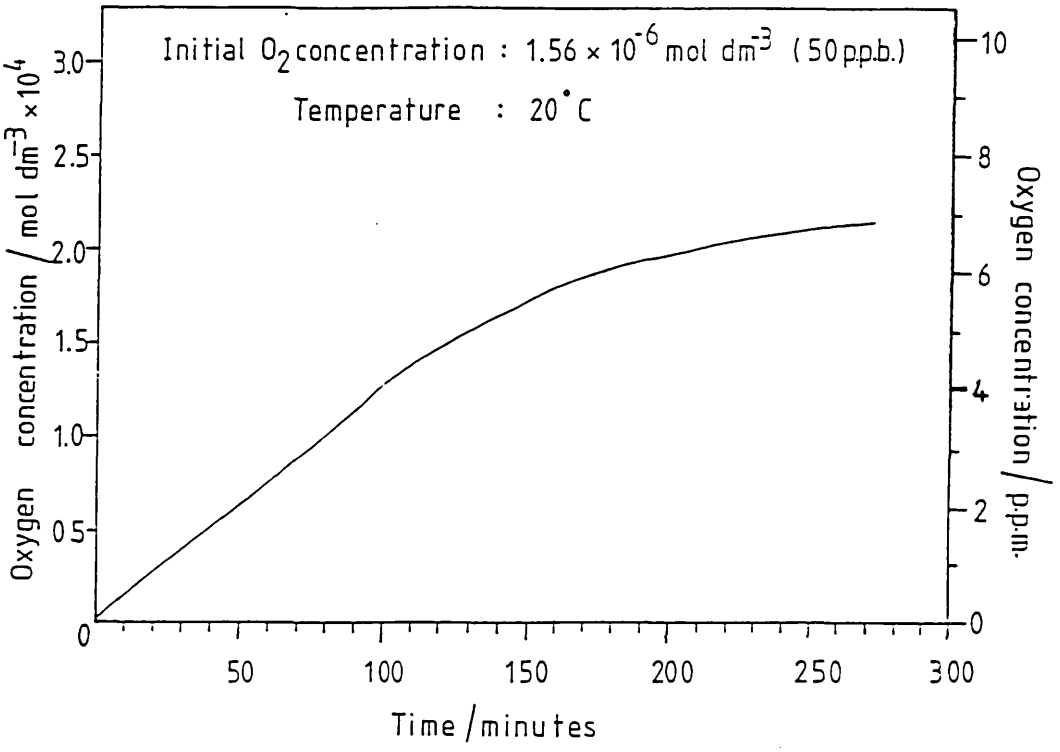


Fig 4.3 Rate of re-oxygenation of water.

4.2 Electrochemical Studies on Sulphide Mineral Electrodes

4.2.1 Preparation of Stationary Mineral Electrodes

Mineral sulphide specimens were cut and polished for electrode preparation and their electrophysical properties determined as described in section 3.2.7.

Electrodes were fabricated by cementing two contact wires to one of the gold sputtered faces of the mineral specimens with silver-loaded epoxy resin. The contact wires were threaded through a length of glass tubing, and the mineral, with about 10 mm of tubing, embedded in epoxy resin in a silicone rubber mould. After hardening, the electrode was removed from the mould and the lower face of the mineral specimen was exposed by grinding away the epoxy resin (Figure 4.4 and Plate 4.1). Only one face of the mineral was exposed to the solution

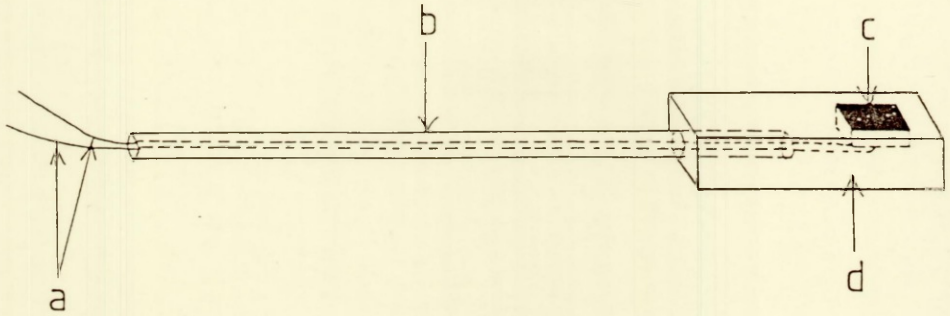


Fig 4.4 Stationary mineral electrode used in cyclic voltammetry, pulse voltammetry and a.c. impedance measurements.
a - contact wires; b - glass tubing; c - sulphide mineral
d - epoxy resin

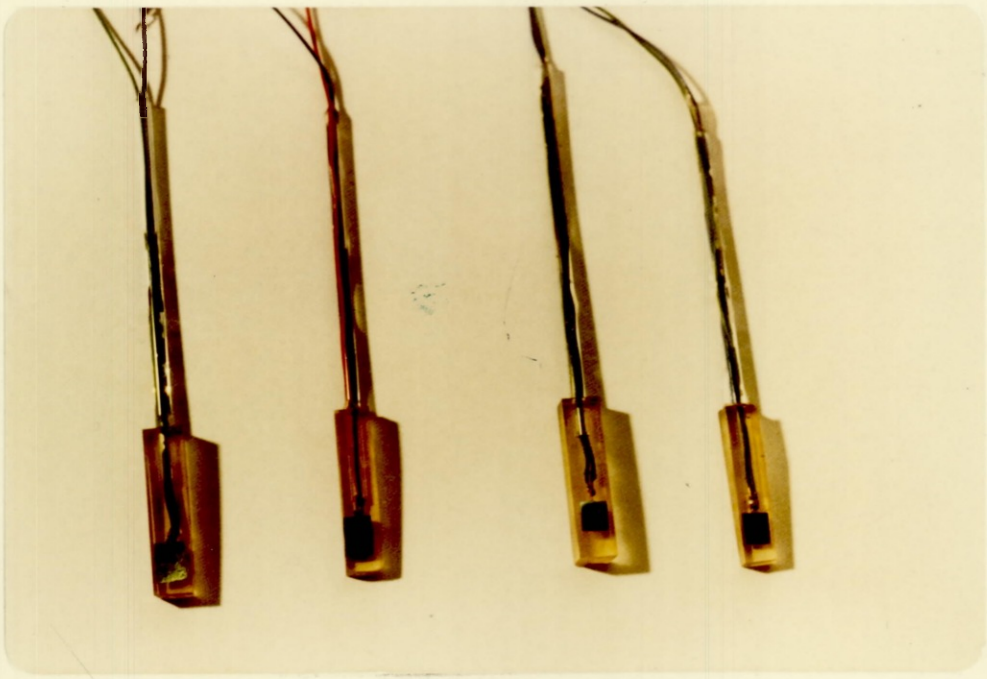


Plate 4.1 Stationary mineral sulphide electrodes used in cyclic voltammetry, pulse voltammetry and a.c. impedance measurements.

during electrochemical experiments: epoxy resin insulated the electrical contact wires and other mineral surfaces from the solution.

If electrode specimens were subsequently analysed by X-ray photoelectron spectroscopy (XPS), a silicon rubber mould, measuring 20 x 20 mm with a cavity 10 x 10 mm by 5 mm on one of its flat surfaces, was used to hold samples during electrochemical experiments (Plate 4.2). The flexibility of silicone rubber allowed the easy

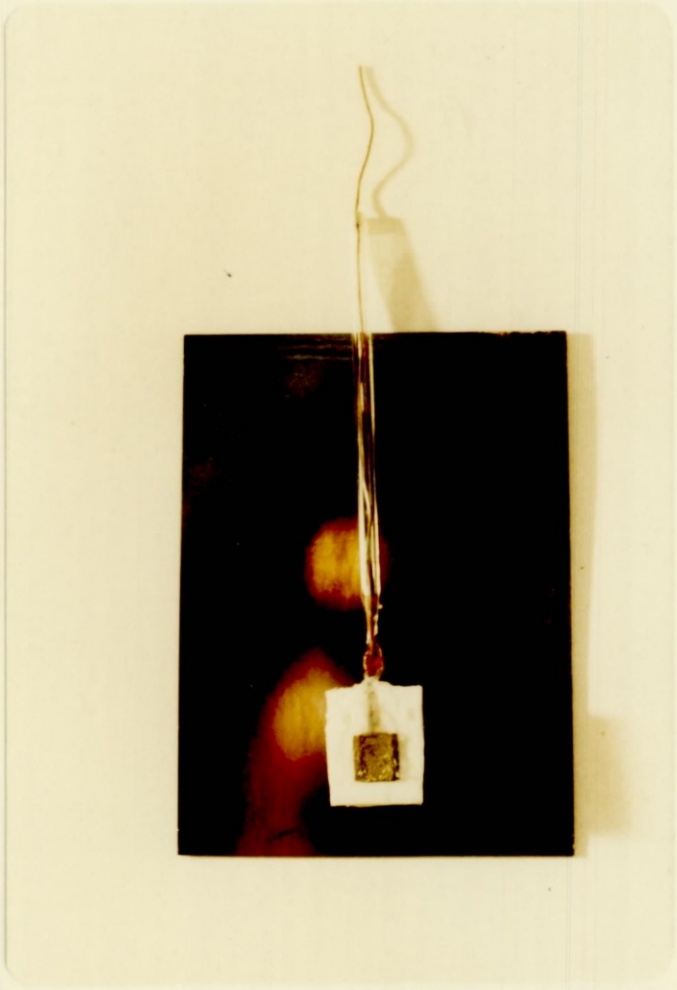


Plate 4.2 Stationary mineral sulphide electrode used in pulse voltammetric experiments subsequently analysed by ESCA.

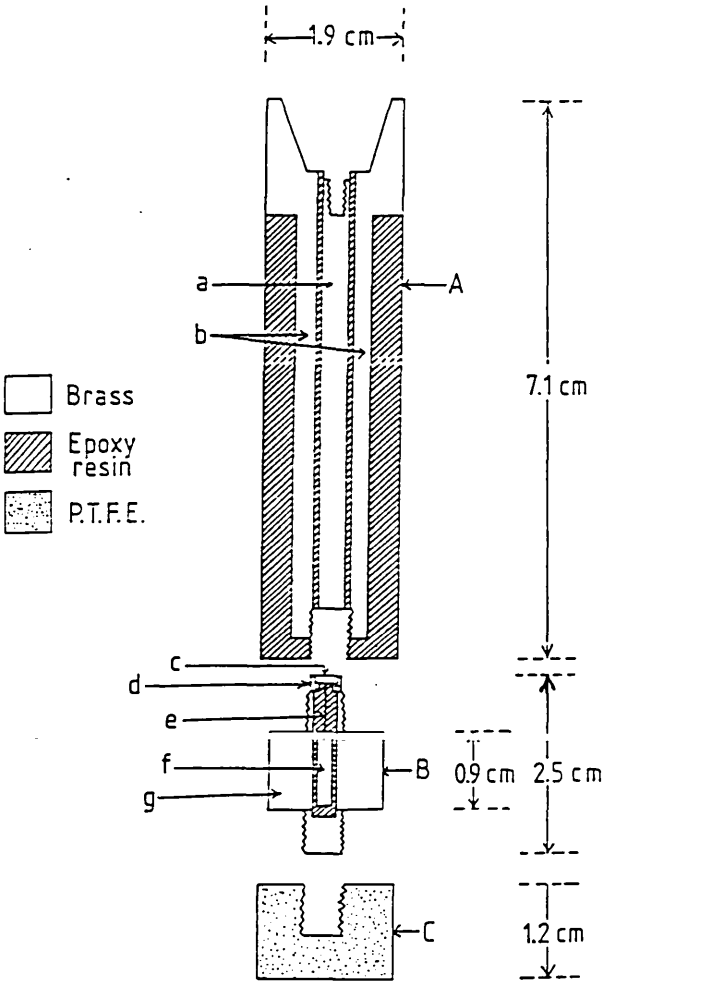
removal of mineral specimens from the holder after electrochemical polarisation.

Electrical contacts to the samples were made as described above. Specimens were then cemented into the cavity with more silicone rubber compound. Care was taken to ensure that the working mineral surface lay proud of the holder's surface, so that subsequent grinding and polishing only affected the mineral sulphide surface, preventing contamination by abraded silicone rubber.

Mineral sulphide electrodes used in electrochemical measurements made on "virgin" sulphide surfaces, and in contact experiments with a Pt feeder electrode, are shown in Figure 4.14 (section 4.3.4). Mineral samples were cemented into the cavity at the end of a glass capillary using epoxy resin, with about 5 mm of the specimen projecting out. Electrical contact wires had previously been cemented to the back of the mineral specimen with silver-loaded epoxy resin and threaded through the capillary and syringe barrel.

4.2.2 Preparation of Rotating Cylinder Collector Electrodes

Convective electrode systems, utilising the rotating disc electrode (RDE) and rotating ring disc electrode (RRDE), for which the convective-diffusion equations have been solved analytically for the steady state, have proved very useful for the study of electrochemical processes[270]. The RRDE was first developed by Frumkin and Nekrasov[271] to detect unstable intermediates in electrode reactions. The electrode consists of a central disc ("source") electrode surrounded by an independent ring ("collector") electrode. The advantages of this electrode system are that experimental investigations can be made at both electrodes: potentials and currents at each electrode can be controlled separately from each other. Paul et al[272] constructed ring-disc electrodes to study the electrochemical behaviour of galena (PbS). However, a RRDE is difficult to construct, requiring the precise alignment of disc and ring and commercial RRDE's are expensive. Therefore a rotating cylinder-collector electrode (RCCE) was constructed (Figure 4.5 and Plate 4.3), similar to that described by McKubre and Macdonald[273]. It has certain characteristics that make it superior to a RRDE for studying the electrochemical behaviour of mineral sulphides:



A) Upper supporting shaft
B) Electrode section
C) PTFE CAP

a) Brass rod
b) Brass cylinder
c) Brass disc
d) PTFE washer
e) Copper wire
f) Mineral working electrode
g) Platinum collector electrode

Fig 4.5 Rotating cylinder - collector electrode

1) It is much easier to construct than a RRDE and the design facilitates the interchanging of different sulphide mineral working electrodes.

2) The system is characterised by a single value for the Reynolds number (Re). In RDE and RRDE systems the Re varies from zero at the rotation axis to a maximum at the outer edge of the disc. Since the shear stress is porportional to Re, surface films are subjected to mechanical stresses that increase with distance from the rotation axis. This is important in film growth processes occurring at the surface of a RDE and/or RRDE.

3) The RCCE has a much larger collector electrode area, making it a more sensitive device for the detection of dissolved electroactive species.

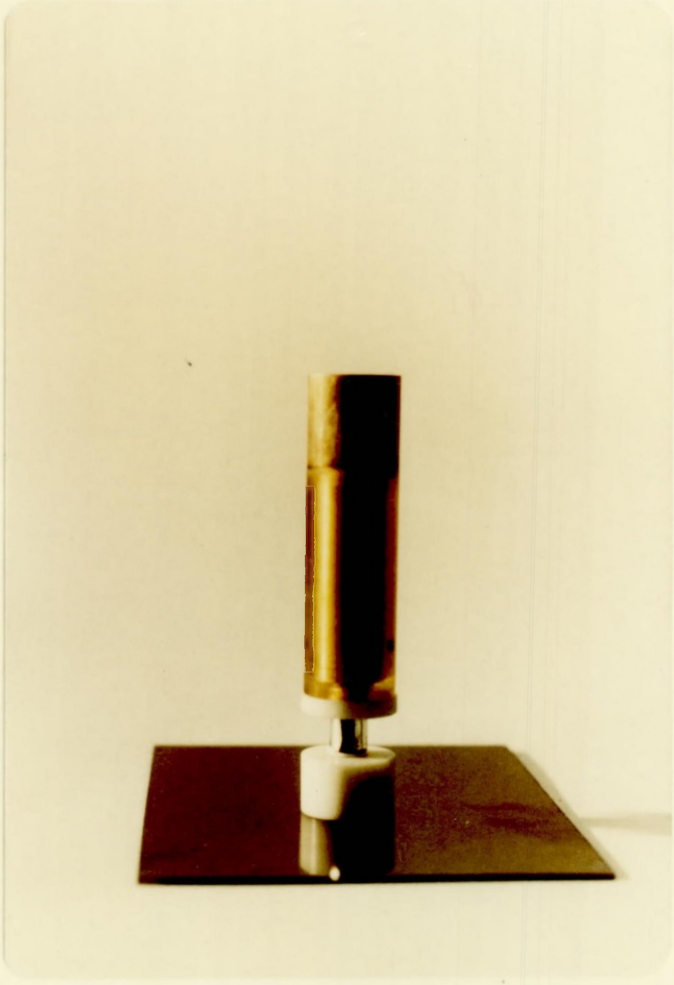


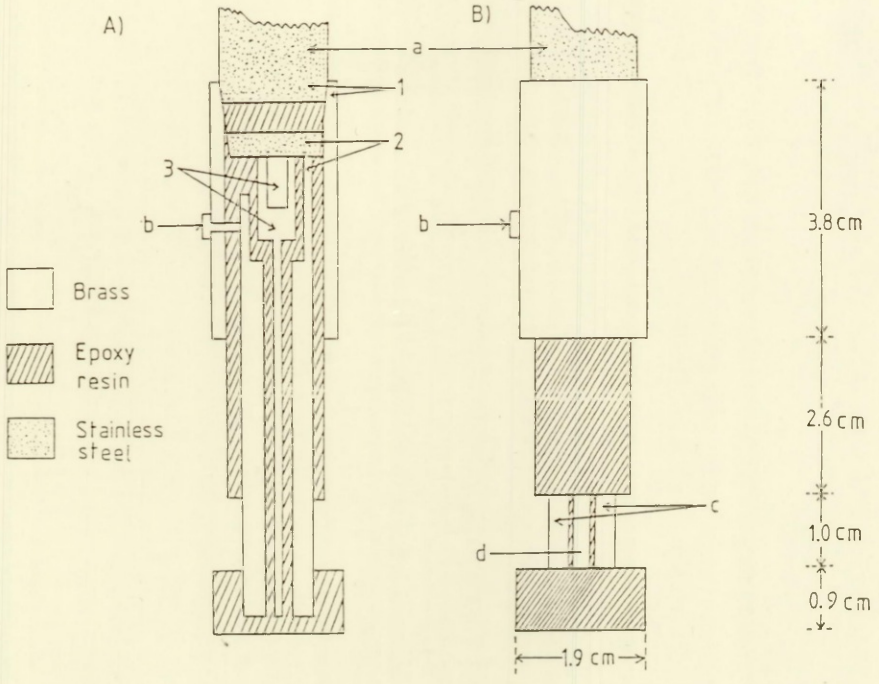
Plate 4.3 Rotating cylinder-collector electrode.

4) The current density distribution across the surface of the RCCE is thought to be more uniform than that for a RDE or RRDE operating below mass transfer limitations[273].

Figure 4.5 shows that the RCCE consisted of three sections. The electrode section was constructed from a brass rod machined at either end to produce two screw threads. A rectangular section was cut out

of the cylinder and lined with PTFE and epoxy resin, to allow the emplacement of a mineral working electrode, and to avoid short-circuiting with the copper cylinder. A mineral sulphide specimen, contacted to a copper wire, was cemented into the cavity with epoxy resin, and then the copper wire was soldered to a brass disc recessed into a PTFE washer. The surface of the copper cylinder was covered with 99.9 % Pt sheet, 1 mm thick, using silver-loaded epoxy resin as a conducting bonding agent. The top of the electrode assembly was then screwed into an internally threaded brass cylinder contained within the upper supporting shaft. This formed the electrical contact, via the brass cylinder of the electrode section, with the Pt collector electrode. The brass disc of the electrode section contacted the brass rod positioned in the centre of the supporting shaft, which was insulated from the surrounding brass cylinder with epoxy resin. The bottom of the electrode assembly was screwed into a PTFE cap to prevent electrolyte penetration. However, the active lifetime of the RCCE in solution was found to be small due to electrolyte leakage between the electrode unit and supporting section, which short-circuited the electrode.

The electrode was therefore redesigned and a rotating split cylinder bi-electrode (RSCBE) constructed, this time as one unit, to prevent electrolyte penetration (Figure 4.6 and Plate 4.4). The RSCBE contained three independent electrodes: two were used as Pt collector electrodes, and one as a mineral working electrode. Running vertically down the electrode were two brass hemi-cylinders positioned around a central brass rod. These sections were encapsulated in epoxy resin. Over a 10 mm length of the electrode epoxy resin was machined away to expose the two brass hemi-cylinders. Then two rectangular slots opposite to one another were cut in the epoxy resin, in the gap between the hemi-cylinders to expose the brass rod. Care was taken to leave a layer of epoxy resin between the hemi-cylinders and cavity to prevent short-circuiting. A mineral specimen was cemented into each cavity, and contacted to the brass rod at the back with silver-loaded epoxy resin. The effective working electrode area and hence the working electrode current of the RSCBE was double that of the RCCE. Two sections of the Pt foil were cemented to the brass hemicylinders to form the collector electrodes. Contacts to the stainless steel motor assembly unit were made as shown in Figure 4.6.



A) Cross section
B) Complete electrode
a) Shaft of motor assembly
b) Screw contact to collector 1
c) Platinum collectors 1 and 2
d) Mineral working electrode
1) Electrical connection for collector 1
2) Electrical connection for collector 2
3) Electrical connection for working electrode

Fig 4.6 Rotating split cylinder bi-electrode

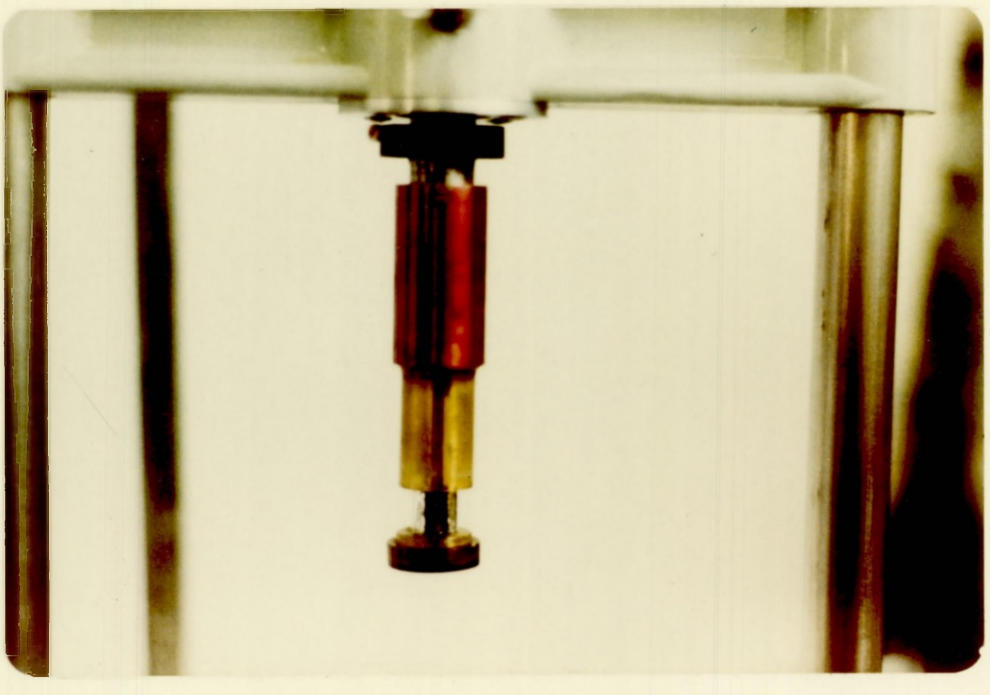


Plate 4.4 Rotating split cylinder bi-electrode.

4.2.3 Cell Design and Electrochemical Instrumentation

Experiments with mineral electrodes were carried out in three compartment electrochemicals cells shown in Figures 4.7 and 4.10 (section 4.3.4). The counter electrode compartments were isolated from the working electrode compartments by sintered glass frits. A Luggin capillary probe, extending from a syringe barrel, was used to connect the working and reference electrode compartments. The tip of the Luggin capillary was placed close to the working electrode surface to minimise the error in the measured potential associated with the uncompensated IR drop in the solution between the tip of the Luggin capillary and the working electrode. A saturated calomel electrode (S.C.E.) was used as a reference electrode although all quoted potentials have been converted to the standard hydrogen electrode (S.H.E.) scale assuming that the SCE has a reversible potential of 0.245 V versus S.H.E.[274]. Both cells had tightly fitting PTFE lids with the necessary openings for stationary minerals electrodes, rotating electrodes, gas bubbler and oxygen electrode.

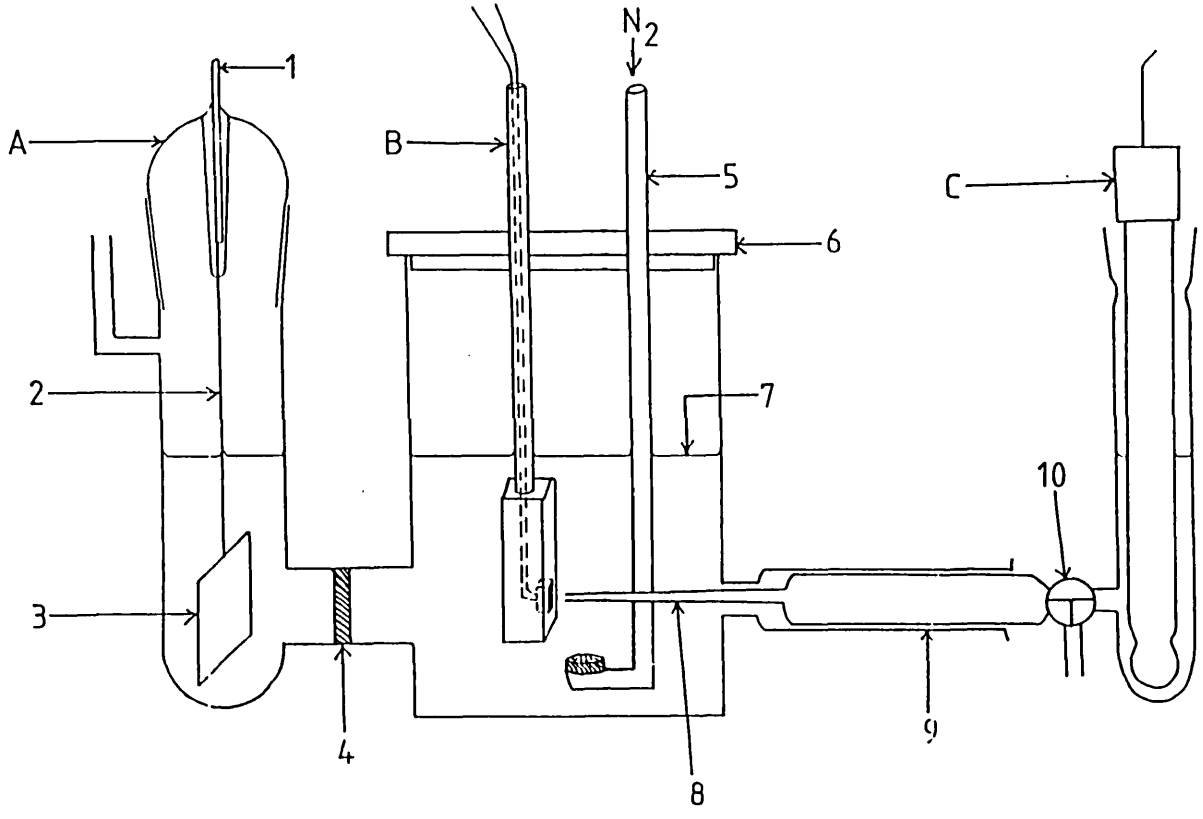
In electrochemical experiments, the potential difference between the working and reference electrodes was controlled by a potentiostat.

The instrumentation available for use during these electrochemical investigations is listed in Table 4.1. In addition, a flexible modular potentiostat system, previously designed and constructed in the laboratory[277], was used in a bi and tri-potentiostat mode to drive the RCCE and RSCBE (see sections 4.2.2 and 4.2.5).

4.2.4 Cyclic Voltammetric Studies

Cyclic voltammetry was employed in initial electrochemical studies to obtain qualitative information about the electrode reactions occurring at sulphide mineral surfaces.

Using repetitive triangular potential scans (RTPS) the surfaces of mineral sulphide electrodes were oxidised during a linear potential



A - counter electrode; B - mineral electrode; C - reference electrode; 1 - tungsten wire; 2 - platinum wire;
3 - platinum foil; 4 - sintered glass frit; 5 - gas bubbler; 6 - PTFE cell lid; 7 - solution level;
8 - Luggin capillary; 9 - syringe barrel; 10 - T - tap.

Fig 4.7 Electrochemical cell

Table 4.1 Instrumentation Used During Electrochemical Experiments

ST72 Wenking potentiostat
Thomson Ministat potentiostat
Hi-Tek PPR1 waveform generator
Hi-Tek gated digital integrator/voltmeter
Nicolet (Explorer I) digital storage oscilloscope
J.J. Lloyd Instruments Limited PL4 XY/t recorder
Solartron 1170 frequency response analyser
Schlumberger electrochemical interface
Sinclair digital voltmeter
380Z Research Machines Limited Microcomputer

sweep and the products of anodic oxidation analysed by the characteristics of their reduction on the reverse cathodic scan. The limit of the anodic scan ($E_{\lambda a}$) was increased after each cycle and the effect on the E/I relationships of cathodic reduction peaks at a fixed cathodic scanning limit ($E_{\lambda a}$) recorded.

Standard electrode potentials calculated from bulk thermodynamic data (see Appendix I), could not be used unambiguously to identify voltammetric peaks because of the requirement of a driving force or overpotential for a kinetically slow reaction, and because monolayers may be non-thermodynamic phases. However, they were useful in eliminating processes which could not occur in a potential region.

At fixed values for $E_{\lambda a}$ and $E_{\lambda c}$, measuring peak currents (I_p) as a function of sweep rate (ν) allowed diffusional processes characterised by I_p being proportional to $\nu^{1/2}$ to be distinguished from surface adsorption/transformation phenomena, for which I_p is proportional to $\nu^{(278)}$.

4.2.4.1 Experimental Procedure

The cell in Figure 4.7 and mineral electrodes in Figure 4.4 and Plate 4.1, described in section (4.2.1), were used (see Plate 4.5). The

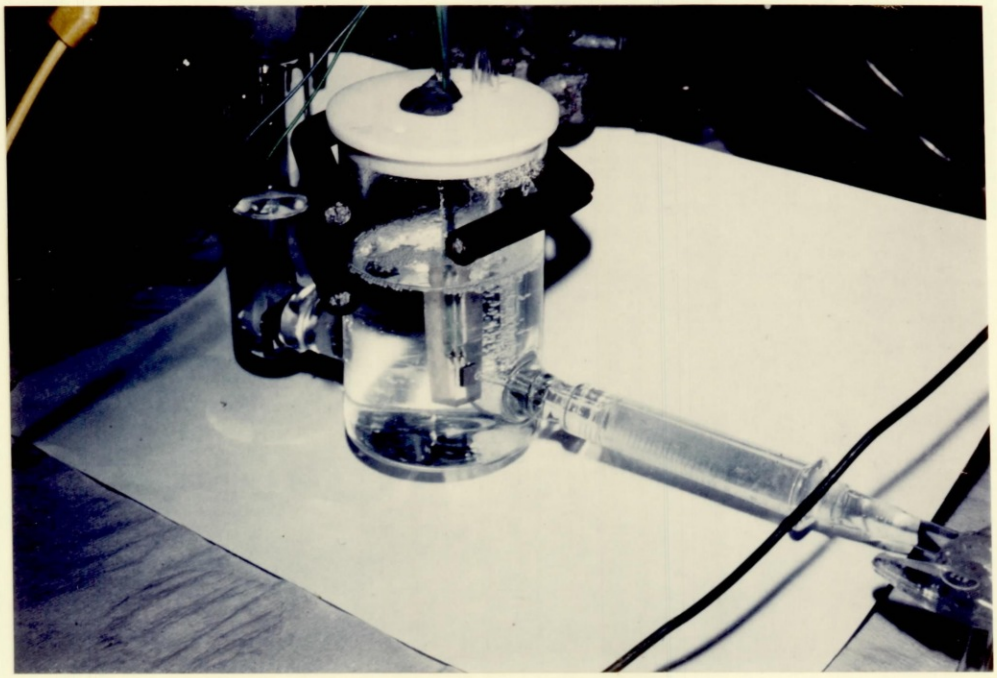


Plate 4.5 Stationary mineral sulphide electrode and electrochemical cell used in cyclic voltammetry, pulse voltammetry and a.c. impedance measurements.

potential of the stationary electrodes was controlled with a ST72 Wenking potentiostat programmed with a Hi-Tek PPR1 waveform generator. Current-potential measurements were made using a Nicolet (Explorer I) digital storage oscilloscope (Plate 4.6) and hard copies recorded on an XY/t chart recorder (J.J. Lloyd PL4). Charge measurements were made using a Hi-Tek gated digital integrator/voltmeter. All the potentials were measured against a saturated calomel electrode (S.C.E.) and reported here against the saturated hydrogen electrode (S.H.E.).

Experiments were carried out in buffer electrolytes of different composition/pH values to minimise the pH change at the mineral/solution interface during oxidation. The composition of

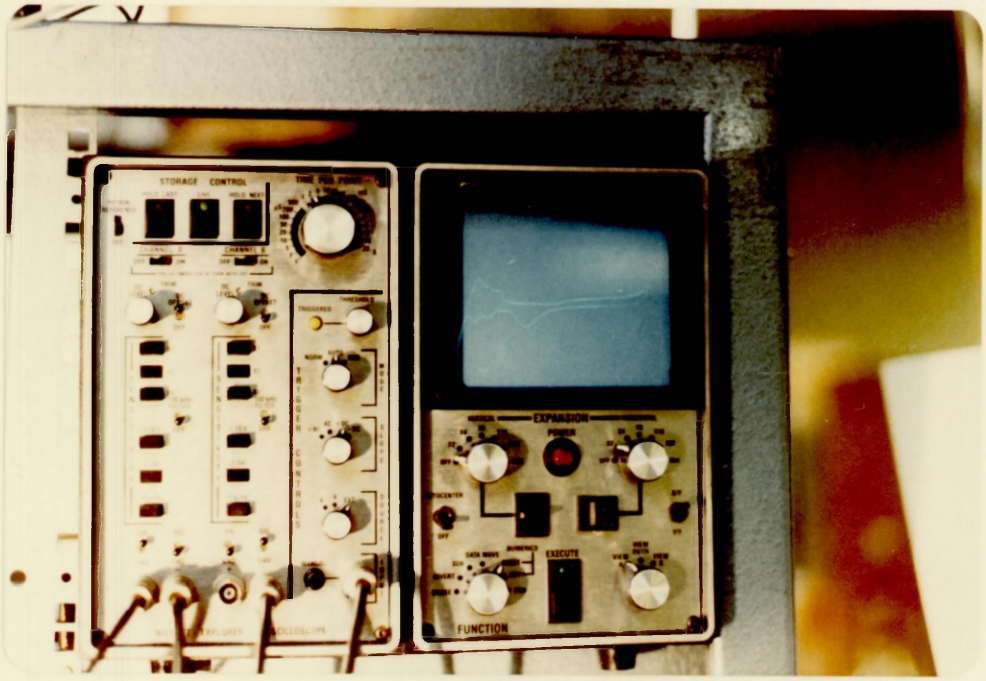


Plate 4.6 Nicolet (Explorer I) digital storage oscilloscope recording a cyclic voltammogram of platinum in 0.05 M $Na_2B_4O_7$.

buffer electrolytes used are shown in Table 4.2. Cell solutions were deoxygenated by bubbling nitrogen for 30 minutes through the cell prior to the introduction of the electrode.

Table 4.2 The Composition of Buffer Electrolytes

pH	Composition of Electrolyte
0.0	1.0 M $HClO_4$
1.0	0.1 M $HClO_4$
4.6	0.5 M CH_3COOH + 0.5 M CH_3COONa
6.97	0.025 M KH_2PO_4 + 0.025 M Na_2HPO_4
9.2	0.05 M $Na_2B_4O_7$
11.0	0.025 M $NaHCO_3$ + 0.023 M NaOH
13.0	0.1 M NaOH

Preliminary experiments showed that voltammetric current values per geometric unit area for mineral electrodes wet ground on 600 grade silicone carbide paper varied after each fresh surface preparation and were eight to ten times those observed for mineral electrodes polished with 3 μm diamonds. These phenomena have been observed by other workers[138,186] and attibuted to differences in surface roughness, i.e. the currents per real unit area are the same for each surface preparation. Therefore, a fresh mineral surface was prepared before each experiment by wet grinding on 600 grade carborundum paper and then polishing with 3 μm diamonds, care being taken to avoid inclusions, cracks and voids. After polishing, each sample was washed with deoxygenated doubly distilled water (DDDW), acetone and the DDDW again before being transferred to the electrochemical cell.

Rest potential measurements on different mineral sulphide electrodes showed that potentials were up to 300 mV positive of the reversible potential for the upper stability limit of the respective sulphide. This indicated that the electrode preparation described above had failed to prevent surface oxides forming. Oxide layers have been shown to form spontaneously on pyrite[128,279] and chalcopyrite[279] when exposed to air. Therefore, the final stage of electrode preparation was concerned with minimising oxidation of the electrode surface before electrochemical experiments were performed. Three methods were explored; each involving electrode preparation as described above up to the point of transfer into the electrochemical cell.

1) The final electrode preparation was carried out in a nitrogen atmosphere in a glove bag. Each electrode was placed in a beaker containing DDDW and transferred into the glove bag with the electrochemical cell. Purified nitrogen was used to flush out the glove bag and to deoxygenate the solution contained in the electrochemical cell. The flowrate was maintained to keep a small excess pressure in the bag. After 2 hours, the oxygen level was $< 6.25 \times 10^{-5}$ mol dm^{-3} (2000 p.p.b.). The electrode was then removed from the beaker and polished wet with 0.3 μm - alumina on a "Selvyt"

cloth, in an attempt to remove any oxide layer that had formed on the surface. The electrode was washed in DDDW to remove alumina particles from the surface and transferred into the electrochemical cell.

Rest potential values, although decreased, were found to still lie positive of the respective thermodynamic stability ranges of the minerals. There were two reasons for this. Firstly, alumina was unable to sufficiently abrade hard, polished sulphide surfaces (especially pyrite) to remove all oxide layers due to its small particle size. The size of the glove bag precluded the use of diamond laps within the glove bag to prepare fresh sulphide surfaces. Secondly, the oxygen level was sufficiently high in the glove bag to oxidise the mineral surface. Longer purging times were impracticable, so that this method of preparation was abandoned.

2) Each electrode was transferred into the cell and cathodically polarised for 60 seconds at a potential 200 mV cathodic of the lower thermodynamic stability limit of the respective sulphide mineral as defined in the E_h-pH diagrams presented for each mineral in Appendix II. Any oxide on the electrode surface was reduced. Conway et al[135] had previously shown that this procedure results in a reproducible electrochemical state for pyrite electrodes. However, the sulphide mineral surface may be reduced to a lower sulphide e.g. pyrite to pyrrhotite, chalcopyrite to chalcocite, so that subsequent cyclic voltammograms may be characteristic of the lower sulphide.

3) The procedure that was usually adopted as a final preparation stage for all stationary mineral electrodes, involved sulphidising electrodes in 100 cm^3 of deoxygenated 5% sodium sulphide solution for 5 minutes. Electrodes were then washed with DDDW in an ultrasonic bath before being transfered into the electrochemical cell. Although Trahar[333] has criticised this technique, since it could result in sulphur deposition due to H_2S oxidation, the procedure produced rest potentials that were within the thermodynamic stability limits of each mineral.

A 5 minute conditioning time was allowed prior to recording cyclic voltammograms. Constant stirring was provided during experiments by nitrogen bubbling, unless otherwise stated.

4.2.4.2 Measurements on Virgin Surfaces Produced by In situ Polishing and First Sweep Voltammetric Curves

Preliminary investigations showed that in general the first potential sweep started from the rest potential in the cathodic direction, differed from those on subsequent cathodic sweeps. The purpose of these measurements was to observe how the rest potential changed after producing a virgin sulphide surface and whether voltammetric curves differed from those of sulphidised mineral electrodes.

The cell in Figure 4.10 and mineral electrode in Figure 4.11 (section 4.3.4), also described in section (4.2.1), were used. A virgin sulphide surface was produced in the cell by abrading the mineral sample with 600 grade silicon carbide paper mounted on the end of a hollow glass rod under nitrogen purged buffer solution. Care was taken to remove any silicon carbide particles from the sulphide surface with a piece of "Selvyt" cloth also mounted on the end of a glass rod. A fresh surface amounting to approximately 80 % of the total exposed electrode area was produced by this method. The rest potential was monitored continuously during this procedure on the Nicolet (Explorer I) digital storage oscilloscope.

4.2.5 Rotating Split Cylinder Bi-electrode Studies

A rotating split cylinder bi-electrode (RSCBE) was employed so that soluble electro-active intermediates formed at a mineral working electrode, might be detected at a potentiostatted platinum collector electrode, by oxidation or reduction.

The effect of electrode rotation on the cyclic voltammograms of sulphide minerals, and the effect of HS^-, $S_2O_3^{2-}$, Fe^{2+}, Fe^{3+}, Cu^{2+} and Ni^{2+} solution additions on cyclic voltammograms of platinum and sulphide minerals, was also investigated.

4.2.5.1 Experimental Procedure

A RSCBE (Figure 4.6 and Plate 4.4) was constructed for each sulphide mineral as described in section (4.2.2). Generally, the two platinum

electrodes were shorted together and experiments performed using the modular bipotentiostat to control the potentials of working and collector electrodes (Plate 4.7). The potential of the mineral

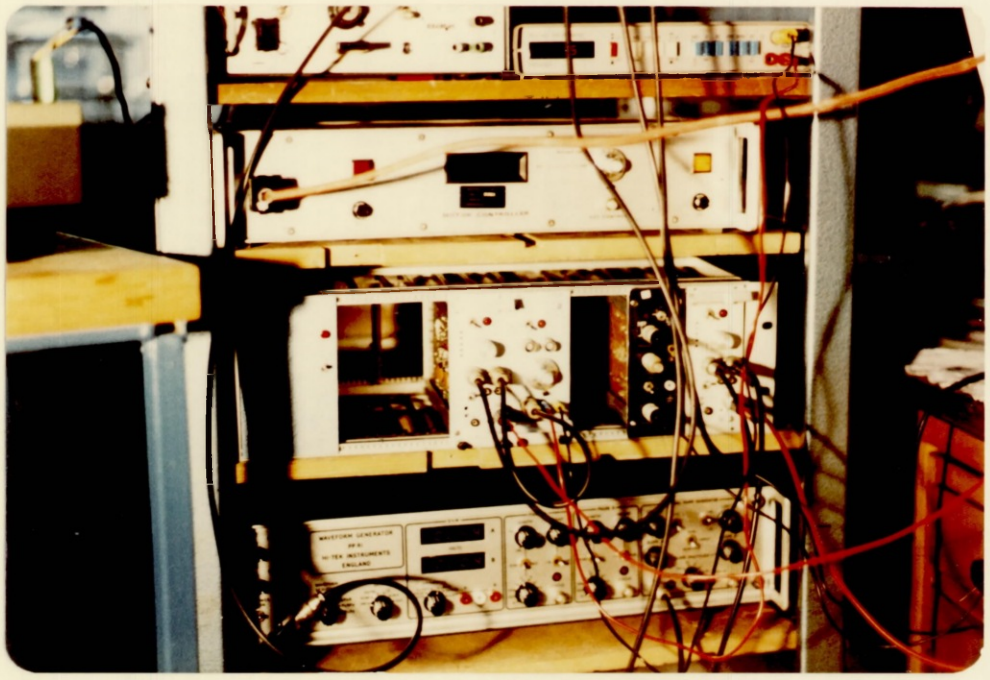


Plate 4.7 The modular potentiostat units used in a bi-potentiostat mode for rotating split cylinder bi-electrode studies.

working electrode was programmed with a Hi-Tek PPR1 waveform generator and that of the collector with a laboratory constructed d.c. voltage source. Electrical contacts between the potentiostats and the RSCBE were made through an Oxford Electrodes rotating electrode contact block (Plate 4.8).

Current-potential measurements were made using the instrumentation described in section (4.2.4.1). The mineral working electrode surfaces were ground with 600 grade carborundum paper followed by wet polishing of mineral and platinum surfaces with 0.3 μm α-alumina. The electrode was washed in deoxygenated doubly distilled water before being screwed onto the motor assembly and lowered into deoxygenated buffer electrolytes, which had been purged with nitrogen for 30 minutes prior to introduction of the electrode. During experiments,

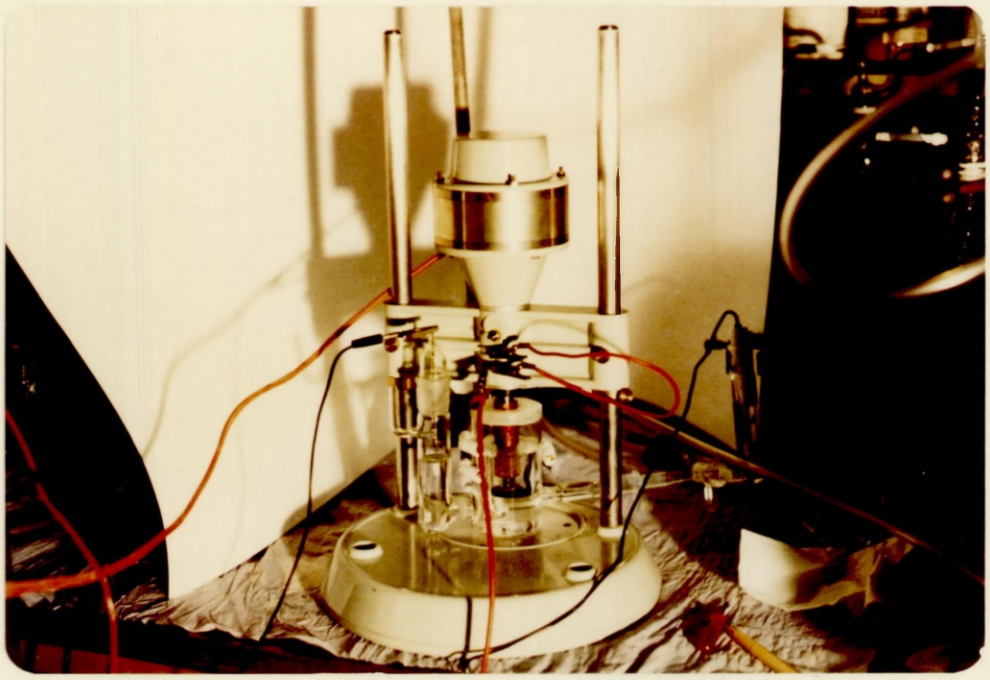


Plate 4.8 Apparatus used in rotating split cylinder bi-electrode studies.

1 - rotating split cylinder bi-electrode.
2 - Oxford Electrode motor.
3 - electrochemical cell.

nitrogen bubbling was stopped to reduce turbulence around the surface of the rotating electrode. The complete experimental arrangement is shown in Plate 4.9. Electrodes were cathodically pretreated as described in section (4.2.4.1) to remove any oxide from the mineral surfaces.

Experiments, similar to those described by McKubre and Macdonald[273], were performed to calibrate the collector efficiency of a pyrite RSCBE in 0.1 M $K_3Fe(CN)_6$ with 1.0 M NaOH supporting electrolyte at 20 °C. The ratio of collector to working electrode current for the removal and generation of electroactive species respectively, defines the collector efficiency (N) for the electrode.

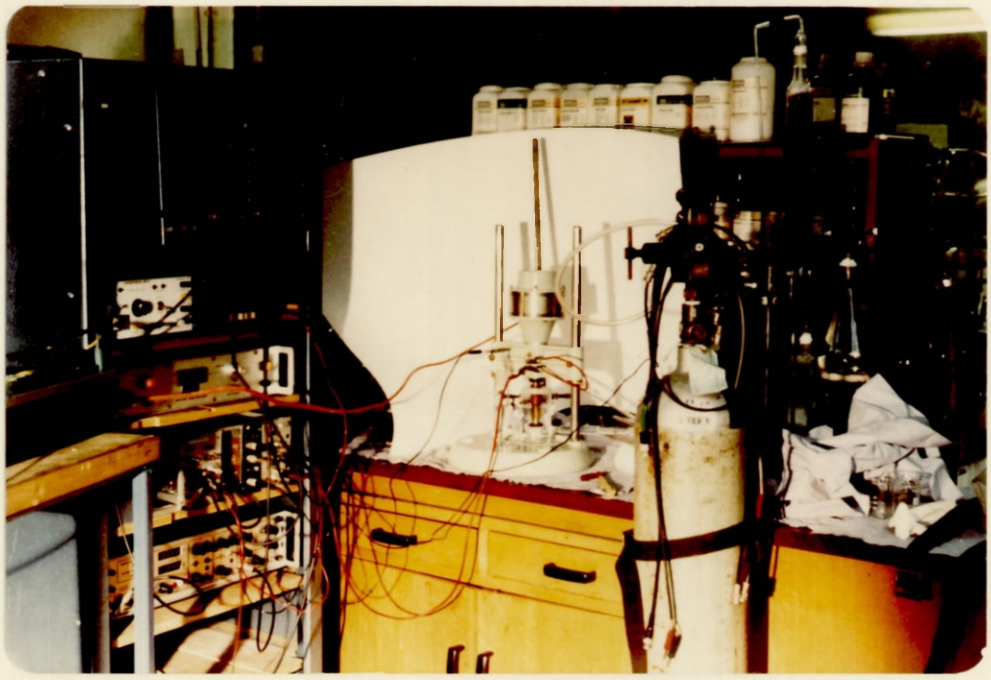


Plate 4.9 Apparatus and electrochemical instrumentation used in rotating split cylinder bi-electrode studies.

The calibration was carried out with both working and collector electrode reactions under mass transfer controlled conditions to eliminate errors introduced by the possible coupling of working and collector currents through uncompensated solution resistance[273]. The pyrite working electrode was held at -0.5 V (S.H.E.) to produce Fe(II), and the collector at 1.0 V vs. S.H.E. to oxidise Fe(II) back to Fe(III). Working and collector electrode currents were measured as a function of electrode rotation speed (ω), and the collector efficiency calibrated.

The working and collector electrode potentials were chosen after cyclic voltammetry was carried out on both electrodes in stirred and quiescent solution, in the absence and presence of $K_3Fe(CN)_6$. From these experiments it was possible to choose an optimum potential for each electrode to invoke the desired mass transport controlled reaction with the minimum background current.

4.2.6 Pulse Voltammetry

The current/time and charge/time responses of sulphide mineral electrodes to anodic potentiostatic pulses was studied to determine the characteristics of the nucleation and growth of solid phases on the electrodes.

4.2.6.1 Experimental Procedure

The electrodes, electrode preparation and instrumentation used during all of these studies was the same as that used for the cyclic voltammetric studies described in section (4.2.4.1).

In some experiments, electrodes were analysed by X-ray photoelectron spectroscopy, after anodic polarisation at constant potential for 10 minutes.

The stationary electrodes described in section (4.2.1) and shown in Plate 4.2 were employed during these investigations. After polarisation, each electrode was removed from the silicone rubber holder and washed in deoxygenated doubly distilled water. The solution remaining on the electrode surface was evaporated in a stream of purified nitrogen to minimise air contamination. Electrical contacts to the sulphide mineral were broken and the sample placed in an air-tight glass container before being sealed under a stream of nitrogen. XPS analysis was carried out by Dr L Hazell at BP Research Centre, Sunbury-on-Thames.

4.2.7 AC Impedance Measurements

AC impedance measurements were made on mineral electrodes by digital frequency response analysis to obtain an in situ measurement of resistance and capacitance for each sample as a function of electrode potential.

The technique involves peturbing the cell with a sinusoidal voltage ($E_{a.c.}$) of small amplitude (< 10 mV peak-to-peak), and measuring the magnitude of the a.c. component of the current ($I_{a.c.}$) at the

frequency of $E_{a.c.}$ and its phase angle (θ) with respect to $E_{a.c.}$. This enables the real and complex part of the electrode impedance to be defined as a function of frequency.

4.2.7.1 Experimental Procedure

The stationary mineral electrodes described in section (4.2.1) see Figure 4.4 and Plate 4.1), and the electrochemical cell shown in Figure 4.7, were used. Electrodes were polished and sulphidised as described in section (4.2.4.1). Deoxygenated buffer electrolytes were employed and the cell was purged for 30 minutes with nitrogen prior to the introduction of the electrode.

A 10 mV peak-to-peak sine wave potential signal, superimposed on a d.c. anodic potential ($E_{d.c.}$), was the potential program applied to the sulphide working electrode. $E_{d.c.}$ was increased in 200 mV steps starting from the rest potential. At each d.c. potential, impedance measurements were made over a range of frequencies using a Solartron 1174 frequency response analyser (FRA) linked to the cell via a Schlumberger Electrochemical Interface (potentiostat) (Plate 4.10).



Plate 4.10 Solartron 1174 frequency response analyser and Schlumberger electrochemical interface.

The FRA consisted of a programmable generator, which provided the perturbing a.c. signal, a correlator to analyse the response to the system, and a display to present the results.

The generator was programmed with the signal amplitude and the frequency range over which measurements were to be made (usually 10 KHz to 0.1 Hz). These were taken sequentially, at equally spaced intervals on a logarithmic scale, generally at 5 points per decade, over the required range. The response was given once a measurement had been completed and could be displayed in three possible notations:-

1) $I_{a.c.}$ and θ

2) Log $I_{a.c.}$ and θ

3) The real (ZR) and imaginary (ZI) parts of the impedance

Using a FRA, measurements could be made very quickly and preliminary experiments produced large amounts of data that were recorded manually. Obviously, this technique lends itself to system control and on-line data processing with a computer. Therefore, in latter work the Solartron FRA was controlled by a Research Machines Limited 380Z micro-computer, using a general purpose interface[280]. The computer programmed the FRA's generator and once a measurement was completed the results, together with the measurement frequency, were transferred to one of the computer's magnetic discs for storage. Simultaneously, the results were plotted on a video monitor to give the complex plane impedance spectrum directly (Plate 4.11). After each frequency scan, the d.c. bias was stepped manually to the next potential.

The software used to control the system and analyse the data acquired, is presented in Appendix III.

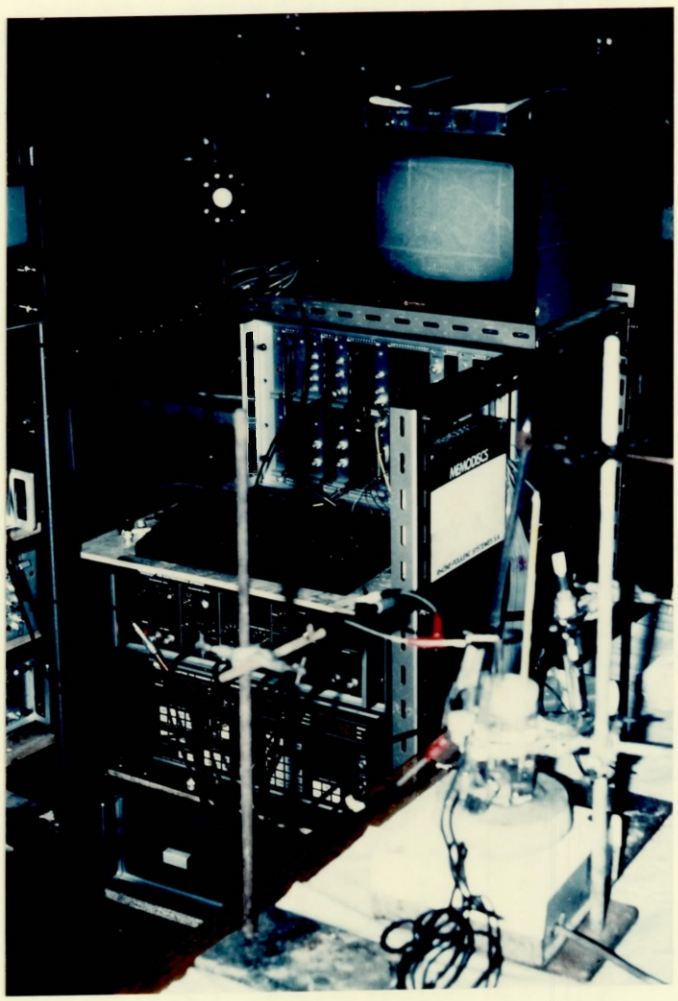


Plate 4.11 Apparatus and electrochemical instrumentation used in a.c. impedance measurements.

4.3 Mineral Pulp/Suspension Electrode Studies

Particulate bed electrodes have previously been used in controlled potential flotation studies to determine the conditions under which sulphide particles are rendered floatable in both the absence[175,282,283] and presence of collectors[281,284,285].

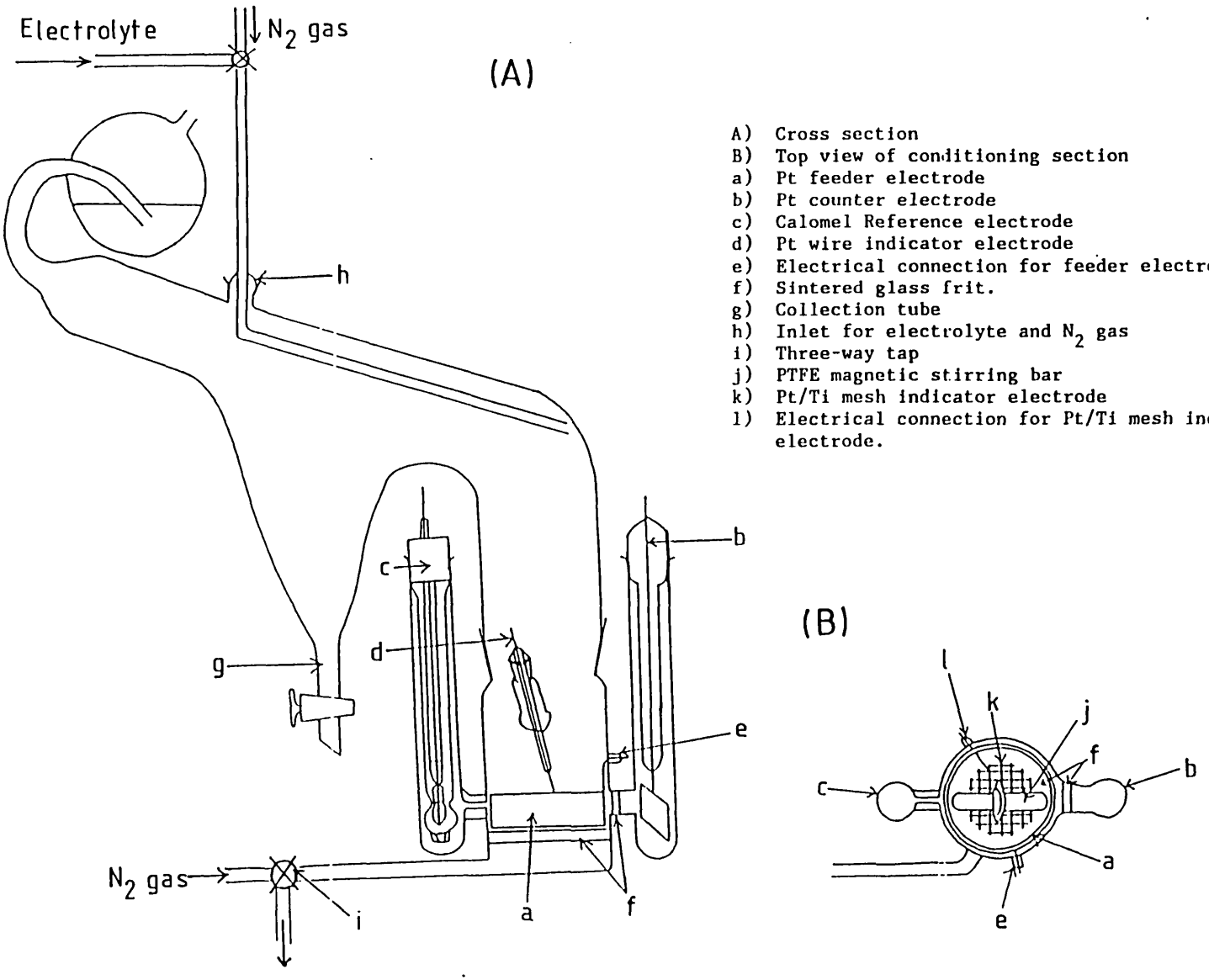
In principle, the cell operates by mineral particles in suspension acquiring the same potential as an inert feeder electrode (usually Pt), by contact with the feeder and/or by contact with "charged" particles during agitation.

4.3.1 Apparatus

A Hallimond tube flotation cell was adapted to allow the potential of mineral particles to be controlled electrochemically as shown in Figure 4.8. A smooth Pt ring around the bottom of the cell served as the feeder electrode. Its potential was controlled against a saturated calomel reference electrode (S.C.E.), which was connected to the flotation compartment through a Luggin capillary probe. A platinum counter electrode was located in a side arm separated from the main cell by a sintered glass disc. Agitation of the bed was achieved with a Teflon-coated magnetic stirrer.

It has been shown that when an inert electrode (Pt or Au) is inserted in a sulphide pulp it adopts a "slurry potential" which differs from that which the inert electrode would have in a filtered solution[73]. Although the potential across the sulphide/solution interface is the important parameter in determining floatability, this can differ from that at a platinum electrode in the same solution because other redox couples may determine the potential of the inert electrode, e.g. Fe^{3+}/Fe^{2+} and PtO_x/Pt (in deoxygenated solutions). Although the E_h potential obtained may not be applicable for theoretical interpretations of the chemistry involved, its measurement can serve as an indicator in monitoring the degree of oxidation or reduction of mineral particles[73,286-290]. Indeed E_h measurements in sulphide flotation circuits have proved a useful guide to plant behaviour[73,286,289,291-293].

However, a Pt electrode is not inert as it is often thought to be. Certain substances, eg H_2S, CN^- and dodecylamine, can seriously effect Eh measurements by forming resistive surface films on Pt, affecting charge transfer[288], so that the validity of E_h measurements in such systems is questionable. The extent of poisoning depends on the type and concentration of the poison, the solution pH and the period of immersion of the indicator electrode[289]. Natarajan and Iwasaki[288] showed that by increasing the pH, adsorbed H_2S on Pt was desorbed or transformed into either HS^- or S^{2-} depending on the pH. A resistive



A) Cross section
B) Top view of conditioning section
a) Pt feeder electrode
b) Pt counter electrode
c) Calomel Reference electrode
d) Pt wire indicator electrode
e) Electrical connection for feeder electrode
f) Sintered glass frit.
g) Collection tube
h) Inlet for electrolyte and N_2 gas
i) Three-way tap
j) PTFE magnetic stirring bar
k) Pt/Ti mesh indicator electrode
l) Electrical connection for Pt/Ti mesh indicator electrode.

Fig 4.8 Electro-Hallimond tube flotation cell

film did not form and by careful cleaning of the electrode reproducible measurements were obtained. They demonstrated that the type of pretreatment given to a platinum electrode determined its behaviour in subsequent measurements.

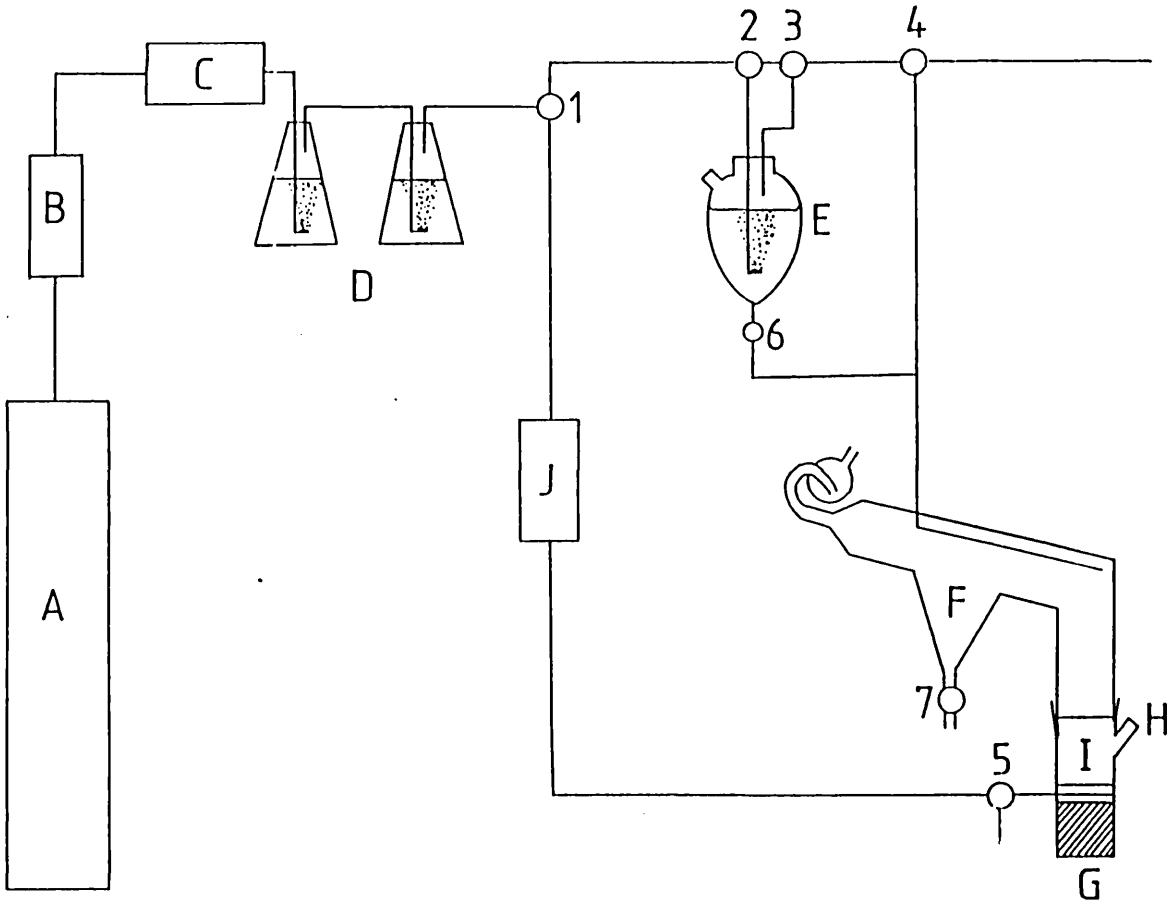
Either anodic or cathodic potential pulse pretreatment could result in oxygen or hydrogen remaining at the electrode surface after cleaning, and therefore influence subsequent E_h measurements. Natarajan and Iwasaki[286,288] recommended that Pt indicator electrodes should be mechanically cleaned since this procedure did not produce surface films and ensured reproducible results. They suggested that indicator electrodes for E_h measurements in flotation circuits should be designed for mechanical cleaning, either periodically or continuously, by contact with an abrading surface attached to a submerged rotating drum[288].

In these studies the E_h of the slurry was monitored with two inert electrodes, a Pt/Ti mesh electrode situated at the bottom of the main cell compartment, and a Pt wire electrode positioned just above the Teflon stirrer. The Pt wire electrode was mechanically polished prior to each experiment (see section 4.3.2).

All experiments were carried out under a nitrogen atmosphere, by using the system shown in Figure 4.9.

4.3.2 Experimental Procedure

Hand-selected mineral sulphide samples were crushed to about 0.5 mm with a hammer and porcelain pestle and mortar. The purest crystals of each sample were hand-picked and ground dry in an agate Tema mill. The product was screened at -212 μm and the oversize returned to the mill for further size reduction. After grinding, the sample was divided into closely sized fractions and each fraction washed in deoxygenated doubly distilled water to remove fines. Each fraction was then dried under vacuum and stored in airtight containers.



A - nitrogen gas cylinder; B - soda asbestos column; C - charcoal column; D - acidified vanadous solution with zinc;
E - electrolyte container; F - flotation cell collection tube; G - magnetic stirrer; H - side-arm; I - conditioning cell
J - flowmeter
1-5-T - taps; 6,7 - two way taps

Fig 4.9 System used in particulate bed electrode studies to exclude oxygen

Before each test, the cell was cleaned with nitric acid and, after placing it into the circuit (Figure 4.9), purified nitrogen was passed through it for 15 minutes by adjusting T-taps 4 and 5 in Figure 4.9. 30 cm^3 of deoxygenated buffer solution containing 1 M NaCl as a background electrolyte was transferred from flask E to the conditioning cell (I) by opening tap 6. The feeder electrode was cathodically polarised in the hydrogen evolution region to remove any oxidation layer on the surface of the electrode. 2 g of mineral sample (generally the -150+106 μm fraction) was transferred into the conditioning cell (I), via the side-arm (H), which housed the Pt-wire indicator electrode. This electrode was wet polished with 0.3 μm α- alumina on a "Selvyt" cloth, then washed with deoxygenated doubly distilled water, before being transferred into the cell. The sample was conditioned at the chosen feeder potential for 30 minutes with nitrogen passing through the cell and the PTFE-coated magnetic stirrer in operation (Plate 4.12). During the conditioning stage, the solution level was kept as low as possible, i.e. sufficient to cover the feeder and counter electrodes, so that feeder-particle and particle-particle contact was enhanced.

A "Ministat" potentiostat (H.B. Thompson Limited), programmed with a Hi-Tek PPR1 waveform generator, was used to control the feeder potential and a home-built buffer amplifier used for impedance matching. Indicator electrode potentials were monitored with, either a Sinclair digital voltmeter, or a Nicolet (Explorer I) digital storage oscilloscope (Plate 4.13).

After conditioning, gas flow through the solution was stopped by adjusting T-taps 1, 4 and 5 in Figure 4.9. Stirring was also stopped to allow the mineral particles in suspension to return to the base of the cell. The cell was then filled with deoxygenated buffer solution and three flotation cuts made after 5, 15 and 30 minutes, with a nitrogen flow-rate of 1 $cm^3\ s^{-1}$ (Plate 4.14). The floats were collected in the collection tube (F) and removed via Tap 7. They were then dried and weighed to determine flotation recovery.

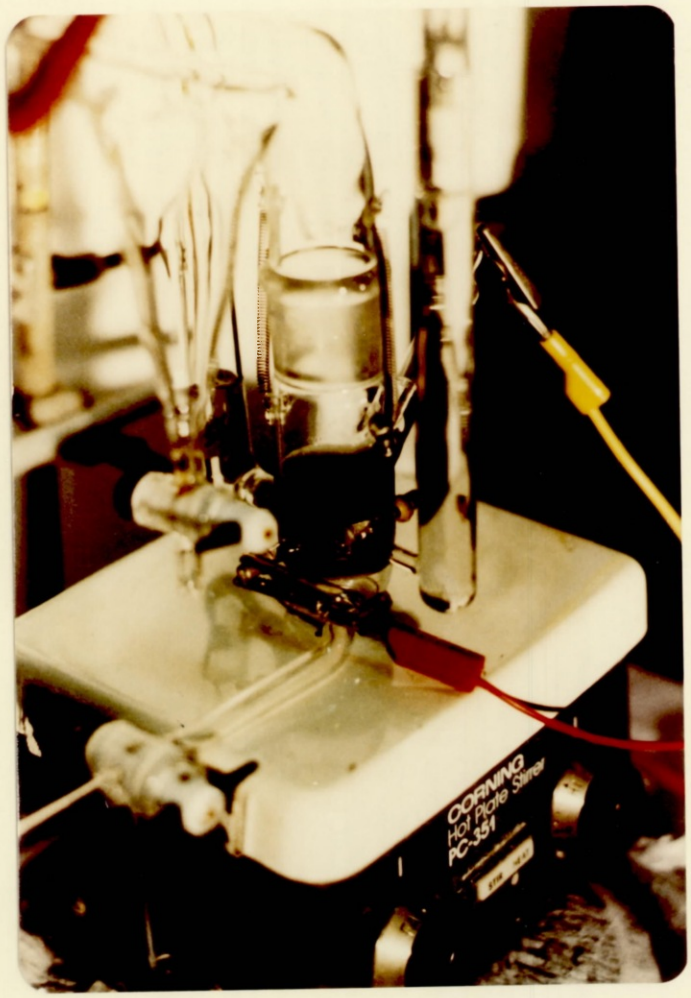


Plate 4.12 Conditioning of agitated mineral sulphide particles in the electro-Hallimond tube flotation cell.

4.3.3 Solution Analysis

The larger area of the particulate bed compared with that of the stationary mineral electrode was utilised to monitor the solution phase by chemical analysis. At various times during the conditioning stage known volumes of solution were withdrawn from the cell (I) via the side-arm (H) using a hypodermic syringe. Total iron and copper were determined by atomic absorption spectroscopy[294].
Analysis for sulphide and oxy-sulphur anions (eg $S_2O_3^{2-}$, $S_4O_6^{2-}$, SO_3^{2-}) was not carried out because these anions may be oxidised to sulphate by Fe(III) species released into solution. Sulphate analysis was not attempted because the usually gravimetric method of

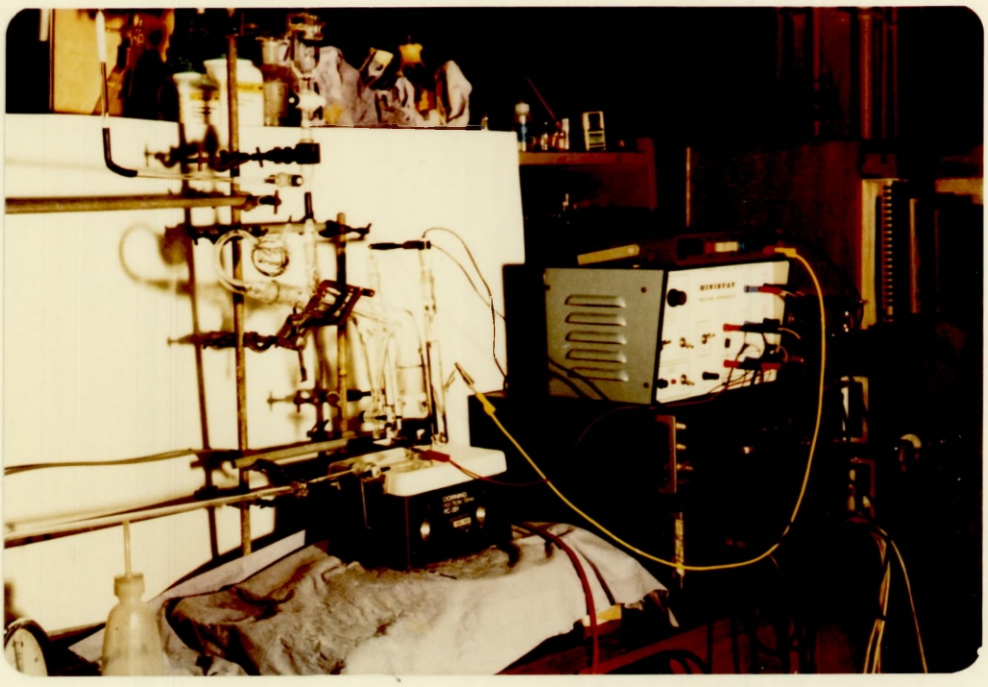


Plate 4.13 The electro-Hallimond tube flotation cell and electrochemical instrumentation used to control the Pt feeder electrode potential during the conditioning stage.

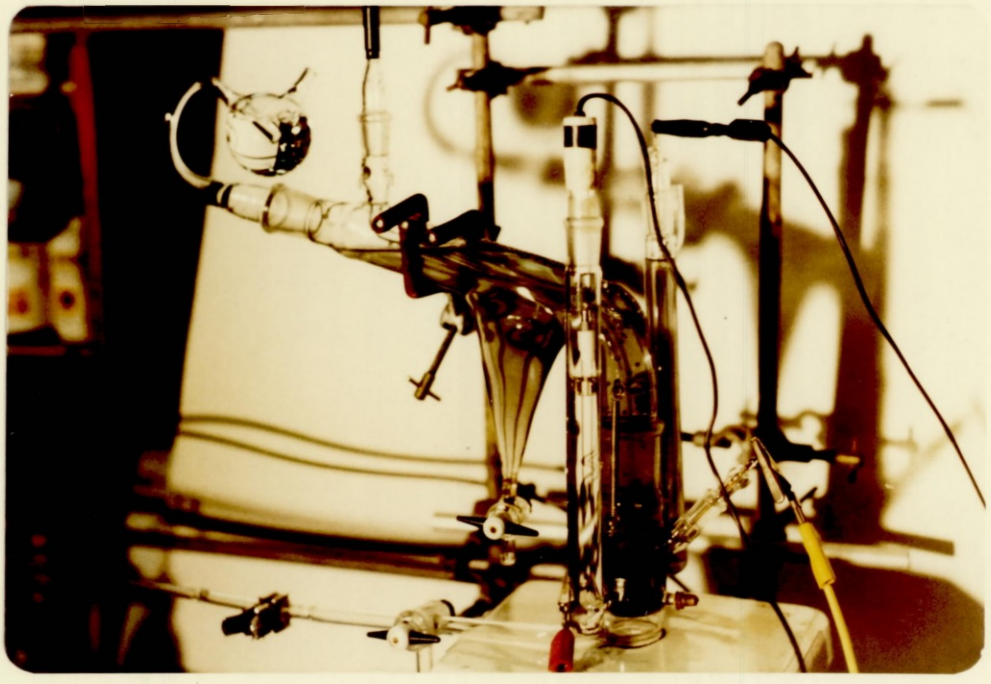


Plate 4.14 The electro-Hallimond tube flotation cell showing the flotation of mineral sulphide particles with purified nitrogen after conditioning.

determination is subject to numerous sources of errors, due mainly to coprecipitation of cations and other anions. This is a result of occlusion, whereby the contaminants are incorporated into the interior of the precipitate by adsorption during growth. Fe^{3+} causes serious errors due to the formation on hydrolysis of a positively charged ferric salt which is strongly adsorbed on the negatively charged barium sulphate[295].

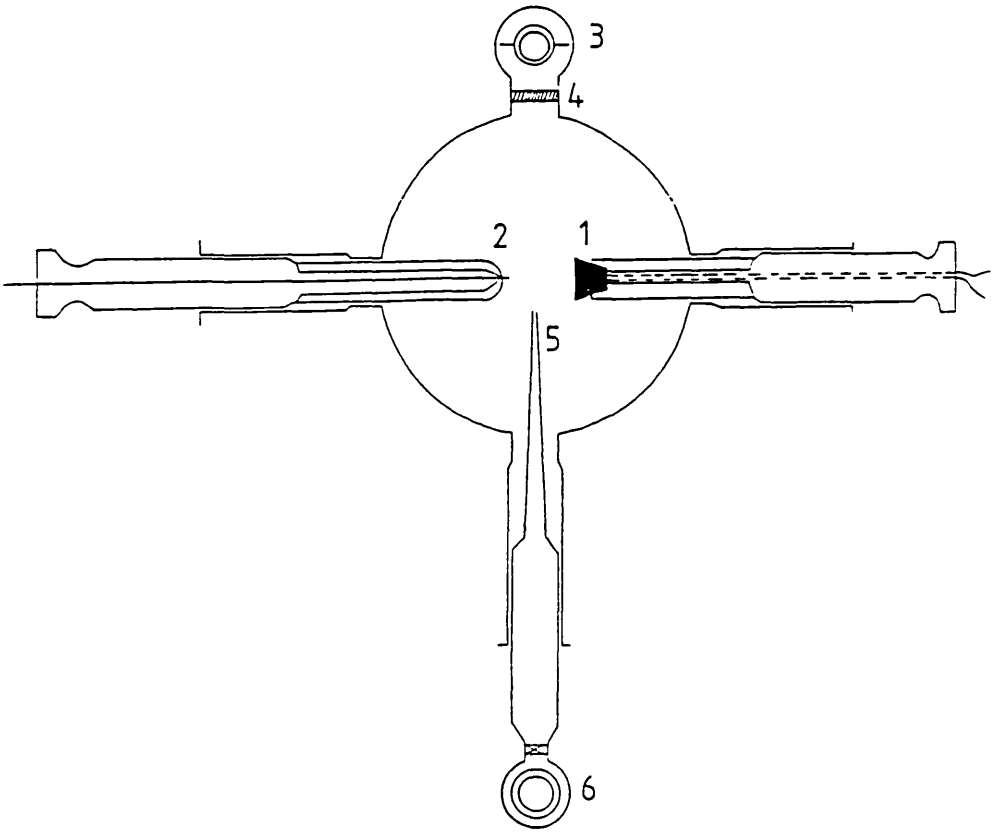
4.3.4 Contact Measurements

To gain a better understanding of the charging mechanism of mineral particles in a pulp/suspension electrode system, a four electrode glass cell was constructed as shown in Figure 4.10. A saturated calomel electrode (SCE) was used as the reference electrode and a Pt foil as the counter electrode. The feeder electrode was a Pt wire sealed through a glass capillary connected to the end of the plunger of a 10 cm glass syringe (Figure 4.11a). The mineral electrodes shown in Figure 4.11b and described in section (4.2.1) were used. Each electrode was wet polished on 600 grade silicon carbide paper and 0.3 μm - alumina, then introduced into the cell followed by the addition of deoxygenated buffer electrolyte.

To simulate feeder-particle contact in the pulp-suspension electrode system, the Pt feeder electrode was polarised at a chosen potential and the mineral electrode contacted to it. The change in the potential of the mineral electrode and the current response at the potentiostated Pt feeder electrode was recorded with a Nicolet (Explorer I) digital storage oscilloscope.

To simulate the contact of "charged" mineral particles with "uncharged" mineral particles in the pulp, a mineral electrode polarised at a chosen potential and an electrode of the same mineral contacted to it. The change in current of the former and potential of the latter was measured as described above for Pt-mineral contact experiments.

Fig 4.10 Electrochemical cell used in contact measurements and experiments on virgin sulphide surfaces. 1 - mineral electrode; 2 - platinum wire feeder electrode; 3 - counter electrode; 4 - sintered glass frit; 5 - Luggin capillary; 6 - reference electrode



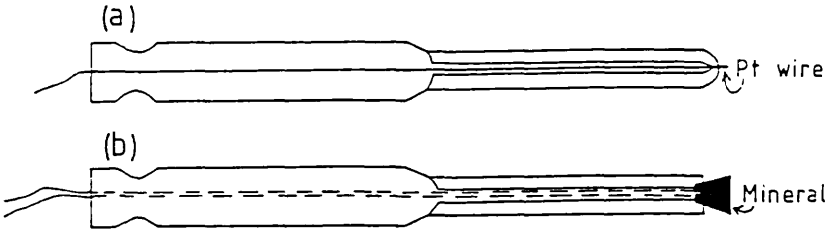


Fig 4.11 (a) Pt feeder electrode used in contact measurements
(b) Mineral electrode used in contact measurements and experiments on virgin sulphide surfaces.

RESULTS AND DISCUSSION

CHAPTER FIVE : THE ROTATING SPLIT CYLINDER BI-ELECTRODE (RSCBE)

5.1 Calibration

A pyrite RSCBE was calibrated over a wide range of rotational frequencies, using the reactions:-

$$Fe(CN)_6^{3-} + e \underset{}{\overset{i_{WE}}{\rightleftharpoons}} Fe(CN)_6^{4-} \quad \ldots\ldots\ldots (r_1)$$

$$E = 0.46 + 0.0591 \log [Fe(CN)_6^{3-}] - 0.0591 \log [Fe(CN)_6^{4-}]$$

The collection efficiency (N) is defined as:-

$$N = - \frac{i_c}{i_{WE}} \qquad (5.1)$$

where i_c and i_{WE} are the collector and working electrode currents, respectively.

The collection efficiency was measured firstly under conditions whereby the reduction of $Fe(CN)_6^{3-}$ to $Fe(CN)_6^{4-}$ at the pyrite working electrode and the reverse reaction at the Pt collector electrode were both under diffusion control.

Cyclic voltammograms of pyrite and platinum in 0.1 M $K_3[Fe(CN)_6]$ with 0.1 M NaOH supporting electrolyte are shown in Figures 5.1 and 5.2 respectively. For comparison, voltammograms of each electrode in the absence of ferricyanide are also shown. Reduction of ferricyanide on pyrite was under mass transfer control at potentials < 0.2 V (Figure 5.1). On platinum, oxidation of the ferrocyanide product formed cathodically was under diffusion control at potentials > 0.8 V (Figure 5.2).

Although the pyrite working electrode currents increased steadily at potentials > 0.5 V no anodic limiting current was observed indicating

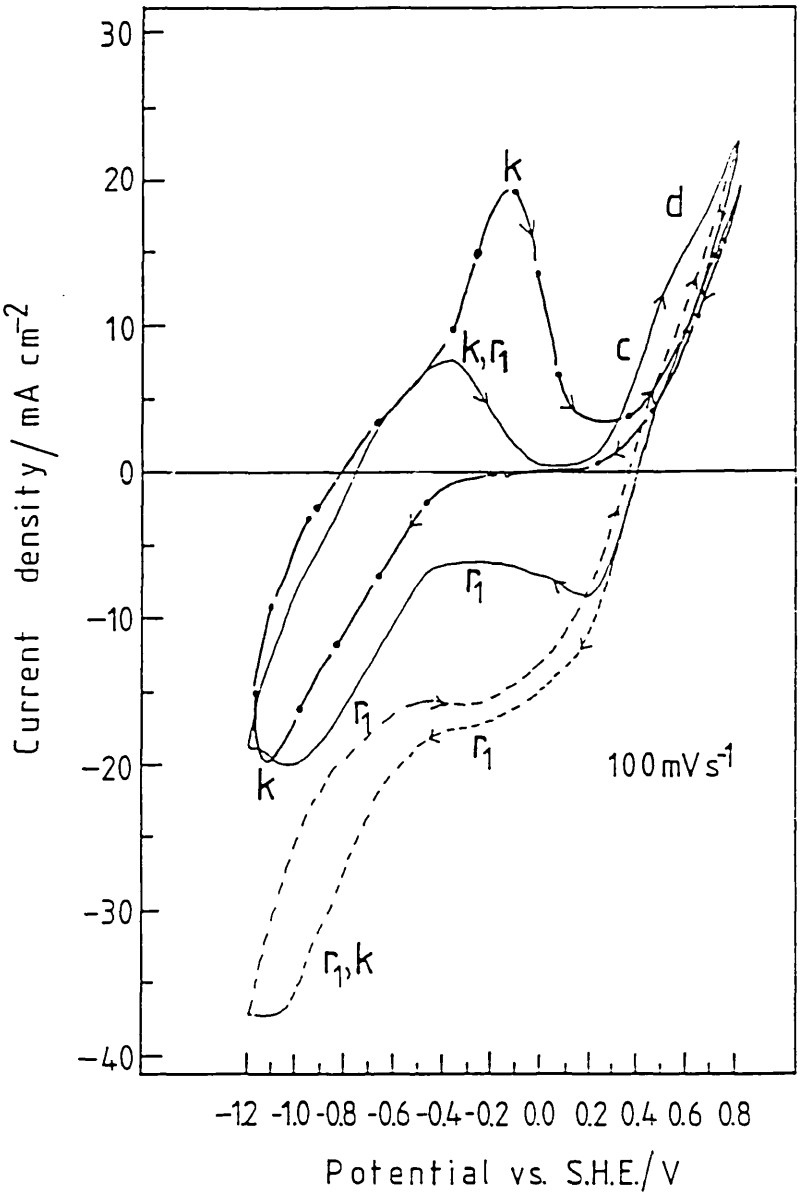


Fig 5.1 Cyclic voltammograms of RSCBE pyrite working electrode in 0.1 M $K_3[Fe(CN)_6]$ + 0.1 M NaOH. (——) ω = 0 Hz; (---) ω = 10 Hz; (-.-) voltammogram in 0.1 M NaOH only, ω = 0 Hz.

that the current at high anodic potentials was due almost exclusively to mineral oxidation (reactions (c) and (d)) and not ferrocyanide oxidation. Similar behaviour has been observed on synthetic millerite (NiS)[296].

The collection efficiency was obtained by holding the pyrite and platinum electrodes at constant potentials of -0.5 V and 1.0 V

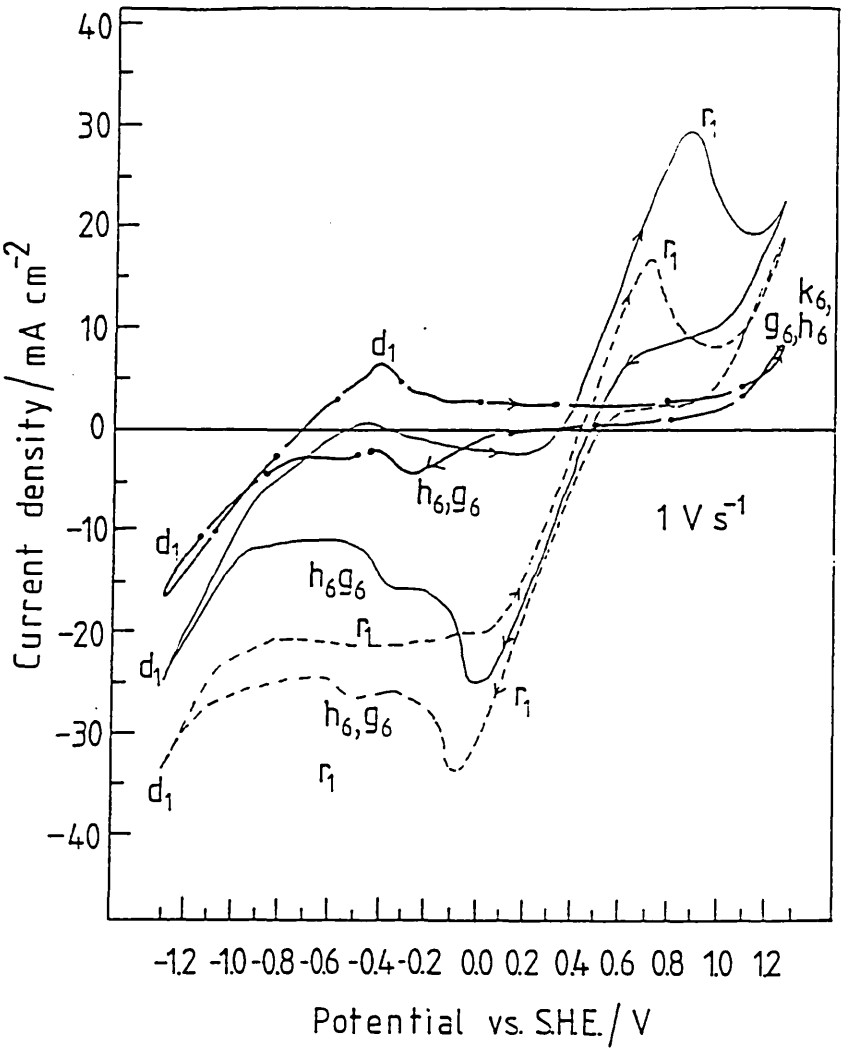


Fig 5.2 Cyclic voltammograms of RSCBE Pt collector electrode in 0.1 M $K_3[Fe(CN)_6]$ + 0.1 M NaOH. (——) ω = 0 Hz; (---) ω = 10 Hz; (-.-) voltammogram in 0.1 M NaOH only, ω = 0 Hz.

respectively, and measuring i_{WE} and i_c as a function of electrode rotation speed (ω).

The mass transfer coefficient K_m has been obtained empirically for a rotating cylinder[297].

$$Sh = 0.079\ Re^{0.70}\ Sc^{0.356} \qquad (5.2)$$

$$\therefore K_m = 0.079\ r^{0.4}\ \nu^{-0.344}\ \omega^{0.7}\ D^{0.644} \qquad (5.3)$$

For a simple steady state diffusion layer model the value of the limiting current i_L is given by:-

$$i_L = nFA\ K_m\ C_o^j \qquad (5.4)$$

where C_o^j = bulk concentration of species j

Substituting (5.3) in (5.4)

$$i_L = 0.079\ nFAr^{0.4}\nu^{-0.344}\omega^{0.7}D^{0.644}C_o^j \qquad (5.5)$$

Thus for a RSCBE a plot of i_{WE} versus (rotation rate, $\omega)^{0.7}$ should be linear as was found to be the case (Figure 5.3). This is in contrast

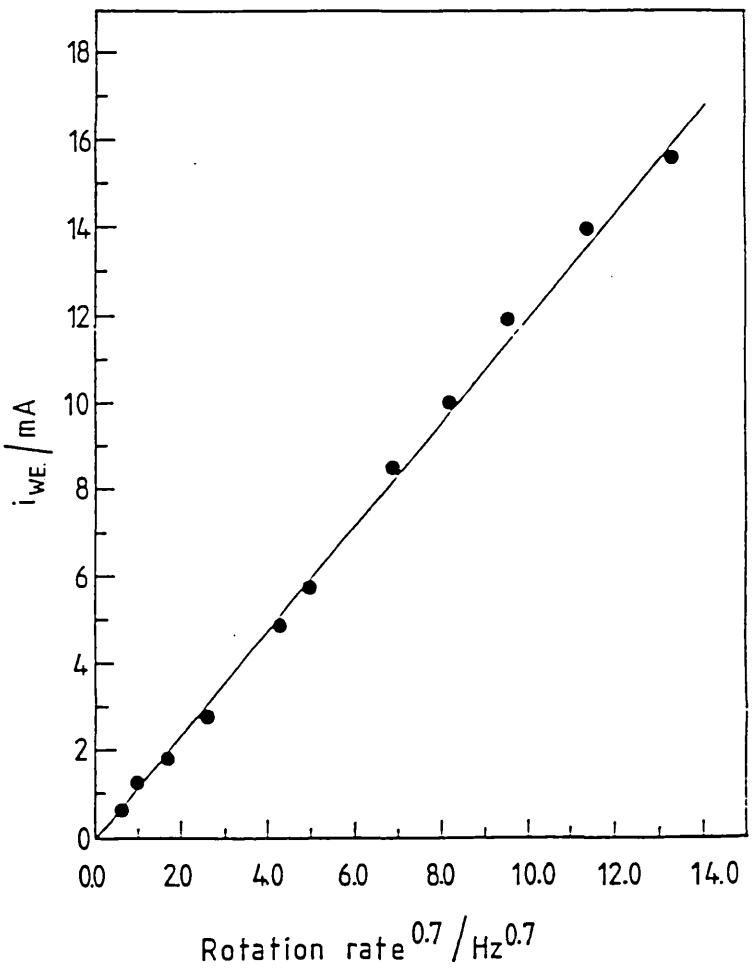


Fig 5.3 0.1 M ferricyanide reduction current at a RSCBE pyrite working electrode in 0.1 M $K_3[Fe(CN)_6]$ + 0.1 M NaOH, as a function of (rotation rate, $\omega)^{0.7}$. ($E_{WE(FeS_2)}$ = -0.5 V).

to the results of McKubre and Macdonald[273], who with a similar bi-electrode system overlooked low rotation rate non-linearity in their limiting current against (rotation rate, ω)$^{0.5}$ plots, chosen by analogy with the behaviour of rotating ring-disc electrode systems [270] (see Figure 5.4).

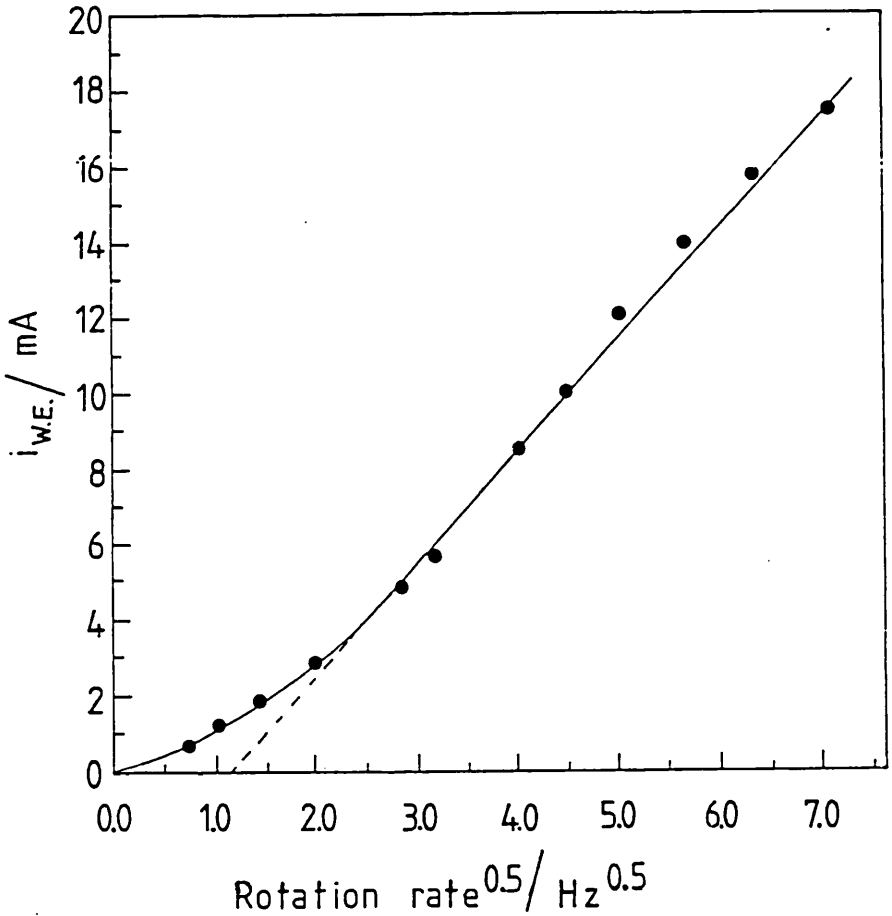


Fig 5.4 0.1 M ferricyanide reduction current at a RSCBE pyrite working electrode in 0.1 M $K_3[Fe(CN)_6]$ + 0.1 M NaOH, as a function of (rotation rate, ω)$^{0.5}$ to show low rotation rate non-linearity. ($E_{WE(FeS_2)}$ = -0.5 V).

i_{WE} was plotted against i_c for rotation rates between 0.5 and 50 Hz (Figure 5.5). A clear linearity was observed with an average collection efficiency of 72% over all rotation rates used. However, if the collection efficiency, calculated at each rotation rate, was plotted as a function of ω (Figure 5.6; ⊙), it was evident that at ω values < 5 Hz the collection efficiency decreased rapidly. This was

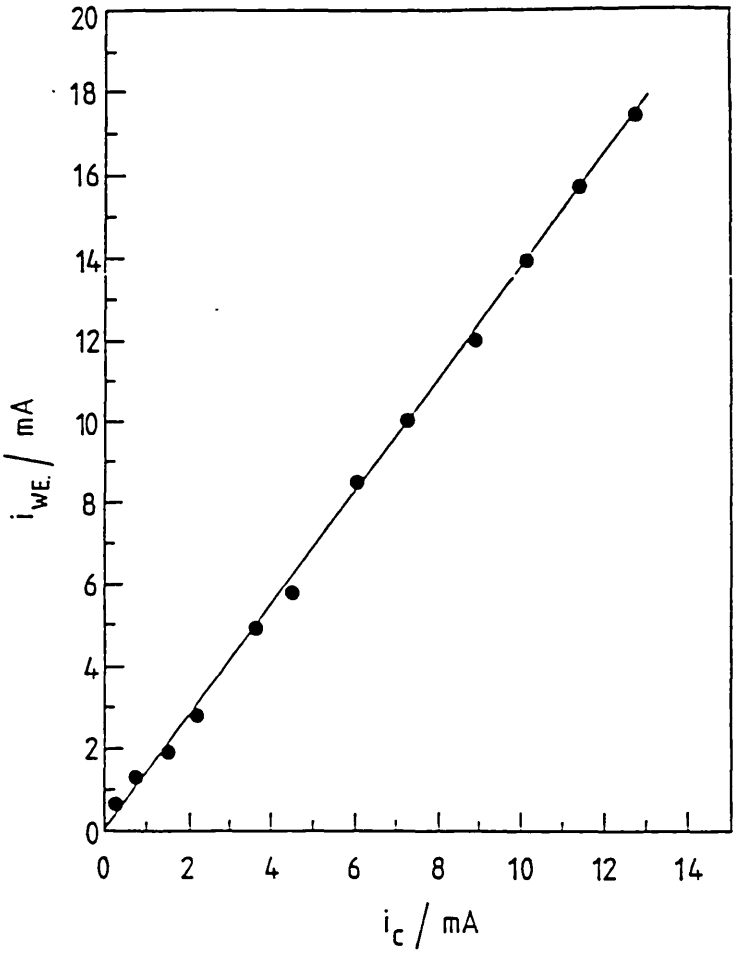


Fig 5.5 Calibration of pyrite working, Pt collector, RSCBE in 0.1 M $K_3[Fe(CN)_6]$ + 0.1 M NaOH. ($E_{WE(FeS_2)}$ = -0.5 V, $E_{c(Pt)}$ = 1.0 V).

presumably due to the increasing influence of radial dispersion with decreasing rotation speed. At ω values > 5 Hz the collection efficiency remained at between 75 and 80 %.

Collection efficiency was also calibrated for conditions at which $Fe(CN)_6^{3-}$ reduction at the mineral working electrode was under electron transfer control and $Fe(CN)_6^{4-}$ oxidation at the Pt collector was under diffusion control. The working electrode was held at 0.4 V where the net current on pyrite was zero. The electrode potential was then pulsed cathodically to 0.3 V for four seconds to reduce $Fe(CN)_6^{3-}$ under electron transfer control (see Figure 5.1). The cathodic charge

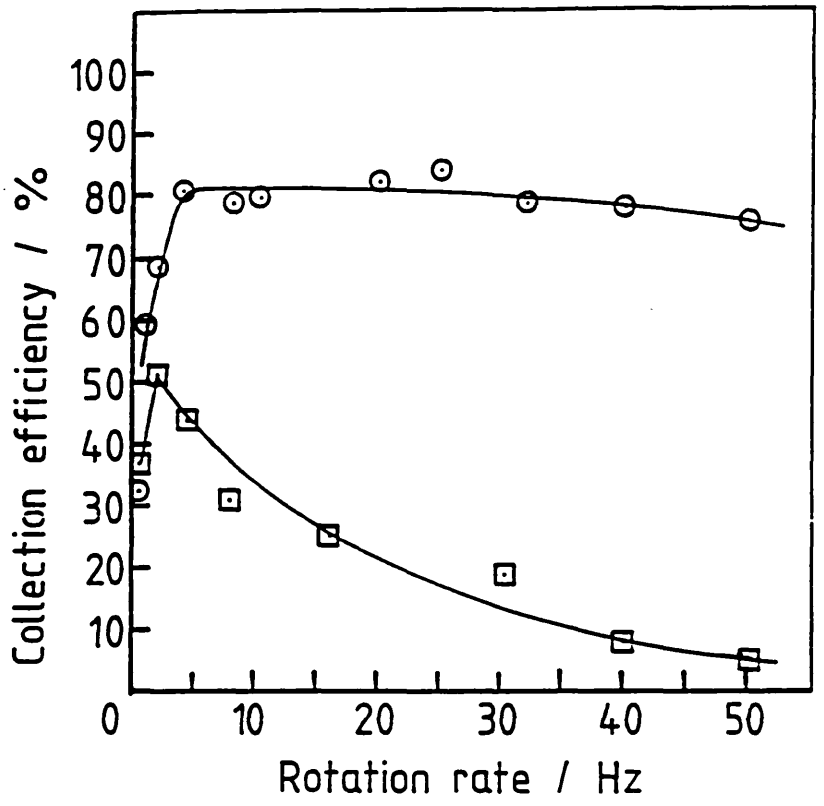


Fig 5.6 Collector efficiency of RSCBE in 0.1 M $K_3[Fe(CN)_6]$ + 0.1 M NaOH, as a function of ω. (⊙) mass transport controlled; (⊡) charge transfer controlled working electrode reaction.

passed at the working electrode, and the anodic charge due to $Fe(CN)_6^{4-}$ oxidation at the Pt collector (held at a constant potential of 1.0 V), was measured and the collection efficiency calculated. The amount of cathodic charge passed was constant for all experiments and independent of rotation rate. The collection efficiency versus ω plot for this situation is also shown in Figure 5.6 (—⊡—).

The collection efficiency passed through a maximum at a rotation rate of 2.25 Hz. At ω values < 2.25 Hz the steady decrease in collection efficiency from a maximum figure of 52% was probably due to the influence of radial dispersion again. The increase in radial dispersion at high rotation rates may be due to the formation of stable hydrodynamic vortices with radial components of convection[298], Figure 5.7 B.

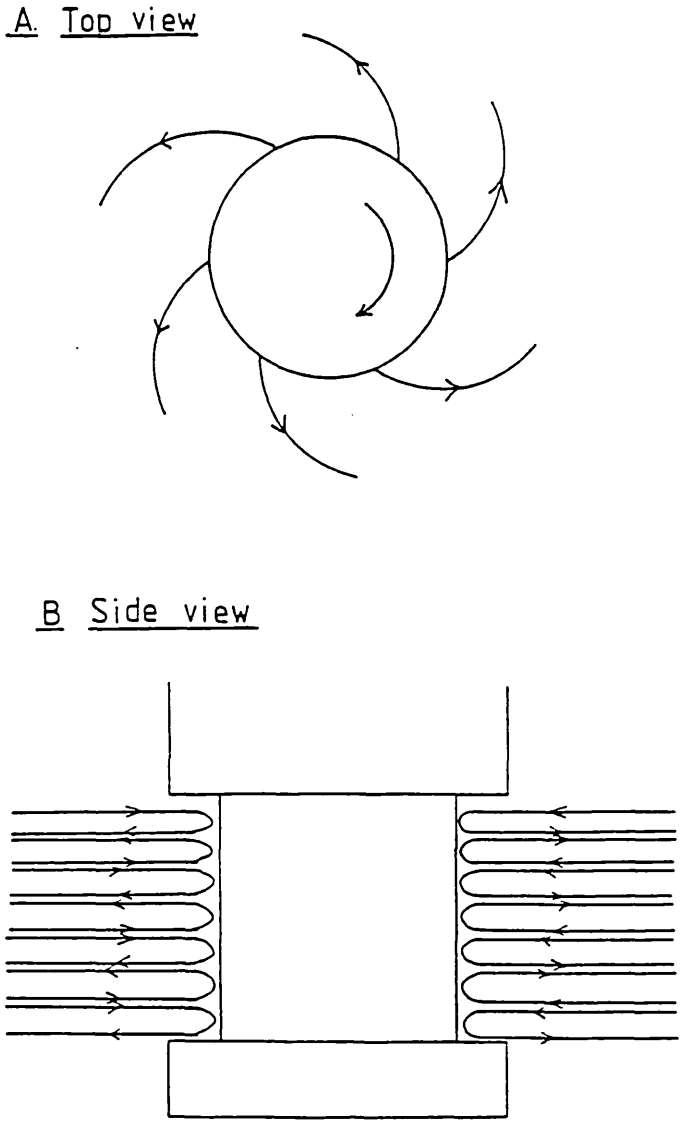


Fig 5.7 Hydrodynamic flow around a RSCBE.

5.2 Detection of Soluble Electroactive Species (Fe^{2+}, Fe^{3+}, H_2S)

Platinum was chosen as the "inert" substrate collector electrode of the RSCBE because it was found that Fe^{3+} reduction to Fe^{2+} at potentials < 0.7 V and Fe^{2+} oxidation to Fe^{3+} in the potential range 0.8 to 1.2 V could be detected in the absence of H_2S oxidation, which occurred only at potentials > 1.2 V (Figure 5.9). Cyclic

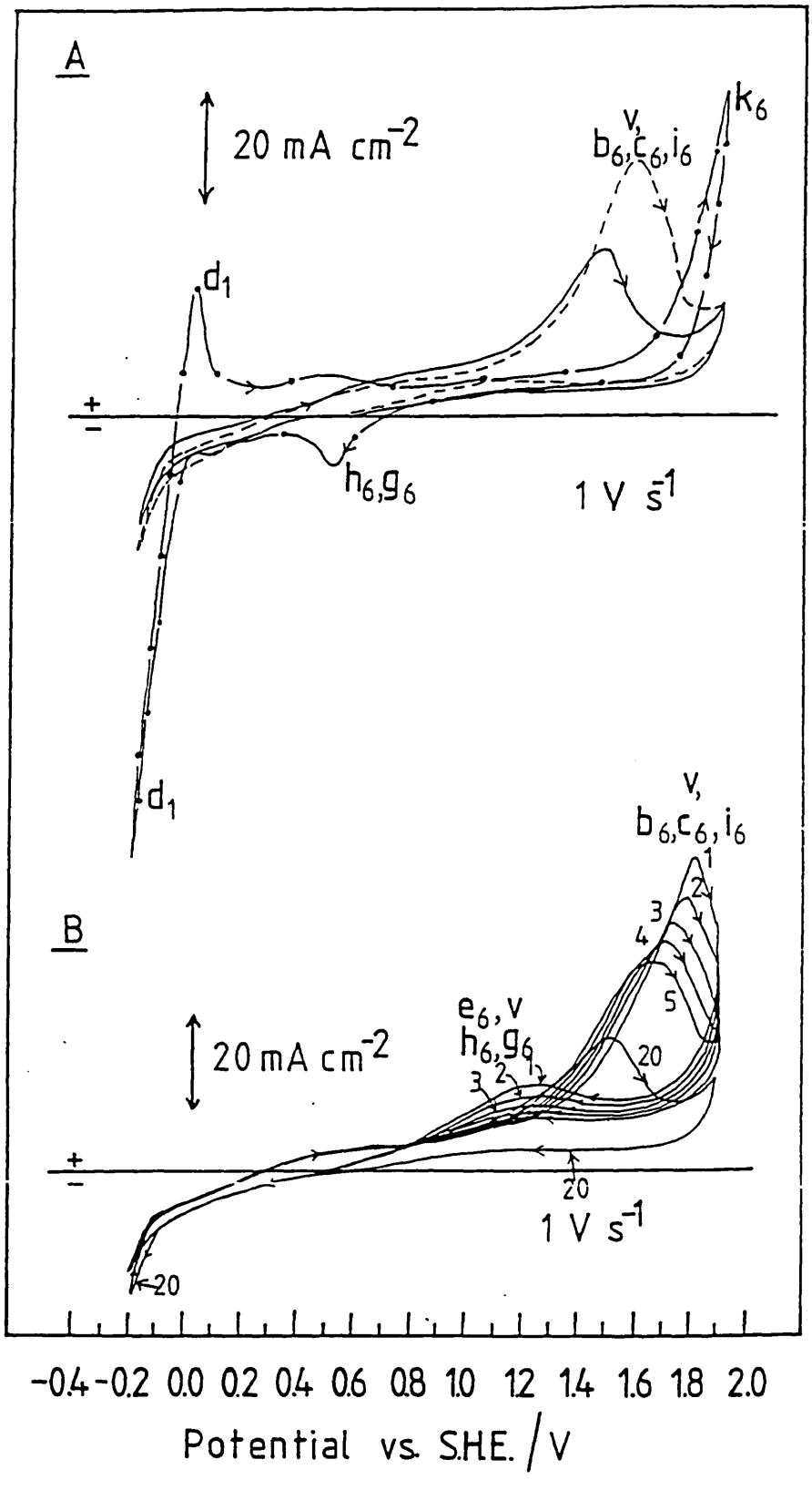


Fig 5.8 Cyclic voltammograms of RSCBE Pt collector electrode in 1M $HClO_4$ + 0.1 M Na_2S. (——) ω = 0 Hz; (---) ω = 10 Hz; (-.-) no sulphide, ω = 0 Hz.

voltammograms of platinum in 1 mol $HClO_4$ plus 0.1 mol Na_2S dm^{-3} are shown in Figures 5.8 and 5.9. A broad oxidation peak with a maximum at about 1.0 V was observed during the first scan only (Figure 5.9). Najdeker and Bishop[137] interpreted this peak in terms of the reaction:-

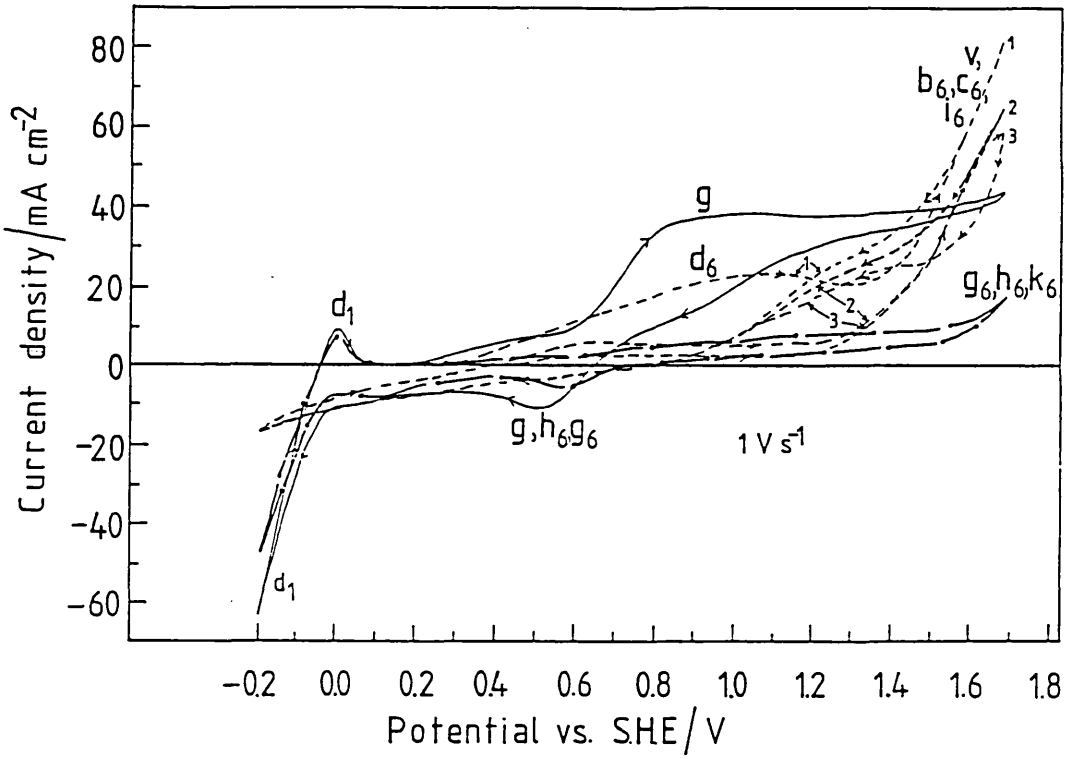


Fig 5.9 Cyclic voltammograms of RSCBE Pt collector electrode in: (——) 1 M $HClO_4$ + 0.1 M $FeSO_4$, ω = 10 Hz; (---) 1M $HClO_4$ + 0.1 M Na_2S (first three cycles), ω = 10 Hz; (-.-) 1 M $HClO_4$, ω = 10 Hz.

$$Pt.(H_2S)_x = PtS_x + 2xH^+ + 2xe \ldots\ldots\ldots(d_6)$$

(where x = 1 or 2)

They assumed that H_2S is strongly adsorbed on the Pt surface immediately on immersion, forming $Pt.(H_2S)_x$.

On the premise that platinum (IV) sulphide is soluble in polysulphides whereas the monosulphide is not, the results of Najdeker and Bishop

suggested that platinum (IV) sulphide is the species formed on the electrode surface during the oxidation of hydrogen sulphide [137]. However, from electrode diffraction data Ramasubramanian[138] concluded that the monosulphide (PtS) was formed.

At potentials anodic of 1.3 V the current increased sharply on the first sweep to given an anodic wave at 1.8 V (Figure 5.8 B). Oxide formation or oxygen chemisorption was not evident, as indicated by the absence of a corresponding cathodic peak at about 0.7 V on the reverse scan. Repeated cycling caused the anodic peak at 1.8 V to decrease in size and for the peak potential to shift to less anodic potentials. After 20 cycles the I/E response remained unchanged; the anodic peak potential being 1.52 V (Figure 5.8 B). The reaction assigned to this peak was oxidation of H_2S in solution to form elemental sulphur (reaction (v)) rather than the oxidation of platinum sulphide formed at lower potential (reactions (b_6), (c_6)), because the peak exhibited a large stirring rate dependence (Figure 5.8 A).

During the first five potential cycles, an anodic peak was observed at 1.2 V on the reverse cathodic potential scans. A similar peak was reported[138,300] at high sulphide concentrations (> 0.2 M). Other workers observed a cathodic peak in this potential region, which grew on repeated cycling; this was assigned to platinum oxide reduction.

Although the main reaction giving rise to the anodic peak at 1.8 V on the forward going scan was H_2S oxidation (reaction (v)), oxidation of PtS_2 to form platinum oxide, elemental sulphur and sulphate (reactions (b_6), (c_6) and (i_6)) probably occurred in parallel with reaction (v) to a lesser extent. On the return scan platinum oxide may be reduced to platinum by reactions (h_6) and (g_6). It is known that PtS_2 film formation decreases the rate of sulphur oxidation and that sulphide oxidation is not observed on oxide covered surfaces[300]. Thus, when platinum oxide was reduced on the reverse potential scan, H_2S oxidation was enhanced on the underlying Pt metal surface, leading to a net anodic peak current. Similar behaviour has been observed in the oxidation of organic substrates[323].

On repetitive cycling a thick sulphur layer was formed on top of the PtS_2 film, retarding H_2S and PtS_2 oxidation, resulting in a decrease in the height of the anodic peaks on the forward and reverse scans. Sulphur reduction was not observed before hydrogen evolution, which occurred at < -0.25 V, under the fast scan rates used in these experiments. The absence of current peaks associated with hydrogen adsorption and desorption indicate that sulphide inhibits these processes and depresses hydrogen evolution by ~ 250 mV (Figure 5.8 A). Clearly, sulphur reduction on Pt is a very slow process. It has been reported that sulphur can be removed galvanostatically at very low current densities[300].

Any further work carried out on the electrochemical behaviour of Pt in sulphide solutions needs to look at the effect of sulphide ion concentration in greater detail. Discrepancies in the results of various authors can be attributed to the wide range of sulphide concentrations used in different investigations. Greater care needs to be taken in the preparation of sulphide solutions to ensure that the surface layers on sulphide crystals are removed before dissolution and that deaerated distilled water is used to make up solutions, thus minimising sulphide oxidation prior to carrying out experiments.

CHAPTER SIX

ELECTROCHEMICAL STUDIES ON PYRITE ELECTRODES

CHAPTER SIX : ELECTROCHEMICAL STUDIES ON PYRITE ELECTRODES

6.1 Thermodynamics

Potential (E_h)-pH and activity-pH diagrams for the S-H_2O and Fe-S-H_2O systems are presented in Appendix II. The thermodynamic equations used to construct these diagrams were calculated from recently published[355], critically assessed free energy of formation data for the various species present in each system (see Tables II(i) and II(ii), Appendix II).

The E_h-pH diagram (Figure 6.1) for the S-H_2O system at 298 K[361] shows that the stability domain of sulphur is triangular and very

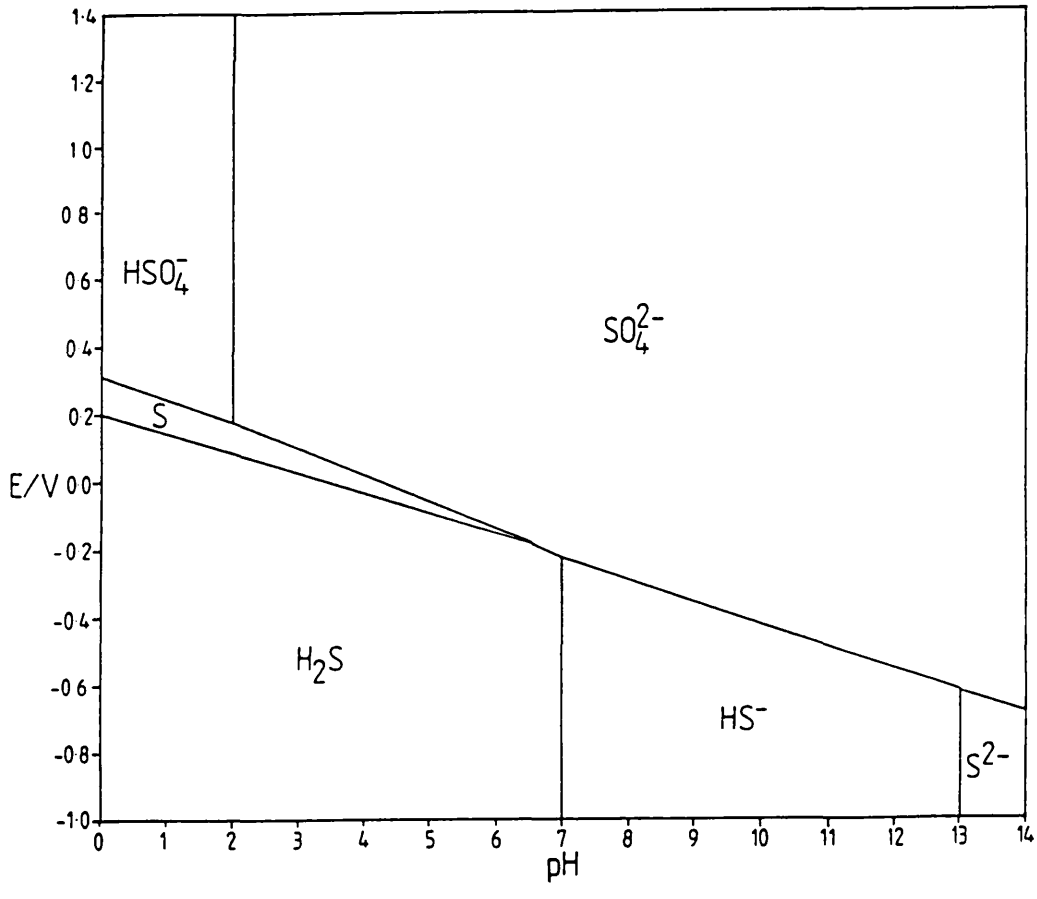


Fig 6.1 Potential-pH diagram for the S-H_2O system at 298 K with a dissolved sulphur activity of 10^{-3}[361].

narrow, but nevertheless appears as a stable phase if the activity of sulphur species in solution is sufficiently high (> 10^{-6} M). Figure 6.1 shows that under oxidising conditions elemental sulphur is not stable at pH < 4. Oxidative acidic dissolution of sulphur has been widely studied using O_2[224,256], HNO_3[357], $KClO_3$[357] and bacteria[358] as the oxidising agents, the major product being sulphuric acid[357]:-

$$S + 4H_2O = H_2SO_4 + 6H^+ + 6e \qquad (at_1)$$

Species such as sulphites do not appear in Figure 6.1 as they are thermodynamically unstable with respect to sulphates. However, electrochemical reactions involving sulphate are kinetically very slow or irreversible[65]. Thus elemental sulphur and/or sulphur-oxygen species such as $S_2O_3^{2-}$, $S_4O_6^{2-}$, SO_3^{2-}, $S_2O_6^{2-}$ may be formed as metastable phases over the relatively short time scales relevant to the interpretation of voltammetric behaviour. Consequently, E_h-pH diagrams for the S-H_2O system, which exclude sulphur (VI) species and then all sulphur-oxygen compounds are also included in Appendix II.

Figure 6.1 shows that at high pH values there is no sulphur stability region, and this correlates well with some of the observed reactions of sulphur at pH > 6. Peters[65] observed that sulphur dissolves at high pH in sulphate solution to yield:-

$$SO_3^{2-} + S^\circ = S_2O_3^{2-} \qquad (bb_1)$$

while Chen et al[165] found that sulphur disproportionates in alkali solutions (pH > 8) to yield both thiosulphate and sulphide ions:-

$$4S^\circ + 6OH^- = S_2O_3^{2-} + 2S^{2-} + 3H_2O \qquad (bc_1)$$

Other workers[65,357] have observed that in aqueous ammonia and $Ca(OH)_2$, polysulphides and thiosulphate are formed:-

$$12S^\circ + 6OH^- = S_2O_3^{2-} + 2S_5^{2-} + 3H_2O \qquad (bd_1)$$

From thermodynamic predictions, the reduction of elemental sulphur to H_2S should be facile. However, sulphur does not readily reduce to lower valence states, though H_2[359], iron powder/HCl[360] and bacteria[358] have been used as chemical reductants.

The E_h-pH diagram (Figure 6.2) for the Fe-S-H_2O system at 298 K was generated for dissolved sulphur and iron activities of 10^{-4} M. Reactions were considered between all possible combinations of species included in Table II(ii) (Appendix II), which incorporated data for nine iron solution species not considered by Bouet et al[354]. The areas of stability for the solid phases considered are enclosed by solid lines and dashed lines define the equilibria between prominant solution species.

Figure 6.2 shows that at low pH, pyrite becomes unstable with respect to Fe^{2+} and H_2S, or at more oxidising potentials with respect to Fe^{2+}, S° and SO_4^{2-}. At neutral and alkaline pH values pyrite oxidises to FeOOH and SO_4^{2-}. The main difference between this diagram and those reported by others[61,64,65,134,354] was the increased area of stability of ferric oxide/hydroxide, which was shifted to lower pH values due to the inclusion of FeOOH in the calculations. In addition, pyrite probably exhibits a meta-stable boundary at more oxidising potentials than those dictated by thermodynamic considerations due to the irreversibility of sulphate formation[65,134]. Such a meta-stable behaviour would result in the formation of FeOOH and SO_4^{2-} over a wider pH range than that shown in Figure 6.2.

6.2 Rest Potential Measurements

The rest potential of polished untreated and sulphidised pyrite electrodes are shown in Figure 6.3. A sulphidising pretreatment of pyrite electrodes with aqueous sodium sulphide solution prior to measuring their open circuit potential lowered the rest potential by about 0.35 V at all pH values. However, the rest potential of the sulphidised electrodes gradually increased with time and eventually reached the potential of untreated electrodes after 45 - 60 minutes.

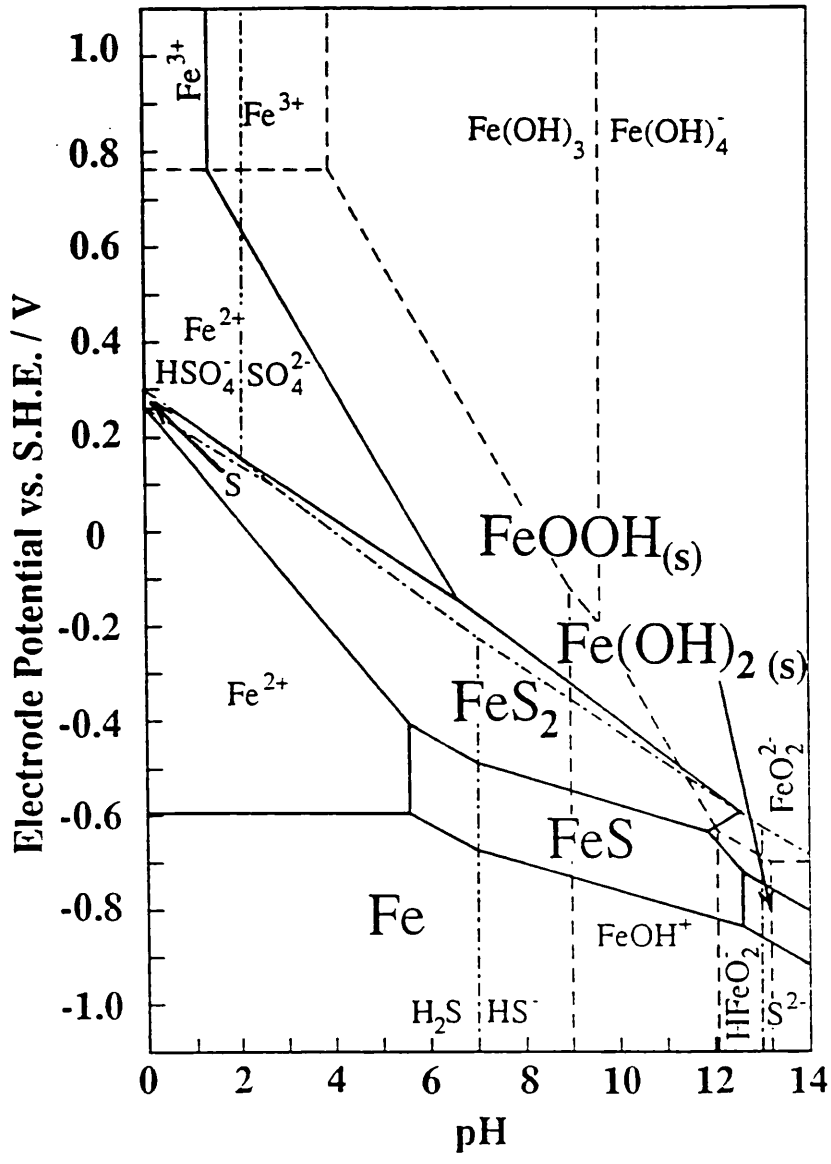


Fig 6.2 Potential-pH diagram for the Fe-S-H_2O system at 298 K with dissolved iron and sulphur activities of 10^{-4}.

The use of sulphidising pretreatments of sulphide mineral electrodes has been rightly criticised by Trahar and Heyes[333] because of the probable deposition of elemental sulphur in oxygen-containing solutions. Therefore the effects of such pretreatments were compared with those of in situ abrasion (see section 6.3).

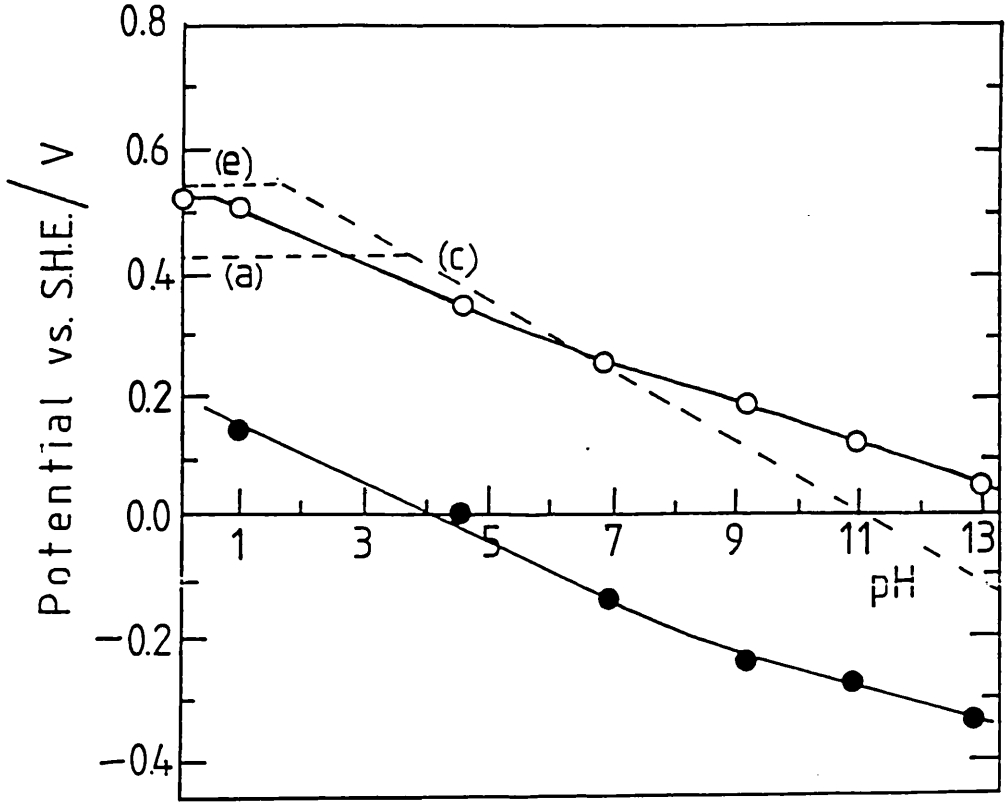


Fig 6.3 The change of rest potential with pH for a pyrite electrode subject to different pretreatments. (O) no pretreatment; (●) sulphidised.

The open-circuit potential of untreated pyrite electrodes showed a pH independent region at pH values < 0.5. Other workers have reported the rest potential to be independent of pH at values < 2 [130,131]. The open circuit potential in the pH independent region was approximately 0.54 V. At pH values > 0.5 the rest potential of pyrite decreased with pH by approximately 40 mV pH^{-1} for both untreated and sulphidised electrodes. As pyrite is a good electrocatalyst for oxygen reduction [185 - 187] a surface iron oxide or hydroxide was probably formed during polishing and washing, even in nominally deoxygenated solutions. At low pH values the hydroxide will dissolve by reaction (o_1).

$$Fe^{3+} + 3H_2O = Fe(OH)_3 + 3H^+ \qquad (o_1)$$

$$\log [Fe^{3+}] = 4.84 - 3\ pH$$

A conditioning time greater than 5 minutes prior to measuring the rest potential in acid solutions is probably needed to remove the oxide layer from the surface by reaction (o_1) and extend the pH independent region up to pH 2.

A pH-independent potential region was not observed for the sulphidised electrodes because the rest potential measured after 5 minutes was not a true equilibrium potential. The potential continued to increase with time until it reached the value obtained for an untreated electrode. Figure 6.2 shows that the potential of freshly polished unoxidised pyrite under oxygen-free conditions is probably controlled by reaction (a) (see Appendix I).

$$FeS_2 = Fe^{2+} + 2S + 2e \qquad (a)$$

$$E = 0.423 + 0.0295 \log [Fe^{2+}]$$

in acid solutions, whereas in neutral and alkaline solutions reaction (c) determines the potential (assuming sulphate formation (reaction (d)) is very slow):-

$$FeS_2 + 3H_2O = Fe(OH)_3 + 2S + 3H^+ + 3e \qquad (c)$$

$$E = 0.64 - 0.0591\ pH$$

These reactions are represented, respectively by the horizontal pH independent line (a) and the diagonal pH dependent line (c) in Figure 6.3. Region (c) corresponds to the potential of a mineral surface passivated by the formation of oxides or hydroxides. Such a passive oxide electrode may function as a pH electrode with a slope of 0.059 V pH^{-1} [287]. Reaction (c) is in reasonable agreement with the potential/pH slope of pyrite electrodes in the pH range 1 to 13.

The measured rest potential of freshly polished pyrite in deoxygenated 1 M $HClO_4$ of 0.537 V was similar to the 0.62 V reported by Peters and Majima[66] for 'passive' pyrite in 1 M $HClO_4$ (solution exposed to air). They also reported a value of 0.2 to 0.3 V for 'active' pyrite (cathodically pretreated), which agrees well with that measured for sulphidised pyrite electrodes. Peters and Majima[66] argued that the cathodic pretreatment generated a clean pyrite surface which had a thermodynamic potential consistent with reaction (a) when corrected for the Fe^{2+} activity. Their results indicated that pyrite in its natural state with a rest potential of 0.62 V is 'passive'. They ascribed the passive film to either adsorbed oxygen or an oxygen sulphur compound. However, they failed to explain why the open-circuit potential of initially active pyrite increases slowly with time to a value ~ 0.3 V higher than that predicted by reaction (a), even in 'deoxygenated' solutions.

Work in acidic solutions has shown that following a cathodic pretreatment to remove either an inhibiting sulphur or oxide layer, the open-circuit potential of binary metal sulphides (ie FeS, PbS, NiS and ZnS) is probably determined by a mixed potential mechanism involving the anodic process:-

$$MS = M^{2+} + S^{\circ} + 2e \qquad (6.1)$$

and the cathodic process:-

$$S^{\circ} + 2H^{+} + 2e = H_2S \qquad (v)$$

$$E = 0.141 - 0.0591\ pH - 0.0295 \log [H_2S]$$

to give an overall non-oxidative dissolution reaction (see section 2.4.3):-

$$MS = M^{2+} + H_2S \qquad (6.2)$$

Scott and Nicol[143] reported that the maximum rate of dissolution was found at potentials several hundred millivolts negative of those expected on thermodynamic grounds for reaction (6.1); thus a mixed potential model could not apply. However, they did not make allowances for the < unit activity of M^{2+} in solution which would shift the equilibrium potential for reaction (6.1) to more negative potentials.

Since pyrite is the most nobel/passive of all sulphide minerals the high potential requirement for reaction (a) ensures that a mixed potential mechanism involving reactions (6.1) and (v) does not occur on pyrite. An alternative mixed potential model is proposed here for pyrite, assuming that $Fe(II)_{lattice}$ is oxidised to $Fe(III)_{lattice}$, either by the residual dissolved oxygen in solution (see below) and/or the photoexcitation of non-bonding t_{2g} electrons localised on the cations (see section 6.7), before dissolution from the pyrite lattice. Once in solution, a mixed potential between the anodic process:-

$$FeS_2 = Fe^{3+} + 2S + 3e \qquad (e)$$

$$E = 0.546 + 0.0196 \log [Fe^{3+}]$$

and cathodic reaction:-

$$Fe^{3+} + e = Fe^{2+} \qquad (g)$$

$$E = 0.771 + 0.059 \log [Fe^{3+}] - 0.0591 \log [Fe^{2+}]$$

could then be established. As the concentration of Fe^{3+} in solution increases, the reversible potential for reaction (g) increases and drives the open-circuit potential for pyrite to more anodic potentials until a film of sulphur passivates the surface, the open-circuit potential being too high for it to be removed by reaction (v).

Peters and co-workers[65,89] have pointed out that pyrite is one of the few sulphide minerals to have a molar volume smaller than its

sulphur content, when the sulphur is in elemental form. Thus sulphur would protect pyrite under these conditions, when pyrite is not oxidised to sulphate to any great extent.

Although rest potentials for pyrite were measured under oxygen free conditions it is known that pyrite is a very good electrocatalyst for oxygen reduction [185 - 187], hence the cathodic reduction of trace amounts of oxygen in solution by reaction (6.3):-

$$O_2 + 4H^+ + 4e = 2H_2O \qquad (6.3)$$

$$E = 1.229 - 0.0591pH - 0.0148 \log P_{O_2}$$

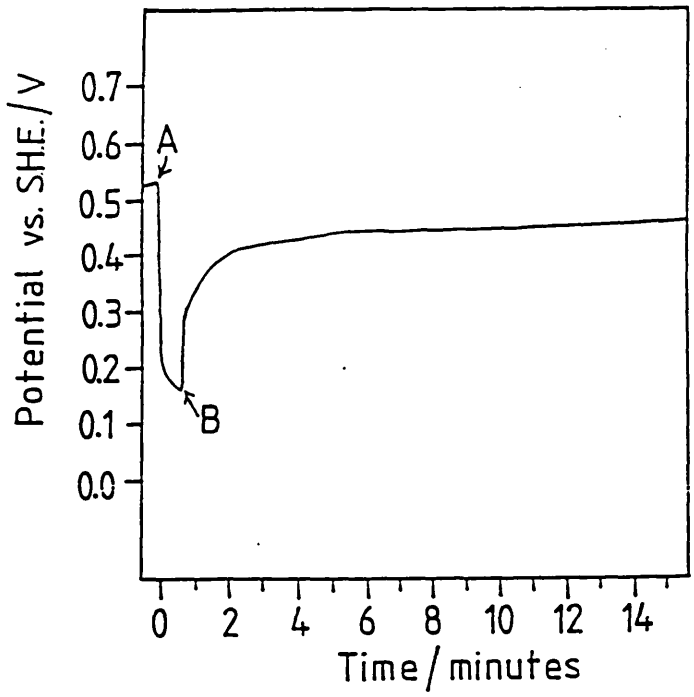
could be the initial driving force in a mixed potential process involving reaction (e), before reaction (g) becomes the dominant cathodic process.

6.2.1 Summary

The open-circuit potential of pyrite in solutions of pH < 0.5 is a mixed potential, the magnitude of which is probably determined by the reversible potential and kinetics of the anodic reaction (e) and the cathodic processes (g) and (6.3). The high anodic potential requirement for the anodic reaction (e) rules out the possibility of sulphur reduction (reaction (v)) contributing to the mixed potential, as it does for the binary sulphides (PbS, NiS, FeS). Thus, a sulphur film formed by reaction (e) could be responsible for passivating the surface of pyrite. An X-ray photoelectron spectroscopic (XPS) study is needed to characterise the nature of the passive film.

6.3 Studies on Virgin Pyrite Surfaces

Figures 6.4 and 6.5 show the effect of in situ grinding to produce a fresh mineral surface on the rest potential of pyrite at pH 0.0 and 9.2 respectively. In both cases the rest potentials were lowered rapidly to values which lay within the thermodynamic stability field for pyrite and which were similar to those obtained for sulphidised pyrite electrodes.



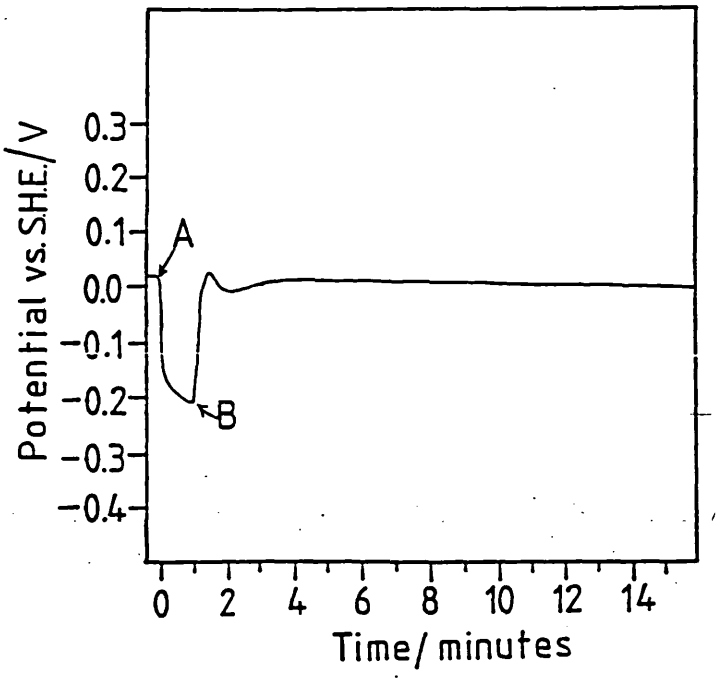


Fig 6.4 (top) The change of rest potential with time (after in situ polishing) of a pyrite electrode at pH 0 (1 M $HClO_4$). (A) commence polishing; (B) finish polishing.

Fig 6.5 (bottom) The change of rest potential with time (after in situ polishing) of a pyrite electrode at pH 9.2 (0.05 M $Na_2B_4O_7$). (A) commence polishing; (B) finish polishing.

When abrading was stopped in 1 M $HClO_4$ the rest potential increased over one or two seconds by 150 mV and then increased gradually until the steady state rest potential of 0.54 V, as observed prior to grinding, was attained after approximately 45 minutes. At pH 9.2 the rest potential returned to its pre-abrasion value within 30 seconds.

A virgin mineral sulphide surface is expected to be very reactive because of the unsatisfied chemical bonds produced by abrasion. Thus the sharp rise in potential observed after abrasion was stopped was probably due to the rapid adsorption of solution species, i.e. H^+ and ClO_4^- at pH 0, Na^+, $B_4O_7^{2-}$ and OH^- at pH 9.2, plus any residual oxygen in solution [302].

The mixed potential mechanism proposed in section 6.2 explains why the open-circuit potential steadily increases at pH 0. However, the model will not apply at pH values > 1.0, at which insoluble ferric oxide/hydroxide is formed and reaction (c) determines the rest potential. At pH 9.2, abrasion did not completely remove oxide layers from the surface of pyrite (see below). Thus the rapid rise in potential to the pre-abrasion value was probably due to re-hydration of the surface oxide layer:

$$FeOOH + H_2O \rightarrow Fe(OH)_3 \qquad (6.4)$$

(N.B. the equilibrium potential for the $Fe(OH)_3/Fe(OH)_2$ couple, reaction (k) lies 0.342 V positive of the $FeOOH/Fe(OH)_2$ potential, reaction (n)).

Cyclic voltammograms of stationary pyrite electrodes in stirred solutions at pH 9.2, recorded immediately after different surface pretreatments, are shown in Figure 6.6. The first diagram (Figure 6.6 A) shows the first sweep voltammogram for a polished, otherwise untreated pyrite electrode. On sweeping the potential negative of the rest potential a cathodic peak was observed at -0.6 V, and on the subsequent reverse scan an anodic peak appeared at 0.08 V similar to those obtained by previous workers[128,129]. Janetski et al[129] assigned the cathodic peak to the reduction of a surface layer of ferric oxide, or hydroxide, to ferrous hydroxide (reaction (k)) and

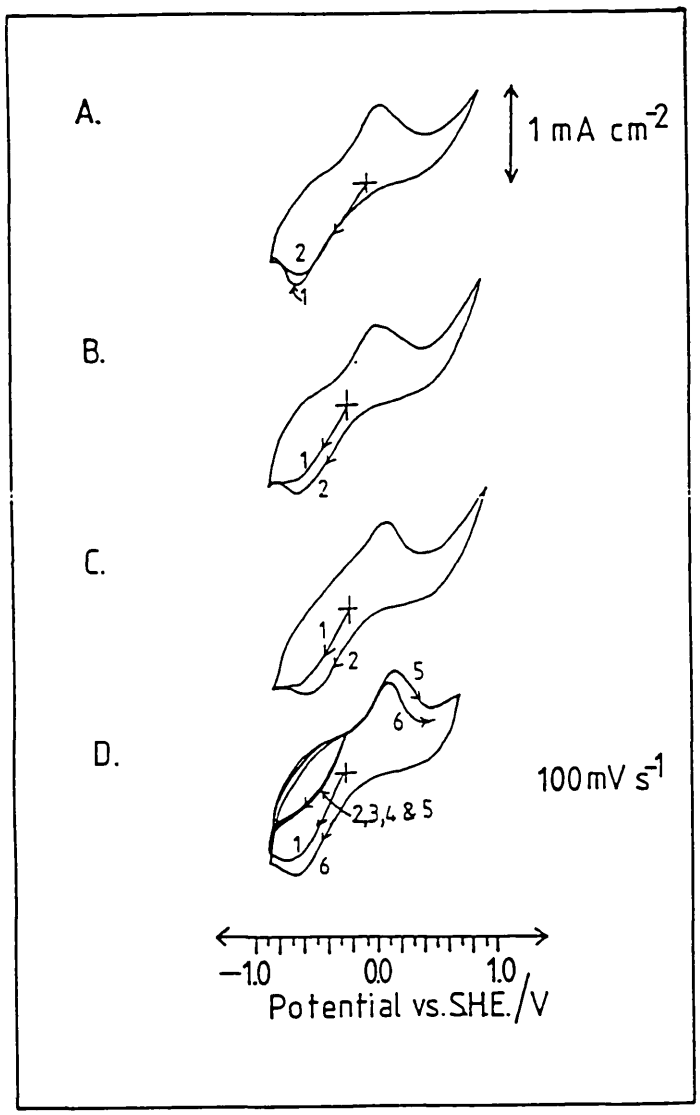


Fig 6.6 Cyclic voltammograms of stationary pyrite electrodes in stirred solutions at pH 9.2 (0.05 M $Na_2B_4O_7$), recorded immediately after different surface pretreatments, starting from the rest potential, first cycled cathodically then anodically at 100 mV s^{-1}. (A) untreated sample; (B) fresh pyrite surface produced by in situ abrasion; (C) electrode potentiostatted at -0.2 V for 5 minutes prior to sweeping the potential; (D) potential of pyrite electrode cycled six times between -0.2 V and -0.9 V before extending the anodic potential limit to 0.8 V.

the anodic peak on the reverse scan to the reverse process. The measured potential of -0.260 V, midway between the anodic and cathodic

peaks, is in good agreement with the reversible potential for reaction (k) of -0.272 V at pH 9.2. Michell and Woods[128] confirmed the presence of an oxygen-containing layer on the surface of pyrite by using x-ray emission spectroscopic analyses and correlating the results with the oxide forming charge passed on potential sweeps.

The structure of α-FeOOH is orthorhombic with a lattice parameter of 0.4569 nm[324]. The charge needed to form a monolayer of α-FeOOH calculated from the lattice parameter assuming a one electron process is 152 μC cm^{-2}. The charge measured under the anodic peaks in Figure 6.6 averaged ~ 1.7 mC cm^{-2}. A roughness factor of ten for a pyrite surface abraded on 600 grade carborundum paper is not unreasonable [128]. Thus the oxide coverage on pyrite was of the order of a monolayer.

In Figure 6.6 B a fresh pyrite surface was produced by in situ abrasion. The rest potential decreased to -0.2 V and a negative-going potential sweep was initiated from this potential before it could return to its pre-abrasion value (Figure 6.5). In Figure 6.6 C a pyrite electrode was potentiostatted at -0.2 V for 5 minutes before commencing the negative scan. This potential lies within the thermodynamic stability field for pyrite and was the open-circuit potential obtained after non-electrochemical pretreatments (ie sulphidising (Figure 6.3) and in situ abrasion (Figure 6.5)). Both Figures 6.6 B and 6.6 C show a first sweep cathodic peak (corresponding to reaction (k)) decreased in magnitude compared with the untreated sample (Figure 6.6 A). This confirmed that neither abrasion, nor the cathodic pretreatment, had removed the proposed oxide monolayer from the pyrite surface.

Although ferrous hydroxide is stable below -0.2 V at pH 9.2 (Figure II (viii); Appendix II), it is soluble to some extent (10^{-5} M, Figure II (vii); Appendix II) and should dissolve and be dispersed into the bulk solution. Thus in a final attempt to remove the oxide monolayer from the surface of pyrite, the potential was cycled five times between -0.2 V and -0.9 V in stirred solution before extending the anodic

scanning limit to 0.8 V (Figure 6.6 D). An anodic peak was still observed at 0.8 V of equal magnitude to that obtained for the untreated pyrite electrode (Figure 6.6 A), indicating that the ferrous oxide layer had not dissolved from the pyrite surface. Increasing the number of cathodic cycles did not decrease the size of the anodic current.

Extending the anodic scanning limit to potentials > 0.3 V caused multilayers of ferric oxide to form on the surface of pyrite by reactions (c) and (d) and the magnitude of the cathodic peak on the reverse scan to increase. This suggested that the oxidation products formed during polishing and on open-circuit were the same as the products formed during anodic polarisation. Continuous potential cycling between -0.2 V and -0.9 V removed the oxide monolayers, presumably due to ferrous oxide dissolution; however, a residual oxide monolayer always remained on the surface.

Similar experiments were carried out in acid solutions (Figure 6.7). Untreated pyrite electrodes exhibited a larger cathodic current on the first sweep from the rest potential than on subsequent sweeps, although no discernable current peak was observed before the onset of hydrogen evolution. Cathodic pretreatment and in situ abrasion were successful in cleaning the mineral surface because the cathodic current on the first sweep was greatly reduced, leaving only the background current due to the reductive dissolution of pyrite by reaction (p).

6.4 Cyclic Voltammetry

6.4.1 Anodic and Cathodic Reactions at pH 1.0 (0.1 M H_2SO_4, 0.1 M $HClO_4$)

Cyclic voltammograms of a stationary pyrite electrode in 0.1 M $HClO_4$ are shown in Figure 6.8; similar behaviour was observed in 0.1 M H_2SO_4. When the anodic potential scanning limit (E_{λ_a}) was extended into the potential range 0.2 - 0.9 V, two cathodic peaks were observed on the return scan at ~ 0.0 V and -0.1 V. Reversing the scan again at

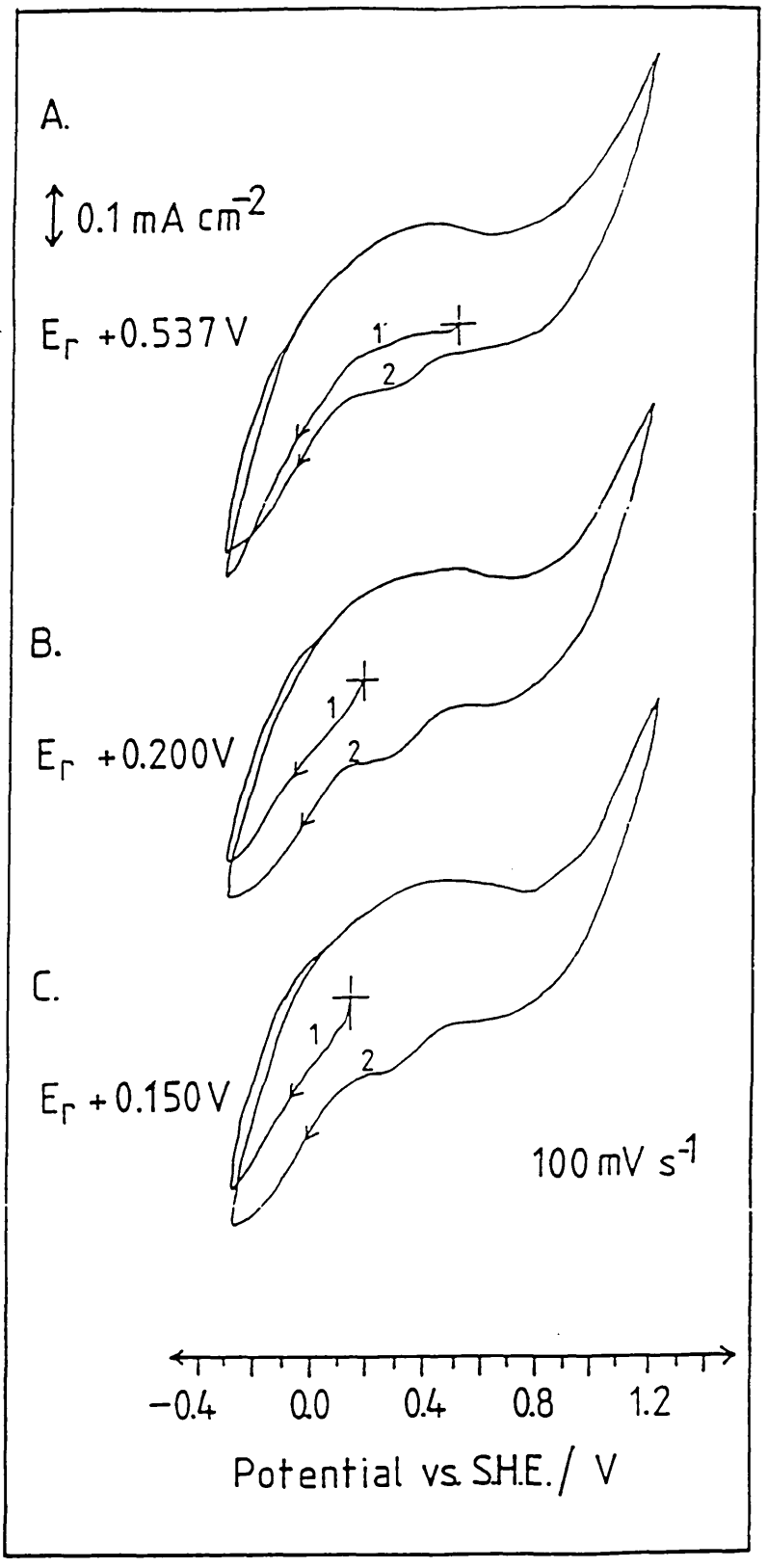


Fig 6.7 Cyclic voltammograms of stationary pyrite electrodes in stirred solutions at pH 0 (1 M $HClO_4$), recorded immediately after different surface pretreatments, starting from the rest potential, first cycled cathodically then anodically at 100 mV s^{-1}. (A) untreated sample; (B) electrode potentiostatted at 0.2 V for 5 minutes prior to sweeping the potential; (C) fresh pyrite surface produced by in situ abrasion.

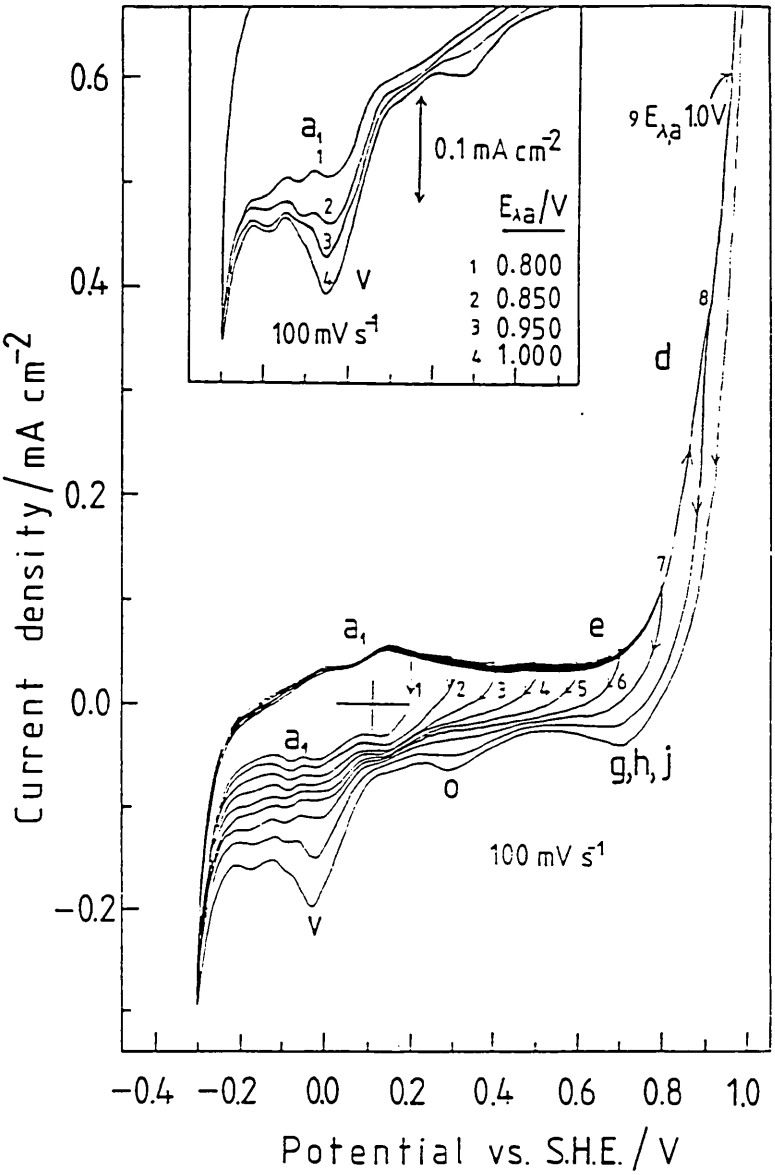


Fig 6.8 The effect of extending the anodic potential scanning limit ($E_{\lambda a}$) on cyclic voltammograms of pyrite at pH 1 (0.1 M $HClO_4$) in stirred solution and a sweep rate of 100 mV s^{-1}. The insert shows an expanded view of the cathodic peaks at potentials < -0.6 V.

-0.3 V produced two anodic peaks displaced ~ 100 mV positive of the cathodic peaks. Both anodic and cathodic currents increased with increasing scan rate (Figure 6.9). The currents for the cathodic peaks x at 0.0 V and y at -0.1 V increased linearly with scan rate (ν) as shown in Figure 6.10. This indicated that surface tranformations

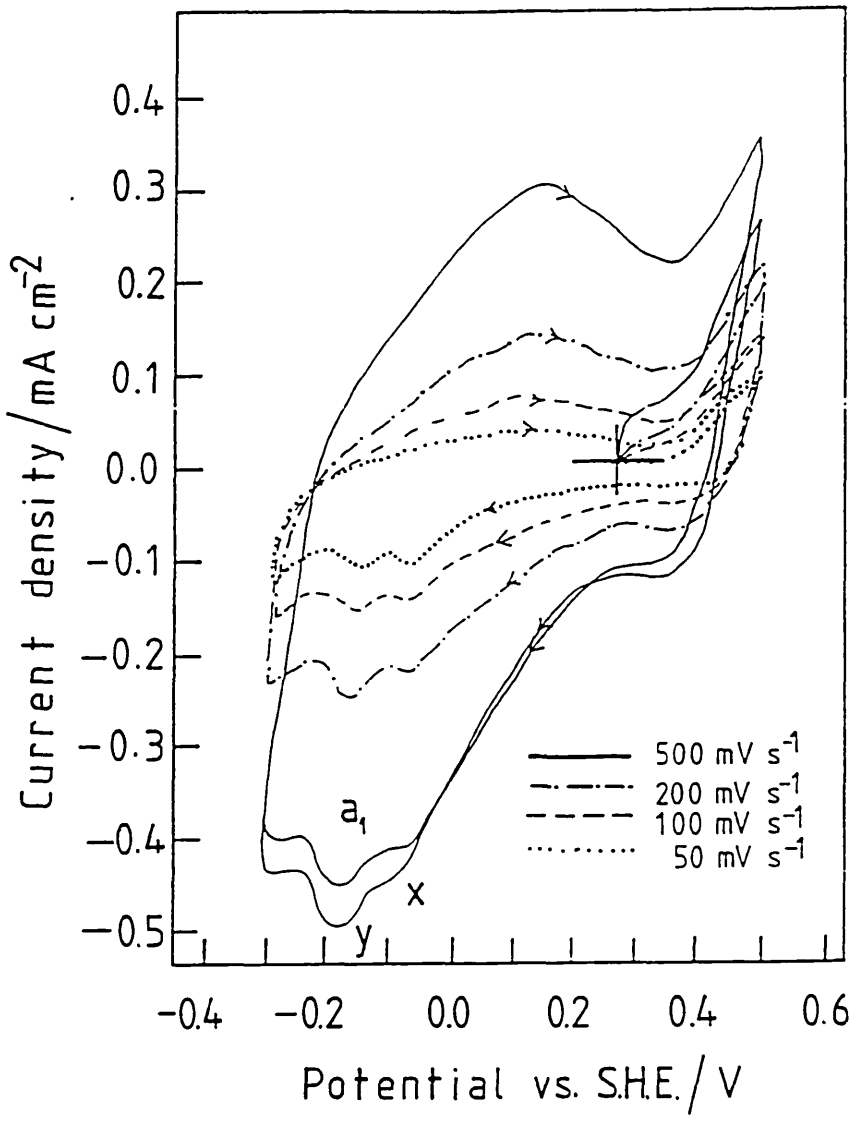


Fig 6.9 Cyclic voltammograms of a pyrite electrode at pH 1 (0.1 M $HClO_4$) as a function of potential sweep rate.

were involved rather than diffusion controlled processes, the peak current (I_p) of which would have been linearly dependent on $\nu^{1/2}$. When these lines were extrapolated back to zero sweep rate, a small residual current was observed on the y-axis (see Figure 6.10), which suggested that a parallel reaction, pyrite reduction by reaction (p), also occurred in this potential region.

When E_{λ_a} was extended to potential > 0.9 V the two cathodic peaks merged to give a single peak at ~ -0.05 V and a third peak appeared at ~ -0.2 V (Figure 6.8).

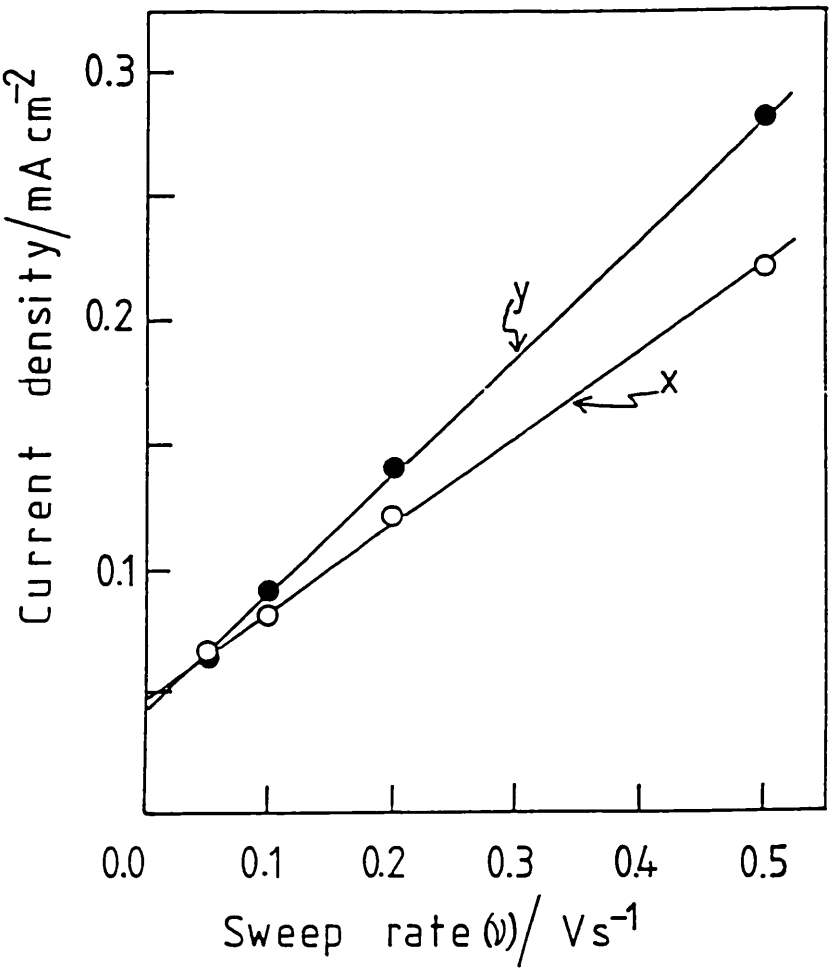


Fig 6.10 Currents for the cathodic peaks x and y plotted as a function of potential sweep rate.

For a positive-going scan, there was a steady rise in anodic current as the potential was increased. From the E_h-pH diagram of the Fe-S-H_2O system (Figure 6.2) pyrite can oxidise to form either sulphur:-

$$FeS_2 = Fe^{2+} + 2S + 2e \qquad (a)$$

$$E = 0.423 + 0.0295 \log [Fe^{2+}]$$

or sulphate (HSO_4^- at pH < 2):-

$$FeS_2 + 8H_2O = Fe^{2+} + 2SO_4^{2-} + 16H^+ + 14e \qquad (b)$$

$$E = 0.367 - 0.067\ pH + 0.008\ \log\ [SO_4^{2-}] + 0.004\ \log\ [Fe^{2+}]$$

The proportion of sulphate formed increased rapidly with increasing potential and accounted for the exponential rise in anodic current. At potentials > 0.8 V, the iron formed would have been in the ferric state (reactions (e) and (f)). Although the solubility of Fe^{3+} with respect to ferric hydroxide ($Fe(OH)_3$) is high at pH 1 ($\log[Fe^{3+}]$ = 1.84; reaction (o_1)), its solubility with respect to goethite (FeOOH) is much less ($\log[Fe^{3+}]$ = -4.85; reaction (u_1)) (see Figures II(iv) and II(v); Appendix II). Hence, assuming that the local concentration of Fe^{3+} ions at the pyrite/solution interface exceeded its solubility on the positive-going scan, the cathodic peak which appeared at ~ 0.35 V when E_{λ_a} was extended to potentials > 0.8 V can be assigned to the reduction of goethite by reaction (o). The cathodic peak at 0.71 V, which appeared on extending E_{λ_a} to potentials > 0.9 V, was attributed to the reduction of Fe^{3+} (reaction (g)) and soluble ferric hydroxy species, i.e. $Fe(OH)^{2+}$ or $Fe(OH)_3$ (reactions (h) and (j)), although stirring did not eliminate this peak completely (Figure 6.8). The effect of stirring on cyclic voltammograms is explained in section 6.4.2.

The anodic polarisation curve in the potential range 0.7 to 1.0 V was not affected by stirring the electrolyte and had a Tafel slope of 94 mV per decade (Figure 6.11), which is in good agreement with values from the literature[78]. However, pulse voltammetry on polished pyrite electrodes produced a current which was strongly time-dependent (see section 6.5), due to the three dimensional growth of corrosion centres. Other workers[66,78,124,126] have not accounted for this in intrepreting Tafel slopes for pyrite electrodes in various electrolytes. Time-dependent surface phenomena preclude the attainment of meaningful steady-state currents and Tafel slopes.

There are three possible explanations of the voltammetric behaviour of pyrite at pH 1 giving rise to the two cathodic peaks at 0.0 V and -0.1 V:

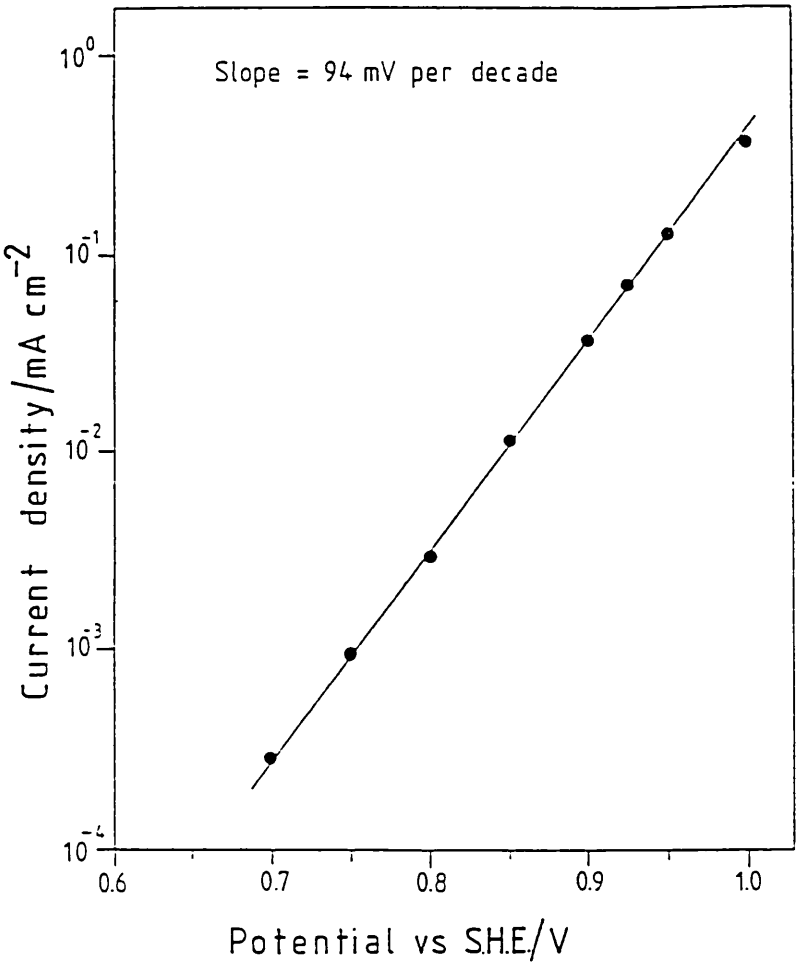


Fig 6.11 Tafel plot for a pyrite electrode at pH 1 (0.1 M $HClO_4$)

1) Assuming that sulphur is nucleated and formed under mild oxidising conditions, the two cathodic peaks can be assigned to the reduction of sulphur in two one electron processes (reactions (x) and (y)).

2) Fe^{2+} is oxidised to Fe^{3+} in the lattice followed by its transfer into the solution, leaving a metal-deficient sulphide film on the pyrite surface supersaturated with S_2^{2-} ions. The S_2^{2-} ions are then reduced in the lattice on the subsequent cathodic sweep by the reversible surface reaction:-

$$S_2^{2-}{}_{(lattice)} + 2e = 2S^{2-}{}_{(lattice)}. \qquad (a_1)$$

which involves two separate one electron reductive steps, although the charges under each peak do not appear to be quite the same (see Figure 6.9). The cathodic charge under both peaks when E_{λ_a} was extended to 0.8 V was 307 μC cm^{-2}, which indicated that a monolayer surface process was occurring. Reaction (a_1) was first suggested by Conway et al[135] who observed two similar, reversible, monolayer surface processes in cyclic voltammograms of pyrite at pH 1. Only when the non-stoichiometry or composition range of pyrite is exceeded (< 1 at-% [303]), i.e. at potentials > 0.9 V, would a sulphur phase form on pyrite's surface and the two cathodic peaks merge to give a single reduction peak due to reaction (v).

3) A third explanation is that sulphur is formed immediately on oxidation by reactions (a) or (e), but is not reduced due to its dielectric nature [304]. Figure 6.12 shows that at an E_{λ_a} value of

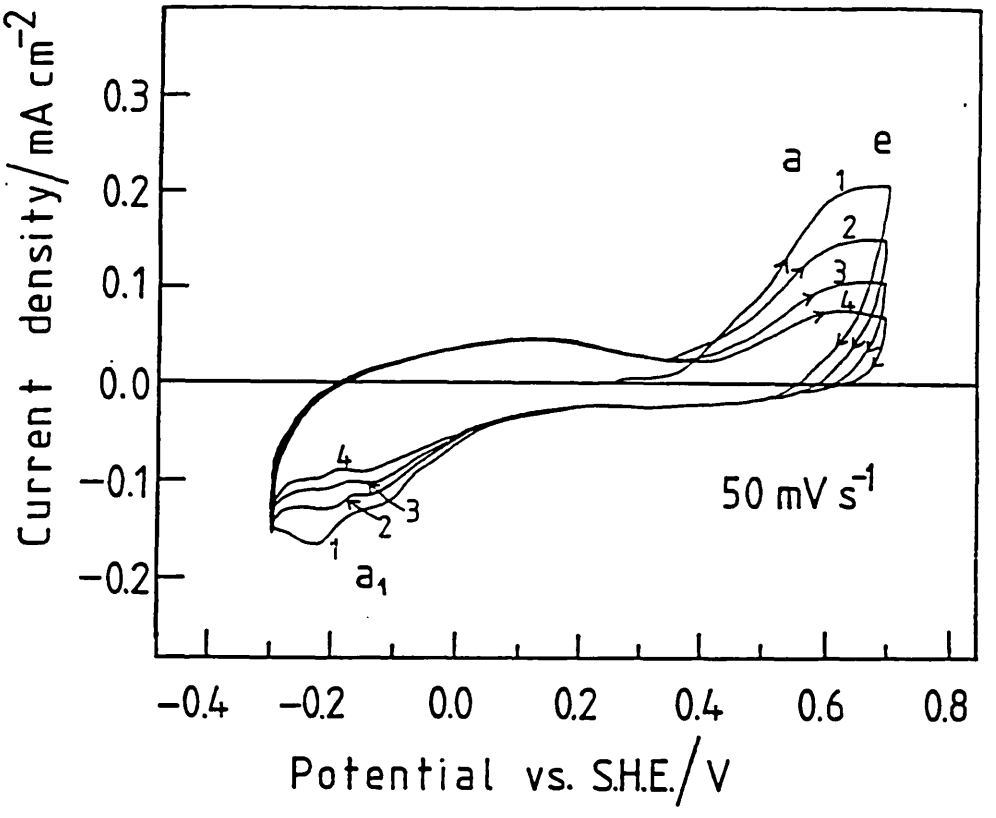


Fig 6.12 Cyclic voltammogram of a pyrite electrode at pH 1 (0.1 M $HClO_4$) and a sweep rate of 50 mV s^{-1}.

0.7 V the magnitude of the anodic and cathodic processes decreased on consecutive cycles due to the formation of a passivating film, attributed to sulphur, which was difficult to reduce. Other redox reactions (i.e. reaction (a_1)) were inhibited. Only an extending E_{λ_a} to potentials > 0.9 V did the passive film breakdown as reaction (d) became the dominant reaction.

The number of moles of pyrite oxidised to sulphur and to sulphate on 100 mV s^{-1} potential scans from the rest potential to different values of E_{λ_a} was determined by integration of the total anodic charge and the cathodic charge under the lower cathodic peaks on the reverse sweep. It was assumed that the charge associated with the lower cathodic peaks was due to sulphur reduction (reaction (v)) and that Fe(III) species, S°, and SO_4^{2-} were the only products of pyrite oxidation in the potential range studied. If x moles of pyrite are oxidised to sulphur and y moles to sulphate by reactions (e) and (f) respectively, then the total anodic charge (Q_A) passed on a potential sweep will be (3x + 15y)F coulombs. The cathodic charge from reaction (v) ($Q_{c(v)}$) will be 4xF. Thus $x = Q_{c(v)}/4F$, $y = (Q_A - 3xF)/15F$ and the number of moles of Fe(III), S° and SO_4^{2-} formed (x + y), 2x and 2y, respectively. The number of moles cm^{-2} of sulphur and pyrite contained in a monolayer, calculated from their respective molar volumes of 16.4 and 24 cm^3 mol^{-1}, was found to be 1.84×10^{-9} moles cm^{-2} for sulphur, and 1.42×10^{-9} moles cm^{-2} for pyrite. Using these values, the number of monolayers of pyrite reacting to form sulphur, sulphate and the number of monolayers of sulphur formed can be ascertained.

Values of x, y, Q_A, $Q_{c(v)}$ etc for pyrite oxidation at pH 1 determined from these equations are presented in Tables 6.1 and 6.2 and Figures 6.13 - 6.16. Figures 6.14 and 6.16 clearly show that sulphate formation accelerated rapidly at potentials > 0.9 V so that at 1.4 V over 96% of pyrite reacted via reaction (f). Under mild oxidising conditions (E_{λ_a} < 0.9 V), the number of monolayers of sulphur formed exceeded the number of monolayers of pyrite reacted (Figure 6.15). This supports the views of Bailey and Peters[89], who claimed that a perfectly non-porous insulating film of sulphur protects the surface

Table 6.1 Quantity of Pyrite Oxidised via Reactions (e) and (f) at pH 1 (0.1 M $HClO_4$) on a 100 mV s^{-1} Potential Sweep from the Rest Potential (E_r) to Different Values of the Anodic Potential Scanning Limit ($E_{\lambda a}$)

E_r = 0.1 V

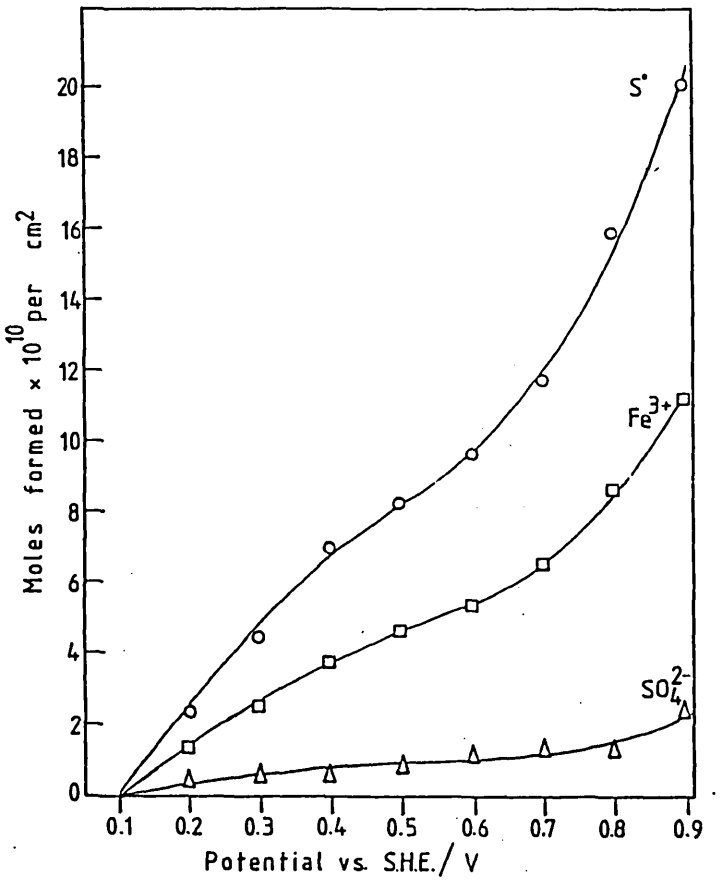
$E_{\lambda a}$/ V vs. S.H.E.	$Q_A/Q_{c(v)}$	Q_A/mC cm^{-2}	$Q_{C(v)}$ /mC cm^{-2}	Moles of pyrite oxidising to sulphur, X x 10^{10}/mol cm^{-2}	No of monolayers FeS_2 reaction via reaction (e)	Moles of pyrite oxidising to sulphate y x 10^{10}/mol cm^{-2}	No of monolayers FeS_2 reacting via reaction (f)
0.2	1.52	0.0668	0.0439	1.13	0.10	0.235	0.02
0.3	1.26	0.1061	0.0843	2.184	0.19	0.296	0.03
0.4	1.07	0.1428	0.1335	3.459	0.31	0.295	0.03
0.5	1.13	0.1808	0.1598	4.141	0.37	0.421	0.04
0.6	1.17	0.2168	0.1857	4.812	0.43	0.536	0.05
0.7	1.14	0.2578	0.2256	5.845	0.52	0.612	0.05
0.8	1.03	0.3148	0.3069	7.952	0.70	0.585	0.05
0.9	1.19	0.4595	0.3874	10.038	0.89	1.167	0.10
1.0	6.50	2.6	0.400	10.364	0.92	15.892	1.40
1.2	50.21	35.9	0.715	18.526	1.64	244.35	21.60
1.3	76.39	86.4	1.131	29.305	2.59	591.13	52.25
1.4	94.07	163.3	1.736	44.981	3.98	1119.3	98.93

Table 6.2 Quantity of Products Formed when Pyrite is Oxidised at pH 1 (0.1 M $HClO_4$) on a 100 mV s^{-1} Potential Sweep as a Function of Anodic Potential Scanning Limit (E_{λ_a})

* One monolayer of FeS_2 = 1.42 x 10^{-9} mol cm^{-2}
** One monolayer of sulphur = 1.84 x 10^{-9} mol cm^{-2}

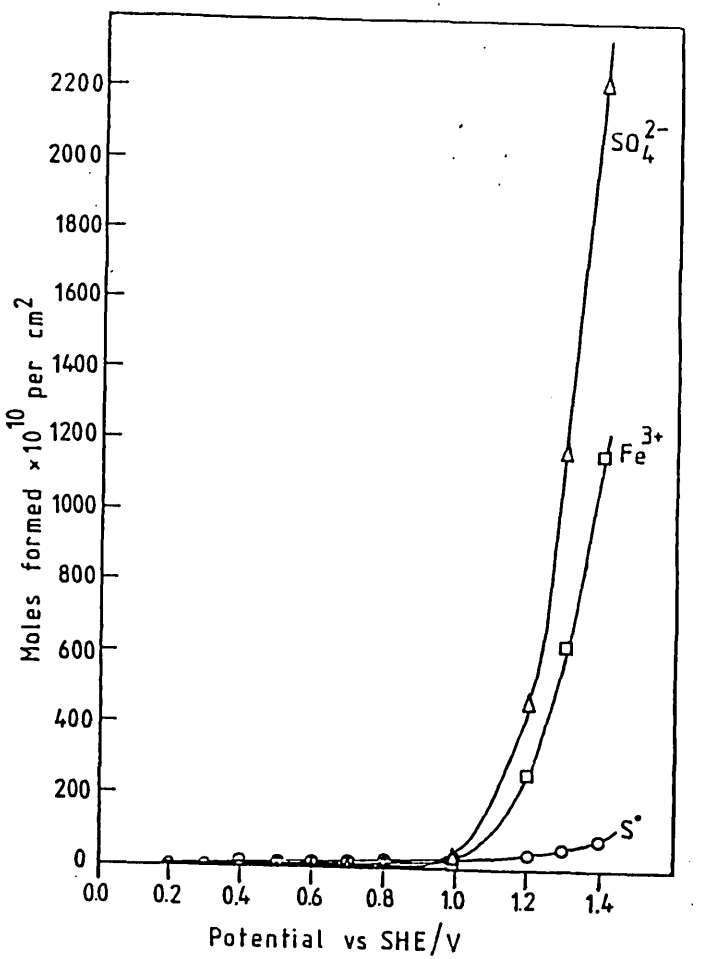
E_{λ_a} /V vs. S.H.E.	Moles of Fe III species formed x 10^{10} cm^{-2} and total moles FeS_2 reacting x 10^{10} cm^{-2}	No of Monolayers of FeS_2 reacting*	Moles of sulphur formed x 10^{10} cm^{-2}	No of monolayers of sulphur formed**	Moles of sulphate formed x 10^{10} cm^{-2}	% pyrite reacting via reaction (f)	Molar ratio of sulphate/ sulphur formed
0.2	1.37	0.12	2.28	0.12	0.47	17.3	0.207
0.3	2.48	0.22	4.37	0.24	0.59	11.9	0.136
0.4	3.75	0.33	6.92	0.38	0.59	7.9	0.085
0.5	4.56	0.40	8.28	0.45	0.84	9.2	0.101
0.6	5.35	0.47	9.63	0.52	1.07	10.0	0.111
0.7	6.46	0.57	11.69	0.64	1.22	9.5	0.105
0.8	8.54	0.75	15.90	0.86	1.17	6.9	0.107
0.9	11.21	0.99	20.08	0.94	2.33	10.4	0.116
1.0	26.26	2.32	20.73	1.13	31.78	60.5	1.53
1.2	262.9	23.23	37.05	2.02	488.7	92.9	13.19
1.3	620.4	54.84	58.61	3.19	1182.3	95.2	20.17
1.4	1164.3	102.91	89.96	4.89	2238.6	96.1	25.15

Fig 6.13



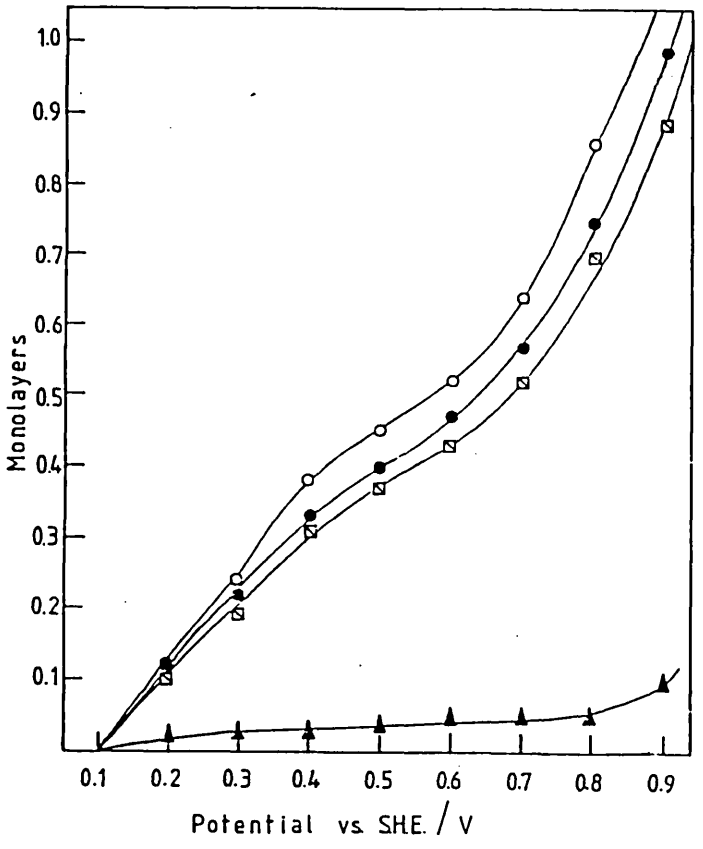
Quantity of sulphur, sulphate, and ferric species formed on a 100 mV s^{-1} potential sweep as a function of the upper potential limit of the sweep (0.1 to 0.9 V) for a pyrite electrode at pH 1 (0.1 M $HClO_4$).

Fig 6.14



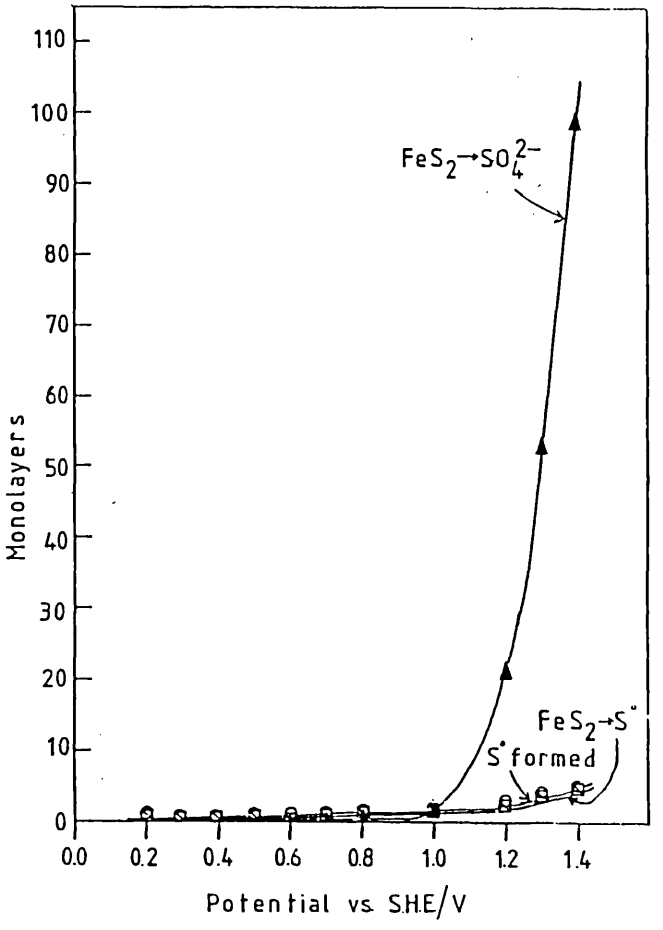
Quantity of sulphur, sulphate, and ferric species formed on a 100 mV s^{-1} potential sweep as a function of the upper potential limit of the sweep (0.1 to 1.4 V) for a pyrite electrode at pH 1 (0.1 M $HClO_4$).

Fig 6.15



Number of monolayers of: pyrite oxidised to form sulphur (⊠); pyrite oxidised to form sulphate (▲); total pyrite oxidised (●); sulphur formed (O), during a 100 mV s^{-1} potential sweep as a function of the upper potential limit of the sweep (0.1 to 0.9 V) for a pyrite electrode at pH 1 (0.1 M $HClO_4$).

Fig 6.16



Number of monolayers of: pyrite oxidised to form sulphur (⊠); pyrite oxidised to form sulphate (▲); sulphur formed (O), during a 100 mV s^{-1} potential sweep as a function of the upper potential limit of the sweep (0.1 to 1.4 V) for a pyrite electrode at pH 1 (0.1 M $HClO_4$).

of pyrite in acidic media. When the volume of sulphur does not occupy all the volume of decomposed pyrite, then protection stops. This occurred at ~ 1.0 V under the non-steady state conditions of the cyclic voltammetry experiments (Figure 6.16) and marked the onset of higher anodic currents/decomposition rate, and reaction (f) as the dominant pyrite oxidation reaction (Figure 6.8).

6.4.2 Pyrite RSCBE at pH 0 (1 M $HClO_4$)

To deconvolute redox reactions that formed/reduced sulphur from those that produced/reduced Fe(III) species, pyrite electrodissolution reactions were investigated further using a RSCBE at pH 0.

Figure 6.17 shows a voltammogram of a FeS_2 RSCBE in 1 M $HClO_4$. At pH 0 the only oxidation product formed on the surface of pyrite should be sulphur. Rotating the pyrite electrode enabled a distinction to be made between reactions which formed soluble products and those in which surface species were produced. For a stationary electrode, dissolved products remain in the vicinity of the surface and can take place in further electrochemical reactions. When the electrode is rotated, soluble products are dispersed as they are formed.

In Figure 6.17 the reduction peak observed at 0.68 V on the reverse cathodic-going potential sweep was assigned to Fe^{3+} reduction by reaction (g). The peak was absent on rotating since the Fe^{3+} ions produced by reactions (e) and (f) were dispersed into the solution. At lower cathodic potentials, the peak at ~ -0.1 V was assigned to the reduction of sulphur by reaction (v) because rotation did not decrease the peak. When the scan was reversed again at -0.3 V, and the electrode was stationary, H_2S and Fe^{2+} remained in the vicinity of the electrode and were oxidised by the reverse of reactions (v) and (g) to give the shoulder on the main oxidation wave at ~ 0.9 V.

In separate experiments, voltammograms were recorded for a pyrite RSCBE in 1 M $HClO_4$ containing ferric, ferrous and sulphide ions (Figures 6.18 - 6.20). The presence of Fe^{2+} and Fe^{3+} in solution were

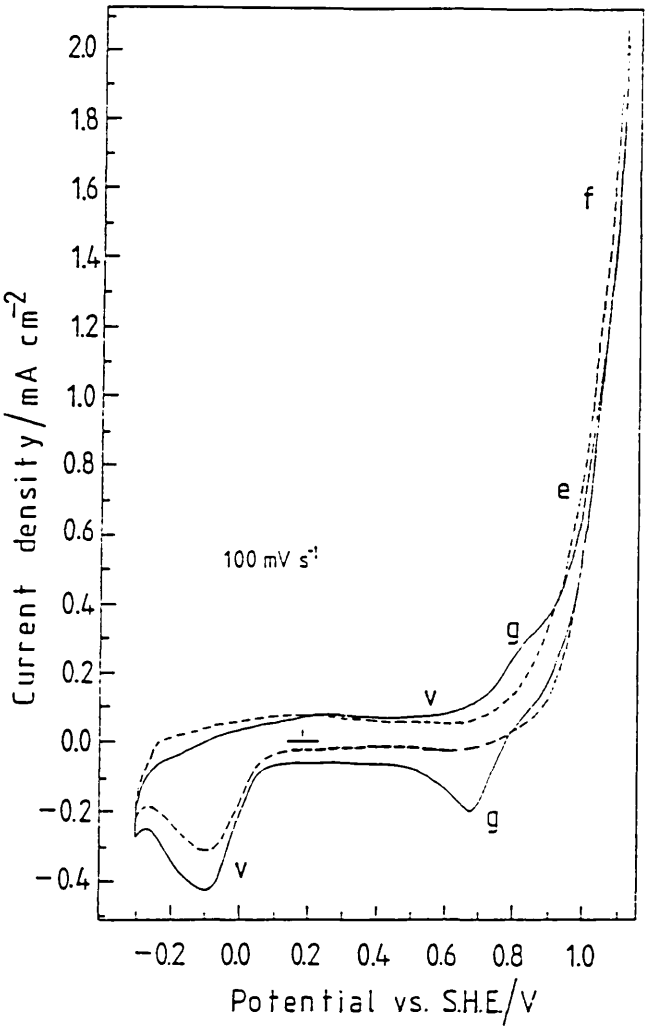


Fig 6.17 Cyclic voltammograms of a pyrite RSCBE in 1 M $HClO_4$ (pH 0).
(—) stationary electrode; (---) rotated electrode.

found to increase the magnitude of peaks assigned to reaction (g), and a saturated solution of H_2S enhanced peak (v), supporting the reaction assignment given above.

Comparing the reduction of Fe^{3+} ions at a pyrite RSCBE (Figure 6.18) with similar voltammograms for pyrite in O_2-saturated 1 M $HClO_4$ recorded by Biegler et al[186], it is clear that Fe^{3+} ions are much more easily reduced than oxygen at a pyrite surface. Fe^{3+} reduction started ~ 0.3 V positive of the potential onset for oxygen reduction.

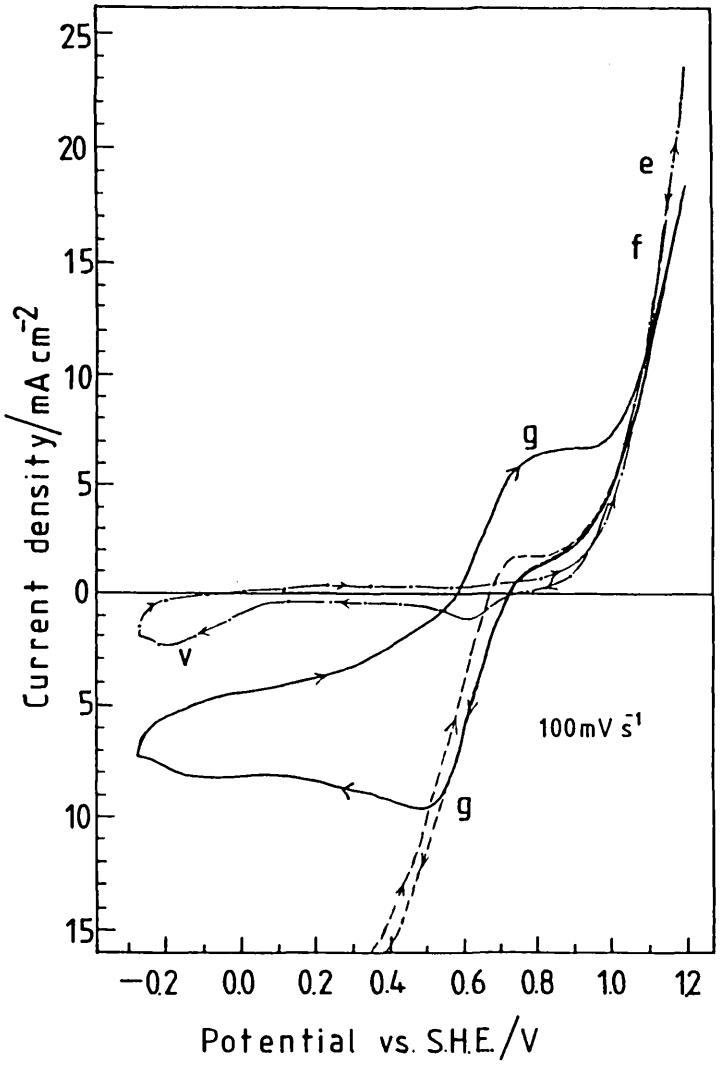


Fig 6.18 Cyclic voltammograms of a pyrite RSCBE in 1 M $HClO_4$ + 0.1 M $FeCl_3$. (——) stationary electrode; (---) rotated electrode; (-•••-) no ferric ions and electrode stationary.

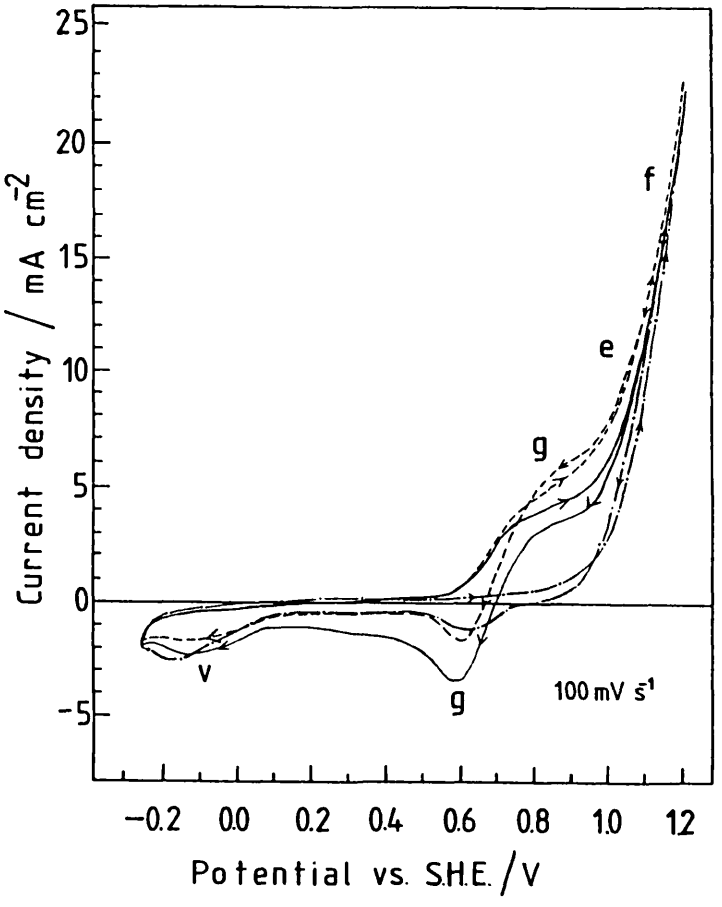


Fig 6.19 Cyclic voltammograms of a pyrite RSCBE in 1 M $HClO_4$ + 0.1 M $FeSO_4$.
(——) electrode stationary; (---) electrode rotated; (-•••-) no ferrous ions and electrode stationary.

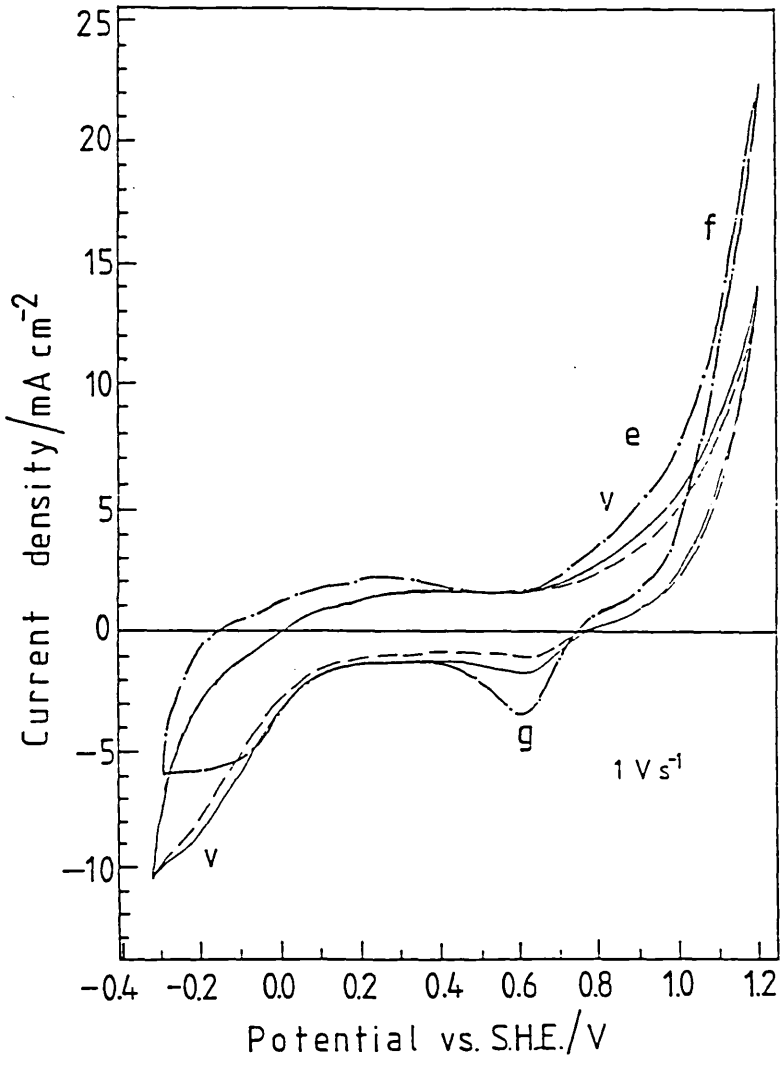


Fig 6.20 Cyclic voltammograms of a pyrite RSCBE in 1 M $HClO_4$ + 0.1 M Na_2S. (—) electrode stationary; (---) electrode rotated; (-•-•-) no sulphide ions and electrode stationary.

In comparison, the oxidation of Fe^{2+} at a pyrite RSCBE was kinetically much slower than Fe^{3+} reduction, because of hinderance due to the competing mineral oxidation reactions (e) and (f) (Figure 6.19). At pH 0, a limiting current of approximately 5 mA cm^{-2} due to Fe^{2+} oxidation was obtained between 0.75 and 1.0 V when the electrode was stationary. This was less than the theoretical limiting current of

~ 20 mA cm^{-2} from the Randles-Sevich equation [305] for a reversible process at a stationary electrode (assuming the diffusion coefficient for Fe^{2+} is 5.2 x 10^{-6} cm^2 s^{-1} [305] and ν = 0.1 V s^{-1}). This suggested that Fe^{2+} oxidation was mainly under kinetic control in this potential region, although a limiting current was observed. The small effect of electrode rotation on the Fe^{2+} oxidation current supported this view. At potentials > 1.0 V the anodic current was almost exclusively due to pyrite oxidation by reactions (e) and (f).

Voltammograms of pyrite at pH 0 in the presence of H_2S exhibited no obvious anodic current peaks due to H_2S oxidation (Figure 6.20). The cathodic peak (v) due to sulphur reduction was enhanced, indicating that H_2S oxidation had taken place but at potentials > 0.65 V, where it competed with pyrite oxidation. The anodic currents at potentials > 0.65 V were less in the presence of H_2S, suggesting that sulphur formed by H_2S oxidation was passivating the pyrite surface. However, the presence of H_2S may also change the activity of dissolved metal ions, thereby changing the overpotentials of the pyrite oxidation reactions, creating the same effect as passivation due to sulphur.

Figure 6.21 shows a voltammogram of a pyrite RSCBE in 1 M $HClO_4$ and the current response at the Pt collector electrode for a range of potentials (E_c). In separate experiments with ferrous and cupric sulphate in 1 M $HClO_4$, though in the absence of sulphide, Fe (II) oxidation and Fe (III) reduction on Pt were found to be transport controlled at potentials > 0.8 V and < 0.5 V, respectively (Figure 6.22).

The oxidation of FeS_2 apparently produced no Fe (II) species judging by the absence of any corresponding collector oxidation current at potentials > 0.8 V (Figure 6.21), contrary to that expected from reactions (a) and (b). Surprisingly, soluble oxidation products were detected only when the working electrode potential was extended to > 1.0 V. Fe^{3+} reduction at the collector electrode (0.2 and 0.0 V) suggested that the main mineral oxidation reactions were (e) and (f). The production of hydrogen ions concomitantly with sulphate formation (reaction (f)) gave rise to the increase in collector reduction

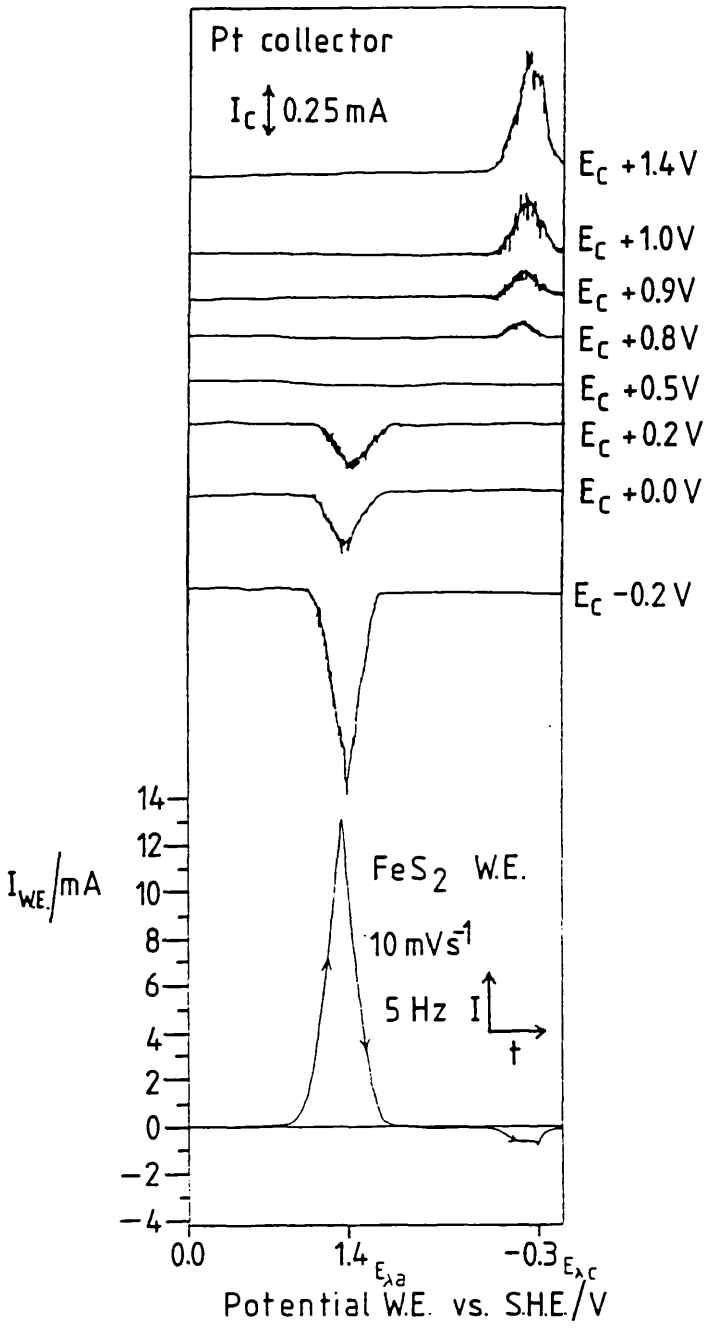


Fig 6.21 Cyclic voltammogram of a RSCBE in 1 M $HClO_4$ (pH 0) with the pyrite working electrode (W.E.) swept anodically from 0.0 to 1.4 V, then cathodically to -0.35 V, with the platinum collector electrode held at various potentials (E_c).

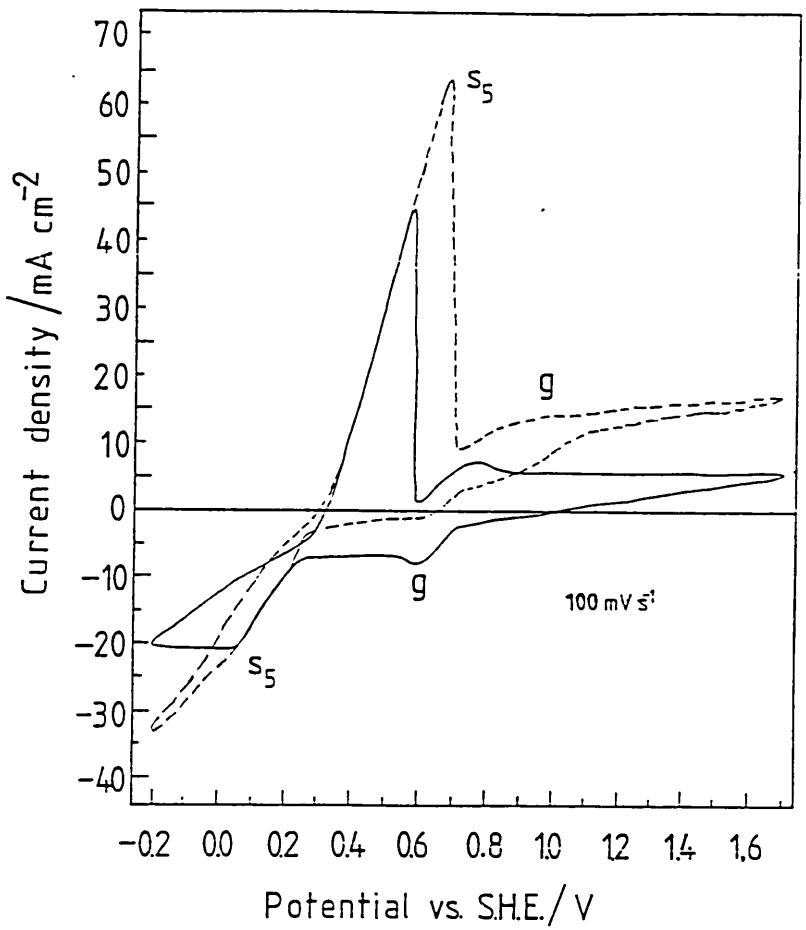


Fig 6.22 Cyclic voltammograms of a RSCBE platinum electrode in 1 M $HClO_4$ + 0.1 M $FeSO_4$ + 0.1 M $CuSO_4$. (—) electrode stationary; (---) electrode rotated.

current at potentials < 0.0 V due to reaction (d_1). At pH 0 and potentials < 0.0 V there was a large collector background current due to hydrogen evolution. Production of H^+ from the pyrite working electrode by reaction (f), effectively lowered the interfacial pH at the collector electrode, increasing the reversible potential for the H_2/H^+ redox couple, thus increasing the collector background current due to reaction (d_1).

The FeS_2 reduction peak at -0.1 V (Figure 6.21) has been attributed, in acidic solutions, to the reduction of anodically formed sulphur (see section 6.4.1)[134]. However, anodic collector current responses at 0.8, 0.9 and 1.0 V suggested that some ferric oxide was formed anodically on the surface of pyrite even at a bulk solution pH of 0, probably by reactions (c) and (d), even though it is thermodynamically unstable at pH 0 (reactions (o_1) and (u_1)) (Figures II(iv) and II(v); Appendix II). At potentials > 1.2 V both Fe^{2+} and H_2S were oxidised at the Pt collector electrode.

6.4.3 pH 4.6 (0.5 M CH_3COOH + 0.5 M CH_3COONa

Voltammograms for a stationary pyrite electrode at pH 4.6 in stirred solution are shown in Figure 6.23. Starting from the rest potential, repetitive triangular potential scans to increasing E_{λ_a} values resulted in decreasing anodic currents on consecutive cycles in the potential range 0.0 to 0.4 V, suggesting a passivating process occurred in this region. Hamilton and Woods[134] assumed that pyrite oxidised by reactions (a) and (b) at these potentials and that ferric hydroxide was formed only at potentials > 0.4 V. However, the pyrite RSCBE results at pH 0 suggested that pyrite oxidised directly to Fe(III) species (see section 6.4.2). In the list of sulphide mineral redox reactions given in Appendix I it has been assumed that ferric hydroxide ($Fe(OH)_3$) rather than FeOOH, is the ferric product of pyrite oxidation so that comparisons can be made with the work of other authors [134]. Initially Fe^{3+} was released into solution and precipitated in the proximity of the electrode when its solubility was exceeded. At pH 4.6 the solubility of Fe^{3+} with respect to $Fe(OH)_3$ is $10^{-8.96}$ mol dm^{-3} (reaction (o_1)). However, thermodynamic predictions indicate that goethite (FeOOH) is the most likely ferric species formed (reactions s_1 and t_1):-

$$FeS_2 + 2H_2O = FeOOH + 2S + 3H^+ + 3e \qquad (s_1)$$

$$E = 0.521 - 0.0591\ pH$$

$$FeS_2 + 10H_2O = FeOOH + 2SO_4^{2-} + 19H^+ + 15e \qquad (t_1)$$

$$E = 0.390 - 0.0749\ pH + 0.0078 \log [SO_4^{2-}]$$

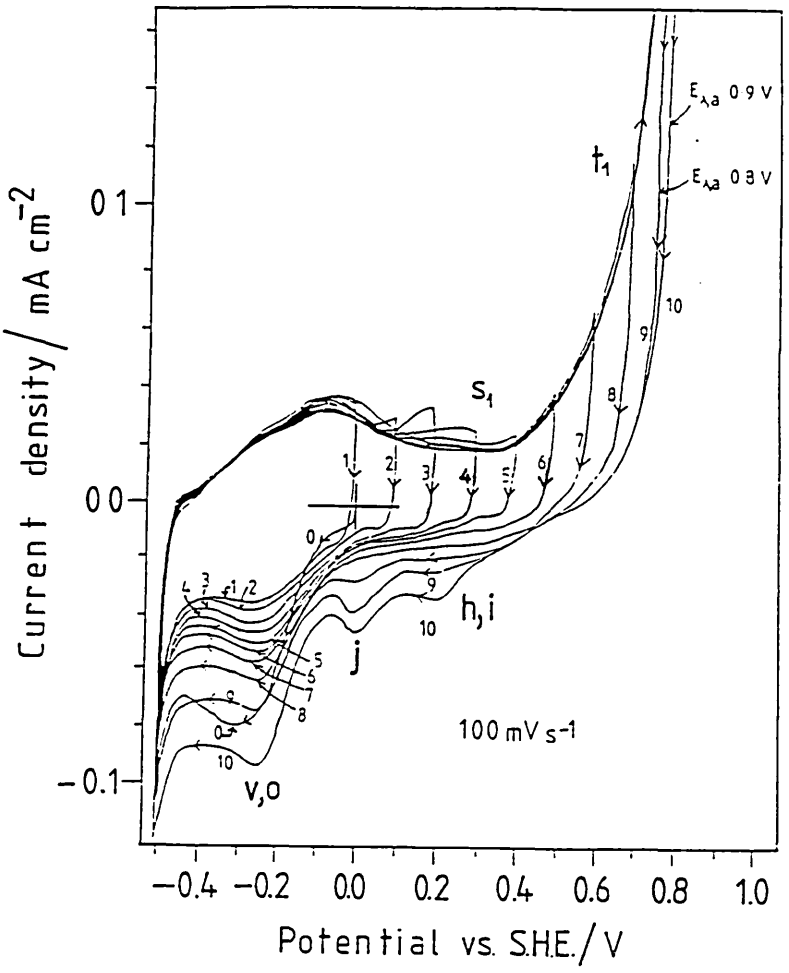


Fig 6.23 The effect of extending the anodic potential scanning limit ($E_{\lambda a}$) on cyclic voltammograms of pyrite at pH 4.6 (0.5 M CH_3COOH + 0.5 M CH_3COONa) in stirred solution and a sweep rate of 100 mV s^{-1}.

At pH 4.6, the reversible potentials for reactions s_1 and t_1 of 0.25 V and 0.045 V respectively, are less positive than those for reactions (c) and (d). Moreover, the solubility of Fe^{3+} with respect to goethite is only $10^{-15.65}$ mol dm^{-3} at pH 4.6 (reaction (u_1); c.f. $10^{-8.96}$ mol dm^{-3} for $Fe(OH)_3$). Thus goethite probably forms spontaneously on the surface of pyrite via a solid state mechanism with no release of ferric ions into solution (c.f. dissolution-precipitation reaction at pH 1; see section 6.4.1).

Hamilton and Woods[134] assigned the cathodic peak at ~ -0.2 V to sulphur reduction only (reaction (v); see Figure 6.21). However, goethite reduction (reaction (o)) has a greater pH dependency than that reaction, and at pH 4.6, goethite can be reduced in the same potential range as sulphur. Hence, only a single reduction peak was observed on the negative-going potential scan for E_{λ_a} values < 0.6 V.

Conway et al[135] reported that the two almost reversible monolayer surface processes, observed in cyclic voltammograms at pH 1 in this work (see section 6.4.1), were present in all their i vs E profiles of pyrite electrodes recorded over the pH range 1 - 11. However, they reported only the potential scanning limits used for cyclic voltammetry experiments at pH 1. Under the potential scanning conditions of these experiments, the two cathodic peaks were not observed at pH 4.6, although there was evidence for two anodic surface processes at ~ -0.25 V and -0.1 V (Figure 6.23). Probably the two cathodic peaks, if present were hidden under the single reduction peak assigned to reactions (v) and (o).

As E_{λ_a} was extended to potentials > 0.6 V, the anodic current increased rapidly and sulphate formation (reaction (t_1)) became the dominant oxidation process (Figure 6.23). Consequently, the local concentration of H^+ ions at the pyrite/solution interface increased, lowering the pH. Hence some of the goethite formed at lower potentials started to dissolve and pyrite started to oxidise by a dissolution-precipitation mechanism (reactions (e), (f), (o_1), (v_1) and (w_1), forming $Fe(OH)_2^+$, $Fe(OH)^{2+}$ and $Fe(OH)_3$ at the higher overpotentials, giving rise to two further cathodic peaks on the return scan at ~ 0.0 V and 0.25 V. The former peak was assigned to $Fe(OH)_3$ reduction (reaction (j)) and the latter to $Fe(OH)^{2+}$ and/or $Fe(OH)_2^+$ reduction (reactions (h) and (i)).

Figure 6.24 shows the effect of increasing the cathodic scanning limit (E_{λ_c}) on the anodic oxidation peaks at a fixed E_{λ_a} in quiescent solution. For E_{λ_c} values in the potential range -0.4 V to -0.7 V, the cathodic current increased rapidly due to the reductive decomposition

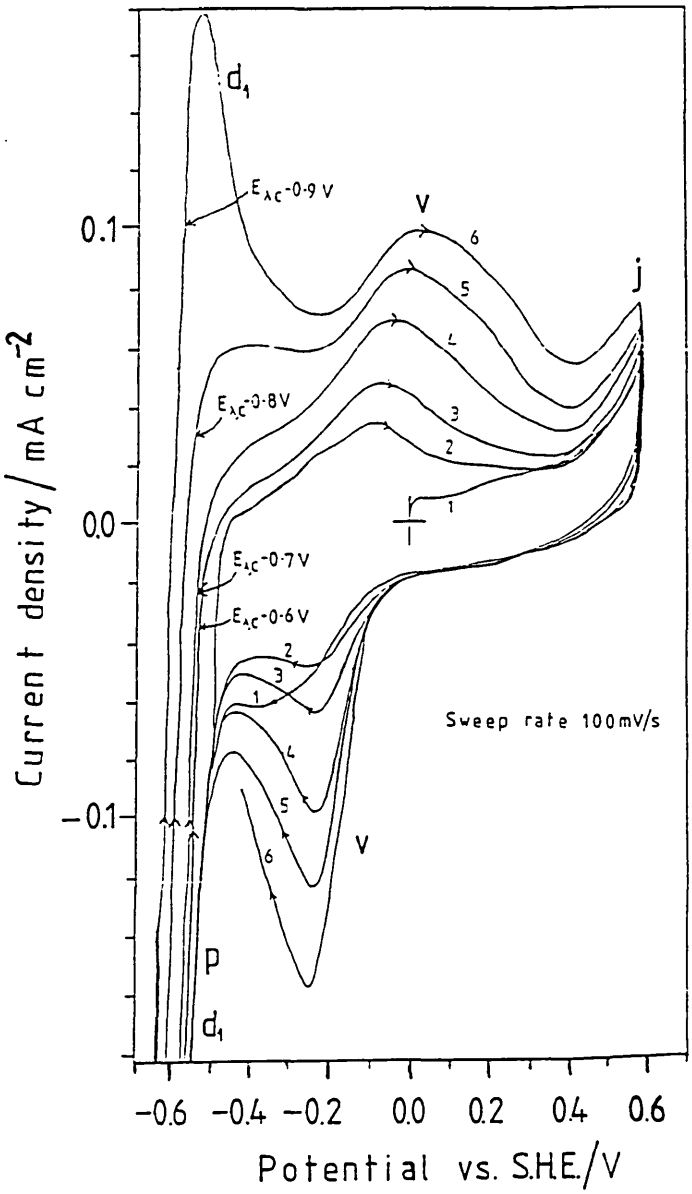


Fig 6.24 The effect of extending the cathodic potential scanning limit ($E_{\lambda c}$) on cyclic voltammograms of pyrite at pH 4.6 (0.5 M CH_3COOH + 0.5 M CH_3COONa) in quiescent solution and a sweep rate of 100 mV s^{-1}.

of pyrite by reaction (p) forming Fe^{2+} and H_2S. On the reverse anodic scan a broad oxidation peak was observed at ~ 0 V assigned to H_2S oxidation (reaction (v)), and at potentials > 0.4 V the anodic current increased due to the oxidation of Fe^{2+} by reaction (j) (see section 6.4.3.1; Figures 6.26 - 6.28). On extending $E_{\lambda c}$ to potentials < -0.7

V, hydrogen ion reduction started to compete with pyrite cathodic decomposition, and a hydrogen oxidation peak, which was absent when a pyrite RSCBE was rotated, began to appear at ~ -0.55 V on the reverse scan (reaction (d_1).

Cyclic voltammograms of stationary pyrite electrodes in stirred solutions, recorded after holding the electrodes at -0.1 V for various times, exhibited an anodic peak at ~ 0.4 V on the first positive going potential sweep. The anodic peak increased in size as the pre-conditioning time at -0.1 V increased (Figure 6.25). Similar behaviour was observed in non-buffered solutions at pH 4.6.

On the reverse cathodic scan the cathodic peaks assigned to $Fe(OH)^{2+}$, $Fe(OH)_2^+$, FeOOH and/or sulphur reduction (reactions (h), (i), (o) and (v), respectively) were enhanced, indicating that these species were products of the oxidation process occurring at 0.4 V on the anodic scan. This suggested that one of the products accumulating on the surface of pyrite during the conditioning stage was probably an adsorbed ferrous hydroxide species ($Fe(OH)^+_{(ads)}$) which was oxidised on the anodic scan by the following reactions:-

$$Fe(OH)^+_{(ads)} = Fe(OH)^{2+}_{(ads)} + e \qquad (6.6)$$

$$Fe(OH)^+_{(ads)} + H_2O = Fe(OH)_2^+{}_{(ads)} + H^+ + e \qquad (6.7)$$

$$Fe(OH)^+_{(ads)} + H_2O = FeOOH + 2H^+ + e \quad (\text{or } Fe(OH)_3) \qquad (6.8)$$

If the ferrous product had been Fe^{2+} ions, stirring would have dispersed them into solution and no oxidation and subsequent reduction of $Fe(OH)^+_{(ads)}$ etc. would have been observed. No net current was measurable during conditioning at -0.1 V and the conditioning potential lay well within the stability field of pyrite at pH 4.6 (See Figure 6.2), which indicated that some kind of chemical redox process was occurring on the surface of pyrite during the conditioning period.

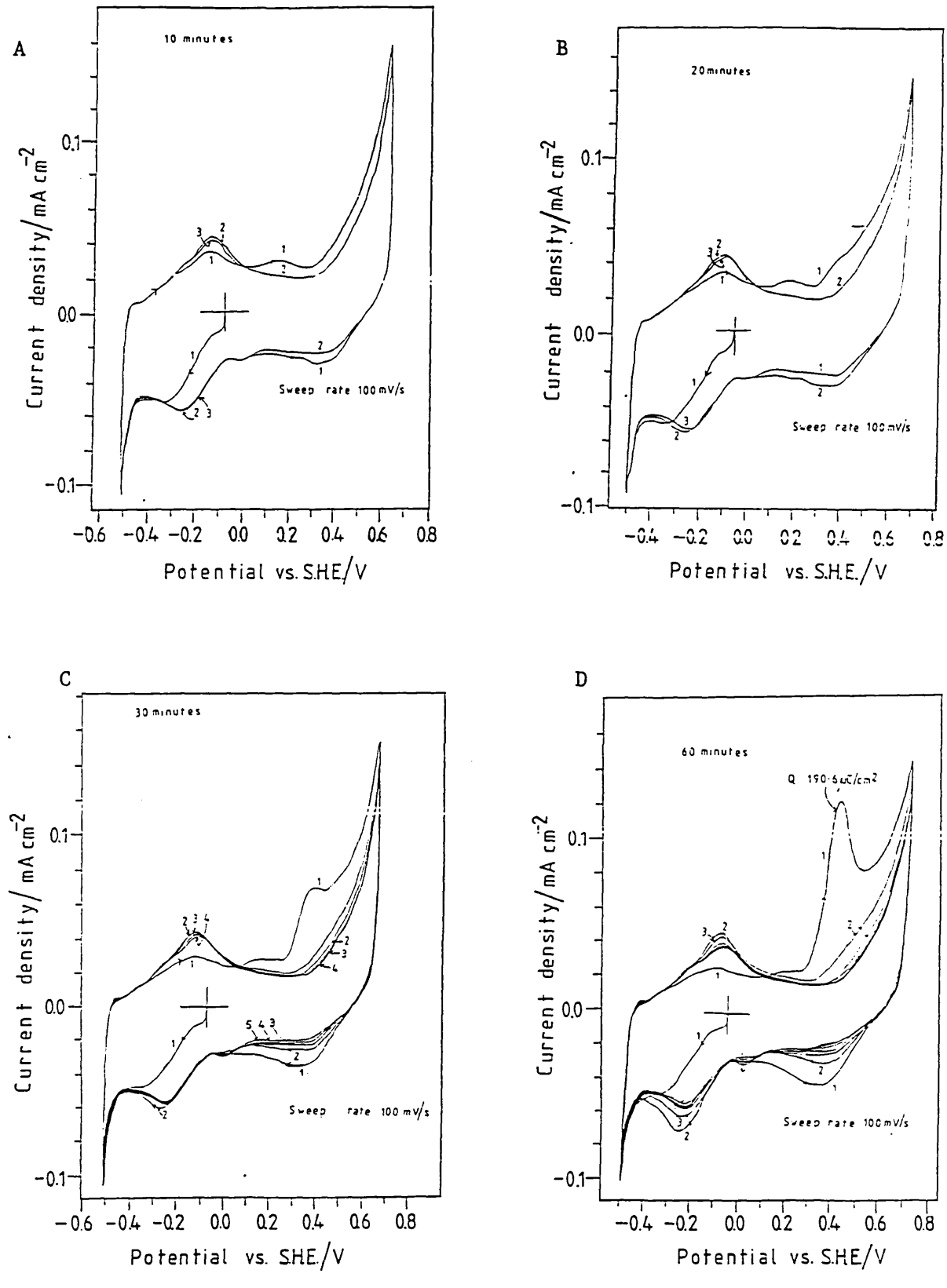


Fig 6.25 Effect of preconditioning at -0.1 V for various times on cyclic voltammograms of pyrite in stirred solution at pH 4.6 (0.5 M CH_3COOH + 0.5 M CH_3COONa), and a sweep rate of 100 mV s^{-1}.

The charges under the anodic peak at 0.4 V and cathodic peaks at ~ 0.4 and ~ -0.2 V were measured, as a function of temperature and conditioning time at -0.1 V (see Table 6.3). Allowing for the dispersion of soluble ferric species formed by reactions 6.6 - 6.8, the high anodic/cathodic charge ratio suggested that sulphur-oxygen compounds were also formed on the surface of pyrite during conditioning, since their electrode reactions, especially those involving sulphate, are irreversible [61]. An anodic/cathodic charge ratio of approximately one would have been obtained if only ferrous/ferric redox processes were involved.

Voltammograms initiated in a cathodic direction after preconditioning at -0.1 V exhibited no cathodic peaks, which precluded the possible formation of sulphur and goethite during the conditioning period.

Separate experiments with a pyrite RSCBE at pH 4.6 in the presence of ferrous and thiosulphate ($S_2O_3^{2-}$) ions showed that at 0.3 V both species started to oxidise on pyrite (see section 6.4.3.1, Figures 6.27 and 6.29 B). This supported the hypothesis that ferrous oxide/hydroxide and sulphur-oxygen compounds were formed on pyrite's surface during conditioning at -0.1 V via a chemical reaction, involving two coupled electrochemical reactions.

Experiments by Biegler et al[186] have shown that at pH 4.6 and -0.1 V, oxygen reduction on pyrite is mass transport controlled. Although solutions were "deoxygenated" in these experiments, the residual oxygen content in solution was still 10^{-5} - 10^{-3} mol m^{-3} (0.5 - 50 ppb) (see section 4.1). For mass transport controlled oxygen reduction, the cathodic current density is given by:-

$$i_L = Z\ F\ \frac{D}{\delta}\ C_o \qquad (6.8)$$

Assuming the diffusion coefficient of oxygen in aqueous solutions is 2×10^{-9} m^2 s^{-1} at 303 K[332], and the diffusion layer thickness under nitrogen sparging $\simeq 2 \times 10^{-3}$ cm[327], then i_L lay between ~ 2×10^{-4}—

Table 6.3 Effect of Temperature and Preconditioning Time at -0.1 V on the Charge (q_A) Measured Under the Anodic Peak at 0.4 V and the Combined Charges (q_c) Under the Cathodic Peaks at ~ 0.4 V and ~ -0.2 V

TEMPERATURE / K																		
293				303				313				323				333			
Time/ secs	Charge x 10^{-3}/ C cm^{-2}		q_A/q_c	Time/ secs	Charge x 10^{-3}/ C cm^{-2}		q_A/q_c	Time/ secs	Charge x 10^{-3} C cm^{-2}		q_A/q_c	Time/ secs	Charge x 10^{-3}/ C cm^{-2}		q_A/q_c	Time/ secs	Charge x 10^{-3}/ C cm^{-2}		q_A/q_c
	q_A	q_c			q_A	q_c			q_A	q_c			q_A	q_c			q_A	q_c	
300	0.0617	-	-	300	0.2034	0.0135	15.07	30	0.431	0.067	6.39	30	1.506	0.533	2.83	60	1.632	0.303	5.39
600	0.1113	-	-	600	0.4035	0.0483	8.35	60	0.717	0.160	4.47	60	1.477	0.492	2.99	120	3.170	0.641	4.95
900	0.1565	0.0108	14.49	900	0.5687	0.0967	5.88	180	1.729	1.444	1.19	120	2.613	0.823	3.17	240	5.934	1.517	3.91
1200	0.1747	0.0145	12.05	1200	0.7317	0.1585	4.62	300	2.547	1.313	1.94	240	4.550	1.61	2.83	960	17.93	6.05	2.96
1800	0.2317	0.0239	9.69	1800	0.9138	0.2630	3.47	600	4.259	2.056	2.07	480	8.24	3.46	2.38	1920	38.31	13.24	2.89
3600	0.2971	0.0415	7.16	3600	1.242	0.3990	3.11	900	6.315	3.456	1.83	960	16.76	7.36	2.28	3600	67.78	17.43	3.89
								1800	11.19	4.50	2.49	1920	35.32	14.41	2.45				
								2700	14.84	5.97	2.49								
								3600	17.34	7.67	2.26								

2×10^{-2} A m^{-2}. Assuming a monolayer coverage of ferrous hydroxide and sulphoxy species is equivalent to 1 mC cm^{-2}, between 1.25×10^{2} and 1.25×10^{4} seconds are required for its formation. Thus a possible corrosion type mechanism for the chemical process giving rise to the anodic peak at 0.4 V is that any residual oxygen in solution is reduced on the surface of pyrite according to reactions 6.9 - 6.13, which has been proposed as the reaction pathway for oxygen reduction in fuel cells[334], and S_2^{2-} ions in the pyrite lattice are oxidised to sulphur atoms (reaction (ag_1)). Oxygen reduction increases the interfacial pH and thereby stabilises $FeOH^+_{(ads)}$ on the pyrite surface (Figure II(vii); Appendix II).

$$O_2 + e = O_2^-{}_{(ads)} \qquad (6.9)$$

$$O_2^-{}_{(ads)} + H^+ = O_2H_{(ads)} \qquad (6.10)$$

$$O_2H_{(ads)} + e = O_2H^-{}_{(ads)} \qquad (6.11)$$

$$O_2^-{}_{(ads)} + H_2O + e = O_2H^-{}_{(ads)} + OH^-{}_{(ads)} \qquad (6.12)$$

$$O_2H^-{}_{(ads)} + H^+ = H_2O_{2(ads)} \qquad (6.13)$$

$$S_2^{2-}{}_{(lattice)} = 2S_{(ads)} + 2e \qquad (ag_1)$$

The hydroxy radicals adsorb onto metal and sulphur sites on the pyrite surface eg:-

$$Fe^{2+}{}_{(lattice)} + OH^{-}\cdot = Fe(OH)^+{}_{(ads)} \qquad (6.14)$$

$$2S_{(ads)} + 2\,{}^{\cdot}O_2H = 2SO_2H \qquad (6.15)$$

$$2S_{(ads)} + H_2O_2 = S_2(OH)_2 \qquad (ax_1)$$

Meyer[126] postulated that the initial step in S^{2-} oxidation involves the formation of $S_2(OH)_2$ (thiosulphurous acid), although it is unknown in the free state. In acidic solutions, thiosulphurous acid is a mild oxidising agent and can breakdown by various reactions[326]:-

$$S_2(OH)_2 = H_2S + SO_2 \qquad (6.16)$$

$$S_2(OH)_2 + H_2S = 3S + 3H_2O \qquad (6.17)$$

$$SO_2 + H_2O = HSO_3^- + H^+ \qquad (6.18)$$

$$HSO_3^- + S = S_2O_3^{2-} + H^+ \qquad (6.19)$$

In summary, $Fe(OH)^+_{(ads)}$, $S_2(OH)_2$ and $S_2O_3^{2-}$ species probably accumulate on the surface of pyrite by a corrosion type process involving the interaction of pyrite with oxygen reduction intermediates, formed as a result of the cathodic conditioning of pyrite.

6.4.3.1 Pyrite RSCBE Results

Figure 6.26 shows a voltammogram of the working electrode of a pyrite RSCBE in pH 4.6 buffer solution. The cathodic peak at -0.2 V was unaffected by stirring, which is consistent with the reduction of adsorbed surface species, viz sulphur and goethite, by reactions (v) and (o), respectively. The cathodic peaks at 0.0 and 0.25 V (Figure 6.23) were enhanced in quiescent solution and merged into a single peak at ~ 0.1 V. This supported the reaction assignment given in section 6.4.3; viz reduction of soluble ferric hydroxide species (ie $FeOH^{2+}$, $Fe(OH)_2^+$ and $Fe(OH)_3$, by reactions (h), (i) and (j) respectively). The H_2S produced by sulphur reduction was reoxidised in quiescent solution when the scan was reversed again to give a broad anodic peak at ~ 0.0 V. Similarly, Fe^{2+} species produced by reduction of the ferric oxide/hydroxides were re-oxidised at potentials > 0.4 V, giving rise to a voltammetric wave. Both these anodic peaks were absent when the electrode was rotated, as H_2S and Fe^{2+} were dispersed into solution.

The reaction assignments were vindicated further by voltammograms recorded separately in pH 4.6 buffer solution containing ferrous and sulphide ion (see Figures 6.27 and 6.28). The anodic step at 0.4 V increased in magnitude when Fe^{2+} was added to the solution, and similarly, sulphide ions enhanced the H_2S oxidation peak at 0.0 V.

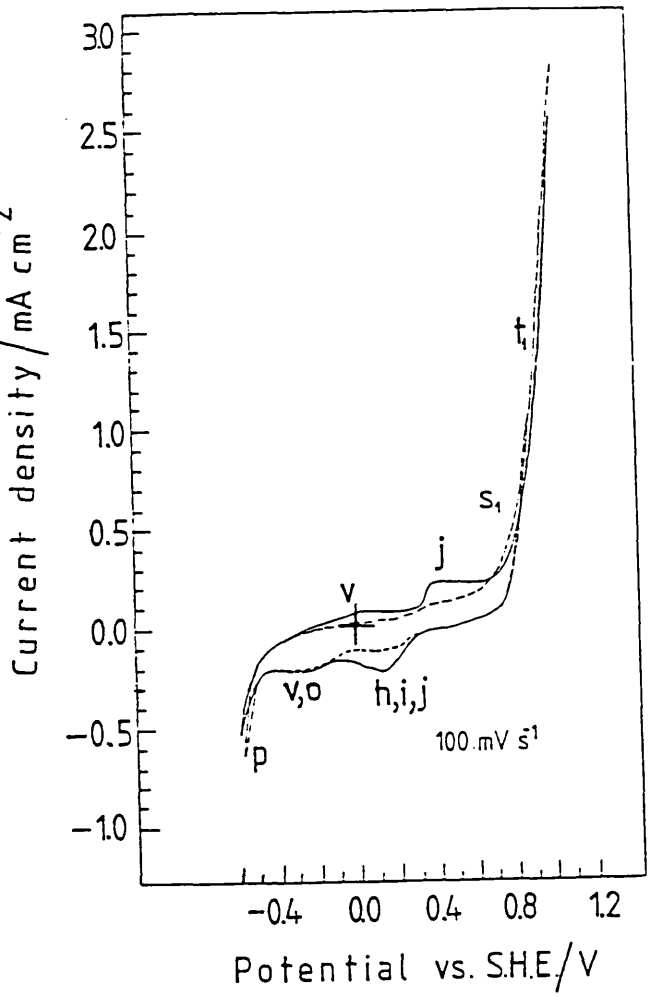


Fig 6.26 Cyclic voltammograms of a pyrite RSCBE in 0.5 M CH_3COOH + 0.5 M CH_3COONa (pH 4.6). (——) stationary electrode; (---) rotated electrode.

The only soluble oxidation products detected at the platinum collector electrode when the potential of pyrite was swept anodically to 1.2 V, were H^+ ion; detected as a reduction current at a collector potential of -0.4 V, which suggested that reactions (s_1) and (t_1) were the main oxidation reactions. Surprisingly, reduction of FeOOH and sulphur, formed on the surface of the pyrite electrode at anodic potentials, produced no oxidation of Fe^{2+} or H_2S at the collector electrode. This may have been due to the precipitation of FeS ($K_{sp} = 10^{-18}$) in the proximity of the electrode by reaction (j_1), which is quite insoluble in mildly acidic and alkaline solutions. Unfortunately, the conditions required to maximise the collection of soluble species

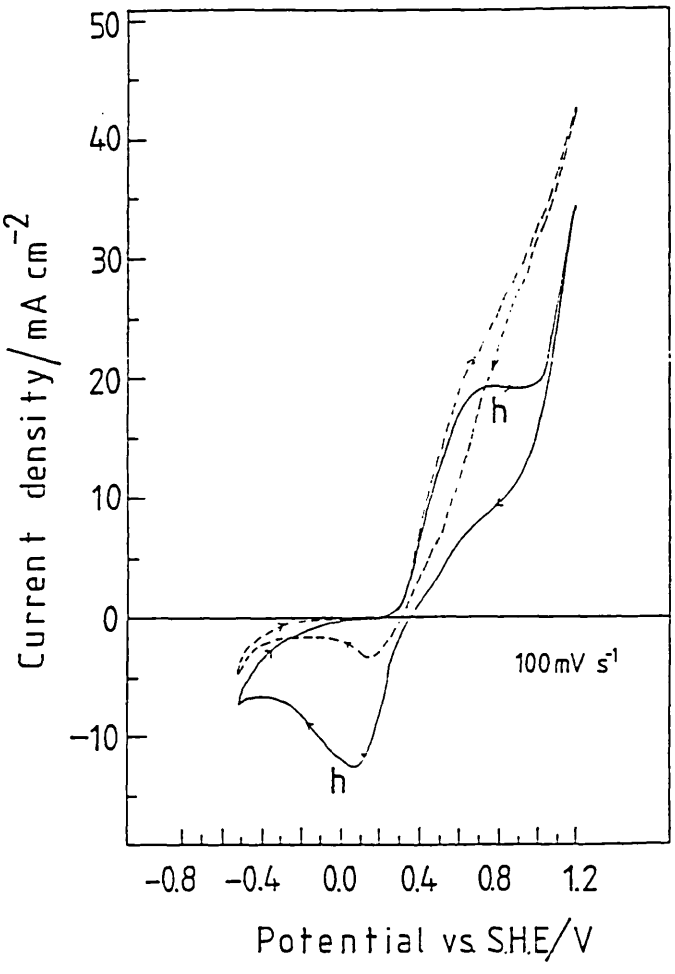


Fig 6.27 Cyclic voltammograms of a pyrite RSCBE in 0.5 M CH_3COOH + 0.5 M CH_3COONa + 0.1 M $FeSO_4$. (——) electrode stationary; (---) electrode rotated.

formed at the pyrite electrode, i.e. low sweep rates (10 mV s^{-1}) to maximise the amount of FeOOH and sulphur formed during pyrite oxidation, and low rotation rates to minimise the dispersion of soluble Fe^{2+} and H_2S, will also create high local concentrations of Fe^{2+} and H_2S and low local concentrations of H^+ at the electrode surface and hence cause FeS precipitation. A similar lack of response at the collector electrode was also observed at pH 7 and 9.2 when the products of FeS_2 oxidation were reduced.

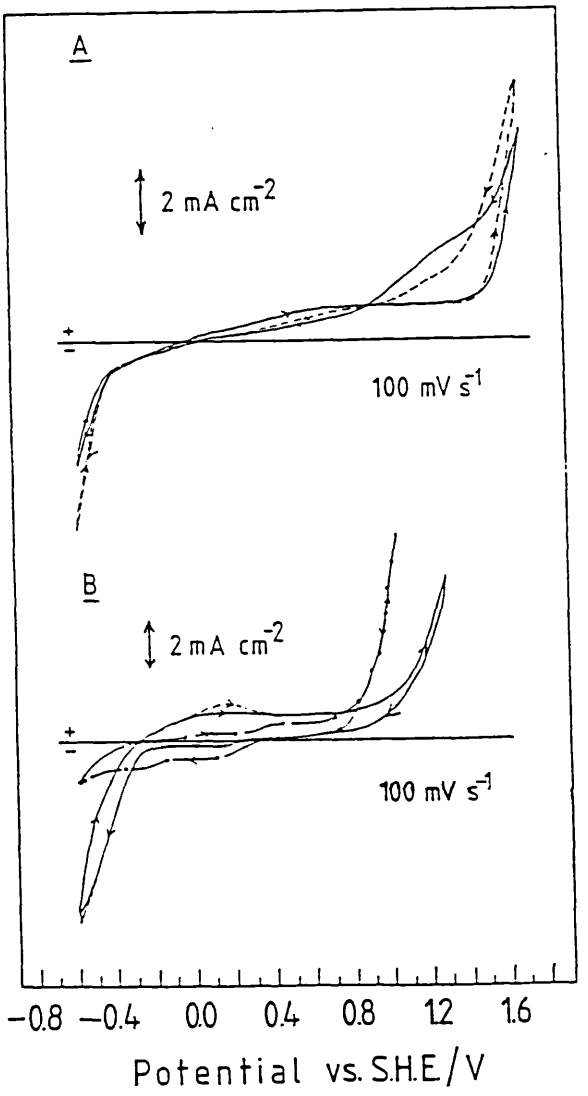


Fig 6.28 Cyclic voltammograms of a RSCBE in 0.5 M CH_3COOH + 0.5 M CH_3COONa + 0.1 M Na_2S. (A) platinum electrode; (B) pyrite electrode; (——) electrode stationary; (---) electrode rotated; (-•-•-) stationary pyrite electrode with no sulphide ions.

Although it is assumed that sulphide mineral oxidation leads directly to either sulphur or sulphate formation, sulphate ions are probably formed via a series of sulphur-oxygen metastable intermediates, i.e. $S_2O_2^{2-}$, $S_2O_3^{2-}$, HSO_3^{2-} etc[75,126,325] (Figure II(ii); Appendix II). To establish the potential range in which thiosulphate ions ($S_2O_3^{2-}$)

are oxidised on pyrite and platinum, cyclic voltammograms were recorded for both substrates using a RSCBE in 0.1 M $Na_2S_2O_3$ solution buffered at pH 4.6 (Figure 6.29).

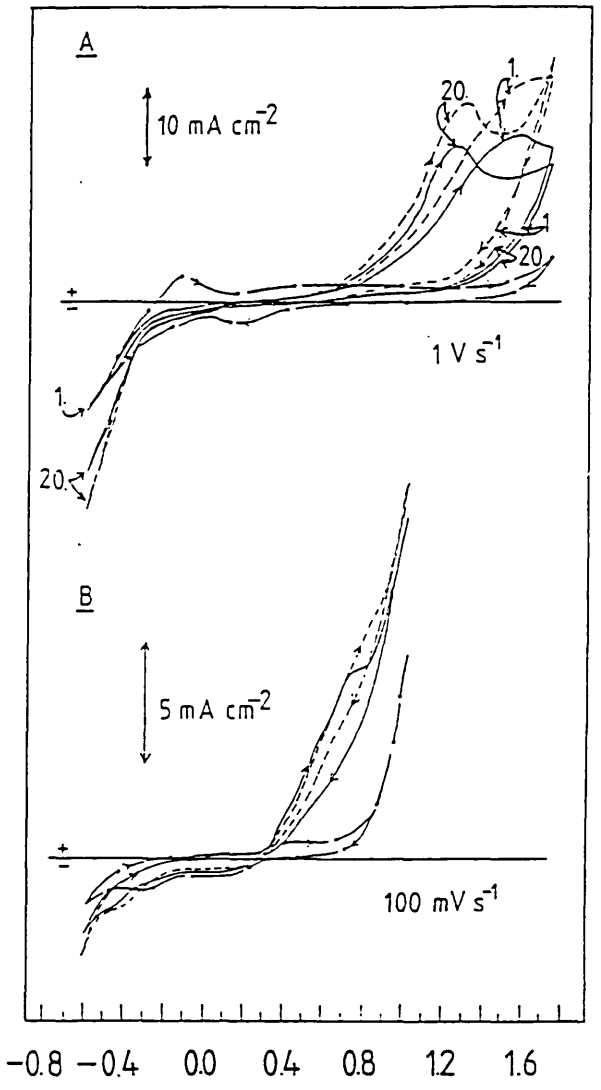


Fig 6.29 Cyclic voltammograms of a RSCBE in 0.5 M CH_3COOH + 0.5 M CH_3COONa + 0.1 M $Na_2S_2O_3$ (A) platinum electrode; (B) pyrite electrode; (——) electrode stationary; (---) electrode rotated; (-·-·-·) stationary pyrite electrode with no thiosulphate ions.

At a sweep rate of 1 V s^{-1} thiosulphate oxidation commenced at 0.6 V on platinum. On the first anodic sweep an oxidation peak was observed at ~ 1.8 V which shifted to less positive potentials on repeated cycling. After 20 cycles the peak potential remained constant at ~ 1.3 V (Figure 6.29 A). Platinum exhibited similar behaviour in Na_2S solution (see section 5.2, Figure 5.8), although the oxidation peak did not decrease in size on cycling and no anodic peak was observed on the negative-going potential scan.

Contractor and Lal[139] and Loucka[301,306] have reported that the species adsorbed on platinum from either solutions of H_2S or SO_2 are virtually identical. Under conditions of potentiodynamic cycling the adsorbed layers from either solution exhibit a large oxidation peak at 1.2 - 1.3 V at room temperature. At low pH thiosulphate decomposes readily [328]. The platinum surface probably acts as a catalytic site for thiosulphate decomposition leading to an adsorbed sulphur and sulphur dioxide layer:-

$$\begin{array}{l} Pt \\ | \\ Pt \end{array} + S_2O_3^{2-} + 2H^+ \rightarrow \begin{array}{l} Pt\text{—}(S)_{(ads)} \\ | + H_2O \\ Pt\text{—}(SO_2)_{(ads)} \end{array} \qquad (6.20)$$

which then oxidises according to the equations:-

$$Pt\text{—}(S)_{(ads)} + 4H_2O = Pt + SO_4^{2-} + 8H^+ + 6e \qquad (6.21)$$

$$Pt\text{—}(SO_2)_{(ads)} + 2H_2O = Pt + SO_4^{2-} + 4H^+ + 2e \qquad (6.22)$$

Thiosulphate oxidation on pyrite was found to commence at potentials > 0.3 V. The presence of $S_2O_3^{2-}$ ions shifted pyrite's anodic polarisation curve (attributed mainly to sulphate formation (reaction (d)) at potentials > 0.8 V) to more negative potentials, which suggested that thiosulphate is probably an intermediate in sulphate formation on pyrite.

6.4.4 pH 7.0 (0.025 M KH_2PO_4 + 0.025 M Na_2HPO_4)

Voltammograms for a stationary pyrite electrode at pH 7.0 in quiescent solution are shown in Figure 6.30. At E_{λ_a} values < 0.0 V, pyrite oxidation proceeded via reaction (s_1) forming goethite and sulphur.

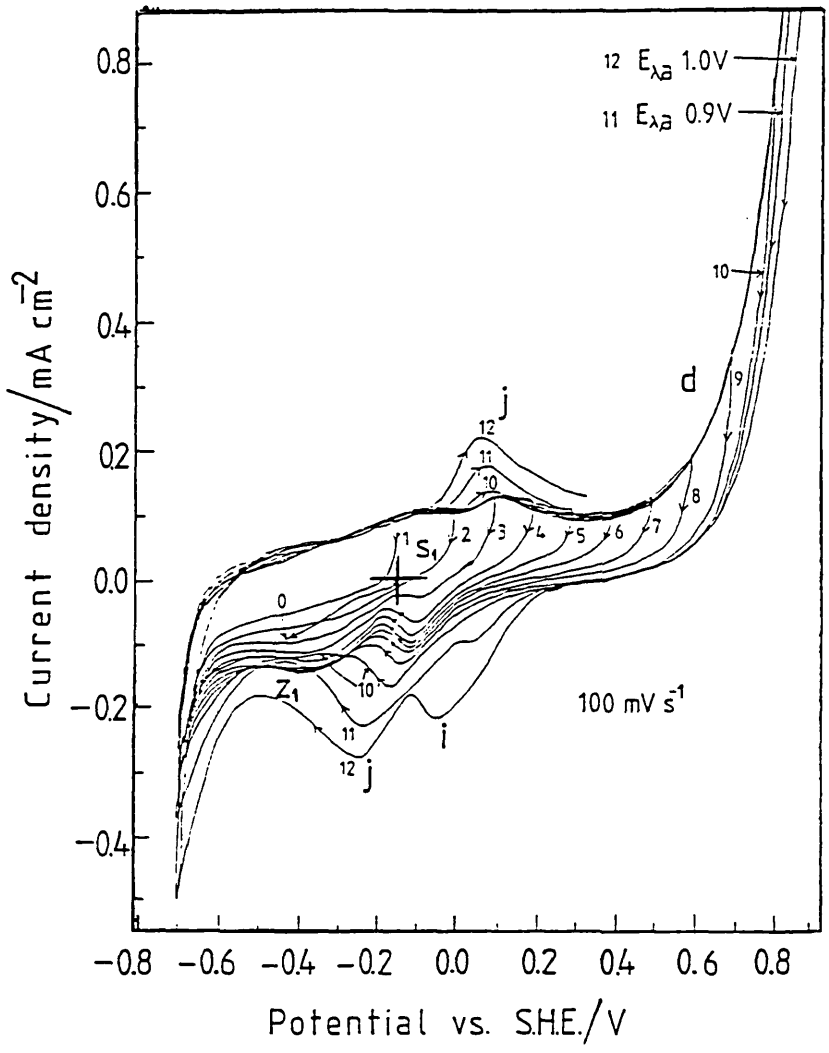


Fig 6.30 The effect of extending the anodic potential scanning limit ($E_{\lambda a}$) on cyclic voltammograms of pyrite at pH 7 (0.025 M KH_2PO_4 + 0.025 M Na_2HPO_4) in quiescent solution and a sweep rate of 100 mV s^{-1}.

As pK_a (H_2S) = 7 (reaction (z)), 50% of the sulphide species in solution, formed as a result of sulphur reduction on the reverse cathodic scan, should comprise HS^- (reaction (w)) and 50% H_2S (reaction (v)). Since the reduction of goethite and sulphur occurred in a similar potential range (a single cathodic peak was observed at ~ -0.4 V on the reverse scan), and because HS^- is probably an intermediate in the formation of H_2S by sulphur reduction (reactions (x), (y) and (z)), it is likely that goethite and sulphur reduction lead to the formation of insoluble ferrous sulphide (FeS), with no release of H_2S into solution:-

$$FeOOH + S + 3H^+ + 3e = FeS + 2H_2O \qquad (z_1)$$

$$E = 0.290 - 0.059\ pH$$

This reaction has a reversible potential of -0.121 V at pH 7.

Pyrite oxidation to sulphate (reactions (d) and (t_1)) became more thermodynamically favourable on increasing the pH from 4.6 to 7. This resulted in an irreversible loss of sulphur from the surface of pyrite, leaving an excess of ferric oxide, even under mild oxidising conditions at pH 7. Thus, at E_{λ_a} values > 0.0 V, a second cathodic peak appeared (initially at -0.1 V), assigned to the reduction of excess ferric oxide by reaction (j). The peak shifted to more negative potential values on increasing E_{λ_a}.

Thus, pyrite oxidised at potentials < 0.0 V by a surface transformation to form sub-monolayer quantities of goethite and sulphur. As sulphate formation became increasingly dominant over sulphur formation at potentials > 0.0 V, the concomitant lowering of pH at the mineral/solution interface resulted in ferric oxide being formed by a dissolution-precipitation process (reactions (e), (f) and (o_1)). Thus at 0.8 V, the oxide layer consisted of an inner monolayer of goethite and sulphur formed by a solid state mechanism and a few outer monolayers of an amorphous, more hydrated ferric oxyhydroxide ($Fe(OH)_3$), formed by a dissolution-precipitation process. Increasing the anodic potential above 0.8 V lowered the interfacial pH sufficiently for some of the precipitated $Fe(OH)_3$ to dissolve, forming soluble $Fe(OH)_2^+$ species (reaction (w_1)). This resulted in a third cathodic peak (Figure 6.30) appearing on the reverse scan at ~ 0.0 V due to $Fe(OH)_2^+$ reduction by reaction (i) in quiescent solution.

Stirring the solution dispersed the soluble ferric species formed by pyrite oxidation into solution. Thus, the cathodic peak assigned to $Fe(OH)_2^+$ reduction was absent, and since less $Fe(OH)_3$ was precipitated on the surface of pyrite, the $Fe(OH)_3$ reduction peak decreased in size

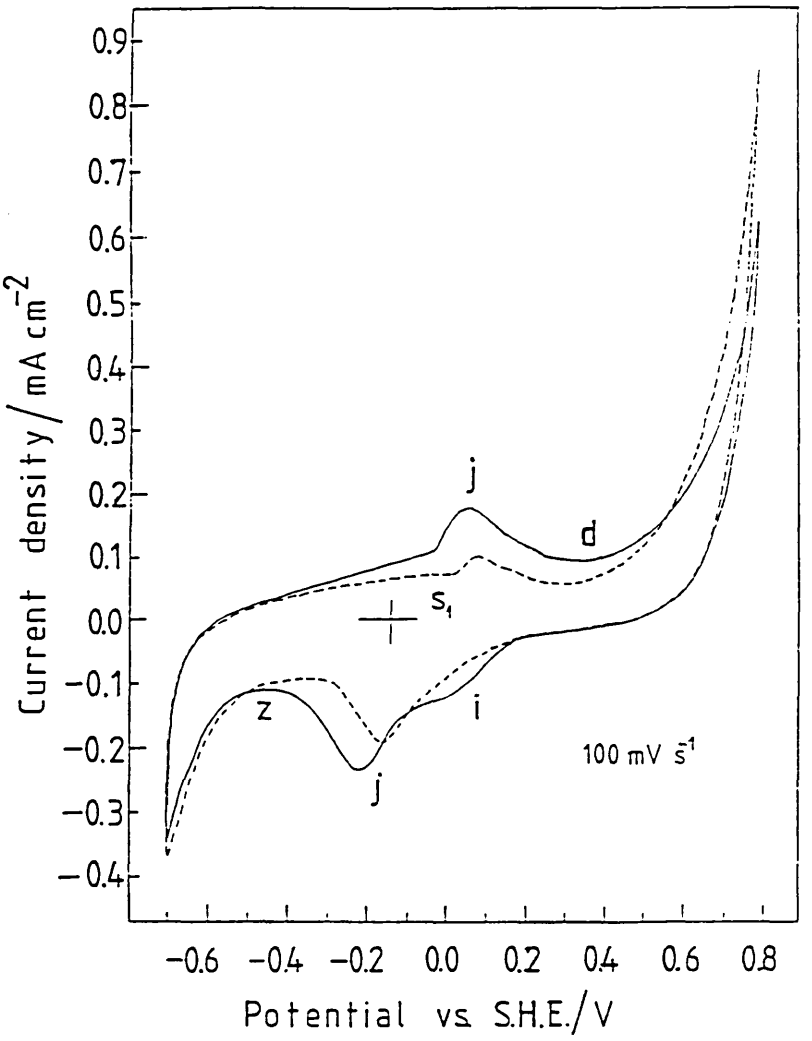


Fig 6.31 Cyclic voltammograms of a pyrite RSCBE in 0.025 M KH_2PO_4 + 0.025 M Na_2HPO_4 (pH 7). (——) stationary electrode (---) electrode rotated.

in stirred solutions (Figure 6.31). The anodic current at potentials > 0.5 V was enhanced in stirred solution, which was consistent with a dissolution-precipitation oxidation mechanism at these potentials, since precipitated ferric hydroxides inhibited pyrite oxidation in quiescent solution.

An interesting characteristic of pyrite voltammograms recorded at pH 7, was that the cathodic peak assigned to goethite and sulphur

reduction (z_1) at -0.4 V, increased in size as $E_{\lambda a}$ was increased to 0.4 V, reached a limiting value for $E_{\lambda a}$ values between 0.4 and 0.7 V, then decreased as $E_{\lambda a}$ was extended to potentials > 0.8 V (Figure 6.30). This phenomena was observed in both quiescent and stirred solution, which implied that the effect was not due to goethite dissolution as a result of the low interfacial pH at high overpotentials.

It is generally assumed that sulphide minerals oxidise by two independent pathways leading to sulphur and sulphate formation, and that sulphate is not formed as a result of sulphur oxidation due to the high overpotential requirement for this reaction [61]. However, the cyclic voltammograms shown in Figure 6.30 suggest that if sub-monolayer quantities of sulphur are formed on pyrite, ie sulphur is present as ad-atoms rather than a separate thermodynamic phase, sulphur may be oxidised to sulphate at potentials > 0.8 V. This resulted in a decrease in the cathodic peak (z_1) at -0.4 V.

Assuming that x moles of pyrite are oxidised to sulphur and y moles to sulphate by reactions (s_1) and (t_1) respectively, then the total anodic charge (Q_A) passed on a potential sweep will be (3x + 15y)F coulombs (see section 6.4.1). The cathodic charge $Q_{c(z_1)}$ arising from reaction (z_1) is given by:-

$$Q_{c(z_1)} = 6xF \text{ coulombs} \qquad (6.23)$$

The total amount of ferric oxide/hydroxide produced is (x + y) moles of which 2x is consumed in reaction (z_1). Thus, the maximum theoretical cathodic charge resulting from the reduction of excess ferric oxide/hydroxide on the surface of pyrite by reaction (j), ($Q_{c(j)}$), equals (x + y - 2x)F coulombs

$$\therefore Q_{c(j)} = (y - x)F \text{ coulombs} \qquad (6.24)$$

This assumes no soluble ferric species are formed and dispersed into the bulk solution, which is a reasonable assumption for quiescent solutions and $E_{\lambda a}$ values < 0.9 V.

Values of x and y were determined from these equations by measuring Q_A, $Q_{c(z1)}$ and $Q_{c(j)}$. Q_A was measured using a gated digital integrator. $Q_{c(z1)}$ and $Q_{c(j)}$ were determined from area measurements of peaks z_1 and j in Figure 6.30 using an image analyser. Corrections were made for peak overlap and the small amount of background charge due to pyrite reduction (reaction(r)). These values, together with the theoretical value of $Q_{c(j)}$ calculated from equation (6.24) are presented in Table 6.4. The theoretical values of $Q_{c(j)}$ were negative for $E_{\lambda a}$ potentials < 0.6 V, which implied that there should have been an excess of sulphur (not ferric oxide) on the surface of pyrite at potentials < 0.6 V and that a cathodic peak due to the reduction of excess ferric oxide would not be observed until $E_{\lambda a}$ exceed 0.6 V. However, cathodic peak (j) appeared once $E_{\lambda a}$ exceeded 0.0 V, and the experimental values of $Q_{c(j)}$ were greater than the theoretical values for all values of $E_{\lambda a}$, so that less anodic charge was needed to form ferric oxides than predicted by this oxidative mechanism. Even if peak (z_1) was assigned to sulphur reduction only (reactions (w) and (x)), and all ferric species were reduced separately under cathodic peak (j), or peak (z_1) was assigned to reaction (s_1), the experimental values of $Q_{c(j)}$ still exceeded the theoretical values. Therefore, under the non-steady state conditions of these experiments, possible anodic reactions which could occur in parallel with pyrite oxidation to sulphur are reactions (6.25), (6.26) and (6.27):-

$$FeS_2 + 5H_2O = Fe(OH)_3 + S_2O_2^{2-} + 7H^+ + 5e \qquad (6.25)$$

$$FeS_2 + 6H_2O = Fe(OH)_3 + S_2O_3^{2-} + 9H^+ + 7e \qquad (6.26)$$

$$FeS_2 + 6H_2O = Fe(OH)_3 + 0.5\ S_4O_6^{2-} + 9H^+ + 8e \qquad (6.27)$$

These reactions require less anodic charge than sulphate formation (c.f. reaction (t_1)), and form meta-stable sulphur-oxygen species which are possible intermediates in sulphate formation. It is assumed that these are irreversible processes since the reduction of soluble sulphoxy species was not observed on the negative going potential scans, even in quiescent solution (see Figure 6.30).

Table 6.4 Quantity of Pyrite Oxidised via Reactions (s_1) and (t_1) at pH 7 (0.025 M Na_2HPO_4 + 0.025 M KH_2PO_4) on a 100 mV s^{-1} Potential Sweep from the Rest Potential (E_r) to Different Values of the Anodic Potential Scanning Limit (E_{λ_a}) in Quiescent Solution

E_r = 0.150 V

E_{λ_a}/ V vs. S.H.E.	Q_A/mC cm^{-2}	$Q_{c(z_1)}$/mC cm^{-2}	Moles of pyrite oxidising to sulphur, x /moles cm^{-2}	Moles of pyrite oxidising to sulphate y/moles cm^{-2}	Theoretical $Q_{c(j)}$ value (equation 6.24)/ mC cm^{-2}	Experimental $Q_{c(j)}$ /mC cm^{-2}
0.0	0.1611	0.0832	1.437×10^{-10}	0.828×10^{-10}	-0.0059	0.0000
0.1	0.2836	0.1402	2.421×10^{-10}	1.475×10^{-10}	-0.0091	0.0549
0.2	0.4208	0.1904	3.289×10^{-10}	2.250×10^{-10}	-0.0100	0.0871
0.3	0.5310	0.2312	3.994×10^{-10}	2.870×10^{-10}	-0.0108	0.1195
0.4	0.6320	0.2751	4.752×10^{-10}	3.416×10^{-10}	-0.0129	0.1387
0.5	0.7838	0.2751	4.752×10^{-10}	4.465×10^{-10}	-0.0028	0.1672
0.6	0.9942	0.2751	4.752×10^{-10}	5.919×10^{-10}	0.0013	0.1888
0.7	1.3033	0.2751	4.752×10^{-10}	8.055×10^{-10}	0.0319	0.2250
0.8	2.0416	0.2235	3.861×10^{-10}	13.330×10^{-10}	0.0914	0.2867

Assuming that x moles of pyrite were oxidised to sulphur, and z moles to sulphoxy anions (the formation of which requires n electrons), the total anodic charge (Q_A) passed on an anodic sweep would be (3x + nz)F coulombs:-

$$\therefore n = \frac{Q_A - 3xF}{zF} \qquad (6.28)$$

Substituting z for y in equation (6.24) the cathodic charge $Q_{c(j)}$ was measured and used to calculate z. Values for Q_A, x and z were then substituted into equation (6.28) and n was determined as a function of E_{λ_a} (see Table 6.5).

n was found to vary between 2 and 3 for E_{λ_a} potentials between 0.1 and 0.5 V. Only at potentials > 0.7 V, when the rate of pyrite oxidation increased sharply, did the value of n exceed 5 and pyrite oxidation proceed by reactions (6.25 - 6.27).

Assuming n equals 3 (for E_{λ_a} values between 0.1 and 0.5 V), it is proposed that the reaction accompanying pyrite oxidation to elemental sulphur at E_{λ_a} potentials between 0.1 and 0.5 V did not involve lattice decomposition and the formation of sulphoxy anions, but involved the oxidation of Fe(II) to Fe(III) in the lattice, and the adsorption and deprotonation of water molecules, by the following reactions:-

$$Fe(II)_{lattice} = Fe(III)_{lattice} + e \qquad (6.29)$$

$$H_2O \rightleftharpoons (O)_{(ads)} + 2H^+ + 2e \qquad (6.30)$$

or

$$2H_2O \rightleftharpoons 2(OH)_{(ads)} + 2H^+ + 2e \qquad (6.31)$$

$$2(OH)_{(ads)} \rightleftharpoons O_2H^-{}_{(ads)} + H^+ \qquad (6.32)$$

Table 6.5 Quantity of Pyrite Oxidised to Sulphur and a Sulphur-Oxygen Anion at pH 7 (0.025 M Na_2HPO_4 + 0.025 M KH_2PO_4) on a 100 mVs^{-1} Sweep from the Rest Potential (E_r) to Different Values of the Anodic Potential Scanning Limit ($E_{\lambda a}$) in Quiescent Solution

E_r = -0.150 V

$E_{\lambda a}$/ V vs. S.H.E.	Q_A/mC cm^{-2}	Moles of pyrite oxidising to sulphur, x /moles cm^{-2}	Experimental $Q_{c(j)}$ /mC cm^{-2}	Moles of pyrite oxidising to sulphur-oxygen anions, z /moles cm^{-2}	Number of electrons (n) required for process z ($n = \frac{Q_A - 3xf}{ZF}$)
0.0	0.1611	1.437×10^{-10}	0.0000	-	-
0.1	0.2836	2.421×10^{-10}	0.549	8.106×10^{-10}	2.73
0.2	0.4208	3.289×10^{-10}	0.0871	12.316×10^{-10}	2.74
0.3	0.5310	3.994×10^{-10}	0.1195	16.379×10^{-10}	2.629
0.4	0.6320	4.752×10^{-10}	0.1387	19.127×10^{-10}	2.679
0.5	0.7838	4.752×10^{-10}	0.1672	22.082×10^{-10}	3.033
0.6	0.9942	4.752×10^{-10}	0.1888	24.320×10^{-10}	3.651
0.7	1.3033	4.752×10^{-10}	0.2250	28.072×10^{-10}	4.304
0.8	2.0416	3.861×10^{-10}	0.2867	33.576×10^{-10}	5.957

Combining reactions (6.31) and (6.32) with reaction (6.29), gives the overall reaction:-

$$FeS_2 + 2xH_2O = Fe_{(1-x)}^{2+}(Fe^{3+}O_2H^-S_2^{2-})_x\ (S_2^{2-})_{(1-x)} + 3xH^+ + 3xe \qquad ...(6.33)$$

This is similar to the reaction proposed by Biegler and Swift[78], viz:-

$$FeS_2 + 2H_2O \rightleftharpoons FeS_2(HO_2)_{ads} + 3H^+ + 3e \qquad (am_1)$$

The mechanism by which water is adsorbed and deprotonated on pyrite at potentials well below the reversible potential for the H_2O/O_2 couple can be accounted for by considering the solid state properties of pyrite and invoking a semiconductor band model to explain the electrochemical behaviour of pyrite. This is described in section 6.7).

Another possibility is that, between 0.1 and 0.5 V, pyrite oxidised by reactions such as:-

$$FeS_2 + 3H_2O = Fe(OH)_3 + 3H^+ + 0.5\ S_4^{2-} + 2e \qquad (an_1)$$

and

$$FeS_2 + 3H_2O = Fe(OH)_3 + 3H^+ + 0.4\ S_5^{2-} + 2.2e \qquad (ao_1)$$

to form ferric oxide/hydroxides and soluble meta-stable polysulphide species. Hamilton and Woods[325,330] have argued that sulphide oxidation on gold occurs via a polysulphide ion intermediate:-

$$xHS^- = S_x^{2-} + xH^+ + (2x - 2)e \qquad (aw_1)$$

$$xS^{2-} = S_x^{2-} + (2x - 2)e \qquad (ap_1)$$

where $2 \leq x \leq 5$

$$S_x^{2-} = xS^\circ + 2e \qquad (aq_1)$$

They observed a slight imbalance in the anodic and cathodic charges, measured during anodic and cathodic sweeps on a gold electrode in 10^{-4} M sulphide solution when the electrode was rotated. This suggested that a soluble polysulphide intermediate was formed during sulphide oxidation and sulphur reduction[325]. It was shown that the composition of the intermediate sulphide deduced from the relative charges passed in stripping a sulphur layer from a stationary and a rotated electrode was S_2^{2-} at all the pH values studied (i.e. 6.8, 9.2 and 13).

Recently Hodgson and Agar[331] have proposed that the formation of polysulphides is an integral part of pyrrhotite oxidation, and from their analysis of voltammetric peaks deduced that the polysulphide formed on pyrrhotite in the pH range of their studies (i.e. 4 - 9), was also S_2^{2-}. However, their reaction assignment of voltammetric peaks observed during anodic scans on pyrrhotite electrodes could be due to ferric oxide dissolution/precipitation, especially since the peak potential for the anodic peak assigned to the reaction,

$$S_2^{2-} = 2S^\circ + 2e \qquad (ar_1)$$

was pH dependent[331].

Both Hamilton and Woods[325] and Hodgson and Agar[331] proposed the formation of S_2^{2-} at all the pH values they studied. However, Chen and Morris[165] computed concentrations of polysulphide species in equilibrium with sulphur over the pH range 6 - 10 for a 10^{-4} M sulphide solution (the same sulphide concentration as that used by Hamilton and Woods[325]), and found that the concentrations of S_2^{2-} and S_3^{2-} were very small compared with S_4^{2-} and S_5^{2-}. This is in general agreement with the general finding that in polysulphide solution only S_4^{2-} and S_5^{2-} are present in significant quantities[328]. Furthermore, it was found that in the pH range 6 - 7 the concentration of these species was small in comparison with the concentration of dissolved sulphur[165]. The solubility of sulphur has been estimated to be approximately 5×10^{-6} mol dm^{-3}[329]. The concentration of polysulphides (S_5^{2-} and S_4^{2-}) only became a significant fraction of the total dissolved sulphur at pH > 8 when the

solution was saturated in sulphur[165]. Thus in Hamilton and Woods'[325] analysis of the reactions of sulphide ions on gold, and in Hodgson and Agar's[331] oxidation mechanism for pyrrhotite, it is unlikely that S_2^{2-} ions are formed, but more probably dissolved sulphur, by the reaction:-

$$S^{2-} = S_{sol} + 2e \qquad (as_1)$$

Wierse et al[327] also studied the oxidation and reduction reactions of sulphide and polysulphide ions on gold. They concluded that only sulphur atoms form on the surface of gold and not larger sulphur chains. Their results showed that the sulphur layers obtained from sulphide or polysulphide solutions were identical and that polysulphide ions split during adsorption. HS^- was the product of sulphur desorption, not S_x^{2-}[327].

Hamilton and Woods[325] concluded that the oxidation of polysulphide to sulphur on gold (reaction (aq_1)) is relatively rapid and that polysulphides were not intermediates in sulphate formation. Sulphur was oxidised to sulphate at higher potentials by the reaction:-

$$S + 4H_2O = SO_4^{2-} + 8H^+ + 6e \qquad (at_1)$$

They also found that little of the soluble polysulphide intermediate (or soluble sulphur, as proposed above) was lost to the solution from a stationary electrode.

Thus if reactions (an_1) and (ao_1) were the oxidation processes occurring on pyrite in parallel with sulphur formation (reaction (s_1)), the reduction of polysulphides/dissolved sulphur would have been observed on the reverse cathodic scan in quiescent solution (see Figure 6.30), and there would have been no imbalance of charge on the anodic and cathodic scans (see Table 6.4). However, since this was not the case, and no soluble species were detected at the collector electrode during anodic potential scans from the rest potential, reaction (6.33) seems the most likely oxidation process, in as much as it does not require the oxidation of S_2^{2-} ions in the pyrite lattice.

6.4.5 Anodic and Cathodic Reactions in Alkaline Solutions (pH > 7)

In alkaline solutions the predominance of sulphate formation and the associated irreversible loss of sulphur from the surface of pyrite produced a high oxide/sulphur ratio with ferric oxide the dominant surface phase.

Once formed, ferric oxide/hydroxide was difficult to remove by cathodic treatment due to the low solubility of ferrous ions in alkali media (10^{-5} M at pH 9.2; reaction (p_1)). Studies on virgin pyrite surfaces at pH 9.2 (see section 6.3) showed that after prolonged cathodic treatment, monolayers of ferric oxide could be removed from the surface of pyrite, presumably due to ferrous oxide dissolution. However, an oxide monolayer was always left on the surface.

Cyclic voltammograms for a stationary pyrite electrode at pH 9.2 are shown in Figure 6.32. Reactions (c) and (d) gave rise to the anodic current above 0.3 V. The number of moles of H^+ formed per mole of $Fe(OH)_3$ produced is high for pyrite oxidation to sulphate (reaction (d)). The large electrode rotation rate dependence of the anodic current at potentials above 0.3 V (Figure 6.33 A) suggested that reaction (d) lowered the interfacial pH sufficiently for ferric oxide/hydroxide to dissolve from the surface and re-precipitate away from the electrode where the pH was higher and/or for ferric hydroxide to be formed directly by a dissolution-precipitation process, thereby decreasing pasivation. This was found to be the case for fast sweep rates ($\geq$ 100 mV s^{-1}) even at pH 13 (Figure 6.34). However, at slower sweep rates ($<$ 100 mV s^{-1}) ferric oxide had more time to build up on the surface of pyrite before the lowering of pH became dominant. Thus, a small potential windov was observed at low anodic overpotentials at which pyrite was passive (e.g. between 0.0 and 0.5 V at pH 11; see Figure 6.35).

Assuming there was never an excess of sulphur on the surface of pyrite at pH 9.2, due to the predominance of sulphate formation, and that insoluble FeS was formed in preference to HS^- (see section 6.4.4),

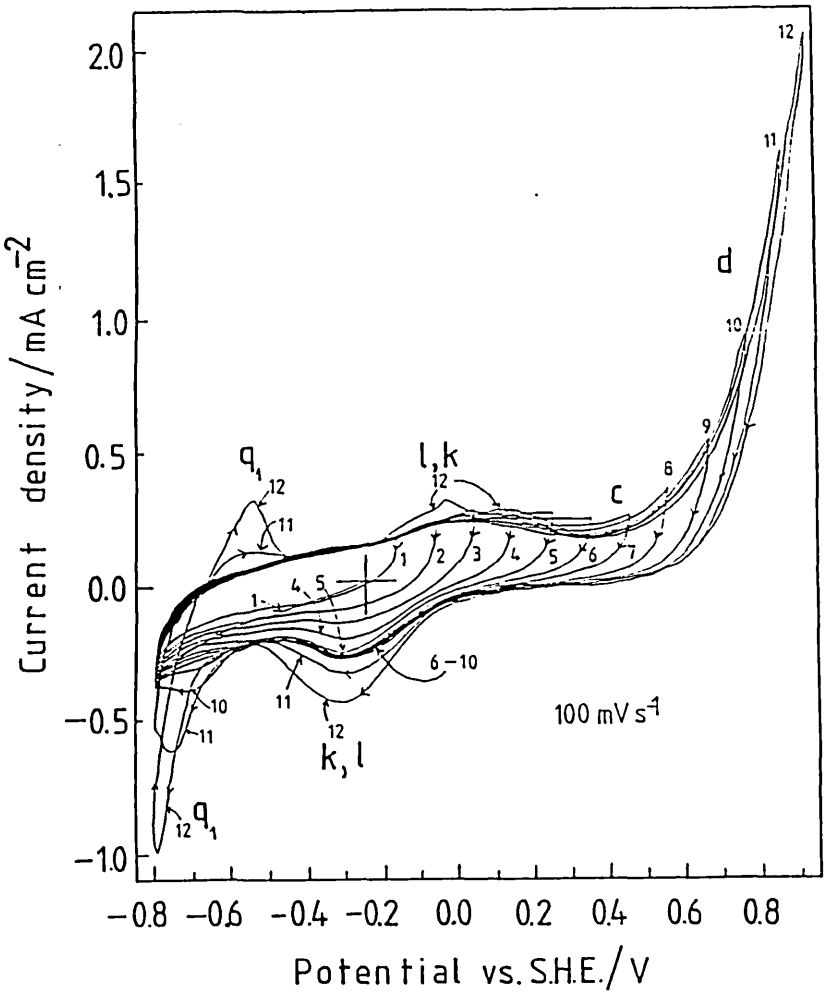


Fig 6.32 The effect of extending the anodic potential scanning limit ($E_{\lambda a}$) on cyclic voltammograms of pyrite at pH 9.2 (0.05 M $Na_2B_4O_7$) in stirred solution and a sweep rate of 100 mV s^{-1}.

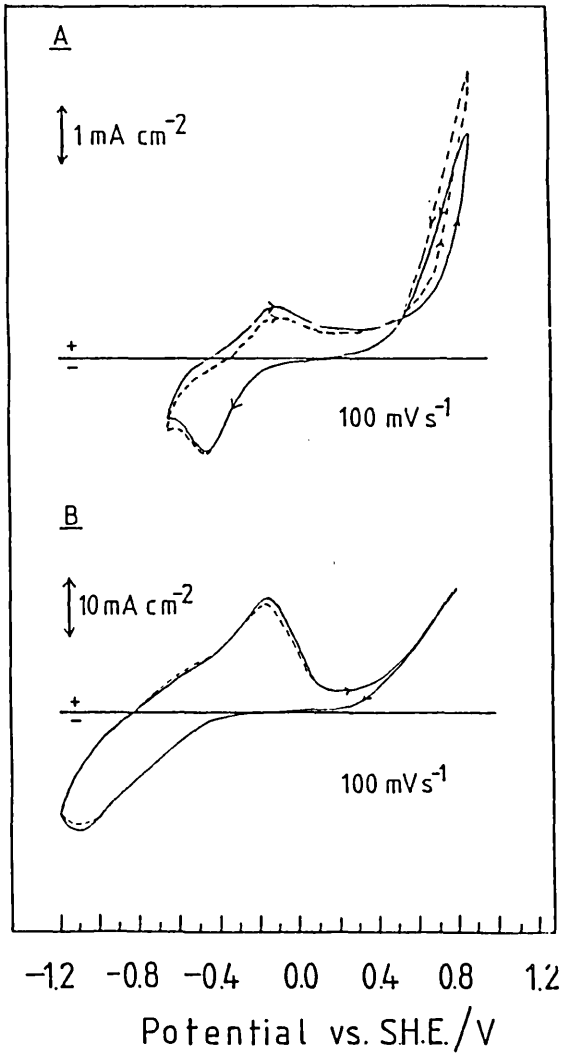


Fig 6.33 Cyclic voltammograms of a pyrite RSCBE in alkaline solutions. (A) pH 9.2 (0.05 M $Na_2B_4O_7$); (B) pH 13 (0.1 M NaOH); (——) electrode stationary; (---) electrode rotated.

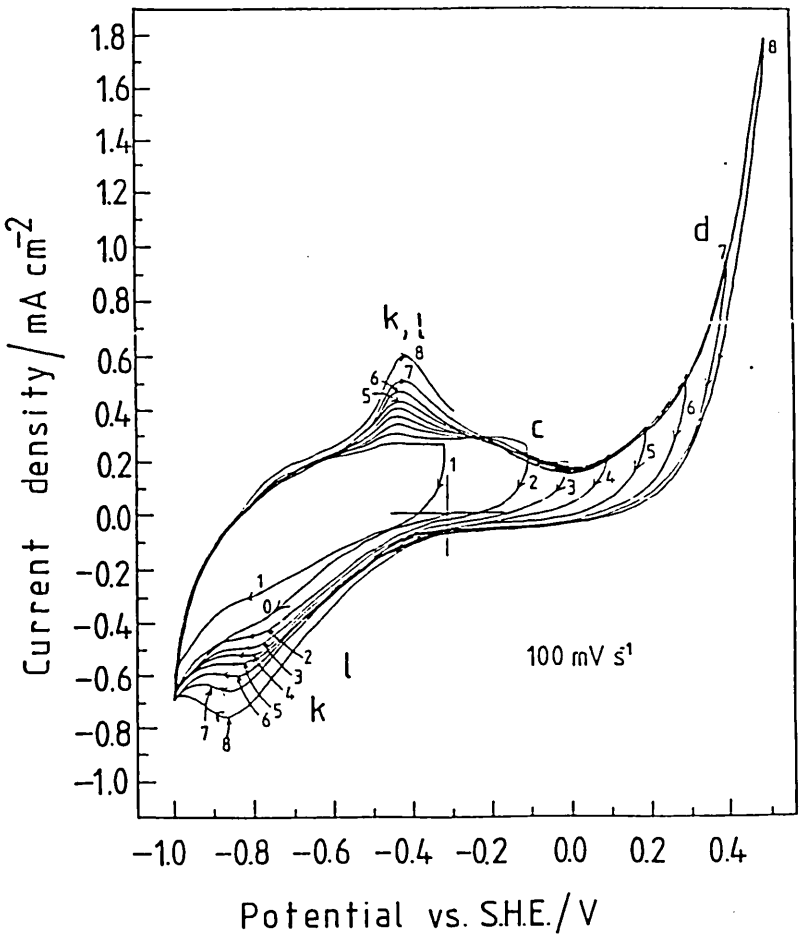


Fig 6.34 The effect of extending the anodic potential scanning limit ($E_{\lambda a}$) on cyclic voltammograms of pyrite at pH 13 (0.1 M NaOH) in stirred solution and a sweep rate of 100 mV s^{-1}.

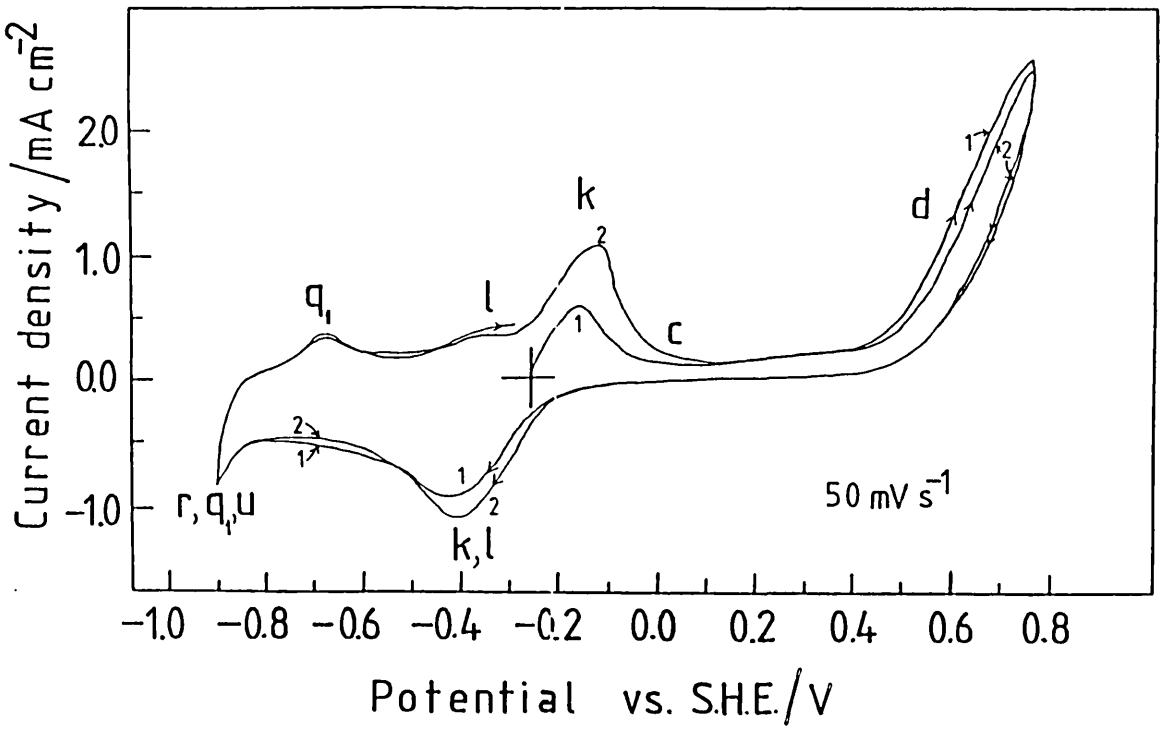


Fig 6.35 Cyclic voltammogram of a stationary pyrite electrode in stirred solution at pH 11 (0.025 M $NaHCO_3$ + 0.023 M NaOH), a scan rate of 50 mV s^{-1}, the anodic potential limit extended to 0.8 V.

then the reduction of ferric oxide/hydroxide and sulphur could occur by three possible reactions:

$$FeOOH + S + H_2O + 3e = FeS + 3OH^- \quad (E - -0.254\ V) \qquad (z_1)$$

$$Fe(OH)_3 + S + 3e = FeS + 3OH^- \quad (E = -0.145\ V) \qquad (l)$$

$$Fe(OH)_3 + e = Fe(OH)_2 + OH^- \quad (E = -0.72\ V) \qquad (k)$$

All these processes occur at similar potentials, thus only a single cathodic peak was observed at ~ 0.3 V for E_{λ_a} values < 0.5 V. Nonetheless, the onset of the cathodic peak at -0.08 V, suggested that sulphur was reduced by reaction (l), rather than (z_1), which was the cathodic process at pH 7. This change in mechanism was further evidence for sulphate formation becoming the dominant anodic process on increasing the pH from 7 to 9. Thus, under mildly oxidising conditions the lowering of interfacial pH resulted in $Fe(OH)_3$ being formed by dissolution-precipitation in preference to the more insoluble FeOOH by a solid-state mechanism.

On extending the anodic potential limit above 0.5 V, a second cathodic peak (q_1) (Figure 6.32) appeared at -0.8 V, with an associated anodic peak at -0.55 V, which were assigned to the reaction:

$$Fe(OH)_2 + 2H^+ + 2e^- = Fe + 2H_2O \qquad (q_1)$$

Although the cathodic peak at -0.3 V showed no stirring rate dependence (Figure 6.33 A), which was consistent with reactions (l) and (k), there was evidence for ferrous hydroxide dissolution (reaction (p_1)), since on the return anodic scan, the anodic current was greatest when the electrode was stationary. This was consistent with Fe^{2+} ions remaining in the vicinity of the electrode and being reoxidised by the reaction:

$$Fe^{2+} + 3H_2O = Fe(OH)_3 + 3H^+ + e \quad (E = -0.572\ V) \qquad (j)$$

At pH 13 the anodic current showed no stirring rate dependence on the return anodic scan, due to a decrease in the solubility of $Fe(OH)_2$ from 10^{-5} M at pH 9.2 to 10^{-13} M at pH 13 (Figure 6.33 B).

Figure 6.36 shows a voltammogram of a pyrite RSCBE in 0.05 M $Na_2B_4O_7$ and the current response at the Pt collector electrode for a range of potentials (E_c). As suggested above, the oxidation of pyrite at potentials > 0.8 V produced soluble ferric species, which were reduced

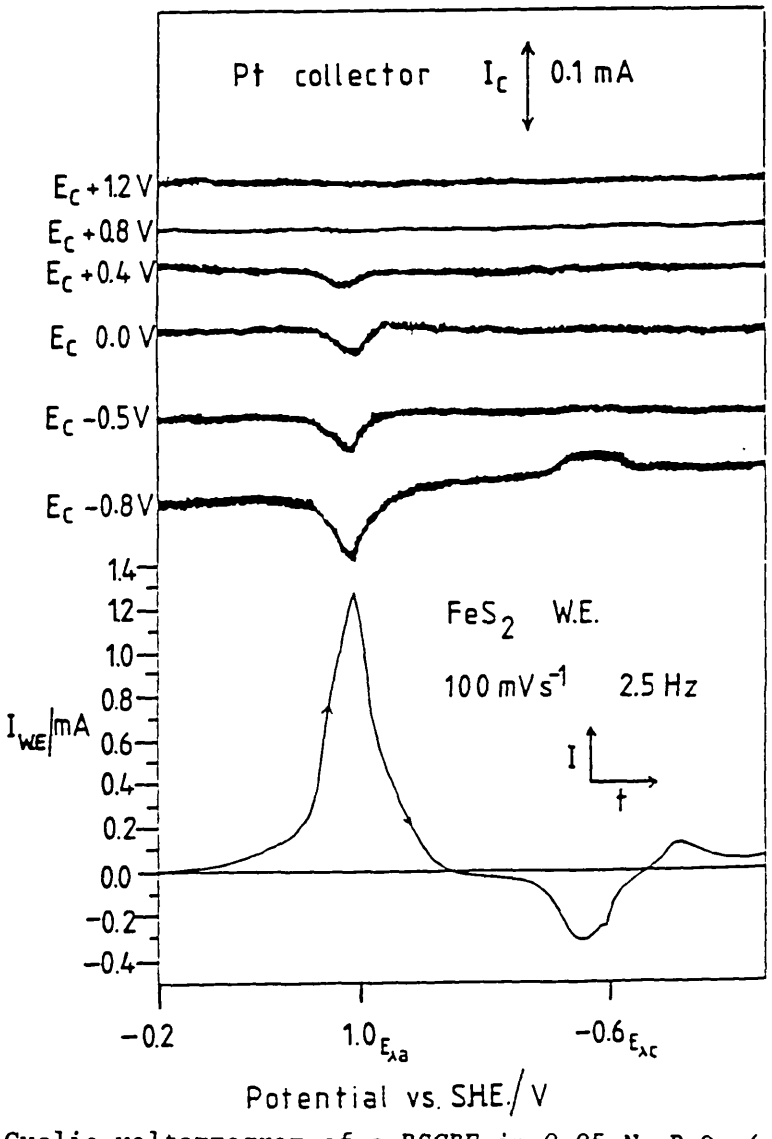


Fig 6.36 Cyclic voltammogram of a RSCBE in 0.05 $Na_2B_4O_7$ (pH 9.2) with the pyrite working electrode (W.E.) swept anodically from -0.2 to 1.0 V, then cathodically to -0.6 V, with the platinum collector held at various potentials (E_c).

at the collector electrode (0.4, 0.0 and -0.5 V). The increase in collector reduction response at collector potentials < -0.5 V and the appearance of an apparent anodic collector current associated with the cathodic processes (l) and (k) was due to interfacial pH changes caused by reactions (c), (d), (l) and (k) at the pyrite mineral electrode, affecting the large background current due to hydrogen evolution at the collector electrode (reaction (d_1); see section 6.4.2).

6.5 Pulse Voltammetry on Stationary Pyrite Electrodes

A computer program was written and used to analyse current-time transients (see Appendix III). Falling curves were fitted to $t^{-1/2}$, $t^{1/2}$, t^{-1} and exp(t) expressions and rising transients to t, $t^{1.5}$, t^2 and t^3 relationships. Regression analysis was performed to give the best fit.

The current-time (i-t) transients observed in response to anodic potential steps applied to "active" pyrite electrodes (ie sulphidised or cathodically pretreated; see sections 6.2 and 6.3) fell into three groups, depending on the anodic overpotential range.

6.5.1 Current-Time Transients at Low Anodic Overpotentials; Transition from "Active" to "Passive" Pyrite

Figures 6.37 and 6.38 show typical I-t responses for pyrite electrodes at pH 4.6 and 9.2 at low anodic overpotentials. Similar curves were obtained at other pH values in the range 0 - 13 at low overpotentials. The transients consisted of a current spike followed by a decay over the first 0.7 seconds. The current then rose to a peak after about 1 second and then decayed again. As the potential was increased, the rising transients became smaller (Figure 6.37), until at a given pH, a "critical potential" was reached; 0.410 V at pH 4.6, above which only a current decay was discernible (see Figure 6.39). The "critical potentials" were very similar to the open-circuit potentials of

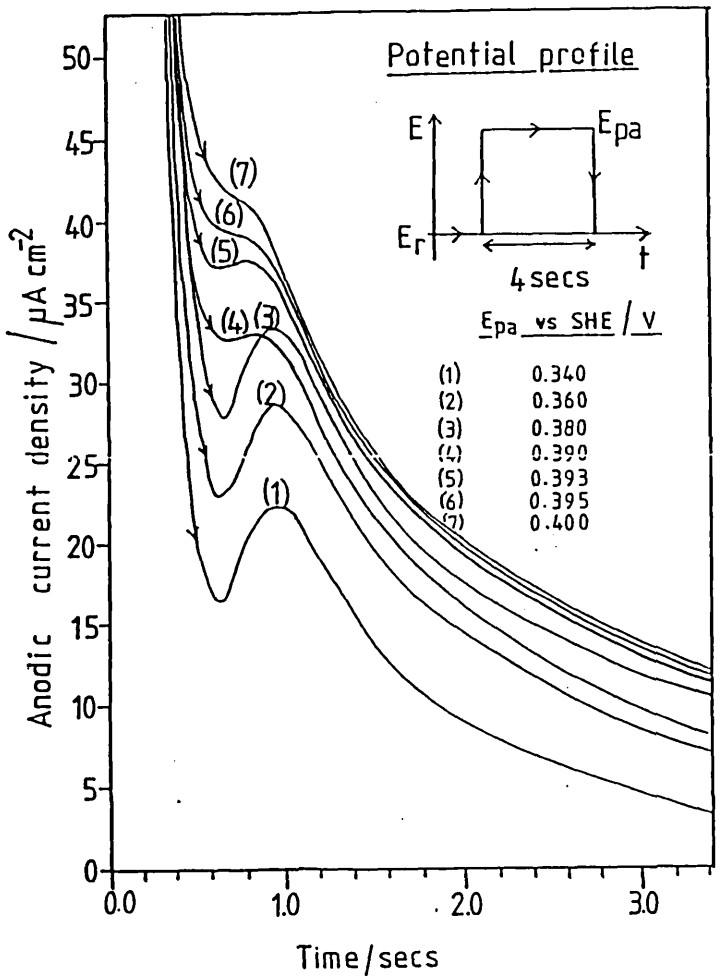


Fig 6.37 Current-time transients for a stationary pyrite electrode pulsed anodically from an "active" rest potential (-0.055 V) in stirred 0.5 M CH_3COOH + 0.5 M CH_3COONa)pH 4.6) buffer solution. E_r rest potential; E_{pa} , anodic pulse potential.

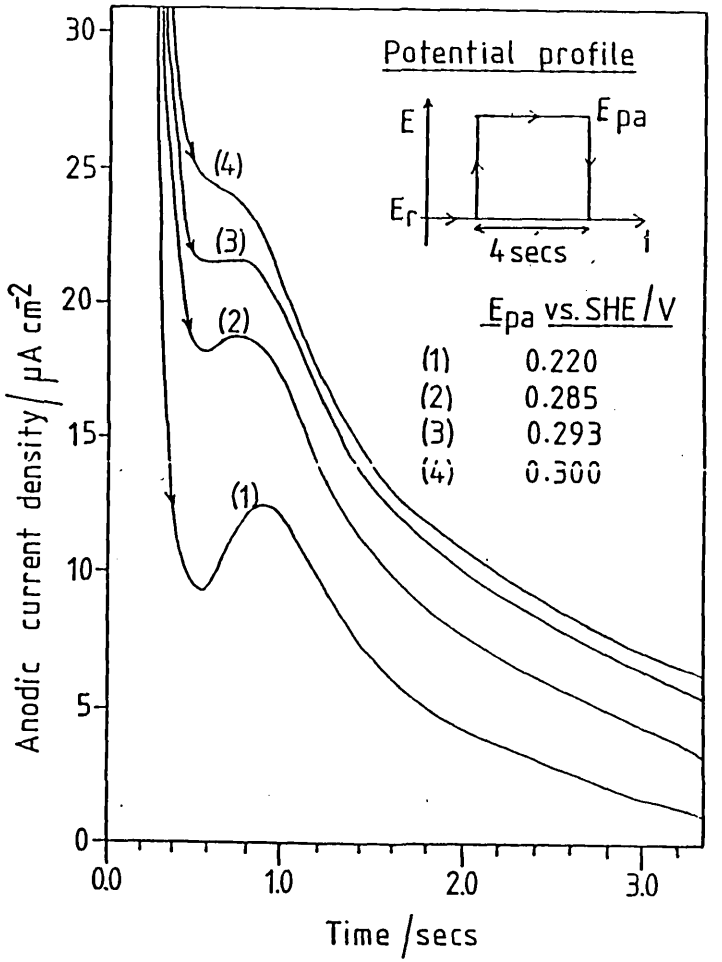


Fig 6.38 Current-time transients for a stationary pyrite electrode pulsed anodically from an "active" rest potential (-0.135 V) in stirred 0.05 M $Na_2B_4O_7$ (pH 9.2) buffer solution. E_r, rest potential; E_{pa}, anodic pulse potential.

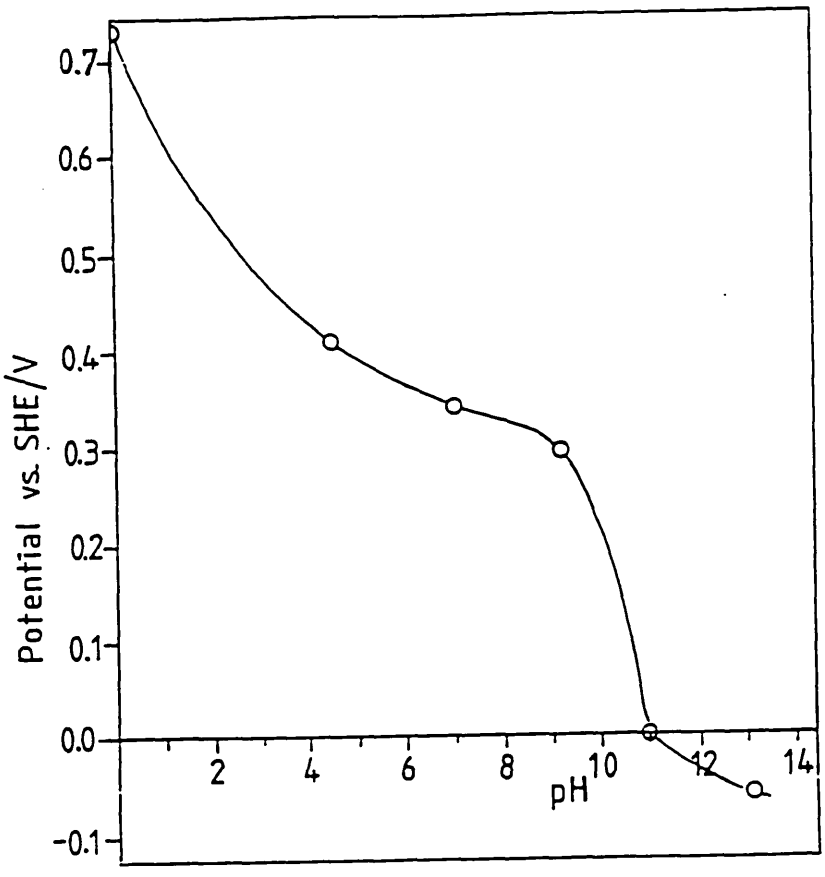


Fig 6.39 "Critical potential" for pyrite electrodes pulsed from "active" rest potentials as a function of pH.

untreated "passive" pyrite electrodes (see Figure 6.3; section 6.2). Since this type of i-t transient was always observed for "active" pyrite in the anodic overpotential range lying between the open circuit potentials of "active" and "passive" pyrite, it probably represented the growth of the oxide and/or sulphur film, postulated by other workers as being responsible for the high open-circuit potential of untreated pyrite[65,66,89].

The form of the i-t response suggested an oxidation process that occurred in three stages:-

I. An Induction Period (0 - 0.7 sec)

The charge under the first current spike was proportional to the potential charge applied to the electrode, but was never

> 130 μC cm^{-2} over the pH range studied (0 - 13). Allowing for roughness factors this was less than would be expected for the double layer charging of a metal. For example, the mean capacity over the induction period, calculated using the equation:-

$$C = \frac{\partial q}{\partial E} \qquad (6.34)$$

varied from 13 to 16 μF cm^{-2}, at pH 1 (assuming a roughness factor of 10), for overpotentials below the critical potential. This was less than 50 μF cm^{-2} which would have been anticipated for the double-layer capacitance on a metal, which suggested that the solid state semiconductor properties of pyrite were dominating the reactions at its surface in this potential region.

After the spike, the current was found to decay linearly with $t^{-1/2}$ over the first 700 milliseconds, which indicated that the process at this stage was diffusion controlled (Figure 6.40). In Section 6.7, a solid state semiconductor model for pyrite oxidation is postulated in which at small anodic overpotentials Fe (II) is oxidised to Fe (III) in the lattice, and partial water oxidation by hole injection into the electrolyte occurs, leading to the formation of deprotonated water molecules $(O_2H)_{ads}$. These adsorb onto the Fe (III) sites maintaining charge neutrality, preventing lattice decomposition (see reaction 6.33; section 6.4.4). It is proposed that the rate of this solid state reaction is determined by the diffusion of O_2H species into the solid which in turn is dependent upon their surface concentration and their solid state diffusion coefficient. The potential applied determines the surface concentration of O_2H. Although the slopes of $i\text{-}t^{-1/2}$ curves increased with increasing potential, a Nernstian slope for $di/dt^{-1/2}$ was not observed; slopes of 300 - 500 mV $decade^{-1}$ were obtained in the pH range 0 - 7. This may be due to a proportion of the applied potential falling across the space-charge layer of the semiconductor and not across the Helmholtz layer.

Compensation of the excess positive charge by O_2H diffusion into the lattice occurs until the surface becomes saturated with FeO_2H^{2+} species (ie $x \rightarrow 1$ in equation 6.33; section 6.4.4).

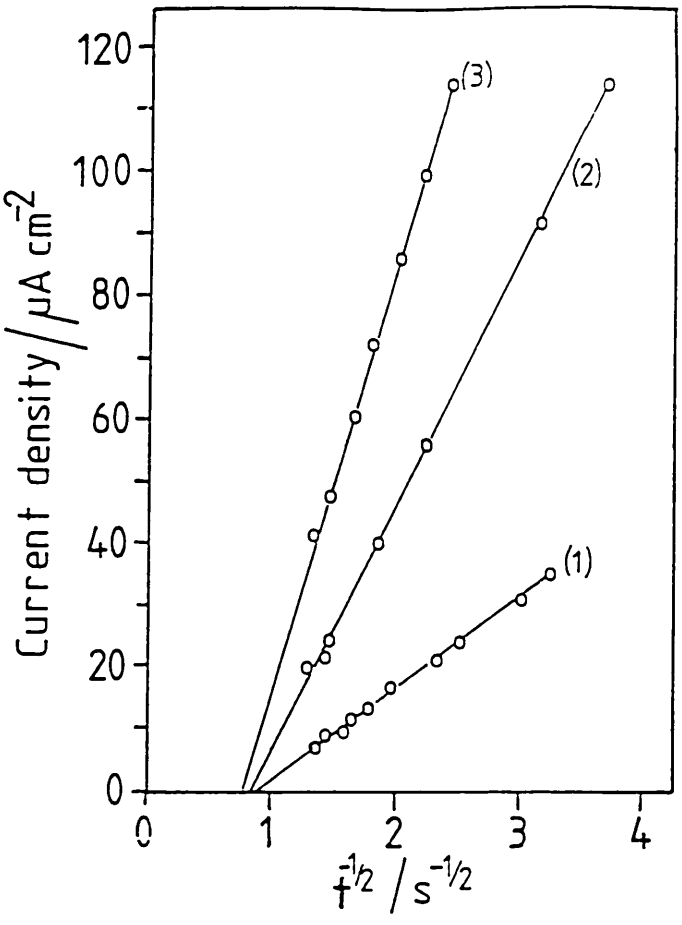


Fig 6.40 Plot of i vs $t^{-1/2}$ for the falling part of the transient from t = 0 to 0.7 s for a pyrite electrode at pH 4.6 (0.5 M CH_3COOH + 0.5 M CH_3COONa), pulsed from an "active" rest potential of -0.055 V to: (1) 0.0 V; (2) 0.1 V; and (3) 0.2 V.

II. Growth or Acceleratory Period (0.7 - 1.0 sec)

At this stage S_2^{2-} ions were the only oxidisable ions in the outer surface layer of the pyrite lattice. The second stage of the oxidation process commenced when these ions started to oxidise, resulting in lattice decomposition and the formation of adsorbed sulphur atoms. This process was characterised by rising current transients from 0.7 to about 1.0 seconds which were found to rise linearly with time when the currents from the initial current fall were subtracted (Figure 6.41). The correction was obtained by extrapolating from Figure 6.40 and similar curves at other potentials.

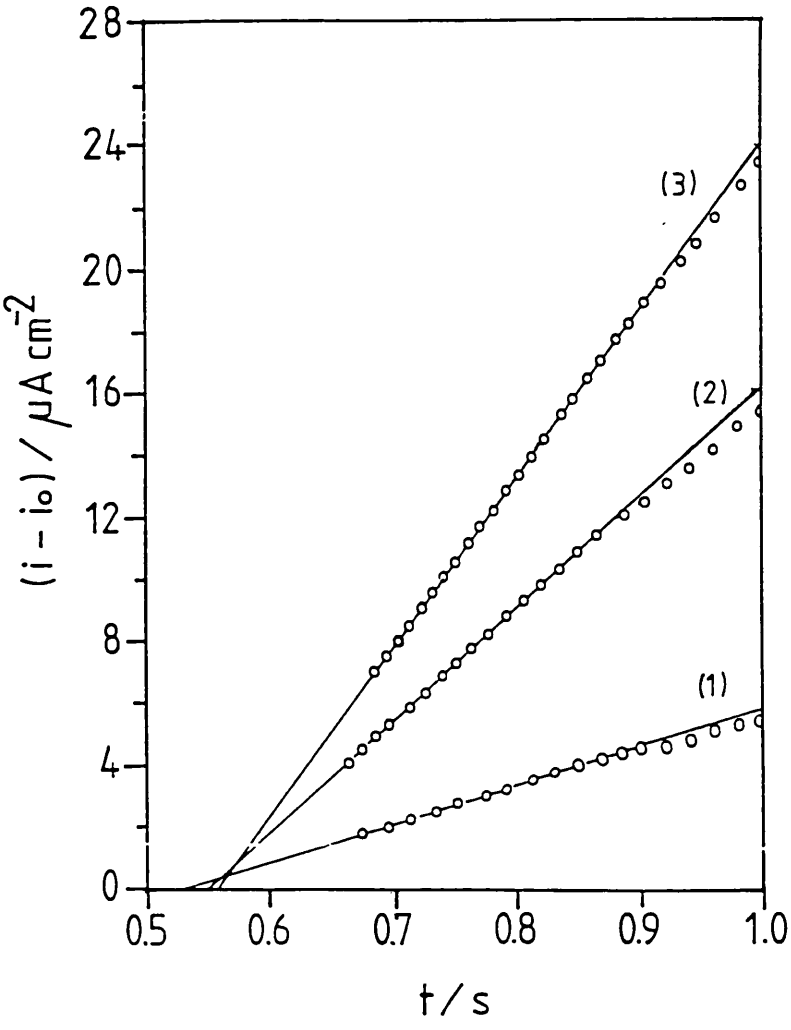


Fig 6.41 i - i_o vs t plot showing the linearity in the rising part of the current-time transient from t = 0.7 to 1.0 s for a pyrite electrode at pH 4.6 (0.5 M CH_3COOH + 0.5 M CH_3COONa). i is the current; i_o is the current attributed to the falling transient (obtained by extrapolation from Figure 6.38). Electrode pulsed from an "active" rest potential of -0.055 V to: (1) 0.0 V; (2) 0.1 V; and (3) 0.2 V.

A linear rise in current is characteristic of the two dimensional growth of a surface phase[362] and the positive intercept on the time axis confirmed that an "incubation period" was necessary before this process commenced.

III. Steady Oxidation (t > 1.0 sec)

There then followed a current decay again after 1.0 seconds which was found to fall with $t^{-1/2}$ again, although less steeply than for stage I (Figure 6.42). Steps I and II produced a resistive film at the

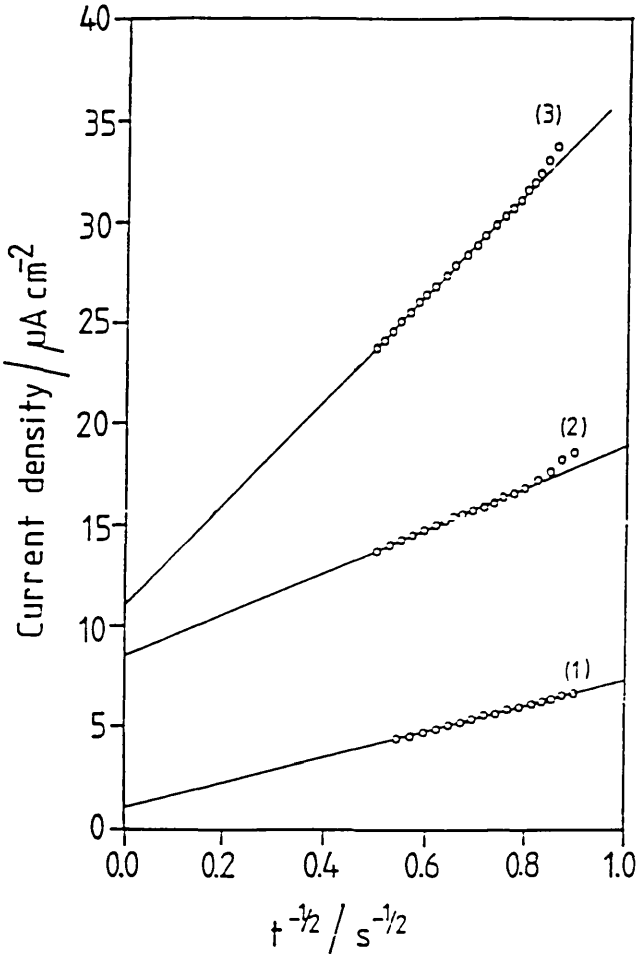


Fig 6.42 i vs $t^{-1/2}$ plot for the falling transient after the current maxima at ~ 1 s for a pyrite electrode at pH 4.6 (0.5 M CH_3COOH + 0.5 M CH_3COONa), pulsed from an "active" rest potential of -0.055 V to: (1) 0.0 V; (2) 0.1 V; and (3) 0.2 V.

surface of pyrite consisting of chemisorbed perhydroxyl ions ($O_2H^-_{ads}$) and sulphur ad-atoms. Most of the applied potential now fell across the passive film and not across the Helmholtz layer. Thus, the rate of oxidation steadily decreased as solid state diffusion and IR losses become rate controlling. During this stage, any excess hydroxy intermediates formed during the partial oxidation of water at the pyrite surface, attached themselves to the sulphur ad-atoms, forming sulphur-oxygen compounds (see reactions 6.14 and 6.15; section 6.4.3).

6.5.2 Current-Time Transients at Intermediate Anodic Overpotentials; ≤ 200 mV Positive of the Critical Potential

Only a current decay was observed for transients in this potential region. At pH 0 and pH 4.6 and short times (t < 1 second) the current decayed with $t^{-1/2}$, indicating that the initial oxidation step probably involved the induction step suggested in section 6.5.1. At these higher anodic overpotentials, the rate of O_2H diffusion into the lattice could not match the rate of Fe (III) formation in the lattice. Therefore charge neutrality was not maintained and pyrite oxidative lattice decomposition occurred before oxidation of S_2^{2-} ions at the surface could occur as a separate process. Thus a rising current transient was not discernable.

At longer times (t > 1 second), the current was found to decay inversely with time, as might be expected of an adsorption (oxide growth) type process. This would be expected at pH 4.6 for which reactions (c) and (d) were the dominant oxidation reactions (Figure 6.43). However, similar behaviour was observed at pH 0 where oxide formation would not be expected from thermodynamic data (see Appendix II). This suggests that partial water oxidation occurred in parallel to the bulk oxidative decomposition of pyrite at these longer times, and the $i\text{-}t^{-1}$ relationship was due to O_2H^- and OH adsorption onto the pyrite surface. Therefore at pH 0, even though the pyrite lattice was decomposing releasing Fe^{3+}, SO_4^{2-} and H^+ into solution. The intermediates OH and O_2H probably attached themselves to some of the Fe (III) sites at the surface just before dissolution occurred forming a meta-stable ferric oxide layer, as was inferred from RSCBE studies (see section 6.4.2). If in excess, these species may have promoted sulphate formation by oxidising sulphur atoms on the surface before they could form a true elemental sulphur phase (see reactions 6.15 and 6.16; section 6.4.3).

In alkaline solution, the predominance of sulphate and proton formation by reaction (d) lowered the interfacial pH sufficiently for ferric oxide to dissolve from the surface and reprecipitate away from the electrode where the pH was higher. Therefore, the rate of

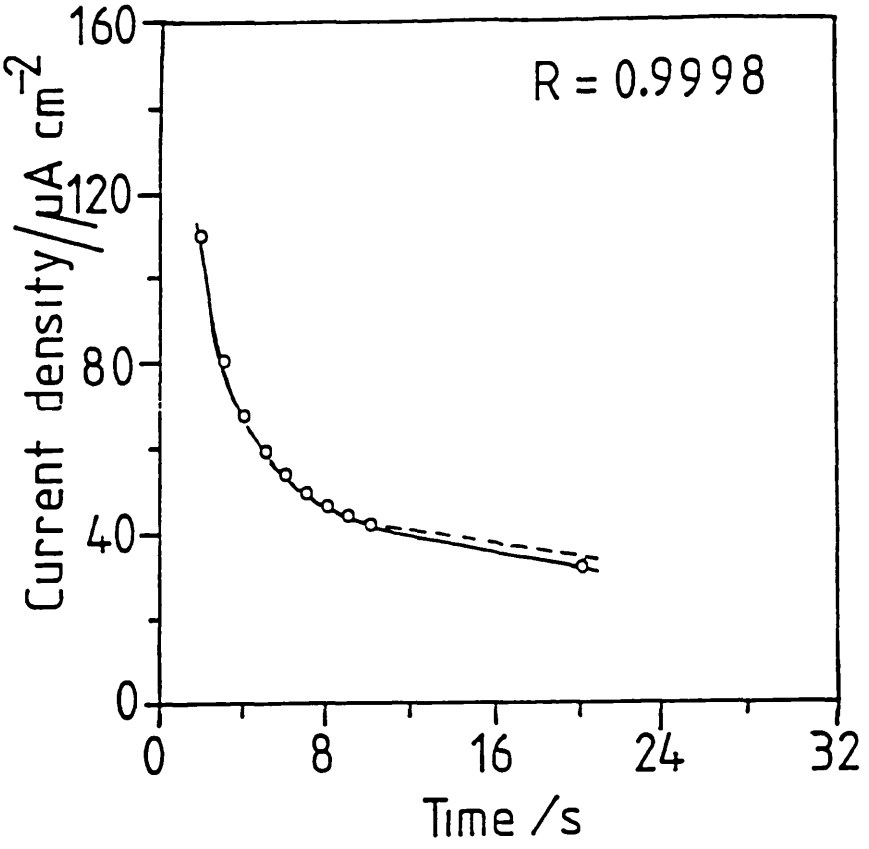
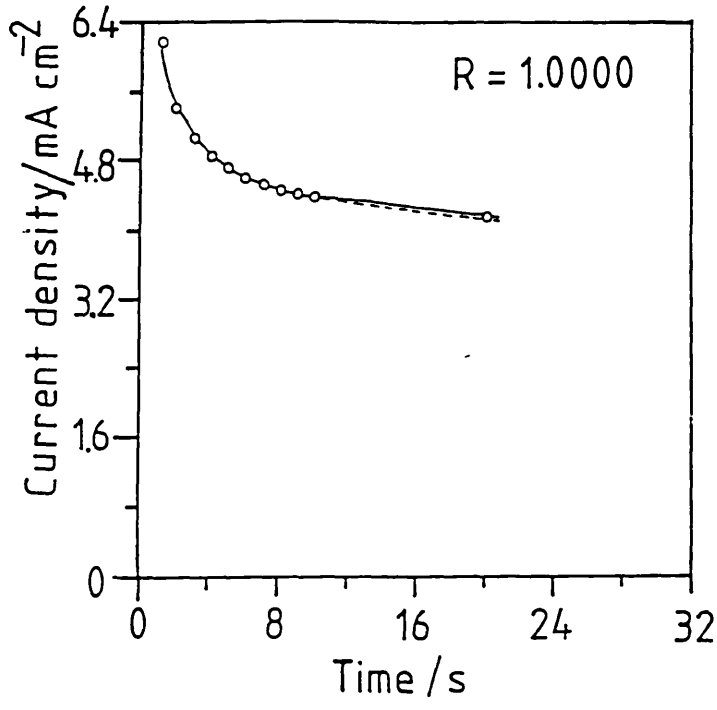


Fig 6.43 Current-time transient for a pyrite electrode at pH 4.6 (0.5 M CH_3COOH + 0.5 M CH_3COONa) pulsed from an "active" rest potential of -0.055 V to 0.7 V. (---) i vs t^{-1}; R = correlation coefficient.

oxidation was effectively controlled by the diffusion of Fe^{3+} and H^+ away from the pyrite surface. Consequently, at pH 9.2 and pH 13 falling transients, best fitted to an i vs $t^{-1/2}$ relationship, were observed at intermediate and high anodic overpotentials (see Figures 6.44 and 6.45).

6.5.3 Current-Time Transients at High Anodic Overpotentials in Acidic Solutions

A second critical potential was reached in acidic solutions at high anodic overpotentials, above which the current passed through a minimum again (i.e. 1.0 V at pH 0 and 0.7 V at pH 4.6).



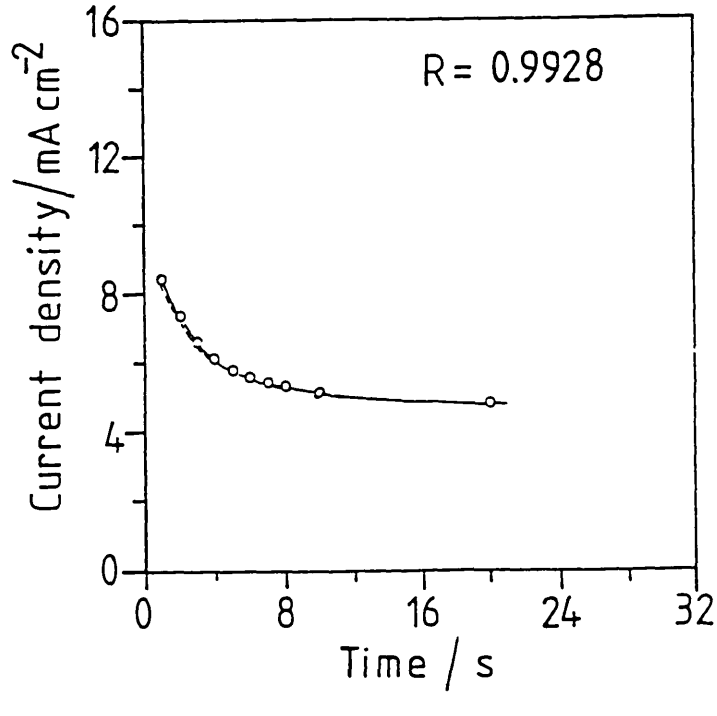


Fig 6.44 (top) Current-time transient for a pyrite electrode at pH 13 (0.1 M NaOH) pulsed from an "active" rest potential of -0.4 V to 0.6 V. (---) i vs. $t^{-0.5}$; R = correlation efficient.

Fig 6.45 (bottom) Current-time transient for a pyrite electrode at pH 9.2 (0.05 M $Na_2B_4O_7$) pulsed from an "active" rest potential of -0.2 V to 1.2 V. (---) i vs. $t^{-0.5}$; R = correlation efficient.

At pH 0, the current at 1.0 V decayed inversely with time over the first 30 seconds; and a charge of 50 mC cm^{-2} was passed (see Figure 6.46). This was thought to be due to the adsorption and deprotonation

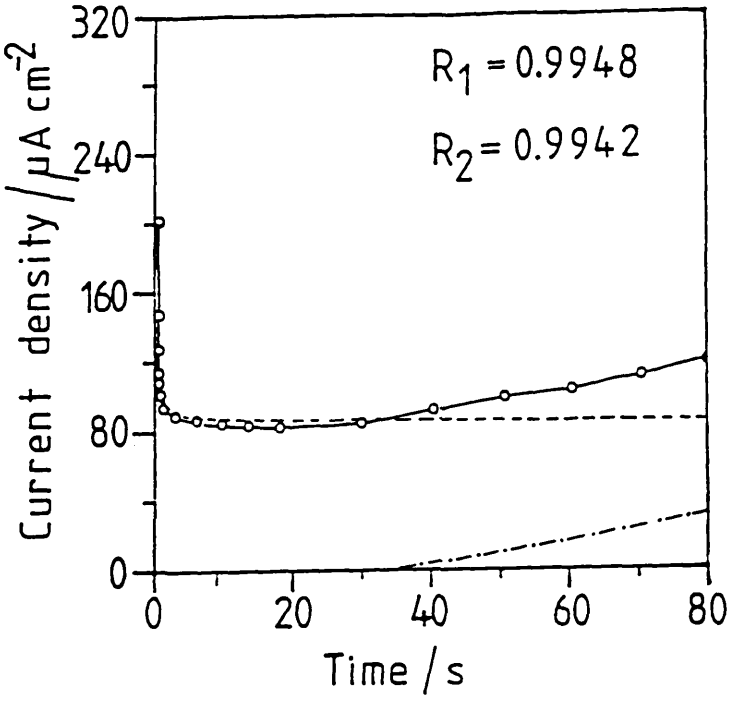


Fig 6.46 Current-time transient for a pyrite electrode at pH 0 (1 M $HClO_4$) pulsed from an "active" rest potential of 0.3 V to 1.0 V. (---) i vs. t^{-1}; (-.-.-) i vs. t; R_1 = correlation coefficient for the decaying i vs. t^{-1} relationship; R_2 = correlation coefficient for the rising i vs. t relationship.

of water molecules (see section 6.7). At longer times (t > 30 sec) the current increased linearly with time, due to pitting dissolution probably resulting from the local pH change produced by reactions (c) and (d).

At higher potentials (> 1.0 V), the initial falling currents were best described by an i vs $t^{-1/2}$ relationship suggesting that the rate of oxidation was fast enough to be controlled by the diffusion of Fe^{3+}, SO_4^{2-} and hydroxy radicals away from the electrode, possibly through a meta-stable oxide or sulphur film. The current then passed through a

minimum, reached in shorter times with higher potentials, before increasing due to pitting dissolution. A second current minimum was then observed at longer times typical of the overlap of growing pits, before rising linearly again and finally reaching a plateau (Figure 6.47). Similar behaviour was observed at pH 4.6 (Figure 6.48 and 6.49).

Figure 6.50 shows the charge passed at a stationary pyrite electrode in stirred solution after 1500 seconds as a function of potential and pH. The high proton yield associated with sulphate formation on pyrite (reactions (d) and (f)) and the increasing dominance of this reaction with increasing pH, prevented a thick ferric oxide layer forming on the pyrite surface, even in alkaline solutions where ferric oxide is very insoluble. Therefore, mild passivation was observed on pyrite only at pH 9.2 and 13 at high potentials.

6.6 Electrode Impedance Measurements

Figure 6.51 shows the imaginary (capacitive and inductive) versus the real (resistive) components of impedance for a stationary pyrite electrode in stirred deoxygenated 1.0 M $HClO_4$ (pH 0), as a function of ac perturbation frequency (0.1 Hz - 10 kHz) and electrode potential. Behaviour at frequencies < 0.1 Hz was not determined, due to the excessive time requirement of carrying out such experiments with a non-stationary (i.e. time-dependent) systems such as FeS_2. The spectra from 0.3 - 1.2 V appeared as capacitive loops in the shape of slightly depressed semicircles. The diameters of these semicircles decreased with increasing anodic potential and a low frequency inductive loop appeared at potentials > 0.9 V (Figure 6.51 B). Inspection of the high frequency region of each spectra revealed the presence of a second capacitive semicircle (Figure 6.52).

The intercept of high frequency points on the real impedance axis gave the sum of the uncompensated solution resistance (R_u), and FeS_2 electrode plus contact resistance (R_s). Careful positioning of the Luggin probe close to the pyrite electrode, and the high conductivity

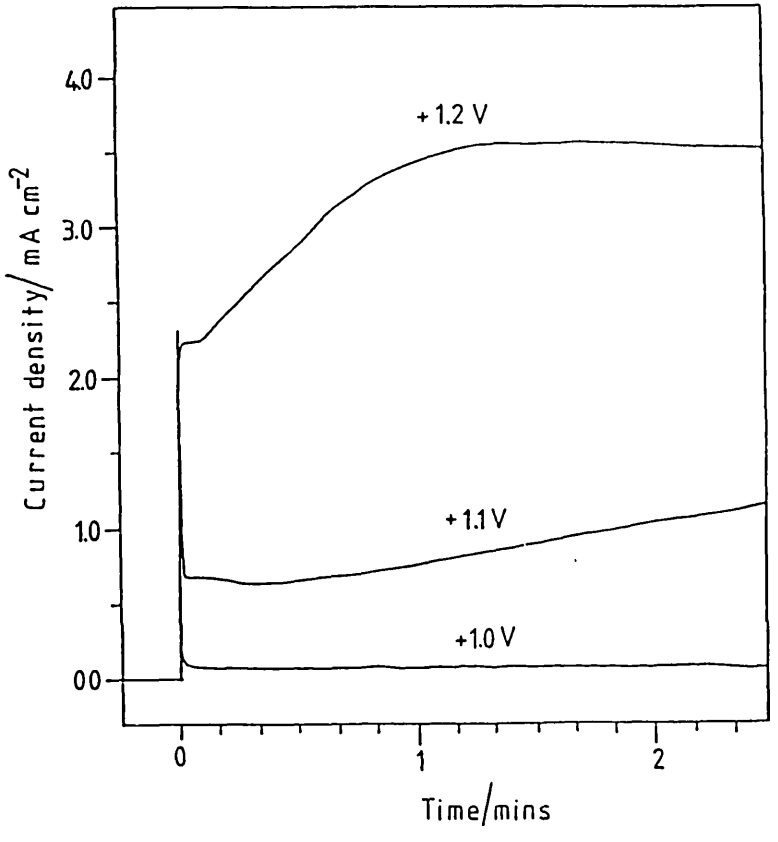


Fig 6.47 Current-time transients for pyrite electrodes at pH 0 (1 M $HClO_4$) pulsed from an "active" rest potential of 0.3 V to various anodic potentials.

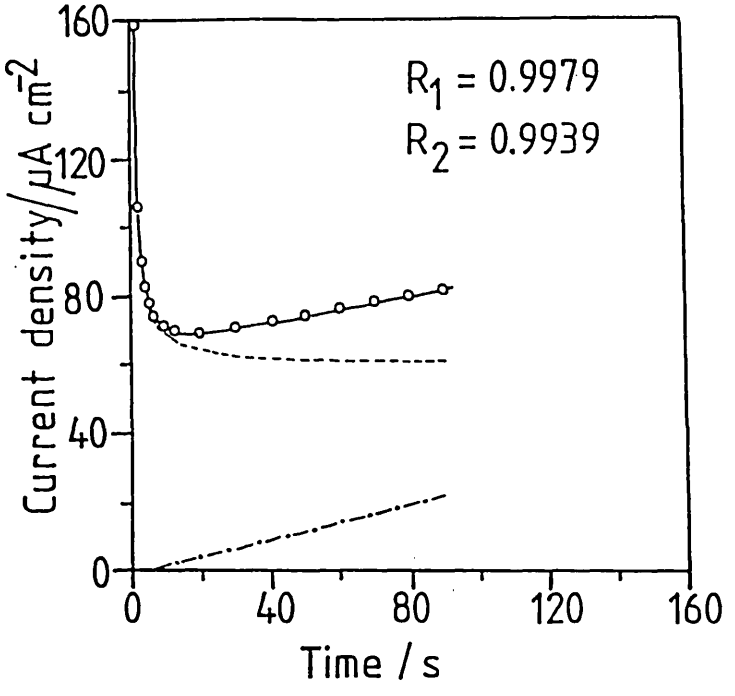


Fig 6.48 Current-time transient for a pyrite electrode at pH 4.6 (0.5 M CH_3COOH + 0.5 M CH_3COONa) pulsed from an "active" rest potential of 0.0 V to 0.8 V. (---) i vs. t^{-1}; (-·-·-) i vs. t; R_1 = correlation coefficient for the decaying i vs. t^{-1} relationship; R_2 = correlation coefficient for the rising i vs. t relationship.

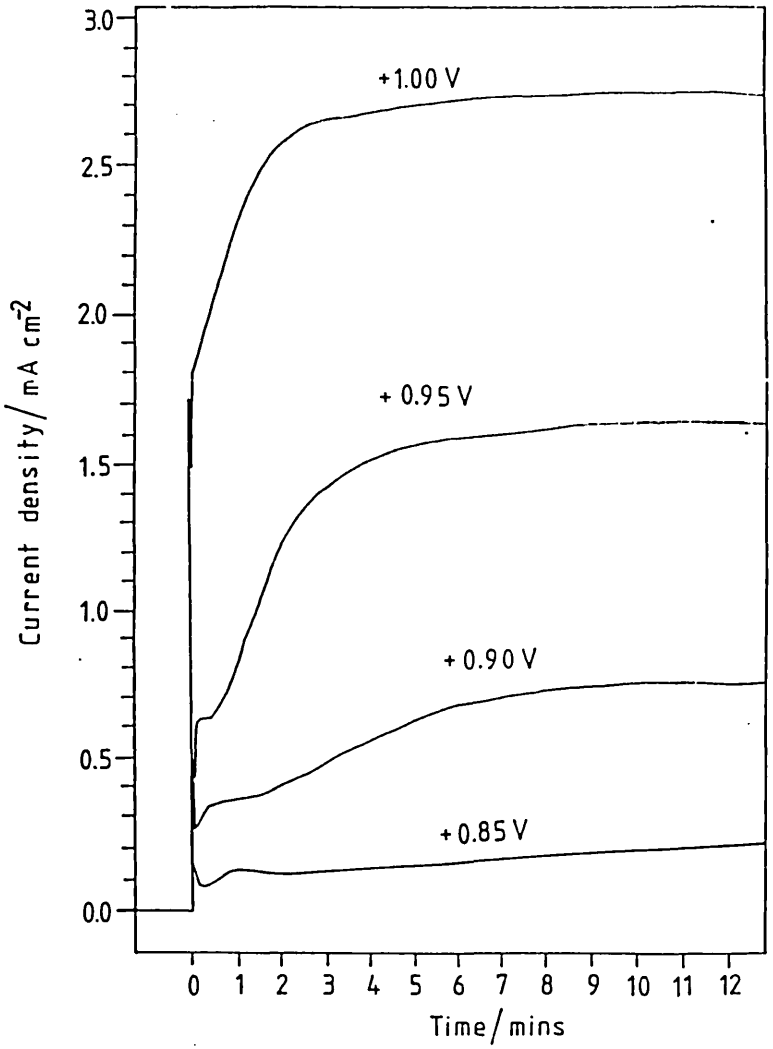


Fig 6.49 Current-time transients for pyrite electrodes at pH 4.6 (0.5 M CH_3COOH + 0.5 M CH_3COONa) pulsed from an "active" rest potential of 0.0 V to various anodic potentials.

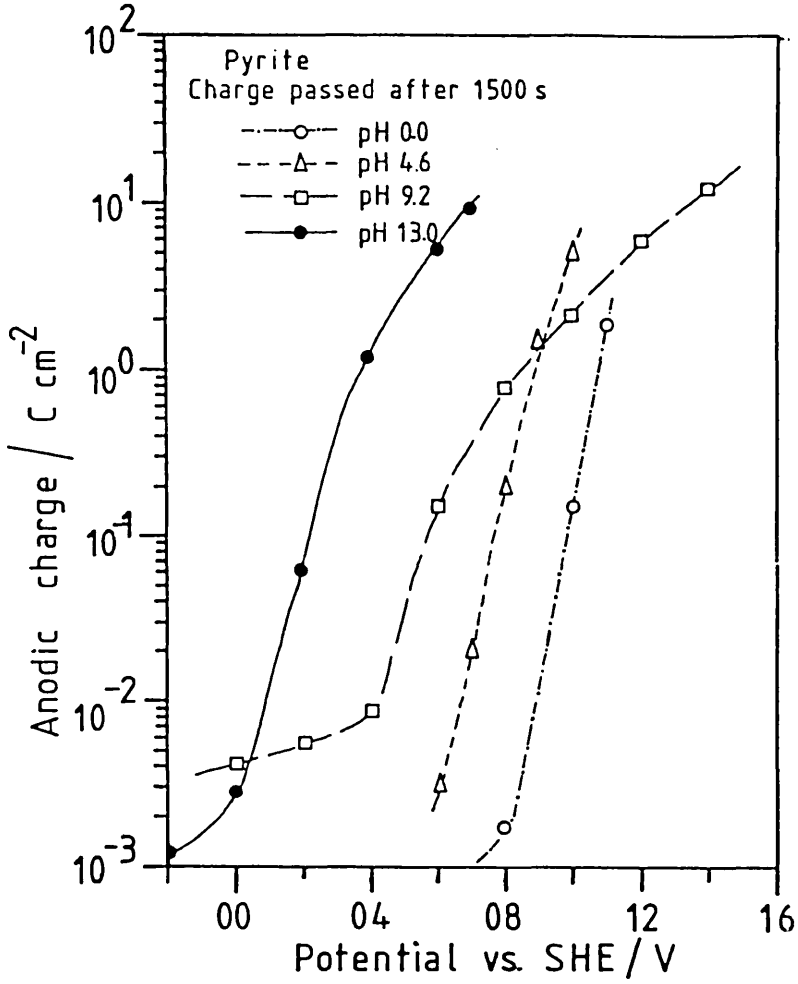


Fig 6.50 Anodic charge passed after 1500 s for a pyrite electrode as a function of potential and pH.

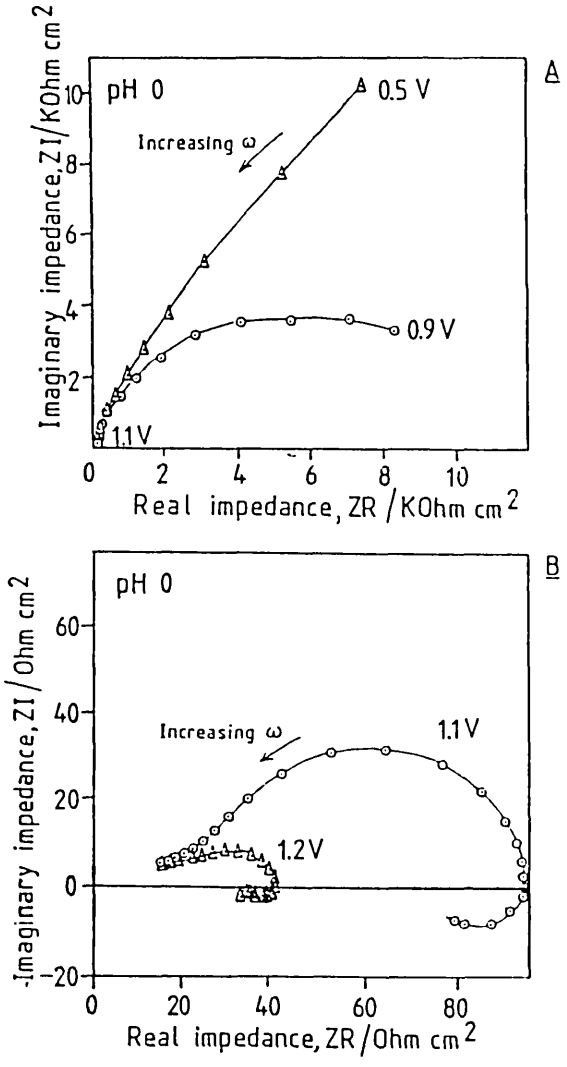


Fig 6.51 Impedance spectra (0.1 Hz - 10 kHz) for a pyrite electrode in 1 M $HClO_4$ (pH 0). A) (Δ) 0.5 V, (⊙) 0.9 V; (⊡) covers the whole spectrum for 1.1 V. B) (⊙) 1.1 V, (Δ) 1.2 V.

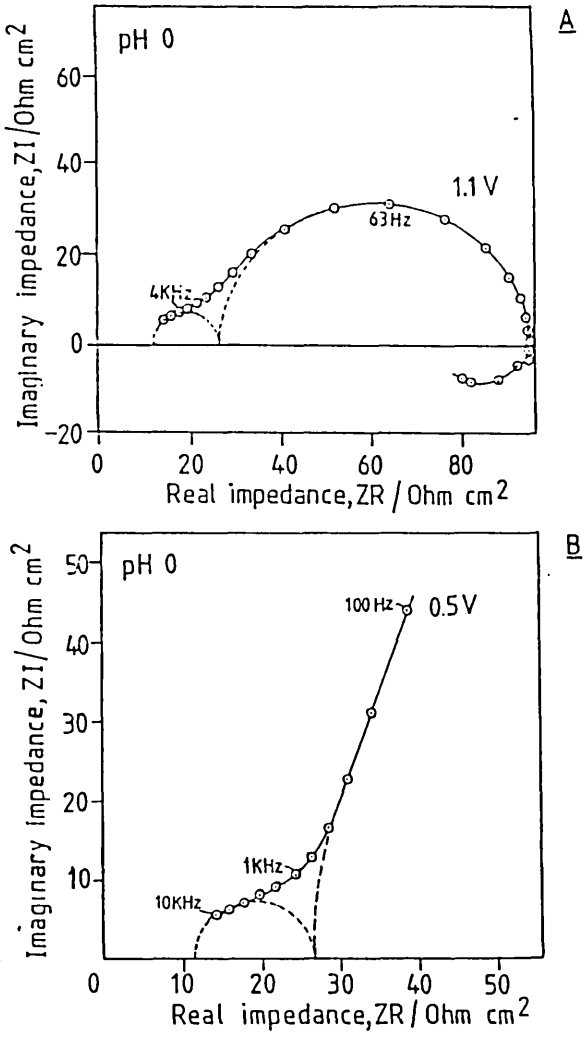


Fig 6.52 Impedance spectra for a pyrite electrode in 1M $HClO_4$ (pH 0) showing the high frequency branch. A) 1.1 V; B) 0.5 V.

of 1.0 M $HClO_4$, reduced R_Q to < 0.1 Ω cm^2. Furthermore, electrical resistivity measurements on the pyrite electrode used to generate the impedance spectra presented in Figure 6.51 showed its resistance to be approximately 11 Ω cm^2 (see section 3.2.7). Thus, although the high frequency points shown in Figure 6.52 fell on a straight line, which if extrapolated back appeared to cut the real impedance axis at zero, the impedance spectra at frequencies > 10 kHz must bend down and cut the real axis at ~ 11 Ω cm^2, since the intercept equals R_u plus R_s. Measurements at frequencies > 10 kHz was beyond the capabilities of the Solartron 1186 Electrochemical Interface used in these experiments. However, by extrapolating the low frequency semicircles and knowing the approximate high frequency real axis intercept, a semi-quantitative estimation of the diameter of the high frequency semicircle was possible at each positive potential bias.

Each semicircle in the impedance diagram can be described by an equivalent RC network electronic analogue model with double layer capacitance (C_{dl}), charge transfer resistance (R_{ct}) and other kinetic parameters relating to adsorption etc. assigned to the various electronic components. The simplest model is a parallel network of resistance and capacitance with an impedance given by:-

$$1/z = \frac{1}{R} + j\omega C \qquad (6.35)$$

The diameter of the semicircle equals the resistance (R), and the capacitance (C) is related to the angular frequency at the maximum of the semicircle (ω_{max}) by:-

$$\omega_{max} = \frac{1}{CR} \qquad (6.36)$$

Figure 6.53 shows the capacitance calculated for the high and low frequency semicircles; C_1 and C_2 respectively, plotted against applied potential. C_1 was approximately independent of potential, having a value between 5 and 9 μF cm^{-2}, which suggested the dominance of a solid state or semiconductor space charge capacitance (C_{sc}) at these frequencies. The low frequency capacitance C_2 had a value of ~ 170 μF cm^{-2} at 0.7 V but decreased with increasing potential to

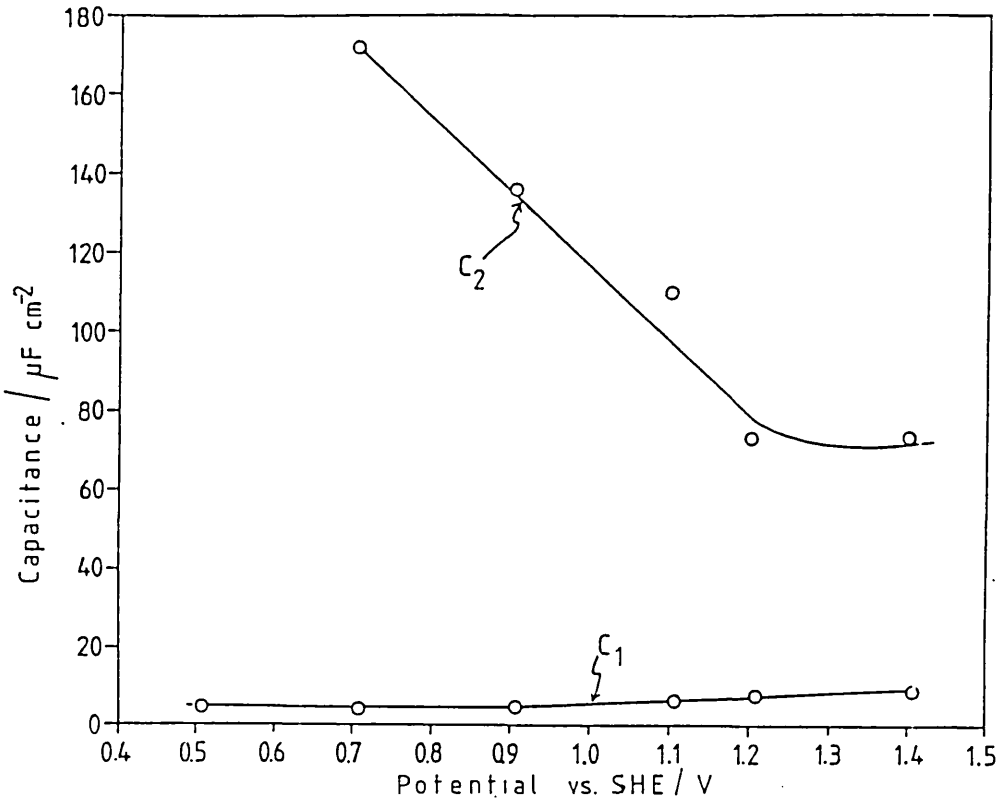


Fig 6.53 The electrode capacitance of a pyrite electrode in 1 M $HClO_4$ (pH 0) for the high frequency (C_1) and low frequency (C_2) semicircles as a function of potential.

level out at ~ 70 μF cm^{-2} at potentials > 1.2 V, a value which probably represented the double layer capacitance (C_{dl}). The higher values of C_2 obtained at lower potentials suggested the presence of a pseudocapacitance or adsorption capacitance (C_a), associated with product adsorption, in parallel to the double layer capacitance.

From this it can be seen that a more sophisticated electronic analogue model than a 2 component RC network is needed to account for all the various RC components mentioned above. In section 6.7 a solid state semiconductor mechanism is proposed to account for the oxidation behaviour of pyrite. An equivalent circuit which is consistent with this mechanism and accounts for the behaviour given above is shown in

Figure 6.54. R_{ct_1} and R_{ct_2} are charge transfer resistances associated

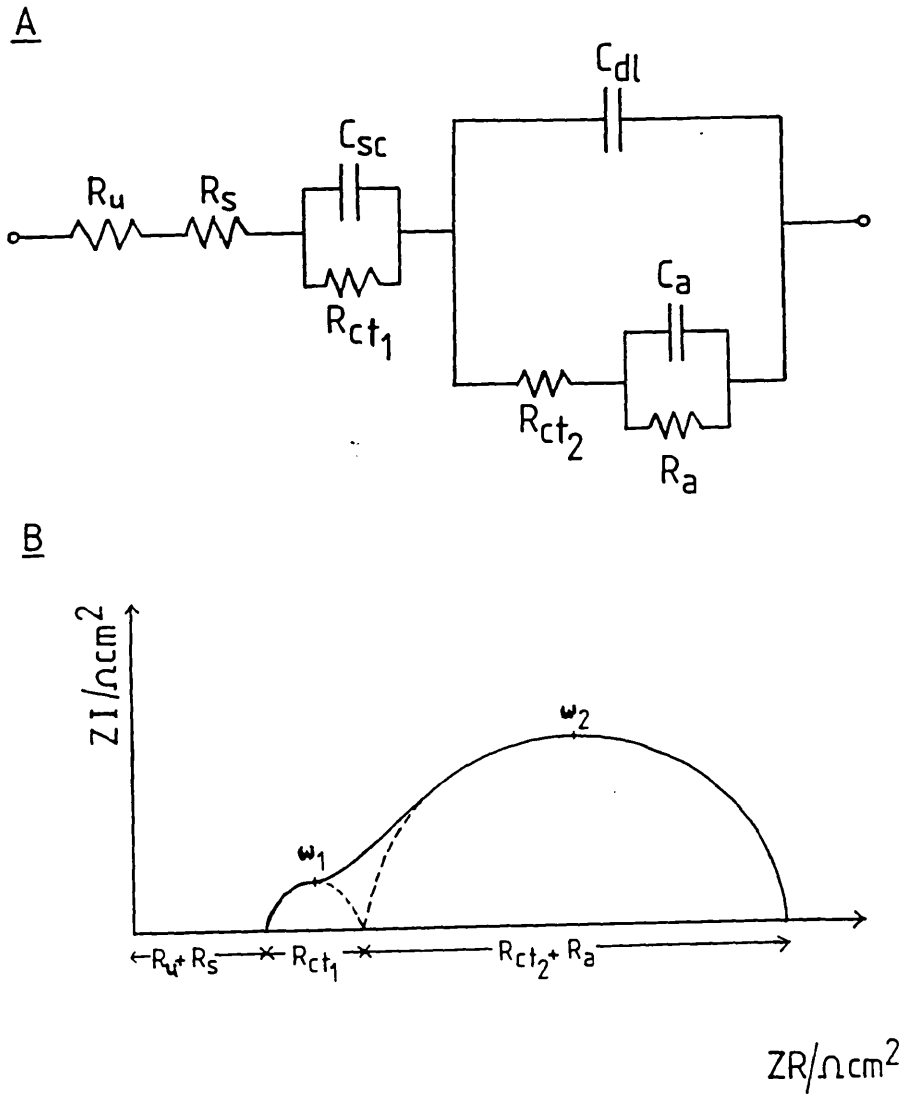


Fig 6.54 Equivalent circuit (A), and complex plane impedance plot (B) for pyrite oxidation in 1 M $HClO_4$ (pH 0). R_u, solution resistance; R_s, electrode resistance; R_{ct_1}, R_{ct_2}, charge transfer resistances; R_a, adsorption resistance; C_{sc}, space charge capacitance; C_{dl}, double layer capacitance; C_a, pseudocapacitance.

with hole injection into solution at the valence band edge and electron injection into the conduction band edge respectively. The former process results in partial water oxidation whereas the

latter process is responsible for lattice decomposition. R_a is an adsorption resistance.

The diameter of the high frequency semicircle, assigned to R_{ct_1}, appeared to be independent of potential. This behaviour can be explained if it is assumed that for a "pseudo-semiconductor" like pyrite, band bending is small and is unaffected by any changes in external polarisation potential applied to the electrode (see section 6.7). Thus the rate of hole injection at the valence band edge, which is proportional to the band bending, will also be independent of potential.

The relatively high values of capacitance (C_2) obtained at low potentials for the low frequency semicircle (see Figure 6.53), were attributed to the adsorption at the interface of hydroxy species (i.e. OH_{ads}, O_{ads} and $O_2H^-_{ads}$), formed as a result of the partial water oxidation process. When adsorbed, they created a passivating oxygen containing layer at the pyrite/solution interface. As the potential increased, a point was reached where the conduction band edge was lowered below the potential required for pyrite lattice decomposition, so the lattice started to oxidise according to reactions (e) and (f). These reactions, and the lowering of interfacial pH accompanying reaction (f), helped to dissolve and desorb the passive film. The desorption process was marked by the appearance of inductive (negative capacitance) loops in the impedance spectra at low frequencies (Figure 6.51 B), and the capacitance of the low frequency semicircle C_2 (which equals $C_a + C_{dl}$), approximating to C_{dl} as C_a tended to zero (Figure 6.53).

At pH 9.2 the impedance spectra consisted of two semicircles between 0.6 - 0.8 V, which could be generated by two RC networks in series (Figure 6.55). Such behaviour has been observed and modelled[317] for passivated metal surfaces. The preferential oxidation of pyrite oxidation to sulphate (reaction (d)), rather than sulphur (reaction (c)), and the insolubility of ferric oxide at pH 9.2 suggested that the impedance spectra between 0.6 and 0.8 V represent a FeS_2/oxide (+ some sulphur)/solution structure, each interface having an associated

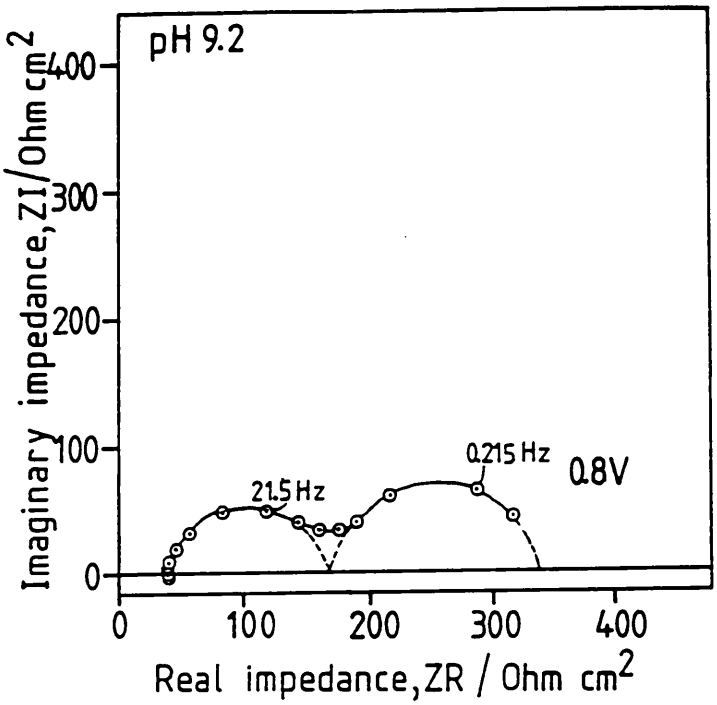


Fig 6.55 Impedance spectrum (0.1 Hz - 10 kHz) for a pyrite electrode in 0.05 M $Na_2B_4O_7$ (pH 9.2) at 0.8 V, showing two semicircles generated by two RC networks in series (see Figure 6.56).

capacitance. In Figure 6.56 the high frequency intercept, real axis resistance (R), for impedance spectra at pH 0, 4.6, and 9.2 is plotted as a function of potential. Subtracting the combined electrode (R_s) plus solution (R_u) resistance (11 Ω cm^2) from R gives the resistance associated with the oxide film (R_f) on the surface of pyrite. Figure 6.56 shows that R_f was negligible at pH 0, but as the pH increased and the insolubility of ferric oxide also increased, the film thickened and R_f increased to ~ 25 Ω cm^2 at pH 9.2, which reflected the low conductivity of the oxide film.

Over the frequency range studied (10 kHz - 0.1 Hz), the capacitance could be calculated for each semicircle only at 0.8 V, since between -0.2 and 0.4 V the spectra only approximated to arcs, and at 0.6 V the low frequency semicircle was not sufficiently defined to allow a

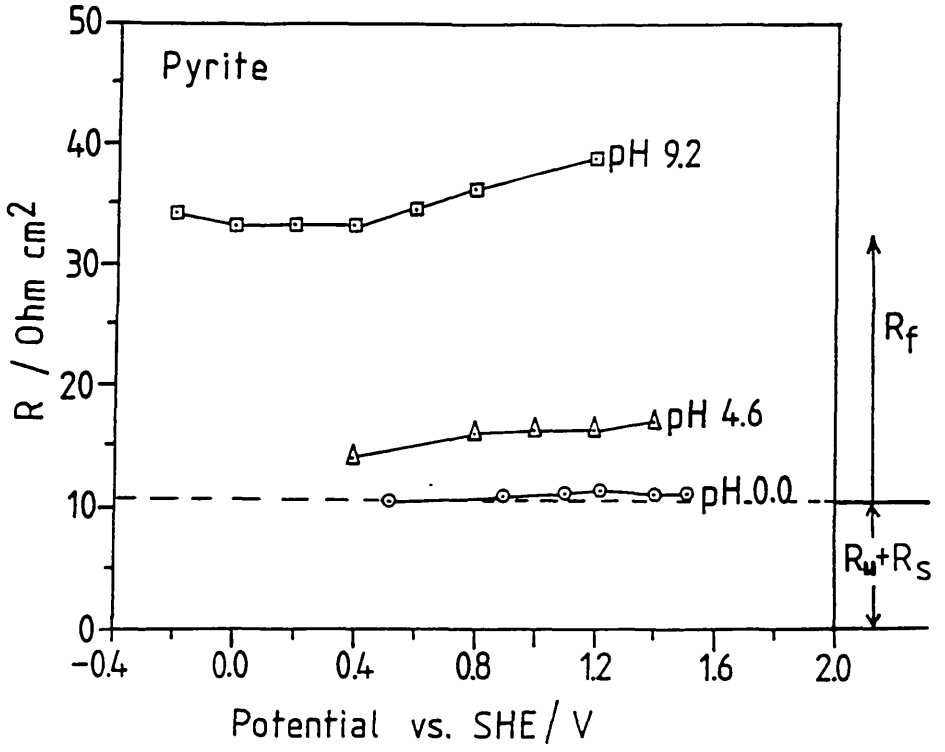


Fig 6.56 Real axis, high frequency intercept resistance (R), for pyrite at pH 0, 4.6 and 9.2, plotted as a function of potential. R_u, solution resistance; R_s, electrode resistance; R_f, electrode surface film resistance.

quantitative analysis of capacitance (Figure 6.57). At 0.8 V the capacitance of FeS_2/oxide interface (C_{d_1}) was 157.6 μF cm^{-2} and that of the oxide/solution interface (C_{d_2}), 7881 μF cm^{-2}. These large values of capacitance suggested that the oxide film was probably quite porous, especially at the oxide/solution interface, giving a large internal surface area and hence large capacitance values. An equivalent circuit[364] for the impedance spectra at pH 9.2 is shown in Figure 6.58. C_g is the geometrical capacitance of the oxide film and is given by:-

$$C_g = \varepsilon_o \varepsilon_r A/l \qquad (6.37)$$

where ε_r is the relative permittivity of the oxide film, A is the electrode area and l is the film thickness.

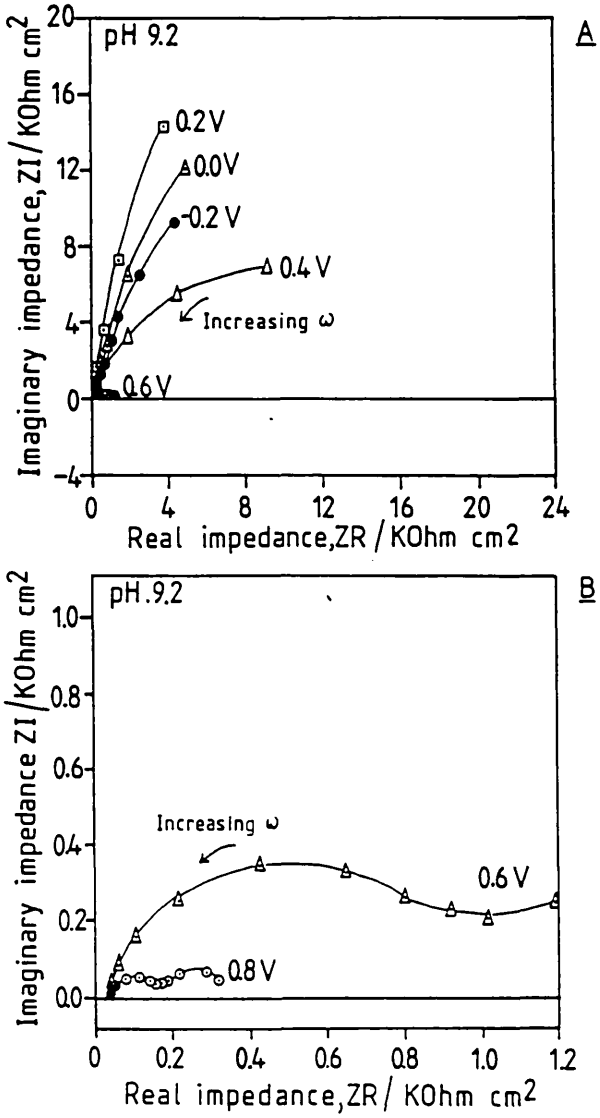


Fig 6.57 Impedance spectra (0.1 Hz - 10 kHz) for a pyrite electrode in 0.05 M $Na_2B_4O_7$ (pH 9.2). A) -0.2 to 0.6 V; B) 0.6 to 0.8 V.

6.7 A Solid State Semiconductor Mechanism for Pyrite Oxidation

There is controversy in the literature as to the nature and mechanism of electrochemical reactions on the surface of pyrite, i.e. passive film formation and the predominance of sulphate over sulphur formation compared with other sulphide minerals, such as CuS and Cu_2S[66,78,89,136]. This may be because the influence of solid state properties on the electrochemical reactions of pyrite (i.e. energy distribution of electronic states and crystal structure) has not been attempted previously.

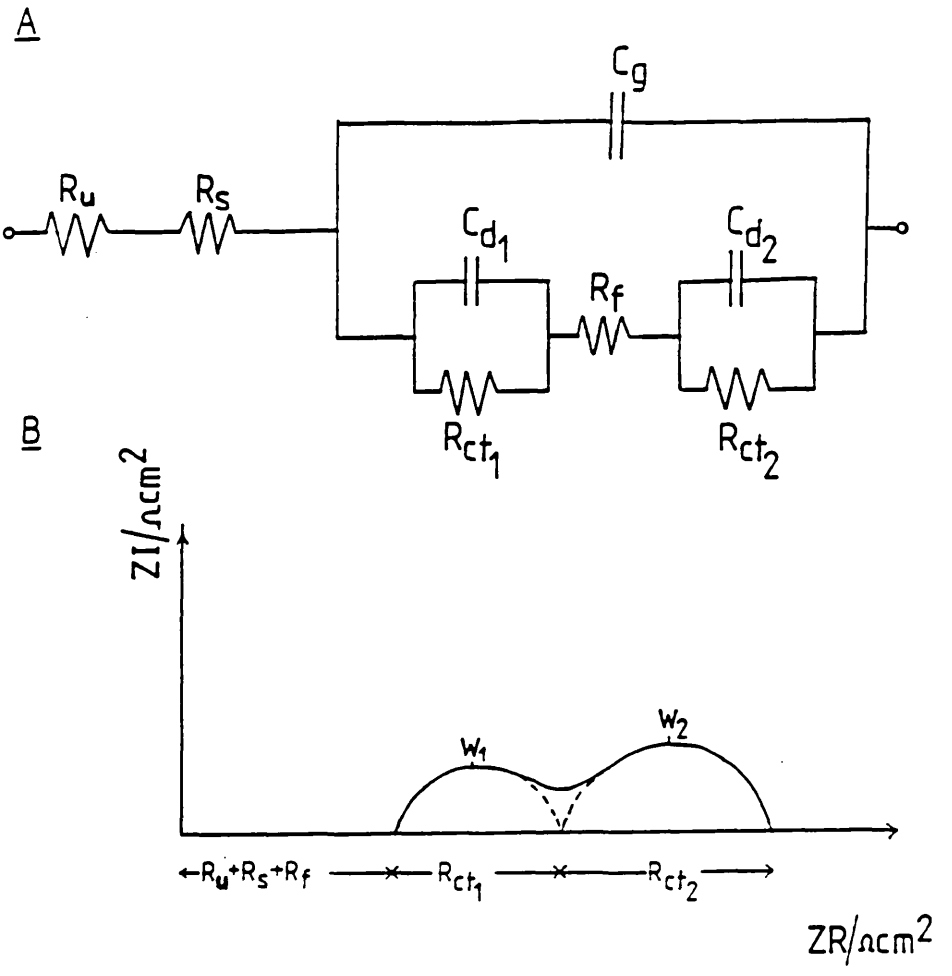


Fig 6.58 Equivalent circuit (A) and complex impedance plot (B) for pyrite oxidation in 0.05 M $Na_2B_4O_7$ (pH 9.2). R_u, solution resistance; R_s, electrode resistance; R_{ct_1}, charge transfer resistance at pyrite oxide interface; R_f, film resistance;; R_{ct_2}, charge transfer resistance at oxide/solution interface; C_g, geometric capacitance of pyrite/oxide interface; C_{d_1}, differential capacitance of pyrite/oxide interface; C_{d_2}, differential capacitance of oxide/solution interface.

Figure 6.59 shows a schematic representation of the electrical double layer at the sulphide mineral/solution interface of a simple binary sulphide e.g. ZnS or PbS, which exhibit a considerable amount of ionic bonding. The sulphide mineral is made up of a lattice of positive metal ions and negative sulphide ions. The first solution layer adjacent to the mineral is occupied largely by water molecules. The locus of the centres of specifically adsorbed ions in this layer defines the Inner Helmholtz Plane. Water molecules are asymmetric, and hence have a dipole with oxygen atoms orientated towards the metal ions, and hydrogen atoms towards the sulphide ions.

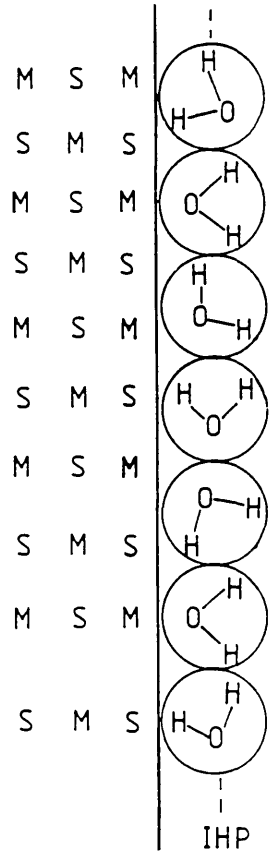


Fig 6.59 Schematic representation of the solid/solution interface for a binary sulphide mineral MS (eg ZnS or PbS), showing the orientation of water molecules in the first solution layer adjacent to the mineral (IHP = Inner Helmhottz Plane).

However, the electronic structure of ZnS and PbS differs widely from that of FeS_2. Both ZnS and PbS are diamagnetic semiconductors with band gaps of 3.67 eV and 0.4 eV respectively. Simple molecular orbital and band models for ZnS are shown in Figure 6.60. The highest filled energy band, the valence band, is derived from sulphur orbitals. Pyrite is also diamagnetic indicating that the six d electrons of Fe^{2+} must be paired and completely fill the t_{2g} orbitals, reflecting the strength of the ligand field due to the disulphide anions[34]. The bonding of Fe^{2+} to sulphur in octahedral coordination is illustrated in the molecular orbital diagram in Figure 6.61. One hybrid sp^3 orbital from each of the six sulphurs, derived from

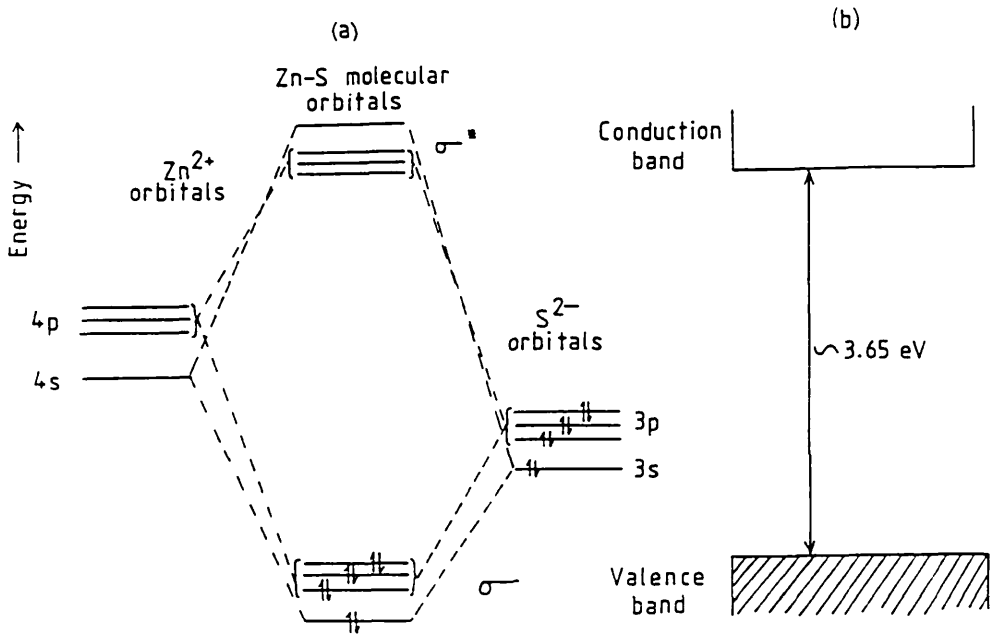


Fig 6.60 Bonding in ZnS. a) schematic molecular orbital diagram for pure ZnS; b) corresponding ZnS band model [34].

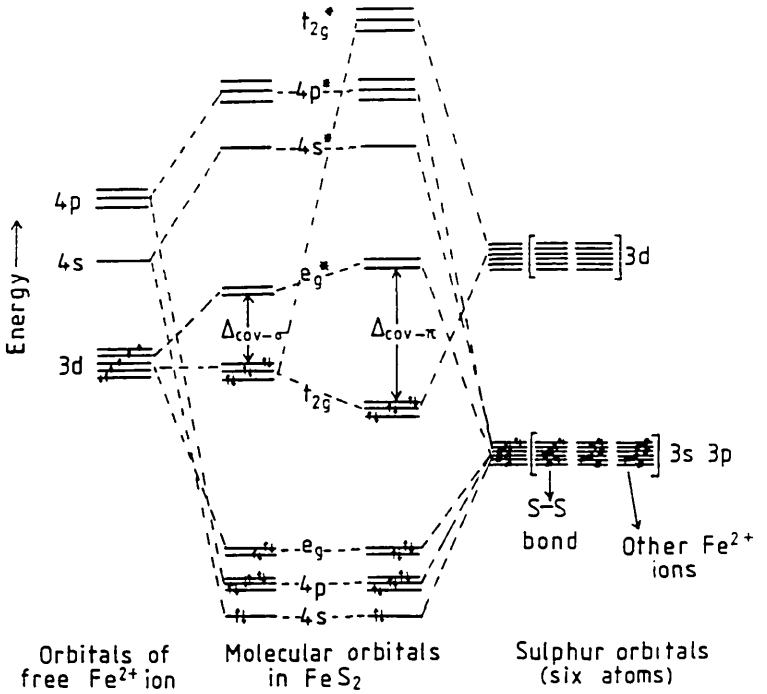


Fig 6.61 Molecular orbital energy level diagram for pyrite[42]. The effect of bonding (if it occurs[34]) on the energy separation between non-bonding t_{2g} and antibonding e_g^* orbitals is also shown.

sulphur's 3s and 3p orbitals forms, six σ bonds with d^2sp^3 hybrid orbitals of the central transition metal ion. The d^2sp^3 hybrids consist of the two e_g orbitals ($d_{x^2-y^2}$ and d_{z^2}), the one 4s orbital and three 4p orbitals. The highest filled orbitals, the three t_{2g} orbitals (d_{xy}, d_{yz}, d_{xz}) of the transition metal, remain nonbonding and apparently do not form π bonds with sulphur's empty 3d orbitals[34]. Overlapping of molecular orbitals generates the corresponding band model shown in Figure 6.62.

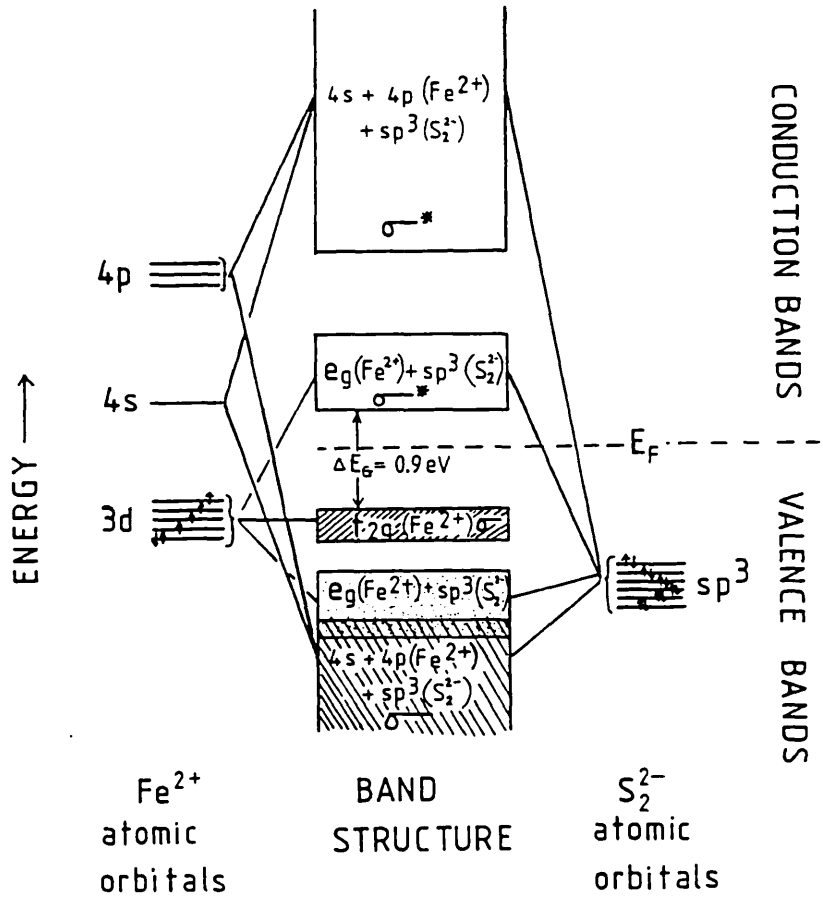


Fig 6.62 Schematic band energy model for pyrite. E_F, Fermi level; hatched bands (valence bands) are filled with electrons (modified after Bither et al[42]).

Conduction in pyrite occurs when electrons are excited into the band formed from e_g* orbitals. The important electrochemical difference between ZnS and FeS_2 is that when electrons are extracted from the highest filled energy band of ZnS, polar chemical bonds are broken and the metal sulphide decomposes by releasing metal ions and producing a film of molecular sulphur. However, when electrons are extracted from

FeS_2, no primary chemical change is to be expected since the t_{2g} electrons are considered to be non-bonding[34].

An important difference between metal and semiconductor electrodes is that in the former, electron exchange with the electrolyte occurs near the Fermi level, whereas in the latter, the electron exchange occurs at the band edges, which are usually well displaced from the Fermi level. Thus electrochemical reactions can occur at significant "underpotentials" on semiconductor electrodes compared with metals. Attempts to determine the flat-band potential of FeS_2 from a.c. impedance measurements were unsuccessful, as capacitance-voltage data could not be analysed in the form of Mott-Schottky plots, since using a simple 3 component series resistor/capacitor equivalent circuit to describe the system proved inadequate (see section 6.6). However, electrochemical studies on other disulphides; viz WS_2 and MoS_2, have shown that their valence band edges are situated below the redox potential of the Fe^{2+}/Fe^{3+} and O_2/H_2O couples[308,310]. Thus, assuming similar behaviour for the FeS_2/H_2O interface, the position of energy bands for FeS_2 in contact with aqueous electrolyte are shown in Figure 6.63 A.

6.7.1 Passive Film Formation

When n-type FeS_2, with its small band gap (0.9 ev) is illuminated with ultra band gap radiation under open-circuit conditions, electron-hole pairs are created in the semiconductor by excitation of Fe^{2+} t_{2g} electrons into e_g^* antibonding orbitals, which constitute the conduction band. Since t_{2g} electrons are non-bonding and localised on the cations, and the e_g^* orbitals are only weakly anti-bonding, electron-hole pairs are produced without affecting the bonding between iron and sulphur at the sulphide surface. A kinetic equilibrium of recombination and generation is established:-

$$Fe(II)_{lattice} \overset{h\nu}{\rightleftharpoons} Fe\ (II)\ h^+_{lattice} + e^- \qquad (6.38)$$

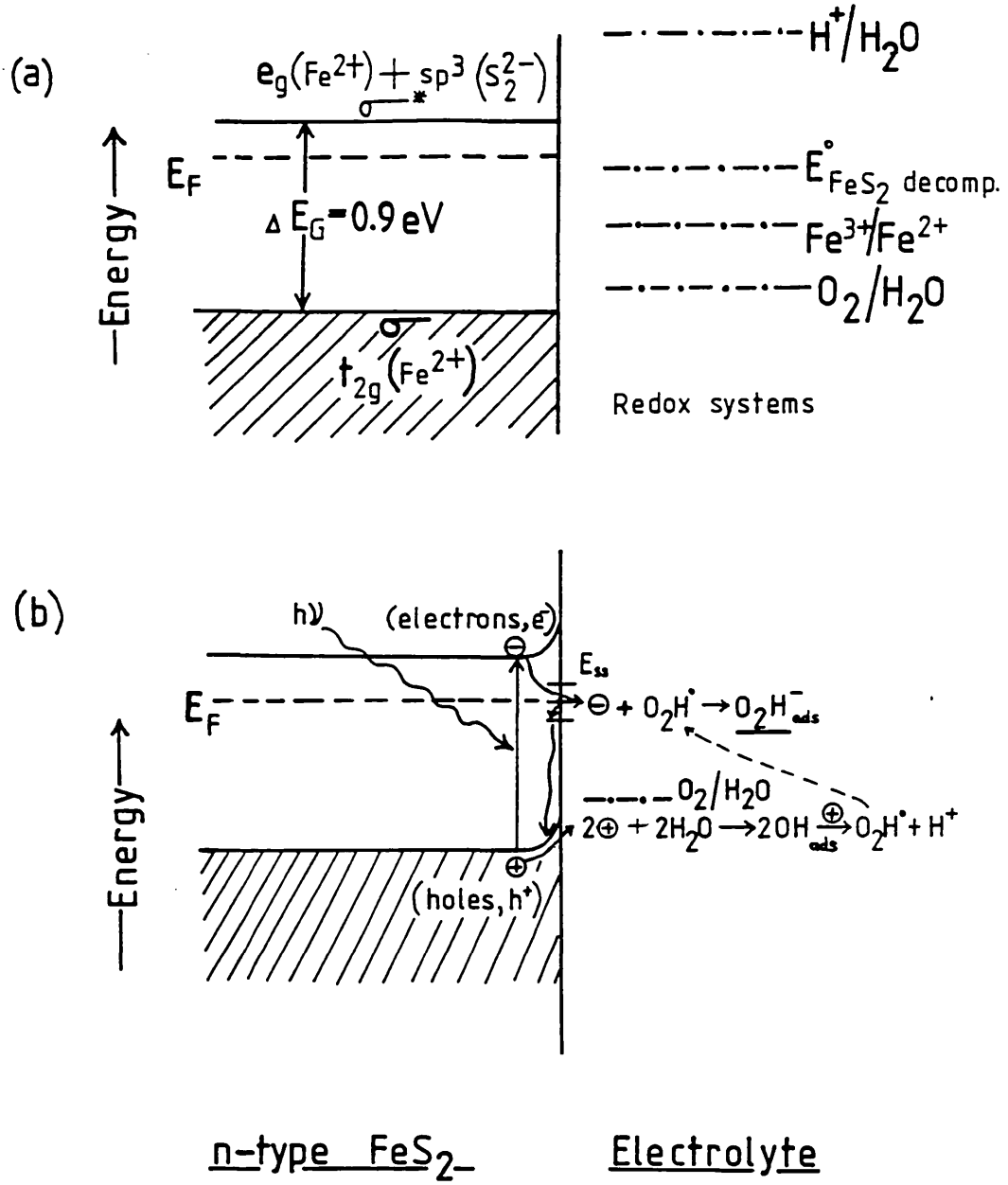


Fig 6.63 Position of energy bands and redox energy levels at the pyrite/electrolyte interface at pH 0. a) Equilibrium condition, no electron photoexcitation; E_F, Fermi level; hatched valence band is filled with electrons. b) Photogeneration of electron-hole pairs results in passive film formation; E_{ss}, interbandgap surface states.

Because the positive hole produced is localised on the cation sites, Fe (II) $h^+_{lattice}$ effectively equals Fe $(III)_{lattice}$.

Assuming that a small depletion layer and surface states exist at the surface of pyrite [309], some of the electrons and holes will react with suitable electron-acceptors/donors in the electrolyte before recombination occurs. In Figure 6.63 A, the O_2/H_2O redox potential lies above the valence band edge of pyrite, so that photogenerated holes arriving at the surface could theoretically oxidise water to oxygen. However, it is more likely that hole injection into the electrolyte under open-circuit conditions results in partial water oxidation, with chemisorption at the valence band edge of the radical intermediates of water oxidation/deprotonation Figure 6.63 B) by the following reactions:-

$$H_2O + 2h^+_{solid} \rightleftharpoons (O)_{ads} + 2H^+ \qquad (ah_1)$$

$$(O)_{ads} + H_2O + h^+_{solid} \rightleftharpoons (O_2H)_{ads} + H^+ \qquad (ak_1)$$

or

$$2H_2O + 2h^+_{solid} \rightleftharpoons 2(OH)_{ads} + 2H^+ \qquad (ai_1)$$

$$2(OH)_{ads} + h^+_{solid} \rightleftharpoons (O_2H)_{ads} + H^+ \qquad (al_1)$$

Therefore, metal-oxide/hydroxide type groups will form spontaneously on the surface of pyrite under open-circuit conditions even in acidic media. This could explain why a passive film forms on pyrite under open-circuit conditions (see sections 6.2 and 6.3). However, Peters and Majima[68] observed that the passive film is not reformed rapidly in the presence of ferric ions. This suggests that passive film formation is not complete until the electrons excited into the e_g* orbitals of the conduction band are transferred from the solid to the $(O_2H)_{ads}$ species on the solution side of the interface by the reaction:-

$$(O_2H)_{ads} + e^-_{solid} \rightleftharpoons O_2H^-_{ads} + H^+ \qquad (av_1)$$

The electrostatic attraction between the negatively charged perhydroxy radical anions, formed on the solution side of the interface, and the positively charged Fe (III) sites in the lattice, would result in the layer of hydroxy-type species at the FeS_2/solution interface becoming more strongly adsorbed at the surface (Figure 6.63 B). This would give rise to the passive nature of pyrite under open-circuit conditions. Ferric ions in solution would prevent passive film formation because they are much faster electron acceptors than oxygen or hydrogen peroxide at sulphide surfaces [370]. Therefore, peroxide radical adsorption would be inhibited. Ferric ions are also known to be good catalysts for hydrogen peroxide decomposition [307], so they may also prevent film formation by preventing the formation of peroxide radical intermediates.

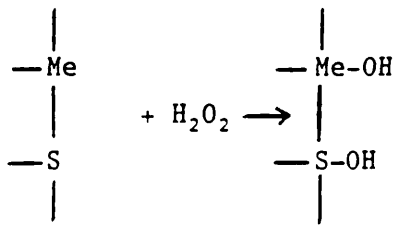
At first sight the injection of photogenerated electrons from the conduction band into the electrolyte may seem improbable, since the conduction and valence band edges of semiconductors are bent at the electrolyte interface, establishing a potential barrier against the transfer of majority carriers into the electrolyte. Thus for an n-type semiconductor, a positive space charge layer (also called the depletion layer) exists in the semiconductor adjacent to the electrolyte, depleted of majority carriers. However, there are two reasons why pyrite's depletion layer does not impair electron transfer into the electrolyte:-

1) Inevitably, surface states or inter-bandgap states will exist at the pyrite/electrolyte interface caused by crystalline imperfections and chemical impurities. They provide a pathway for electrons to tunnel across the interface, thereby delaying recombination and increasing the "lifetime" of electron-hole pairs (Figure 6.63 B).

2) As pyrite has a small band gap (0.9 eV), it will have a high surface concentration of conducting electrons and positive holes (see reaction 6.38). Thus, the thickness of the depletion layer and the amount of "band bending", will both be small, so that the probability of excited electrons being able to surmount the potential barrier will be significant.

For a "pseudo-semiconductor" like pyrite these solid state properties allow efficient anodic and cathodic electrochemical activity to be developed in the presence of ultra-bandgap radiation. Simultaneously, neither the cathodic supply of electrons nor the anodic supply of positive holes limit electrochemical reactions, which may occur at significant "underpotentials" compared with metals.

Although there is very little literature available about the reaction of hydrogen peroxide with metal sulphides [195,196,197], pyrite has been shown to act as a catalyst for hydrogen peroxide decomposition [311], which tends to support this mechanism. Furthermore, experiments with other semiconductors have demonstrated that reactions such as:-



(6.39)

occur easily on solid surfaces [312]. To find out what degradation products are formed on the surface of pyrite under open-circuit conditions, a pyrite sample was placed in triply distilled water (pH ~ 6 and not deoxygenated) for 1 hour, then subjected to XPS analysis (see section 4.2.6). A fresh surface was prepared initially by in situ wet grinding on a steel file, followed by ultrasonic cleaning to remove any abraded particles. The Fe_{2p} spectrum (see Figure 6.64) suggests that surface iron is present in four forms: pyrite (peak centred at 707.9 eV), ferrous oxide/hydroxide (709.9 eV), ferric hydroxy-sulphate (712.2 eV) and ferric sulphate (713.8 eV), which supports the postulated passive film formation mechanism given above.

6.7.2 Pyrite Oxidation

It is generally assumed that for classical semiconductor/electrolyte junctions, electrode polarisation does not change the relative positions of the energy levels available for electron exchange (i.e.

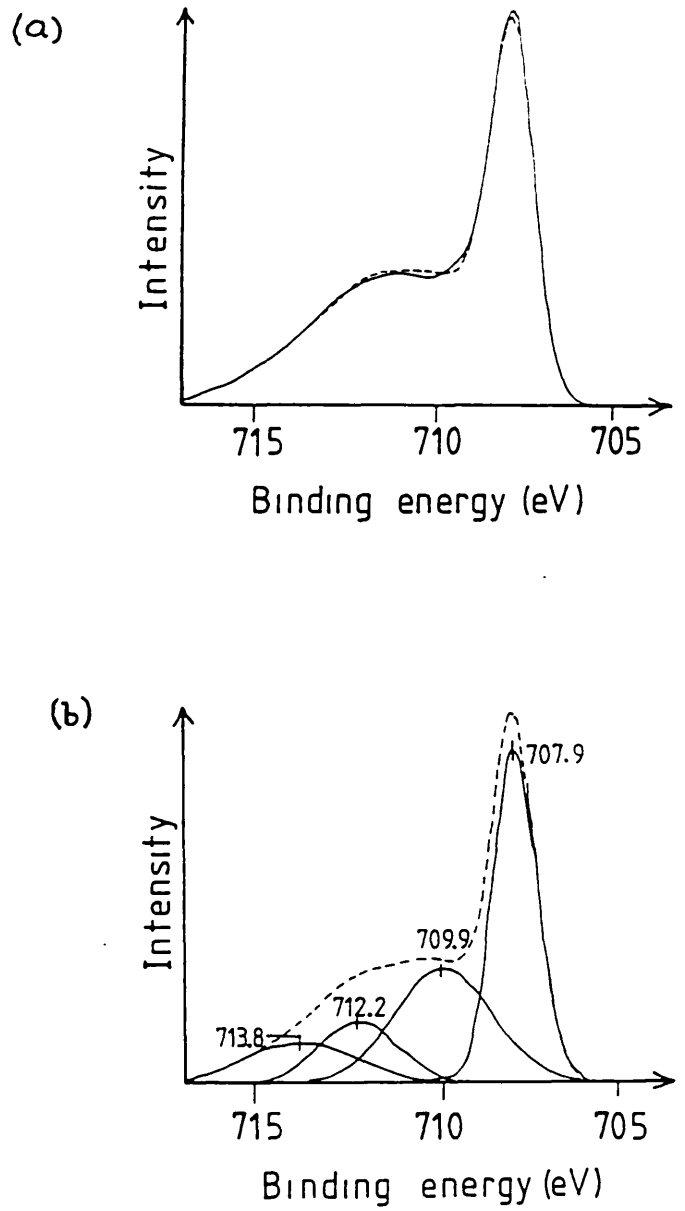


Fig 6.64 Fe 2p xps spectrum for pyrite oxidised in aerated triply distilled water for 1 hour. a) (——) experimental spectrum; (---) fitted curve (least squares). b) (——) fitted curve; (---) components of fitted curve.

band edges at the electrolyte interface), whereas for metals the available energy levels (ie the Fermi levels) change with polarisation. For a "pseudo-semiconductor" like pyrite, with a very thin depletion layer, Jaegermann and Tributsch[309] have argued that

most of the potential drop will occur through the Helmholtz layer, and that the band edges are not fixed at the surface but shift in parallel to the bulk band shift [309]. Thus, the reactions proposed above to explain passive film formation on pyrite under open-circuit conditions, can also be used to help explain the nature of pyrite oxidation under external polarisation conditions, since band bending is postulated to be independent of the external anodic potential applied to the electrode.

During pulse experiments at low overpotentials linear rising current-time transients suggested that a sub-monolayer of sulphur atoms was also formed on the surface (see section 6.5.1), before pseudo steady state conditions were achieved. However, under equilibrium conditions it is unlikely that elemental sulphur is ever formed on pyrite, since it is proposed that peroxide radicals are reactive enough to chemically oxidise sulphur atoms as they form on the surface producing intermediates such as SO_2H and $S_2(OH)_2$ (see Figure 6.65 A) by the reactions:-

$$S_{(ads)} + O_2H_{(ads)} = SO_2H \qquad (6.40)$$

$$2S_{(ads)} + O_2H_{(ads)} + H^+ = S_2(OH)_2 \qquad (6.41)$$

These species are unstable, and would be oxidised further, either electrochemically, or chemically (by molecular oxygen or hydrogen peroxide) through to sulphate.

On increasing the anodic bias, a potential would be reached at which the lowest energy levels of the conduction band were lowered below the potential required for pyrite decomposition according to reactions (c), (d), (e) and (f) and below the O_2/H_2O redox couple in the electrolyte. Under these conditions, continuous electron injection into the conduction band would occur and the anodic current would rise sharply (Figure 6.65 B).

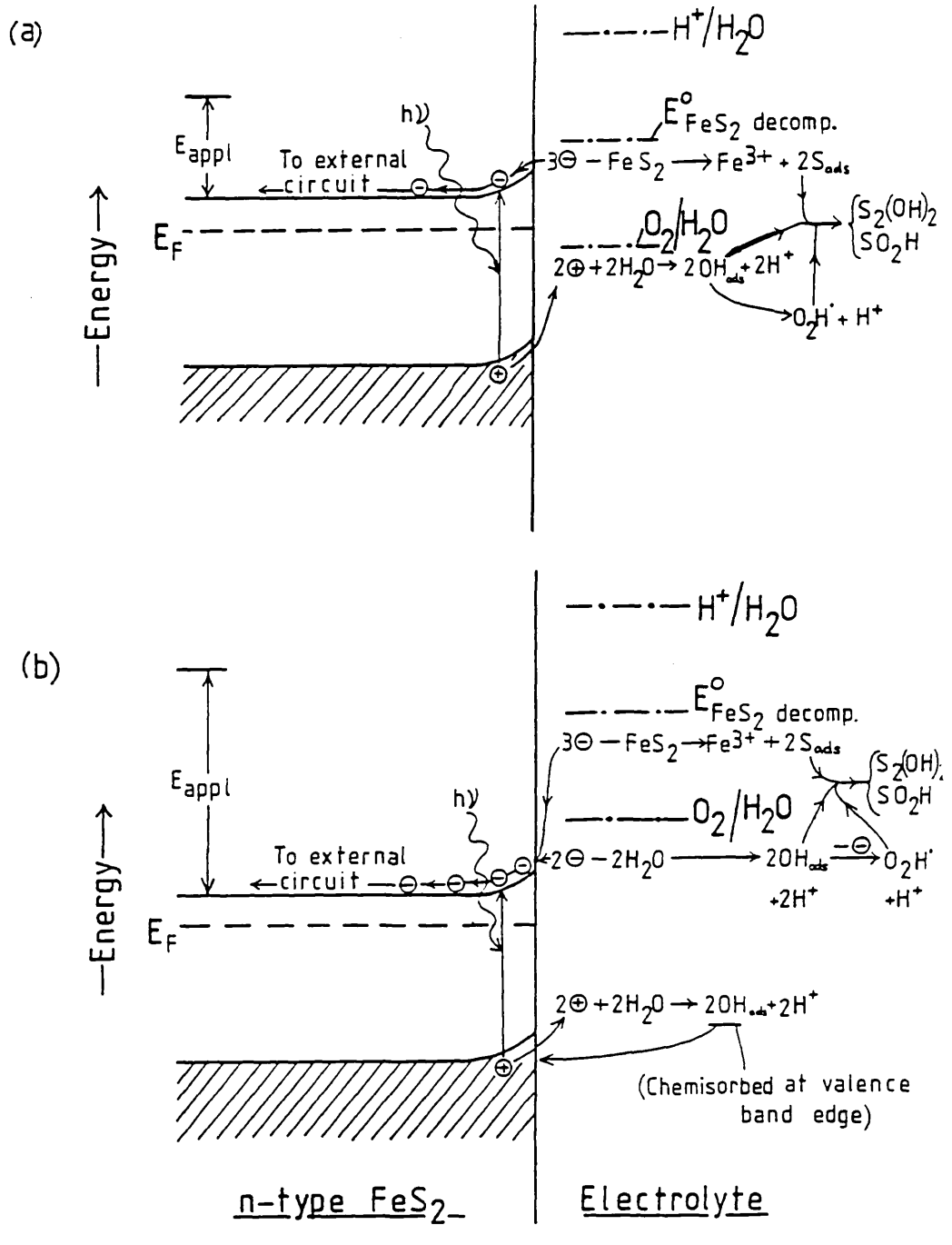


Fig 6.65 Energy level diagram for pyrite oxidation. Band bending is assumed to be approximately constant (independent of the applied potential). E_F, Fermi level; E_{appl}, externally applied anodic potential. a) Small anodic bias; photocurrent = dark current. b) Large anodic bias; photocurrent < dark current.

The position of the O_2/H_2O and H^+/H_2 electrolyte redox couples shift to more negative potentials with increasing pH by -59 mV/pH unit. Previous work on metal oxide semiconductors [313,314] suggested that the conduction and valences band edges move to more negative potentials with increasing pH by -59 mV/pH unit as well. This implies that the relative positions of the electrolyte O_2/H_2O and H^+/H_2 redox couples with the semiconductor band edges is pH independent.

However studies on HgS [315], $PbCrO_4$ [316], and MoS_2 [310], have shown that the band edges move by more than -59 mV/pH unit: ~ -90 mV/pH unit for $PbCrO_4$ [316]. Assuming FeS_2 behaves in a similar manner, the conduction band will lie nearer to the O_2/H_2O redox couple in basic media. Thus on increasing the pH, the external anodic bias required before continuous electron injection into the conduction band can occur, either by water oxidation or pyrite oxidative decomposition, decreases. Water oxidation by hole injection from the conduction band also becomes more favourable. This suggests that the rate of sulphate formation should increase with increasing pH, as expected, due to water oxidation and lattice decomposition becoming more favourable. Furthermore, faradaic background currents should increase with increasing pH. This has been observed in this work (Figures 6.8 and 6.34) previously by Conway et al[135].

6.8 Relevance of These Results to Pyrite Flotation

Figure 6.66 shows a typical flotation recovery curve for pyrite using potassium ethyl xanthate as a collector. Although spectroscopic [318], electrokinetic [318] and electrochemical [72,319,320] investigations have shown that dixanthogen is the species responsible for rendering pyrite hydrophobic, the depression of pyrite in the pH range 4.5 - 6, which cannot be due to a lack of dixanthogen, remains unexplained.

Over the last 25 years most flotation researchers have recognised that oxygen (or some other oxidising agent) is necessary for thio-type collectors to render sulphide minerals hydrophobic. This led to the

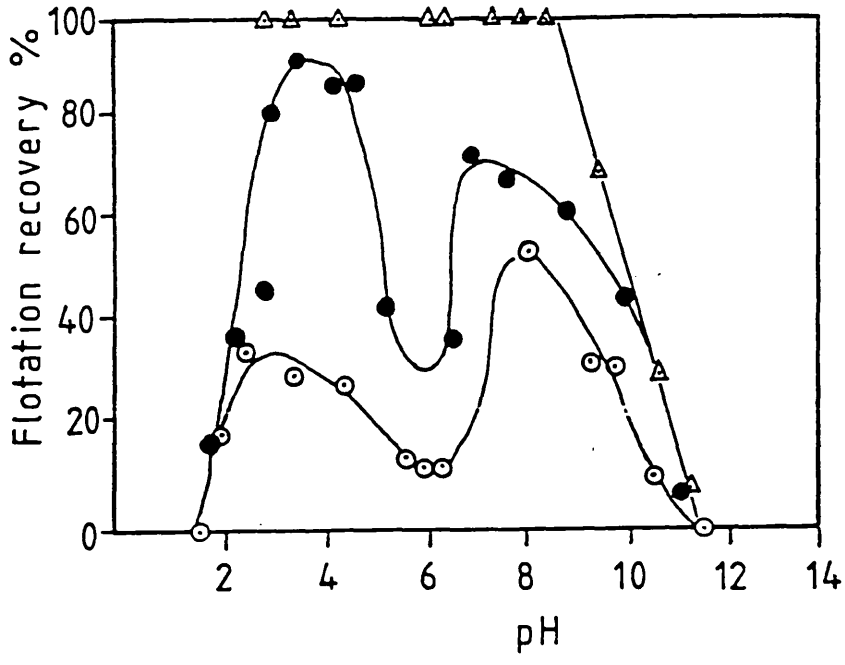


Fig 6.66 Flotation recovery of pyrite as a function of pH for various additions of potassium ethyl xanthate (from Fuerstenau et al [318]). (△) 1 x 10^{-5} mol dm^{-3}; (●) 2 x 10^{-5} mol dm^{-3}; (⊙) 2 x 10^{-4} mol dm^{-3}.

now generally accepted electrochemical theory for the action of thio-type collectors on mineral sulphides, first proposed by Salamy and Nixon [121]. Their hypothesis involved the formation of dixanthogen by the anodic oxidation of xanthate ions on the surface of pyrite, coupled to the cathodic reduction of adsorbed oxygen, i.e.

$$\text{Anodic reaction : } 2ROCS_2^- = (ROCS_2)_2 + 2e \qquad (6.42)$$

xanthate dixanthogen

$$\text{Cathodic reaction: } 1/2O_2 + H_2O + 2e = 2OH^- \qquad (6.43)$$

where R is an alkyl hydrocarbon group, usually of length C_2-C_5. Since metal sulphides are electronic conductors, electron transfer occurs through the solid, and the overall reaction is:-

$$2ROCS_2^- + 1/2O_2 + H_2O = (ROCS_2)_2 + 2OH^- \qquad (6.44)$$

Majima and Takeda[319] and Usul and Tolun[320] favour the above mechanism for dixanthogen formation on pyrite. However, Fuerstenau et al[318] postulated that the oxidation of xanthate to dixanthogen on pyrite was due to either Fe^{3+} or $Fe(OH)_3$ by the reactions:-

$$2Fe^{3+} + 2ROCS_2^- = 2Fe^{2+} + (ROCS_2)_2 \qquad (6.45)$$

$$2Fe(OH)_3 + 6H^+ + 2ROCS_2^- = 2Fe^{2+} + 6H_2O + (ROCS_2)_2 \qquad (6.46)$$

Mössbauer studies by Sheikh[321] showed that ferric xanthate is formed only at pH values < 3.5, unlike on other systems such as lead and copper sulphides, due to the greater insolubility of ferric oxide/hydroxide at higher pH values. Thus it seems unlikely that ferric xanthate plays any role in the flotation behaviour of pyrite.

A criticism of many published electrochemical investigations of sulphide mineral/xanthate systems is that they have involved xanthate concentrations 20 to 100 times greater than would normally be encountered in real flotation systems [72,129,319,320], which typically use 1×10^{-5} - 5×10^{-5} mol dm^{-3}. Since the current due to xanthate oxidation is linearly dependent on xanthate concentration under mildly oxidising conditions (i.e. under diffusion control), by using a relatively high xanthate concentration, the rate of xanthate oxidation has appeared much faster than the rate of sulphide mineral oxidation. However, at the lower xanthate concentrations encountered in sulphide flotation circuits, the effect of sulphide mineral oxidation on the overall hydrophobicity of the mineral and the inhibiting effect of mineral oxidation products (metal oxide, sulphur etc.) on xanthate oxidation will be much more significant.

Recent electrochemical studies carried out on the pyrrhotite/xanthate system [322] have shown that the overall hydrophobicity of a pyrrhotite electrode surface depends on the relative amounts of hydrophobic (dixanthogen)/hydrophilic (ferric oxide) species on the surface at a given E_h, pH, and xanthate concentration. Thus, any attempt to explain the pyrite recovery vs pH flotation curve should consider not only the xanthate oxidation reactions but also the sulphide mineral oxidation reactions.

Using the results from the electrochemical studies presented in this chapter for pyrite electrodes in aqueous solutions containing no xanthate collectors, and considering this data in relation to an E_h-pH diagram which contains all the relevant redox couples for the pyrite/xanthate/oxygen system, it is possible to rationalise the flotation behaviour of pyrite.

In Figure 6.67 the horizontal line (A) at 0.217 V represents the

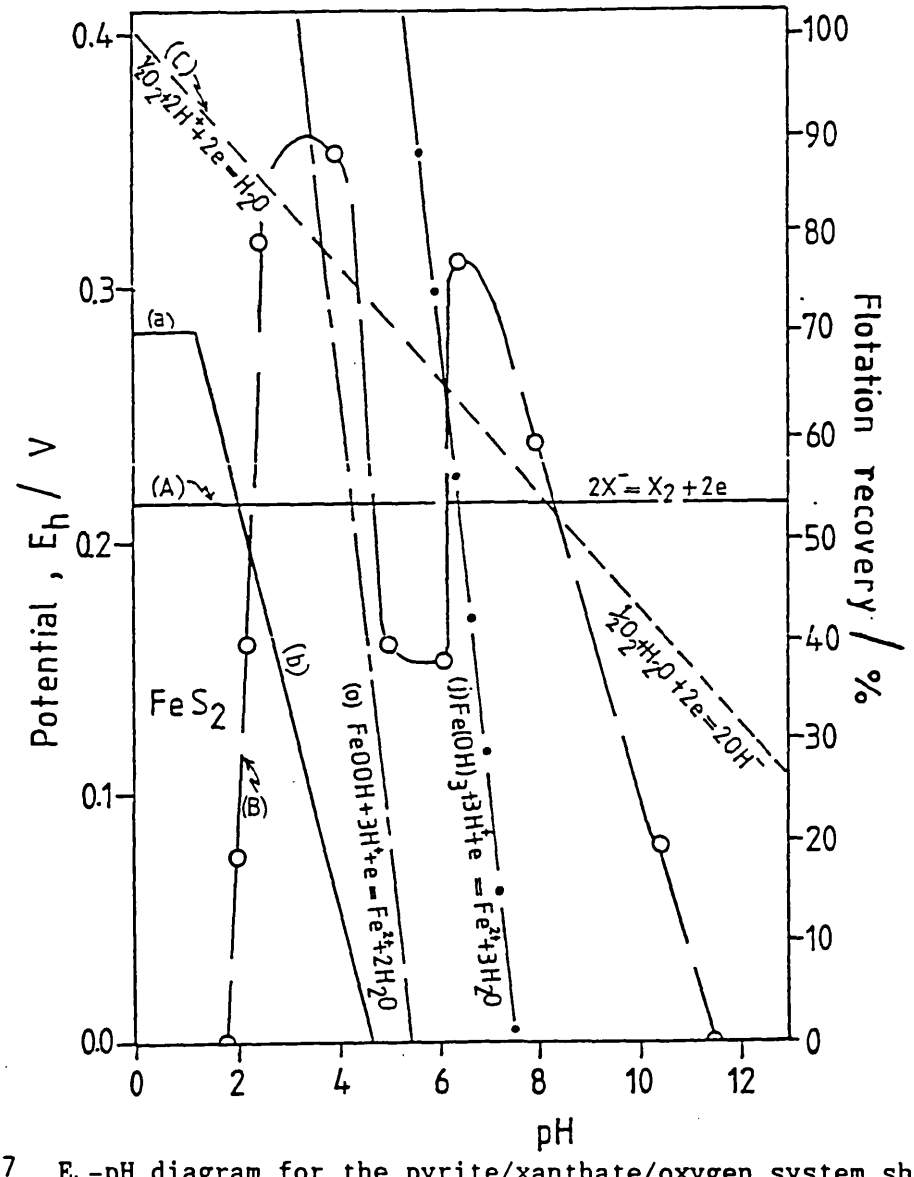


Fig 6.67 E_h-pH diagram for the pyrite/xanthate/oxygen system showing the redox couples relevant to the flotation behaviour of pyrite at 298 K and 10^{-5} M solution species. X^-, ethyl xanthate anion; X_2, dixanthogen; Line (B), pyrite flotation recovery with 10^{-5} M potassium ethyl xanthate solution (after Fuerstenau et al[318]). Line (C), potential onset of oxygen reduction on pyrite (after Biegler et al[186]).

reversible potential of the xanthate/dixanthogen couple for a 2 x 10^{-5} mol dm^{-3} solution of potassium ethyl xanthate (KEX)[365]. Line (C) represents the potential at which oxygen reduction from an air saturated solution commences on the surface of pyrite (> 10 μA cm^{-2}), as constructed from the results of Biegler et al[186]. Superimposed on the E_h-pH diagram is the flotation response of pyrite in a KEX solution at the same concentration (Line B - after Fuerstenau et al[318]).

At pH values < 2.5 the flotation recovery of pyrite decreased rapidly as a result of xanthate ion decomposition according to the reactions:-

$$ROCS_2^- + H^+ \rightleftharpoons \underset{\text{xanthic acid}}{ROCS_2H} \rightarrow ROH + CS_2 \qquad (6.47)$$

It can be seen that in the pH range 2.5 - 4 the potential onset for oxygen reduction occurs at values more positive than both the upper stability limit of pyrite and the xanthate/dixanthogen reversible potential (Figure 6.67). Hence, in this pH range, a mixed potential will operate involving the cathodic reduction of oxygen according to:-

$$1/2O_2 + 2H^+ + 2e = H_2O \qquad (6.48)$$

and the anodic oxidation of xanthate ions (reaction 6.42) and the mineral itself (reactions (s_1) and (t_1). Recent work by Pillai and Bockris[335] suggests that the reduction of oxygen on pyrite is catalysed about forty times in the presence of xanthate. Cyclic voltammograms, recorded for pyrite electrodes in the pH range 1 - 4.6 (see sections 6.4.1 and 6.4.3), suggested that the products of pyrite oxidation under mildly oxidising conditions were mainly goethite (FeOOH), elemental sulphur, with some sulphate ions. Obviously, the elemental sulphur will contribute to the hydrophobicity of pyrite. However, Figure 6.67 also shows that in the pH range 2.5 - 4, xanthate ions are capable of reducing FeOOH to Fe^{2+}, which leads to the formation of dixanthogen by the reaction:-

$$2FeOOH + 6H^+ + 2ROCS_2^- = 2Fe^{2+} + 4H_2O + (ROCS_2)_2 \qquad (6.49)$$

Thus the flotation recovery of pyrite is high in this pH range because dixanthogen can be formed by reaction (6.44) and by reaction (6.49) after pyrite oxidation has occurred.

Figure 6.65 shows that the potential onset for oxygen reduction converges on the xanthogen/dixanthogen reversible potential with increasing pH, indicating that the rate of xanthate oxidation by reaction (6.44) will decrease with increasing pH. More importantly, the diagram shows that at pH values > 4.2 xanthate ions can no longer reduce FeOOH. Thus dixanthogen formation by reaction 6.49 will cease and hydrophilic FeOOH will accumulate on the surface of pyrite as a result of mineral oxidation, decreasing the overall hydrophobicity of pyrite. This explains why there is a sudden decrease in the flotation recovery of pyrite in the pH range 4.5 - 6.

At pH values > 6, pyrite flotation recovery showed a second maximum of ~ 70 % recovery at pH 6.5 This was probably due to the increasing dominance of sulphate over elemental sulphur formation as the main pyrite oxidation pathway under mildly oxidising conditions. Voltammograms recorded at pH 7 (see section 6.4.4) showed that at potentials > 0.0 V there was evidence for both the formation of FeOOH and a more hydrated ferric hydroxide ($Fe(OH)_3$) on the surface of pyrite. The high yield of H^+ ions accompanying pyrite oxidation to sulphate (reaction t_1) lowered the interfacial pH sufficiently for goethite to partially dissolve, forming soluble ferric species which precipitate as $Fe(OH)_3$ on moving away from the surface as the pH increased to its original value.

There are two ways in which the formation of $Fe(OH)_3$, rather than FeOOH, can enhance the formation of dixanthogen and hence increase the hydrophobicity of pyrite. Firstly, whereas the formation of a resistive FeOOH layer (by a solid state mechanism) prevents reaction (6.44) from occurring, by blocking the passage of xanthate ions to the underlying pyrite surface, the formation of $Fe(OH)_3$ by a dissolution-precipitation mechanism allows xanthate ions to penetrate through to the pyrite surface so that dimerisation can still occur. Secondly,

Figure 6.67 shows that at pH values $\leq$ 6.5 xanthate ions will reduce any $Fe(OH)_3$ present by reaction (6.46), which also generates dixanthogen. Both these processes will increase the ratio of hydrophobic (dixanthogen)/hydrophilic (ferric oxide) species on the surface of pyrite, and give rise to the second maximum at pH 6.5 in the flotation recovery curve of pyrite.

At pH values > 6.5, the hydrophobicity/flotation recovery of pyrite decreases steadily for the following reasons:-

1. At pH values > 6.5 dixanthogen formation by the reduction of $Fe(OH)_3$ ceases.

2. At pH values > 8.0 pyrite oxidation and oxygen reduction occur at potentials less negative than required for xanthate oxidation. Thus, dixanthogen formation by reaction (6.46) is no longer possible and only pyrite oxidation (reaction (d)) by dissolved oxygen can occur.

3. From impedance measurements (see section 6.6; Figure 6.56) it was clear that the increasing insolubility of ferric oxide/hydroxide with increasing pH also increases the resistance/thickness of the hydrophilic oxide layer.

4. Dixanthogen decomposition occurs at pH values > 9 according to the reaction:-

$$(ROCS)_2 + OH^- \xrightarrow{H_2O} ROCS_2^- + ROH + CS_2 \qquad (6.50)$$

although the kinetics of this reaction is relatively slow ($k = 0.24 \pm 0.005$ l mol^{-1} sec^{-1} at 296 K)[363].

CHAPTER SEVEN

ELECTROCHEMICAL STUDIES ON PYRRHOTITE ELECTRODES

CHAPTER SEVEN : ELECTROCHEMICAL STUDIES ON PYRRHOTITE ELECTRODES

7.1 Thermodynamics

Figure 7.1 shows the E_h-pH diagram for pyrrhotite at 298 K calculated using the thermodynamic data presented in Table II(ii) (Appendix II). Pyrite was excluded from the diagram since the oxidation of pyrrhotite to pyrite by a reaction such as:-

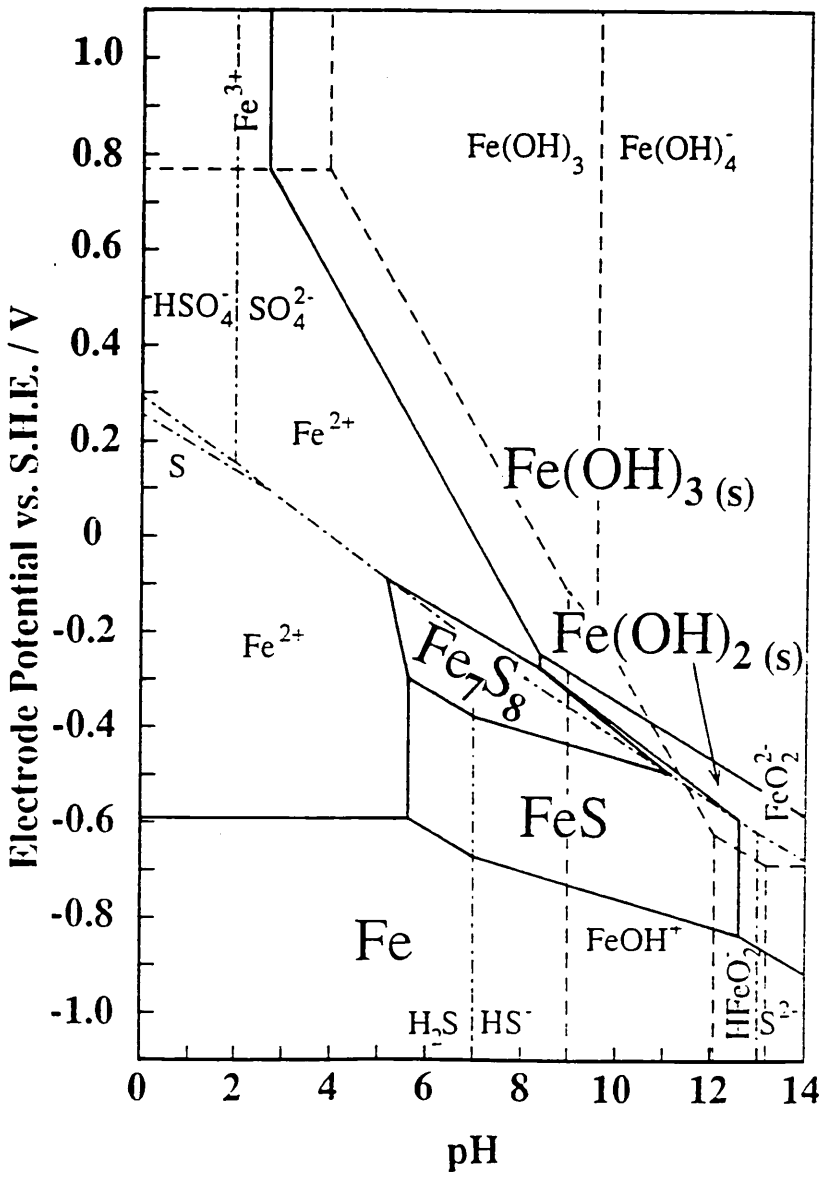


Fig 7.1 Potential-pH diagram for the Fe-S-H_2O system at 298 K for dissolved sulphur and iron activities of 10^{-4}. FeS_2 excluded.

$$Fe_{1-x}S = (1-2x)Fe^{2+} + FeS_2 + 2(1-2x)e \qquad (be_1)$$

is slow even at 100°C[371]. Moreover there is no evidence of pyrite formation during the leaching of pyrrhotite[67]. Indeed, reactions in nature which give rise to pyrite are known to be particularly slow[372].

At low dissolved sulphur activities (typical of solutions initially containing no dissolved sulphur on immersion of a pyrrhotite electrode), pyrrhotite is unstable at pH values < 5 (Figure 7.1). Unlike pyrite (see section 6.1), FeS dissolves non-oxidatively under such conditions, the reaction:-

$$FeS + 2H^+ + Fe^{2+} + H_2S \qquad (j_1)$$

being favoured.

Under oxidising conditions, iron-rich pyrrhotite (α-FeS) oxidises to form an iron-deficient, or sulphur-rich, pyrrhotite phase (shown as Fe_7S_8 in Figure 7.1):-

$$FeS = (1-x)Fe^{2+} + Fe_xS + 2(1-x)e \qquad (l_1)$$
$$\text{where } x < 1$$

which becomes unstable with respect to Fe^{2+} and SO_4^{2-} at more oxidising potentials. In alkaline solutions, pyrrhotite oxidises to $Fe(OH)_2$ and SO_4^{2-}. However, due to the irreversibility of sulphate formation[65,134], it can be expected that pyrrhotite will exhibit a meta-stable boundary at more oxidising potentials than those dictated by thermodynamic considerations. Thus $Fe(OH)_3$ or FeOOH is more likely to be formed than $Fe(OH)_2$.

7.2 Studies on Virgin Pyrrhotite Surfaces

Figure 7.2 shows the effect of in situ grinding to produce a fresh mineral surface on the rest potential of hexagonal pyrrhotite

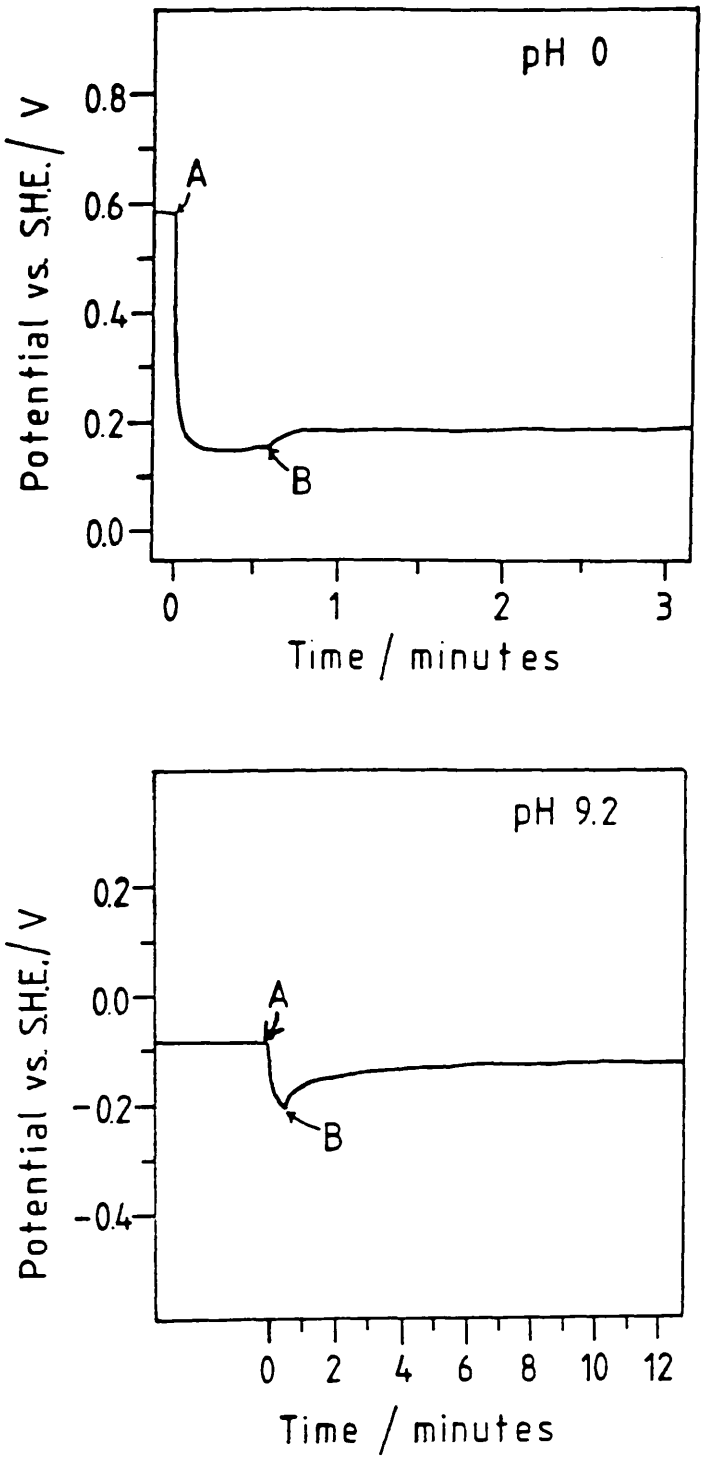


Fig 7.2 The change of rest potential with time (after in situ polishing) of a pyrrhotite electrode at pH 0 (top) and pH 9.2 (bottom). (A) commence polishing; (B) finish polishing.

($Fe_{0.905}S$) at pH 0 and 9.2. In 1 M $HClO_4$ pyrrhotite acquired a rest potential of ~ 0.6 V, which was lowered to 0.15 V almost instantaneously on abrading the pyrrhotite surface (Figure 7.2 (top)), and remained at this value thereafter. In contrast, at pH 9.2 the rest potential returned to its pre-abrasion potential after about 15 minutes (Figure 7.2 (bottom)). This was different from the behaviour of pyrite whose rest potential returned to its preabrasion value at both pH 0 and pH 9.2, taking only 30 seconds in the latter case (see section 6.3).

Cyclic voltammograms of hexagonal pyrrhotite in 1 M $HClO_4$ recorded before and after in situ abrasion of the electrode surface are shown in Figure 7.3. Potential sweeps were commenced in a negative direction from the open-circuit potential. On the first negative sweep a sharp, narrow cathodic peak (I) was observed at ~ 0.0 V. On subsequent sweeps the peak was shorter, broader and its E_p was shifted to more negative potentials. Abrading the electrode surface reduced the size of the peak considerably, the charge associated with the peak decreasing from 76 mC cm^{-2} to 9 mC cm^{-2}.

Previous work has shown that the open-circuit dissolution of iron sulphides is dependent on the potential of the sulphide surface (see section 2.4.3), a cathodic process (associated with peak I) being a prerequisite for dissolution. The cathodic process may involve the removal of a passivating sulphur film [201,202,205] and/or dissolution of a ferric oxide layer [200,204], or it may decrease the non-stoichiometry of the sulphide to produce an exactly stoichiometric compound at the surface, which then dissolves non-oxidatively (reaction (l_1) and (j_1)) [143,205,210,211]. However, since physical abrasion of the pyrrhotite surface in 1 M $HClO_4$ lowered its open-circuit potential into a region where non-oxidative dissolution occurs, it seems likely that a layer of sulphur and/or more likely a ferric oxide film is responsible for inhibiting the dissolution of pyrrhotite. Once the film is removed the open-circuit potential is "pinned" at the corrosion potential for the non-oxidative dissolution process, the process being comprised of an anodic and a cathodic half-cell reaction (see section 6.2; reactions 6.1 and (v) respectively).

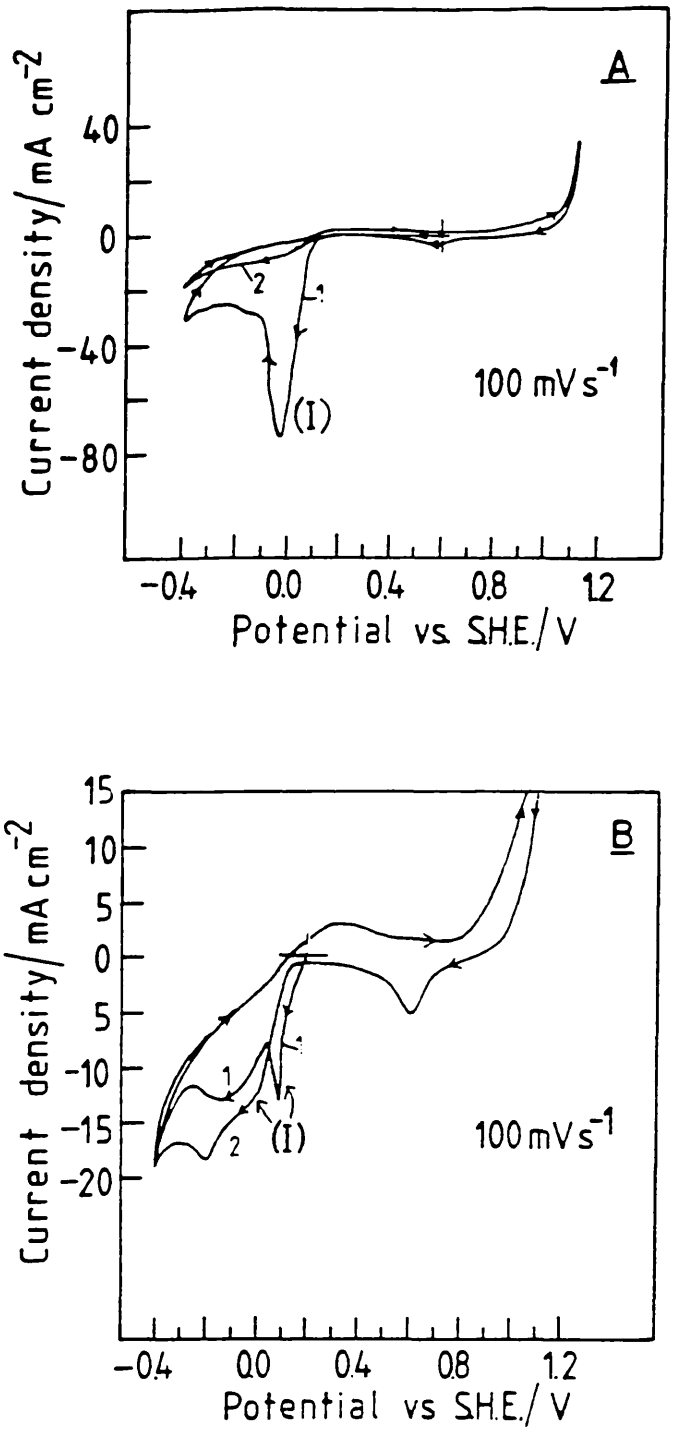


Fig 7.3 Cyclic voltammograms of a stationary pyrrhotite electrode in stirred solution at pH 0 (1 M $HClO_4$), recorded immediately after different surface pretreatments, starting from the rest potential, first cycled cathodically then anodically at 100 mVs^{-1}. (A) untreated sample; (B) fresh pyrrhotite surface produced by in situ abrasion.

7.3 Cyclic Voltammetry

7.3.1 Anodic and Cathodic Reactions at pH 1 (0.1 M $HClO_4$)

Cyclic voltammograms of a stationary pyrrhotite electrode in stirred 1 M $HClO_4$ are shown in Figure 7.4. The two-peak reversible

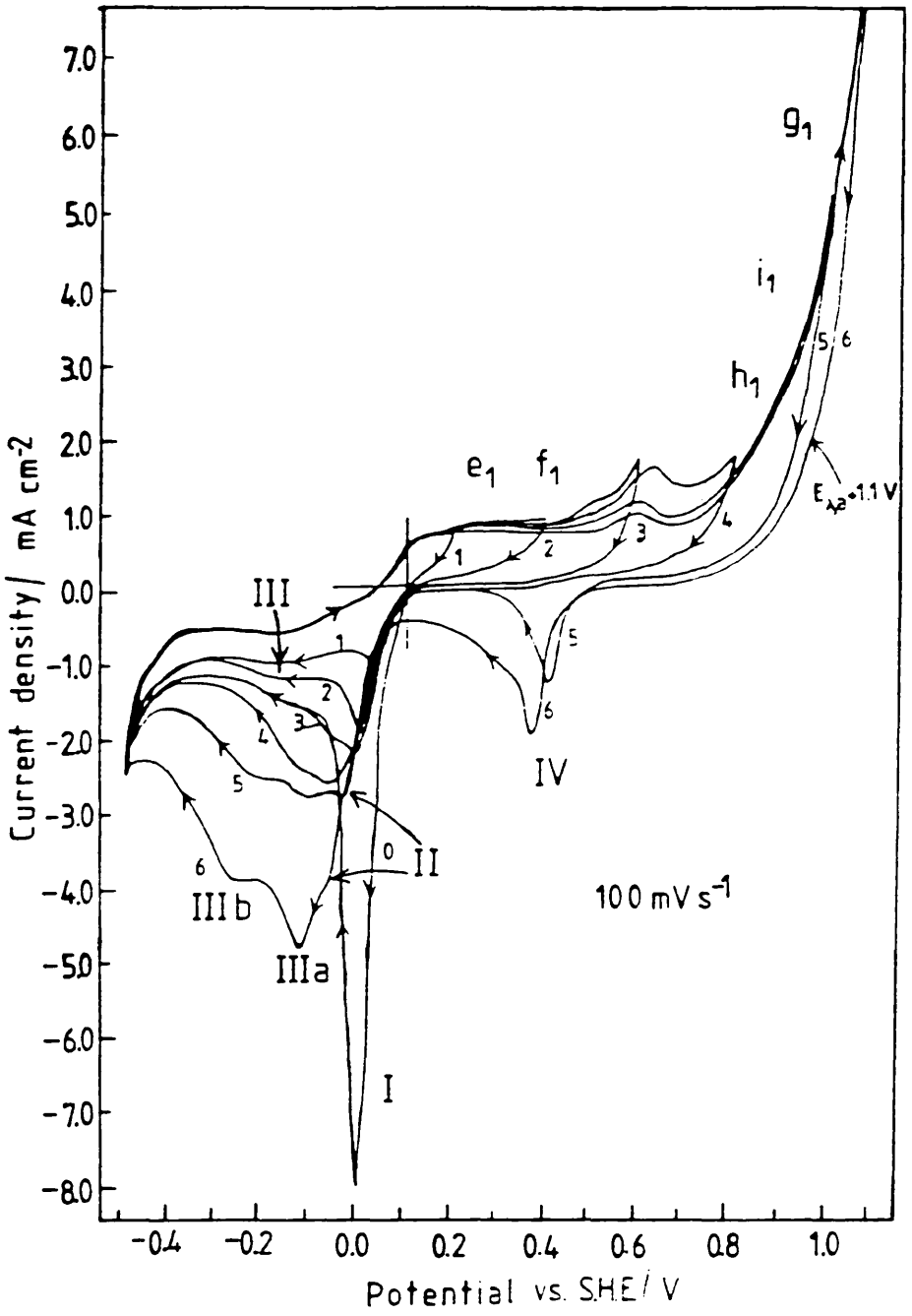


Fig 7.4 The effect of extending the anodic potential scanning limit ($E_{\lambda a}$) on cyclic voltammograms of pyrrhotite at pH 1 (0.1 M $HClO_4$) in stirred solution and a sweep rate of 100 mVs^{-1}.

process(es) observed in the potential range -0.2 - 0.2 V with pyrite were absent in voltammograms of pyrrhotite. This is probably due to the different electrochemical reactivities of S_2^{2-} ions and S^{2-} ions in the lattice structures of pyrite and pyrrhotite respectively [135].

When E_{λ_a} was extended to potentials in the range $E_r < E_{\lambda_a} < 0.4$ V, two cathodic peaks ((II) and (III)) were observed on the reverse scan. Although smaller in size, peak (II) occurred at similar potentials (~ 0.0 V) and was similar in shape and form to peak (I); the large narrow cathodic peak observed on the first negative potential sweep from the rest potential (see section 7.2). Peak (III) was broader and smaller than peak (II) and became split into two peaks ((IIIa) and (IIIb)) when E_{λ_a} was increased above 0.5 V. Repetitive triangular potential scans to increasing E_{λ_a} values above 0.4 V resulted in decreasing anodic currents on consecutive cycles in the potential range 0.4 to 0.8 V. This suggested that a passivating process occurred in this potential region.

The anodic current increased sharply at potentials > 0.8 V and a fourth cathodic peak appeared on the reverse scan at 0.4 V. In addition, as E_{λ_a} was extended above 0.8 V, the height of peaks (IIIa) and (IIIb) increased more rapidly than that of peak (II) so that peak (II) became discernible only as a shoulder on peak (IIIa). All the cathodic peaks shifted to more negative potentials on increasing E_{λ_a} due to the irreversible nature of pyrrhotite oxidation. Peaks (IV), (II) and (IIIa) were unaffected by electrode rotation (see Figure 7.5), which suggested that, in addition to sulphur, other insoluble and/or adsorbed oxidation products were formed on the surface of pyrrhotite at pH 1.

The voltammetric behaviour of pyrrhotite described above can be interpreted in two ways:-

(i) Metal-Deficient Sulphide Film Formation

It is proposed that at E_{λ_a} potentials < 0.4 V the hexagonal pyrrhotite

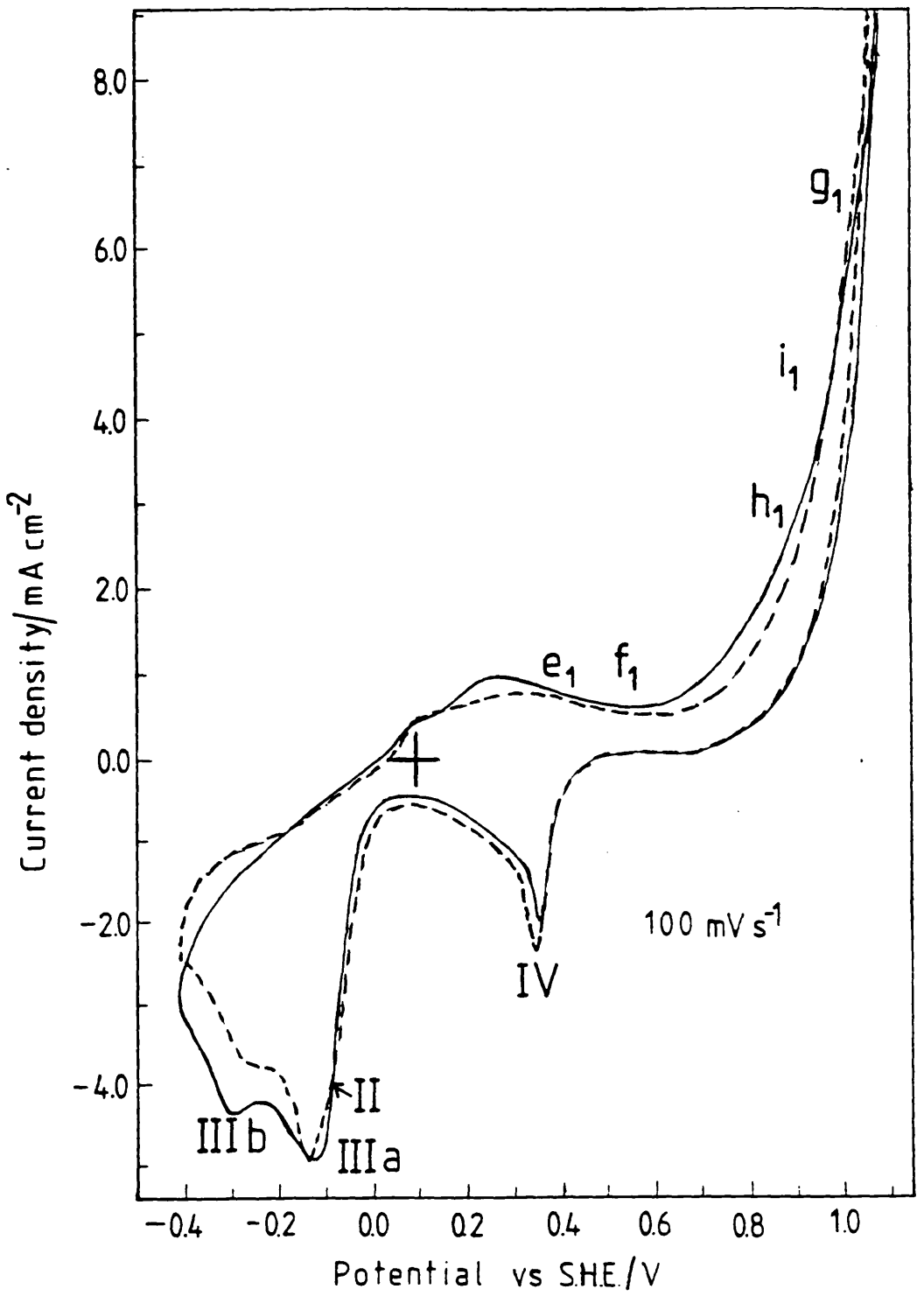


Fig 7.5 The effect of electrode rotation on cyclic voltammograms of a pyrrhotite RSCBE at pH 1 (0.1 M $HClO_4$). (——) stationary electrode; (---) rotated electrode.

sample ($Fe_{0.905}S$) oxidised by reaction 7.1, forming a metal-deficient sulphide film (MDSF):-

$$Fe_{0.905}S = xFe^{2+} + Fe_{(0.905-x)}S + 2xe \qquad (7.1)$$

where: $0 \leq x \leq 0.011$, since $Fe_{0.894}S$ represents the lower limit of iron deficiency in hexagonal pyrrhotite (see section 2.1.1.2).

On the subsequent negative going potential scan, peak (II) was assigned to the reduction of the MDSF (Fe_yS) by the following reaction:-

$$Fe_yS + 2(1-y)H^+ + 2(1-y)e = yFeS + (1-y)H_2S \qquad (7.2)$$

where: $0.905 \leq y \leq 0.894$

Elemental sulphur formed electrochemically once the compositional range of hexagonal pyrrhotite was exceeded (reaction (7.3)) and/or possibly by chemical decomposition of the MDSF (reaction (7.4)).

$$Fe_{0.905}S = xFe^{2+} + Fe_{0.894}S + (x-0.011)S + 2xe \qquad (7.3)$$

where: $x > 0.011$

$$Fe_yS = yFeS + (1-y)S \qquad (7.4)$$

where: $0.905 \leq y \leq 0.894$

Sulphur reduction (reaction (v)) was assigned to the broad single cathodic peak (III), which occurred between -0.05 and -0.35 V.

At E_{λ_a} values > 0.4 V the rate of reaction (7.3) increased, depositing sulphur which passivated the surface in the potential range 0.4 to 0.8 V. Also peak (III) split into two, suggesting that sulphur reduction then involved a two-step process. Soluble intermediates were probably formed during this process since the height of peak (IIIb) decreased when the electrode was rotated.

Hodgson and Agar[331] proposed that the polysulphide S_2^{2-} is formed as an intermediate when pyrrhotite is oxidised to elemental sulphur and when the sulphur so produced is reduced to H_2S or HS^-. In section 6.4.4 it was argued that the formation of S_2^{2-} during sulphide mineral oxidation is unlikely, especially in acidic media where polysulphide-type species are unstable, and sulphide mineral oxidation further lowers the interfacial pH (eg reactions (b), (c), (d), (l), (f_1) and (g_1)). Even in basic solutions S_4^{2-} and S_5^{2-} (not S_2^{2-}) are the only polysulphide species present in significant quantities[165]. However, the formation of polysulphides during sulphur reduction seems a more reasonable proposition, since the process consumes hydrogen ions (reaction (v)) and hence increases the interfacial pH. Initially, the sulphur formed at E_{λ_a} values < 0.5 V gave rise to a single cathodic peak (III) which was not affected by electrode rotation. Therefore, this layer was probably reduced in a single step (reaction (v)). However, as more sulphur was formed on the positive potential sweep, the interfacial pH increased sufficiently on the reverse scan for polysulphide formation to occur. Hence peaks (IIIa) and (IIIb) appeared. The former peak was assigned to the reaction:-

$$xS^\circ + H^+ + 2e = HS_x^- \qquad (ay_1)$$

and the latter to:-

$$HS_x^- + (2x-1)H^+ + 2xe = xH_2S \qquad (az_1)$$

Thus, when the electrode was rotated some of the polysulphide ions formed by reaction (ay_1) (peak (IIIa)) were dispersed into the bulk solution so that less remained at the electrode surface to be reduced further to H_2S (reaction (az_1)). Hence peak (IIIb) decreased in size.

At potentials > 0.8 V the iron formed was in the ferric state (reactions (h_1), (i_1) and (g_1)) and goethite formation occurred, even at pH 1 (section 6.3.1). Thus the cathodic peak at 0.4 V which appeared on extending E_{λ_a} to > 0.8 V was assigned to the reduction of geothite by reaction (o).

(ii) Underpotential Deposition of Ferric Oxide

An alternative explanation of the voltammetric behaviour of pyrrhotite is to assign peaks (I), (II) and (IV) to the reduction of ferric oxide/hydroxide type species, peak (III) being ascribed to sulphur reduction as before.

Earlier work, described in section 7.2, showed how abrading the surface of pyrrhotite in 1 M $HClO_4$ substantially decreased the size of peak (I) on the first negative going potential sweep. This suggested that the process associated with peak (I) involved the cathodic reduction of an insoluble surface film (probably of ferric oxide formed by air oxidation), which was responsible for inhibiting the non-oxidative dissolution of pyrrhotite. An induction period prior to pyrrhotite dissolution has been observed by other workers [200,201,204] and can be explained by assuming that the meta-stable ferric oxide film slowly dissolves during this period. Since peaks (I) and (II) occurred at the same potential and were similar in shape, it seems reasonable to suggest that both peaks were due to the same cathodic process. This implied that pyrrhotite oxidised by reactions (1) and (z_1) at potentials < 0.8 V and pH 1, at which the formation of ferric oxide/hydroxide species should not occur according to thermodynamic predictions (see Appendix II).

Unlike pyrite, whose semiconductor properties can be invoked to explain ferric oxide film formation in acidic solutions, pyrrhotite is a good electronic conductor and can be regarded as metallic (see sections 2.1.2). The only evidence to support the interpretation described above is from studies of the electrochemical behaviour of simple and mixed iron (III) oxides using carbon paste electrodes in 1 M acids (HCl, $HClO_4$, H_3PO_4 and H_2SO_4) [336-339]. Chemical dissolution of the oxides was relatively slow, the dissolution rate being dependent on the type of oxide involved and particle size. A cathodic peak due to the electrochemical reduction of the solid ferric oxide was observed in the potential range 0.4 to -0.2 V. The shape, position and amplitude of the peak was greatly influenced by the morphology of the oxide. Sharp peaks, similar to peaks (I) (II) and (IV), were obtained when the size distribution of the oxide particles

was narrow[336]. The more hydrolysed the oxide, the more the cathodic peak was shifted to positive potentials [337,338].

Thus peak (IV) was probably due to the reduction of a ferric oxide more hydrolysable than that giving rise to peak (I)/(II).

7.3.2 Pyrrhotite RSCBE at pH 0 (1 M $HClO_4$)

Figure 7.6 shows the current-time response of a hexagonal pyrrhotite

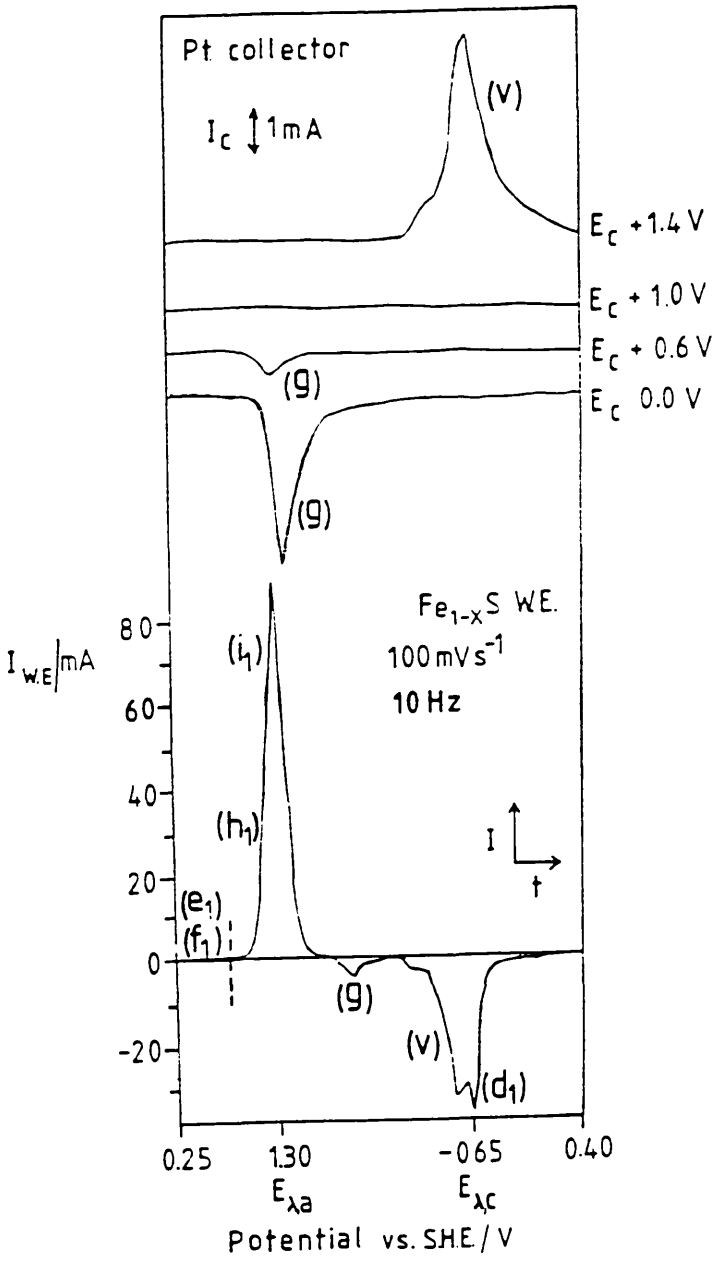


Fig 7.6 Cyclic voltammogram of a RSCBE in 1 M $HClO_4$ (pH 0), with the pyrrhotite working electrode (WE) swept anodically from 0.25 to 1.3 V, then cathodically to -0.65 V, and the platinum collector electrode held at various potentials (E_c).

RSCBE to potential cycling in 1 M $HClO_4$. The current response at the Pt collector electrode for a range of potentials (E_c) is also shown.

Similar to the behaviour of pyrite, the oxidation of pyrrhotite apparently produced no Fe(II) species judging by the absence of any corresponding collector oxidation current at potentials > 0.8 V. This may be because the amount of Fe^{2+} produced was below the detection capability of the RSCBE under these non-steady state conditions. At potentials > 0.7 V the main mineral oxidation reactions were (h_1) and (i_1) producing Fe^{3+}, sulphur and SO_4^{2-}. Fe^{3+} was reduced to Fe^{2+} by reaction (g) at collector potentials < 0.7 V. On sweeping the pyrrhotite electrode to negative potentials, any Fe^{3+} remaining at the mineral surface was reduced to Fe^{2+} giving rise to peak (g) at 0.736 V. Increasing the rotation rate to 40 Hz dispersed all the Fe^{3+} ions from the mineral surface and the peak disappeared.

At lower potentials (< 0.08 V), the sulphur on pyrrhotite was reduced to H_2S (reaction (v)), giving a peak at -0.43 V and a shoulder at -0.17 V. This suggested that either two forms of sulphur were formed during pyrrhotite oxidation, or sulphur was reduced in a two-step process (see Section 7.3.1; reactions (ay_1) and (az_1)). Oxidation of the H_2S formed was detected at the Pt collector electrode at potentials > 1.2 V, confirming H_2S and not Fe^{2+} to be the reacting species.

7.3.3 pH 4.6 (0.5 M CH_3COOH + 0.5 M CH_3COONa)

The voltammetric behaviour of pyrrhotite in pH 4.6 buffer solution is shown in Figure 7.7. Thermodynamics predict that at pH 4.6 pyrrhotite oxidises by reaction (z_1) at potentials > 0.02 V forming goethite and sulphur. For E_{λ_a} potentials < 0.5 V only one cathodic peak was observed on the reverse negative-going potential scan. This was assigned to goethite and sulphur reduction (reactions (o) and (v) respectively) since both occur in the same potential range.

At E_{λ_a} potentials > 0.5 V the anodic current increased rapidly as sulphate formation (reaction (ba_1)) became the dominant oxidation reaction. A second cathodic peak also appeared at 0.2 V due to the

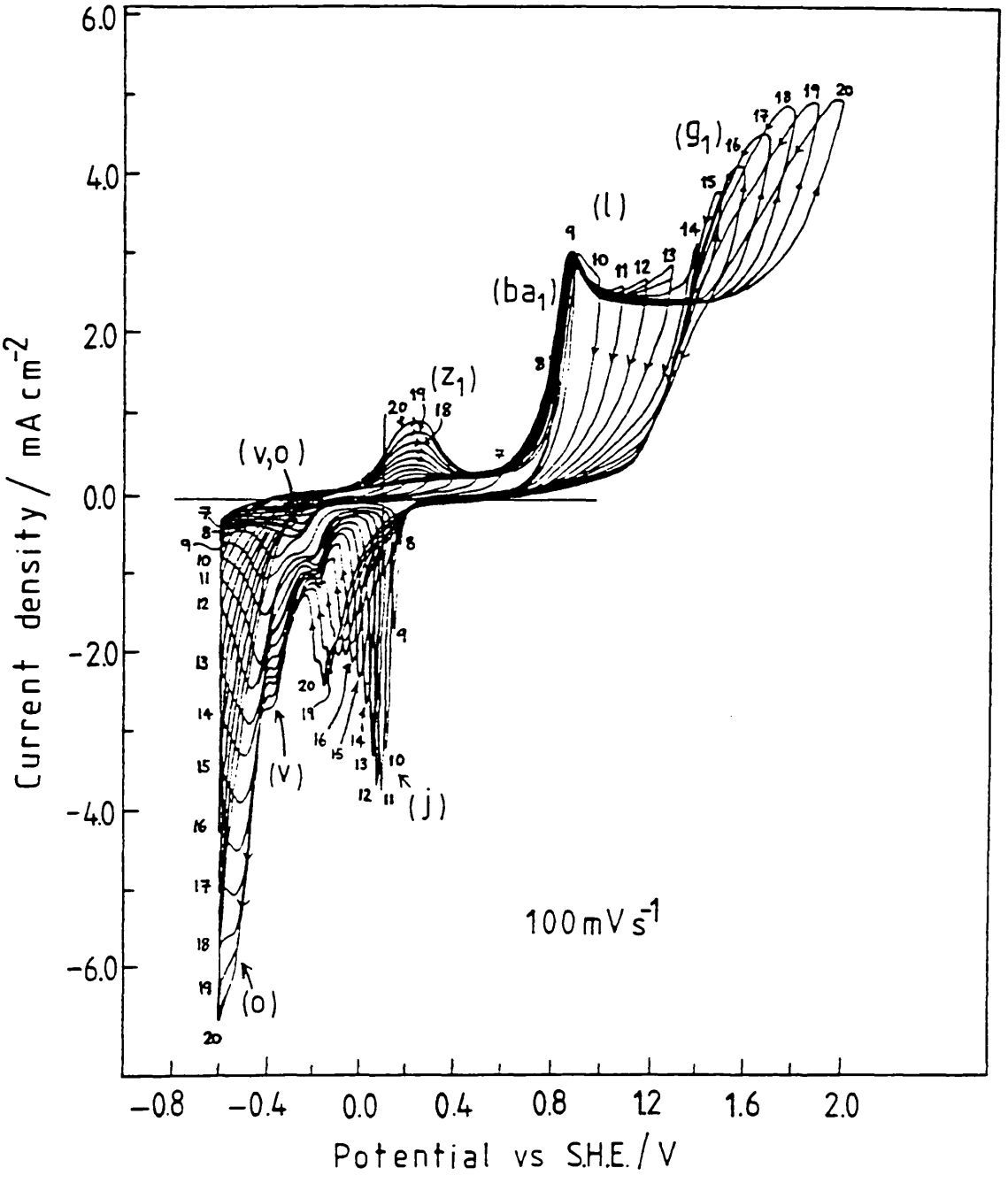


Fig 7.7 The effect of extending the anodic potential scanning limit (E_{λ_a}) on cyclic voltammograms of pyrrhotite at pH 4.6 (0.5 M CH_3COOH + 0.5 M CH_3COONa) in stirred solution and a sweep rate of 100 mV s^{-1}.

reduction of a more hydrated ferric oxide, $Fe(OH)_3$ (reaction (j)). This was formed because sulphate formation lowered the interfacial pH at the mineral electrode so that ferric oxide started to form by dissolution-precipitation, rather than by a solid state mechanism. As

the rate of sulphate formation increased with increasing potential the ferric oxide/sulphur ratio on the surface of pyrrhotite also increased. Thus at E_{λ_a} potentials > 0.6 V, peaks (o) and (v) became distinguishable from one another as the goethite reduction peak (o) shifted to more negative potentials and increased in size more rapidly than the sulphur reduction peak (v).

Eventually a "limiting current" region was reached between 0.9 and 1.3 V in which pyrrhotite oxidation was inhibited by the ferric oxide film formed on its surface, the current at 1.3 V being 25 times lower at pH 4.6 than at pH 0. The limiting current also showed no stirring rate dependence (Figure 7.8), implying that the passivating oxide film had been formed by a solid state reaction and not by dissolution-precipitation (cf pyrite; section 6.4.3). On extending E_{λ_a} to 1.0 V, the charge measured under peaks (j), (v) and (o) was 1.50, 0.99 and 5.65 mC cm^{-2} respectively. Assuming cubic close packing and neglecting roughness factors, this corresponds to 10, 2 and 37 monolayers, respectively. Thus the passivating film consisted mostly of Fe(III) species, with an outer, easily reduced, hydrated $Fe(OH)_3$ layer and an inner, less easily reduced, less hydrated FeOOH layer with a little interspersed sulphur.

At potentials > 1.4 V, the anodic current increased again (Figure 7.7) and there was considerable hysteresis between the current on the forward and reverse scans in this region. The upward trend of the current after the scan was reversed was probably due to the visible growth of hydrated ferric oxide in pits nucleated at the high potential. As the pits expanded, they caused the passive film to breakdown. A shoulder also appeared on peak (o) at -0.3 V (Figure 7.7; scan 13 onwards). This may have been associated with a more reducable ferric oxide, or sulphur reduction occurring via a two-step process (see section 7.3.1, reactions (ay_1) and (az_1)). On the return positive scan an anodic current peak was observed at 0.4 V, which increased when E_{λ_a} was increased above 1.2 V and was slightly decreased by stirring the solution (Figure 7.8). The peak was assigned to the oxidation of stoichiometric FeS (reaction (z_1)) precipitated in the proximity of the electrode (reaction (j_1)) when ferric oxide and sulphur were reduced on the preceding negative-going potential sweep.

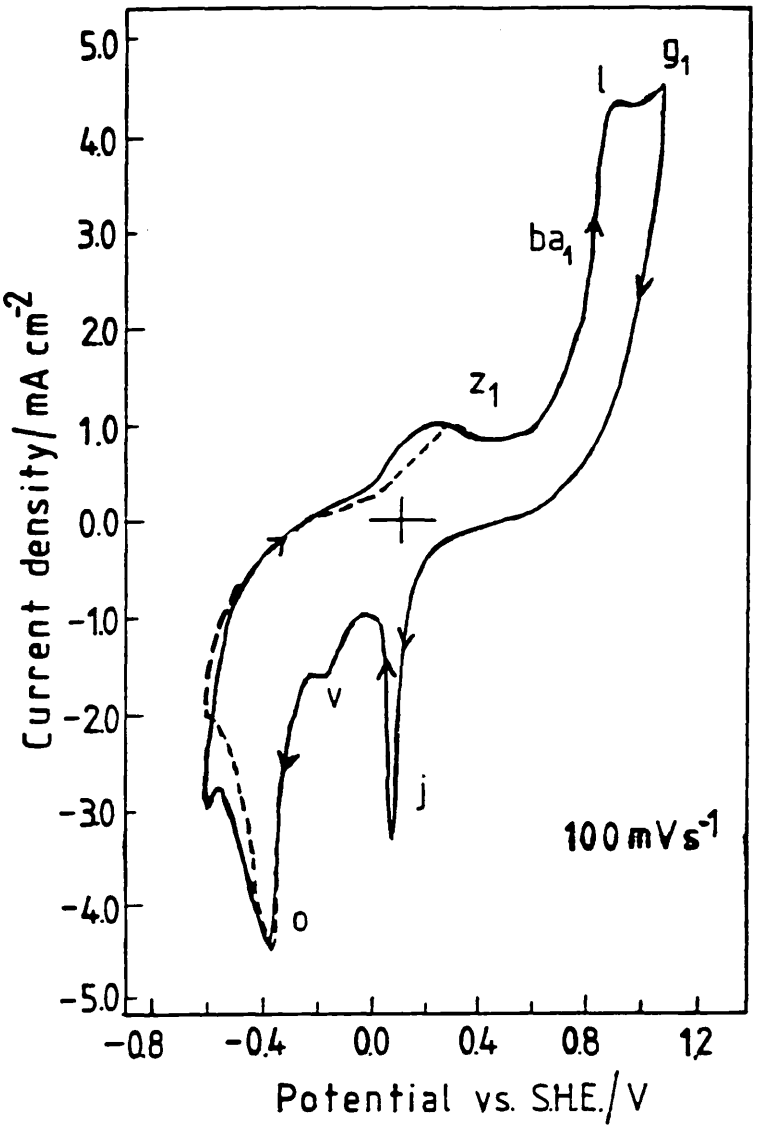


Fig 7.8 The effect of electrode rotation on cyclic voltammograms of a pyrrhotite RSCBE at pH 4.6 (0.5 M CH_3COOH + 0.5 M CH_3COONa) (——) stationary electrode; (---) rotated electrode.

There were two reasons why pyrrhotite was passivated by ferric oxide at pH 4.6 whereas pyrite (see section 6.3.3) and pentlandite (section 8.2.1) were not:-

1. More ferric hydroxide/oxide was formed on pyrrhotite than on the other two minerals because it has a higher iron content: 50 at. %, compared with 33.3 at. % and 26.5 at. % for pyrite and pentlandite respectively.

2. At 0.9 V (the onset of passivation for pyrrhotite), sulphate formation was the dominant anodic reaction on all three minerals. For the sulphate oxidation pathway, the number of moles of H^+ produced per mole of $Fe(OH)_3$ formed was much greater for pyrite and pentlandite, than for pyrrhotite, as shown in Table 7.1.

Table 7.1 Molar $H^+/Fe(OH)_3$ Ratio for Sulphur and Sulphate Formation on Pyrrhotite, Pyrite and Pentlandite

Mineral	$H^+/Fe(OH)_3$ molar ratio	
	Sulphur Formation reactions 1, c, e_2	Sulphate formation reactions g_1, d, f_2
Pyrrhotite	3.0	11
Pyrite	3.0	19
Pentlandite	3.0	17.2

Hence, the interfacial pH was lowered to a greater extent on pyrite and pentlandite than on pyrrhotite, leading to the partial dissolution of any inhibiting goethite layer formed at lower potentials and the oxidation of pyrite and pentlandite by a dissolution-precipitation mechanism.

7.3.3.1 Open-Circuit Decomposition of the Passivating Film

In separate experiments the potential of a pyrrhotite electrode in stirred solution was held potentiostatically at 0.8 V and 1.0 V for 30 seconds to grow the passivating oxide film, then interrupted, and the open-circuit potential monitored as a function of time. When the potential was held in the limiting current region the specularly reflective surface of the pyrrhotite electrode darkened before

a red-brown film of ferric oxide became visible on the surface. On open-circuit the film gradually decomposed/dissolved and the reflective surface was restored. Typical profiles of the open-circuit are shown in Figure 7.9. They were characterised by an arrest in the

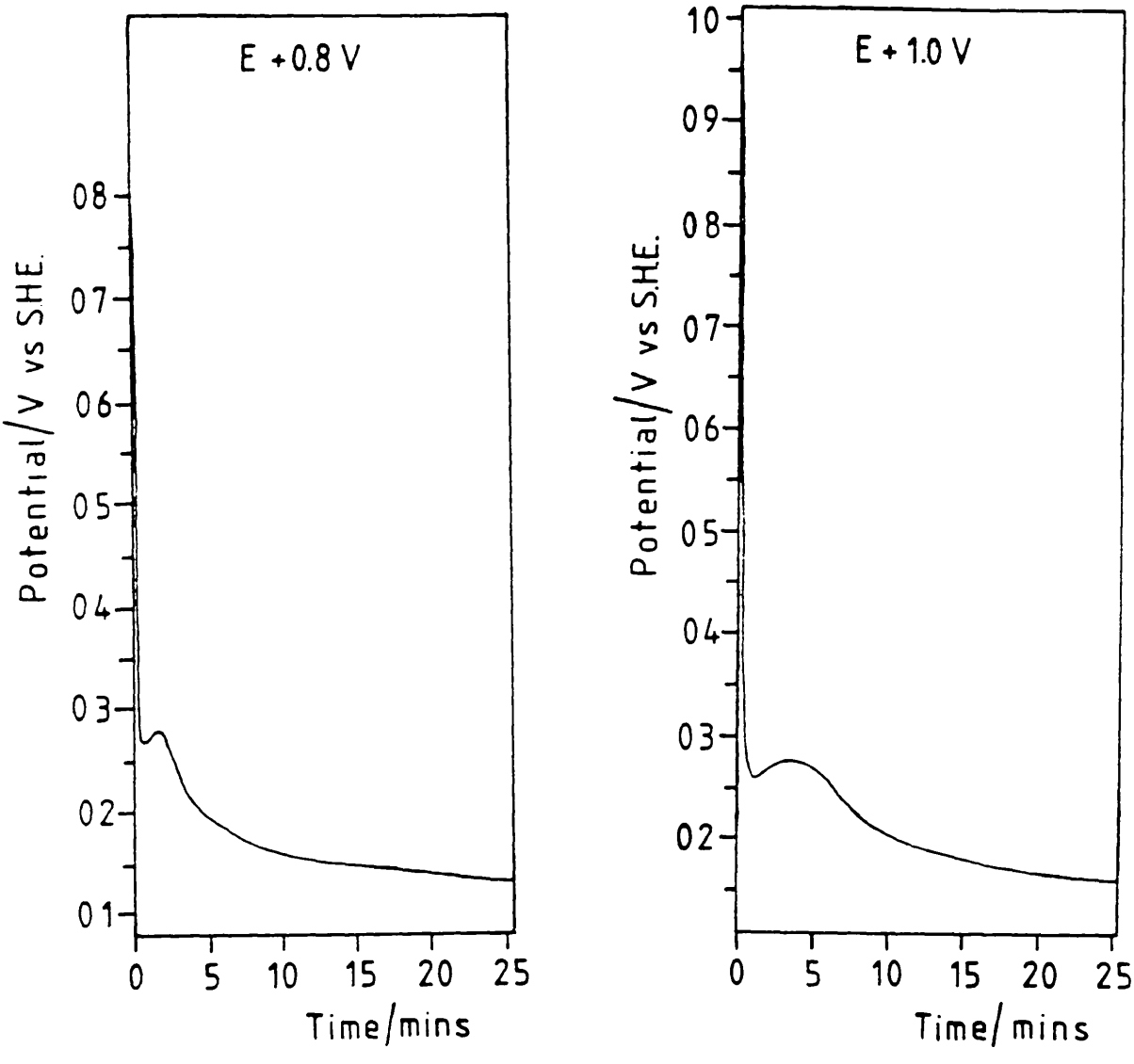


Fig 7.9 The decay of open-circuit potential with time at pH 4.6 (0.5 M CH_3COOH + 0.5 M CH_3COONa) observed after potentiostatting a pyrrhotite electrode to 0.8 V (left) and 1.0 V (right) for 30 s then interrupting the current.

potential decay at ~ 0.27 V as the film started to dissolve. The potential increased by 20 - 30 mV during this stage before undergoing another sharp fall once dissolution was complete.

The potential arrest at 0.27 V was probably due to a mixed potential mechanism being established between the anodic oxidation of pyrrhotite according to reaction (e_1):-

$$FeS = Fe^{2+} + S + 2e \qquad (e_1)$$

$$E = 0.078 + 0.0295 \log [Fe^{2+}]$$

and the cathodic reduction of the passivating oxide film by reactions (j) and (o):-

$$Fe(OH)_3 + 3H^+ + e = Fe^{2+} + 3H_2O \qquad (j)$$

$$E = 1.056 - 0.177\ pH - 0.059 \log [Fe^{2+}]$$

$$FeOOH + 3H^+ + e = Fe^{2+} + 2H_2O \qquad (o)$$

$$E = 0.715 - 0.177\ pH - 0.059 \log [Fe^{2+}]$$

with the underlying FeS surface acting as a reductant by solution contact through pores in the oxide film.

Assuming the Fe^{2+} concentration was 10^{-6} mol dm^{-3}, then the reversible electrode potentials at pH 4.6 for reactions (e_1) and (j) are -0.099 V and 0.596 V, respectively. Thus, the "corrosion" potential established between 0.27 and 0.29 V provided a negative overpotential for the cathodic reaction (j) and a positive overpotential for the anodic reaction (e_1).

Under the above conditions, the corrosion potential appeared to provide no driving force for the cathodic reaction (o) ($E_{(reaction(o))}$ = 0.255 V). However, assuming sulphate formation (reactions (g_1) and (ba_1)) lowered the interfacial pH at the pyrrhotite electrode during oxide growth by 0.5 - 1.0 pH units only (see section 7.3.3), the local decrease in pH in the pores of the film would have been sufficient to shift the equilibrium potential for reaction (o) to potentials

positive of the corrosion potential. Thus reaction (o) probably occurred albeit at a slower rate than reaction (j).

There was evidence for this in Figure 7.10 where the potential of a

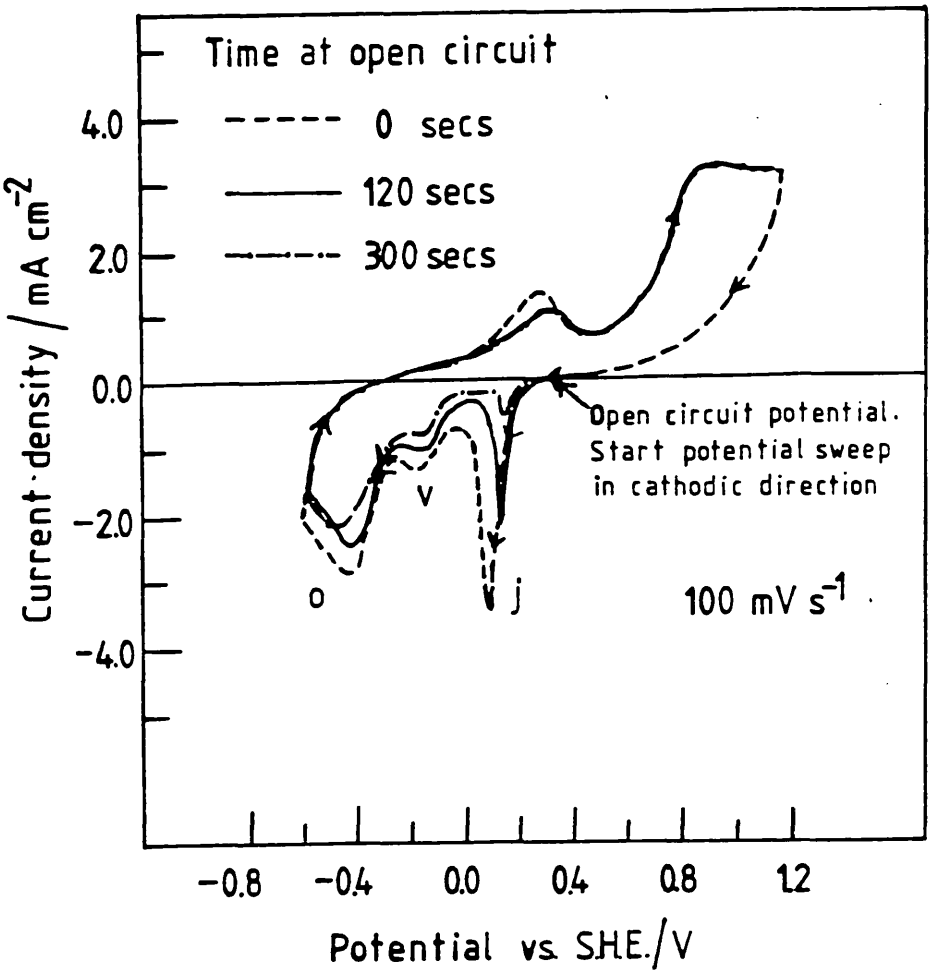


Fig 7.10 Cyclic voltammograms of a stationary pyrrhotite electrode in stirred solution at pH 4.6 (0.5 M CH_3COOH + 0.5 M CH_3COONa), sweeping the potential cathodically from the open-circuit potential (E_{oc}); attained after pulsing the potential anodically to 1.2 V for 10 seconds and then leaving the electrode at open-circuit for (---) 0 s, (——) 120 s, and (-•-•-) 300 s.

stationary pyrrhotite electrode in stirred solution was pulsed to 1.2 V for 10 seconds, and then interrupted. The electrode was then left at open-circuit for a given time interval (0, 2 and 5 minutes) before

sweeping the electrode potential in a negative direction from the E_{oc} value acquired after that time. The cathodic charge under peaks (j) and (o) decreased as the time at open circuit was increased; the reduction in peak height being greater for $Fe(OH)_3$ (peak (j)) than for FeOOH (peak (o)). Peak (v), assigned to sulphur reduction, also appeared to decrease in height with time at open circuit. However, it was difficult to ascertain whether this was a real effect since peak (v) appeared as a shoulder on peak (o). Hence goethite dissolution may account for the apparent decrease in the height of peak (v).

7.3.3.2 Pyrrhotite RSCBE Results

Figure 7.11 shows the current-time response of a pyrrhotite RSCBE to potential cycling in pH 4.6 buffer solution. No soluble iron species were detected at the platinum collector electrode when the potential of the mineral electrode was swept in a positive direction. On the reverse negative-going scan, the ferric oxide/hydroxide species formed anodically were reduced to Fe^{2+} (peaks (j) and (o) respectively). The Fe^{2+} formed was oxidised at the collector electrode using a potential of 1.0 V. At 1.4 V, where H_2S is oxidised on Pt, oxygen evolution reduced the collector efficiency and consequently the detection currents, as shown in Figure 7.10. Therefore it was not possible to ascertain from these results whether the shoulder at -0.220 V was due to sulphur reduction (reaction (v)) or ferric oxide/hydroxide reduction.

7.3.4 Voltammetry in Neutral and Basic Solutions

The limiting anodic current observed in voltammograms recorded at pH 4.6 was also present in stirred solutions at pH 7 (Figure 7.12) and 9.2 (Figure 7.13). At pH 13 (Figure 7.14), an anodic peak was observed rather than a limiting current as the passivating effect of the oxide layer increased with increasing pH. At pH 7 and 9.2 the ferric oxide/hydroxide layer was difficult to remove by cathodic treatment due to the low solubility of ferrous ions in alkaline solutions (reaction (p_1) see Figure II(vii), Appendix II). Thus pyrrhotite oxidation was inhibited on subsequent positive

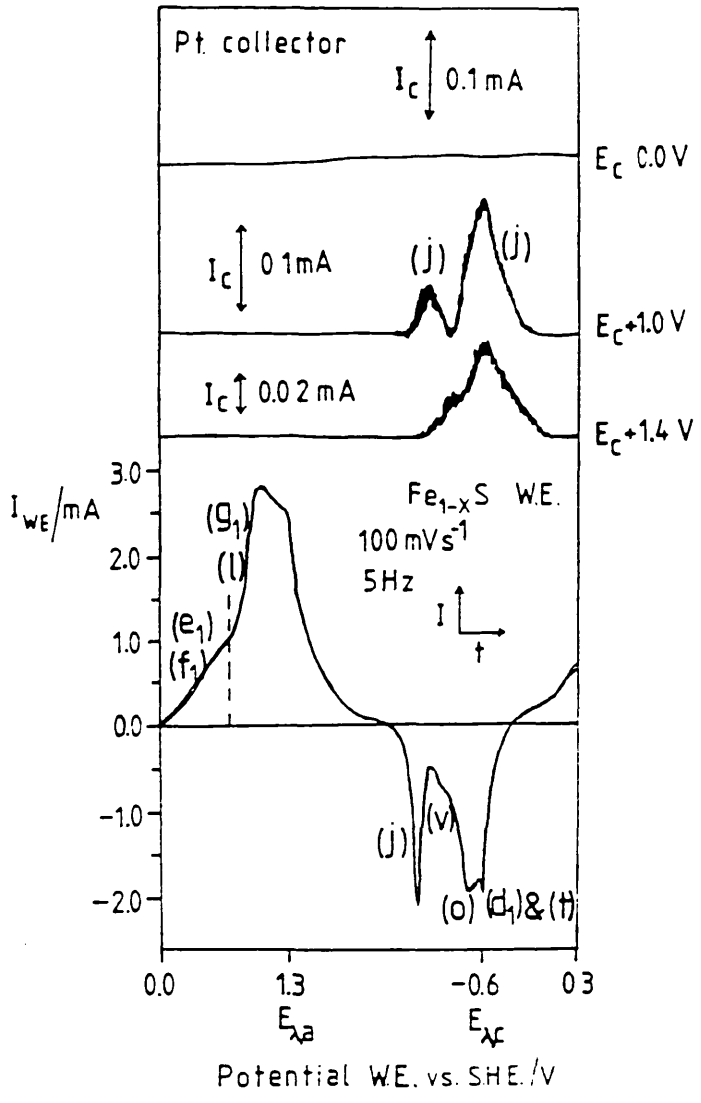


Fig 7.11 Cyclic voltammogram of a RSCBE in 0.5 M CH_3COOH + 0.5 M CH_3COONa (pH 4.6), with the pyrrhotite working electrode (WE) swept anodically from 0.0 to 1.3 V, then cathodically to -0.6 V, and the platinum collector electrode held at various potentials (E_c).

potential sweeps and the anodic current shifted to more positive potentials; the effect being greater at pH 9.2 than at pH 7. At pH 13 and $E_{\lambda a}$ values > 0.6 V an anodic peak was observed at 0.4 V on the

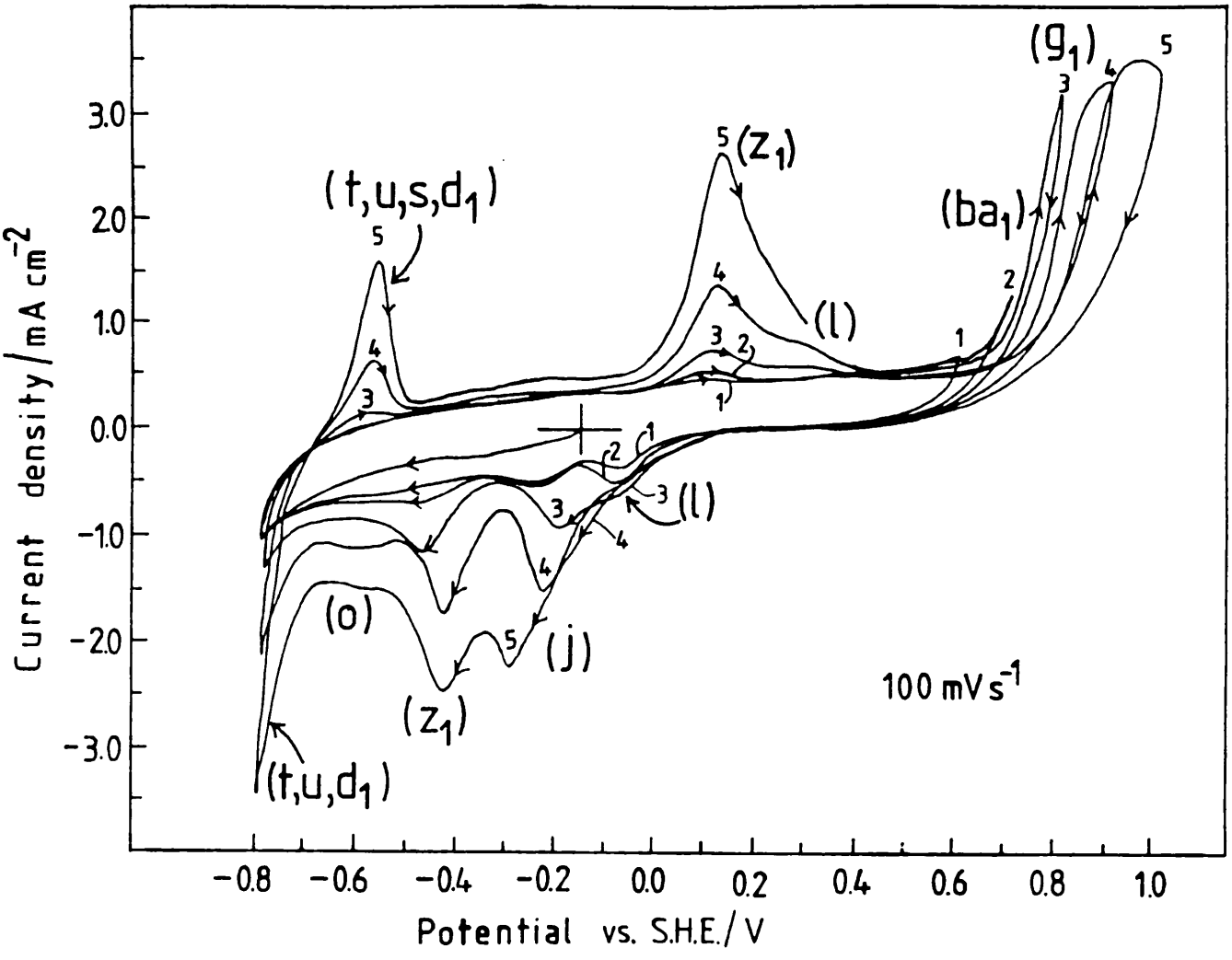


Fig 7.12 The effect of extending the anodic potential scanning limit (E_{λ_a}) on cyclic voltammograms of pyrrhotite at pH 7 (0.025 M KH_2PO_4 + 0.025 M Na_2HPO_4) in stirred solution and a sweep rate of 100 mV s^{-1}.

reverse negative-going potential sweep. This probably reflected a transformation in the solid state properties of the oxide film from, an electronic conductor in the passive state, to an electrical insulator in the pre-passive region [340].

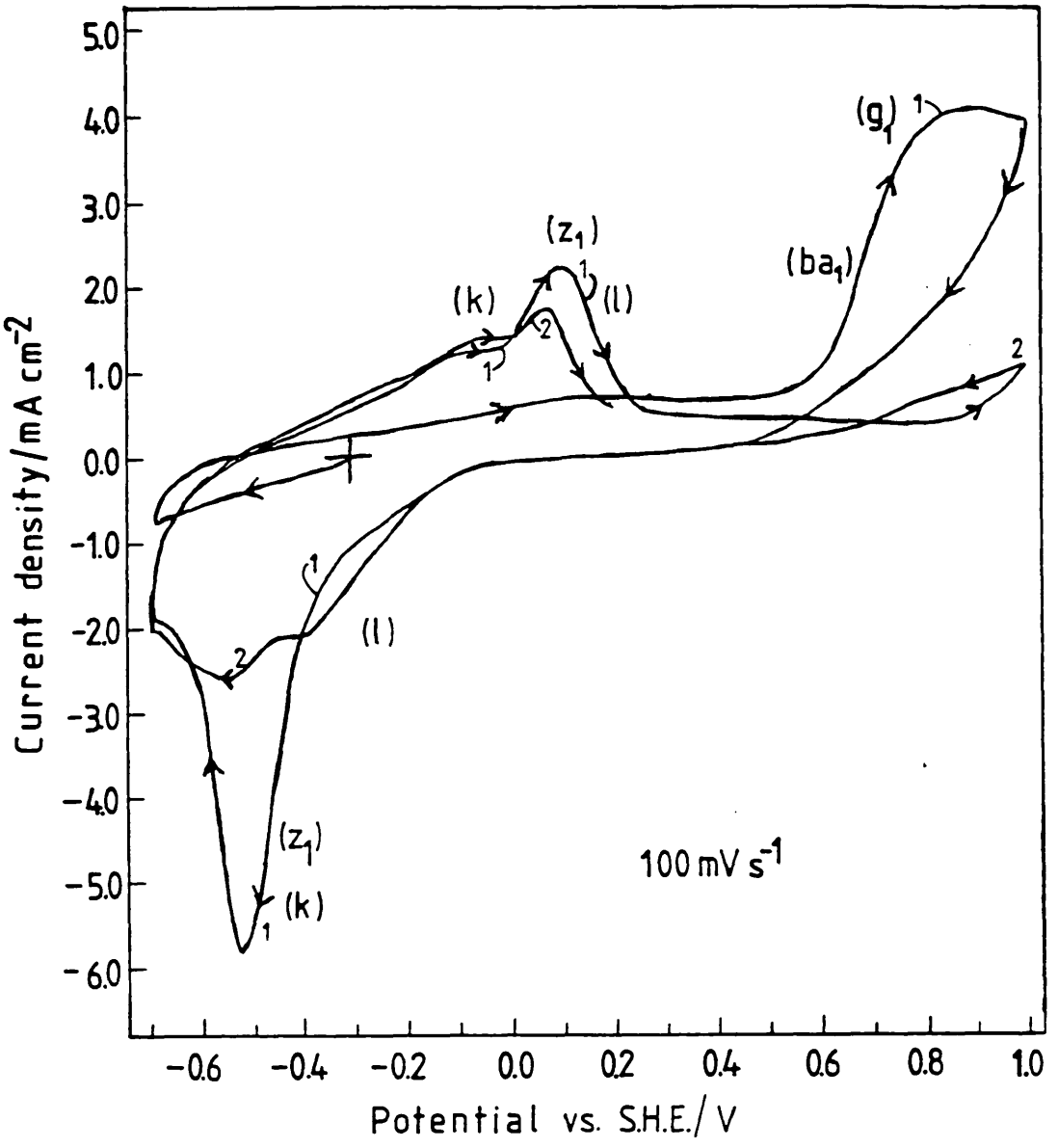


Fig 7.13 The effect of repetitive cycling between 1.0 and -0.7 V at 100 mV s^{-1} on the voltammetric behaviour of a stationary pyrrhotite electrode in stirred solution at pH 9.2 (0.05 M $Na_2B_4O_7$).

Stirring the solution had no effect on current-potential profiles and no soluble reaction products were observed in RSCBE experiments which suggested that all the oxidation reduction reactions involved solid species. Assuming FeS formed in preference to HS^-, when ferric

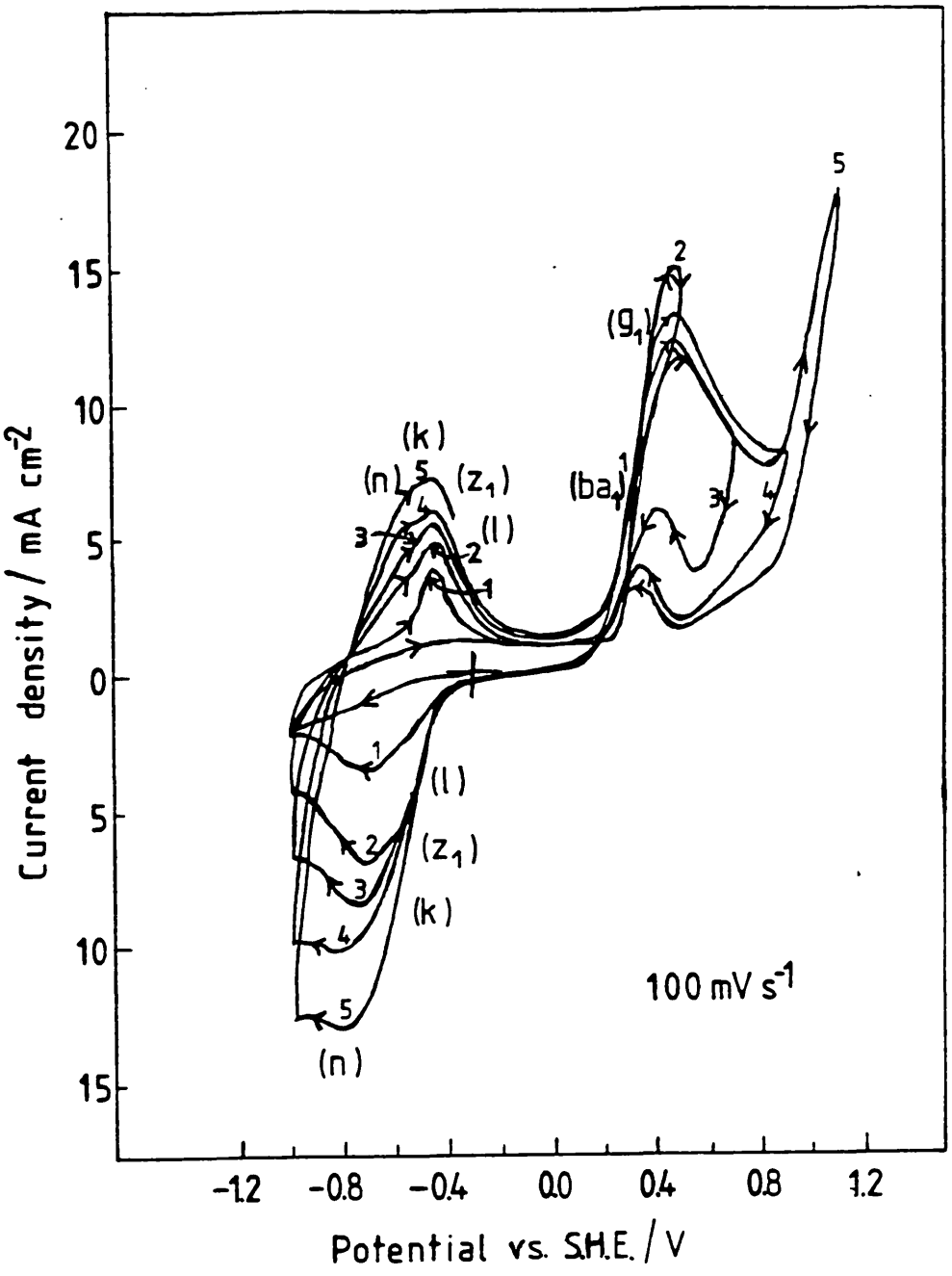


Fig 7.14 The effect of extending the anodic potential scanning limit (E_{λ_a}) on cyclic voltammograms of pyrrhotite at pH 13 (0.1 M NaOH) in stirred solution and a sweep rate of 100 mV s^{-1}.

oxide and sulphur were reduced in neutral and basic solutions, and that the ratio of ferric oxide/sulphur on the surface was > 1, due to the predominance of anodic sulphate formation, then the reduction of ferric oxide/hydroxide and sulphur probably occurred by reactions (l), (z_1), (j) and (o) at pH 7 and by reactions (l), (z_1) and (k) at pH 9.2 and 13. These reactions occur at similar potentials in basic solutions and therefore could only be assigned tentatively to the

voltammetric peaks in Figures 7.12 to 7.14. However, it appeared that the cathodic peak assigned to FeS formation (reaction (z_1)), on the second and subsequent negative-going potential sweeps, was larger on pyrrhotite than on pyrite. This was due to less sulphate being formed on pyrrhotite, hence the interfacial pH at the surface of pyrrhotite was higher, which favoured the precipitation/formation of FeS.

7.4 Pulse Voltammetry on Stationary Pyrrhotite Electrodes

7.4.1 pH 0 (1 M $HClO_4$)

There was no evidence of rising current-time transients at short times, under mildly oxidising conditions as there was for pyrite. However, like pyrite, rising transients were observed at high anodic overpotentials (> 0.9 V vs. S.H.E., see Figure 7.15).

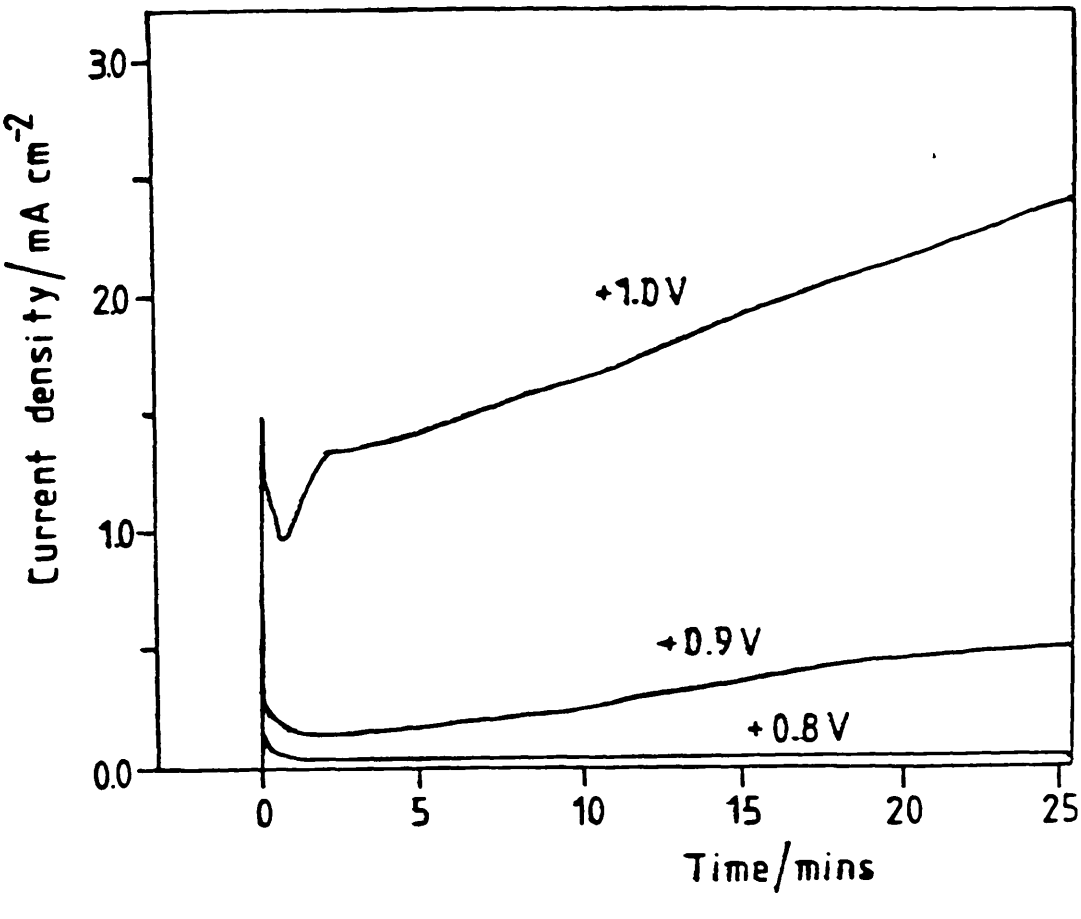


Fig 7.15 Current-time transients for a stationary pyrrhotite electrode held at various anodic potentials in stirred solution at pH 0 (1 M $HClO_4$).

At each of the potentials shown in Figure 7.15, the falling current transients were best fitted to an i vs t^{-1} relationship, characteristic of an adsorption (sulphur growth) type process. At 0.9 V the current passed through a minimum after ~ 250 s, reached in shorter times with higher potentials, before increasing with $t^{1.5}$ as sulphur grew in 3-dimensional pits nucleated in the falling current transient region (Figure 7.16). At potentials $\geq$ 1.0 V a second

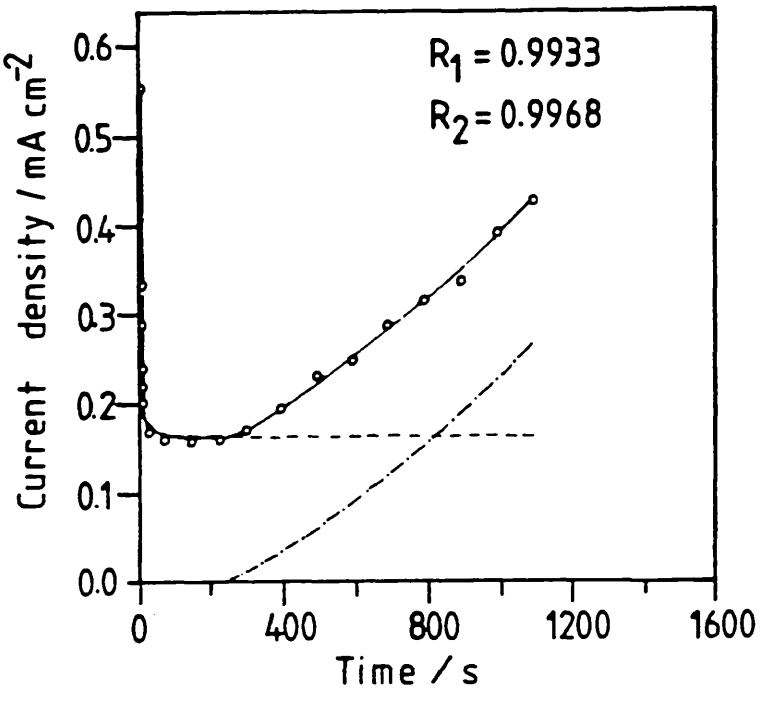


Fig 7.16 Current-time transient for a stationary pyrrhotite electrode held at 0.9 V in stirred solution at pH 0 (1 M $HClO_4$). (---) i vs t^{-1}; (-•-•-•-) i vs $t^{1.5}$;
R_1 = correlation coefficient for the i vs t^{-1} relationship;
R_2 = correlation coefficient for the i vs $t^{1.5}$ relationship.

minimum was observed in current transients due to the overlap of growing pits. After these experiments were completed, sulphur was clearly visible on the surface of each electrode (see plate 7.1). The sulphur had a reddish colouration in regions where dissolving ferric ions were diffusing through the sulphur barrier.

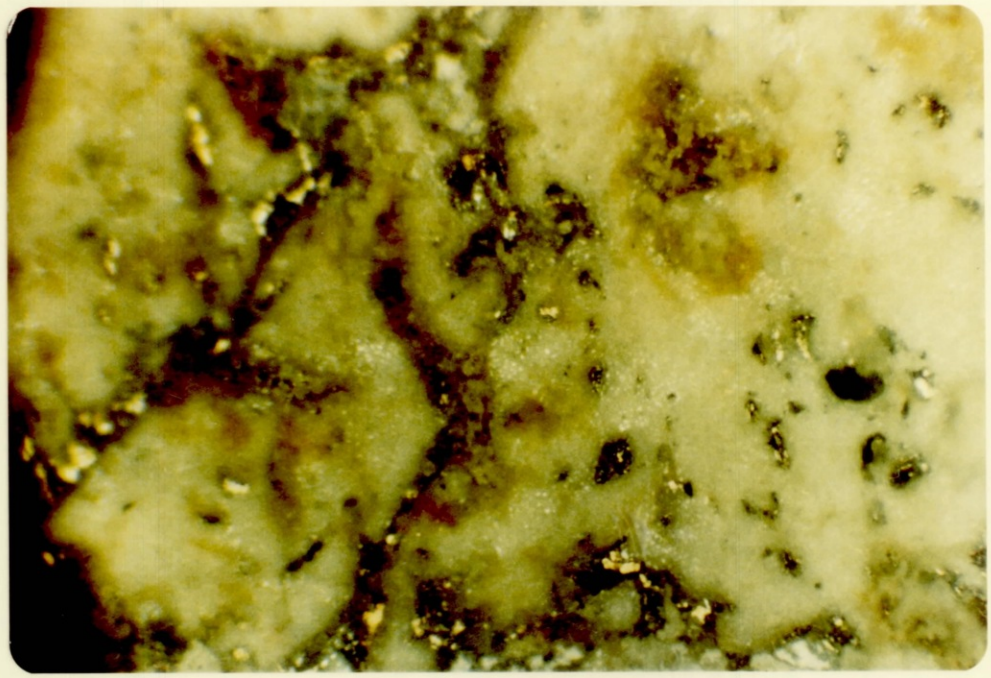


Plate 7.1 Optical photomicrograph of a pyrrhotite electrode after oxidation at 1.1 V (vs. S.H.E.) for 1500 s in 1 M $HClO_4$.

7.4.2 pH 4.6 (0.5 M CH_3COOH + 0.5 M CH_3COONa) and pH 9.2 0.05 M $Na_2B_4O_7$)

At pH 4.6 in the potential range 0.5 to 1.3 V, at which a ferric oxide film forms on the surface of pyrrhotite (see section 7.3.3), only falling current transients were observed (Figure 7.17). These decayed according to an i vs $t^{-0.5}$ relationship (Figure 7.18), which suggests that diffusion through the passive oxide film limited the current. At potentials > 1.4 V the breakdown of the passive film by pitting lead to rising current transients after a long induction period (400 s, 40 mC cm^{-2}), during which time pits nucleated and grew and the current decayed with t^{-1}. Similar behaviour was observed at pH 9.2 (0.05 M $Na_2B_4O_7$).

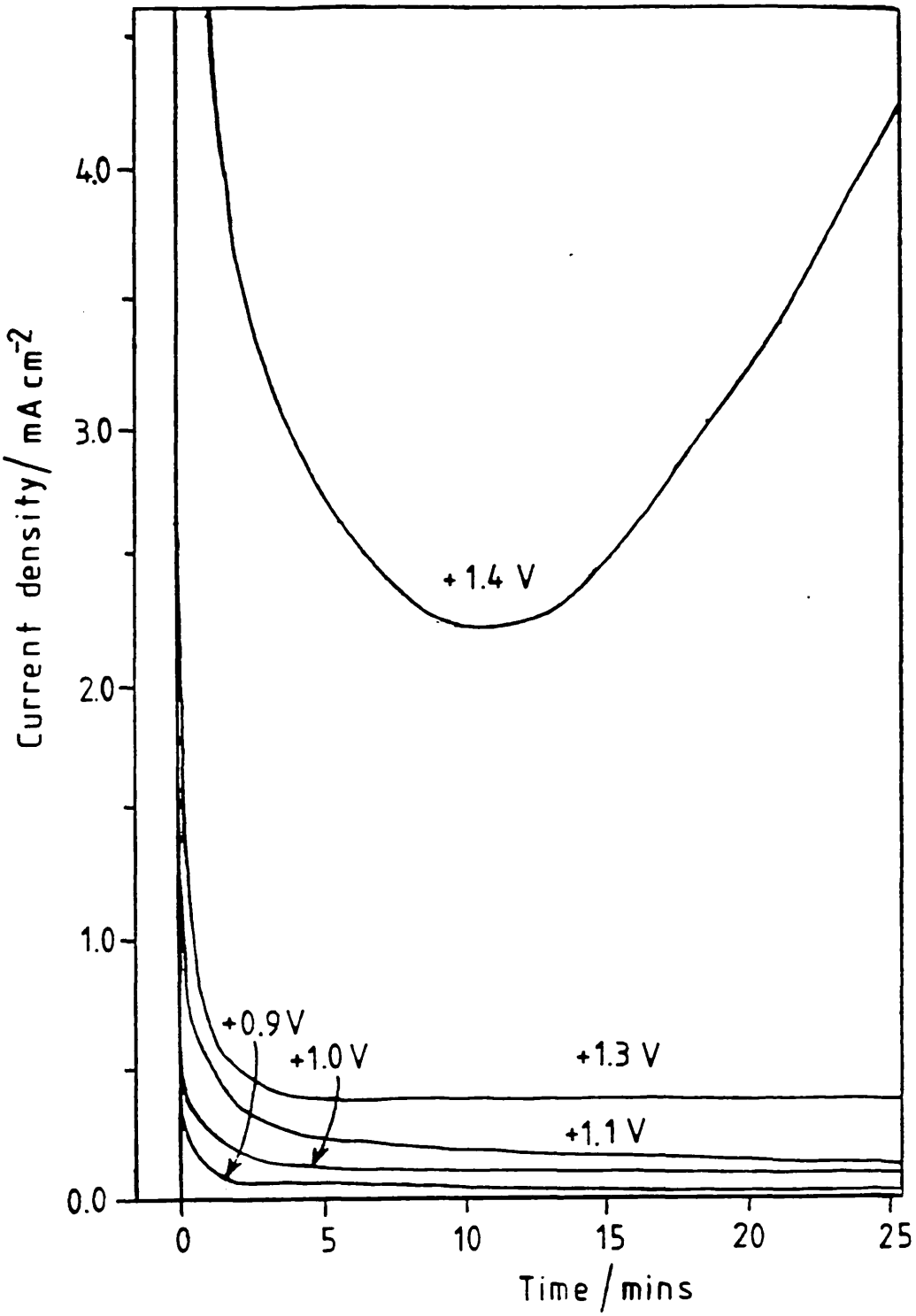


Fig 7.17 Current-time transients for a stationary pyrrhotite electrode held at various anodic potentials in stirred solution at pH 4.6 (0.5 M CH_3COOH + 0.5 M CH_3COONa).

7.4.3 pH 13 (0.1 M NaOH)

At pH 13 the response differed from that observed at pH 4.6 and 9.2. In the prepassive region (0.1 to 0.4 V at pH 13), where the current

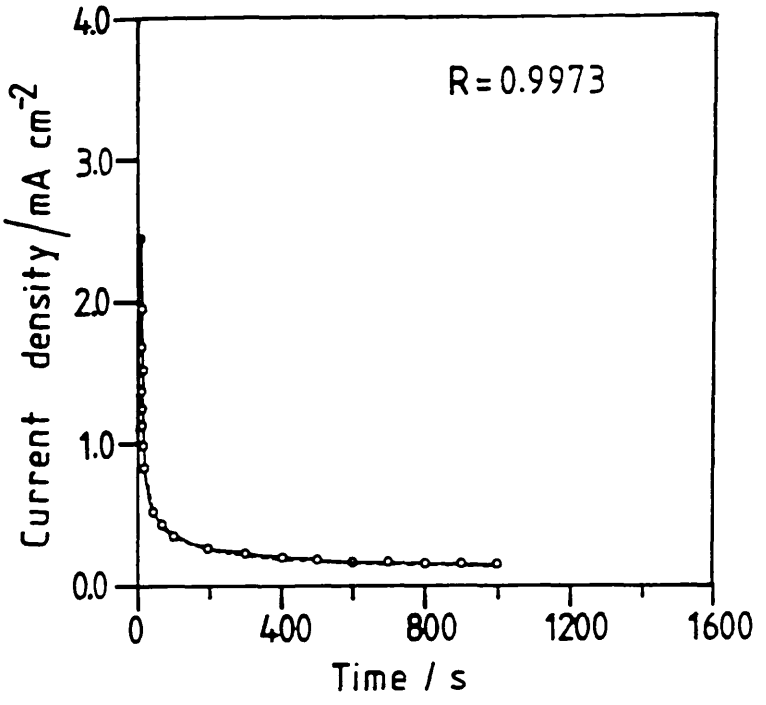


Fig 7.18 Current-time transient for a stationary pyrrhotite electrode held at 1.1 V in stirred solution at pH 4.6 (0.5 M CH_3COOH + 0.5 M CH_3COONa). (---) i vs $t^{-0.5}$;
R = correlation coefficient.

was found to increase rapidly in cyclic voltammetry experiments (see section 7.3.4, Figure 7.14), rising current transients were observed (Figure 7.19). At pH 4.6 and 9.2, the current only decayed with time in this region (e.g. between 0.5 and 0.9 V at pH 4.6). In the passive region (0.4 to 1.0 V at pH 13) falling transients were observed, as at pH 4.6 and 9.2, closely fitting an i vs $t^{-0.5}$ relationship, but over a much longer period of time (1500 s, see Figure 7.20).

7.4.4 Charge vs Time Measurements

Log charge (q) vs potential plots for stationary pyrrhotite electrodes in stirred solutions after 1500 seconds are shown in Figure 7.21 as a function of pH. At pH 0, log q increased linearly with potential (120 mV per decade) and there was no evidence of sulphur inhibiting the oxidative processes. Plateaux in the log q versus potential plots at

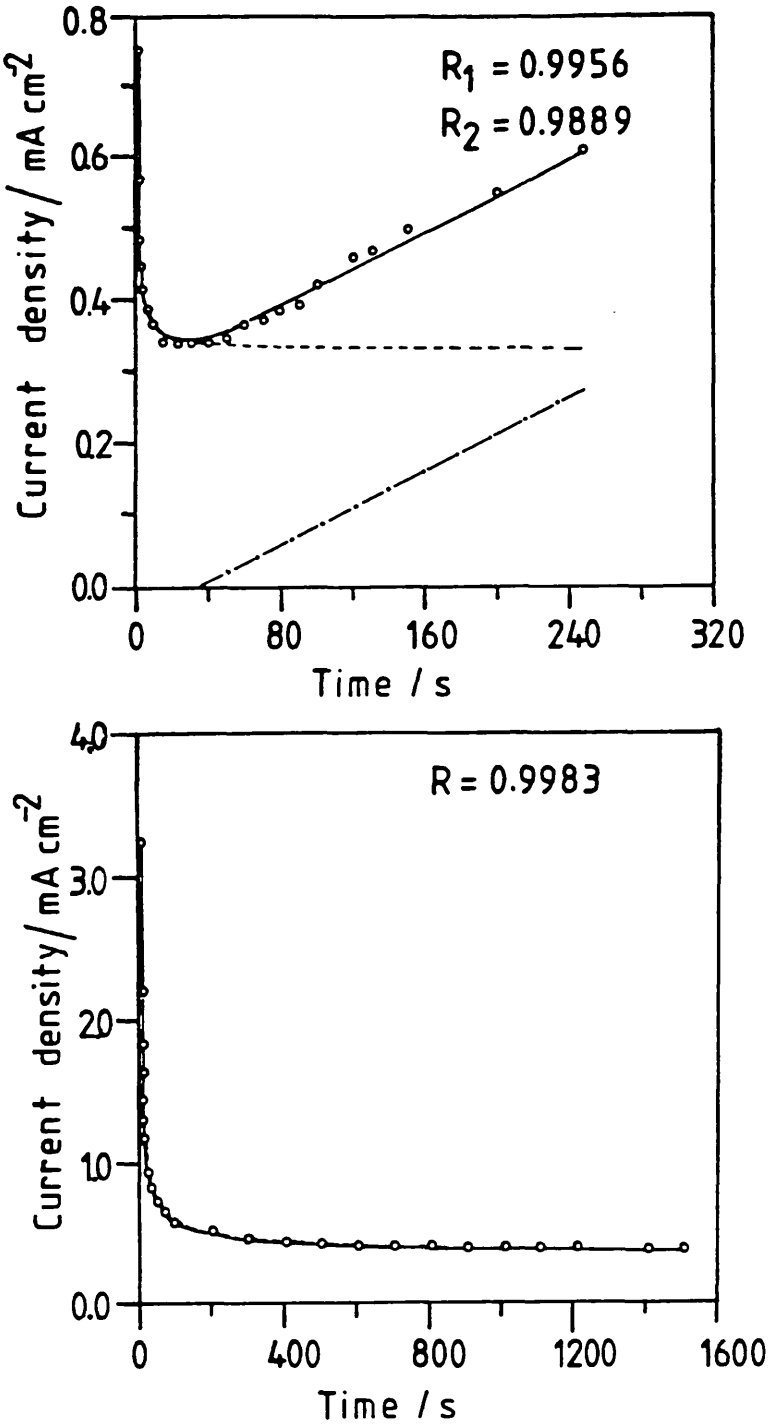


Fig 7.19 (top) Current-time transient for a stationary pyrrhotite electrode held at 0.150 V in stirred solution at pH 13 (0.1 M NaOH). (---) i vs t^{-1}; (-•-•-) i vs t;
R_1 = correlation coefficient for the i vs t^{-1} relationship;
R_2 = correlation coefficient for the i vs t relationship.

Fig 7.20 (bottom) Current-time transient for a stationary pyrrhotite electrode held at 0.6 V in stirred solution at pH 13 (0.1 M NaOH) (---) i vs $t^{-0.5}$; R = correlation coefficient.

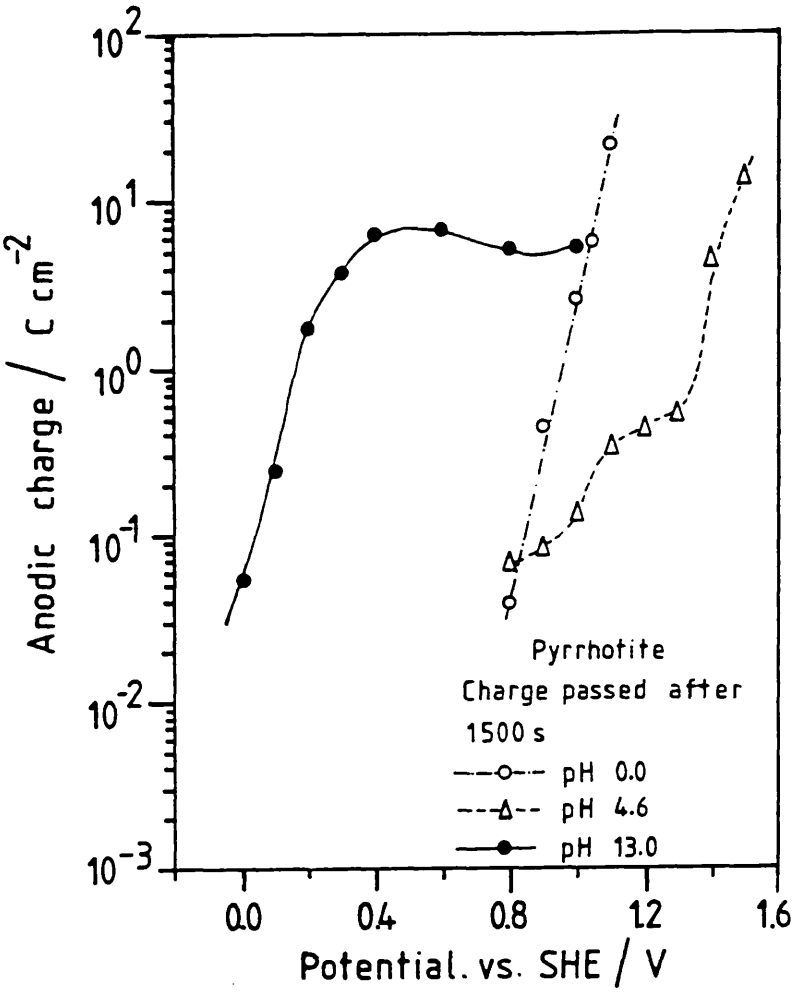


Fig 7.21 Anodic charge passed after 1500 s for a pyrrhotite electrode as a function of potential and pH.

pH 4.6 and 13 characterised the potential regions in which pyrrhotite oxidation was inhibited by ferric oxide film formation, the width of the plateau increasing with increasing pH. The amount of charge passed before passivation occurred was much greater at pH 13 than at 4.6, because sulphate formation, which has a higher charge requirement than sulphur formation, was more dominant at the former pH value.

7.5 Impedance Measurements on Stationary Pyrrhotite Electrodes

Unlike pyrite, ac impedance measurements on pyrrhotite electrodes did not reveal a small high frequency capacitive semicircle associated

with a possible space charge layer (see sections 6.6 and 6.7). The impedance diagrams for pyrrhotite were characterised by a single, slightly distorted, depressed capacitive semicircle at all the pH values studied (pH 0, 4.6 and 9.2), the diameter generally decreasing with increasing potential. The impedance dispersion, caused by the overlapping of one or more capacitive semicircles of slightly different time constants, was more pronounced on pyrrhotite than on pyrite. More specifically, it prevented any meaningful quantitative evalution of equivalent circuit parameters using customary graphical methods. The high frequency, real axis intercept was the only parameter that could be ascertained from the impedance spectra with any real certainty. Since the uncompensated solution resistance (R_u) gave a direct measure of the changes in ohmic resistance (R_f) incurred when sulphur and ferric oxide films were formed on the electrode surface.

Figure 7.22 compares the values of R_f obtained from impedance spectra at pH 0, 4.6 and 9.2 as a function of electrode potential. In comparison with pyrite, the R_f values for pyrrhotite were found to vary quite noticeably with potential.

At pH 0, R_f was negligible (< 0.2 Ω cm^2) at potentials < 1.1 V, but increased with increasing potential to 15 Ω cm^2 at 1.4 V, as a resistive, porous layer of elemental sulphur was formed on the electrode surface. In contrast, R_f was negligible on pyrite in the potential range 0.45 to 1.5 V (see section 6.6, Figure 6.56), which emphasises the dominance of sulphate formation on pyrite.

At pH 4.6 the resistance increased from 2 Ω cm^2 at 0.6 V to ~ 10 Ω cm^2 in the current limiting region between 0.8 and 1.4 V. This increase in R_f was attributed to the passivating ferric oxide/hydroxide/sulphur film formed in this potential region. Above 1.4 V, breakdown of the passive film was marked by a decrease in R_f.

The R_f values at pH 9.2 were much higher (> 14 Ω cm^2), which reflected the decrease in solubility and increased thickness of the ferric oxide

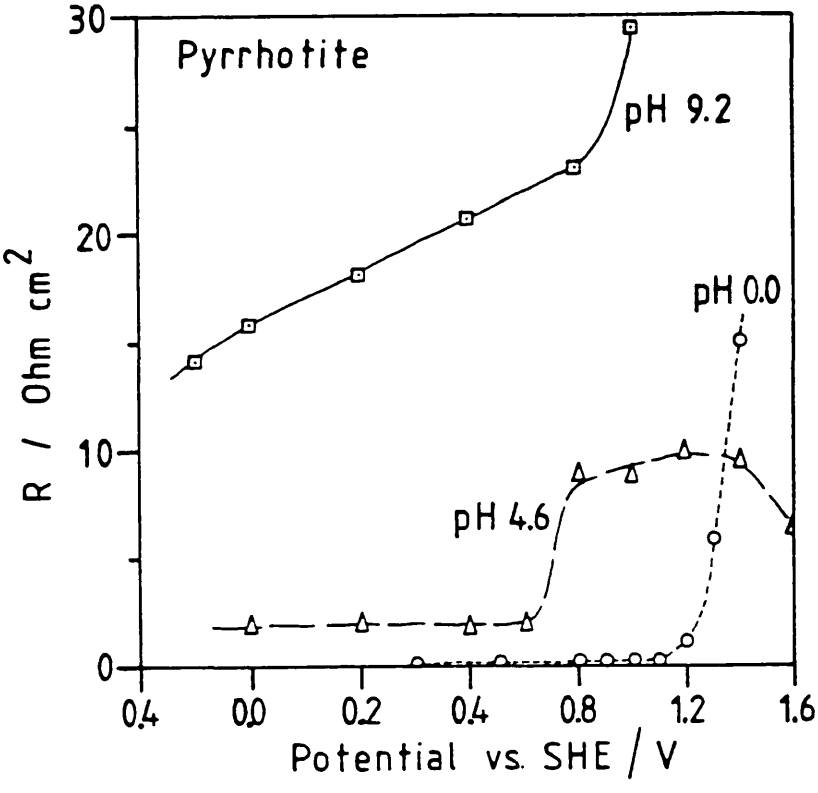
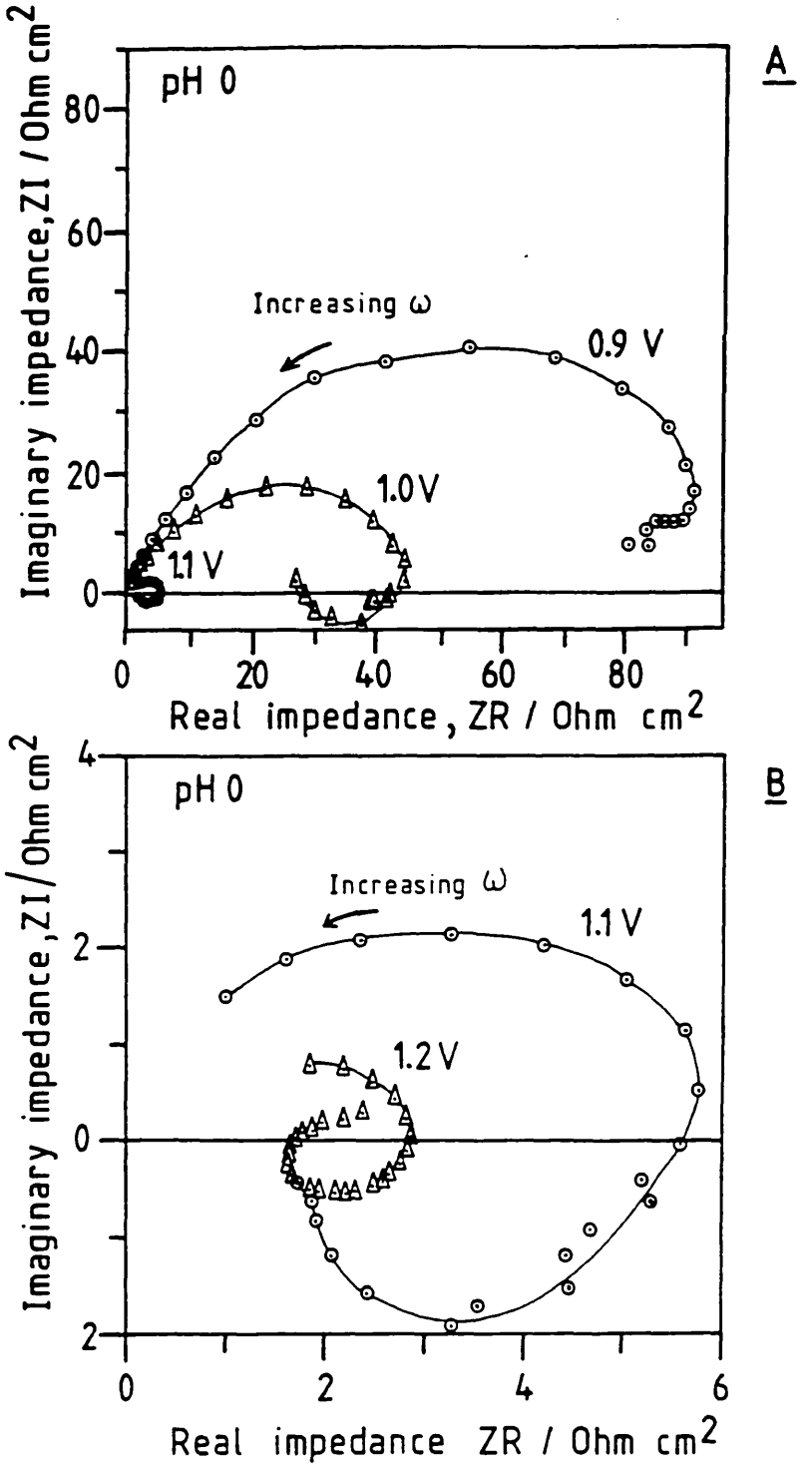


Fig 7.22 Real axis, high frequency intercept resistance, R (equivalent to the surface film resistance, R_f), for pyrrhotite at pH 0, 4.6 and 9.2, plotted as a function of potential.

film in basic solutions. As passivation increased above 0.4 V (see section 7.3.4, Figure 7.13) the value of R_f also increased.

The impedance spectra of stationary pyrrhotite electrodes in stirred deoxygenated solutions at pH 0, 4.6 and 9.2 are presented in Figures 7.23 - 7.25 as a function of electrode potential. The following points are of significance:-

1. At pH 0 a low frequency inductive loop appeared at potentials > 0.9 V. This probably originated from the potential dependence of the surface coverage by adsorbed sulphur and/or sulphur-oxygen intermediates in the formation of sulphate (Figure 7.23).



7.23 Impedance spectra (0.1 Hz - 10 kHz) for a stationary pyrrhotite electrode in stirred solution at pH 0 (1 M $HClO_4$). A) 0.9 to 1.1 V; B) 1.1 and 1.2 V.

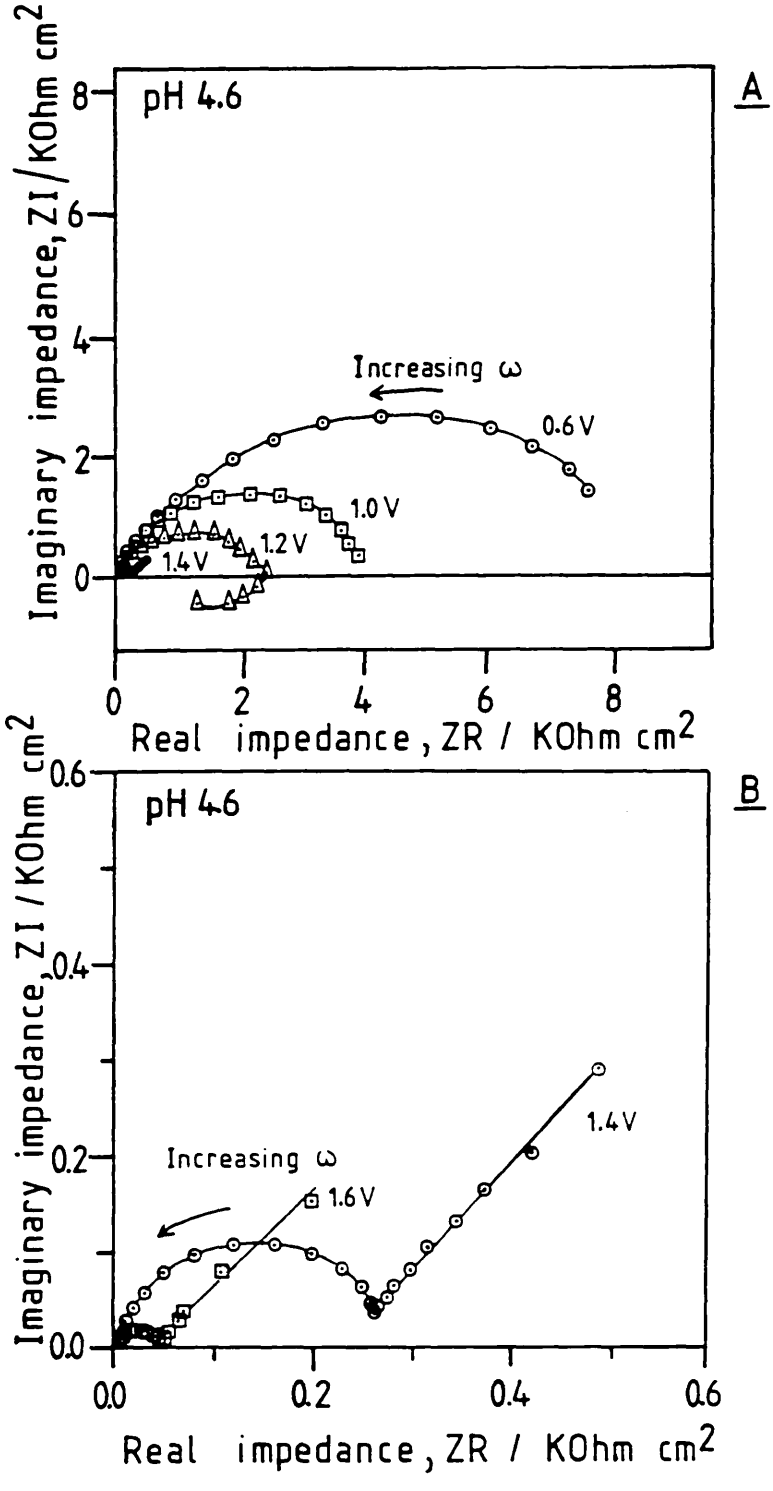


Fig 7.24 Impedance spectra (0.1 Hz - 10 kHz) for a stationary pyrrhotite electrode in stirred solution at pH 4.6 (0.5 M CH_3COOH + 0.5 M CH_3COONa). A) 0.6 to 1.4 V; B) 1.4 and 1.6 V.

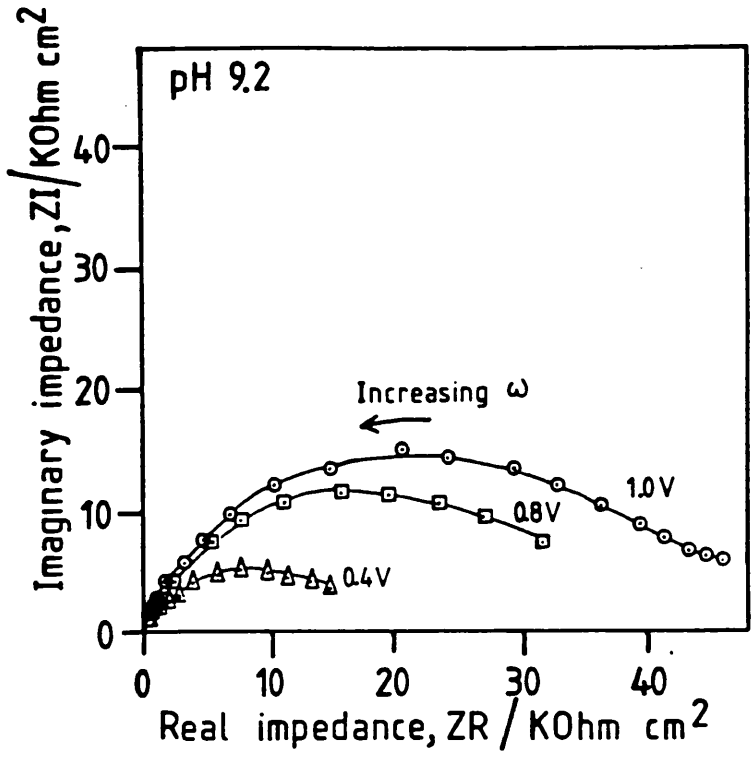


Fig 7.25 Impedance spectra (0.1 Hz - 10 kHz) for a stationary pyrrhotite electrode in stirred solution at pH 9.2 (0.05 M $Na_2B_4O_7$).

2. In the limiting current region at pH 4.6 (see section 7.3.3), a low frequency inductive loop was observed at 1.2 V (Figure 7.24 A). However, once the passive film began to break up as a result of pitting at potentials > 1.4, the impedance spectra were characterised by the appearance of a low frequency Warburg impedance line (Figure 7.24 B). This was interpreted as being due to pyrrhotite oxidation becoming diffusion limited in the pits or pores.

3. At pH 9.2 the charge transfer resistence (diameter of the semicircles) increased as the electrode potential was increased above 0.4 V (Figure 7.25). This signified an increase in the passivation of pyrrhotite by ferric oxide (see section 7.3.4).

CHAPTER EIGHT

ELECTROCHEMICAL STUDIES ON PENTLANDITE ELECTRODES

CHAPTER EIGHT : ELECTROCHEMICAL STUDIES ON PENTLANDITE ELECTRODES

8.1 Thermodynamics

Free energy of formation values for iron-nickel sulphides are not available in collections of reliable thermodynamic data. Craig[368] obtained a ΔG°_f value for violarite ($FeNi_2S_4$) of -319.66 kJ mol^{-1} by extrapolating high temperature thermodynamic data back to 298 K. However, Young[373] critically assessed the evaluation of free energies by the method adopted by Craig and claimed that the accuracy was "at best" ± 42 kJ. Melling[374] considered the effect of such an error in the free energy value of violarite on its stability domain in the Fe-Ni-S-H_2O diagram. He found that there was a large effect on the stability of violarite with respect to pH and reducing conditions. However, under oxidising conditions the effect on stability was much smaller, the main contribution to the overall free energy change coming from sulphate rather than violarite.

Sajek[369] estimated a theoretical ΔG°_f for pentlandite at 298 K by extrapolating high temperature data for the reaction:-

$$Fe_{4.5}Ni_{4.5}S_8 = 4.5\ FeS + 1.5\ Ni_3S_2 + 0.25\ S_{2(g)} \qquad (8.1)$$

back to 298 K. A value of -751.70 kJ mol^{-1} was obtained, which was adjusted afterwards[369] to -794.96 kJ mol^{-1} so as to be consistent with the observed stability of pentlandite and its occurrence with other iron and nickel sulphides in nature. Other workers have quoted ΔG°_f values for pentlandite that lay either side of this value, notably Abramov[69] (-716.18 kJ mol^{-1}) and Thornber[70] (836.80 kJ mol^{-1}).

All the free energy of formation data used to calculate the E_h-pH and activity-pH diagrams for the Fe-Ni-S-H_2O system is listed in Table III(iii) (Appendix II). Higher nickel oxides (Ni_3O_4, Ni_2O_3, NiO_2) were not considered, since the data for these species is now thought to be uncertain[355] due to the poor characterisation of these phases. Moreover, the solution species $HNiO_2^-$, considered by Pourbaix[63], is no longer thought to exist[355]; this is congruent with the well known corrosion resistance of nickel in alkaline solutions[375].

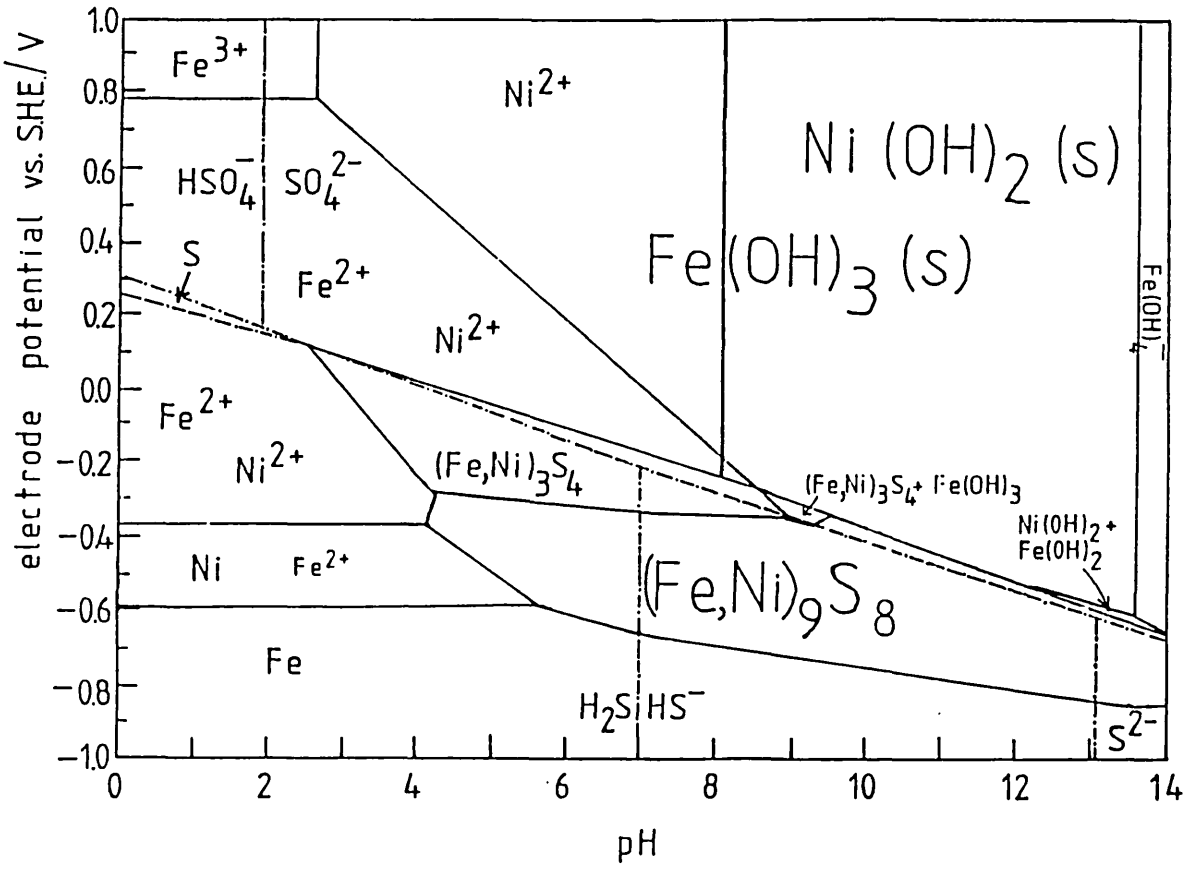


Fig 8.1 Potential-pH diagram for the Fe-Ni-S-H_2O system at 298 K for dissolved sulphur, nickel and iron activities of 10^{-4}.

The E_h-pH diagram (Figure 8.1) for the Fe-Ni-S-H_2O system at 298 K was generated for dissolved sulphur, nickel and iron activities of 10^{-4}. Pyrite was omitted from the diagram as its formation by reactions such as:-

$$FeNi_2S_4 + Fe^{2+} = 2FeS_2 + 2Ni^{2+} + 2e \qquad (8.2)$$

was unlikely under the experimental conditions[372] (see section 7.1).

Figure 8.1 shows that at low dissolved sulphur activities pentlandite is thermodynamically unstable at pH values < 4. However, it cannot dissolve non-oxidatively in the true sense as dissolution must involve an increase in the formal oxidation state of the metal atoms from < +2 in the lattice to +2 in solution.

Violarite shows a region of stability between pH 3 and 10 which lies directly above the stability domain of pentlandite. Therefore, a product layer of violarite can be expected to form on the surface of pentlandite under mildly oxidising conditions. At more oxidising potentials, violarite becomes unstable with respect to Fe^{2+}, Ni^{2+} and SO_4^{2-} in acidic media, whereas $Fe(OH)_3$ and $Ni(OH)_2$ are formed in neutral and alkaline solutions.

8.2 Studies on Virgin Pentlandite Surfaces

The effect of in-situ grinding to produce a fresh mineral surface on the rest potential of pentlandite at pH 0 and 9.2 is shown in Figure 8.2. The E_{oc} versus time responses were similar to those observed for pyrite (see section 6.3).

In 1 M $HClO_4$ the rest potential of an untreated pentlandite electrode was lowered from 0.695 V to 0.127 V on abrading the mineral surface. However, when the abrasion treatment was stopped, the rest potential increased instantaneously to ~ 0.4 V and then climbed slowly back to its pre-abrasion value over the next 30 minutes.

Under non-oxidising conditions, pentlandite and pyrite respond very slowly to attack by acids due to the formation of a passivating film on their surfaces. Pentlandite dissolves 60 times slower than pyrrhotite under the same acid leaching conditions (see section 2.4.3). Although an inhibiting layer also forms on pyrrhotite it dissolves in highly acidic solutions during an "induction period" prior to rapid pyrrhotite dissolution[200,201,204,205]. The results presented in section 7.2 suggested that the layer formed as a result of air oxidation, since it was removed by abrasion under non-oxidising conditions and did not reform subsequently. In contrast, abrasion did not prevent the open-circuit potential of pentlandite and pyrite electrodes returning to high values, which suggested that a passive layer formed on these minerals even in deoxygenated solutions. The results also suggested that the nature and form of the film formed on pyrite differed from that on pentlandite. Untreated pyrite electrodes exhibited larger cathodic currents on the first negative-going

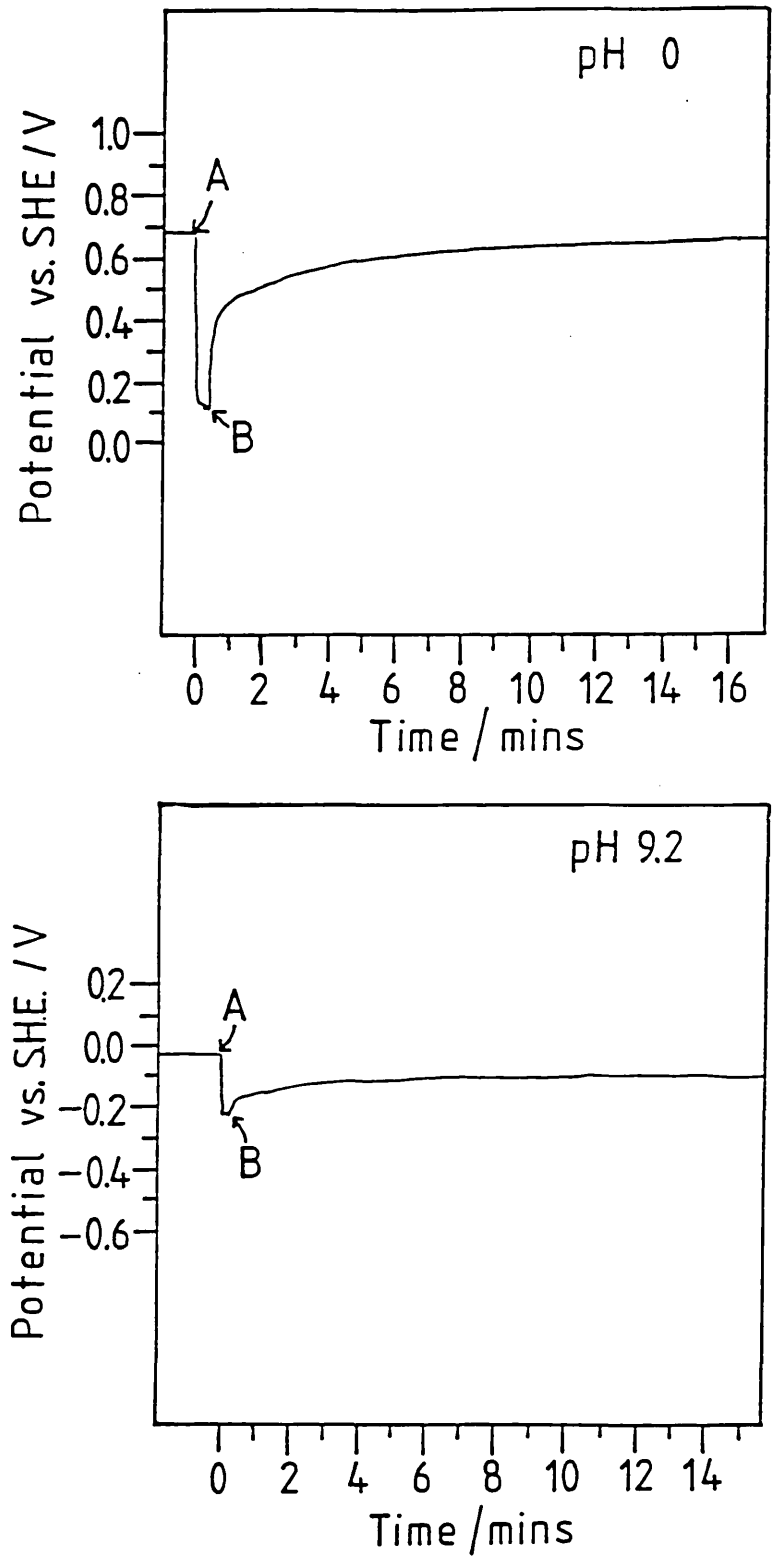


Fig 8.2 Change in the rest potential of a pentlandite electrode with time (after in situ polishing) at pH 0 (top) and pH 9.2 (bottom). (A) commence polishing; (B) finish polishing.

potential sweep from the rest potential than on subsequent sweeps, but with no discernable cathodic peak(s) (section 6.3). Current versus time curves and charge measurements (section 6.5.1) indicated that the passive film was of monolayer thickness. In addition, a mechanism involving the semiconductor properties of pyrite was postulated to describe its formation (section 6.7). The mechanism proposed that partial oxidation/deprotonation of water molecules occurs spontaneously at a "clean" pyrite surface, producing hydroxy-species which chemisorb onto the mineral surface, causing passivation.

In contrast, a large cathodic peak was observed on the first negative-going potential sweep with untreated pentlandite electrodes (see Figure 8.3 A). The 55 mC cm^{-2} of charge associated with the peak suggested that the passive layer is several monolayers thick. Cathodic pretreatment at 0.15 V (Figures 8.3 B and 8.3 C) and in-situ abrasion (Figure 8.3 D) were both successful in removing the passive layer, although it did reform even in deoxygenated solution if the electrode was left at open-circuit for a period of time. There is no justification in using a semiconductor-type mechanism to explain why a passive film forms on pentlandite because the mineral is metallic in nature (see section 3.2.7). However, at pH values < 1 pentlandite is a very active electrocatalyst for oxygen reduction, being more active than pyrite and only slightly less active than gold [188]. Thus, the high rest potential acquired at pH 0 (Figure 8.2) may be due initially to a mixed potential being established between the anodic process:-

$$(Fe, Ni)_9S_8 = 4.5\ Ni^{2+} + 4.5\ Fe^{2+} + 8S + 18e \qquad [a_2]$$

$$E = 0.067 + 0.015 \log [Ni^{2+}] + 0.015 \log [Fe^{2+}]$$

and cathodic reduction of the trace amounts of oxygen in solution (10^{-5} - 10^{-3} mol m^{-3}; see section 4.1) by reaction (k_6). Hence, a passivating layer of "sulphur" was formed, the open-circuit potential being too high for it to be removed by reaction (v).

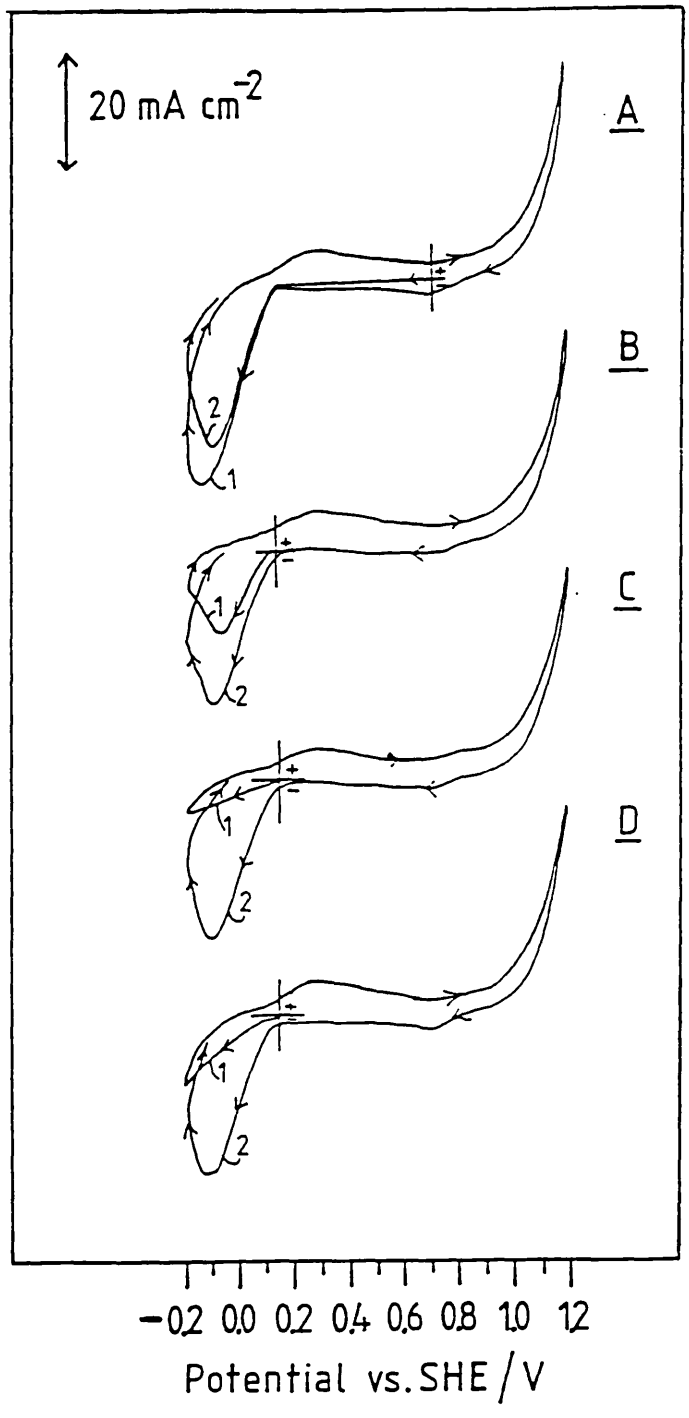


Fig 8.3 Cyclic voltammograms of a stationary pentlandite electrode in stirred solution at pH 0 (1 M $HClO_4$), recorded immediately after different surface pretreatments, starting from the rest potential, first cycled cathodically then anodically at 100 mV s^{-1}. (A) no pretreatment; (B) cathodic pretreatment at 0.15 V for 15 s; (C) cathodic pretreatment at 0.15 V for 2 min; (D) fresh pentlandite surface produced by in situ abrasion.

8.3 Cyclic Voltammetry

8.3.1 Anodic and Cathodic Reactions in Acidic Solutions (pH < 7)

The voltammograms recorded for stationary pentlandite electrodes in acidic media (Figure 8.4 (pH 1) and Figure 8.5 (pH 4.6)) were similar

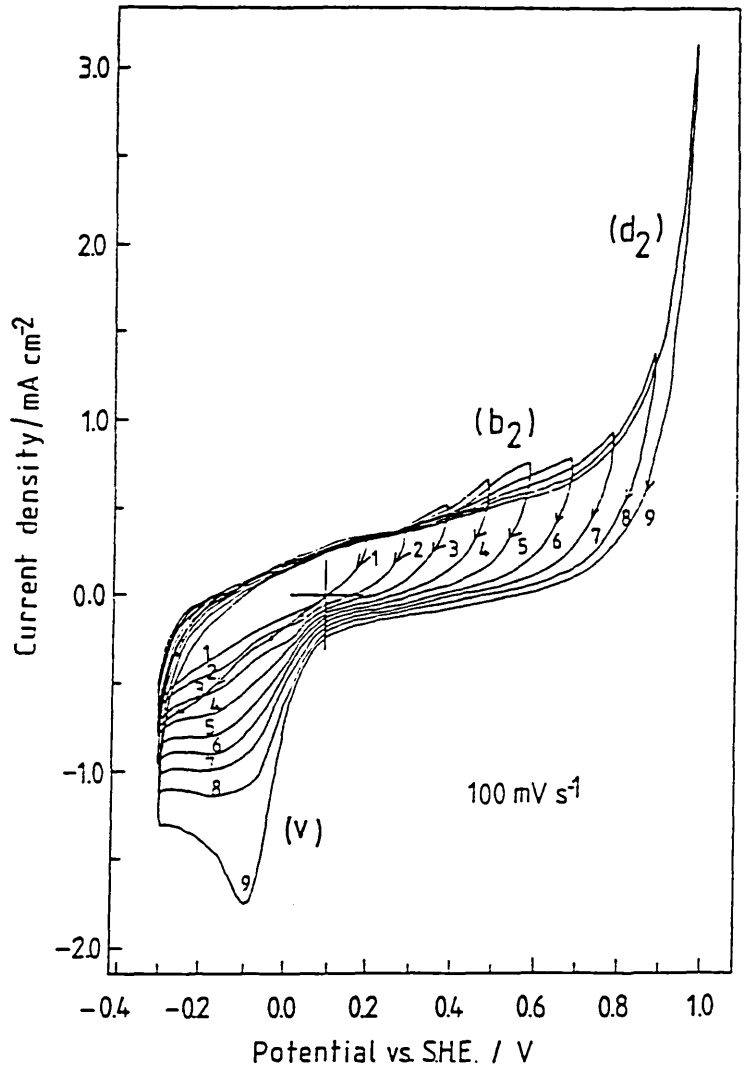


Fig 8.4 The effect of extending the anodic potential scanning limit (E_{λ_a}) on cyclic voltammograms of pentlandite at pH 1 (0.1 M $HClO_4$) in stirred solutions and a sweep rate of 100 mV s^{-1}.

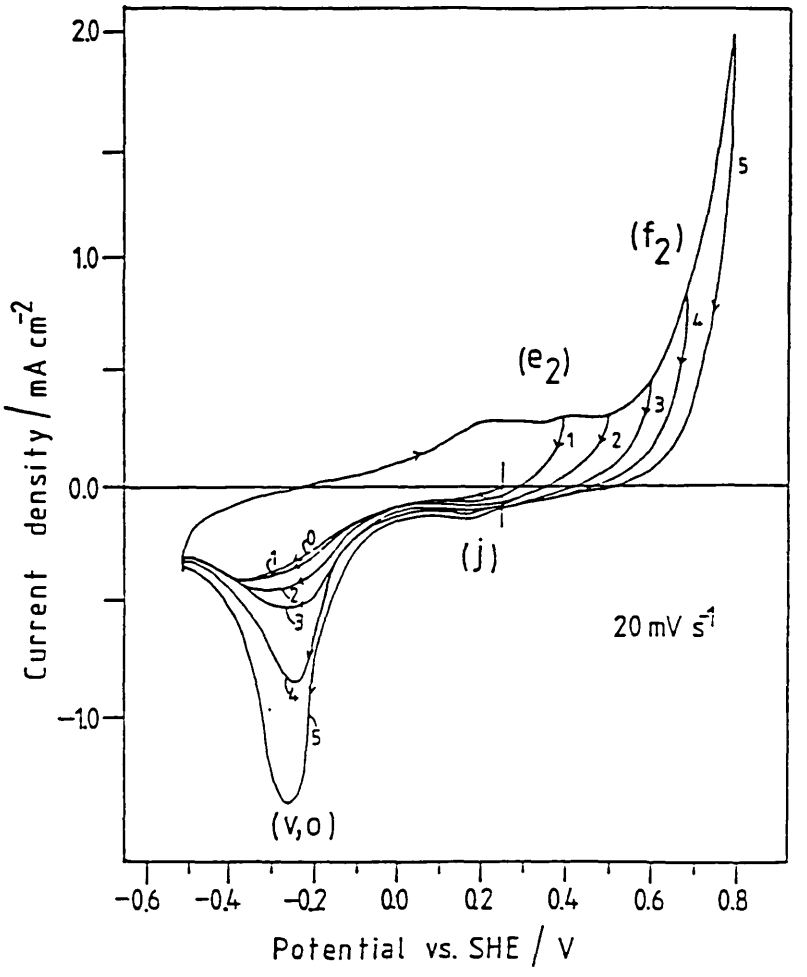


Fig 8.5 The effect of extending the anodic potential scanning limit (E_{λ_a}) on cyclic voltammograms of pentlandite at pH 4.6 (0.5 M CH_3COOH + 0.5 M CH_3COONa) in stirred solution and a sweep rate of 20 mV s^{-1}.

in general shape and form to those observed for pyrite at the same pH values (see sections 6.4.1 and 6.4.3). However, the E_{λ_a} potential required before the reduction of adsorbed/soluble ferric species was observed on the reverse scan was much higher on pentlandite (eg > 1.1 V at pH 1, compared with > 0.8 V for pyrite). This was probably because the amount of ferric species formed at the surface of pentlandite, per mole of sulphide oxidised, was less than that formed at the surface of pyrite (see section 7.3.3).

At pH 1 (Figure 8.4) the products of pentlandite oxidation were Ni^{2+}, sulphur, sulphate and mainly Fe^{3+} (see section 8.3.1.1), formed by reactions (b_2) and (d_2). The sulphate yield and ferric/sulphur ratio increased with increasing potential similar to pyrite and pyrrhotite. However, in contrast to pyrite and pyrrhotite, the broad cathodic peak at -0.1 V, assigned to sulphur reduction (reaction (v)), appeared to have no fine structure(s) (shoulders etc) associated with it.

Thornber[70] postulated that pentlandite oxidation proceeds via the formation of an intermediate phase, viz violarite ($FeNi_2S_4$, reaction (r_2)), which then oxidises by reactions (q_3) and (r_3) to give the same final product.

Violarite and pentlandite both have cubic-close packed sulphur lattices, so any metal atom depletion of a few monolayers from the pentlandite surface could be interpreted as surface alteration to form violarite, although the altered layer may not be a true thermodynamic phase.

At pH 4.6 (Figure 8.5) the main oxidation reactions were (e_2) and (f_2); forming ferric hydroxy species, Ni^{2+}, S° and SO_4^{2-}. Figures 8.6 and 8.7 show that the anodic oxidation curves for pentlandite exhibited a large stirring rate dependence at potentials > 0.6 V, where SO_4^{2-} formation (reactions (d_2) and (f_2)) was the dominant oxidation process. Moreover, the effect of stirring increased with increasing pH and had a greater effect on the anodic oxidation curves for pentlandite than it had on pyrite at similar pH and potential values (cf Figure 8.5 with Figure 6.26). This behaviour is typical of a dissolution-precipitation reaction (see section 6.4.3). It would appear that sulphate formation lowered the interfacial pH sufficiently to solubilise any insoluble ferric oxide/hydroxide layers formed on the surfaces of pentlandite and pyrite electrodes at lower overpotentials. Hence, Fe^{3+}, $Fe(OH)^{2+}$ and $Fe(OH)_2^{+}$ ions were released into solution and precipitated "near" the mineral electrode surface in regions where the pH is relatively high (> 1). (NB. near is taken to

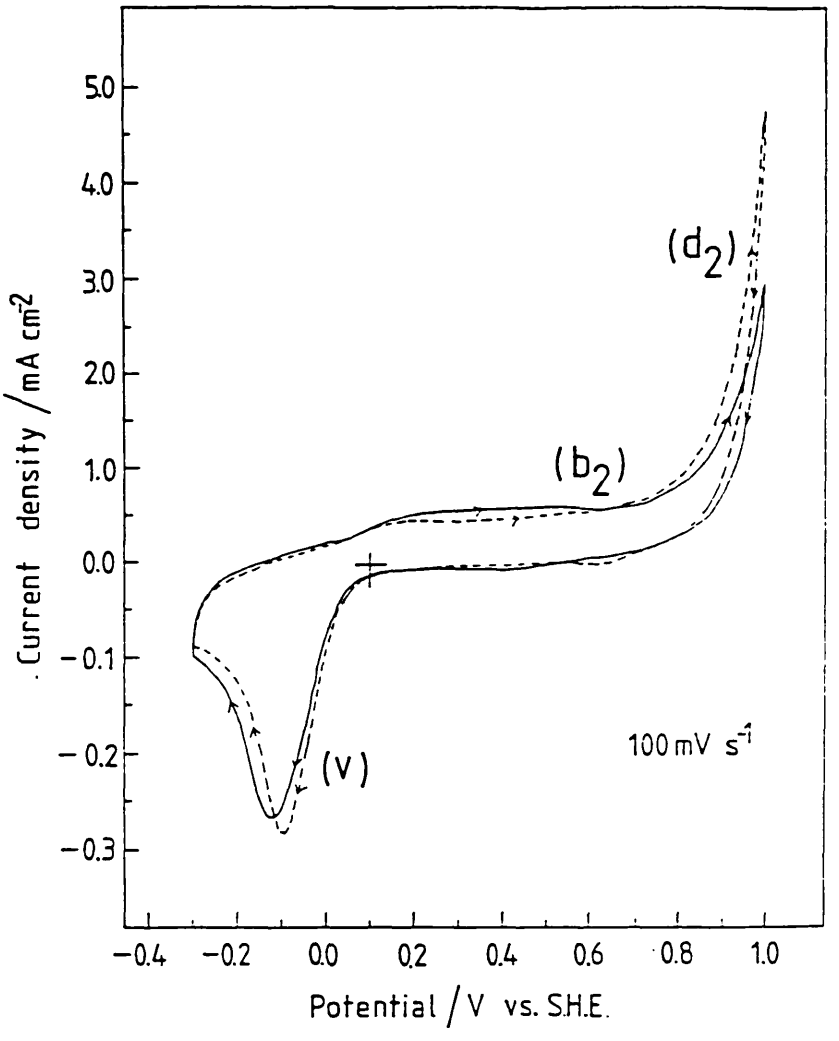


Fig 8.6 The effect of electrode rotation on cyclic voltammograms of a pentlandite RSCBE at pH 1 (0.1 M $HClO_4$). (——) stationary electrode; (---) rotated electrode.

mean a distance greater than the thickness of the electrical double layer). In quiescent solutions, ferric hydroxide reprecipitated on the surfaces of pentlandite and pyrite, inhibiting their anodic oxidation reactions, which were shifted to more positive potentials. However, in stirred solutions, some of the soluble ferric species were

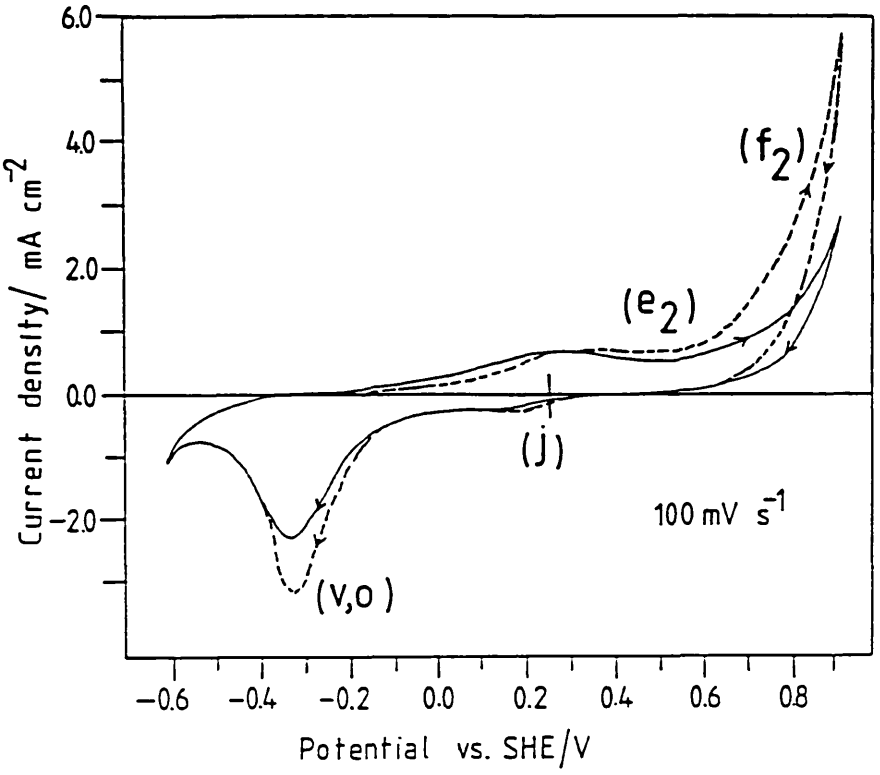


Fig 8.7 The effect of electrode rotation on cyclic voltammograms of a pentlandite RSCBE at pH 4.6 (0.5 M CH_3COOH + 0.5 M CH_3COONa) (——) stationary electrode; (---) rotated electrode.

dispersed into solution and precipitated further away from the mineral surfaces than before, so decreasing the inhibiting effect of the product layers. As the pH increased and the solubility of ferric species decreased, the effect of stirring on the anodic oxidation curves for pentlandite and pyrite became more noticeable (cf Figure 8.6 and 8.7). Moreover, since sulphate formation yielded a higher $H^+/Fe(OH)_3$ product ratio at the surface of pyrite than at the surface of pentlandite (see section 7.3.3, Table 7.1), and sulphate formation appeared to be the dominant oxidation pathway for pyrite (see section 6.7), it follows that ferric hydroxide species were more likely to

inhibit pentlandite oxidation than pyrite oxidation. Consequently, the anodic oxidation current of pentlandite exhibited a larger stirring rate dependence.

Indeed at pH 4.6, the potential of pyrite could be extended to 2.0 V without passivation, whereas with pentlandite at E_{λ_a} values > 1.3 V, the anodic current decreased gradually on consecutive potential cycles (Figure 8.8) and the surface of the electrode darkened. Clearly, the

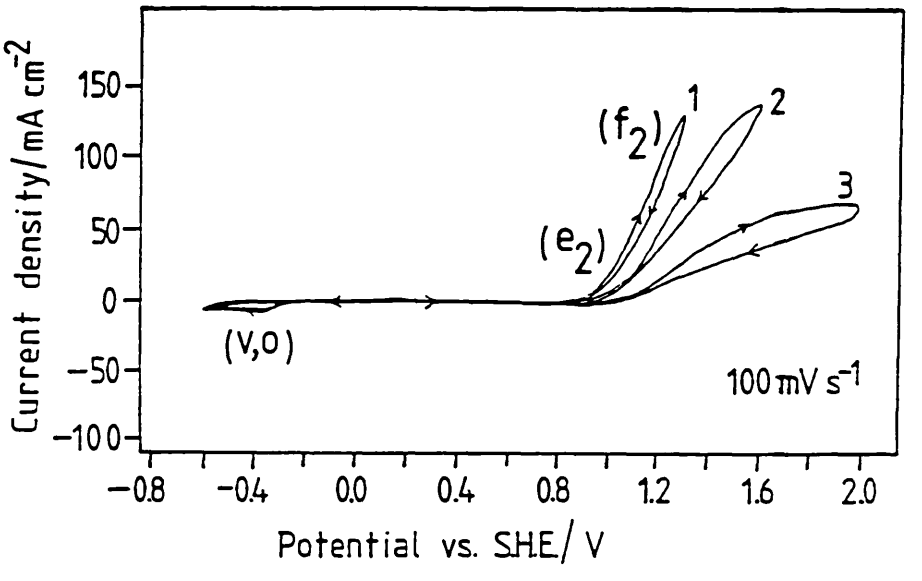


Fig 8.8 Cyclic voltammograms of pentlandite at pH 4.6 (0.5 M CH_3COOH + 0.5 M CH_3COONa) in stirred solution. (1) E_{λ_a}, 1.3 V; (2) E_{λ_a}, 1.6 V; (3) E_{λ_a} 2.0 V.

passive layer formed on pentlandite at high anodic potentials is not reduced easily and is different in thickness and/or in nature to the passive ferric oxide film formed on pyrrhotite, which was reduced on each negative-going potential sweep (see section 7.3.3). Most probably the passive layer on pentlandite is a mixed oxide/sulphur dielectric film with a higher sulphur content than that formed on pyrrhotite at similar potentials, making it more resistive.

8.3.1.1 Pentlandite RSCBE at pH 0 (1 $HClO_4$)

The current-time response of a pentlandite RSCBE to potential cycling in 1 M $HClO_4$ is shown in Figure 8.9. Once again, no Fe(II) species

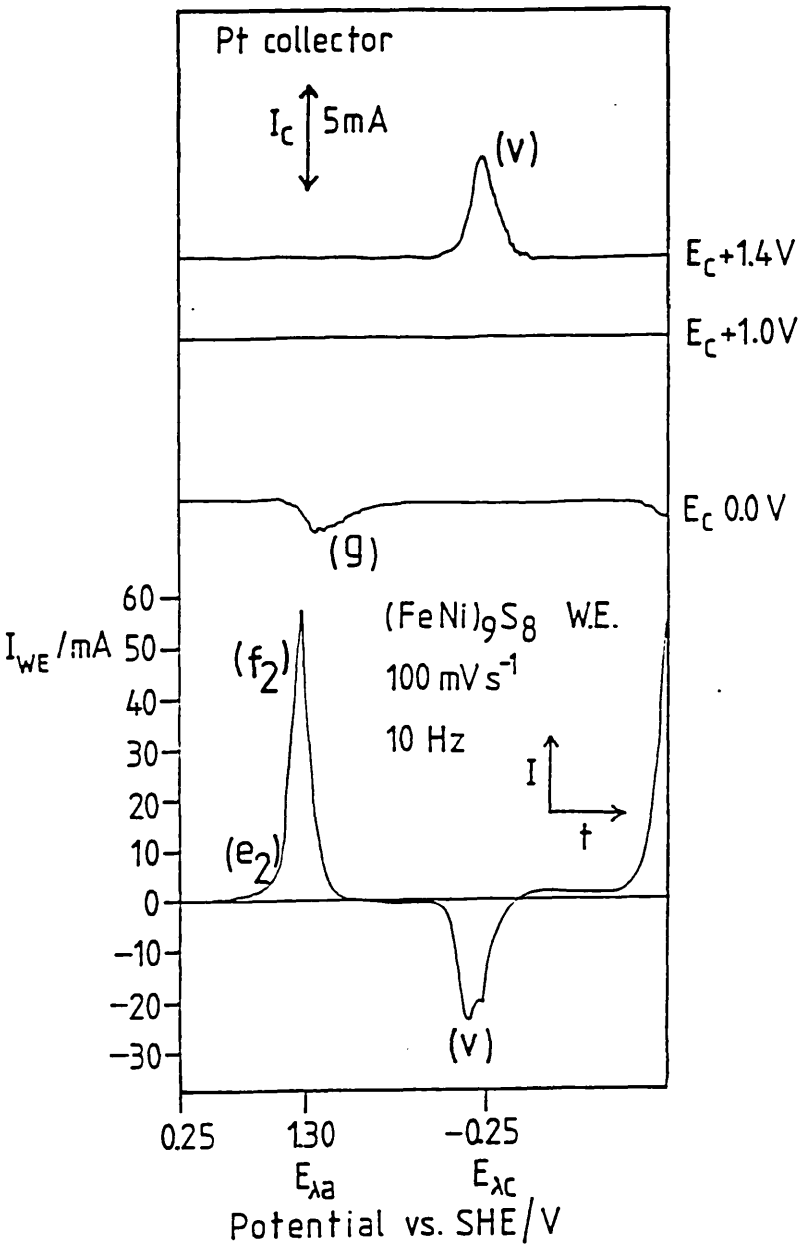


Fig 8.9 Cyclic voltammograms of a RSCBE in 1 M $HClO_4$ (pH 0) with the pentlandite working electrode (WE) swept anodically from 0.25 to 1.3 V, then cathodically to -0.25 V, and the platinum collector electrode held at various potentials (E_c).

were detected at the platinum collector (held at potentials > 0.8 V) when the potential of the mineral electrode was swept in a positive direction (see sections 6.4.2 and 7.3.2). At potentials > 0.8 V the main pentlandite oxidation reactions were (b_2) and (d_2) producing Fe^{3+}, Ni^{2+}, sulphur and sulphate. Over the range of collector potentials (E_c) studied, viz 0.0 - 1.4 V, Ni^{2+} ions were electro-inactive. Thus only Fe^{3+} ions were detected at the collector electrode (reduced to Fe^{2+} by reaction (g) at E_c potentials < 0.7 V), when the mineral electrode was swept to positive potentials.

The pentlandite cathodic peak at -0.1 V, attributed to the reduction of anodically formed sulphur, gave rise to an anodic collector current response at E_c values > 1.2 V, as a result of H_2S oxidation.

8.3.2 Voltammetry in Neutral and Basic Solutions

Voltammograms of pentlandite recorded over the pH range 7 - 13 were very similar in character, exhibiting an anodic wave/current plateau, between 0.4 and 0.6 V, followed by a rapid increase in current on the first positive-going potential scan (see Figures 8.10 and 8.12). Both features shifted to more negative potentials with increasing pH and the anodic wave was observed irrespective of whether the electrode potential was initially swept in a negative (Figures 8.10), or positive (Figure 8.11 - 8.13) direction from the rest potential.

The E_h/pH diagram for the Fe-Ni-S-H_2O system at 298 K (Figure 8.1) predicts that at neutral pH values and low anodic potentials pentlandite can oxidise to form a surface layer consisting of a nickel-rich violarite ($FeNi_2S_4$)-type phase mixed with ferric oxide/hydroxide (reaction (s_2)). As the potential increased, violarite oxidised (reactions (m_3) and (n_3)), giving rise to the anodic prewave between 0.4 and 0.6 V. The Ni^{2+} ions released into solution precipitated once their solubility was exceeded (reaction (a_3)). At pH 7, thermodynamics predicts the solubility of $Ni(OH)_2$ to be $10^{-1.82}$ mol dm^{-3} Figure II(xii) (Appendix II), although the experimental results of various workers lie in the range 10^{-1} to

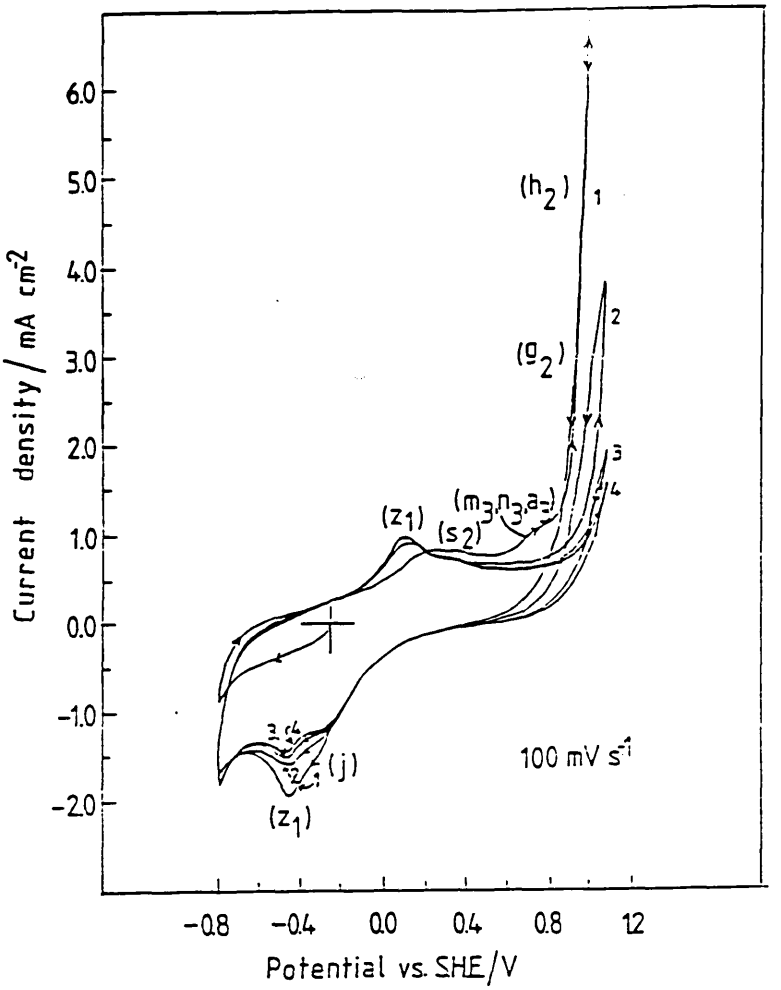
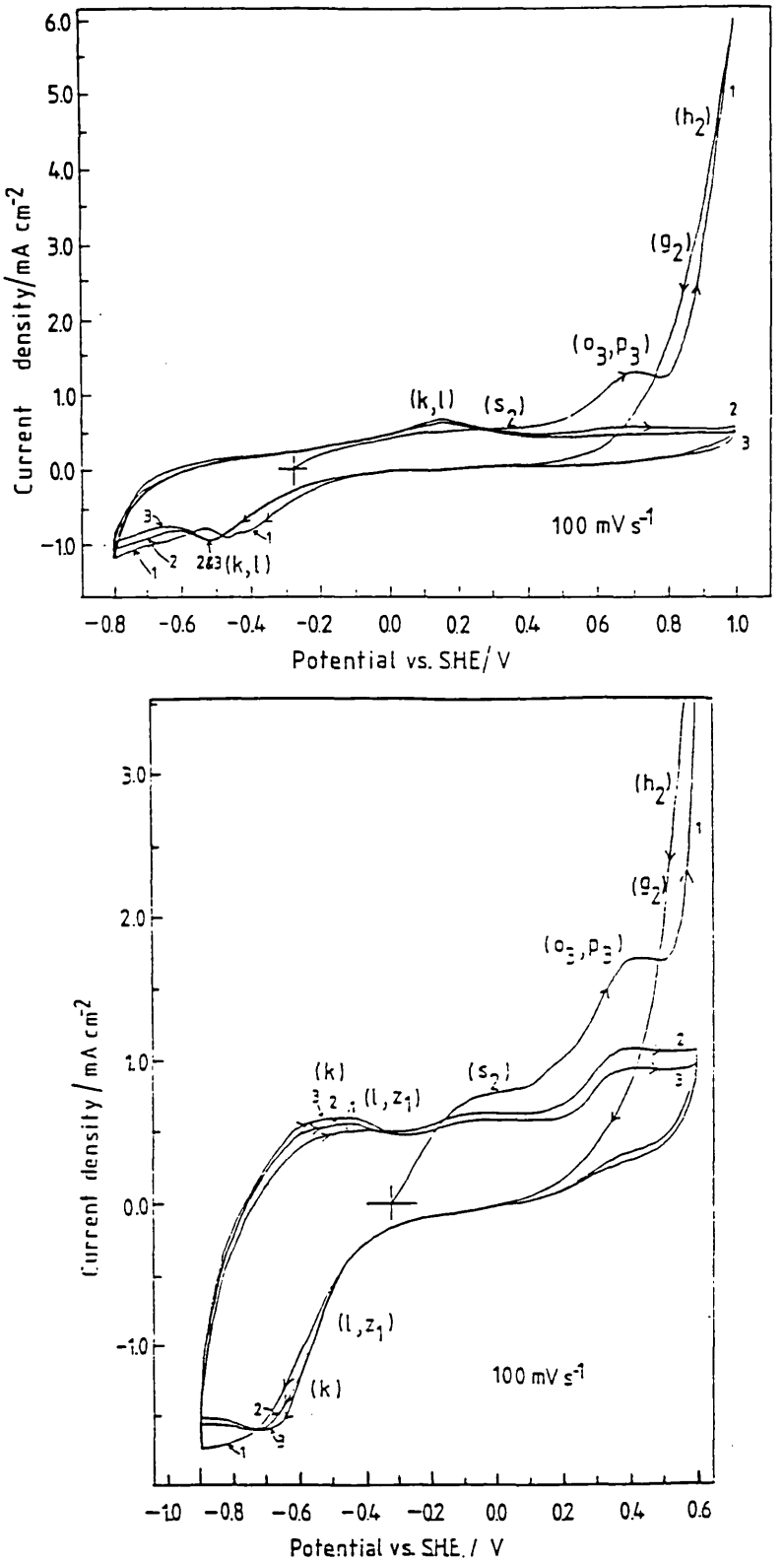


Fig 8.10 The effect of repetitive potential cycling between 1.1 and -0.8 V at 100 mV s^{-1} on the voltammetric behaviour of a stationary pentlandite electrode in stirred solution at pH 7 (0.025 M KH_2PO_4 + 0.025 M Na_2HPO_4).

10^{-5} mol dm^{-3} [63]. In comparison, the solubility of Fe^{3+} with respect to $Fe(OH)_3$ and FeOOH is much lower, viz $10^{-16.2}$ and $10^{-22.9}$ mol dm^{-3}, respectively (reactions (o_1) and u_1)). Thus, the stirring rate dependence of the anodic current in the prewave region at pH 7 (Figure 8.13) was more likely to be due to the anodic dissolution-precipitation of $Ni(OH)_2$ rather than of ferric hydroxy species since at low anodic overpotentials the interfacial pH was probably not lowered sufficiently to solubilise ferric species, except perhaps within the pores of the sulphur layer formed during violarite oxidation. Although $Ni(OH)_2$ precipitation inhibited the anodic



8.11 (top) The effect of repetitive potential cycling between 1.0 and -0.8 V at 100 mV s^{-1} on the voltammetric behaviour of a stationary pentlandite electrode in stirred solution at pH 9.2 (0.05 M $Na_2B_4O_7$).

8.12 (bottom) The effect of repetitive potential cycling between 0.6 and -0.9 V at 100 mV s^{-1} on the voltammetric behaviour of a stationary pentlandite electrode in stirred solution at pH 13.0 (0.1 M NaOH).

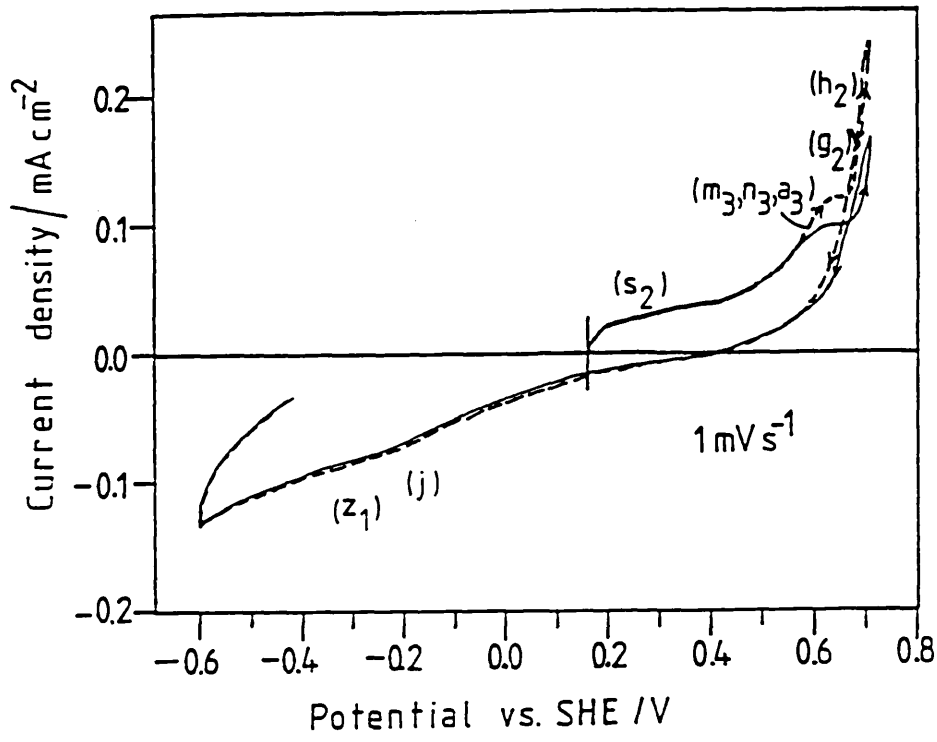


Fig 8.13 The effect of electrode rotation on cyclic voltammograms of a pentlandite RSCBE at pH 7 (0.025 M Na_2HPO_4 + 0.025 M KH_2PO_4) (——) stationary electrode; (---) rotated electrode.

processes and accounted partly for the observed prewave, the molar volume change associated with violarite oxidation to sulphur also contributed to the decrease in the rate of pentlandite oxidation. Table 8.1 shows the molar volume changes that occur when one mole of sulphide mineral is converted to elemental sulphur and dissolved metal ions (assuming metal ion hydroxylation occurs subsequently as a separate reaction).

The table shows that pentlandite oxidation to sulphur (reaction (b_2)) causes a relatively large negative change in the molar volume (-22.5%). With such a large shrinkage the sulphur formed anodically would be expected to form in a cracked or porous morphology which would not prevent further oxidation of the mineral lying underneath. Similarly, any anodic surface transformation, or change in the surface stoichiometry of pentlandite towards a nickel-rich violarite type phase, should not obstruct the passage of dissolving metal ions

Table 8.1 Volume Changes Associated with Sulphide Mineral Oxidation Reactions

Mineral	Molar Volume (cm^3)
Pentlandite ($(Fe,Ni)_9S_8$)	160
Pyrrhotite (FeS)	18.5
Violarite ($FeNi_2S_4$)	64
Sulphur (S^o)	15.5
Reaction	**Volume Change (%)**
(b_2) $(Fe,Ni)_9S_8 = 4.5Ni^{2+} + 4.5Fe^{3+} + 8S + 22.5e$	-22.5
(r_2) $(Fe,Ni)_9S_8 = 2FeNi_2S_4 + 2.5Fe^{3+} + 0.5Ni^{2+} + 8.5e$	-20
(q_3) $FeNi_2S_4 = Fe^{3+} + 2Ni^{2+} + 4S + 7e$	- 3
(h_1) $FeS = Fe^{3+} + S + 3e$	-16

(reaction (r_2)). However, the decrease in molar volume associated with violarite oxidation to sulphur (reaction (q_3)) is quite small (-3%). Thus assuming a violarite-type intermediate phase was formed on the surface of pentlandite, and its subsequent oxidation at low anodic overpotentials gave a high sulphur yield, the transport of metal ions through the sulphur film formed on violarite would be much slower than if pentlandite oxidised directly to sulphur. This might explain why an anodic prewave was observed and why the current in the prewave potential region exhibited a stirring rate dependence.

At potentials > 0.7 V the current increased rapidly due to the bulk oxidation of pentlandite (reactions (g_2) and (h_2)) and an upward trend in the current was observed after the scan was reversed,

characteristic of a nucleation and growth process. Moreover, on subsequent potential cycles the anodic current decreased, though more gradually at pH 7 (Figure 8.10) than at pH 9.2 and 13 (Figure 8.11 and 8.12). Clearly, the surface layer nucleated and grown on the first anodic sweep, passivated the surface and was not reduced on the reverse negative-going potential scan. This behaviour was similar to that observed at pH 4.6 at E_{λ_a} potentials > 1.3 V (see Figure 8.8), where passivation was attributed to the formation of a mixed ferric oxide/sulphur film. However, in neutral and basic solutions the passive layer was probably composed of a mixed ferric/nickelous oxide film due to the predominance of sulphate formation in alkali media.

The S 2p and Ni 2p 3/2 XPS spectra of pentlandite electrodes polarised for 10 minutes at 1.0 V in pH 4.6, 7.0 and 9.2 buffer solutions is shown in Figure 8.14. The S 2p spectra exhibited a large sulphide peak at 162 eV and a smaller sulphate peak at 168 eV. As expected, the sulphate peak became more pronounced with increasing pH. At pH 4.6 the S 2p peak at 162 eV was skewed and slightly displaced to higher binding energies, indicating that elemental sulphur was also present on the surface. At pH 9.2 the sulphide peak was at its most intense. Similarly, the Ni 2p 3/2 spectra exhibited a peak at 853 eV, characteristic of Ni(0) and/or Ni(II), which became more intense and shifted to lower binding energies with increasing pH. In addition, the Fe 2p and O 1s spectra showed that ferric hydroxy and hydroxy-sulphate species were also present on the pentlandite surface at each pH value.

These results suggested that the level of Ni(II) and sulphide sulphur at the pentlandite surface, under oxidising conditions, increases with increasing pH, which supports an oxidation mechanism involving the formation of a violarite-type intermediate phase. The violarite-type phase appeared to be formed even at the relatively high anodic potentials used in these experiments, although Thornber's Eh-pH diagram for the Fe-Ni-S-H_2O[70] system suggests that if the local concentration of dissolved Ni^{2+} ions at the surface is high ($> 10^{-4}$ mol dm^{-3}), e.g. at high anodic potentials, then millerite (NiS) may be the intermediate phase formed (reactions (t_2) and (u_2)).

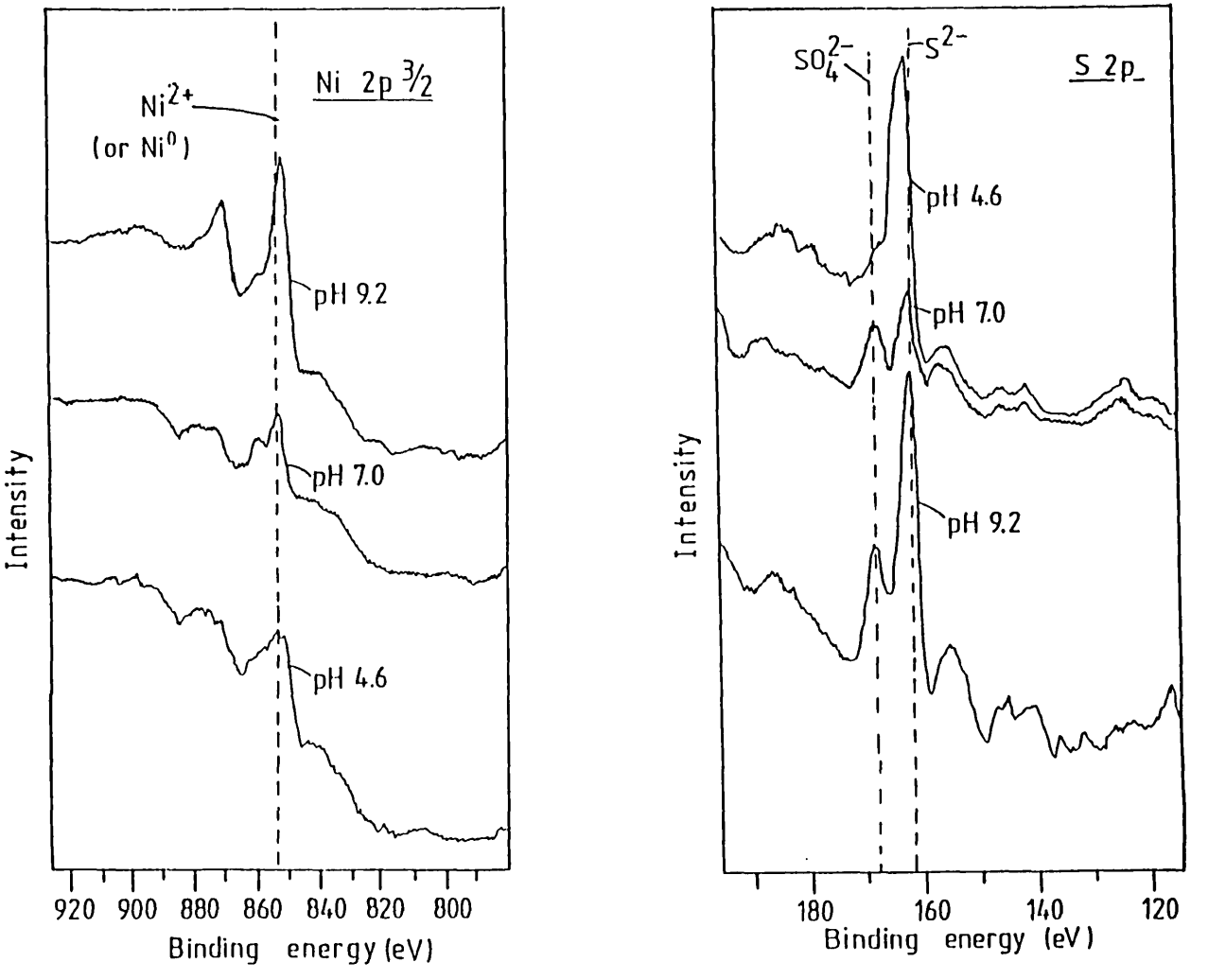


Fig 8.14 S 2p and Ni 2p 3/2 XPS spectra of pentlandite electrodes polarised for 10 minutes at 1.0 V in pH 4.6, 7.0 and 9.2 buffer solutions.

8.4 Pulse Voltammetry on Stationary Pentlandite Electrodes

Figure 8.15 shows the current-time transients recorded in 1 M $HClO_4$ on

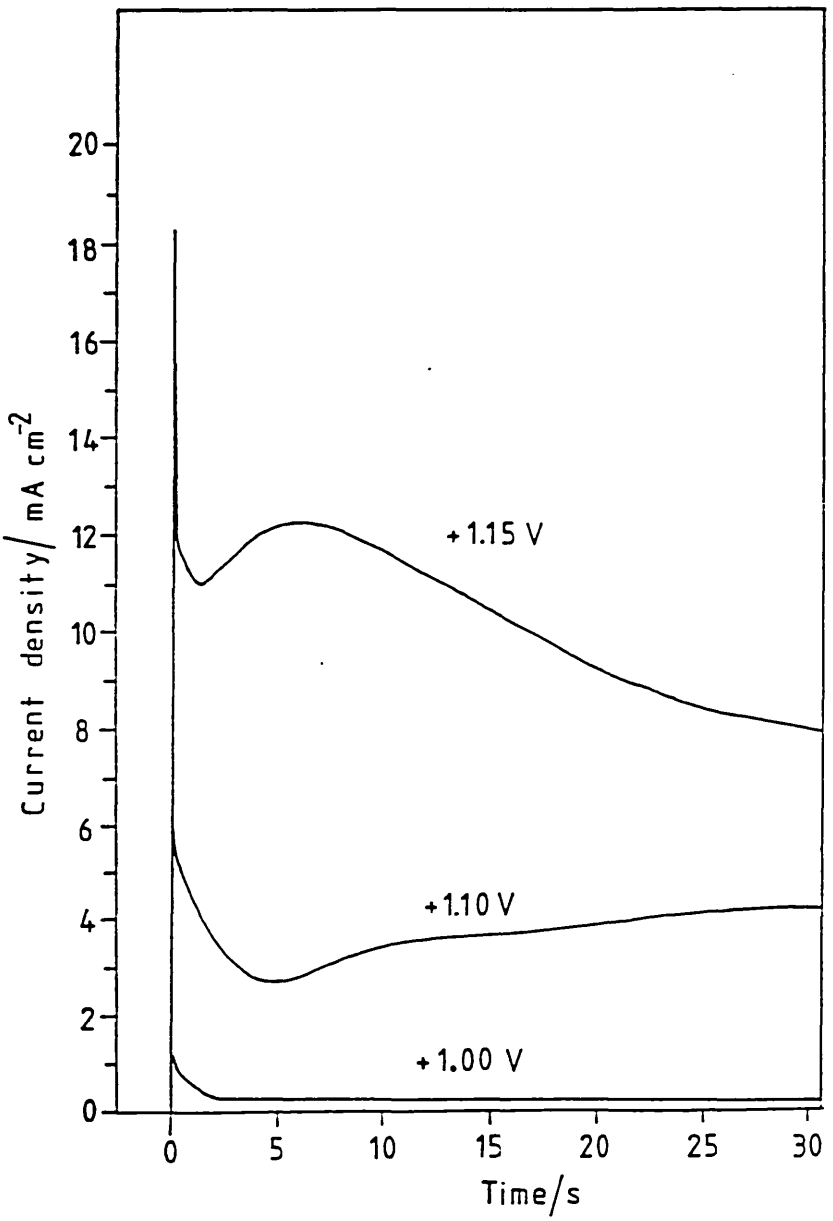


Fig 8.15 Current-time transients for a stationary pentlandite electrode held at various anodic poentials in stirred solution at pH 0 (1 M $HClO_4$).

pulsing the potential of pentlandite electrode from its rest potential to a series of anodic overpotentials. Over the potential range studied (0.6 - 1.3 V), the current always decayed initially as a function of $t^{-0.5}$ (Figure 8.16), indicating that the diffusion of

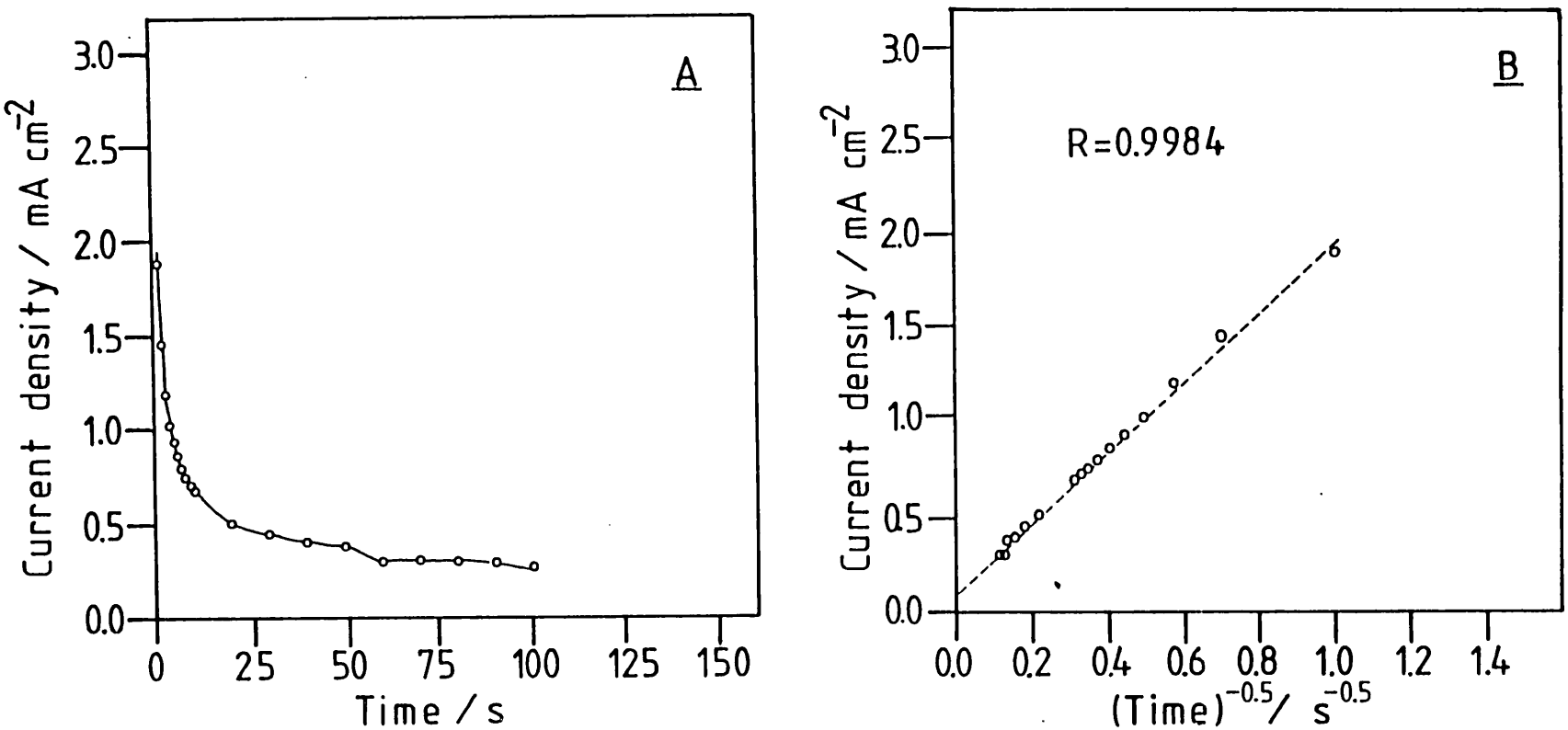


Fig 8.16 Current-time transient for a stationary pentlandite electrode held at 1.0 V in stirred solution at pH 0 (1 M $HClO_4$). (A) i vs t; (B) i vs $t^{-0.5}$; R = correlation coefficient.

metal ions away from the electrode surface was rate-determining. At potentials > 1.0 V, the i-t data showed a minimum, which was reached at shorter times as the potential was increased. The current then increased due to the nucleation and growth of sulphur before passing through a maximum (Figure 8.15). The time associated with the rising portion of the transient was dependent on the overpotential. The subsequent current decay was caused by the thickening sulphur layer inhibiting further anodic dissolution. Similar behaviour was observed at pH 4.6 (Figure 8.17).

Only falling current transients were observed in alkaline solutions. When the potential was stepped into the potential region where the anodic prewave was observed in cyclic voltammograms, the current decayed according to a t^{-1} relationship, characteristic of an adsorption/oxide growth ($Ni(OH)_2$)-type process (Figure 8.18). At higher potentials the current decayed as a function of $t^{-0.5}$, with the diffusion of metal ions through a thickening oxide film rate-determining. Further evidence of this diffusion controlled region in alkaline solutions was detected in plots of log charge (q) vs potential, where the charge curve levelled out at high anodic overpotentials (Figure 8.19).

8.5 Impedance Measurements on Stationary Pentlandite Electrodes

The complex plane impedance spectra (0.1 Hz - 10 kHz) of stationary pentlandite electrodes in stirred deoxygenated solutions at pH 0, 4.6 and 9.2 are presented as functions of potential in Figures 8.20 - 8.22. In acidic solutions (Figure 8.20 and 8.21), a single semicircle was obtained, corresponding to the charge transfer resistance, which decreased in size as the anodic potential was increased. At high potentials (> 1.0 V), an inductive loop also appeared, indicating that an adsorbed sulphur and/or sulphur-oxygen intermediate product layer was probably forming on the electrode surface (see section 7.5). In addition, the charge transfer semicircles became less depressed which allowed capacitance values to be calculated from the imaginary impedance maxima by equation (6.36). As expected pentlandite exhibited quasi-metallic behaviour. At pH 0, the double layer

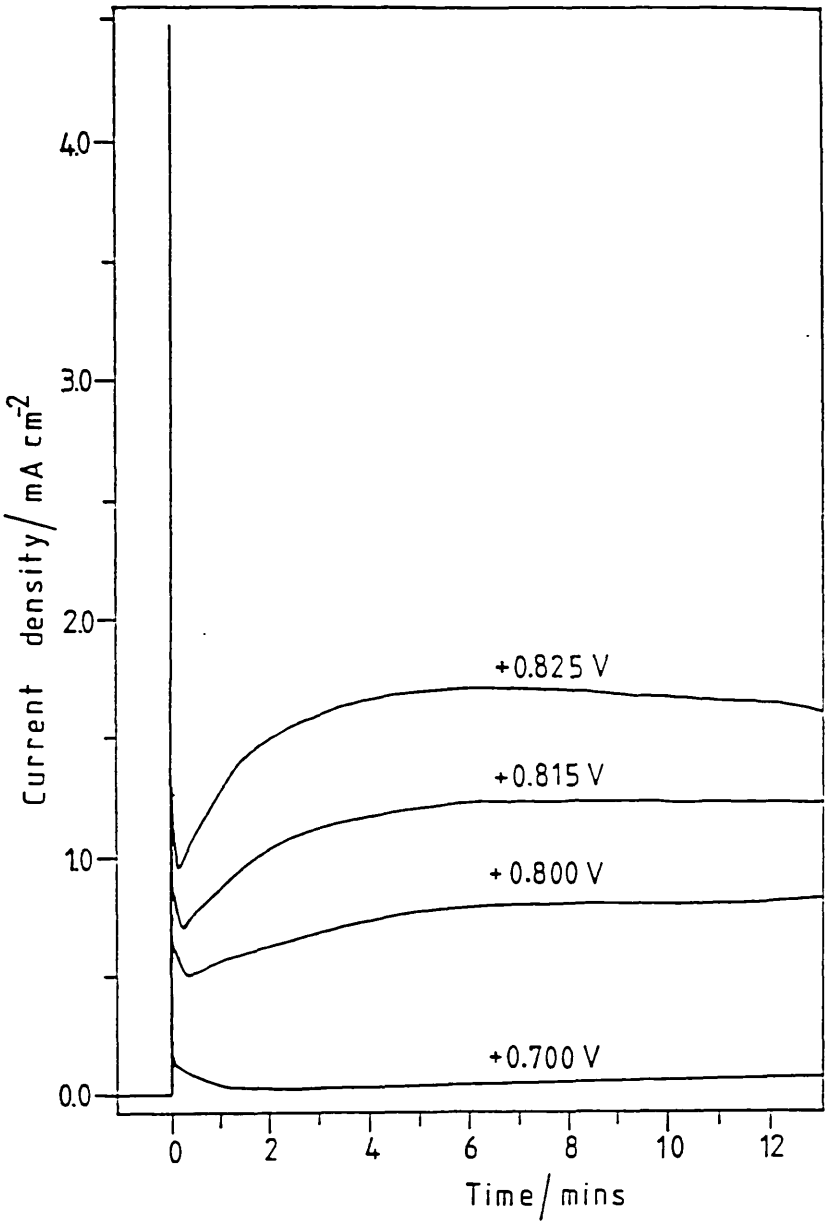


Fig 8.17 Current-time transients for a stationary pentlandite electrode held at various anodic potentials in stirred solution at pH 4.6 (0.5 M CH_3COOH + 0.5 M CH_3COONa).

capacitance increased from 13 to 48 μF cm^{-2} as the potential was increased from 1.0 V to 1.2 V. This rise in capacitance was most probably due to the nucleation and growth of sulphur in corrosion

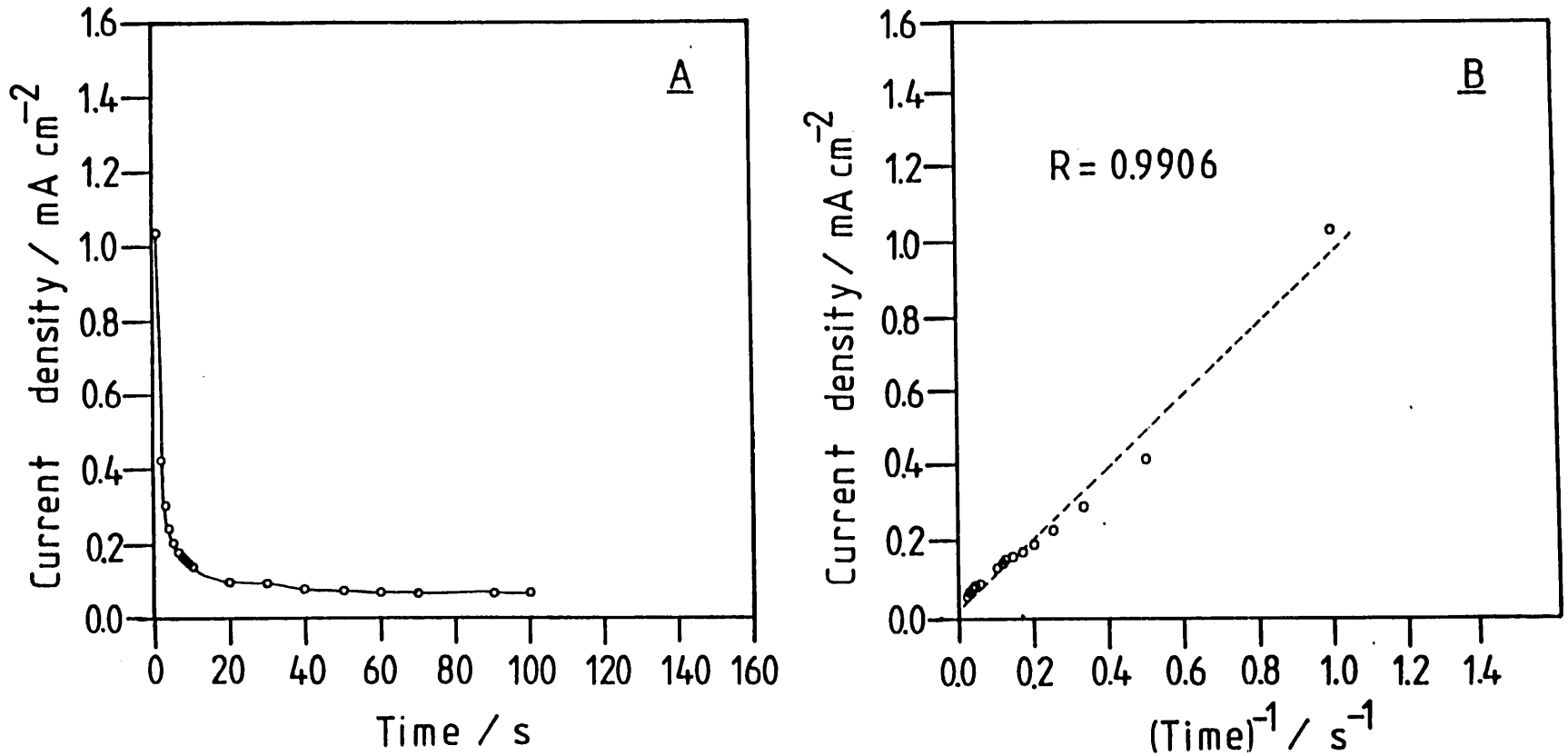


Fig 8.18 Current-time transient for a stationary pentlandite electrode held at 0.6 V in stirred solution at pH 9.2 (0.05 M $Na_2B_4O_7$). (A) i vs t; (B) i vs t^{-1}; R = correlation coefficient.

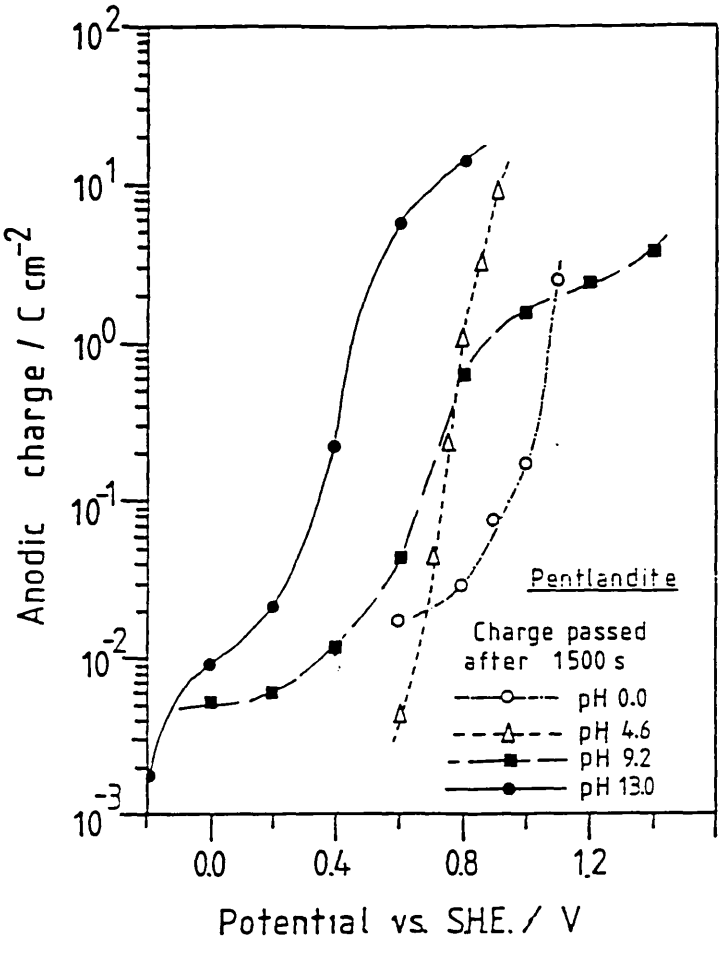


Fig 8.19 Anodic charge passed after 1500 s for a pentlandite electrode as a function of potential and pH.

pits, which increased the surface area of the pentlandite electrode, although the increase may have been caused by an additional pseudo-capacitance associated with the adsorption of the sulphur product layer. At 1.4 V, the double layer capacitance decreased to 24 μF cm^{-2} while the uncompensated ohmic resistance increased from 0.65 Ω cm^2 at 1.2 V to 1.07 Ω cm^2 at 1.4 V. This was attributed to a thickening of the sulphur layer which decreased the double layer capacitance by decreasing the reactive surface area of the electrode. Similarly behaviour was observed at pH 4.6.

Figure 8.23 shows the variation in uncompensated ohmic resistance (R_u) as a function of potential and pH. Over the potential range investigated (0.3 - 1.2 V), resistance values were generally low in acidic media (< 1 Ω cm^2 at pH 0 and < 2 Ω cm^2 at pH 4.6),

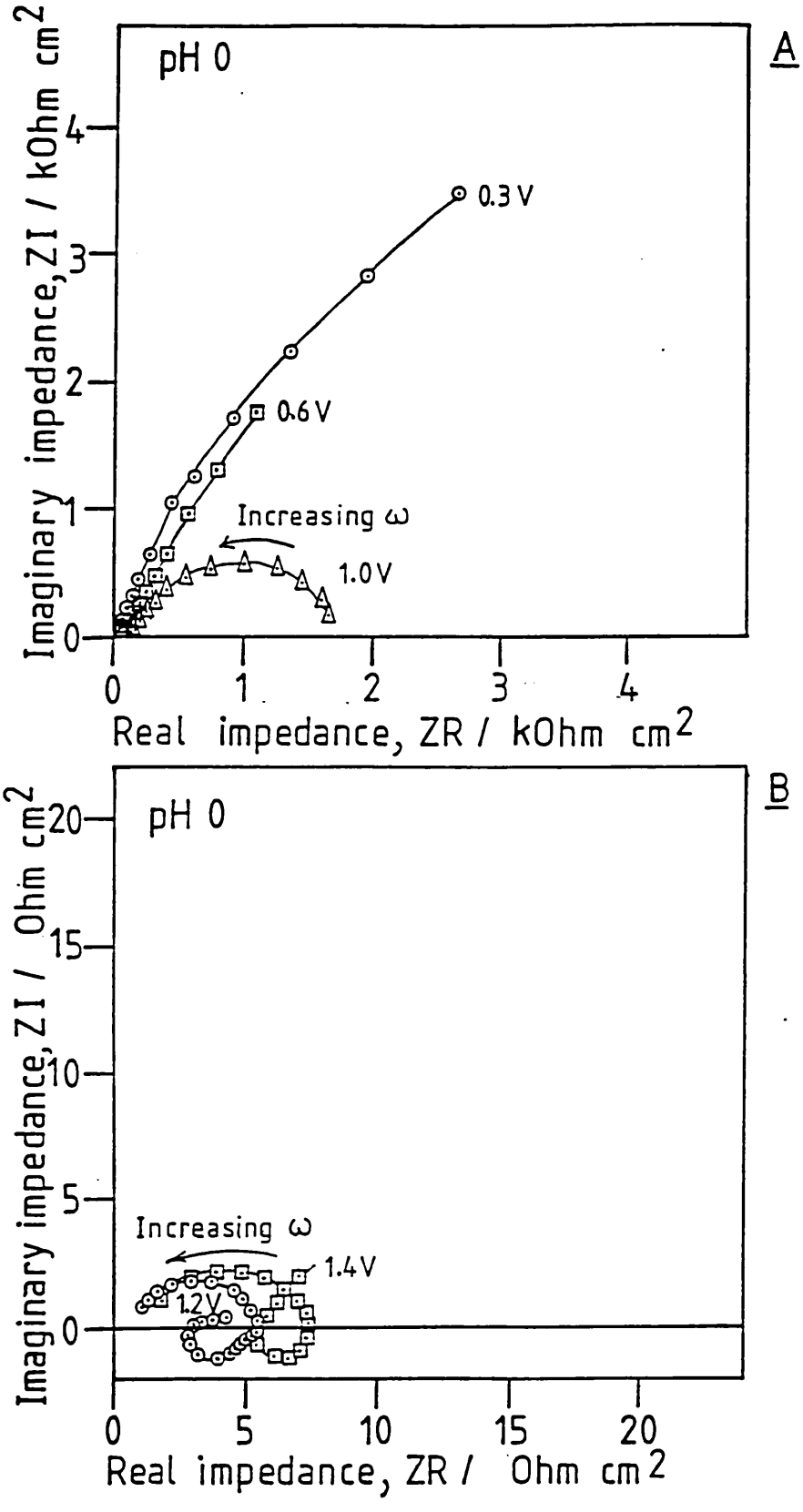
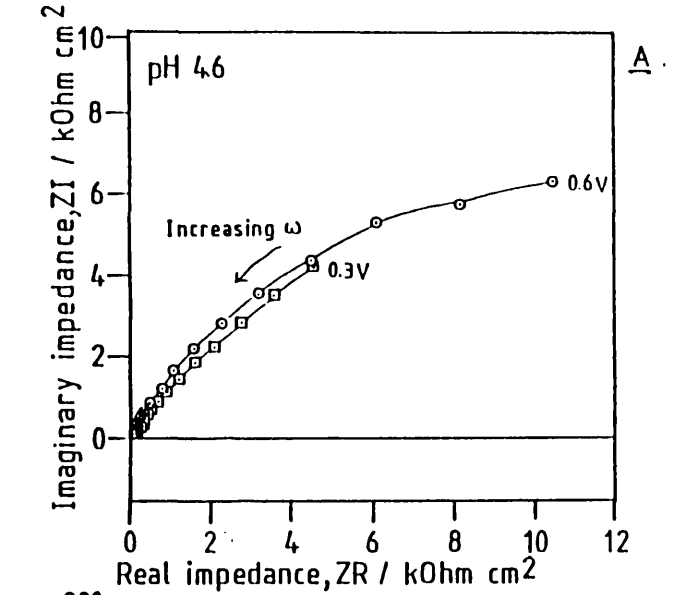
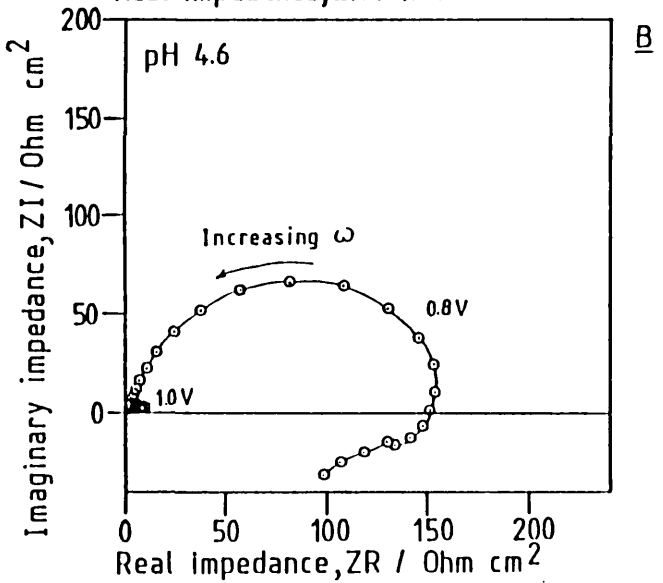


Fig 8.20 Impedance spectra (0.1 Hz - 10 kHz) for a stationary pentlandite electrode in stirred solution at pH 0 (1 M $HClO_4$). (A) 0.3 to 1.0 V; (B) 1.2 and 1.4 V.





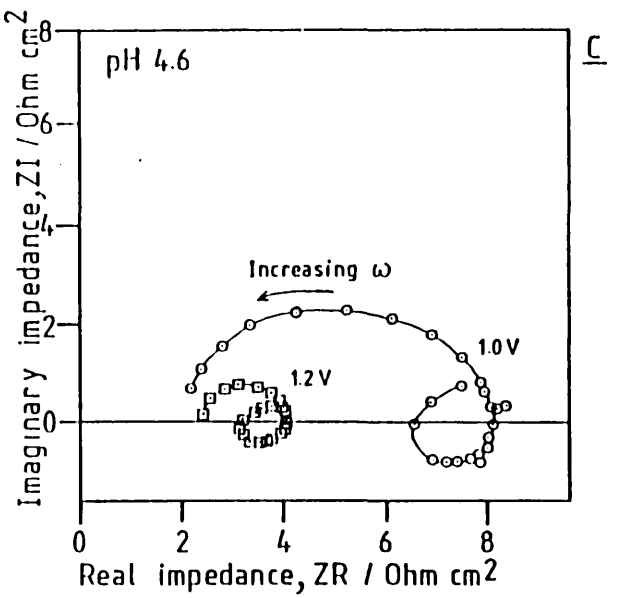


Fig 8.21 Impedance spectra (0.1 Hz - 10 kHz) for a stationary pentlandite electrode in stirred solution at pH 4.6 (0.5 M CH_3COOH + 0.5 M CH_3COONa). (A) 0.3 and 0.6 V; (B) 0.8 and 1.0 V; (C) 1.0 and 1.2 V.

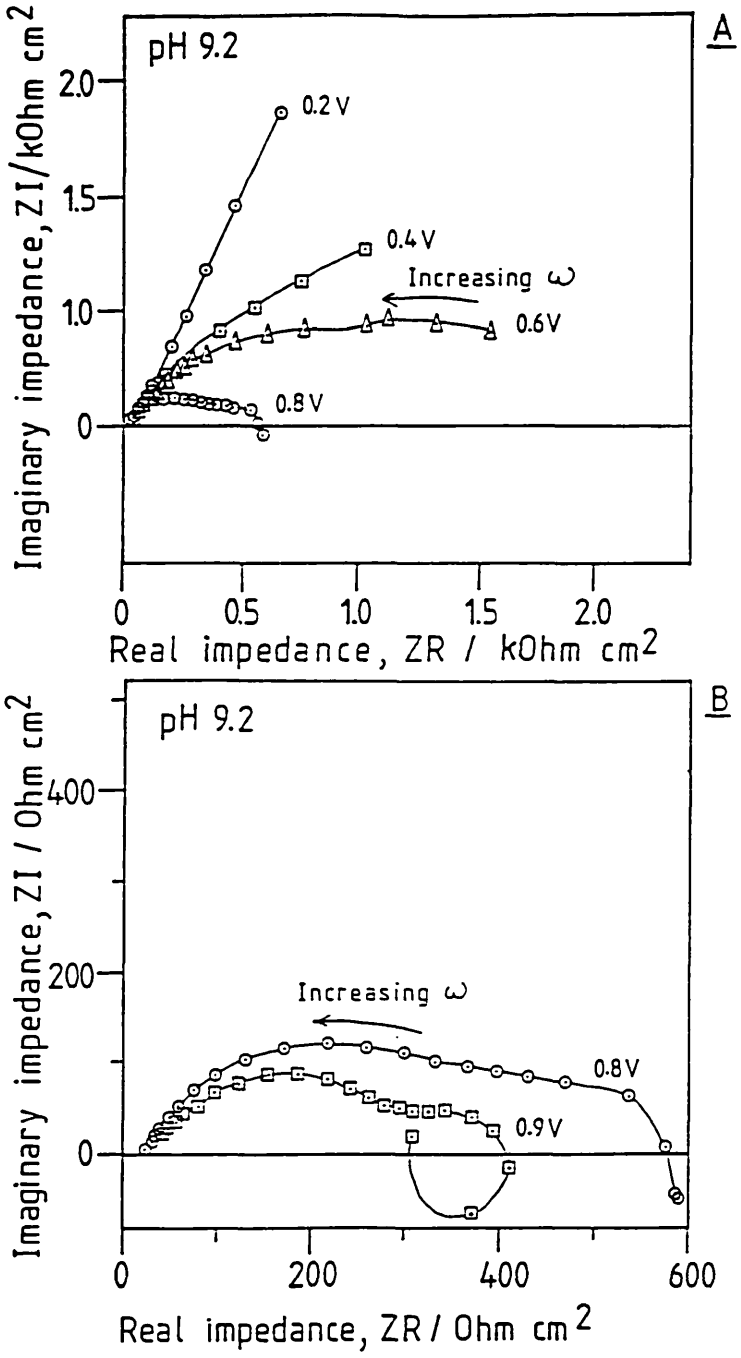


Fig 8.22 Impedance spectra (0.1 Hz - 10 kHz) for a stationary pentlandite electrode in stirred solution at pH 9.2 (0.05 M $Na_2B_4O_7$). (A) 0.2 to 0.8 V; (B) 0.8 and 0.9 V.

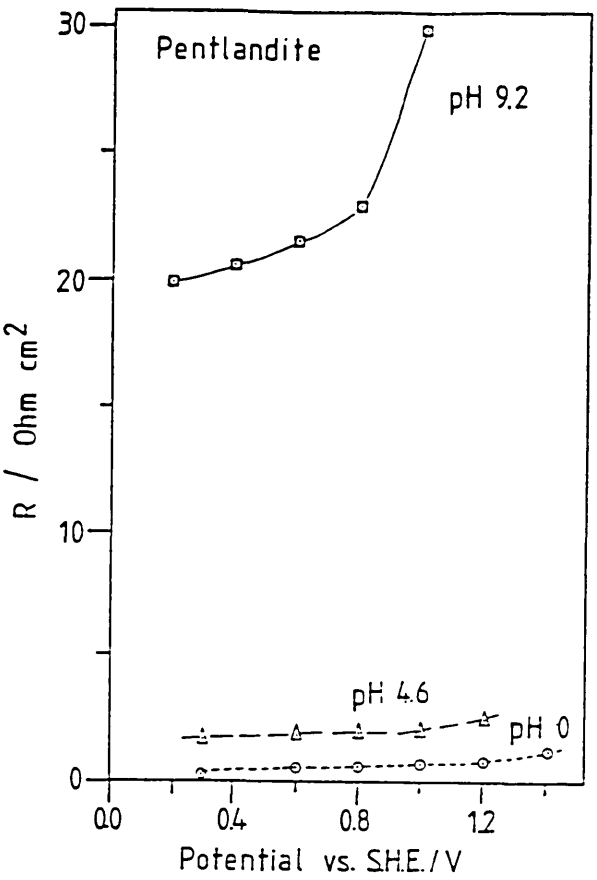


Fig 8.23 Real axis, high frequency intercept resistance, R (equivalent to the surface film resistance, R_f), for pentlandite at pH 0, 4.6 and 9.2, plotted as a function of potential.

increasing only slightly with increasing anodic overpotential, which suggested that the product layer formed on pentlandite (sulphur at pH 0, sulphur and ferric hydroxide at pH 4.6) was relatively thin. Similar behaviour was observed with pyrite and can be attributed to the lower overpotential requirement for sulphate formation on these minerals, in comparison to pyrrhotite, on which sulphur formation was dominant even at high anodic potentials (see section 7.4.1 and 7.5).

At pH 9.2, under mildly oxidising conditions (0.2 V), the impedance spectrum exhibited the beginning of a Warburg diffusion line at low frequencies (Figure 8.22). This was attributed to the diffusion of Fe^{3+} and Ni^{2+} ions out through a porous layer consisting of a nickel rich violarite-type phase and ferric oxide/hydroxide formed during anodic polarisation (reaction (s_2)). The Fe^{3+} ions precipitate out as ferric oxide/hydroxide once they reach the surface.

A major change in the Nyquist plot was observed on increasing the anodic potential to 0.7 V. Two depressed semicircles were obtained, which coincided with the electrode surface becoming covered in a brown/grey deposit of ferric/nickelous oxide. Double layer capacitance values of 46.4 and 46.9 $\mu F\ cm^{-2}$ were derived (using equation (6.36)) from an analysis of the high frequency loops at 0.8 and 0.9 V. These values were typical of a metal/aqueous solution interface and similar to those values obtained in acidic media. Capacitance values calculated from the low frequency loops increased from 1,933 $\mu F\ cm^{-2}$ at 0.8 V to 2,439 $\mu F\ cm^{-2}$ at 0.9 V, consistent with the pseudo-capacitance associated with the nucleation and growth of a thickening ferric/nickelous oxide film (reactions (g_2) and (h_2)). This was also reflected in values obtained for the total uncompensated resistance, which increased from 23 $\Omega\ cm^2$ at 0.8 V to 30 $\Omega\ cm^2$ at 0.9 V. Furthermore at 0.9 V, a low frequency inductive loop appeared, which suggests that adsorbed sulphur-oxygen species (e.g. $S_2O_3^{2-}$ etc.) may also have been present in the oxide film.

CHAPTER NINE

ELECTROCHEMICAL STUDIES ON CHALCOPYRITE ELECTRODES

CHAPTER NINE: ELECTROCHEMICAL STUDIES ON CHALCOPYRITE ELECTRODES

9.1 Thermodynamics

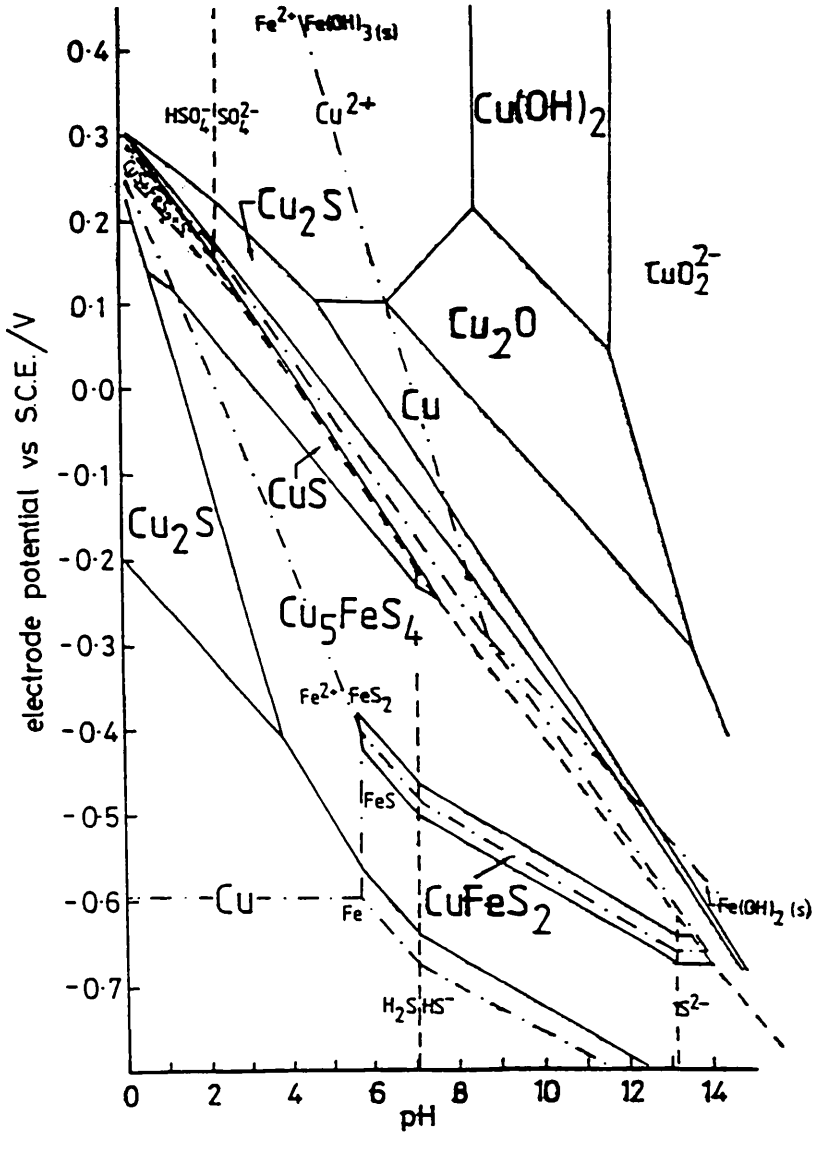


Fig 9.1 Potential-pH diagram for the Cu-Fe-S-H_2O system at 298 K for dissolved copper, iron and sulphur activities of 10^{-8}, 10^{-4} and 10^{-4}, respectively[370].

The E_h-pH diagram (Figure 9.1) for the Cu-Fe-S-H_2O system at 298 K calculated from the thermodynamic data presented in Table II(iv) (Appendix II) shows that oxidative decomposition paths for

chalcopyrite in acidic solutions call for H_2S as a reactant and FeS_2 as a product, e.g.:-

$$CuFeS_2 + 0.4\ H_2S = CuFe_{0.2}S_{0.8} + 0.8FeS_2 + 0.8\ H^+ + 0.8e \quad (9.1)$$

$$2CuFeS_2 + H_2S = Cu_2S + 2FeS_2 + 2H^+ + 2e \quad (9.2)$$

$$CuFeS_2 + H_2S = CuS + FeS_2 + 2H^+ + 2e \quad (9.3)$$

However, if H_2S is not available as a reactant, i.e. at the low dissolved sulphur activities typical of solutions initially containing no dissolved sulphur on immersion of an electrode, then these reactions cannot occur. Moreover, the slow rate of pyrite nucleation/formation[372] (see section 7.1) probably explains why none of these reactions have been observed in any of the numerous atmospheric or pressure leaching studies that have been carried out on chalcopyrite [153,154,158,168,169,172-174].

Also, Figure 9.1 does not adequately predict the kinetic behaviour of the oxidation of copper sulphides, which, unlike the iron sulphides, produce predominantly elemental sulphur, rather than sulphate[65], as the product of oxidation in non-chloride aqueous acid solutions. Moreover, a metallic copper stability domain lies above that of chalcocite (Cu_2S) and is derived from the oxidation of Cu_2S to sulphur (VI):-

$$Cu_2S + 4H_2O = 2Cu^\circ + SO_4^{2-} + 8H^+ + 6e \quad (9.4)$$

However, this reaction requires geological time scales to give rise to detectable products[377]. To account for the observed kinetic behaviour of the oxidation of copper sulphides, Goodenough[376] and Woods et al[377] have recently constructed E_h-pH diagrams for the Cu-S-H_2O system which allow for the irreversibility of sulphate formation. If sulphoxy species (i.e. sulphur species with oxidation states > 0) are excluded from consideration, then Figure 9.2B[376] is obtained. The effect is to expand the regions of copper sulphide stability to much higher potentials (compare Figure 9.2A and Figure 9.2B). Covellite (CuS) has a band of meta-stability lying above that

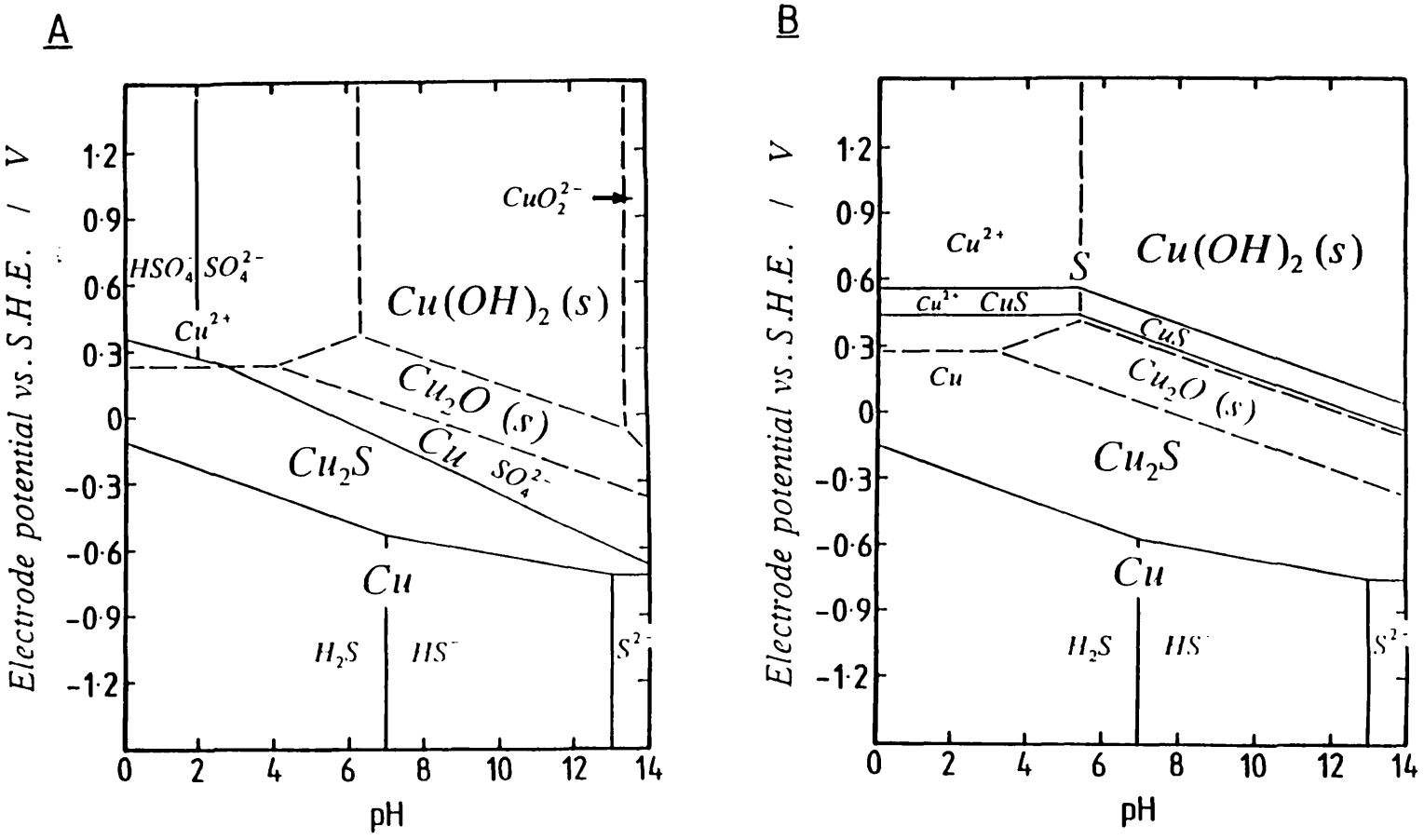


Fig 9.2 Potential-pH diagrams for the Cu-S-H_2O system[376] at 298 K for dissolved sulphur and copper activities of:-

(A) 10^{-6} and 10^{-4}, respectively.

(B) 10^{-5} and 5×10^{-3}, respectively (meta-stable diagram excluding sulphur species with oxidation states > 0).

of Cu_2S, hence Cu_2S is predicted to oxidise to CuS which in turn oxidises to elemental sulphur and Cu^{2+} ions or $CuO/Cu(OH)_{2(s)}$, depending on the pH. Furthermore, Figure 9.2B shows the copper sulphides to be more noble electrochemically than Cu_2O and Cu, thus predicting that the latter species are not formed as products of copper sulphide oxidation in neutral and basic solutions.

9.2 Rest Potential Measurements

Open-circuit potential (E_{oc}) versus time profiles for chalcopyrite electrodes subjected to in situ grinding at pH 0 and 9.2 are shown in Figure 9.3. In 1 M $HClO_4$, the rest potential was lowered from 0.559 V to 0.197 V on abrading the mineral surface. However, when the abrasion was stopped the rest potential increased and levelled off at ca. 0.46 V after 3 minutes. Similar behaviour was observed at pH 9.2, except that the difference between the initial and final rest potential was much less (ca. 50 mV).

9.3 Cyclic Voltammetry

9.3.1 Anodic and Cathodic Processes in Acidic Solutions (pH < 7)

Cyclic voltammograms of stationary chalcopyrite electrodes in acidic solutions were characterised by an anodic peak or prewave which occurred between 0.4 and 0.7 V (Figures 9.4 and 9.5). The prewave was observed irrespective of the type of acid electrolyte used or the direction of the initial potential sweep. In 0.1 M $HClO_4$, the peak current decreased on subsequent cycles until a reproducible voltammogram was obtained after about five cycles (Figure 9.6A), indicating that passivation was occurring to a degree in the prewave region; the extent of passivation being dependent on the negative-going potential scanning limit ($E_{\lambda c}$) (see section 9.3.1.1).

The main oxidation reactions in the prewave region could be attributed to the reactions:-

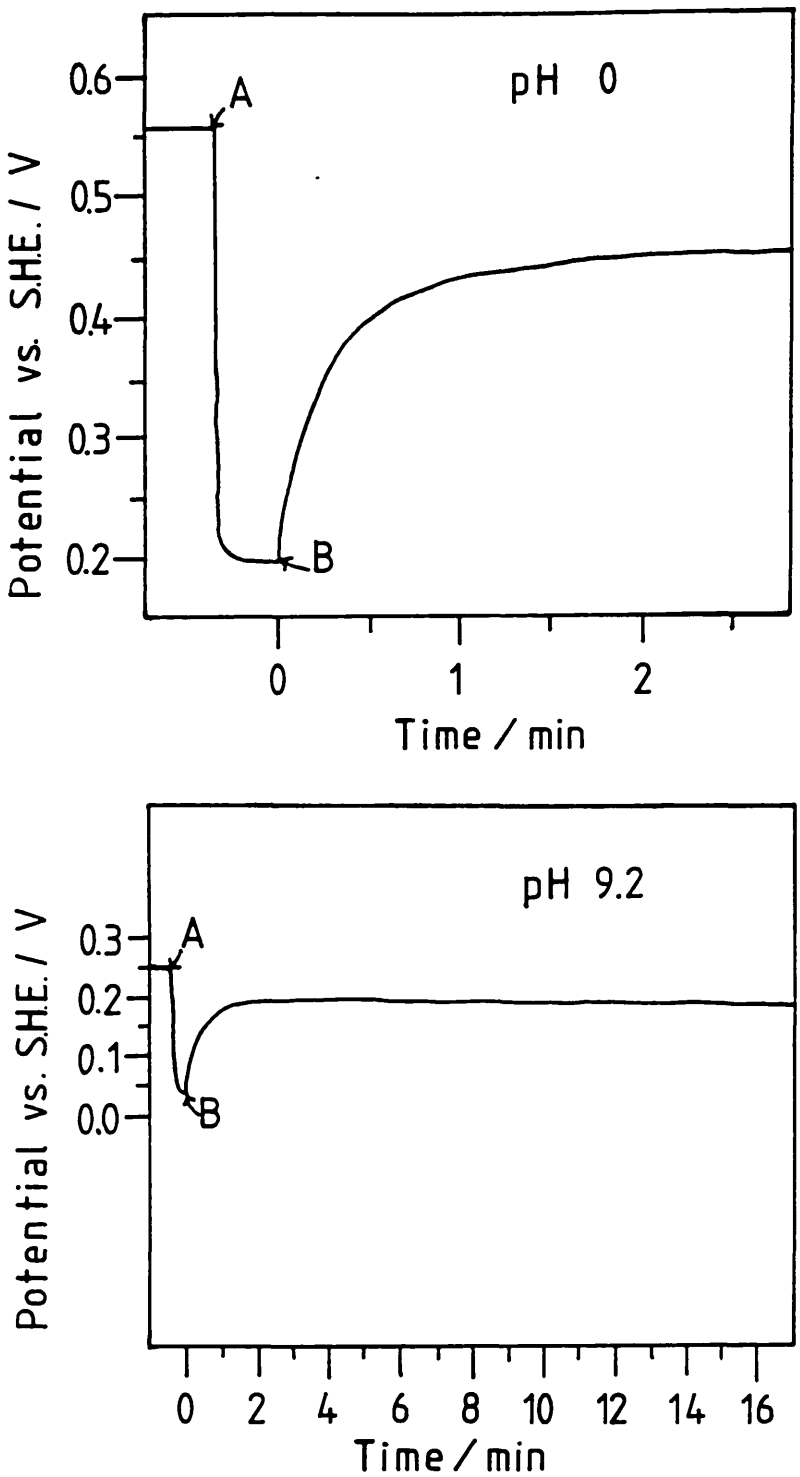


Fig 9.3 Change in the open-circuit potential of a chalcopyrite electrode with time after in situ polishing at pH 0 (top) and pH 9.2 (bottom). (A) commence polishing; (B) finish polishing.

$$CuFeS_2 = CuS + Fe^{2+} + S + 2e \qquad (a_4)$$

$$E = 0.232 + 0.0295 \log [Fe^{2+}]$$

$$CuFeS_2 = CuS + Fe^{3+} + S + 3e \qquad (b_4)$$

$$E = 0.412 + 0.197 \log [Fe^{3+}]$$

occurring in series with reaction (r_4):-

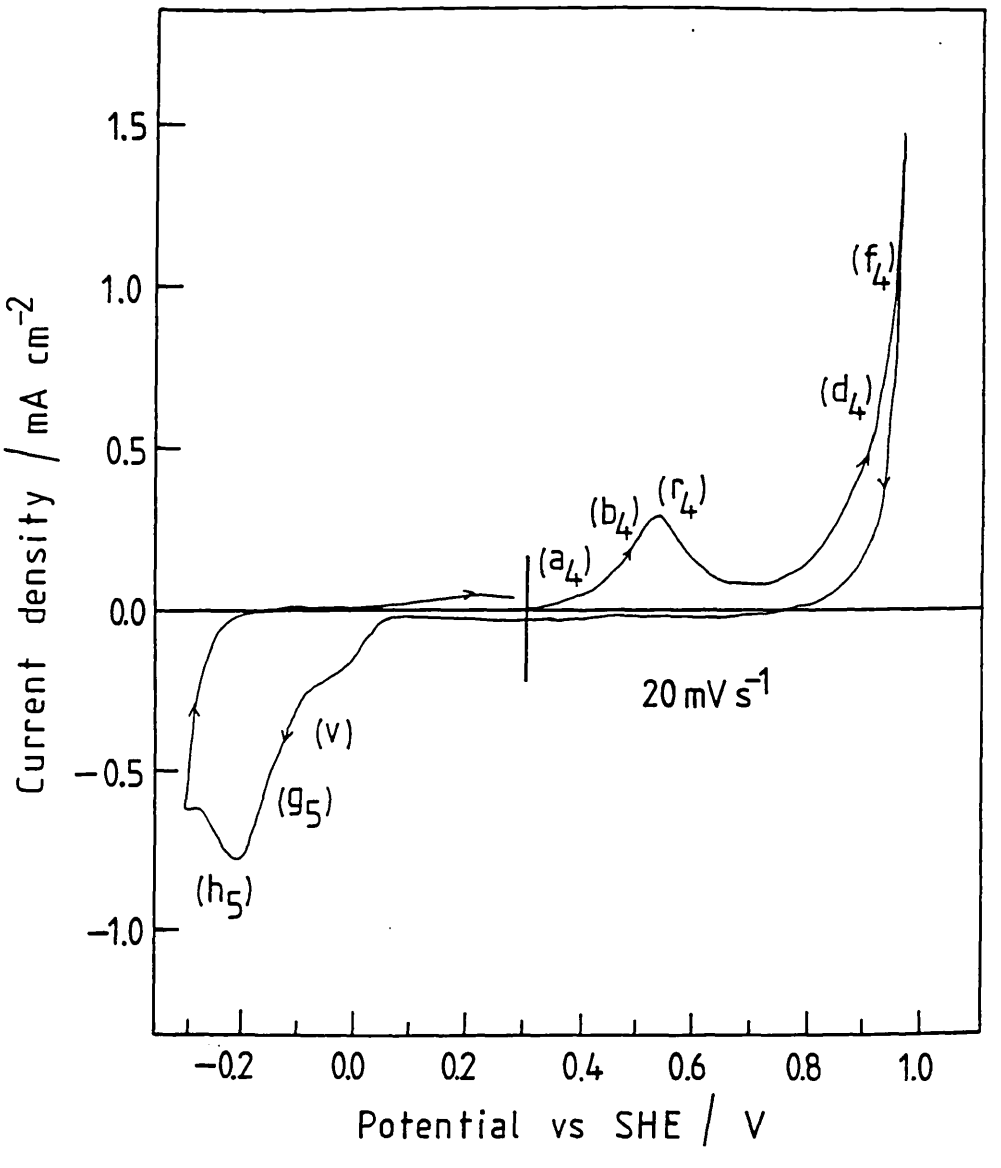


Fig 9.4 Cyclic voltammogram of a stationary chalcopyrite in stirred solution at pH 1 (0.1 M H_2SO_4) and a sweep rate of 20 mV s^{-1}.

$$CuS = Cu^{2+} + S + 2e \qquad (r_4)$$

$$E = 0.590 + 0.0295 \log [Cu^{2+}]$$

the latter reaction becoming more significant at high potentials. On the negative-going potential sweep, a reduction peak was observed at 0.35 V in quiescent solution (Figure 9.6A) assigned to the reverse

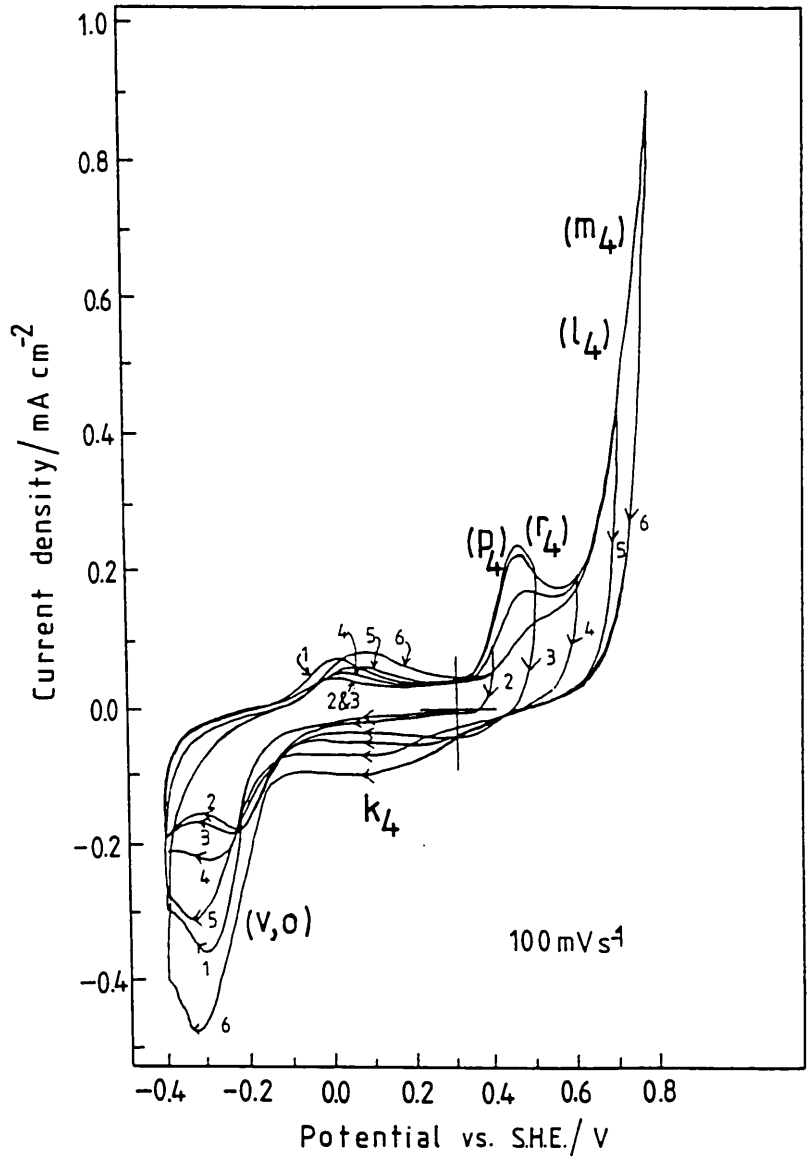


Fig 9.5 The effect of extending the anodic potential scanning limit (E_{λ_a}) on cyclic voltammograms of chalcopyrite at pH 4.6 (0.5 M CH_3COOH + 0.5 M CH_3COONa) in stirred solution and a sweep rate of 100 mV s^{-1}.

of reaction (k_4), since stirring decreased the current by dispersing the Cu^{2+} produced by reaction (r_4). At lower cathodic potentials the reduction of chalcopyrite to bornite (reaction (g_5))[179] and sulphur reduction (reaction (v)) gave rise to the reduction peak at -0.1 V, the latter reaction being reversed at 0.05 V on the subsequent anodic sweep, again with stirring dispersing the H_2S and decreasing the

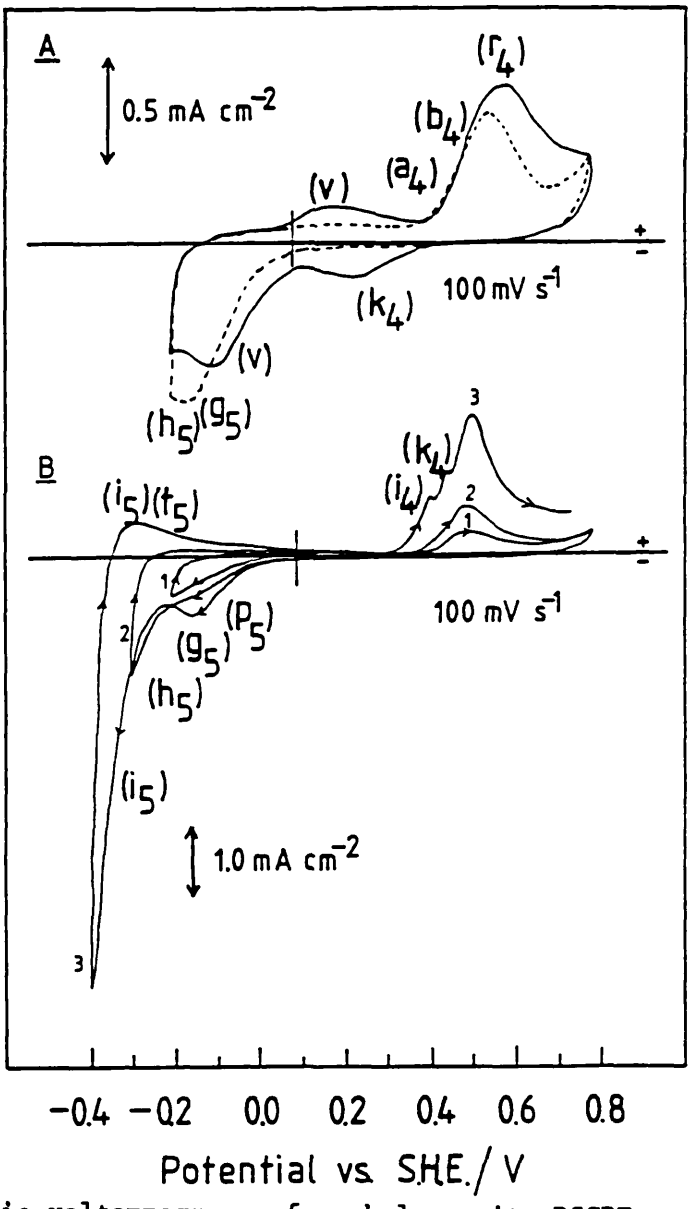


Fig 9.6 Cyclic voltammograms of a chalcopyrite RSCBE at pH 1 (0.1 M $HClO_4$) and a sweep rate of 100 mV s^{-1}. (A) effect of electrode rotation; (——) stationary electrode; (---) rotated electrode. (B) effect of extending the cathodic potential scanning limit ($E_{\lambda c}$) on the anodic prewave peak height (rotated electrode).

oxidation peak current. At the cathodic limit ($E_{\lambda c}$ = -0.2 V) chalcopyrite reduction to chalcocite (reaction (h_5)) could also occur (Figure 9.6A).

The presence of Fe^{2+} at a concentration of 0.1 mol dm^{-3} in 1 M $HClO_4$ increased the magnitude of the prewave peak only slightly (Figure 9.7A), consistent with the known irreversible nature of this redox

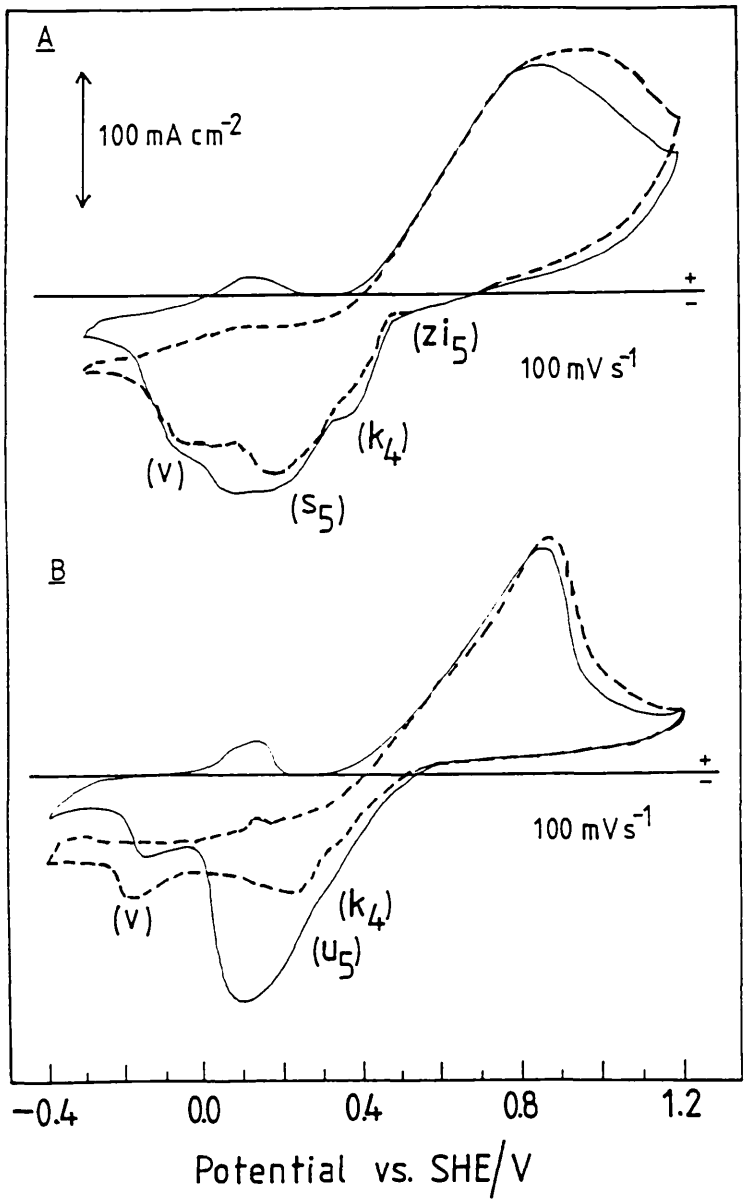


Fig 9.7 Cyclic voltammograms of a chalcopyrite RSCBE in:
(A) 1 M $HClO_4$ + 0.1 M $CuSO_4$ + 0.1 M $FeSO_4$
(B) 1 M HCl + 0.1 M $CuSO_4$
(——) stationary electrode; (---) rotated electrode.

system on chalcopyrite[160]. The addition of Cu^{2+} at the same concentration enhanced the magnitude of the peak assigned to reaction (k_4), supporting the reaction assignment given above. In addition, a cathodic peak was observed at 0.2 V due to the reduction of Cu(II) to Cu^0 (reaction (s_5); Figure 9.7A). In 1 M HCl (Figure 9.7B), peak (s_5) was absent, presumably due to the stability of Cu(I) in chloride media; the cathodic peak at 0.1 V being attributable to reaction (k_4) occurring in parallel with the reduction of Cu^{2+} to $CuCl_2^-$ (reaction (u_5)).

In separate experiments with ferrous (0.1 mol dm^{-3}) and cupric sulphate (0.1 mol dm^{-3}) in 1 M HCl, though in the absence of sulphide, the reduction of Cu^{2+} to $CuCl_2^-$ (reaction (u_5)) and $CuCl_2^-$ to Cu (reaction (v_5)) on platinum occurred at ~ 0.4 V and 0.08 V, respectively (Figure 9.8).

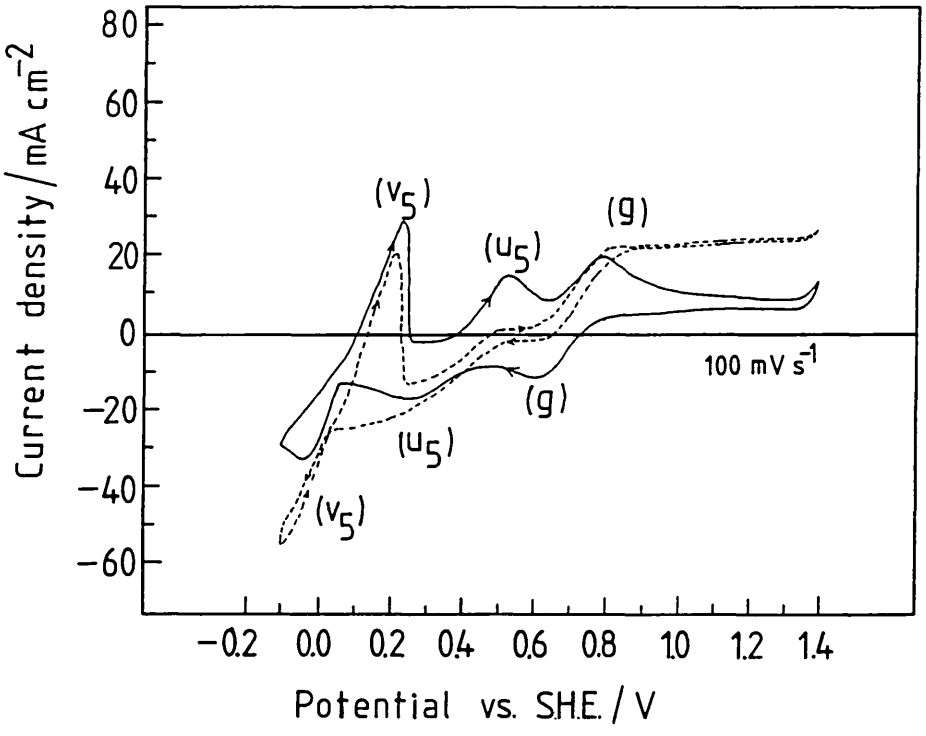


Fig 9.8 Cyclic voltammograms of a RSCBE Pt collector electrode in 1 M HCl + 0.1 M $CuSO_4$ + 0.1 M $FeSO_4$ (——) stationary electrode; (---) rotated electrode.

9.3.1.1 The Prewave Process

As so little solid product is formed in the prewave region it cannot be identified by X-ray diffraction. However, it has been well documented that the initial oxidation of chalcopyrite involves the selective dissolution of iron[152,158]; the shorter the time, the higher the Fe/Cu molar ratio found in solution; decaying from 4:1 to a final value of 2:1[155].

There are several possible mechanisms to explain the anodic prewave process:-

(i) Gardner and Woods[175] assigned the prewave process to reaction (a_4), producing Fe^{2+}, sulphur and covellite (CuS). The latter was said to oxidise at potentials above the prewave region to give Cu^{2+} and sulphur by reaction (r_4), implying that the prewave process does not involve the release of Cu^{2+} ions into solution. Therefore this mechanism fails to explain the Fe/Cu ratio found in solution.

(ii) While others[152,167] have observed the prewave peak, its dependence on the cathodic potential limit has not been reported. By sweeping the potential to $E_{\lambda c}$ values < -0.2 V (Figure 9.6B), the reduction of chalcopyrite occurred (probably by reactions (p_5), (g_5), (h_5) and (i_5)), leading to the reactivation of the prewave peak at 0.55 V. The formation of metallic copper by reactions (i_5) gave rise to a broad oxidation peak at -0.3 V due to the reverse reaction occurring in parallel with reaction (t_5), producing Cu_2S. The subsequent anodic peaks observed at 0.4 V and 0.45 V (Figure 9.6B), superimposed on the prewave, could then be assigned to the oxidation of bornite (reaction (i_4)) and chalcocite (reaction (k_4)) formed on the previous cathodic sweep.

This suggested that the prewave process involved the oxidation of copper sulphide phases with a Cu/Fe ratio greater than that of chalcopyrite. Thus chalcopyrite oxidation may have proceeded via bornite ($CuFe_{0.2}S_{0.8}$ - reaction (g_4)) and chalcocite (Cu_2S - reaction (i_4)) to produce covellite (reaction (k_4)) by an overall reaction (n_4):-

$$CuFeS_2 = CuFe_{0.2}S_{0.8} + 0.8Fe^{2+} + 1.2S + 1.6e \qquad (g_4)$$

$$E = 0.260 + 0.0295 \log [Fe^{2+}]$$

$$CuFe_{0.2}S_{0.8} = 0.5\ Cu_2S + 0.2Fe^{2+} + 0.3S + 0.4e \qquad (i_4)$$

$$E = 0.273 + 0.0295 \log [Fe^{2+}]$$

$$0.5\ Cu_2S = 0.5\ CuS + 0.5\ Cu^{2+} + e \qquad (k_4)$$

$$E = 0.530 + 0.295 \log [Cu^{2+}]$$

Overall $$CuFeS_2 = 0.5\ CuS + 1.5S + Fe^{2+} + 0.5\ Cu^{2+} + 3e \qquad (n_4)$$

$$E = 0.437 + 0.01 \log [Cu^{2+}] + 0.02 \log [Fe^{2+}]$$

This mechanism explains the high dissolved Fe/Cu ratio and its final value of two, and is also consistent with the E_h-pH diagram shown in Figure 9.2, which allows for the irreversibility of sulphate formation (see section 9.1).

(iii) Alternatively, the prewave process could represent the dissolution of metal ions from the mineral lattice leaving a metal-deficient sulphide film ($Cu_xFe_yS_2$, where $x < 1$, $y < 1$) which is formed by reaction (l_5):-

$$CuFeS_2 = (1-x)Cu^{2+} + (1-y)Fe^{2+} + Cu_xFe_yS_2 + 4(2-x-y)e \qquad (l_5)$$

Open circuit potential decay measurements, recorded after pulsing the potential into the prewave region, showed that a small potential arrest occurred after ~ 15 s (Figure 9.9). This could be due to the galvanic reduction of the porous metal-deficient film by the underlying, unaltered chalcopyrite, forming sulphur by the reaction:-

$$Cu_xFe_yS_2 = (x+y)\ CuFeS_2 + (2-x-y)S \qquad (m_5)$$

XPS studies of chalcopyrite oxidation in air and air-saturated solutions by Woods et al[330,379-381] tend to support this mechanism. In early studies[381], the sulphur spectrum for an oxidised surface was interpreted in terms of three different environments with binding

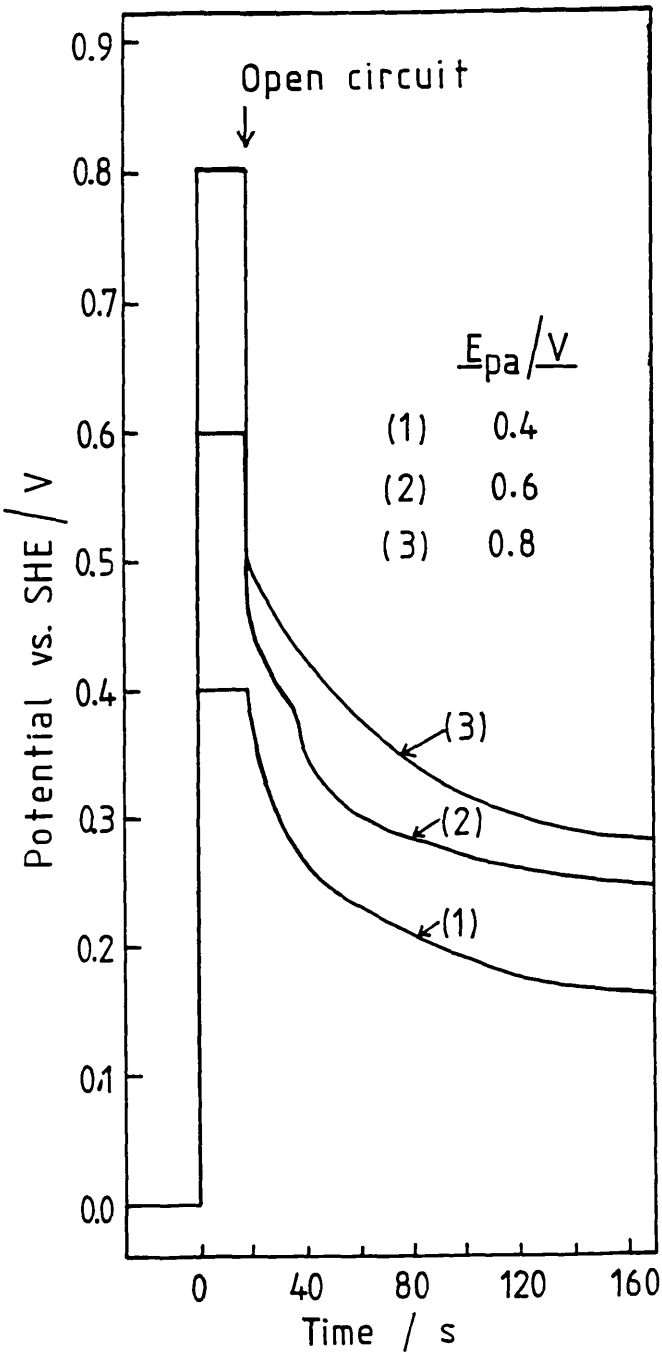


Fig 9.9 Open-circuit potential versus time profiles for a chalcopyrite electrode at pH 4.6 (0.5 M CH_3COOH + 0.5 M CH_3COONa) recorded after pulsing to various anodic potentials for 20 seconds.

energies consistent with the presence of CuS, S and unaltered chalcopyrite. This observation appeared to substantiate the conclusions from previous electrochemical studies[175], that anodic oxidation was represented by reaction (a_4).

However, reappraisal of the sulphur spectra for surfaces oxidised by air[379] revealed that they were best fitted by one additional doublet shifted by at least 1.7 eV from that of chalcopyrite, with the shift increasing towards 1.9 eV as the exposure time increased. It was concluded that this was due to the formation of a copper sulphide of stoichiometry close to CuS_2 and that in acidic solutions reaction (a_4) should be presented as:-

$$CuFeS_2 = CuS_2 + Fe^{2+} + 2e \qquad (9.5)$$

although the copper content of the surface was less than expected from the equivalent of reaction (9.5)[379,380]. The peak intensities were consistent with a layer of composition $Cu_{0.8}S_2$[379,380] indicating that some copper was leached from the surface in addition to iron during the prewave process.

(iv) When a previously passivated electrode was held at its rest potential the anodic prewave peak was enhanced on the subsequent anodic potential sweep. The peak current also increased with the time interval (0 - 80 minutes) between potential cycles. However, the initial current value obtained with a freshly polished electrode was not achieved, except by repolishing, or extending the cathodic potential limit to < -0.2 V.

The dependence of the anodic prewave peak current on the immersion time at the initial rest potential and the cathodic potential limit is consistent with chalcopyrite decomposition occurring via a path involving both non-oxidative and oxidative dissolution. Some non-oxidative decomposition paths indicated by the thermodynamics of Figure 9.1 include the following:-

$$CuFeS_2 + 0.2H^+ = CuFe_{0.2}S_{0.8} + 0.8Fe^{2+} + 0.8H_2S \qquad (9.6)$$

$$CuFeS_2 + 2H^+ = CuS + Fe^{2+} + H_2S \qquad (9.7)$$

However, if non-oxidative dissolution produced a non-thermodynamic metal-deficient sulphide film (depleted in iron more than copper), the process is best described by the following equation:-

$$CuFeS_2 + 2xH^+ = CuFe_{(1-x)}S_{(2-x)} + xH_2S + xFe^{2+} \qquad (9.8)$$

the copper-rich sulphide phase being oxidised on the subsequent positive-going potential sweep. Alternatively, Fe(III) could oxidise the Cu(I) to Cu(II) in the lattice to maintain solid state electroneutrality on dissolution of Fe(II):-

$$Cu^+Fe^{3+}(S^{2-})_2 = Cu^+_{(1-x)}Cu^{2+}_xFe^{3+}_{(1-x)})(S^{2-})_2 + xFe^{2+}_{(aq)} \qquad (z_5)$$

or, as suggested by Linge[155], Fe(III) could dissolve and three protons enter the vacant cation sites to maintain charge neutrality:-

$$Cu^+Fe^{3+}(S^{2-})_2 + 3xH^+ = Cu^+Fe^{3+}_{(1-x)}H^+_{3x}(S^{2-})_2 + xFe^{3+}_{(aq)} \qquad (za_5)$$

9.3.1.2 Chalcopyrite RSCBE at pH 0 (1 M $HClO_4$ and 1 M HCl)

Figure 9.10 shows a voltammogram of a chalcopyrite RSCBE in 1 M $HClO_4$ and the current response at the Pt collector electrode for a range of potentials (E_c); similar behaviour was observed in 1 M HCl. In separate experiments with ferrous and cuprous sulphate in 1 M $HClO_4$, though in the absence of sulphide, Fe(II) oxidation and Fe(III) reduction were found to be transport controlled at potentials > 1.0 V and < 0.5 V, respectively. Cu(II) reduction to Cu metal occurred at potentials < 0.28 V (see Figure 6.22, section 6.4.2). The chalcopyrite reduction doublet at 0 V was attributed to the reduction of anodically formed sulphur (reaction (v)) and lattice decompostion by reaction (g_5), producing Fe(II) and H_2S, which were reoxidised at the Pt collector electrode. The former species gave rise to the current response at 1.0 V, and both species were oxidised at 1.4 V. The main reduction process at the cathodic potential limit was due to reactions (h_5) and (i_5), again producing Fe(II) and H_2S, which were reoxidised at the Pt collector electrode.

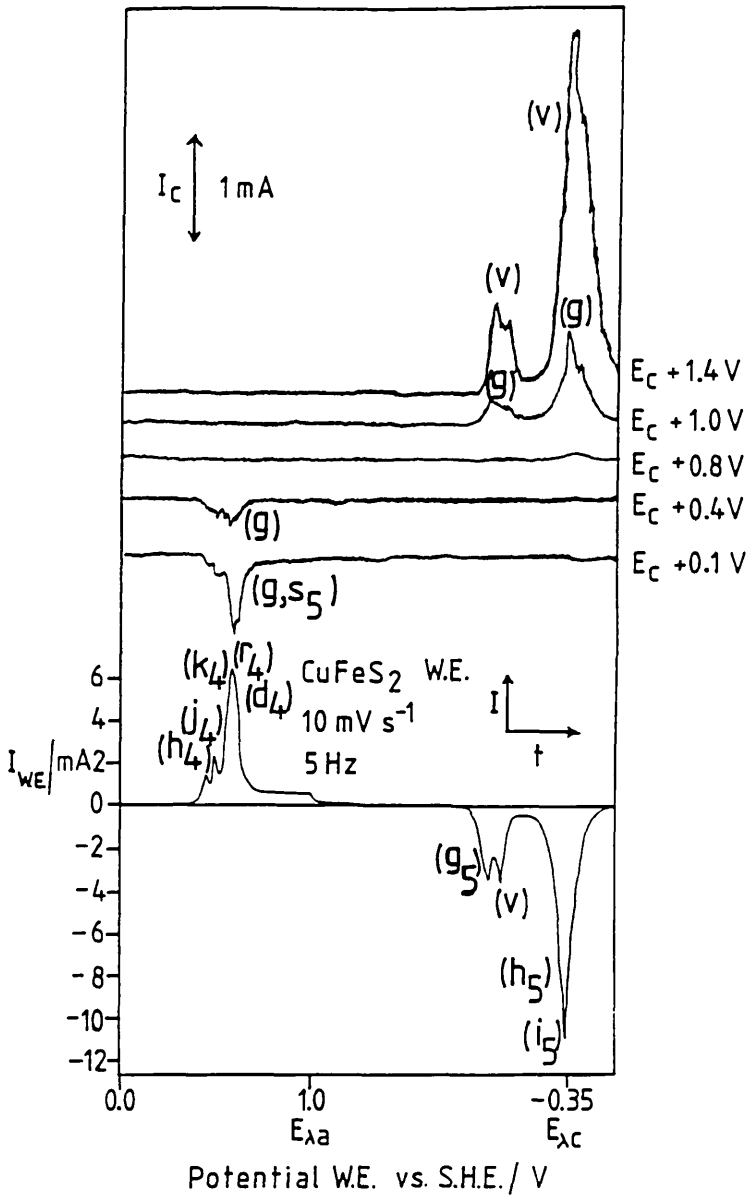


Fig 9.10 Cyclic voltammogram of a RSCBE in 1 M $HClO_4$ (pH 0) with the chalcopyrite working electrode (W.E.) swept anodically from 0.0 to 1.0 V, then cathodically to -0.35 V, and the platinum collector electrode held at various potentials (E_c).

The oxidation of chalcopyrite apparently produced no Fe(II) species judging by the absence of any corresponding collector oxidation current at potentials > 0.8 V contrary to that expected from reactions (a_4), (g_4) and (i_4). The two small oxidation peaks at 0.4 V and 0.45 V were associated with Fe(III) reduction at the collector electrode (E_c potentials < 0.5 V), precluding the oxidation of chalcopyrite by reaction (a_4), which would have produced Fe(II). Thus the following reactions may have been involved:-

$$CuFeS_2 = CuFe_{0.2}S_{0.8} + 0.8Fe^{3+} + 1.2S + 2.4e \qquad (h_4)$$

$$E = 0.430 + 0.197 \log [Fe^{3+}]$$

$$CuFe_{0.2}S_{0.8} = 0.5\ Cu_2S + 0.2Fe^{3+} + 0.3S + 0.6e \qquad (j_4)$$

$$E = 0.439 + 0.0197 \log [Fe^{3+}]$$

followed by reactions (k_4) and (r_4) giving rise to the main oxidation peak at 0.55 V (reaction (b_4)). If the Pt collector electrode responses at 0.45 V (0.25 mA) and 0.1 V (0.75 mA) are taken as being due to Fe(III) and (Fe(III) + Cu(II)) reduction, respectively and proportional to the concentration of these species (i.e. transport controlled), then approximately equal amounts of copper and iron are dissolved at 0.58 V, as expected from reaction (d_4). However, quantitative interpretation of the RSCBE results is complicated by the voltammetry necessarily being non-steady state, unlike the collector efficiency data (see Chapter 5). Also the presence of H_2S in solution may change the behaviour of the Pt collector electrode, such that mass transport controlled currents may not be observed at the potentials expected from experiments in the absence of sulphide, which may also change the activity of dissolved metal ions, before they can be detected at the collector electrode.

9.3.2 Voltammetry in Neutral and Basic Solutions

In neutral and alkaline solutions, the decrease in the solubility of Fe(II), Fe(III) and Cu(II) species, increased the number of surface transformation reactions detected in the voltammetry, and so restricted the usefulness of the RSCBE. Cyclic voltammograms for chalcopyrite recorded over the pH range 7 - 13 are presented in Figures 9.11 - 9.13. The anodic potential scanning limit ($E_{\lambda a}$) was extended to much higher values than those used in previous studies by Gardner and Woods[175].

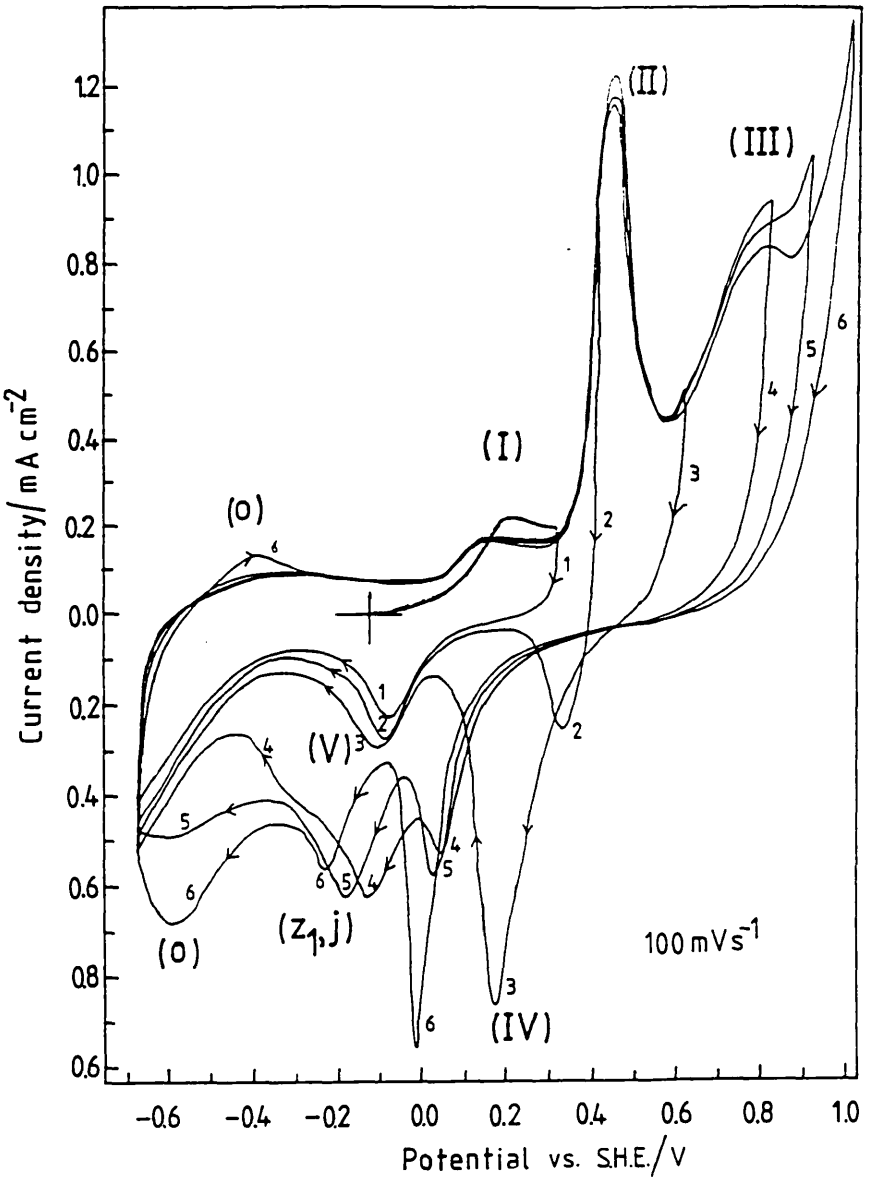


Fig 9.11 The effect of extending the anodic potential scanning limit (E_{λ_a}) on cyclic voltammograms of chalcopyrite at pH 7 (0.025 M KH_2PO_4 + 0.025 M Na_2HPO_4) in stirred solution and a sweep rate of 100 mV s^{-1}.

In contrast to pyrite and pyrrhotite, for which sulphate formation was the dominant oxidation reaction in neutral and basic solutions (see sections 6.4.5 and 7.3.4), the equality of anodic and cathodic charges observed in the voltammograms for chalcopyrite indicated that oxidation of this mineral produced negligible quantities of sulphate.

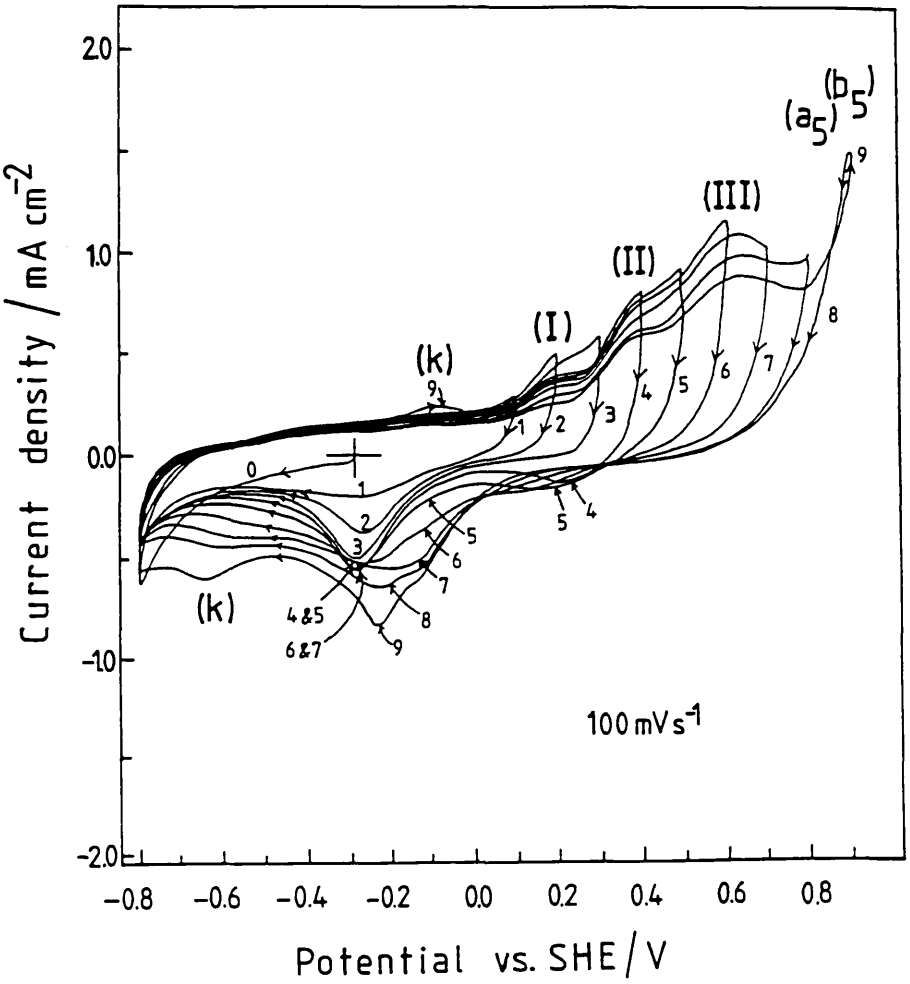


Fig 9.12 The effect of extending the anodic potential scanning limit (E_{λ_a}) on cyclic voltammograms of chalcopyrite at pH 9.2 (0.05 M $Na_2B_4O_7$) in stirred solution and a sweep rate of 100 mV s^{-1}.

9.3.2.1 pH 7 (0.025 M KH_2PO_4 + 0.025 M Na_2HPO_4)

At pH 7 (Figure 9.11) an oxidation peak (I) was observed at 0.15 V on the first positive-going potential scan, which shifted to 0.1 V on subsequent anodic potential scans. Gardner and Woods[175] observed a similar oxidation peak in their voltammetric studies of chalcopyrite oxidation over the pH range 4.6 - 13 and concluded that the reaction giving rise to the peak in neutral and basic solutions was:-

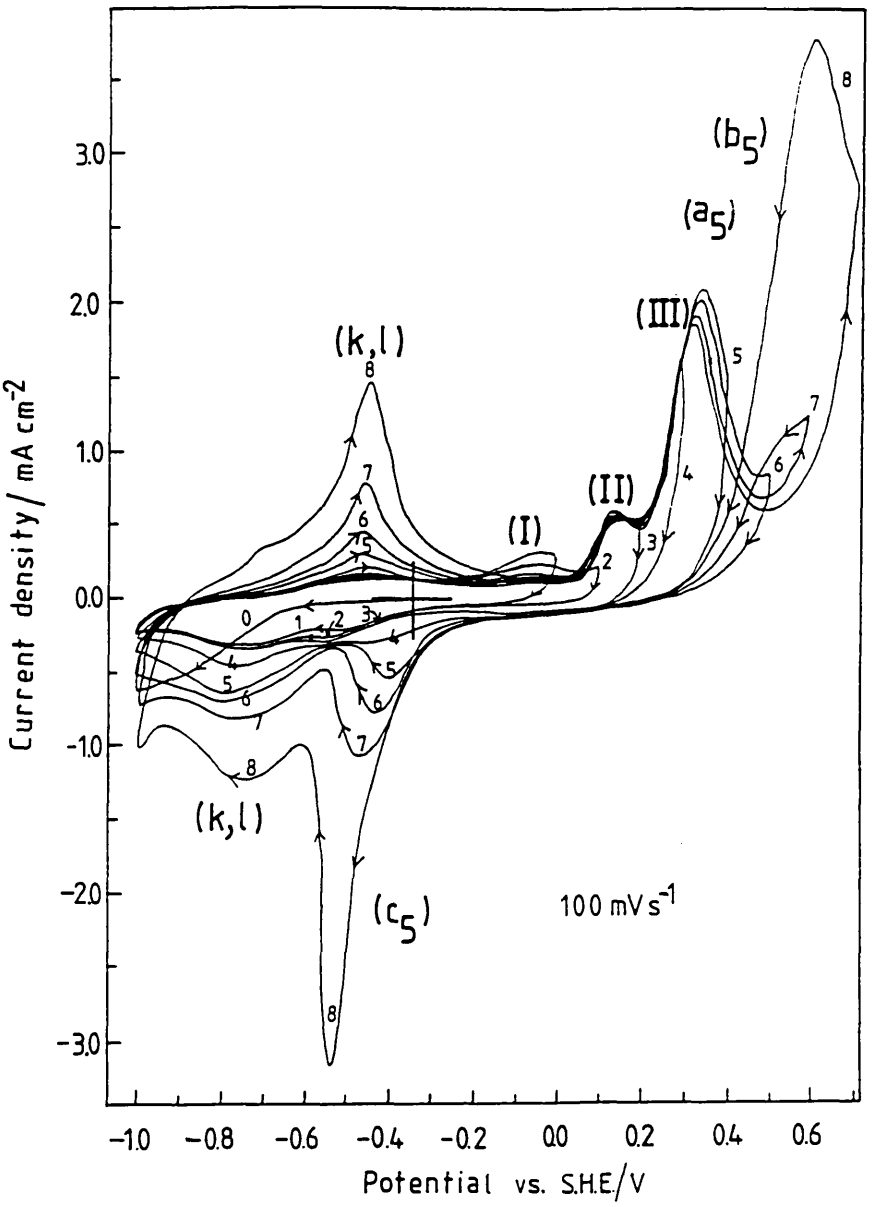


Fig 9.13 The effect of extending the anodic potential scanning limit (E_{λ_a}) on cyclic voltammograms of chalcopyrite at pH 13 (0.1 M NaOH) in stirred solution and a sweep rate of 100 mV s^{-1}.

$$CuFeS_2 + 3H_2O = CuS + S + Fe(OH)_3 + 3H^+ + 3e \qquad (p_4)$$

$$E = 0.507 - 0.0591\ pH$$

However, if sulphoxy species were not formed under mild oxidising conditions, as the reversibility of the system suggests, then thermodynamic considerations predict that bornite and chalcocite should form as intermediate phases during the oxidation of chalcopyrite to covellite (see section 9.3.1.1, mechanism **(ii)**):-

$$CuFeS_2 + 2.4H_2O = CuFe_{0.2}S_{0.8} + 0.8Fe(OH)_3 + 1.2S + 2.4H^+ + 2.4e \quad (s_4)$$

$$E = 0.525 - 0.0591\ pH$$

$$CuFe_{0.2}S_{0.8} + 0.6H_2O = 0.5Cu_2S + 0.2Fe(OH)_3 + 0.6H^+ + 0.3S + 0.6e \quad (u_4)$$

$$E = 0.534 - 0.0591\ pH$$

$$Cu_2S + 2H_2O = CuS + Cu(OH)_2 + 2H^+ + 2e \quad (w_4)$$

$$E = 0.802 - 0.0591\ pH$$

Since the reversible potential (0.39 V at pH 7) for reaction (w_4) coincided closely with the onset of the anodic current giving rise to the second oxidation peak (II), this indicated that peak (I) was probably associated with the formation of chalcocite by the overall reaction:-

$$CuFeS_2 + 3H_2O = 0.5\ Cu_2S + 1.5S + Fe(OH)_3 + 3H^+ + 3e \quad (zg_5)$$

$$E = 0.527 - 0.0591\ pH$$

rather than covellite, as Gardner and Woods had claimed earlier[175]. Peak (II) was assigned to chalcocite oxidation (reaction w_4), forming covellite, which oxidised by reaction (x_4):-

$$CuS + 2H_2O = Cu(OH)_2 + S + 2H^+ + 2e \quad (x_4)$$

$$E = 0.863 - 0.0591\ pH$$

producing cupric oxide/hydroxide and elemental sulphur.

On the reverse negative-going potential sweep and for E_{λ_a} values < 0.6 V, the charge associated with reduction peaks (IV) and (V) approximated to that associated with anodic peaks (II) and (I), respectively (Figure 9.11); the charge could not be measured accurately due to peak overlap. This observation suggested that peaks (IV) and (V) arise from the reverse of reactions (x_4+w_4) and (zg_5), respectively. Indeed, current-potential profiles were identical in both stirred and quiescent solutions, indicating that all the oxidation/reduction reactions involved solid species.

If the reaction assignment given above was correct, then the anodic charge for peak (II) should have been 2/3 times that of peak (I). However, the observed charge ratio was much higher (Figure 9.11), the charge for peak (II) (1.86 mC cm^{-2}) being approximately four times greater than that for peak (I) (0.47 mC cm^{-2}). The extra charge associated with peak (II) could not be ascribed to the formation of sulphoxy species, since the process(es) occurring in this potential region were reversible. The most plausible explanation for the disparity in the observed and expected charge ratio was that the chalcopyrite surface had already been partially oxidised and depleted in iron and sulphur whilst polishing the electrode. This resulted in the formation of Cu_2O/CuOH on the surface, peak (ii) corresponding closely with the thermodynamic reversible potentials for the oxidation of either one, or both, of these products (reactions (w_4+x_4) and (c_5)); peak (I) being ascribed to the oxidation of unaltered chalcopyrite. Since copper in chalcopyrite occurs in the Cu(I) valence state, this should help stabilise Cu(I) oxide/hydroxide on the surface of chalcopyrite.

On extending E_{λ_a} to potentials > 0.6 V the current increased rapidly due to the bulk oxidation of chalcopyrite occurring by reactions (a_5) and (b_5); a small anodic wave (III) being observed at 0.85 V (Figure 9.11). The decrease in interfacial pH associated with sulphate formation (reaction (b_5)) increased the solubility of metal oxide/hydroxide species on the chalcopyrite surface. Since $Cu(OH)_2$ is more soluble than $Fe(OH)_3$ or FeOOH (see Figures II(iv), II(v) and II(xvi); Appendix II), the net effect was for the surface to become depleted in copper and sulphur as the potential increased. Thus,

cathodic peak (IV), assigned to the reduction of $Cu(OH)_2$ and sulphur by reactions (w_4+x_4) and (c_5), decreased initially on increasing E_{λ_a} above 0.6 V, and cathodic peaks appeared at -0.2 V and -0.6 V, ascribed to Fe(III) hydroxide reduction by reactions (j), (z_1) and (o).

Recent XPS studies of chalcopyrite oxidation in air-saturated solutions[380,381] (i.e. corresponding to the potential region of peak I) have confirmed that ferric oxide and a copper sulphide phase are formed in neutral and basic media. However, the exact identify of the copper sulphide phase is not clear, since the interpretation of the sulphur spectra was complicated by the possible loss of elemental sulphur in the spectrometer vacuum prior to recording the spectra. Covellite and sulphur[381], or a copper sulphide of stoichiometry close to CuS_2[380], may have been formed (see section 9.3.1.1):-

$$CuFeS_2 + 3H_2O = Fe(OH)_3 + CuS_2 + 3H^+ + 3e \qquad (zf_5)$$

with the CuS_2 product retaining the sulphur lattice of the original mineral.

Clearly the voltammograms are not sufficiently discriminating to distinguish between all the possible reactions occurring during chalcopyrite oxidation due to the overpotential requirements of phase transitions. The interpretation of the voltammetric behaviour given above was based on the assumption that the oxidation products behaved as definite chemical entities. However, if non-thermodynamic phases were formed, such as CuS_2, then assigning reactions to the voltammetric peaks becomes very difficult.

9.3.2.2 pH 9.2 (0.05 M $Na_2B_4O_7$) and pH 13 (0.1 M NaOH)

Oxidation peaks (I), (II) and (III) were also evident in the voltammograms recorded at pH 9.2 (Figure 9.12) and pH 13 (Figure 9.13). However, the peaks were less distinct at pH 9.2 than at pH 7, and at pH 13, peak (I) appeared only on the first positive going scan. Furthermore, at pH 9.2 (Figure 9.12), the anodic current decreased with each positive-going potential scan, even at low E_{λ_a} potentials (< 0.5 V), in the region where peaks (I) and (II) occurred. Although

two cathodic peaks were observed on the reverse scan at 0.2 and -0.25 V, assigned to the reverse of reactions (zh_5) and (zf_5), respectively, or (x_4+w_4) and (zg_5), depending on the oxidation mechanism chosen (CuS_2 versus CuS + S; see section 9.2.2.1), clearly, not all of the mixed sulphur, ferric and cupric oxide/hydroxide product layer formed anodically was reduced back to chalcopyrite on the reverse negative-going scan. That which remained on the surface, inhibited chalcopyrite oxidation each time the potential was again swept in the positive direction.

Peak (III) occurred in the potential region assigned to the bulk oxidation of chalcopyrite by reactions (a_5) and (b_5) and was caused by the passivating effect of the cupric and ferric oxide/hydroxide oxidation products. As sulphate formation (reaction b_5), with its higher charge requirement, became more dominant with increasing pH, then the peak current at which passivation occurred also increased. At higher potentials, > 0.9 V at pH 9.2 (Figure 9.12) and > 0.5 V at pH 13 (Figure 9.13), the local decrease in pH caused by the predominance of reaction (b_5) was sufficient to breakdown the passive layers and the anodic current increased once more. The upward trend was continued after the scan was reversed due to pitting dissolution.

9.4 Pulse Voltammetry on Stationary Chalcopyrite Electrodes

9.4.1 pH 0 (1 M $HClO_4$)

In acidic media, rising current-time transients were observed at high anodic potentials (> 1.0 V at pH 0).

Figure 9.14 shows the i-t transient in response to a potential step from the chalcopyrite rest potential to 1.1 V. The initial decay (< 0.2 s, 8 mC cm^{-2}) was described best by an i vs. $t^{-0.5}$ relationship, characteristic of a diffusional process.

This suggested that sulphur, produced by reaction (d_4), and possibly covellite, formed by reaction (b_4), were presenting a diffusion

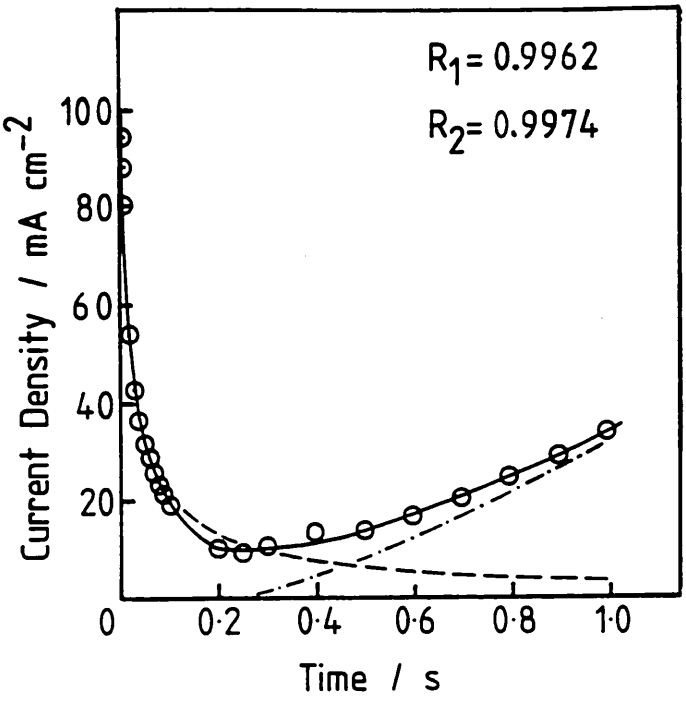


Fig 9.14 Current-time transient for a stationary chalcopyrite electrode held at 1.1 V in stirred solution at pH 0 (1 M $HClO_4$). (---) i vs. $t^{-0.5}$; (-•-•-) i vs $t^{1.5}$.
R_1 = correlation coefficient for the i vs. $t^{-0.5}$ relationship;
R_2 = correlation coefficient for the i vs. $t^{1.5}$ relationship.

barrier to the dissolving Cu^{2+} and Fe^{3+} ions. At longer times (> 0.2 s), the transient was best fitted to a i vs. $t^{1.5}$ relationship as further sulphur was formed and 3-dimensional pits were nucleated and grown. The formation of sulphate and protons, by reaction (f_4), was probably responsible for the pitting behaviour. At longer times, the current passed through a maximum presumably due to the overlap of growing pits[167] and the further growth of sulphur by reaction (d_4).

9.4.2 pH 9.2 (0.05 M $Na_2B_4O_7$)

Rising current-time transients were also observed in basic solutions on pulsing into the potential region where an upward trend in the anodic current was detected in cyclic voltammograms after reversing the scan (i.e. > 0.9 V at pH 9.2 (Figure 9.12) and > 0.5 V at pH 13 (Figure 9.13)).

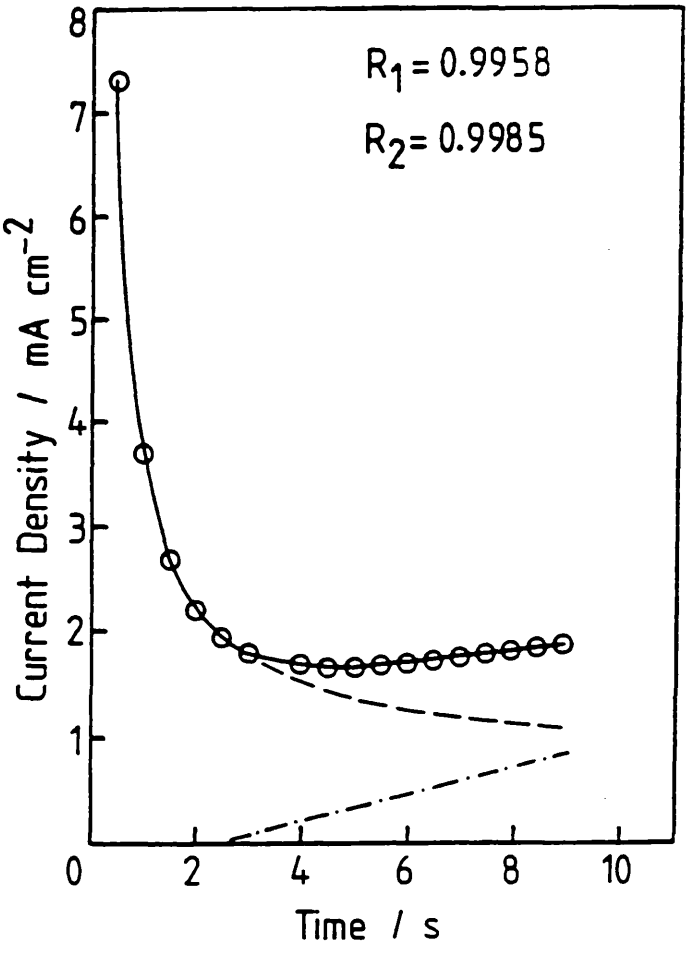


Fig 9.15 Current-time transient for a stationary chalcopyrite electrode held at 1.2 V in stirred solution at pH 9.2 (0.05 M $Na_2B_4O_7$). (---) i vs t^{-1}. (-·-·-) i vs. t.
R_1 = correlation coefficient for the i vs. t^{-1} relationship;
R_2 = correlation coefficient for the i vs. t relationship.

For example, at pH 9.2 (Figure 9.15), the current at 1.2 V was found to decay inversely with time at short times (t < 3 s, 50 mC cm^{-2}), as might be expected of an adsorption (oxide/growth) type of process, probably involving reactions (a_5) and (b_5). However, at longer times (t > 3 s), the current increased linearly with time due to pitting dissolution.

9.4.3 Charge vs. Time Measurements

Figure 9.16 shows the charge passed at a $CuFeS_2$ electrode after

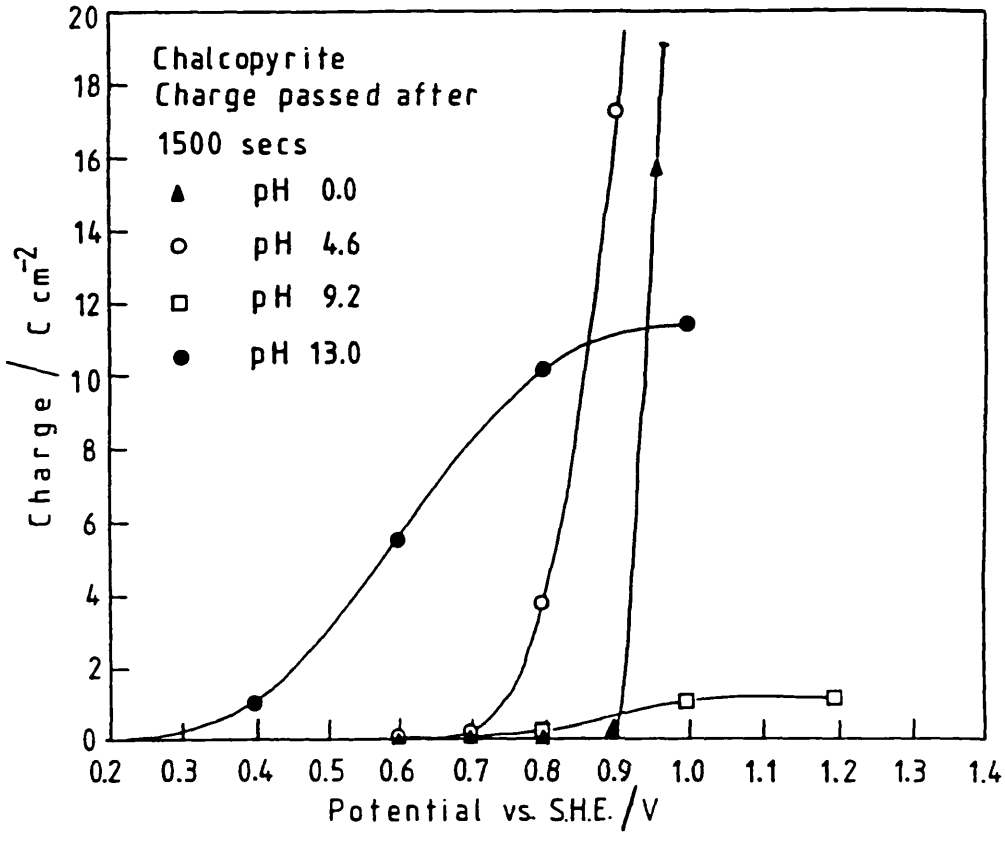


Fig 9.16 Anodic charge passed after 1500 s for a chalcopyrite electrode as a function of potential and pH.

1500 s, as a function of potential and pH. As was evident from the cyclic voltammetry as a function of pH (section 9.3), the formation of oxide/hydroxide phases near the pH of minimum solubility of Cu(II) and Fe(II)/Fe(III) species, caused passivation; hence the low charge at high potentials at pH 9.2 and the plateau for pH 9.2 and 13. At the latter pH, the formation of the anionic metal hydroxy complexes caused the solubility and hence the currents to be higher than at pH 9.2.

9.5 Impedance Measurements on Stationary Chalcopyrite Electrodes

The complex plane impedance spectra (0.1 Hz - 10 KHz) of stationary chalcopyrite electrodes in stirred deoxygenated solutions at pH 0 and

pH 9.2 are presented as a function of potential in Figures 9.17 and 9.18, respectively.

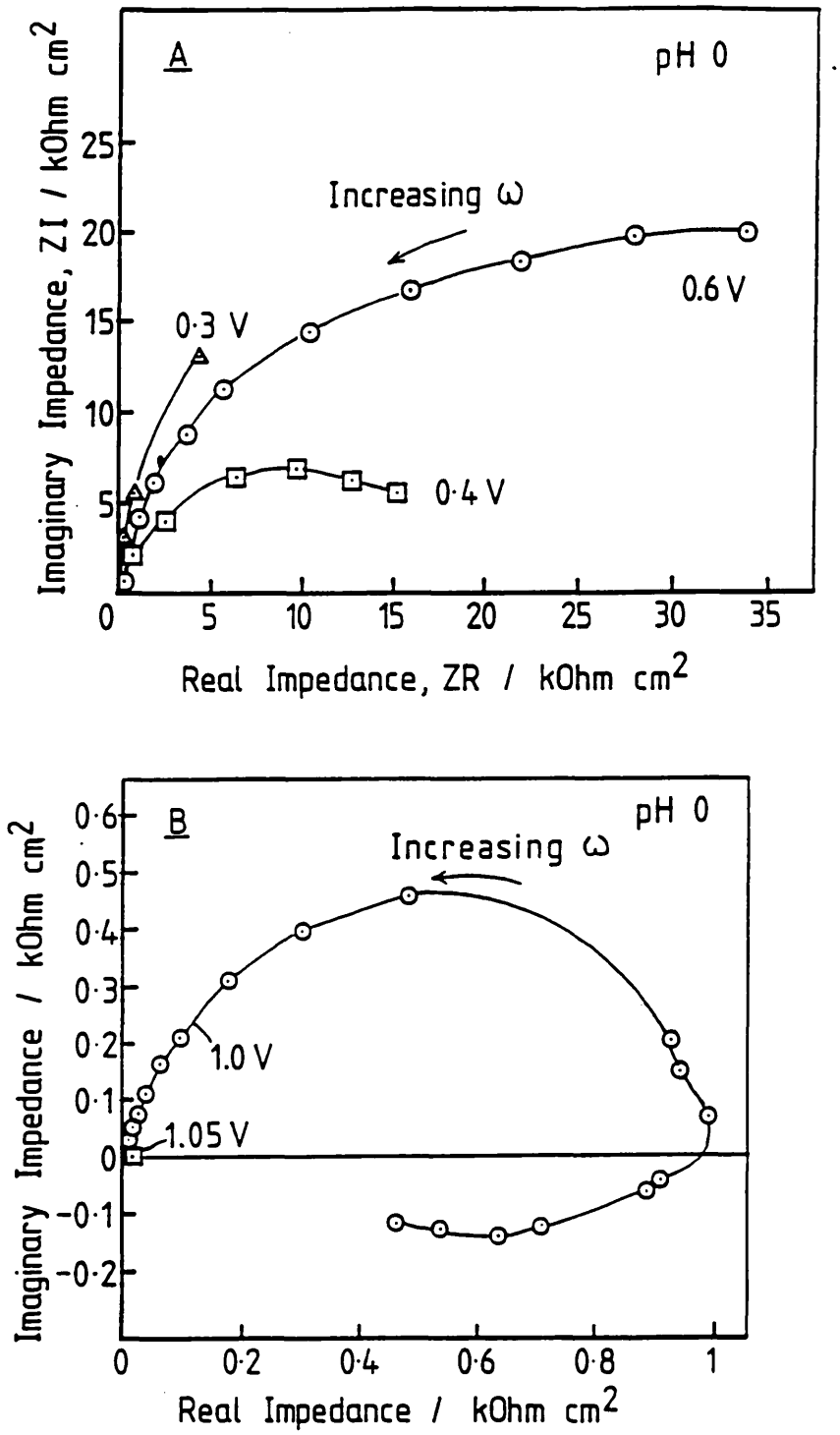


Fig 9.17 Impedance spectra (0.1 Hz - 10 kHz) for a stationary chalcopyrite electrode in stirred solution at pH 0 (1 M $HClO_4$).
(A) 0.3 to 0.6 V; (B) 1.0 and 1.05 V.

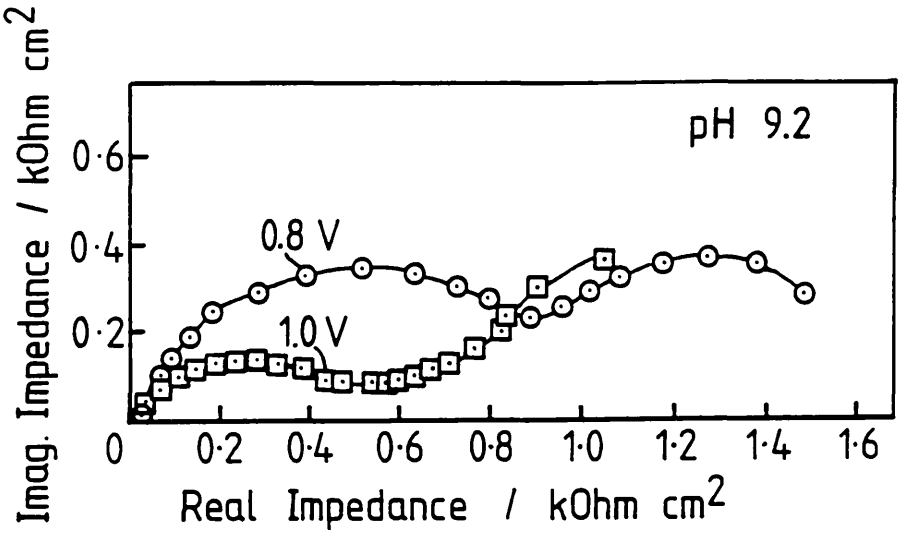


Fig 9.18 Impedance spectra (0.1 Hz - 10 kHz) for a stationary chalcopyrite electrode in stirred solution at pH 9.2 (0.05 M $Na_2B_4O_7$).

At pH 0, the spectra for 0.3 - 0.6 V (Figure 9.17) approximated to arcs of (depressed) semicircles. At high potentials (> 1.0 V), an inductive loop also appeared due to sulphur and/or sulphur-oxygen intermediate products adsorbing on the electrode surface. Capacitance values calculated from the imaginary impedance maximima by equation (6.36) increased at these high potentials from 20 μF cm^{-2} at 1.0 V to 1050 μF cm^{-2} at 1.3 V (Figure 9.19), due to the pseudocapacitance associated with product adsorption. However, the formation of porous sulphur by reactions (d_4), and possibly (b_4), caused only a small increase in the high frequency intercept, real axis resistance (R) (Figure 9.20), which indicated that the product layer conductivity was high.

At pH 9.2, the R value increased dramatically to 20 - 30 Ω cm^2, reflecting the low conductivity of the metal oxide/hydroxide phases formed by reactions such as (a_5) and (b_5) (Figure 9.20). The impedance spectra (Figure 9.18) showed evidence of two semicircles at potentials > 0.4 V which could be generated by two RC networks in

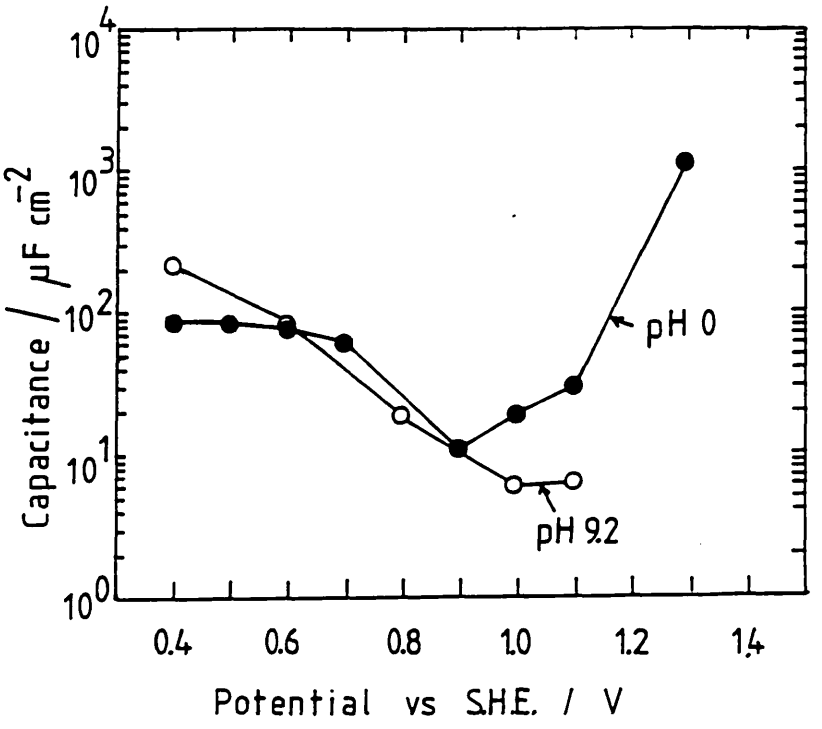


Fig 9.19 Chalcopyrite electrode capacitance at pH 0 (1 M $HClO_4$) and pH 9.2 (0.05 M $Na_2B_4O_7$) as a function of potential.

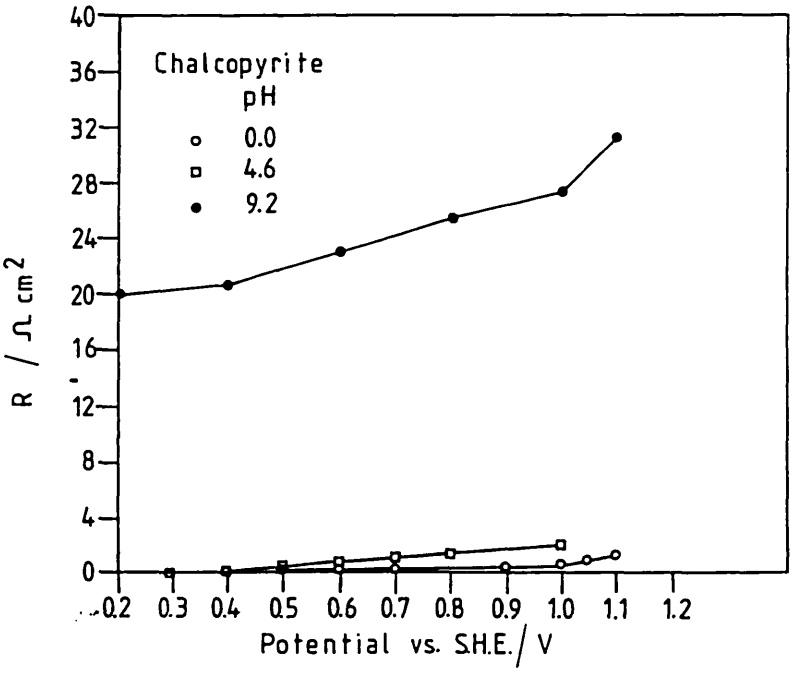


Fig 9.20 Real axis, high frequency intercept resistance, R (equivalent to the surface film resistance, R_f) as a function of potential and pH.

series. This behaviour suggested that the oxide/hydroxide surface phases produced by reactions (a_5) and (b_5), create a $CuFeS_2$/oxide (+sulphur)/solution structure, each interface having an associated capacitance (see section 6.6). With increasing potential the capacitance of the high frequency semicircle decreased from quasi-metallic values (tens of $\mu F\ cm^{-2}$) at low potentials to $< 1\ \mu F\ cm^{-2}$ at 1.1 V (Figure 9.19), which possibly indicated the dominance of a small solid state capacitance in the series sum.

CHAPTER TEN

MINERAL PULP SUSPENSION ELECTRODE STUDIES

CHAPTER 10: MINERAL PULP SUSPENSION ELECTRODE STUDIES

10.1 Introduction

Most sulphide minerals are rendered floatable by the adsorption of xanthates as collectors. However, there have been various reports in the literature of certain sulphide minerals, notably chalcopyrite[175,341-345,350-352] and pyrite[299,342,344-345,349] being floated in the absence of collectors. Having used mineral electrodes to study the electrochemical behaviour of pyrite and chalcopyrite in aqueous solutions (Chapters 6 and 9), their flotation response after electrochemical pretreatment was studied to correlate the surface reactions with "natural" (i.e. collectorless) hydrophobicity.

10.2 Chalcopyrite

Figure 10.1 shows the flotation response of chalcopyrite (-150 +106 μm) in 0.025 M $NaHCO_3$ + 0.023 M NaOH buffer solution with NaCl (1 mol dm^{-3}) used as a background electrolyte (pH 10.5). Flotation recovery after conditioning in the electro-Hallimond tube[175] at a controlled potential for 30 minutes is plotted as a function of time for different conditioning potentials. The recovery after 30 minutes flotation is shown as a function of feeder potential in Figure 10.2. The results showed that flotation recovery increased above a potential of about 0.0 V and increased rapidly above 0.4 V; at > 0.8 V the recovery decreased again. Similar behaviour was observed at pH 9.0 (0.05 M $Na_2B_4O_7$ + 1 M NaCl) although the flotation response was shifted to slightly more negative potentials (Figure 10.3). These results were in general agreement with those of Gardner and Woods[175] who studied the flotation response of chalcopyrite at pH 11 between -0.4 and 0.8 V. Figure 10.4 shows the charge passed at the Pt feeder electrode during conditioning at pH 10.5 and constant potential in the absence of any mineral. At potentials > 0.8 V the anodic charge passed began to increase rapidly, due to the oxidation of Cl^- ions in the background electrolyte to ClO^-, ClO_2^-, ClO_3^- and eventually ClO_4^{2-}.

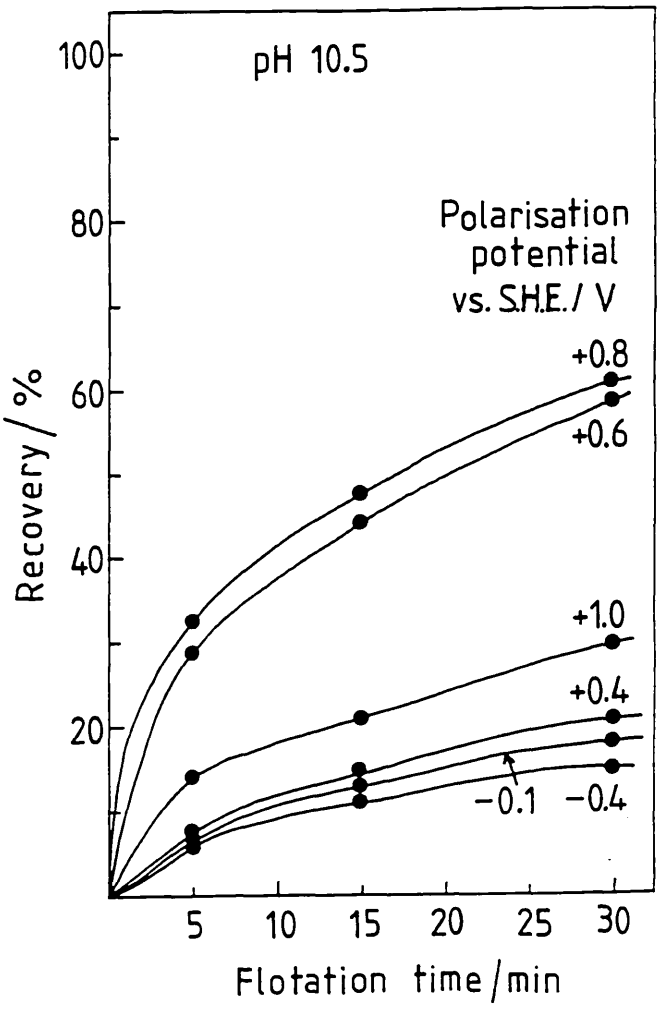


Fig 10.1 Rate of flotation of chalcopyrite (-150 +106 μm) conditioned at different potentials in 0.025 M $NaHCO_3$ + 0.023 M NaOH + 1 M NaCl buffer solution (pH 10.5).

With chalcopyrite in suspension a net anodic charge was passed at potentials > 0.0 V, Figure 10.5. Knowing the weight of sample used (2 g), the density of the mineral (ρ_{CuFeS_2} = 4.2 g cm^{-3}) and by assuming that each particle was cubic of length equal to the average of the size fraction (-150 +106 μm), the charge passed at the feeder electrode per cm^2 of mineral bed was calculated. This is also shown in Figure 10.5.

The effect of conditioning time on flotation recovery, charge passed, and dissolved Cu and Fe at a Pt feeder electrode potential of 0.8 V is

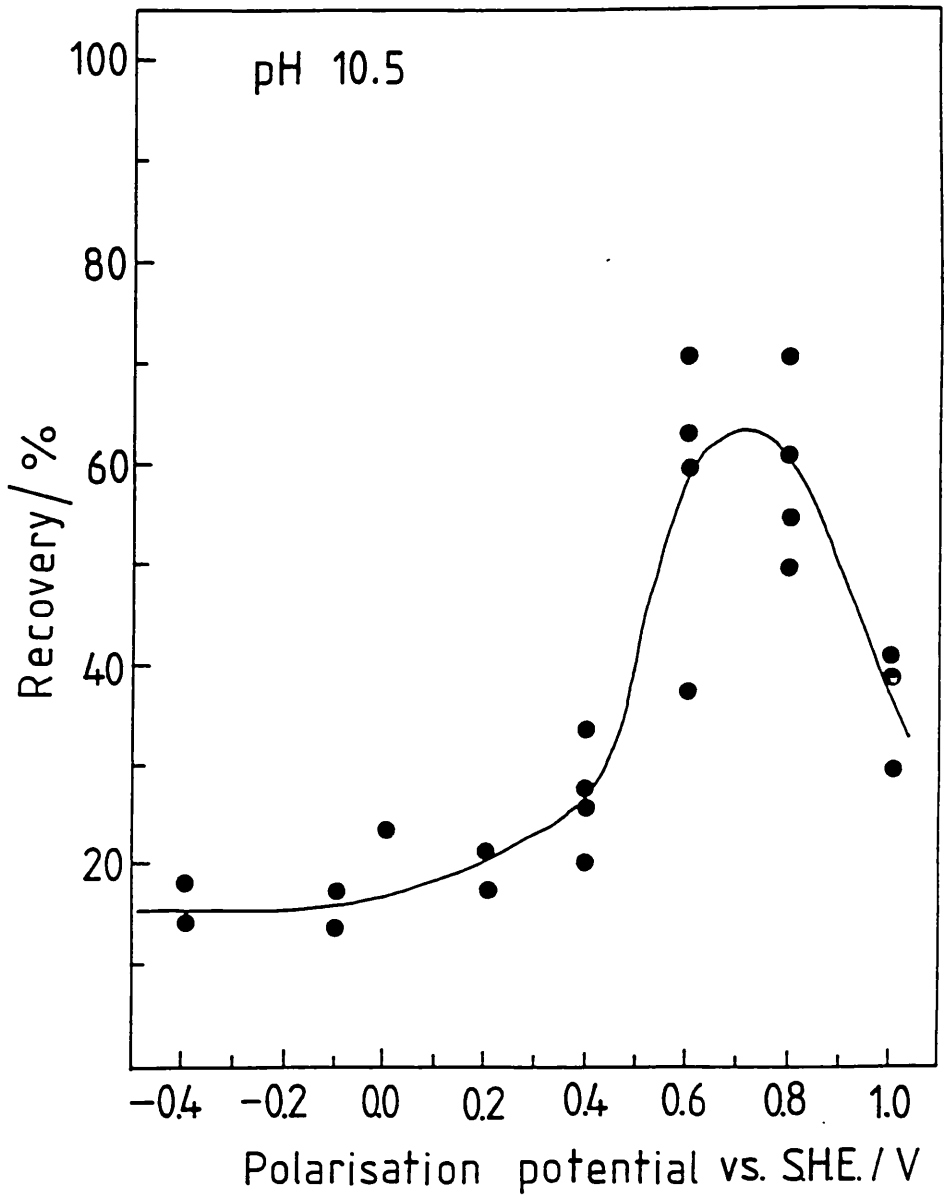


Fig 10.2 Recovery of chalcopyrite after 30 minutes flotation as a function of polarisation potential in pH 10.5 buffer solution.

shown in Figures 10.6 and 10.7. The flotation recovery increased with conditioning time and then began to decrease at times > 30 minutes (Figure 10.6). The decrease in recovery appeared to be associated with a decrease firstly in the amount of dissolved copper in solution and then in the amount of dissolved iron (Figure 10.7). This suggested that the hydrolysis of soluble Fe(II), Fe(III) and Cu(II) species to insoluble $Fe(OH)_2$, $Fe(OH)_3$ and $Cu(OH)_2$ was relatively slow.

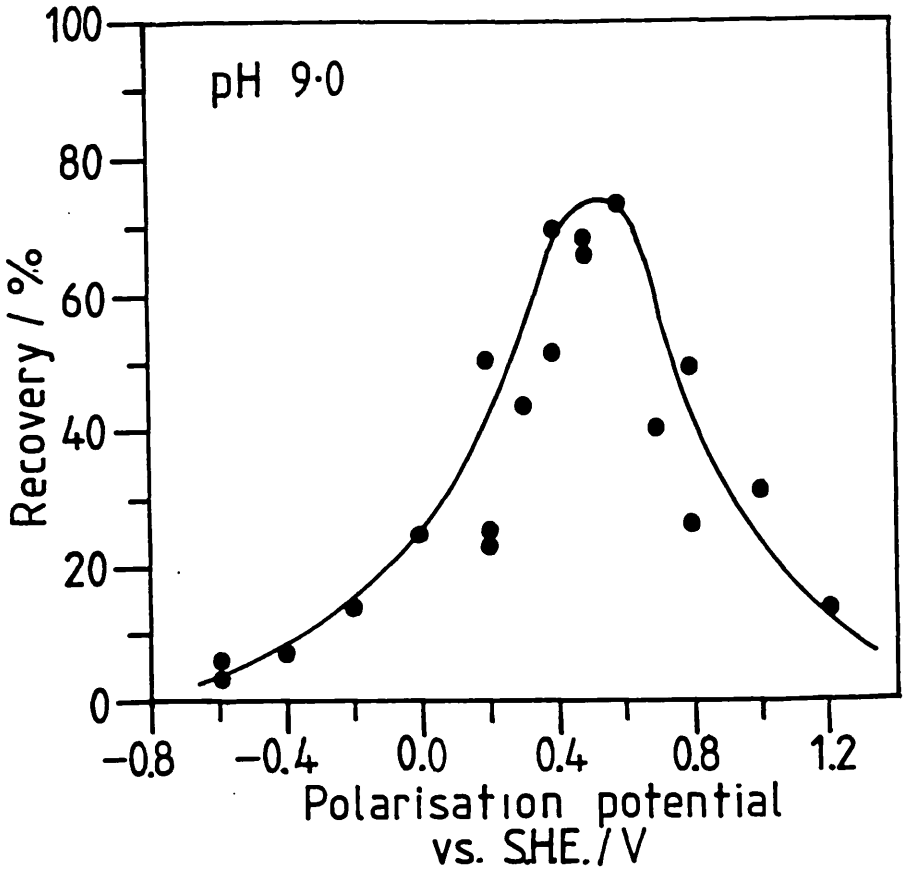


Fig 10.3 Recovery of chalcopyrite after 30 minutes flotation as a function of polarisation potential in pH 9.0 buffer solution (0.05 M $Na_2B_4O_7$ + 1 M NaCl).

However, at pH 10.5 the solubility of Fe^{3+} with respect to $Fe(OH)_3$ is very low (log $[Fe^{3+}]$ = -26.66; reaction (o_1)). Thus it seems more likely that the species being hydrolysed were Fe(II) and Cu(II) species (viz. Fe^{2+}, $FeOH^+$, CuO_2^{2-} and $HCuO_2^-$; see Appendix II), which have finite solubilities at pH 10.5.

The most obvious mechanism to account for the hydrophobicity assuming the original chalcopyrite surface to be hydrophilic, is the formation of sulphur, a known hydrophobic species, on the surface of the mineral. However, Finkelstein et al[344] were unable to establish a correlation between the amount of sulphur on the surface and flotability for several sulphide minerals including chalcopyrite.

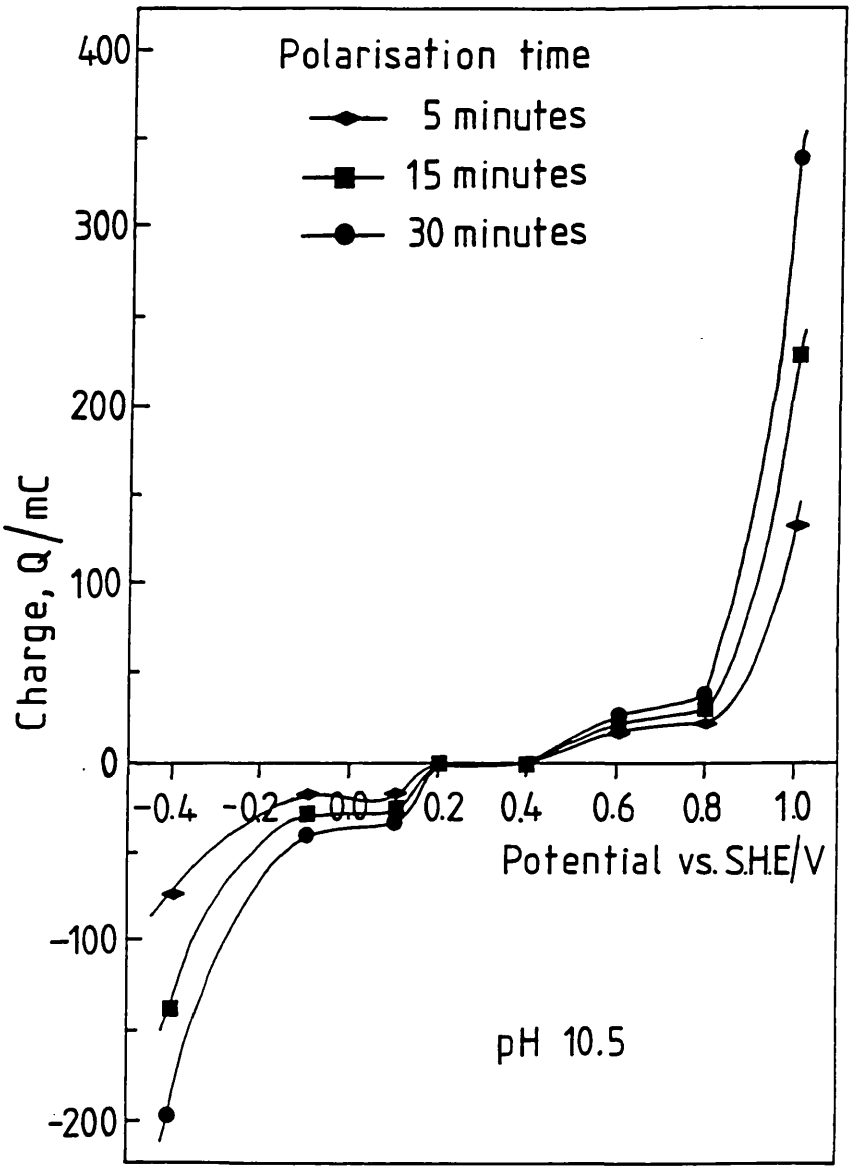


Fig 10.4 Charge passed at Pt feeder electrode in pH 10.5 buffer solution as a function of polarisation potential in the absence of a mineral suspension.

Gardner and Woods([175]) suggested that the oxidation reaction in alkaline solution can be represented by equation (p_4) to produce CuS, $Fe(OH)_3$ and S°. However, iron oxide/hydroxide layers are hydrophilic and there is no evidence to suggest that CuS is naturally hydrophobic. It is most probable that maximum natural flotation occurs when there is either elemental sulphur or an excess of sulphide in the lattice at the mineral/solution interface (reaction l_5), brought about by the transfer of copper and iron ions from the lattice into solution.

Two processes operate to increase the hydrophobicity of the surface. Removal of metal ions from the first few layers of the mineral surface reduces the opportunity for specific interaction with water molecules.

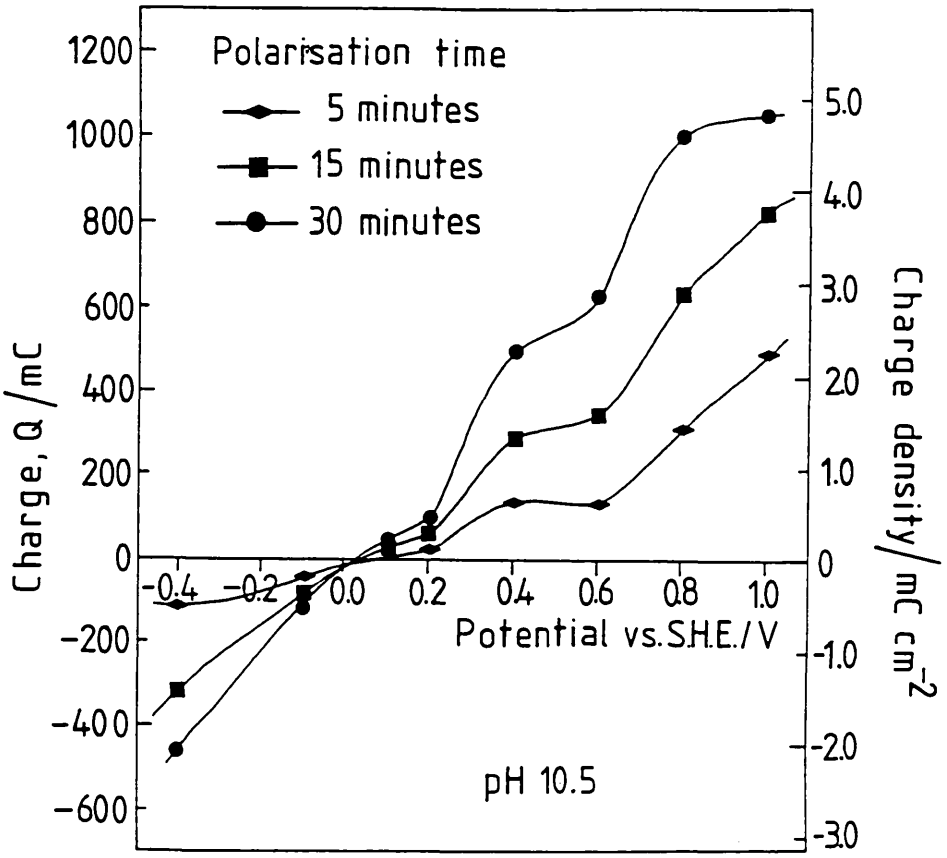


Fig 10.5 Charge passed at Pt feeder electrode in pH 10.5 buffer solution as a function of polarisation potential with chalcopyrite particles (-150 +106 μm) in suspension.

At the same time the reduction of the formal charge on sulphur diminishes further any weak interaction between water and sulphide ions. Indeed, recent XPS studies[380,381] have indicated that $Fe(OH)_3$ and a copper sulphide of stoichiometry close to CuS_2 are formed (reaction zf_5); see section 9.3.2.1).

The solution analysis suggested that the metal-deficient sulphide was more deficient in iron than copper at maximum flotation recovery. Mossbauer spectroscopy has shown that the copper and iron in chalcopyrite are in the Cu(I) and Fe(III) oxidation states[35]. A characteristic of the cuprous oxidation state is that Cu(I) has a low heat of hydration and forms complexes of coordination number two, eg $(CuCl_2)^-$. Thus Cu(I) ions in a sulphide lattice will make less contribution to the wetting of the sulphide than Cu(II), Fe(II) or Fe(III). The conclusion to be drawn from this is that although alteration of the chalcopyrite surface stoichiometry to increase the

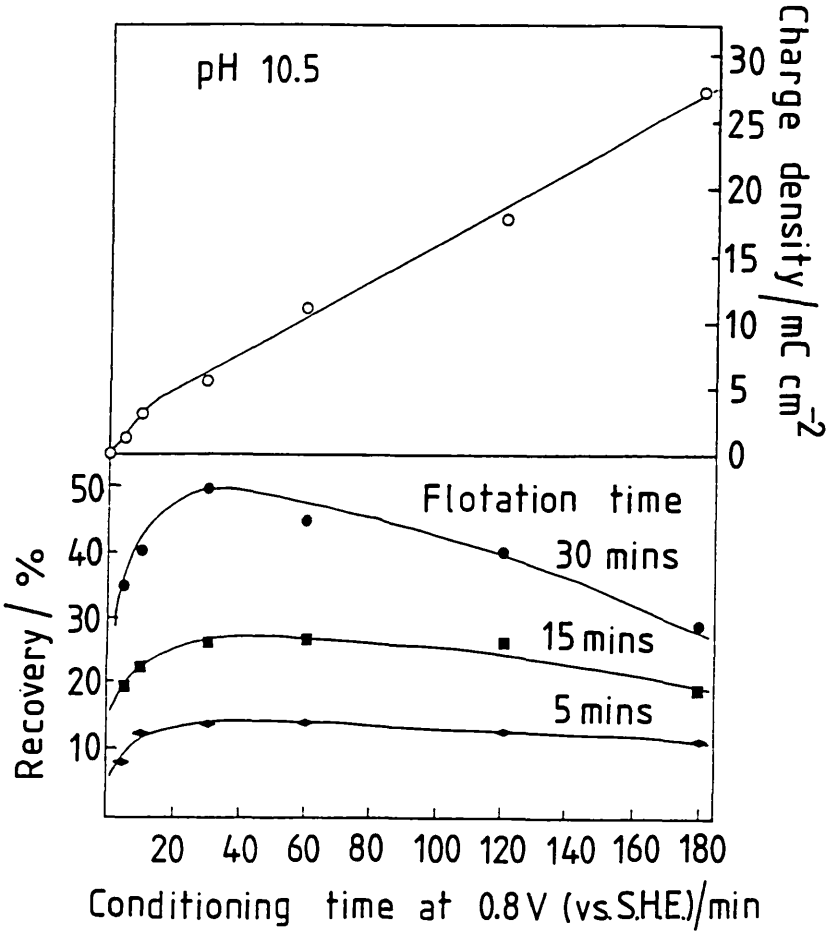


Fig 10.6 Charge density for the chalcopyrite mineral suspension and flotation recovery at pH 10.5 as a function of conditioning time at 0.8 V.

sulphide/metal ion ratio will increase hydrophobicity, an increase in the Cu(I)/Fe(III) ion ratio at the surface will also help significantly.

The fall in flotation recovery at potentials > 0.8 V at pH 10.5 (Figure 10.2) and > 0.6 V at pH 9.0 (Figure 10.3) seemed to coincide with the oxidation of Cl^- ions in the background electrolyte. The formation of hypochlorite according to the reaction (10.1):-

$$Cl^- + H_2O = ClO^- + 2H^+ + 2e \qquad (10.1)$$

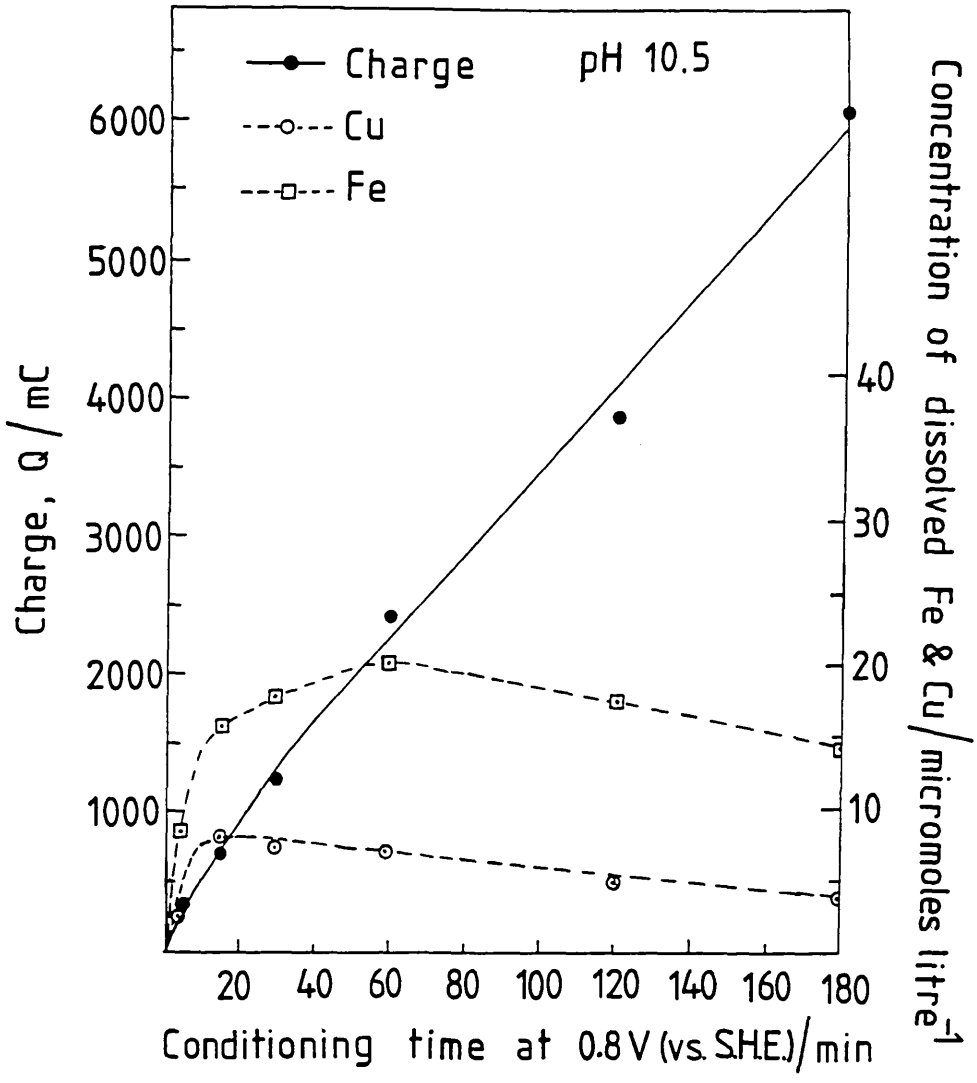


Fig 10.7 Dissolved Cu and Fe, plus charge passed at a Pt feeder electrode in pH 10.5 buffer solution at a polarisation potential of 0.8 V with chalcopyrite particles (-150 +106 μm) in suspension, as a function of conditioning time.

was the dominant chloride ion oxidation reaction at pH values > 9 and low current densities. Consequently, chalcopyrite oxidation occurred both electrochemically by feeder/particle contact and chemically by the oxidising action of electrogenerated hypochlorite (reactions (10.2) and (10.3)). The effect was to increase the rate of chalcopyrite oxidation, which at these relatively high positive feeder potentials was likely to lead to sulphate formation (reaction (10.3)). This left a hydrophilic layer of Fe(III) and Cu(II) oxides on the surface of the chalcopyrite particles, which reduced their floatability.

$$2CuFeS_2 + 5ClO^- + 5H_2O = 2Cu(OH)_2 + 2Fe(OH)_3 + 4S + 5Cl^- \quad (10.2)$$

$$2CuFeS_2 + 17ClO^- + 9H_2O = 2Cu(OH)_2 + 2Fe(OH)_3 + 4SO_4^{2-} + 17Cl^- + 8H^+ \quad (10.3)$$

10.3 Pyrite

Figure 10.8 shows the recovery of pyrite (-150 +106 μm) after 30

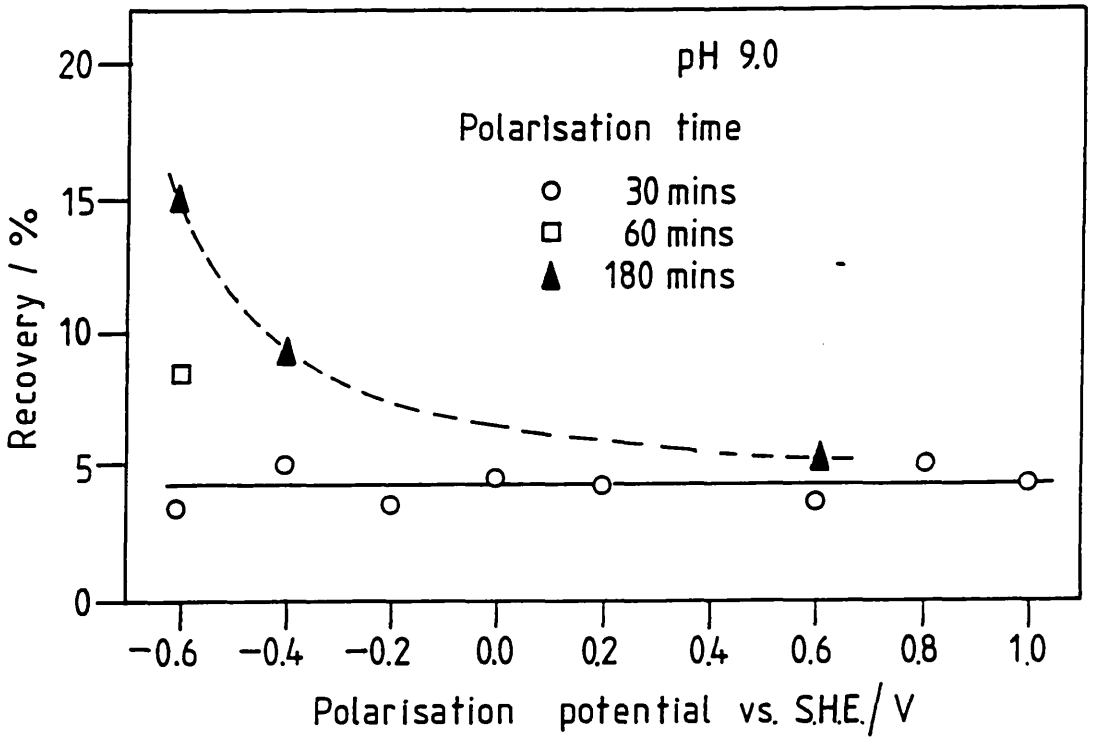


Fig 10.8 Recovery of pyrite after 30 minutes flotation as a function of polarisation potential and polarisation time in pH 9.0 buffer solution.

minutes flotation as a function of feeder potential and polarisation time at pH 9.0 (0.05 M $Na_2B_4O_7$ + 1 M NaCl). In contrast to chalcopyrite, pyrite exhibited no increase in flotation recovery under mild oxidising conditions. However, at cathodic potentials the recovery did increase slightly, although only after prolonged polarisation (1 - 3 hours). The inability of pyrite to float at oxidising potentials was probably due to the presence of a hydrophilic layer of ferric oxide/hydroxide on the surface of the pyrite particles, which was reduced to ferrous hydroxide at cathodic

potentials (reaction (k)). The hydrophilic ferrous hydroxide film then dissolved slowly (log $[Fe^{2+}]$ = -4.71 at pH 9.0 (reaction (p_1); see section 6.3.5), thereby increasing the hydrophobicity/floatability of pyrite.

Although the hydrophobicity of pyrite increased under reducing conditions the recovery of pyrite by flotation was still much less than that obtained for chalcopyrite under oxidising conditions. Pyrite's poorer hydrophobicity may have been due to:-

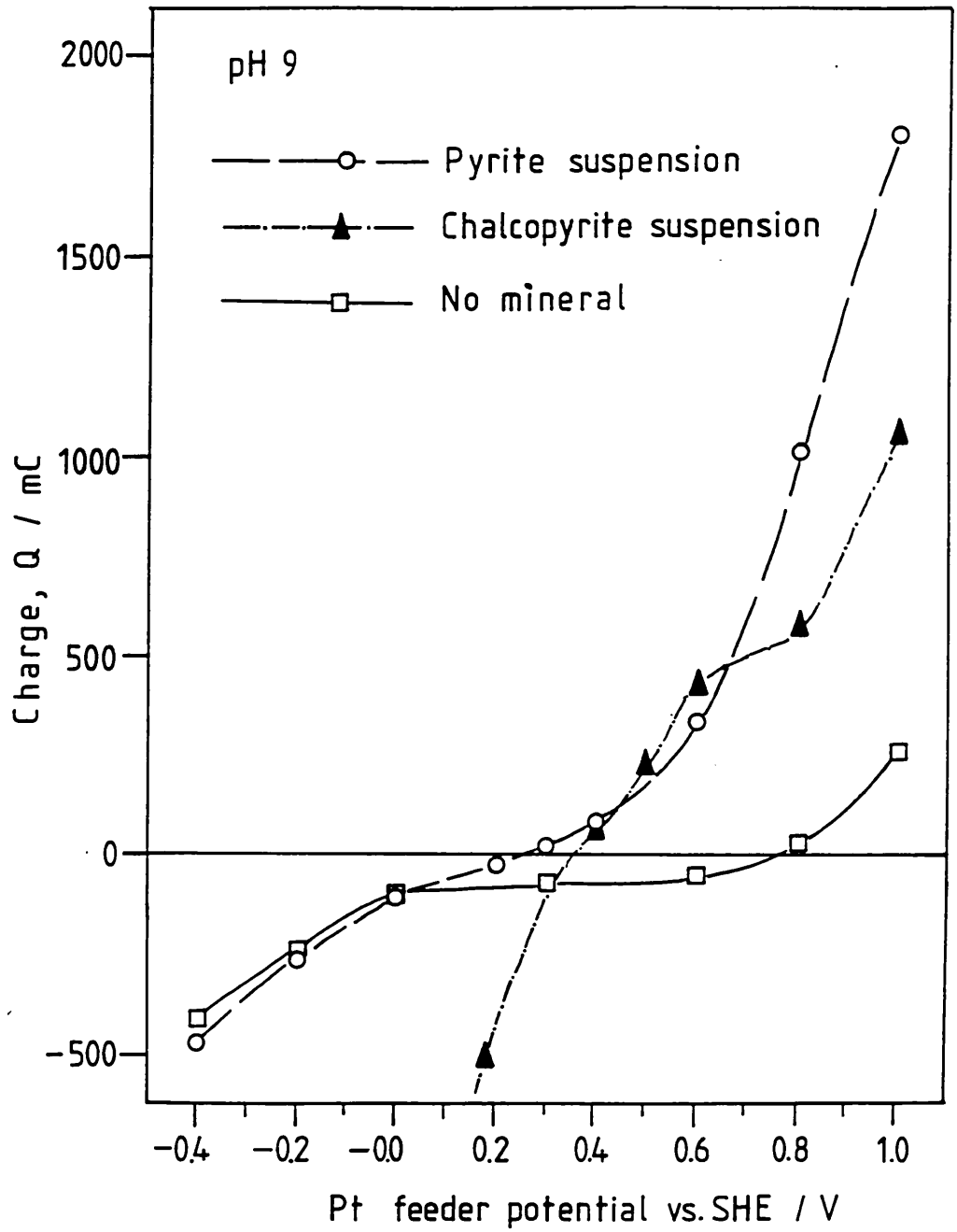
(i) the slow, or incomplete dissolution of ferrous hydroxide from the surface of pyrite.

(ii) differences in the relative hydrophobicity of the sulphur and/or metal-deficient sulphide layer on chalcopyrite and the covalently saturated sulphur atoms on an "iron oxide-free" pyrite surface.

(iii) feeder electrode-particle and/or particle-particle contact resistances may have prevented pyrite from attaining the feeder electrode potential, and hence reduced charge transfer. For example, Figure 10.9 shows that the charge passed at the Pt feeder electrode at cathodic potentials increased only slightly in the presence of a pyrite suspension. This suggested that under these conditions, charge injection into the pyrite particles was relatively slow and hence might explain why long polarisation times were required before any changes were observed in the hydrophobicity/floatability of pyrite.

(iv) In flotation, to ensure continuing contact between particle and bubble during levitation, the force of adhesion generated over the finite area of contact must exceed any disruptive force associated with the weight of the particle. Therefore, although reduced pyrite and oxidised chalcopyrite surfaces might have the same degree of hydrophobicity, for a given size fraction, the flotation recovery of pyrite would be less, because it has a higher specific gravity (ρ_{FeS_2} = 5.0 g cm^{-3}) than chalcopyrite (ρ_{CuFeS_2} = 4.2 g cm^{-3}).

Thus, further studies were carried out to ascertain whether (iii) and/or (iv) were responsible for the lower flotation recoveries obtained with pyrite.



10.9 Charge passed at Pt feeder electrode after 30 minutes polarisation in pH 9.0 buffer solution as a function of polarisation potential in the absence and presence of pyrite and chalcopyrite mineral suspensions.

10.4 Contact Potential Measurements

To gain a greater insight into the charging mechanism of mineral particles in a pulp/suspension electrode system, contact potential

measurements were made using Pt, pyrite and chalcopyrite electrodes to simulate the potential changes that occur upon feeder-particle and particle-particle contact.

Figures 10.10 and 10.11 show that at pH 9.0 (0.05 M $Na_2B_4O_7$ + 1 M NaCl) and pH 0 (1 M $HClO_4$) chalcopyrite reached the applied potential almost instantaneously when contacted either with a Pt or chalcopyrite feeder electrode.

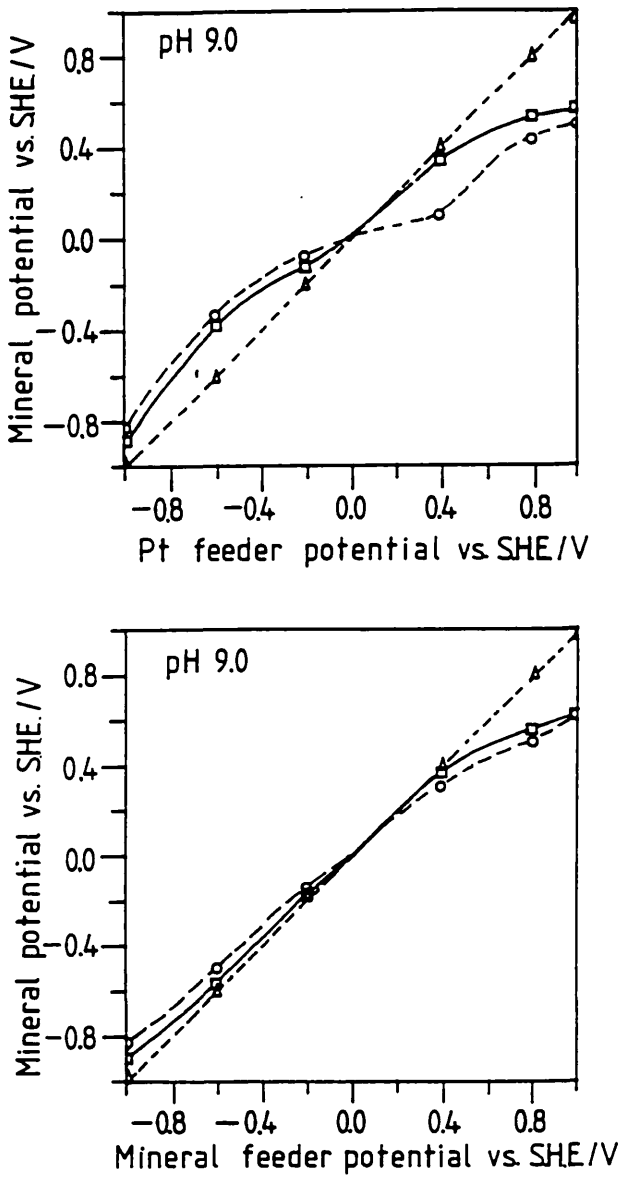


Fig 10.10 Pt feeder - mineral and mineral feeder - mineral contact experiments for pyrite (o, □) and chalcopyrite (Δ) in pH 9.0 buffer solution. (- - -) immediate potential after contact; (——) potential after contact for 2 minutes.

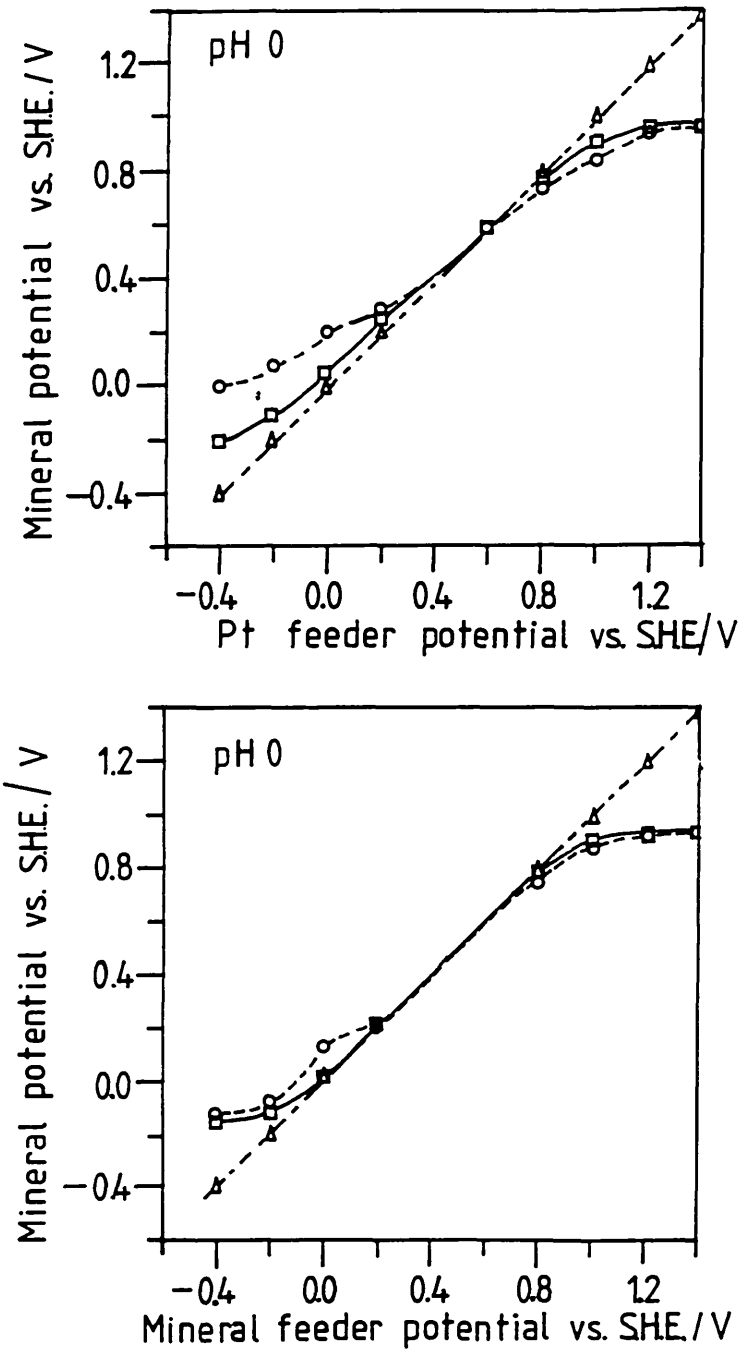


Fig 10.11 Pt feeder-mineral and mineral feeder-mineral contact experiments for pyrite (o,□) and chalcopyrite (Δ) in 1 M $HClO_4$ (pH 0). (- - -) immediate potential after contact; (——) potential after contact for 2 minutes.

In contrast, the potential of pyrite was generally much less than the applied potential, the difference becoming more pronounced at high anodic and cathodic potentials, where pyrite did not achieve the feeder potential even after prolonged contact (15 minutes). Moreover, it was found that the difference between the applied and mineral potential was less significant for pyrite-pyrite contacts than for Pt-pyrite contacts, especially at cathodic potentials.

Increasing the pressure applied during contact increased the rate of change of potential. This suggested that the charging of coarse pyrite particles would be more effective than that of fine pyrite particles, since the former would have a higher momentum and hence would make better contact with the feeder electrode.

Since the results obtained with pyrite were similar both in acid and alkaline solutions, the contact resistance cannot be attributed solely to the presence of oxides on the surface of pyrite. Differences in the work functions of Pt and pyrite at the Pt (metal)/pyrite (semiconductor) interface may also contribute to the observed contact potential.

These results indicate that in comparison with pyrite the charging of chalcopyrite particles, by feeder-particle or particle-particle contact, occurs much more readily and might explain why changes in the flotation response of pyrite were only observed after prolonged periods of polarisation.

10.5 Effect of Particle Size

To study the effect of particle size on the flotation behaviour of pyrite and chalcopyrite under oxidising and reducing conditions, different size fractions of each mineral were polarised for 30 minutes either at 0.6 V, or -0.6 V, and then floated for 30 minutes to determine the flotation response. All the tests were carried out at pH 9 (0.05 M $Na_2B_4O_7$ + 1 M NaCl) both in the presence and absence of a frothing (redistilled analar grade n-pentanol) agent, viz amyl alcohol, which was added to reduce bubble size and enhance the probability of particle-bubble contact.

Recovery-size curves, in which the recovery from a particular size fraction is plotted against the average size of particle in that fraction, are presented in Figures 10.12 and Figures 10.13 for pyrite and chalcopyrite, respectively.

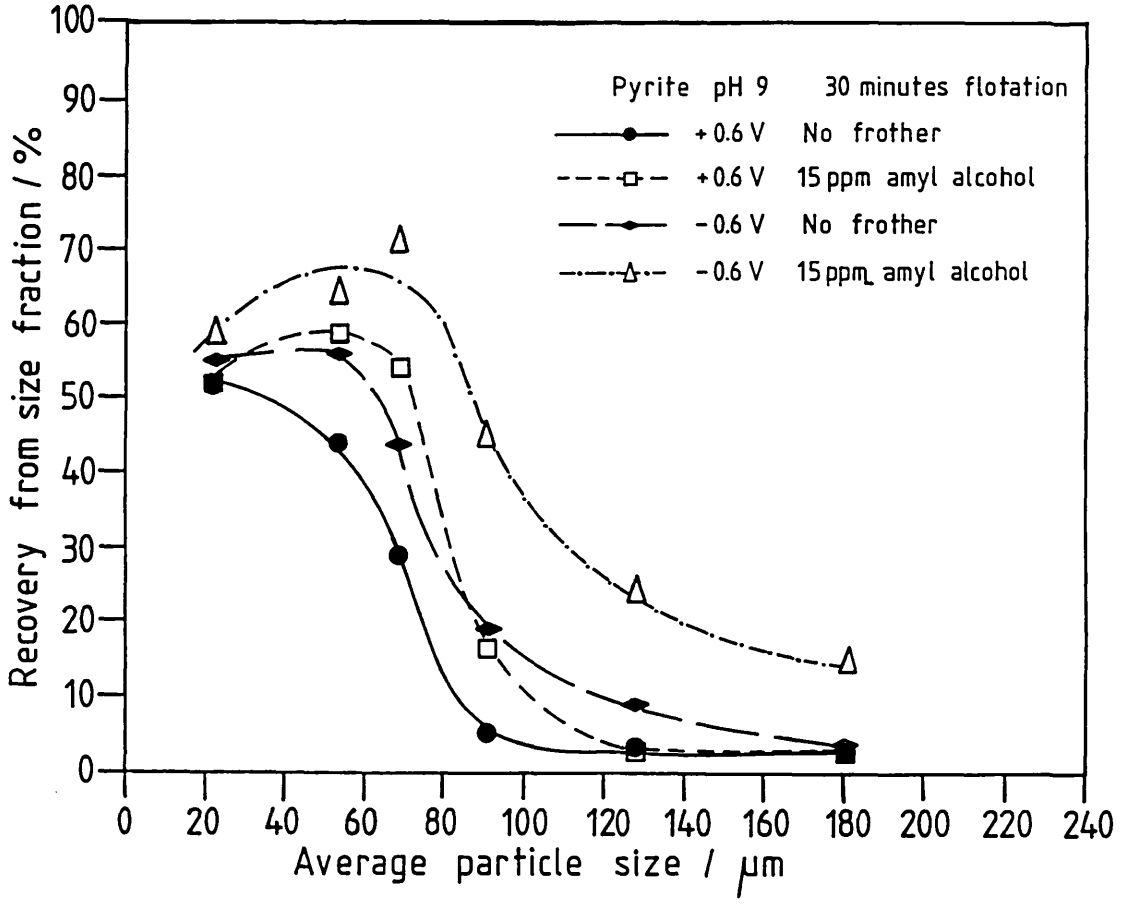


Fig 10.12 Recovery-size curves for pyrite polarised for 30 minutes in pH 9.0 buffer solution prior to flotation. Flotation carried out in the absence/presence of amyl alcohol.

All the curves were similar in shape, the tendency to float increasing with decreasing particle size as entrainment became the dominant recovery method. However, significant differences in flotation recovery were observed at a given particle size, depending on the mineral type, anodic/cathodic pretreatment, absence/presence of frother etc.

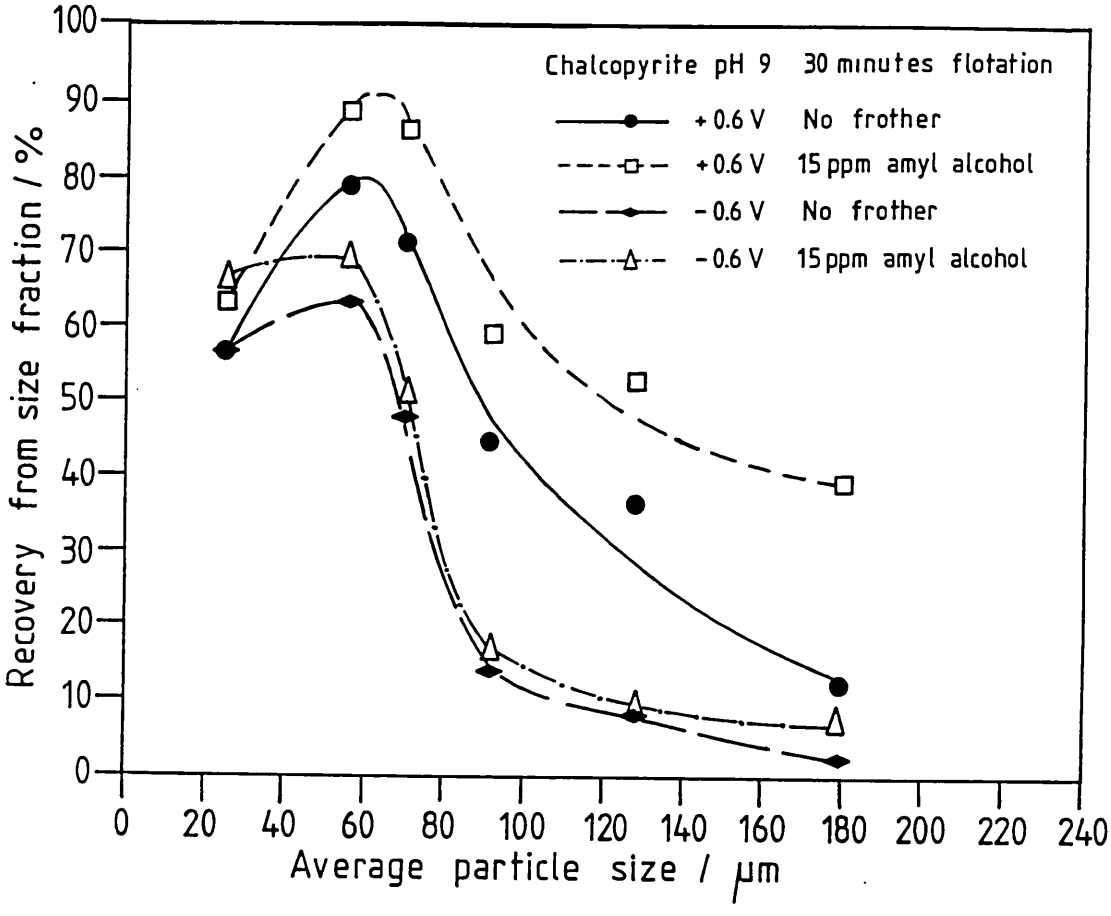


Fig 10.13 Recovery-size curves for chalcopyrite polarised for 30 minutes in pH 9.0 buffer solution prior to flotation. Flotation carried out in the absence/presence of amyl alcohol.

To separate the effect of these variables on genuine flotation (bubble attachment and levitation) from that of entrainment, it was assumed that the recovery curves for oxidised pyrite (0.6 V, no frother) and reduced chalcopyrite (-0.6 V, no frother) were due to entrainment only. By subtracting these "base-line" curves from those acquired for reduced pyrite (-0.6 V) and oxidised chalcopyrite (0.6 V) in the absence/presence of frother, recovery curves were obtained which reflected real changes in hydrophobicity/floatability brought about solely by the electrochemical pretreatment and/or frother addition. These are shown in Figures 10.14 and 10.15.

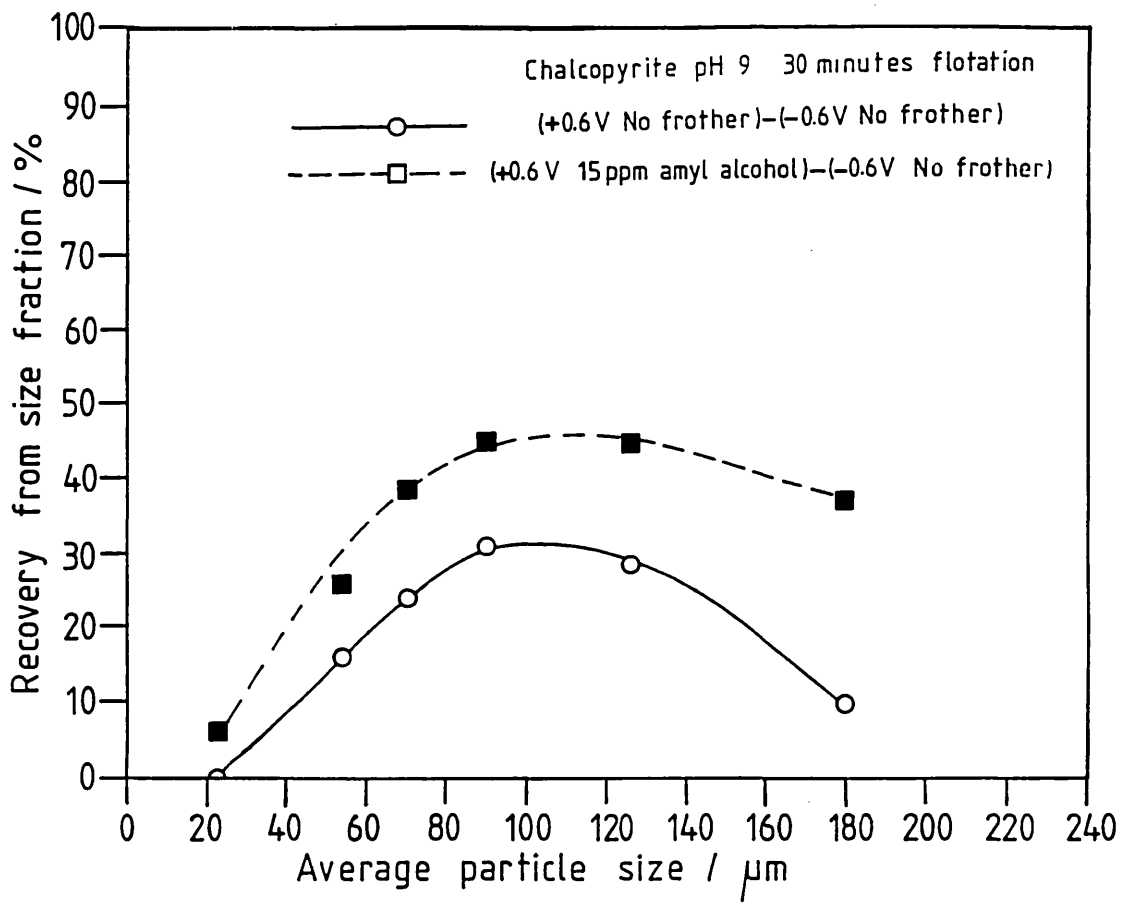


Fig 10.14 Recovery-size curves for oxidised chalcopyrite (0.6 V, 30 min polarisation, 30 min flotation) corrected for entrainment.

In the absence of frother pyrite and chalcopyrite behaved similarly. Electrochemical conditioning caused the greatest enhancement in flotation recovery at intermediate particle sizes, the maximum recovery occurring at a coarser average particle size for oxidised chalcopyrite (~ 100 μm) than for reduced pyrite (~ 70 μm). Although electrochemical conditioning was probably more efficient at coarse particle sizes, this advantage was outweighed by an increase in the degree of hydrophobicity required to overcome gravitational effects and so promote high floatability. Therefore the recovery decreased with increasing particle size.

The degree of surface oxidation incurred during grinding tended to increase with decreasing particle size. Therefore, feeder-particle

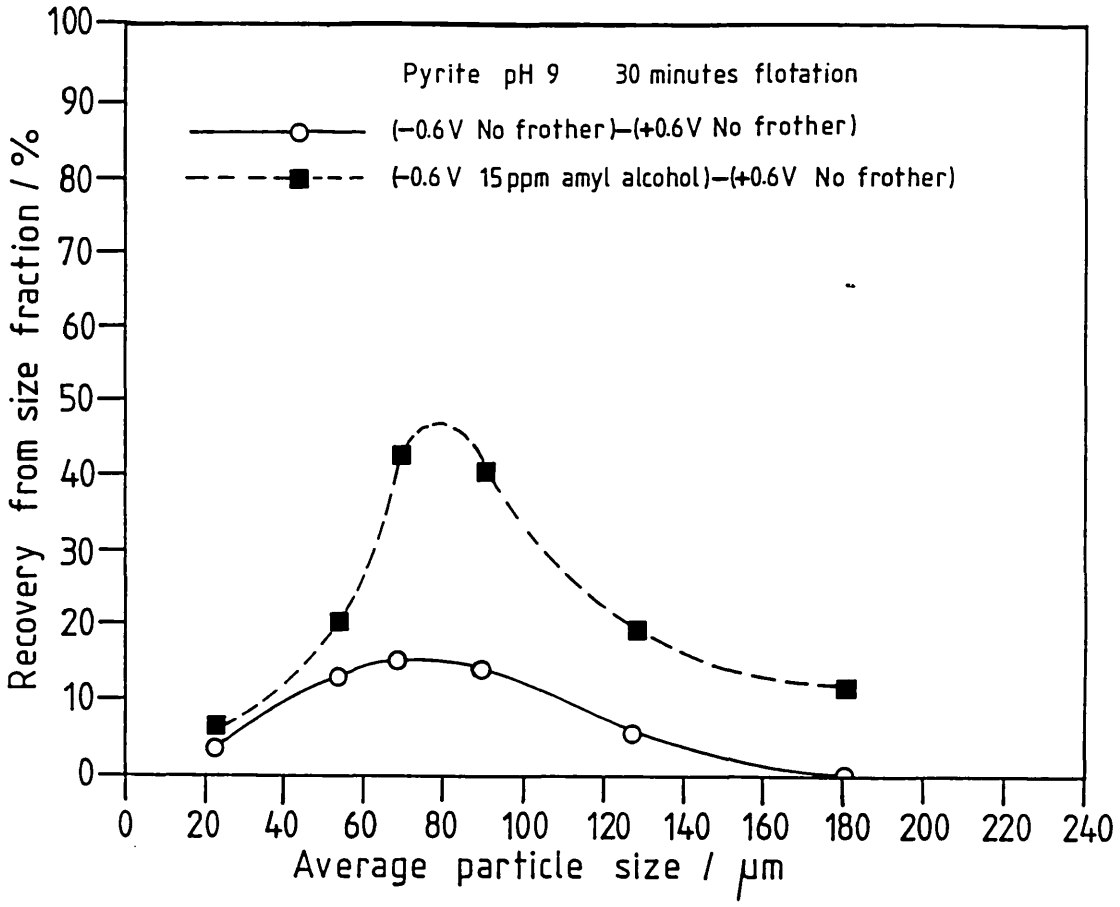


Fig 10.15 Recovery-size curves for reduced pyrite (-0.6 V, 30 min polarisation, 30 min flotation) corrected for entrainment.

and particle-particle contact resistances were higher for the finer size fractions, which meant that charging was less effective. As a result the flotation recovery decreased.

Adding frother (15 ppm amyl alcohol) to an electrochemically oxidised chalcopyrite surface increased recovery over the entire particle size range, the improvement increasing steadily with increasing particle size. No significant improvement was observed with reduced chalcopyrite (Figure 10.13), except for a a slight increase in recovery at particles sizes < 40 µm. In contrast, frother addition increased the recovery of both oxidised and reduced pyrite, the increase being greater for reduced pyrite surfaces, especially at coarse particle sizes (Figure 10.12). At particle sizes < 40 µm, frother addition had little effect on pyrite recovery with either type of surface

pretreatment. These results suggested that amyl alcohol was acting as a dipolar collector as well as a frother.

The adsorption of non-ionic molecules, such as alcohols, at the solid-liquid interface is maximised at the zero point of surface charge (z.p.c.) of the solid[382].

For oxides like Fe_2O_3, the surface reactions involved in the establishment of a surface charge and the electrical double layer may be represented formally as:-

$$Fe(OH)_2^{+}{}_{(surface)} + H^+ \rightleftharpoons Fe(OH)_{3(surface)} \qquad (10.4)$$

$$Fe(OH)_{3(surface)} + H_2O \rightleftharpoons Fe(OH)_4^{-}{}_{(surface)} + OH^- \qquad (10.5)$$

the z.p.c. of the solid being determined by the pH of the aqueous solution for which the activities of adsorbed surface hydroxy species ($Fe(OH)^{2+}$, $Fe(OH)_4^-$) are equal. This pH corresponds to the point of minimum solubility of the solid[383]. The activity-pH diagram for Fe(III) species in equilibrium with Fe_2O_3 (Figure II(vi); Appendix II) shows that the minimum solubility of Fe_2O_3 occurs at pH 6.1, although the minimum is not sharply defined due to the high concentration of undissociated $Fe(OH)_3$ species. Parks[385] quoted z.p.c. values for α-Fe_2O_3 ranging from 5.0 to 9.05, the actual value for a particular sample being influenced by its source, method of preparation, type of pretreatment and the presence of trace impurities.

In contrast, the use of electrokinetic techniques as a means of studying the mineral sulphide-solution interface has not received as much attention. Healy and Moignard[384] carried out a survey of previous electrokinetic studies on metal sulphides and reported z.p.c. values for pyrite and chalcopyrite of 6.2-6.9 and 3.0, respectively. However, the survey showed that little attention had been given to experimental detail. Often no account had been taken of sample equilibration and conditioning effects and there had been a lack of preventative measures to control sulphide mineral oxidation before or during the experiment. Nevertheless, it may be expected that oxidation or reduction of a given sulphide mineral surface would shift its z.p.c. towards the characteristic z.p.c. of the product layer.

Table 10.1 The point of zero charge of some metal sulphide and metal hydroxide compounds.

Compound	z.p.c.
$CuFeS_2$	pH 3[384]
FeS_2	pH 6.2-6.9[384]
$Fe(OH)_{3(s)}$	pH 7.4-8.4[385]
$Fe(OH)_{2(s)}$	pH 11.3-12.4[385]
$Cu(OH)_{2(s)}$	pH 9.4-10.1[385]

For example, in the experiments described above, carried out at pH 9 under oxidising conditions, the formation of metal hydroxide coatings on the surfaces of pyrite and chalcopyrite would have increased the z.p.c. values of the sulphide minerals towards pH 9 (see Table 10.1) and hence promoted the adsorption of amyl alcohol. Moreover, the increase in z.p.c./frother adsorption would also be greater for surfaces having a higher ratio of $Fe(OH)_2$ and/or $Cu(OH)_2$ relative to $Fe(OH)_3$ (Table 10.1). As $Fe(OH)_2$ was probably the major component on the surface of reduced pyrite, this would explain why frother addition increased the recovery of reduced pyrite more than that of oxidised pyrite.

10.6 Summary

The results have shown that pyrite is rendered naturally hydrophobic under reducing conditions, whereas chalcopyrite is rendered hydrophobic under oxidising conditions. The surfaces which generated the natural hydrophobicity were probably a sulphur and/or metal deficient sulphide layer on chalcopyrite and for pyrite an iron-oxide free surface containing covalently saturated sulphur atoms.

Increases in genuine flotation recovery, i.e. no entrainment, due solely to electrochemical conditioning, passed through a maximum which occurred at a coarser particle size for oxidised chalcopyrite than for reduced pyrite.

CHAPTER ELEVEN

CONCLUSIONS

CHAPTER ELEVEN: CONCLUSIONS

1. Voltammetric studies at pH 1 (0.1 M H_2SO_4, 0.1 M $HClO_4$) suggested that under mild oxidising conditions, anodic scanning potential limits (E_{λ_a}) < 0.9 V, pyrite oxidation occurred mainly by the following reaction:-

$$FeS_2 = Fe^{3+} + 2S + 3e \qquad (e)$$

$$E = 0.546 + 0.0196 \log[Fe^{3+}]$$

forming a passivating layer of sulphur on the surface. Although charge measurements showed that sub-monolayer quantities of sulphur were formed, the fractional monolayer coverage of sulphur exceeded the fraction of a monolayer of pyrite reacted, hence the sulphur film protected the underlying pyrite surface. Protection stopped once the volume of sulphur produced became less than the volume of pyrite decomposed. Under the non-steady state conditions of cyclic voltammetry experiments, this occurred at > 1.0 V and marked the onset of higher anodic currents/ decomposition rate, as pyrite oxidation to sulphate (reaction (f)) became the dominant decomposition pathway:-

$$FeS_2 + 8H_2O = Fe^{3+} + 2SO_4^{2-} + 16H^+ + 15e \qquad (f)$$

$$E = 0.394 - 0.063\ pH + 0.008 \log[SO_4^{2-}] + 0.004 \log[Fe^{3+}]$$

For example, the amount of pyrite oxidised by reaction (f) increased from 10% at 0.9 V to 96% at 1.4 V.

2. Cyclic voltammograms of pyrite recorded at pH 0 (1 M $HClO_4$) using a rotating split cylinder bi-electrode (RSCBE) suggested that pyrite oxidation produced no Fe(II) species judging by the absence of any corresponding oxidation current at the Pt collector electrode when held at potentials (E_c) > 0.8 V. Indeed, soluble oxidation products were detected only when the working electrode

potential was extended to > 1.0 V. Fe^{3+} reduction at the collector electrode (E_c = < 0.5 V) confirmed that the main mineral oxidation reactions were (e) and (f). However, reduction of the oxidation product layer (sulphur) gave rise to anodic collector current responses at E_c potentials of 0.8, 0.9 and 1.0 V, which suggested that ferric oxide was also formed on the surface of pyrite during oxidation, even though it is thermodynamically unstable at pH 0.

3. Electrochemical studies at pH 4.6 (0.5 M CH_3COOH + 0.5 M CH_3COONa) suggested that, under mild oxidising conditions (< 0.6 V), goethite formed spontaneously on the surface of pyrite via a solid state mechanism (reaction (s_1)):-

$$FeS_2 + 2H_2O = FeOOH + 2S + 3H^+ + 3e \qquad (s_1)$$

$$E = 0.521 - 0.0591\ pH$$

As pyrite oxidation to sulphate (reaction (t_1)) became the dominant oxidation process at potentials > 0.6 V:-

$$FeS_2 + 10H_2O = FeOOH + 2SO_4^{2-} + 19H^+ + 15e \qquad (t_1)$$

$$E = 0.390 - 0.0749\ pH + 0.0078\ \log[SO_4^{2-}]$$

the concomitant production of H^+ ions sufficiently lowered the interfacial pH at the pyrite/solution interface for ferric oxide/hydroxide to form by a dissolution-precipition mechanism (reactions (e), (f), (o_1), (v_1) and (w_1)), producing $Fe(OH)_2^+$, $Fe(OH)^{2+}$ and $Fe(OH)_3$ at the higher overpotentials.

4. Cathodic conditioning of pyrite at pH 4.6 resulted in the formation of oxygen reduction intermediates, which reacted with the pyrite surface by a corrosion type process, producing $Fe(OH)^+_{(ads)}$, $S_2(OH)_2$ and $S_2O_3^{2-}$ species on the mineral surface.

5. Pyrite oxidation to sulphate became even more favourable on increasing the pH from 4.6 to 7 (0.025 M Na_2HPO_4 + 0.025 M KH_2PO_4). This resulted in an irreversible loss of sulphur from the surface of pyrite, leaving an excess of ferric oxide, even under mild oxidising conditions (0.0 V). At 0.8 V, the oxide layer consisted of an inner monolayer of goethite and sulphur, formed by a solid state mechanism, and a few outer monolayers of an amorphous, more hydrated ferric oxyhydroxide ($Fe(OH)_3$), formed by a dissolution-precipitation process. Increasing the anodic potential above 0.8 V lowered the interfacial pH sufficiently for some of the precipitated $Fe(OH)_3$ to dissolve, forming soluble $Fe(OH)_2^+$ species (reaction (w_1)).

6. It is generally assumed that sulphide mineral oxidation to sulphur and sulphoxy species (sulphate) occurs by two independent pathways and that sulphate is not formed as a result of elemental sulphur oxidation due to the high overpotential requirement for this reaction[61]. However, cyclic voltammograms for pyrite recorded at pH 7, suggested that if sub-monolayer quantities of sulphur are formed, i.e. sulphur is present as ad-atoms rather than a separate thermodynamic phase, sulphur may be oxidised to sulphate at E_{λ_a} potentials > 0.8 V.

7. A charge balance revealed that the reaction accompanying pyrite oxidation to sulphur, at E_{λ_a} potentials < 0.5 V, approximated to a 3 electron process and was assigned to the reaction:-

$$FeS_2 + 2xH_2O = Fe_{(1-x)}^{2+}(Fe^{3+}O_2H^-S_2^{2-})_x\ (S_2^{2-})_{(1-x)} + 3xH^+ + 3xe \quad \ldots(6.33)$$

This process involved the oxidation of Fe(II) to Fe(III) in the lattice, and the adsorption and deprotonation of water molecules. It did not involve lattice decomposition. The number of electrons associated with the reaction accompanying pyrite oxidation to sulphur only exceeded 5 when the potential was extended to 0.8 V, signifying that sulphoxy species such as $S_2O_2^{2-}$ and $S_2O_3^{2-}$ were

being formed as intermediates in the oxidation pathway to sulphate.

8. In alkaline solutions, the predominance of sulphate formation and the associated irreversible loss of sulphur from the surface of pyrite produced a high oxide/sulphur ratio with ferric oxide the dominant surface phase.

9. Once formed, ferric oxide/hydroxide was difficult to remove by cathodic treatment due to the low solubility of ferrous ions in alkali media (e.g. 10^{-5} M at pH 9.2; reaction (p_1)). Studies on virgin pyrite surfaces at pH 9.2 showed that after prolonged cathodic treatment, monolayers of ferric oxide could be removed from the surface of pyrite, presumably due to ferrous oxide dissolution. However, an oxide monolayer was always left on the surface.

10. The spontaneous formation of a passive film on the surface of pyrite, even in acidic solutions, and the predominance of sulphate over sulphur formation, was accounted for by considering the solid state properties of pyrite and invoking a semiconductor band model to explain its electrochemical behaviour.

11. Abrading the surface of a pyrrhotite electrode, while in 1 M $HClO_4$, lowered its open-circuit potential (E_{oc} = 0.6 V) into a region where non-oxidative dissolution occurred (E_{oc} = 0.15 V). This suggested that a layer of sulphur and/or more likely a ferric oxide film was responsible for inhibiting the dissolution of pyrrhotite. Once the film was removed the open-circuit potential was "pinned" at the corrosion potential for the non-oxidative dissolution reaction:-

$$MS = M^{2+} + H_2S$$

the process being comprised of an anodic:-

$$MS = M^{2+} + S + 2e$$

and cathodic process:-

$$S + 2H^{+} + 2e = H_2S$$

12. The voltammetric behaviour of hexagonal pyrrhotite at pH 1 (0.1 M $HClO_4$) and potentials < 0.8 V suggested that pyrrhotite oxidation results either in the formation of a metal-deficient sulphide film (MDSF):-

$$Fe_{0.905}S = xFe^{2+} + Fe_{(0.905-x)}S + 2xe \qquad (7.1)$$

where: $0 \leq x \leq 0.011$, since $Fe_{0.894}S$ represents the lower limit of iron deficiency in hexagonal pyrrhotite.

or in the underpotential deposition of a meta-stable ferric oxide/hydroxide layer (reactions (1) and (z_1)).

13. RSCBE studies at pH 0 (1 M $HClO_4$) suggested that pyrrhotite oxidation, like pyrite oxidation, produced no Fe(II) species judging by the absence of any corresponding collector oxidation current at E_c potentials > 0.8 V. On extending the working electrode potential to > 0.7 V, the main pyrrhotite oxidation reactions were (h_1) and (i_1), producing Fe^{3+}, sulphur and SO_4^{2-}. Fe^{3+} was reduced to Fe^{2+} at collector potentials < 0.7 V, and on the reverse negative-going scan, sulphur was reduced to H_2S in a two-step process (reactions (ay_1) and (az_1)), the H_2S giving rise to an anodic collector current at E_c potentials > 1.2 V.

14. In cyclic voltammetry experiments carried out at pH 4.6 (0.5 M CH_3COOH + 0.5 M $CH_3COO.Na$ buffer solution), pyrrhotite oxidised by reaction (z_1) at $E_{\lambda a}$ potentials < 0.5 V forming goethite and sulphur. On extending $E_{\lambda a}$ to > 0.5 V, the anodic current increased rapidly as sulphate formation (reaction (ba_1)) became the dominant oxidation reaction.

15. Eventually a "limiting current" region was reached between 0.9 and 1.3 V. In this region, pyrrhotite oxidation was inhibited by a passivating ferric oxide film, the current at 1.3 V being 25 times lower at pH 4.6 than at pH 0. The limiting current also showed no stirring rate dependence, implying that the film had been formed by a solid state mechanism and not by dissolution-precipitation. At an E_{λ_a} of 1.0 V, the passivating film consisted mostly of Fe(III) species, with an outer, easily reduced, hydrated $Fe(OH)_3$ layer (about 10 monolayers in thickness) and an inner, less easily reduced, less hydrated, FeOOH layer (37 monolayers) interspersed with a little sulphur (2 monolayers).

16. In contrast, ferric hydroxide/oxide species did not passivate the surfaces of pyrite and pentlandite in the potential region 0.9 - 1.3 V at pH 4.6, although oxidation was inhibited to an extent. There were two reasons for this:-

    (i) More ferric hydroxide/oxide was formed on pyrrhotite than on the other two minerals because pyrrhotite has a higher iron content: 50 at. %, compared with 33.3 at. % and 26.5 at. % for pyrite and pentlandite, respectively.

    (ii) Although sulphide oxidation to sulphate was the dominant oxidation pathway for all three minerals, the number of moles of H^+ produced per mole of $Fe(OH)_3$ formed was much greater for pyrite (19) and pentlandite (17.2), than for pyrrhotite (11). Thus, the interfacial pH was lowered to a greater extent at the surfaces of pyrite and pentlandite, which allowed ferric hydroxy species to disperse and precipitate further away from the surfaces of these minerals, hence, decreasing the inhibiting effect of ferric oxide/hydroxide on oxidation.

17. At potentials > 1.4 V, the anodic current increased once more, the the upward trend in current continuing after the scan was reversed. This behaviour was ascribed to the visible growth of hydrated ferric oxide in pits nucleated at the high potential. As the pits expanded they caused the passive film to breakdown.

18. The anodic limiting current region was also observed in cyclic voltammograms of pyrrhotite recorded at pH 7 and pH 9.2. At pH 13 an anodic peak was observed, rather than a limiting current, as the passivating effect of the oxide layer increased with increasing pH. Moreover, stirring the solution had no effect on current-potential profiles at these pH values, and no soluble reaction products were observed in RSCBE experiments, which suggested that all the oxidation reduction reactions involved solid species.

19. Pentlandite is thermodynamically unstable at pH values < 4. However, in deoxygenated acidic solutions it cannot dissolve non-oxidatively in the true sense, like for example pyrrhotite, as its dissolution must involve an increase in the formal oxidation state of the metal atoms from < +2 in the lattice to +2 in solution. In this sense pentlandite was similar to pyrite. Furthermore, like pyrite, it was found to have a high positive rest potential in 1 M $HClO_4$ (0.695 V). This was ascribed to the high electrocatalytic activity of pentlandite for oxygen reduction, which allowed a mixed potential to be established between the anodic process:-

$$(Fe,Ni)_9S_8 = 4.5Ni^{2+} + 4.5Fe^{2+} + 8S + 18e \qquad (a_2)$$

and cathodic reduction of the trace amounts of oxygen in solution (10^{-5} - 10^{-3} mol m^{-3}):-

$$O_2 + 4H^+ + 4e = 2H_2O \qquad (k_6)$$

Thus, a passivating layer of sulphur was formed, the open circuit potential being too high for it to be removed by reaction (v).

20. RSCBE studies at pH 0 (1 M $HClO_4$), showed that the products of pentlandite oxidation were mainly Fe^{3+}, Ni^{2+}, sulphur and sulphate (reactions (b_2) and (d_2)), and at pH 4.6, ferric hydroxy species, Ni^{2+}, sulphur and sulphate (reactions (d_2) and (f_2)).

21. Cyclic voltammograms for stationary pentlandite electrodes in acidic media were similar in general shape and form to those observed for pyrite at a given pH value. However, the anodic oxidation curves for pentlandite exhibited a larger stirring rate dependence at $E_{\lambda a}$ potentials > 0.6 V, due to the greater inhibiting effect of the ferric oxide/hydroxide species formed on its surface. This behaviour was attributed to sulphate formation yielding a lower $H^+/Fe(OH)_3$ product ratio on the surface of pentlandite than on pyrite (17.2 versus 19), and sulphide oxidation to sulphate being the more dominant oxidation pathway for pyrite (see conclusion (16)).

22. Cyclic voltammograms of pentlandite recorded over the pH range 7 - 13 were very similar in character, exhibiting an anodic prewave/current plateau, between 0.4 and 0.6 V, followed by a rapid increase in current on the first positive-going potential scan. Both features shifted to more negative potentials with increasing pH and the anodic wave was observed irrespective of whether the electrode potential was initially swept in a negative or positive direction from the rest potential. The E_h/pH diagram for the Fe-Ni-S-H_2O system at 298 K predicted that, at neutral pH values and low anodic potentials, pentlandite oxidation occurred by the reaction:-

$$(Fe,Ni)_9S_8 + 7.5H_2O = 2FeNi_2S_4 + 2.5Fe(OH)_3 + 0.5Ni^{2+} + 7.5H^+ + 8.5e \qquad (s_2)$$

to form a surface layer consisting of a nickel-rich violarite ($FeNi_2S_4$)-type phase mixed with ferric oxide/hydroxide. Violarite oxidised by reactions (m_3) and (n_3) as the potential increased,

giving rise to the anodic prewave between 0.4 and 0.6 V. The Ni^{2+} ions released into solution precipitated once their solubility was exceeded (reaction (a_3)).

23. X-ray photoelectron spectroscopy confirmed that the level of Ni(II) and sulphide sulphur at the pentlandite surface increased under oxidising conditions and with increasing pH, which supported the oxidation mechanism proposed above, involving the formation of a violarite-type intermediate phase.

24. Cyclic voltammograms of stationary chalcopyrite electrodes in acidic solutions were characterised by an anodic peak or prewave which occurred between 0.4 and 0.7 V. The prewave was observed irrespective of the type of acid electrolyte used, or the direction of the initial potential sweep.

25. RSCBE studies in 1 M $HClO_4$, coupled with thermodynamic considerations, suggested that the prewave process involved initially the oxidation of chalcopyrite to covellite (CuS) and sulphur by the reaction:-

$$CuFeS_2 = 0.5CuS + 1.5S + Fe^{3+} + 0.5Cu^{2+} + 4e \qquad (o_4)$$

with bornite ($CuFe_{0.2}S_{0.8}$ - reaction (h_4)) and chalcocite (Cu_2S - reactions (j_4) followed by (k_4)) formed as intermediate phases during this stage of the process. At the peak maximum (0.55 V in 1 M $HClO_4$), covellite was oxidised to Cu^{2+} and sulphur by reaction (r_4):-

$$CuS = Cu^{2+} + S + 2e \qquad (r_4)$$

giving an overall reaction:-

$$CuFeS_2 = Cu^{2+} + Fe^{3+} + 2S + 5e \qquad (d_4)$$

The RSCBE results indicated that approximately equal amounts of copper and iron were dissolved at the peak maximum, as expected from reaction (d_4).

26. The above interpretation of the prewave process assumed that the oxidation products behaved as definite chemical entities. However, the process may have involved the dissolution of metal ions from the mineral lattice producing a non-thermodynamic metal-deficient sulphide film, depleted in iron more than copper:-

$$CuFeS_2 + 2xH^+ = CuFe_{(1-x)}S_{(2-x)} + xH_2S + xFe^{2+} \qquad (9.8)$$

The film was then oxidised on the first positive-going potential sweep. Alternatively, Fe(III) may oxidise the Cu(I) to Cu(II) in the lattice to maintain solid state electroneutrality on dissolution of Fe(II):-

$$Cu^+Fe^{3+}(S^{2-})_2 = Cu^+_{(1-x)}Cu^{2+}_xFe^{3+}_{(1-x)}(S^{2-})_2 + xFe^{2+}_{(aq)}$$

$$\ldots\ldots\ldots(z_5)$$

27. In contrast to pyrite and pyrrhotite, where sulphate formation was the dominant oxidation reaction in neutral and basic solutions, the equality of anodic and cathodic charges observed in cyclic voltammograms for chalcopyrite indicated that oxidation of this mineral produced negligible quantities of sulphate.

28. Three anodic peaks, (I), (II) and (III), were observed in cyclic voltammograms for chalcopyrite recorded at pH 7, 9.2 and 13. The results suggested that the chalcopyrite surface had already been partially oxidised and depleted in iron and sulphur whilst polishing the electrode. This resulted in the formation of $Cu_2O/CuOH$ on the surface, peak (ii) corresponding closely with the thermodynamic reversible potentials for the oxidation of either one, or both of these products (reactions ($w_4 + x_4$) and (c_5)). Peak (I) was ascribed to the oxidation of unaltered chalcopyrite by the reaction:-

$$CuFeS_2 + 3H_2O = 0.5Cu_2S + 1.5S + Fe(OH)_3 + 3H^+ + 3e \quad .....(zg_5)$$

Peak (III) occurred in the potential region assigned to the bulk oxidation of chalcopyrite by reactions (a_5) and (b_5), producing $Fe(OH)_3$, $Cu(OH)_2$, sulphur and sulphate, and was caused by the passivating effect of the metal oxide/hydroxide products.

29. The flotation response of chalcopyrite and pyrite in alkaline solutions was studied, after electrochemical conditioning in an electro-Hallimond tube, to correlate their surface reactions with "natural" (i.e. collectorless) hydrophobicity.

30. Chalcopyrite (-150 +106 μm) was rendered hydrophobic under mild oxidising conditions (0.0 to 0.8 V) in pH 10.5 buffer solution (0.025 M $NaHCO_3$ + 0.023 M NaOH + 1M NaCl), the recovery increasing with potential, before decreasing again at potentials > 0.8 V. Similar behaviour was observed at pH 9.0 (0.05 M $Na_2B_4O_7$ + 1 M NaCl), although the flotation response was shifted to more negative potentials. Maximum natural flotation was ascribed to the formation of sulphur, or a metal-deficient sulphide film with a high Cu(I)/Fe(III) ion ratio at the surface. At pH 10.5, the fall in flotation recovery at potentials > 0.8 V coincided with the electro-oxidation of chloride ions in the background electrolyte to hypochlorite. Hypochlorite enhanced the oxidation of chalcopyrite to sulphate, leaving a hydrophilic layer of Fe(III) and Cu(II) oxides on the mineral surface, which reduced floatability.

31. In contrast, pyrite (-150 +106 μm) exhibited no increase in flotation recovery under mild oxidising conditions. However, at cathodic potentials the recovery did increase after prolonged polarisation (1 - 3 hours). The inability of pyrite to float at oxidising potentials was due to the presence of a hydrophilic layer of ferric oxide/hydroxide on the surface of the pyrite particles, which was reduced to ferrous hydroxide at cathodic

potentials. The hydrophilic ferrous hydroxide film then dissolved slowly (reaction (p_1), increasing the hydrophobicity/floatability of pyrite.

32. Electrochemical conditioning caused the greatest enhancement in flotation recovery at intermediate particle sizes, the maximum recovery occurring at a coarser average particle size for oxidised chalcopyrite (~ 100 μm) than for reduced pyrite (~ 70 μm).

33. Adding frother (15 ppm amyl alcohol) to an electrochemically oxidised chalcopyrite surface increased recovery over the entire particle size range, the improvement increasing steadily with increasing particle size. No significant improvement was observed with reduced chalcopyrite, except for a slight increase in recovery at particle sizes < 40 μm. In contrast, frother addition increased the recovery of both oxidised and reduced pyrite, the increase being greater for reduced pyrite surfaces, especially at coarse particle sizes. At particle sizes < 40 μm, frother addition had little effect on pyrite recovery with either type of surface pretreatment. These results suggested that amyl alcohol was acting as a dipolar collector as well as a frother.

REFERENCES

1. Ross, V. "Geochemistry", mineralogy and crystal structure of sulphides". Econ. Geol., 52, 1957, pp 755-74.

2. Hellnor, E. "A structural scheme for sulphide minerals". J. Geol., 66, 1958, pp 503-25.

3. Povarennyk, A.S. "On a further development of the crystallochemical classification of minerals", Bull. Acad. Sci. USSR, Sci. Geol., 12, 1956, pp 91-114.

4. Povarennyk, A.S. "Crystal Chemical Classification of Minerals", (two vols.), (trans. J.E.S. Bradley), Plenum Press, New York, 1972.

5. Zoltai, T. "Systematics of Sulphide Structures", Department of Geology and Geophysics, University of Minnesota, Minneapolis, Minn., 1974.

6. Bray, L., and Claringbull, C.F. "Crystal Structures of Minerals", G Bell and Sons, London, 1965, p 55.

7. Brostingen, G., and Kjekshus, A., "Redetermined crystal structure of FeS_2 (pyrite)" Acta. Chem. Scand., 23, 1969, pp 2186-2188.

8. Kullerud, G., and Yoder, H.S. "Pyrite stability relations in the Fe-S system", Econ. Geol., 54, 1959, pp 533-72.

9. Anderson, H., and Chesley, K., Am. Jour. Sci., 25, 1933, p 315.

10. Carpenter, R.H. and Desborough, G.A. "Ranges in solid, solution and structure of naturally occurring triolite and pyrrhotite", Amer. Mineral., 49, 1964., pp 1350-1365.

11. Clark, A.H. "Stability field of monoclinic pyrrhotite", Trans IMM, B75, 1966, pp 232-235.

12. Yund, R.A., and Hall, H.T. "Hexagonal and monoclinic pyrrhotite", Econ. Geol., 64, 1969, pp 420-423.

13. Arnold, R.G. "Range in composition and structure of 82 natural terrestrial pyrrhotites", Canadian Mineral., 9, 1967, pp 31-50.

14. Arnold, R.G. "Pyrrhotite phase relations below 304 $\pm$ 6°C at $<$ 1 atm total pressure". Econ. Geol., 64, 1969, pp 405-419.

15. Morimoto, N., Nakazawa, H., Nighiguchi, K., and Tokonami, M. "Pyrrhotites" stoichiometric compounds with composition $Fe_{n-1}S_n$ ($n \geq 8$), Science, 168, 1970, pp 964-966.

16. Evans, H.T. "Lunar troilite: crystallography", Science, 167, 1970, pp 621-623.

17. Bertaut, E.F. "Contribution a l'etude des structures lacunaires: la pyrrhotine", Acta Crystallogr., 6, 1953, pp 557-61.

18. Tokonami, M., Nishiguchi, K., and Morimoto, N. "Crystal structure of a monoclinic pyrrhotite Fe_7S_8" Amer. Mineral., 57, 1972, pp 1066-1080.

19. Nakazawa, H., Morimoto, N. and Watanabe, E. "Direct observation of metal vacancies by high resolution electron microscopy. I. 4C type pyrrhotite (Fe_7S_8)" Amer. Mineral., 60, 1975, pp 359-66.

20. Clark, A.H., and Clark, A.M. "Electron microprobe analysis of mackinawite from the Ylojarvi, Finland", Neues. Jahrb. Mineral. Monatsch., 8, 1968, pp 259-68.

21. Kuovo, O., Vuorelainen, Y. and Long, J.V.P. "A tetragonal iron sulphide", Amer. Mineral., 48, 1963, pp 511-24.

22. Alson, N., Geol. Forening Stockholm Forh., 47, 1925, p 19.

23. Lindqvist, M., Lindqvist, D., and Westgren, H. "The crystal structure of CoS_8 and of pentlandite $(Ni,Fe)_9S_8$", Svensk Kem. Tidskr., 48, 1936, pp 156-60.

24. Rajamani, V., and Pravitt, C.T. "Crystal chemistry of natural pentlandites", Can. Mineral, 12, 1973, pp 178-87.

25. Burdick, C.L. and Ellis, J.H., J. Amer. Chem. Soc., 39, 1917, pp 2518.

26. Pauling, L., and Brockway, L.O. "The crystal structure of chalcopyrite", Z. Kristallogr., 82, 1932, pp 188-94.

27. Donnay, G., Corliss, L.M., Donnay, J.D.H., Elliot, N., and Hastings, J.H. "Symmetry of magnetic structures: magnetic structure of chalcopyrite", Phys. Rev., 112, 1958, pp 1917-23.

28. Hall, S.R. and Stewart, J.M. "The crystal structure refinement of chalcopyrite, $CuFeS_2$", Acta Crystallogr., 29B, 1973, pp 579-85.

29. Cabri, L.J. "A new copper-iron sulphide", Econ. Geol., 62, 1967, pp 910-25.

30. Cabri, L.J., and Hall, S.R. "Mooihoiekite and Haycockite, two new copper-iron sulphides and their relationship to chalcopyrite and talnakite", Amer. Mineral., 57, 1972, pp 689-708.

31. Hall, S.R. "Crystal structures of the chalcopyrite series", Can. Mineral., 13, 1975, pp 168-72.

32. Myamlin, V.A., and Pleskov, T.V. "Electrochemistry of Semiconductors", Plenum Press, New York, 1967.

33. Pridmore, D.F. and Shuey, R.T. "The electrical resistivity of galena, pyrite and chalcopyrite", Amer. Mineral., 61, 1976, p 248-259.

34. Vaughan, D.T., and Craig, J.R. "Mineral Chemistry of Metal Sulphides",, Cambridge Earth Science Series, Cambridge University Press, 1978, 493 pp.

35. Shuey, R.T. "Semiconducting Ore Minerals", Developments in Economic Geology No 4, Elsevier, Amsterdam, 1975.

36. Miyahara, S. and Teranishi, T. "Magnetic properties of FeS_2 and CoS_2" J. Appl. Phys., 39, 1968, pp 896-897.

37. Russell, P.E. and Montans, P.A., J. Appl. Phys., 49, 1978, p 4615.

38. Vaughan, D.J. and Ridout, M.S. "Mössbauer studies of some sulphide minerals", J. Inorg. Nucl. Chem., 33, 1971, pp 741-7.

39. Smith, F.G. "Variation in the properties of pyrite", Amer. Mineral., 27, 1947, pp 1-19.

40. Hill, P.A. and Green, R. "Thermoelectricity and resistivity of pyrite from Renison Bell and Mt. Bischoff, Tasmania", Econ. Geol., 57, 1962, pp 579-586.

41. Marinace, J.C. "Some electrical properties of natural crystals of iron pyrite", Phys. Rev., 96, 1954, p 593.

42. Bither, T.A., Bouchard, R.J., Cloud, W.H., Donohue, P.C., and Siemons, W.J. "Transition metal pyrite dichalogenides, high pressure synthesis and correlation of properties", Inorg. Chem., 7, 1968, pp 2208-2220.

43. Horita, H. "Some semiconducting properties of natural pyrite", Japan. J. Appl. Physics", 12, 1973, pp 617-618.

44. Hawley, J.E. "Spectrographic studies of some Eastern Canada gold mines", Econ. Geol., 47, 1952, pp 260-304.

45. Levinson, L.M., and Treves, D. "Mössbauer study of the magnetic structure of Fe_7S_8", J Phys. Chem. Solids, 29, 1968, pp 2227-31.

46. Parasnis, D.S. "The electrical resistivity of some sulphide and oxide minerals and their ores", Geophysical Prosp., 4, 1956, pp 249-278.

47. Thesdossiou, A. "Measurements of the Hall effect and resistivity in pyrrhotite", Phys. Rev., A137, 1965, pp 1321-1326.

48. Hihara, T. "Magnetic and electric properties of iron sulphide single crystals", J. Sci. Hiroshima Univ., A24, 1960, pp 31-53.

49. Kaplan, H.I., and Worrell, W.L. "The variation of the electrical conductivity of FeS with sulphur pressure at temperatures between 670 and 900°C". (eds. Eyring, L. and O'Keefe, M.) "The Chemistry of Extended Defects in Non-Metallic Solids", North-Holland, Amsterdam, 1970, 672 pp.

50. Knop, O., Huang, C. and Woodhams, F.W.D. "Chalcogenides of the transition elements. VII. A Mössbauer study of pentlandite", Amer. Mineral., 55, 1970, pp 1115-30.

51. Rosenquist, T. "A thermodynamic study of the iron, cobalt and nickel sulphides", J. Iron Steel Inst., 176, 1954, pp 37-59.

52. Koch, D.F.A. "Electrochemistry of sulphide minerals", Modern Aspects of Electrochemistry, 10, (Eds. J.O.M. Bockris, B.E. Conway), Plenum Press, New York, 1975, p 211-237.

53. Wyckoff, R.W.G. "Deux especes de chalcopyrites mises en evidence pas les bacteries", Bull. Soc. Fr. Miner. Cristallogr., 93, 1970, pp 120-2.

54. Greenwood, N.N. and Whitfield, H.J. "Mössbauer effect studies on cubanite ($CuFe_2S_4$) and rotated iron sulphides", J. Chem. Soc., 1968A, 1968, pp 1697-9.

55. Telkes, M. "Thermoelectric power and electrical resistivity of minerals", Amer. Mineral., 35, 1950, pp 536-555.

56. Austin, I.G., Goodman, C.H.L. and Pengelly, A.E. "New semiconductors with the chalcopyrite structure", J. Electrochem. Soc., 103, 1956, pp 609-610.

57. Teranishi, T., Sato, K., and Kondo, K. "Optical properties of a magnetic semiconductor: Chalcopyrite $CuFeS_2$. I. Absorption spectra of $CuFeS_2$ and Fe-doped $CuAlS_2$ and $CuGaS_2$", J. Phys. Soc. Japan, 36, 1974, pp 1618-24.

58. Donovan, B., and Reichenbaum, G. "Electrical properties of chalcopyrite", Brit. J. Appl. Phys., 9, 1958, pp 474-477.

59. Barton, P.B. "Solid solutions in the system Cu-Fe-S. Part I: The Cu-S and CuFe-S joins". Econ. Geol., 68, 1973, pp 455-465.

60. Harvey, R.D. "Electrical conductivity and polished mineral surfaces", Econ. Geol., 23, 1928, pp 778-803.

61. Peters, E. "The electrochemistry of sulphide minerals", Trends in Electrochemistry, (Eds. J.O.M. Bockris, D.A.J. Rand and B.J. Welch), Plenum Press, New York, 1977, pp 267-290.

62. Sato, M. "Half-cell potentials of semiconductive simple binary sulphides in aqueous solution", Electrochim. Acta, 11, 1966, p 361-373.

63. Pourbaix, M. "Atlas of Electrochemical Equilibria", Gauthiers-Villars, Paris, 1963.

64. Garrels, R.M., and Christ, C.L. "Solution Minerals and Equilibria", Harper and Row, New York, 1965.

65. Peters, E. "Direct leaching of sulphides: chemistry and applications", 1976 Extract. Met. Lecture, Met. Soc., AIME, Metallurgical Transactions, 7B, 1976, pp 505-517.

66. Peters, E., and Majima, H. "Electrochemical reactions of pyrite in acid perchlorate solutions", Canadian Metallurgical Quarterly, 7, 1968, pp 111-117.

67. Peters, E. "The physical chemistry of hydrometallurgy", Int. Symposium on Hydrometallurgy, AIME, (eds. D.J.I. Evans and R.S. Shoemaker), 1973, Chicago, Illinois, pp 205-228.

68. Safin, Kh. Sh. "Calculation of the thermodynamic functions of pentlandite", Obogashchenie Rud, 5, 1977, pp 62-66.

69. Abramov, A.A. "Theoretical Bases of Optimising Selective Flotation of Sulphide Ores", Hedra, Moscow, 1978.

70. Thornber, M.R. "Mineralogical and electrochemical stability of the nickel-iron sulphides-pentlandite and violarite", J. Applied Electrochemistry, 13, 1983, pp 253-267.

71. Peres, A.E.C. "The interaction between xanthate and sulphur dioxide in the flotation of nickel-copper sulphide ores", Ph.D. Thesis, Univ. British Columbia, Vancouver, Canada, 1979.

72. Woods, R. "Electrochemistry of sulphide flotation", Flotation, A.M. Gaudin Memorial Volume, 1, American Institute of Mining, Metallurgical, and Petroleum Engineers Inc, 1976, pp 298-333.

73. Natarajan, K.A., Iwasaki, I. "E_h measurements in hydrometallurgical systems", Min. Sci. Engng., 6(1), 1974, pp 35-53.

74. Harkins, W.D. "Physical Chemistry of Surface Films", New York, Reinhold, 1952.

75. Forward, F.A., and MacKiw, V.N. "Chemistry of the ammonia pressure process for leaching nickel, copper, and cobalt from Sherritt Gordon Sulphide Concentrates", Trans. Met. Soc. of AIME, 203, 1955, pp 457-463.

76. Allen, E.T., and Johnston, J., J. Ind. Eng. Chem., 2, 1910, p 196.

77. Allen, E.T., and Crenshaw, J.L., Amer. J. Sci., 33, 1914, p 393.

78. Biegler, T., and Swift, D.A. "Anodic behaviour of pyrite in acid solutions", Electrochimica Acta., 24, 1979, pp 415-420.

79. Kim, J.W., and Choi, D.J., Kumsok Hakkoe Chi., 6, 1968, p 83.

80. Nagai, T., and Kuichi, T. "Formation of the pyramidal etch hills on pyrite and its role in dissolution kinetics", J. Mining. Met. Inst. Japan, 90(1040), 1974, pp 653-58.

81. Nagai, T., and Kuichi, T. "Kinetic studies on the leaching of pyrite with plate specimens", J. Mining Met. Inst. Japan, 91(1049), 1975, pp 473-477.

82. Nagai, T., and Kuichi, T. "Electrochemical studies on the pressure leaching of pyrite", J. Mining Met. Inst. Japan,, 91(1050), 1975, pp 547-553.

83. Warren, I.H., Australian J. Appl. Sci., 7, 1956, p 346.

84. Stenhouse, J.F., and Armstrong, W.M. "The aqueous oxidation of pyrite", Trans. Can. Inst. Mining Met., 55, 1951, pp 48-52.

85. Downes, K.W. and Bruce, R.W. "The recovery of elemental sulphur from pyrite and pyrrhotite", Trans. Can. Inst. Mining Met., 58, 1955, pp 77-82.

86. Mizoguchi, T., and Habashi, F. "Aqueous oxidation of zinc sulphide, pyrite and their mixtures in hydrochloric acid", Trans. IMM, C92, 1983, pp 14-19.

87. Majima, H. and Peters, E., IUPAC Conference, Sydney, Australia, 1969.

88. McKay, D.R., and Halpern, J. "A kinetic study of the oxidation of pyrite in aqueous suspension", Trans. Metall. Soc. AIME, 212, 1959, pp 301-309.

89. Bailey, L.K. and Peters, E. "Decomposition of pyrite in acids by pressure leaching and anodisation: the case for an electrochemical mechanism", Can. Metall. Quarterly, 15(4), 1976, pp 333-344.

90. Thomas, G., and Whalley, B.J.P., Can. J. Chem. Eng., 36, 1958, p 37.

91. Burkin, A.R., and Edwards, A.M. "The formation of insoluble iron oxide coatings during the alkali pressure leaching of pyrite" Proc. VI Int. Min. Proc. Congress., Cannes, France, 1964.

92. Gerlach, J., Haehne, H., and Pawlek, F.Z., Erzbergbau Metalhuettenwes, 19, 1966, p 66.

93. Kunda, W., Rudyk, B., and MacKiw, V.N., CIM Bulletin, 61, 1968, p 819.

94. Thornhill, P.G., Can. Metall. Quarterly, 8, 1969, p 219.

95. Habashi, F., Trans AIME, 254, 1973, p 328.

96. Sandefur, B.T., Econ. Geol., 37, 1942, pp 173-187.

97. Michener, C.E., and Yates, A.B., Econ. Geol., 39, 1944, pp 506-14.

98. Nickel, E.H., Ross, J.R., and Thornber, M.R. "The supergene alteration of pyrrhotite-pentlandite ore at Kambalda, Western Australia", Econ. Geol., 69, 1974, pp 93-107.

99. Nickel, E.H., Allchurch, P.D., Mason, M.G. and Wilmshurst, J.R. "Supergene alteration at the Perseverance nickel deposit, Agnew, Western Australia", Econ. Geol., 72, 1977, pp 184-203.

100. Keele, R.A., and Nickel, E.H. "The geology of a primary millerite-bearing sulphide assemblage and supergene alteration at the Otter Shoot, Kambalda, Western Australia", Econ. Geol., 69, 1974, pp 1102-1117.

101. Dutrizac, J.E., and MacDonald, R.J.C. "Percolation leaching of pentlandite ore", CIM Bulletin, 67, 1974, pp 169-75.

102. Kelt, S. "The leaching of certain nickel sulphides", Ph.D. Thesis, Imperial College, London, 1975.

103. Subramanian, K.N., Jennings, P.H. "Review of the hydrometallurgy of chalcopyrite concentrates", Can. Metall. Quarterly, 11, 1972, pp 387-400.

104. Woodcock, J.T. "Some aspects of the oxidation of sulphide minerals in aqueous suspensions", Proc. Aust. IMM, No 198, 1961, pp 47-84.

105. Dutrizac, J.E., MacDonald, R.J.C., and Ingraham, T.R. "The kinetics of the dissolution of synthetic chalcopyrite in aqueous acidic ferric sulphate solution", Trans. Metall. Soc. AIME, 245, 1969, pp 955-959.

106. Dutrizac, J.E., and MacDonald, R.J.C. "Ferric ion as a leaching medium", Minerals Sci. Eng., 6(2), 1974, pp 59-100.

107. Wadsworth, M.E. "Advances in the leaching of sulphide minerals", Minerals Sci. Eng., 4(4), 1972, pp 36-47.

108. Linge, H.G. "A study of chalcopyrite dissolution in acidic ferric nitrate by potentiometric titration", Hydrometallurgy, 2, 1976, pp 51-64.

109. Munoz, P.B., Miller, J.D., Wadsworth, M.E. "Reaction mechanism for the acid ferric sulphate leaching of chalcopyrite", Metall. Trans. AIME., B10, 1979, pp 149-159.

110. Warren, G.W., Wadsworth, M.E., and El-Raghy, S.M. "Passive and transpassive anodic behaviour of chalcopyrite in acid solutions", Metall. Trans. AIME, B13, 1982, pp 571-579.

111. Dutrizac, J.E. "The kinetics of dissolution of chalcopyrite in ferric ion media", Metall. Trans. AIME, B9, 1978, pp 431-439.

112. Kruesi, P.R. "Cymet copper reduction process", Min. Congr. J., 60(9), 1974, pp 22-23.

113. Kruesi, P.R., Allen, E.S., and Lake, J.L. "Cymet process - hydrometallurgical conversion of base metal sulphides to pure metals", Bull. Can. IMM, 66, 1973, pp 81-87.

114. Wagner, C., and Traud, W., Z. Elektrochem., 44, 1938, pp 391.

115. Plaksin, I.N. "Study of superfacial layers of flotation reagents on minerals and the influence of the structure of minerals on their interaction with reagents", Proc. Int. Mineral Processing Cong., Group III, Paper No 13, 1960, London.

116. Plaksin, I.N. and Shafeyev, R.S. "On properties of distributions of xanthates on the surface of sulphide minerals; J. Mines Metals and Fuels, 1960, pp 1-8.

117. Fox, R.W., Phil Trans, 2, 1830, p 309.

118. Sato, M., and Mooney, H.M. "The electrochemical mechanism of sulphide self-potentials", Geophysics, 25, 1960, pp 226-249.

119. Kamienski, B. "So-called flotation", Przemysl Chemiczny, 15, 1931, pp 201-202.

120. Kamienski, B. "Electrostatic potentials at the phase boundary: electrolyte unattackable electrode, and the physical chemistry of the flotation process" Z. Phys. Chem., A158, 1932, pp 441-444.

121. Salamy, S.G. and Nixon, J.C. "The application of electrochemical methods to flotation research". Recent Developments in Mineral Dressing, London, Institution of Mining and Metallurgy, 1953, pp 503-516.

122. Gottschalk, V.H. and Buhler, H.A., Econ. Geol., 7, 1915, p 15.

123. Klein, J.D., and Shuey, R.T. "Nonlinear impedance of mineral electrolyte interfaces: Part I. pyrite", Geophysics, 43(6), 1978, pp 1222-1234.

124. Springer, G. "Observations on the electrochemical reactivity of semiconducting minerals", Trans. IMM, C79, 1970, pp 11-14.

125. Kunori, S., and Ishui, F., J. Mining Met. Inst. Japan, 79, 1963, pp 35.

126. Meyer, R.E. "Electrochemistry of FeS_2" J. Electroanl. Chem., 101, 1979, pp 59-71.

127. Yashina, G.M., Smirnova, E.N., Olerskaya, N.L., and Levin, A.I., Izv. Vyssh. Uchebn. Zaved., Khim. Khim. Tekhnol., 20, 1977, p 1579.

128. Michell, D., and Woods, R. "Analysis of oxidised layers on pyrite surfaces by x-ray emission spectroscopy and cyclic voltammetry", Aust. J. Chem., 31, 1978, pp 27-34.

129. Janetski, N.D., Woodburn, S.I., and Woods, R. "An electrochemical investigation of pyrite flotation and depression" Int. J. Miner. Proc., 4, 1977, pp 227-239.

130. Sato, M. "Oxidation of sulphide ore bodies - I. Geochemical environments in terms of E_h and pH", Econ. Geol., 55, 1960, pp 928-1201.

131. Sato, M. "Oxidation of sulphide ore bodies - II. Oxidation mechanisms of sulphide minerals at 25°C", Econ. Geol., 55, 1960, pp 1202-1231.

132. Ahmed, S.M. "Electrochemical studies of sulphides, I. The electrocatalytic activity of galena, pyrite and cobalt sulphide for O_2 reduction in relation to xanthate adsorption and flotation", Int. J. Miner. Proc., 5, 1978, pp 163-174.

133. Ahmed, S.M. "Electrochemical studies of sulphides, II. Measurement of the galvanic currents in galena and the general mechanism of O_2 reduction and xanthate adsorption on sulphides in relation to flotation", Int. J. Miner. Proc., 5, 1978, pp 175-182.

134. Hamilton, I.C., and Woods, R. "An investigation of surface oxidation of pyrite and pyrrhotite by linear potential sweep voltammetry", J. Electroanal. Chem., 118, 1981, pp 327-344.

135. Conway, B.E., Ku, J.C.H., and Ho, F.C. "The electrochemical surface reactivity of iron sulphide, FeS_2" J. Colloid Interface Sci., 75(2), 1980, pp 357-72.

136. Lowson, R.T. "Aqueous oxidation of pyrite by molecular oxygen", Chem. Rev., 82(5), 1982, pp 461-497.

137. Najdeker, E., and Bishop, E. "The formation and behaviour of platinum sulphide on platinum electrodes", J. Electroanal. Chem., 41, 1973, pp 79-87.

138. Ramasubramanian, N. "Anodic behaviour of platinum electrodes in sulphide solutions and the formation of platinum sulphide", J. Electroanal. Chem., 64, 1975, pp 21-37.

139. Contractor, A.Q. and Hira Lal "Two forms of chemisorbed sulphur on platinum and related studies", J. Electroanal. Chem., 96, 1979, pp 175-181.

140. Onuchukiou, A.I. "Hydrogen evolution on iron pyrite (FeS_y) in sodium chloride solution", Electrochim. Acta, 27(4), 1982, pp 529-533.

141. Venkatachalam, S., and Mallikarjunan, R. "Electrode potentials and anodic polarisation of sulphides", Trans. IMM, C79, 1970, pp 181-188.

142. Henry, B., Lecuire, J.M., and Bessiere, J. "Reduction electrochimique des sulfines de fer application a la mesure de la non stoechiometric" J. Electroanal. Chem., 83, 1977, pp 111-115.

143. Scott, P.D., and Nicol, M.H. "The kinetics and mechanisms of the non-oxidative dissolution of metal sulphides", Trends in Electrochemistry (eds. J. O'M. Bockris, D.A.J. Rand and B.J. Welch), Plenum Press, New York, 1977, pp 303-316.

144. Kuhn, A.T., and Chan, C.Y. "pH changes at near-electrode surfaces", J. Applied Electrochemistry, 13, 1983, pp 189-207.

145. Jones, D.L., and Peters, E. "Electrochemical experiments with chalcopyrite electrodes in aqueous solutions up to 200°C", High Temperature High Pressure Electrochemistry in Aqueous Solutions, National Association of Corrosion Engineers, Houston, 1976, pp 443-458.

146. Jones, D.L., and Peters, E. "The leaching of chalcopyrite with ferric sulphate and ferric chloride", Extractive Metallurgy of Copper II, Trans. Metall. Soc. AIME, New York, 1976, pp 633-653.

147. Jones, D.L., "The leaching of chalcopyrite" Ph.D. Thesis, Dept. of Metallurgy, Univ. of British Columbia, Vancouver, B.C., 1974.

148. Warren, G.W., "Electrochemical oxidation of chalcopyrite", Ph.D. Thesis, Dept. of Metallurgy and Metallurgical Engineering, Univ. of Utah, Salt Lake City, Utah, 1978.

149. Warren, G.W., Wadsworth, M.E., and El-Raghy, S.M. "Passive and transpassive anodic behaviour of chalcopyrite in acid solutions", Metallurgical transactions SME-AIME, 13B, 1982, pp 571-579.

150. Warren, G.W., Wadsworth, M.E., and El-Raghy, S.M. "Anodic behaviour of chalcopyrite in acid sulphuric acid", Int. Symposium on Hydrometallurgy, AIME, 1983, Atlanta, Georgia, USA.

151. Miller, J.D., and Portillo, H.Q. "Silver catalysis in ferric sulphate leaching of chalcopyrite", XII Int. Miner. Proc. Cong., Warsaw, Poland, 1979, (ed. J. Laskowski), Elsevier, New York (1981), pp 851-901.

152. Ammou-Chokroum, M., Sen, P.K. and Fouques, F. "Electroxidation of chalcopyrite in acid chloride medium; kinetics, stoichiometry and reaction mechanism", XII Int. Miner. Proc. Cong., Warsaw, Poland, 1979, (ed. J. Laskowski), Elsevier, New York (1981) pp 759-809.

153. Ichikuni, M. "The dissolution of sulphide minerals in various media, III. Factors intervening in the dissolution of chalcopyrite", Bulletin of the Chemical Society of Japan, 33, 1960, pp 1159-1162.

154. Ichikuni, M. "The action of ferric ions on chalcopyrite", Bulletin Chem. Soc. Japan, 35, 1962, pp 1765-1768.

155. Linge, H.G. "Reactivity comparison of Australian chalcopyrite concentrates in acidified ferric solution", Hydrometallurgy, 2(3), 1976, pp 219-232.

156. Beckstead, L.W., and Miller, J.D. "Ammonia leaching of chalcopyrite-reaction kinetics", Metallurgical Transactions SME-AIME, 8B(1), 1977, pp 19-30.

157. Beckstead, L.W., and Miller, J.D. "Acid ferric sulphate leaching of attrition-ground chalcopyrite concentrates", in Extractive Metallurgy of Copper II, Trans. Metall. Soc. AIME, New York, 1976, pp 611-632.

158. Baur, J.P., Gibbs, H.L., and Wadsworth, M.E. "Initial-stage sulphuric leaching kinetics of chalcopyrite using radiochemical techniques", US Bureau of Mines, R.I. 7823, 1974.

159. Hillrichs, E., Greulich, H., and Bertram, R. "Investigations of the electrochemical dissolution of copper sulphide ores in sulphuric acid solutions", Int. Symposium on Hydrometallurgy, Annual Meeting SME-AIME, 1983, Atlanta, Georgia, USA.

160. Parker, A.J., Paul, R.L., and Power, G.P. "Electrochemical aspects of leaching copper from chalcopyrite in ferric and cupric salt solutions", Aust. J. Chem., 34, 1981, pp 13-34.

161. Parker, A.J., Paul, R.L. and Power, G.P. "Electrochemistry of the oxidative leaching of copper from chalcopyrite", J. Electroanal. Chem., 118, 1981, pp 305-316.

162. Zevgolis, E. "Electrochemical kinetics and anodic dissolution of chalcopyrite", Ph.D. Thesis, Dept. of Chemical Engineering and Materials Science, University of Minnesota, Minneapolis, Minnesota, 1971.

163. Zevgolis, E., and Cooke, S.R.B. "Electrochemical properties of the semiconductor mineral chalcopyrite", XI Int. Miner. Proc. Cong., Calgiari, Italy, 1975.

164. McMillan, R.S., Mackinnon, D.J. and Dutrizac, J.E. "Anodic dissolution of n-type and p-type chalcopyrite", J. Applied Electrochem., 12, 1982, pp 743-757.

165. Chen, J.H. and Harvey, W.W. "Cation self-diffusion in chalcopyrite and pyrite", Metallurgical Transactions SME-AIME, 6B, 1975, pp 331-339.

166. Price, D.C. and Chilton, J.P. "The electroleaching of bornite and chalcopyrite", Hydrometallurgy, 5(4), 1980, pp 381-394.

167. Biegler, T., and Swift, D.A. "Anodic electrochemistry of chalcopyrite", J. Applied Electrochem., 9, 1979, pp 545-554.

168. Ferreira, R.C.H. "Leaching of chalcopyrite, Ph.D. Thesis, Dept. of Metallurgy and Materials Science, Imperial College, University of London, 1972.

169. Warren, I.H. "A study of the acid pressure leaching of chalcopyrite, chalcocite and covellite", Aust. J. Appl. Sci., 9, 1958, pp 36-51.

170. Ammou-Chokroum, M., Cambazoglu, M., and Steinmetz, D. "Oxidation menagee de la chalcopyrite en solution acide: analyse cinetique des reactions. I. Modeles chimiques", Bull. Soc. Fr. Mineral Cristallogr., 100, 1977, pp 149-161.

171. Ammou-Chokroum, M., Steinmetz, D., and Malve, A. "Etude electrochimique de l'oxydation de la chalcopyrite en milieu acid chlorure, Bull. Soc. Fr. Mineral. Cristallogr., 101, 1978, pp 26-43.

172. Dobrokhotov, G.N., and Maiorova, E.V. "Kinetics of autoclave leaching of chalcopyrite", J. Appl. Chem. USSR, 35, 1962, pp 1637-42.

173. Majima, H., and Peters, E. "Oxidation rates of sulphide minerals by aqueous oxidation at elevated temperatures", Trans. AIME, 236, 1966, pp 1409-13.

174. Vizsolyi, A. "Copper and elemental sulphur from chalcopyrite by pressure leaching", J. Metals, NY, 19, 1967, pp 52-9.

175. Gardner, J.R., and Woods, R. "An electrochemical investigation of the natural flotability of chalcopyrite", Int. J. Miner. Proc., 6, 1979, pp 1-16.

176. Filmer, A.O., Parker, A.J., and Wadley, L.G.B. "Oxidation of copper sulphides in aqueous ammonia. I. Formation of sulphur", Aust. J. Chem., 32, 1979, pp 961-73.

177. Filmer, A.O., Parker, A.J. and Wadley, L.G.B. "Oxidation of copper sulphides in aqueous ammonia. II. Electrochemical aspects" Aust. J. Chem., 32, 1979, pp 975-87.

178. Nicol, M.J. "Mechanisms of aqueous reduction of chalcopyrite by copper, iron and lead", Trans. IMM, C84, 1975, pp 206-209.

179. Biegler, T., and Swift, D.A. "The electrolytic reduction of chalcopyrite in acid solution", J. Applied Electrochem., 6, 1976, pp 229-235.

180. Biegler, T., and Constable, D.C. "Upgrading and activation of chalcopyrite concentrates by slurry electrolysis", Trans. IMM, C85, 1976, pp 40-44.

181. Biegler, T., and Constable, D.C. "Continuous electrolytic reduction of a chalcopyrite slurry" J. Applied Electrochem., 7, 1977, pp 175-179.

182. Biegler, T., "Reduction kinetics of a chalcopyrite electrode surface", J. Electroanal. Chem., 85, 1977, pp 101-106.

183. Macleod, I.D., and Muir, D.M. "Reduction of chalcopyrite with copper (I)" J. Applied Electrochem., 13, 1983, pp 411-416.

184. Cerda, P.A.M. "Electrodissolution of chalcopyrite concentrates", M.Sc. Thesis, Dept. of Metallurgy and Materials Science, Imperial College, University of London, 1977.

185. Biegler, T., Rand, D.A.J. and Woods, R. "Oxygen reduction on sulphide minerals", Trends in Electrochemistry, (eds. J.O.M. Bockris, D.A.J. Rand, and B.J. Welch), Plenum Press, New York, 1977, pp 291-302.

186. Biegler, T., Rand, D.A.J. and Woods, R. "Oxygen reduction on sulphide minerals. Part I. Kinetics and mechanism at rotated pyrite electrodes", J. Electroanal. Chem., 60, 1975, pp 151-162.

187. Biegler, T. "Oxygen reduction on sulphide minerals. Part II. Relation between activity and semiconducting properties of pyrite electrodes", J. Electroanal. Chem., 70, 1976, pp 265-275.

188. Rand, D.A.J. "Oxygen reduction on sulphide minerals. Part III. Comparison of activities of various copper, iron, lead and nickel mineral electrodes", J. Electroanal. Chem., 83, 1977, pp 19-32.

189. Majima, H., and Peters, E. "Electrochemistry of sulphide dissolution in hydrometallurgical systems", VIIIth. Int. Miner. Proc. Cong., Leningrad, USSR, 1968.

190. Granville, A., Finkelstein, N.P., and Allison, A.S. "Review of reactions in the flotation system galena-xanthate-oxygen", Trans. IMM, C81, 1972, pp 1-30.

191. Tolun, R., and Kitchener, J.A. "Electrochemical study of the galena-xanthate-oxygen flotation system", Trans. IMM, 73, 1964, pp 312-322.

192. Usul, A.H., And Tolun, R. "Electrochemical study of the pyrite-oxygen-xanthate system", Int. J. Miner. Proc., 1, 1974.

193. Plaksin, I.N., and Bessonov, S.V. "Role of gases in flotation reactions", Proceedings of the 2nd International Congress on Surface Activity, 3, 1957, pp 361-367.

194. Behret, H., Binder, H., and Sandstede, "Electrocatalytic oxygen reduction with thiospinels and other sulphides of transition metals", Electrochimica Acta, 20, 1975, pp 111-117.

195. Tributsch, H., and Bennett, J.C. "Hydrogen peroxide induced periodical catalysis on copper-containing sulphides", Ber. Bunsenges. Phys. Chem., 80, 1976, pp 321-327.

196. Tributsch, H. "Sustained oscillations during catalytic reduction of hydrogen peroxide on copper-iron-sulphide electrodes I", Ber. Bunsenges. Phys. Chem., 79, 1975, pp 570-579.

197. Tributsch, H. "Sustained oscillations during catalytic reduction of hydrogen peroxide on copper-iron-sulphide electrodes II, Ber. Bunsenges. Phys. Chem., 79, 1975, pp 580-587.

198. Subramarvan, K.N., Stratigakos, E.S., and Jennings, P.H. "Hydrometallurgical processing of pyrrhotite", Can. Metall. Quarterly, 11, 1972, pp 425-434.

199. Parsons, H.W., and Ingraham, T.R. "The hydrogen sulphide route to sulphur recovery from base metal sulphides", Ottawa, Dept. of Energy, Mines and Resources, Inf. Cir., IC242, June 1970.

200. Jibicki, K. "Acid decomposition reactions on compounds and minerals in the Fe-Ni-sulphide system", Ph.D. Thesis, University of British Columbia, Canada, May 1974.

201. Ingraham, T.R., Parsons, H.W., and Cabri, L.J. "Leaching of pyrrhotite with hydrochloric acid", Can. Metall. Quarterly, 11, 1972, pp 407-411.

202. Van Weert, G., Mah, K., and Piret, N.L. "Hydrochloric acid leaching of nickeliferous pyrrhotites from the Sudbury district", Can. Min. Metall. Bull., 77, 1974, pp 97-103.

203. Tewari, P.H., and Campbell, A.B. "Dissolution of iron sulphide (troilite) in aqueous sulphuric acid", J. Phys. Chem., 80, 1976, pp 1844-1848.

204. Yazawa, A., and Eguchi, M., Bulletin of the Research Inst. of Mineral Dressing and Metallurgy, Tohoku Univ. Sendai, Japan, 23, 1967, pp 147.

205. Nicol, M.J. and Scott, P.D. "The kinetics and mechanism of the non-oxidative dissolution of some iron sulphides in aqueous acidic solutions", J. S. Afr. Inst. Min. Metall., 79, 1979, pp 298-305.

206. Dyson, N.F., and Scott, T.R. "Acid leaching of nickel sulphide concentrates", Hydrometallurgy, 1, 1976, pp 361-372.

207. Filmer, A.O., and Nicol, M.J. "The non-oxidative dissolution of nickel sulphides in aqueous acid solutions", J.S. Afr. Inst. Min. Metall., 80(12), 1980, pp 415-424.

208. Filmer, A.O. "The non-oxidative dissolution of nickel mattes in aqueous acidic solutions", J. S. Afr. Inst. Min. Metall., 81, 1981, pp 74-84.

209. Majima, H., and Awakura, Y. "Non-oxidative leaching of base metal sulphide ores", XII Int. Miner. Proc. Cong., Warsaw, Poland, 1979.

210. Nicol, M.J. "The non-oxidative leaching of oxides and sulphides: an electrochemical approach", Int. Symposium on Hydrometallurgy, AIME, 1983, Atlanta, Georgia, USA.

211. Scott, P.D., and Nicol, M.J. "The kinetics and mechanisms of the non-oxidative dissolution of some iron sulphides in aqueous acidic solutions", Johannesburg, National Institute for Metallurgy, Report No 1858, Nov. 1976.

212. Vermilyea, D.A. "The dissolution of some compounds in aqueous media" J. Electrochem. Soc., 113, 1966, pp 1067-1070.

213. Habashi, F. "The electrometallurgy of sulphides in aqueous solutions", Minerals Sci. Engng., 3(3), 1971, pp 3-12.

214. Wright, J.K. "Electrochemical aspects of sulphide hydrometallurgy", Bulletin of the Aust. Min. Development Laboratories, Amdel Bulletin, No 12, 1971, pp 47-73.

215. Wright, J.K. "The electrolytic processing of sulphide concentrates, possible applications", Bulletin of the Aust. Min. Development Laboratories, Amdel Bulletin, No 13, 1972, pp 27-40.

216. Bautista, R.G., and Flett, D.S. "Electrodissolution in hydrometallurgy", Warren Springs Report, England, Rep. No. LR226(ME), 1976, 7 pp.

217. Renzoni, L.S., McQuire, R.C., and Barker, W.V. "Direct electrorefining of nickel matte", J. Metals, 10(6), 1958, pp 414-418.

218. Boldt, J.R., and Queneau, P. "The Winning of Nickel", Methuen and Co. Ltd., London, 1967, pp 336-370.

219. Shimura Nickel Manufacturing Company, "Direct electrorefining of nickel matte anode", French Patent 1,360,675, (1964).

220. Krasnonosov, V.P., and Borbat, V.F. "Electrolytic refining of nickel by using high-sulphur anodes", Tsvetn. Metal., 38(10), 1965, pp 38-41.

221. Papademetriou, T., and Grasso, J.R. "Recovery of precious metals from South African matte", Engelhard Ind. Tech. Bull. 10(4), 1970, pp 121-129.

222. Spence, W.W., and Cook, W.R., "The Thompson refinery", Trans. Can. IMM, 67, 1964, pp 55-62.

223. Loshkarev, A.G., and Vozisov, A.F., "Anodic solution of copper sulphide", Zh. Prikl. Khim., 26, 1953, pp 55-62.

224. Habashi, F., and Torres-Acuna, N., "The anodic dissolution of copper (I) sulphide and the direct recovery of copper and elemental sulphur from white metal", Trans. Metall. Soc., AIME, 242, 1968, pp 780-787.

225. Venkatachalem, S. And Mallikarjunan, R. "Direct electrorefining of cuprous sulphide and copper matte", Trans. IMM, C77, 1968, pp 45-52.

226. Chizhikov, D.M. "Effect of the concentration of chloride ions in a sulphuric acid electrolyte on the anodic dissolution of a copper-nickel converter matte", Issled Protsessov Met. Isvet. Redk. Met., (ed. D.M. Chizhikov), 1969, pp 166-171.

227. Venkatachalem, S., and Mallikarjunan, R. "Laboratory scale studies on a new procedure for the recovery of electrolytic copper", Trans. Ind. Inst. Metals, June 1971, pp 29-38.

228. Etienne, A. "Electrochemical aspects of the aqueous oxidation of copper-sulphides,", Ph.D. Thesis, Dept. of Metallurgy, Univ. of British Columbia, Vancouver, Canada, 1970.

229. Kato, T., and Oki, T., "Anodic reaction of copper (II) sulphide in sulphuric acid solution", Denki Kagaku, 40, 1972, pp 670-674.

230. Wright, J.K. "An electrochemical investigation of the hydrometallurgy of synthetic copper sulphides", Ph.D. Thesis, University of New South Wales, Australia, 1970.

231. Biegler, T., and Swift, D.A. "Dissolution kinetics of copper sulphide anodes", Hydrometallurgy, 2, 1976/1977, pp 335-349.

232. Hojo, M., and Peters, E. "Direct electrorefining of chalcocite", J. Electroanal. Chem., 118, 1981, pp 345-364.

233. MacKinnon, D.J. "Fluidised-bed anodic dissolution of chalcocite", Hydrometallurgy, 1, 1976, pp 241-257.

234. MacKinnon, D.J. "Fluidised-bed anodic dissolution of covellite", Hydrometallurgy, 2, 1976, pp 65-76.

235. Cole, S.H. "Electrochemical investigation of the dissolution of copper sulphide", Ph.D. Thesis, University of Columbia, Ohio, USA, 1972.

236. Ilangovan, S., Nagaraj, D.R. and Vasu, K.I. "Electrometallurgy of chalcopyrite: copper powder from slurry anodes", J. Electrochem. Soc., India, 24(4), 1975, pp 195-199.

237. Oki, T., and Ono, S. "On the anodic dissolution in direct electrolysis of chalcopyrite concentrate", J. Min. & Met. Inst. Japan, 83, 1967, pp 1159-62.

238. Majima, H. "How oxidation affects selective flotation of complex sulphide ores", Can. Metall. Quarterly, 8, 1969, pp 269-273.

239. Hiskey, J.B., and Wadsworth, M.E. "Galvanic conversion of chalcopyrite", Metall. Trans., SME-AIME, 6B, 1975, pp 183-190.

240. Berry, V.K., Murr, L.E., and Hiskey, J.B. "Galvanic interaction between chalcopyrite and pyrite during leaching of low-grade waste", Hydrometallurgy, 3, 1977, pp 309-326.

241. Peters, E., and Majima, H., Paper presented at the Annual Meeting of the AIME, New York, 1968.

242. Jeffrey, P.G., and Hutchison, D. "Chemical Methods of Rock Analysis", 3rd edition, Pergamon Press, Oxford, 1981.

243. Zussman, J. "X-ray diffraction", Physical Methods in Determinative Mineralogy, (ed. J. Zussman), Academic Press, New York and London, 1977, pp 391-473.

244. J.C.P.D.S. "Powder Diffraction File and Index", Data Books (1-5, 6-10, 11-15, 16-18, 18-22, 22-24), Data Cards (25-30). Search Manuals ("Hanawault" and "Fink" methods). "Selected Powder Diffraction Data for Minerals", (Data Book and Search Manuals). Joint Committee on Powder Diffraction Standards, 1601 Park Lane, Swarthmore, Pa. 19081, USA.

245. Hewins, R.H. "The petrology of some marginal mafic rocks along the north range of the Sudbury irruptive", Ph.D. Thesis, University of Toronto, Canada, 1971.

246. Abel, M.K., Buchan, R., Coats, C.J.A., and Penstone, M.E. "Copper mineralisation in the footwall complex, Strathcona Mine, Sudbury, Ontario", Canadian Mineralogist, 17, 1979, pp 275-285.

247. Battey, M.H. "Mineralogy for Students", Longman, London and New York, 1972, 323 pp.

248. Long, J.V.P. "Electron probe microanalysis" Physical Methods in Determinative Mineralogy, (ed. J. Zussman), Academic Press, New York and London, 1977, pp 273-341.

249. Estep-Barnes, P.A. "Infrared spectroscopy" Physical Methods in Determinative Mineralogy, (ed J. Zussman), Academic Press, New York and London, 1977, pp 529-603.

250. Lyon, R.J.P. "Minerals in the Infrared. A Critical Bibliography", Stanford Research Institute, California, 1963, 63 pp.

251. Rao, C.N.R. "Chemical Applications of Infrared Spectroscopy", Academic Press, New York, 1963, p 370.

252. Gillieson, A.H. "Infrared spectroscopy of some sulphide minerals", Bol. Geol. Min., 80, 1969, p 429.

253. Nyqvist, R.A., and Kagel, R.O. "Infrared Spectra of Inorganic Compounds (3800-45 cm^{-1})", Academic Press, New York, 1971, 495 pp.

254. Liese, H.C. "Infrared absorption (435 to 250 cm^{-1}) and ultraviolet emission analyses of selected sulphides and sulfosalts: a correlative study", Appl. Spectroscopy, 28, 1974, pp 135-138.

255. Poling, G.W., and Leja, J. "Infrared study of xanthate adsorption on vacuum deposited films of lead sulphide and metallic copper under conditions of controlled oxidation", J. Phys. Chem., 67, 1963, pp 2126-26.

256. Lowe, K. "The instrumentation developed for electrochemical studies of the leaching of uranium dioxide", South African National Institute for Metallurgy, Report No 1509, 1973, 17 pp.

257. Berger, H.H. "Contact resistance and contact resistivity", J. Electrochem. Soc., 119(4), 1972, pp 507-514.

258. Read, A.D. and Kitchener, J.A., Society of Chemical Industry, Monograph No 25, 1967, pp 300-313.

259. Meites, L. and Meites, T., "Removal of oxygen from gas streams", Anal. Chem., 20, 1948, pp 984-985.

260. Potter, E.C. "The microdetermination of dissolved oxygen in water. I. The nature of the problem", J. Applied Chem., 7, 1957, pp 285-297.

261. Potter, E.C. "The microdetermination of dissolved oxygen in water. II. The design of water-sampling vessels", J. Applied Chem., 7, 1957, pp 297-308.

262. Potter, E.C., and White, J.F. "The microdetermination of dissolved oxygen in water. III. Titrimetric determination of iodine in submicrogramme amounts", J. Applied Chem., 7, 1957, pp 309-317.

263. Potter, E.C., and White, J.F. "The microdetermination of dissolved oxygen in water. IV. Test of Winkler's reaction to below 0.001 ppm of dissolved oxygen", J. Applied Chem., 7, 1957, pp 317-328.

264. Gilroy, D., and Mayne, J.E.O. "The de-aeration of aqueous solutions", J. Applied Chem., 12, 1962, pp 382-384.

265. Bar-lev, A. "Semiconductors and Electronic Devices", Prentice-Hall, London, 1979.

266. Adams, D.M. "Inorganic Solids", John Wiley & Sons, London, 1974, 336 pp.

267. King, E.G., Mah, A.D., and Pankratz, L.B. "Thermodynamic properties of copper and its inorganic compounds", INCRA Series on the Metallurgy of Copper, 1973.

268. Latimer, W.M. "Oxidation Potentials", 2nd Ed., Prentice Hall, Englewood Cliffs, New Jersey, 1961.

269. Mellor, J.W., "A Comprehensive Treatise on Inorganic and Theoretical Chemistry: Vol XIV. Fe (Part 3) - Cobalt", Longmans, Green and Co., New York, 1935.

270. Albery, W.J. and Hitchman, M.L. "Ring-Disc Electrodes", Clarendon Press, Oxford, 1971.

271. Frumkin, A.N., and Nekrasov, L.I. Dokl. Akad. Nawk. SSSR, 126, 1959, p 115.

272. Paul, R.L., Nicol, M.J., Diggle, J.W., and Saunders, A.P. "The electrochemical behaviour of galena PbS", Electrochim. Acta, 23(7), 1978, pp 625-633, and pp 635-639.

273. McKubre, M.C.H., and Macdonald, D.D. The rotating cylinder-collector electrode (RCCE)", J. Electrochem. Soc., 127(3), 1980, pp 632-641.

274. Milazzo, G., and Caroli, S. "Tables of Standard Electrode Potentials", Project of the IUPAC Electrochemistry Commission, Wiley-Interscience, New York, 1978.

275. Sawyer, D.T., Roberts, J.L. "Experimental Electrochemistry for Chemists", Wiley-Interscience, London, 1974.

276. Schwarz, W.M., and Shain, I., Anal. Chem., 35, 1963, p 1770.

277. Savage, S., and Kelsall, G. "A study of the coupled electrochemical oxidation of cyanide and cathodic zinc electrodeposition", Mineral Res. Engng. Research Progress Report No 1, Royal School of Mines, Imperial College, January 1981.

278. Srinivasan, S., and Gileadi, E. "The potential-sweep method: A theoretical analysis", Electrochim. Acta, 11, 1966, pp 321-335.

279. Brion, D. "Etude par spectroscopie de photoelectrons de la degradation superficielle de FeS_2, $CuFeS_2$, ZnS et PbS a l'air et dans l'eau", Applications of Surface Science, 5, 1980, pp 133-152.

280. Goddard, N.J. "Using the "C" programming language for interface control", to be published in Laboratory Microcomputer.

281. Chander, S., and Fuerstenau, D.W. "Effect of potential on the flotation and wetting behaviour of chalcocite and copper" Trans. Society of Mining Engineers, AIME, 258, 1975, pp 284-5.

282. Walker, G.W., Stout, J.V., and Richardson, P.E. "Electrochemical flotation of sulphides: Reactions of chalcocite in aqueous solution", Int. J. Miner. Proc., 12, 1984, pp 55-72.

283. Bhaskar Raju, G., and Khangronkar, P.R. "Electro-flotation of chalcopyrite fines", Int. J. Miner. Proc., 9, 1982, pp 133-143.

284. Chander, S., and Fuerstenau, D.W. "On the floatability of sulphide minerals with thiol collectors: the chalcocite-diethyldithiophosphate system", XIth. Int. Min. Proc. Cong., Rome Italy, 1975.

285. Gardner, J.R., and Woods, R. "The use of particulate bed electrodes for the electrochemical investigation of metal and sulphide flotation", Aust. J. Chem., 26, 1973, pp 1635-44.

286. Natarajan, K.A., and Iwasaki, I. "Behaviour of platinum electrodes as redox potential indicators in some systems of metallurgical interest", Trans. Society of Mining Engineers, AIME, 247, 1970, pp 317-324.

287. Natarajan, K.A. and Iwasaki, I. "E_h-pH response of noble metal and sulphide mineral electrodes", Trans. Society of Mining Engineers, AIME, 252, 1972, pp 437-9.

288. Natarajan, K.A. and Iwasaki, I. "Effect of poisoning of platinum electrodes on E_h measurements", ", Trans. Society of Mining Engineers, AIME, 254, 1972, pp 22-28.

289. Natarajan, K.A. and Iwasaki, I. "Practical implications of E_h measurements in sulphide flotation circuits", Trans. Society of Mining Engineers, AIME, 254, 1973, pp 323-328.

290. Natarajan, K.A. and Iwasaki, I. "Significance of mixed potentials in E_h measurements with platinum electrodes", Trans. Society of Mining Engineers, AIME, 255, 1974, pp 82-86.

291. Graham, R., and Heathcote, C.R. "The effect of the oxidation state of the pulp on the selective flotation of chalcopyrite from Black Mountain ore", Proceedings XIIth CMMI Congress, Johannesburg, S. Afr. Inst. Min. Metall., 1982, pp 867-877.

292. Johnson, N.W., Jowett, A., and Heyes, G.W. "Oxidation-reduction effects in galena flotation: observations on Pb-Zn-Fe sulphides separation", Trans. IMM, C91, 1982, pp 32-37.

293. Woodcock, J.T., and Jones, M.H. "Oxygen concentrations, redox potentials, xanthate residuals, and other parameters in flotation plant pulps", Proceedings IXth CMMI Congress, London, Inst. Min. Metall., 1969, pp 439-468.

294. Vogel, A. "A Textbook of Quantitative Inorganic Analysis", Longmans, Green, London, 1966, 371 pp.

295. Williams, W.J. "Handbook of Anion Determination", Butterworths, London, 1976, 630 pp.

296. Power, G.P. "The electrochemistry of the Nickel Sulphides. I. NiS", Aust. J. Chem., 34, 1981, pp 2287-96.

297. Schiffrin, D.J. "Rotating electrodes", Advanced Instrumental Methods in Electrode Kinetics, University of Southampton Lecture Course Notes, 1982.

298. Schlicting, H. "Boundary Layer Theory", McGraw Hill, New York, 1960.

299. Heyes, G.W., and Trahar, W.J., "The flotation of pyrite and pyrrhotite in the absence of conventional collectors", Electrochemistry in Minerals and Metallurgical Processing, Meeting of Electrochem. Soc. Symposium, Cincinnatti, 1984, pp 219-232.

300. Kapusta, S., Viehbeck, A., Wilhelm, S.M., and Hackerman, N. "The anodic oxidation of sulphide on platinum electrodes", J. Electroanal. Chem., 153, 1983, pp 157-174.

301. Loucka, T. "Adsorption and oxidation of sulphur and of sulphur dioxide at the platinum electrode", J. Electroanal. Chem., 31, 1971, pp 319-332.

302. Richardson, P.E., and Maust, E.E. "Surface stoichiometry of galena in aqueous electrolytes and its effect on xanthate interactions". Flotation A.M. Gaudin Memorial Volume, 1, American Institute of Mining, Metallurgical and Petroleum Engineers Inc., 1976, pp 364-392.

303. Bouchard, R.J. "The preparation of single crystals of FeS_2, CoS_2 and NiS_2 pyrites by chlorine transport", J. Cryst. Growth, 2, 1968, pp 40-44.

304. Ghali, E., and Dandapani, B. "Anodic behaviour of lead sulphide in hydrochloric acid", J. Appl. Electrochem., 10, 1980, pp 335-344.

305. Bard, A.J., and Faulkner, L.R. "Electrochemical Methods. Fundamentals and Applications", John Wiley & Sons, New York, 1980, 718 pp.

306. Loucka, T. "Adsorption and oxidation of organic compounds on a platinum electrode partly covered by adsorbed sulphur" J. Electronal. Chem., 36, 1972, pp 355-367.

307. Tributsch, H., and Gerischer, H. "The oxidation and self-heating of metal sulphides as an electrochemical corrosion phenomenon", J. Appl. Biotechnol., 26, 1976, pp 747-761.

308. Tributsch, H. and Bennett, J.C. "Semiconductor-electrochemical aspects of bacterial leaching. I. Oxidation of metal sulphides with large energy gaps", J. Chem. Tech. Biotechnol., 31, 1981, pp 565-577.

309. Jaegermann, W. and Tributsch, H. "Photoelectrochemical reactions of FeS_2 (pyrite) with H_2O and reducing agents", J. Appl. Electrochem., 13, 1983, pp 743-750.

310. Tributsch, H., and Bennett, J.C. "Electrochemistry and photochemistry of MoS_2 Layer Crystals. I.", J. Electroanal. Chem., 81, 1977, pp 97-111.

311. Schumb, C.W., Satterfield, C.N., and Wenthworth, R.L. "Hydrogen Peroxide", Reinhold Publ. Corp., 1955.

312. Gerischer, H., and Wallem-Mattes, I., Z. Phys. Chem. Neue Folge, 64, 1969, p 187.

313. Bolts, J., and Wrighton, M., J. Phys. Chem., 80, 1976, p 2641.

314. Gerischer, H., in "Physical Chemistry", Vol. IXA, (eds Eyring, H., Hunderson, D., and Jost, W.) Academic Press, 1970, Chapter 5.

315. Davidson, R.S., and Willsher, C.J. "The electrochemical behaviour of light-sensitive electrodes formed by coating a platinum mesh with a powdered semiconductor", J. Appl. Electrochem., 12, 1982, pp 517-523.

316. Page, P.W. "Conversion of solar to electrical energy using lead (II) chromate as a photochemical electrode", Internal Report, Leicester University, 1979.

317. Armstrong, R.D., and Edmondson, K. "The impedance of metals in the passive and transpassive regions", Electrochim. Acta, 18, (1973), pp 937-943.

318. Fuerstenau, M.C., Kuhn, M.C., and Elgillani, C.A. "The role of dixanthogen in xanthate flotation of pyrite", Trans. AIME, 241, (1968), pp 148-156.

319. Majima, H., and Takeda, M. "Electrochemical studies of the xanthate-dixanthogen system on pyrite", Trans. AIME, 241, (1968), pp 431-436.

320. Usul, A.H., and Tolun, R. "Electrochemical study of the pyrite-oxygen-xanthate system", Int. J. Miner. Proc., 1, (1974), pp 135-140.

321. Sheikh, N., and Leja, J. "Mössbauer spectroscopy of iron xanthates", Separation Science, 12(5), 1977; pp 529-540.

322. Page, P.W., Unpublished work.

323. Lamy, C., Leger, J.M., Clavilier, J., and Parsons, R., "Structural effects in electrocatalysis. A comparative study of the oxidation of CO, HCOOH and CH_3OH on single crystal Pt electrodes", J. Electroanal. Chem., 150, 1983, pp 71-77.

324. Robie, R.A., Bethke, P.M., and Beardsley, K.M. "X-ray crystallographic data, molar volumes and densities of minerals and related substances", US Geological Survey Bulletin, 1248.

325. Hamilton, I.C., and Woods, R. "An investigation of the deposition and reactions of sulphur on gold electrodes", J. Applied Electrochem., 13, 1983, pp 783-794.

326. Lyons, D., and Nickless, G. "The lower oxy-acids of sulphur", Inorganic Sulphur Chemistry, (ed. Nickless, G.), Elsevier, Holland, 1968.

327. Wierse, D.G., Lohrengel, M.M., and Schultze, J.W. "Electrochemical properties of sulphur adsorbed on gold electrodes", J. Electroanal. Chem., 92, 1978, pp 121-131.

328. Schwarzenbach, G., and Fisher, A., Helv. Chem. Acta., 169, 1960, pp 1365-90.

329. La Mer, V.K., and Kenyon, A.S., J. Colloid Sci., 2, 1947, pp 257-264.

330. Hamilton, I.C., and Woods, R. "A voltammetric study of the surface oxidation of sulphide minerals", Electrochemistry in Minerals and Metallurgical Processing, Electrochem. Soc. Symposium, Cincinnatti, 1984, pp 259-285.

331. Hodgson, M., and Agar, G.E. "An electrochemical investigation into the natural flotability of pyrrhotite", Electrochemistry in Minerals and Metallurgical Processing, Electrochem. Soc. Symposium, Cincinnatti, 1984, pp 185-201.

332. Hoare, J.P. "The Electrochemistry of Oxygen". Int. Sci. Publishers, 1968.

333. Trahar, W.J., and Heyes, G.W., "The flotation of pyrite and pyrrhotite in the absence of conventional collectors", Electrochemistry in Minerals and Metallurgical Processing, Electrochem. Soc. Symposium, Cincinnatti, 1984, pp 185-201.

334. Liebhafsky, H.A., and Cairns, E.J. "Fuel Cells and Fuel Batteries", John Wiley, 1967, 370 pp.

335. Pillai, K.C., and Bockris, J. O'M "A quantitative examination of the mixed potential mechanism in mineral flotation", J. Electrochem. Soc., 131, 1984, pp 558-578.

336. Mouhandess, M.T., Chassagneux, F., and Vittori, O. "Electrochemical behaviour of α-Fe_2O_3 using carbon paste electrodes: influence of particle size", J. Electroanal. Chem., 131, 1982, pp 367-371.

337. Sharara, Z.Z., Vittori, O., and Durand, B. "Electrochemical reduction of alkaline iron (III) oxides, $LiFeO_2$ and $NaFeO_2$, using carbon paste electrodes", Electrochim. Acta, 29(12), 1984, pp 1685-88.

338. Mouhandess, M.T., Chassagneux, F., Durand, B., Sharara, Z.Z. and Vittori, O. "Some advantages of carbon paste electrodes in the morphological study of finely divided iron oxides", J. of Mat. Sci., 20, 1985, pp 3289-3299.

339. Lecuire, Jean-Marie, Evrard, O. "Reduction electrochimique des oxydes de fer. Confrontation des caracteristiques electrochimiques et christallographiques", J. Electronal. Chem., 78, 1977, pp 331-339.

340. Bockris, J. O'M., and Reddy, A.K.N. "Modern Electrochemistry", Volume 2, Plenum/Rosetta, New York, 1973.

341. Heyes, G.W. and Trahar, W.J. "The natural flotability of chalcopyrite", Int. J. Min. Proc., 4, 1977, pp 317-344.

342. Stewart, B.V., and Finkelstein, N.P. "A preliminary investigation of the flotation of copper activated sphalerite without the use of collectors", Nat. Inst. Metall. Repub. S. Afr., Rept. No. 1587, 1973, 13 pp.

343. Lepetic, V.M. "Flotation of chalcopyrite without collectors after dry autogeneous grinding", CIM Bulletin, June 1974, pp 71-77.

344. Finkelstein, N.P., Allison, S.A., Lovell, V.M., and Stewart, B.V. "Natural and induced hydrophobicity in sulphide mineral systems", Am. Inst. Chem. Eng. Sym. Ser., 71, (150), 1975, pp 165-175.

345. Fuerstenau, M.C., and Sabacky, B.J. "On the natural flotability of sulphides", Int. J. Min. Proc., 8, 1981, pp 79-84.

346. Boyce, J.H., Venter, W.J., and Adam, J. "Beneficiation practice at the Tsumeb concentrator", Proc. World Symp. Min. Metal. Lead and Zinc, AIME, New York, N.Y., 1970, p 542.

347. Sen, P.K., Ray, K.C., and Ray, S. "Role of semiconductor properties of galena in flotation", Trans. Indian Inst. Met., 28, 1975, pp 337-342.

348. Rey, M., and Formanek, V. "Some factors affecting selectivity in differential flotation of lead-zinc ores", Proc. 5th Int. Miner. Process. Congr., I.M.M., London 1960, pp 343-354.

349. Allison, S.A. "The role of sulphur in the flotation of sulphide minerals", Nat. Inst. Metall. Repub. S. Afr., Rept. No. 1597, 1974, 14 pp.

350. Yoon, R.H. "Collectorless flotation of chalcopyrite and sphalerite ores by using sodium sulphide", Int. J. Miner. Process., 8, 1981, pp 31-48.

351. Luttrell, G.H., and Yoon, R.H. "The collectorless flotation of chalcopyrite ores using sodium sulphide", Int. J. Miner. Process., 13, 1984, pp 271-283.

352. Trahar, W.J. "A laboratory study of the influence of sodium sulphide and oxygen on the collectorless flotation of chalcopyrite", Int. J. Miner. Process., 11, 1983, pp 57-74.

353. House, C.I. "The electrogeneration of reductants and the aqueous reduction of minerals", Ph.D. Thesis, Dept. of Mineral Resources Engineering, Imperial College, University of London, 1985.

354. Bouet, J. et Brenet, J.P. "Contribution at l'etude du diagramme tension/pH du fer en mileux sulfures", Corrosion Science, 3, 1963, pp 51-63.

355. Bard, A.J., Parsons, R., Jordon, J. "Standard Potentials in Aqueous Solution", Dekker, N.Y., 1985.

356. Schoeffel, E.W. Brit. Patent 779,506, 1957.

357. Sander, U.H.F., Fischer, H., Roth, U., and Kola, R. "Sulphur, Sulphur Dioxide and Sulphuric Acid", (ed. More, A.I.), The British Sulphur Corp., 1982.

358. Meyer, B. "Sulphur, Energy and Environment", Elsevier, 1977.

359. Okuno, I., Morris, J.C., and Haines, W.E., Anal. Chem., 32, 1960, p 1007.

360. Marjanovic-Krayovan, V., and Turina, S., Kem. Ind. (Zagreb), 10, 1961, p 159.

361. Thompson, I., Ph.D. Thesis, University of London, 1987.

362. Fleischmann, M. and Thirsk, H.R. "Advances in Electrochem. and Electrochem. Engng.", (ed. Delahay, D.), 3, Interscience, N.Y., 1963.

363. Tipman, R.N. "The reactions of potassium ethyl xanthate in aqueous solution", Ph.D. Thesis, University of British Columbia, 1970.

364. Peverelli, K.J., and Van Leeuwen, H.P. "A kinetic study of the silver/silver iodide film electrode in aqueous solution using the coulostatic pulse technique. Part I. Properties in 0.1 M KNO_3 solution", J. Electroanal. Chem., 110, (1980), pp 119-135.

365. Kakovskii, I.A., and Areshkevitch, V.M., VII Int. Miner. Proc. Cong., Leningrad, USSR, 2, 1968, pp 300-314.

366. Misawa, T. "The thermodynamic considerations for Fe-H_2O system at 25°C", Corrosion Science, 13, 1973, pp 659-676.

367. Wagman, D.D., N.B.S. Technical Note 270-4, Washington D.C., 1969.

368. Craig, J.R., Amer. Mineral., 56, 1971, pp 1303-1311.

369. Sajek, B., Ph.D. Thesis, University of London, 1980.

370. Kostuch, J.A., Ph.D. Thesis, University of London, (1986), to be published.

371. Taylor, P., Rummery, T.E., and Owen, D.G., J. Inorg. Nucl. Chem., 4, 1979, p 1683.

372. Barton, P.B., and Skinner, B.S. "Geochemistry of Hydrothermal Ore Deposits", (ed. Barnes, H.L.), Hott, Rinehart and Winston, N.Y., 1967, pp 236-333.

373. Young, P.A., Amdel Bulletin, 3, 1967, pp 1-19.

374. Melling, J. "Potential-pH diagrams for the Fe-Ni-S-H_2O system at 25°C", Unpublished report, Warren Spring Laboratory, 1980.

375. Guzman, R.S.S., Vilche, J.R., and Arvia, A.J. "Rate processes related to the hydrated nickel hydroxide electrode in alkaline solutions", J. Electrochem. Soc., 125(10), 1976, pp 1578-1587.

376. Goodenough, M., Ph.D. Thesis, University of London, 1987.

377. Woods, R., Yoon, R.H., and Young, C.A. "E_h-pH diagrams for stable and metastable phases in the copper-sulphur-water system", Int. J. Miner. Proc., 20, 1987, pp 109-120.

378. Buckley, A.N., Hamilton, I.C., and Woods, R. "Investigation of the surface oxidation of bornite by linear potential sweep voltammetry and x-ray photoelectron spectroscopy", J. Applied Electrochem., 14, 1984, pp 63-74.

379. Buckley, A.N., Woods, R. "An x-ray photoelectron spectroscopic investigation of the surface oxidation of sulphide minerals", in Electrochemistry in Minerals and Metallurgical Processing, Electrochem. Soc. Symposium, Cinncinnatti, 1984, pp 286-288.

380. Buckley, A.N., Hamilton, I.C., and Woods, R., in Flotation of Sulphide Minerals,, (ed. Forssberg, K.S.E.), Developments in Mineal Processing, 6, Elsevier, 1980.

381. Buckley, A.N., Woods, R., in Interfacial Phenomena in Mineral Processing, Engineering Foundation, (eds. Yarar, B., and Spottiswood, D.J.), New York, 1982, pp 3-17.

382. Hunter, R.J. "Zeta Potential in Colloid Science - Principles and Applications", Academic Press, N.Y., 1981, 385 pp.

383. Parks, G.A., and de Bruyn, P.L. "The zero point of charge of oxides", J. Phys. Chem., 66, 1962, pp 967-973.

384. Healy, T.W., and Moignard, M.S. "A review of electrokinetic studies of metal sulphides", Flotation, A.M. Gaudin Memorial Volume, 1, American Institute of Mining Metallurgical, and Petroleum Engineers Inc., 1976, pp 275-297.

385. Parks, G.A. "The isoelectric points of solid oxides, solid hydroxides, and aqueous hydroxo complex systems", Chem. Rev., 65, 1965, pp 177-198.

APPENDIX I: Thermodynamics Equations (A separate "pull-out" copy of the equations listed below is enclosed at the end of the thesis).

(1) Pyrite (FeS_2), Pyrrhotite (FeS, ($Fe_{1-x}S$)) and Sulphur

(a) $FeS_2 = Fe^{2+} + 2S = 2e$

$$E = 0.423 + 0.0295 \log[Fe^{2+}]$$

(b) $FeS_2 + 8H_2O = Fe^{2+} + 2SO_4^{2-} + 16H^+ + 14e$

$$E = 0.367 - 0.067\ pH + 0.008 \log[SO_4^{2-}] + 0.004 \log[Fe^{2+}]$$

(c) $FeS_2 + 3H_2O = Fe(OH)_3 + 2S + 3H^+ + 3e$

$$E = 0.64 - 0.0591\ pH$$

(d) $FeS_2 + 11H_2O = Fe(OH)_3 + 2SO_4^{2-} + 19H^+ + 15e$

$$E = 0.412 - 0.0749\ pH + 0.0078 \log[SO_4^{2-}]$$

(e) $FeS_2 = Fe^{3+} + 2S + 3e$

$$E = 0.546 + 0.0196 \log[Fe^{3+}]$$

(f) $FeS_2 + 8H_2O = Fe^{3+} + 2SO_4^{2-} + 16H^+ + 15e$

$$E = 0.394 - 0.063\ pH + 0.008 \log[2SO_4^{2-}] + 0.004 \log[Fe^{3+}]$$

(g) $Fe^{2+} = Fe^{3+} + e$

$$E = 0.771 + 0.0591 \log[Fe^{3+}] - 0.0591 \log[Fe^{2+}]$$

(h) $Fe^{2+} + H_2O = Fe(OH)^{2+} + H^+ + e$

$$E = 0.914 = 0.0591\ pH + 0.0591 \log[FeOH^{2+}] - 0.0591 \log[Fe^{2+}]$$

(i) $Fe^{2+} + 2H_2O = Fe(OH)_2^+ + 2H^+ + e$

$$E = 1.191 - 0.1182\ pH + 0.0591 \log[Fe(OH)_2^+] - 0.0591 \log[Fe^{2+}]$$

(j) $Fe^{2+} + 3H_2O = Fe(OH)_3 + 3H^+ + e$

$$E = 1.056 - 0.177\ pH - 0.0591 \log[Fe^{2+}]$$

(k) $Fe(OH)_2 + H_2O = Fe(OH)_3 + H^+ + e$

$$E = 0.271 - 0.0591\ pH$$

(l) $FeS + 3H_2O = Fe(OH)_3 + S + 3H^+ + 3e$

$E = 0.398 - 0.0591\ pH$

(m) $FeS + 2H_2O = FeOOH + S + 3H^+ + 3e$

$E = 0.290 - 0.0591\ pH$

(n) $Fe(OH)_2 + FeOOH + H^+ + e$

$E = -0.071 - 0.0591\ pH$

(o) $Fe^{2+} + 2H_2O = FeOOH + 3H^+ + e$

$E = -0.715 - 0.177\ pH - 0.0591 \log[Fe^{2+}]$

(p) $Fe^{2+} + 2H_2S = FeS_2 + 4H^+ + 2e$

$E = -0.106 - 0.0591\ pH - 0.0295 \log[H_2S] - 0.0295 \log[Fe^{2+}]$

(q) $FeS + H_2S = FeS_2 + 2H^+ + 2e$

$E = -0.216 - 0.0591\ pH - 0.0295 \log[H_2S]$

(r) $FeS + HS^- = FeS_2 + H^+ + 2e$

$E = -0.423 - 0.0295\ pH - 0.0295 \log[HS^-]$

(s) $Fe = Fe^{2+} + 2e$

$E = -0.440 + 0.0295 \log[Fe^{2+}]$

(t) $Fe + H_2S = FeS + 2H^+ + 2e$

$E = -0.364 - 0.0591\ pH - 0.0295 \log[H_2S]$

(u) $Fe + HS^- = FeS + H^+ + 2e$

$E = -0.571 - 0.0295\ pH - 0.0295 \log[HS^-]$

(v) $H_2S = S + 2H^+ + 2e$

$E = 0.141 - 0.059\ pH - 0.0295 \log[H_2S]$

(w) $HS^- = S + H^+ + 2e$

$E = 0.065 - 0.0295\ pH - 0.0295 \log[HS^-]$

(x) $S + H^+ + e = HS$

(y) $HS + e = HS^-$

(z) $HS^- + H^+ = H_2S \qquad \log \frac{[HS^-]}{[H_2S]} = -7.00 + pH$

(a_1) $2S^{2-}_{lattice} = S_2^{2-}_{lattice} + 2e$

(b_1) $Fe + 2HS^- = FeS_2 + 2H^+ + 4e$

$E = -0.497 - 0.0295\ pH - 0.0295 \log[HS^-]$

(c_1) $Fe + 2H_2S = FeS_2 + 4H^+ + 4e$

$E = -0.290 - 0.0591\ pH - 0.0295 \log[H_2S]$

(d_1) $H_2 = 2H^+ + 2e$

$E = 0.000 - 0.0591\ pH - 0.0295 \log p_{H2}$

(e_1) $FeS = Fe^{2+} + S + 2e$

$E = -0.078 + 0.0295 \log [Fe^{2+}]$

(f_1) $FeS + 4H_2O = Fe^{2+} + SO_4^{2-} + 8H^+ + 8e$

$E = 0.0287 - 0.0591\ pH + 0.007 \log [SO_4^{2-}] + 0.007 \log[Fe^{2+}]$

(g_1) $FeS + 7H_2O = Fe(OH)_3 + SO_4^{2-} + 11H^+ + 9e$

$E = 0.372 - 0.072\ pH + 0.007 \log[SO_4^{2-}]$

(h_1) $FeS = Fe^{3+} + S + 3e$

$E = 0.301 + 0.020 \log [Fe^{3+}]$

(i_1) $FeS + 4H_2O = Fe^{3+} + SO_4^{2-} + 8H^+ + 9e$

$E = 0.114 - 0.053\ pH + 0.007 \log [SO_4^{2-}] + 0.007 \log [Fe^{3+}]$

(j_1) $FeS + 2H^+ = Fe^{2+} + H_2S$

$\log [Fe^{2+}] = 2.582 - 2\ pH - \log [H_2S]$

(k_1) $FeS_2 + 2H^+ = Fe^{2+} + H_2S + S$

$\log [Fe^{2+}] = -9.531 - 2\ pH - \log [H_2S]$

(l_1) $FeS = (1-x)Fe^{2+} + Fe_xS + 2(1-x)e$

(m_1) $Fe_xS = xFeS + (1-x)S \quad (x < 1)$

(n_1) $Fe_xS + 2(1-x)H^+ + 2(1-x)e = xFeS + (1-x)H_2S$

(o_1) $Fe^{3+} + 3H_2O = Fe(OH)_3 + 3H^+$

$\log [Fe^{3+}] = 4.84 - 3\ pH$

(p_1) $Fe^{2+} + 2H_2O = Fe(OH)_2 + 2H^+$

$\log [Fe^{2+}] = 13.29 - 2\ pH$

(q_1) $Fe + 2H_2O = Fe(OH)_2 + 2H^+ + 2e$

$E = -0.047 - 0.0591\ pH$

(r_1) $Fe(CN)_6^{4-} = Fe(CN)_6^{3-} + e$

$E = 0.46 + 0.0591 \log[Fe(CN)_6^{3-}] - 0.0591 \log[Fe(CN)_6^{4-}]$

(s_1) $FeS_2 + 2H_2O = FeOOH + 2S + 3H^+ + 3e$

$E = 0.521 - 0.0591\ pH$

(t_1) $FeS_2 + 10H_2O = FeOOH + 2SO_4^{2-} + 19H^+ + 15e$

$E = 0.390 - 0.0749\ pH + 0.0078 \log [SO_4^{2-}]$

(u_1) $Fe^{3+} + 2H_2O - FeOOH + 3H^+$

$\log [Fe^{3+}] = -1.85 - 3\ pH$

(v_1) $FeOH^{2+} + 2H_2O = Fe(OH)_3 + 2H^+$

$\log[FeOH^{2+}] = 2.41 - 2\ pH$

(w_1) $Fe(OH)_2^+ + H_2O = Fe(OH)_3 + H^+$

$\log [Fe(OH)_2^+] = -2.28 - pH$

(x_1) $FeOH^{2+} + H_2O = FeOOH + 2H^+$

$\log [FeOH^{2+}] = -3.37 - 2\ pH$

(y_1) $Fe(OH)_2^+ = FeOOH + H^+$

$\log [Fe(OH)_2^+] = -8.06 - pH$

(z_1) $FeS + 2H_2O = FeOOH + S + 3H^+ + 3e$

$E = 0.290 - 0.591\ pH$

(ab_1) $FeS + HS^- = FeS_2 + H^+ + 2e$

$E = -0.423 - 0.0295\ pH - 0.0295 \log [HS^-]$

(ac_1) $FeS + S^{2-} + 2e$

$E = -0.837 - 0.0295 \log [S^{2-}]$

(ad_1) $Fe + HS^- = FeS + H^+ + 2e$

$E = -0.571 - 0.0295\ pH - 0.0295 \log ([HS^-]$

(ae_1) $Fe + S^{2-} = FeS + 2e$

$E = -0.985 - 0.0295 \log [S^{2-}]$

(af_1) $Fe = Fe^{2+} + 2e$

$E = -0.440 + 0.0295 \log[Fe^{2+}]$

(ag_1) $S_2^{2-}{}_{(lattice)} = 2S_{(ads)} + 2e$

(ah_1) $H_2O + 2h^+ \rightleftharpoons (O)_{ads} + 2H^+$

(ai_1) $2H_2O + 2h^+ \rightleftharpoons 2(OH)_{ads} + 2H^+$

(aj_1) $(O)_{ads} + (O)_{ads} \rightleftharpoons (O_2)_{ads}$

(ak_1) $(O)_{ads} + H_2O + h^+{}_{solid} \rightleftharpoons (O_2H)_{ads} + H^+$

(al_1) $2(OH)_{ads} + h^+{}_{solid} \rightleftharpoons (O_2H)_{ads} + H^+$

(am_1) $FeS_2 + 2H_2O \rightleftharpoons FeS_2(HO_2)_{ads} + 3H^+ + 3e$

(an_1) $FeS_2 + 3H_2O = Fe(OH)_3 + 3H^+ + 0.5S_4^{2-} + 2e$

(ao_1) $FeS_2 + 3H_2O = Fe(OH)_3 + 3H^+ + 0.4S_5^{2-} + 2.2e$

(ap_1) $xS^{2-} = S_x^{2-} + (2x-2)e$ when $2 \leq x \leq 5$

(aq_1) $S_x^{2-} = xS + 2e$ (where $2 \leq x \leq 5$)

(ar_1) $S_2^{2-} = 2S + 2e$

(as_1) $S^{2-} = S_{solid} + 2e$

(at_1) $S + 4H_2O = SO_4^{2-} + 8H^+ + 6e$

$E = 0.357 - 0.0788\ pH + 0.0098\ \log[SO_4^{2-}]$

(au_1) $(OH)_{ads} + (O)_{ads} \rightleftharpoons (O_2H)_{ads}$

(av_1) $(O_2H)_{ads} + e_{solid}^- \rightleftharpoons O_2H^-_{ads}$

(aw_1) $xHS^- = S_x^{2-} + xH^+ + (2x-2)e$

(ax_1) $2S_{(ads)} + H_2O_2 = S_2(OH)_2$

(ay_1) $xS + H^+ + 2e = HS_x^-$

(az_1) $HS_x^- + (2x-1)H^+ + 2xe = xH_2S$

(ba_1) $FeS + 6H_2O = FeOOH + SO_4^{2-} + 11H^+ + 9e$

$E = 0.341 - 0.072\ pH + 0.007\ \log[SO_4^{2-}]$

(bb_1) $SO_3^{2-} + S = S_2O_3^{2-}$

(bc_1) $4S + 6OH^- = S_2O_3^{2-} + 2S^{2-} + 3H_2O$

(bd_1) $12S + 6OH^- = S_2O_3^{2-} + 2S_5^{2-} + 3H_2O$

(be_1) $Fe_{1-x}S = (1-2x)Fe^{2+} + FeS_2 + 2(1-2x)e$

2. Pentlandite ($(Fe,Ni)_9S_8$), Violarite ($FeNi_2S_4$) and Millerite (NiS)

(a_2) $(Fe,Ni)_9S_8 = 4.5Ni^{2+} + 4.5Fe^{2+} + 8S + 18e$

$E = 0.067 + 0.015\ \log[Ni^{2+}] + 0.015\ \log[Fe^{2+}]$

(b_2) $(Fe,Ni)_9S_8 = 4.5Ni^{2+} + 4.5Fe^{3+} + 8S + 22.5e$

$E = 0.208 + 0.0118 \log[Ni^{2+}] + 0.118 \log [Fe^{3+}]$

(c_2) $(Fe,Ni)_9S_8 + 32H_2O = 4.5Fe^{2+} + 4.5Ni^{2+} + 8SO_4^{2-} + 64H^+ + 66e$

$E = 0.278 - 0.0573\ pH + 0.004 \log[Fe^{2+}] + 0.004 \log[Ni^{2+}] + 0.072 \log[SO_4^{2-}]$

(d_2) $(Fe,Ni)_9S_8 + 32H_2O = 4.5Ni^{2+} + 4.5Fe^{3+} + 8SO_4^{2-} + 64H^+ + 70.5e$

$E = 0.310 - 0.054\ pH + 0.0038 \log[Ni^{2+}] + 0.0038 \log[Fe^{3+}] + 0.0067 \log[SO_4^{2-}]$

(e_2) $(Fe,Ni)_9S_8 + 13.5H_2O = 4.5Ni^{2+} + 4.5Fe(OH)_3 + 8S + 13.5H^+ + 22.5e$

$E = 0.265 - 0.0355\ pH + 0.0118 \log[Ni^{2+}]$

(f_2) $(Fe,Ni)_9S_8 + 45.5H_2O = 4.5Ni^{2+} + 4.5Fe(OH)_3 + 8SO_4^{2-} + 77.5H^+ + 70.5e$

$E = 0.0328 - 0.065\ pH - 0.0038 \log[Ni^{2+}] + 0.0067 \log[SO_4^{2-}]$

(g_2) $(Fe,Ni)_9S_8 + 22.5H_2O = 4.5Ni(OH)_2 + 4.5Fe(OH)_3 + 8S + 22.5H^+ + 22.5e$

$E = 0.409 - 0.059\ pH$

(h_2) $(Fe,Ni)_9S_8 + 54.5H_2O = 4.5Ni(OH)_2 + 4.5Fe(OH)_3 + 8SO_4^{2-} + 86.5H^+ + 70.5e$

$E = 0.374 - 0.0725\ pH + 0.0067 \log[SO_4^{2-}]$

(i_2) $(Fe,Ni)_9S_8 + 22.5H_2O + 4.5NiOOH + 4.5Fe(OH)_3 + 8S + 27H^+ + 27e$

$E = 0.513 - 0.0591\ pH$

(j_2) $(Fe,Ni)_9S_8 + 54.5H_2O = 4.5NiOOH + 4.5Fe(OH)_3 + 8SO_4^{2-} + 91H^+ + 75e$

$E = 0.413 - 0.0716\ pH + 0.006 \log[SO_4^{2-}]$

(k_2) $(Fe,Ni)_9S_8 + 10.5H_2O = FeNi_2S_4 + 3.5Fe(OH)_3 + 2.5Ni^{2+} + 4S + 10.5H^+ + 15.5e$

$E = 0.225 - 0.040\ pH + 0.0095 \log[Ni^{2+}]$

(m_2) $(Fe,Ni)_9S_8 + 26.5H_2O = FeNi_2S_4 + 3.5Fe(OH)_3 + 2.5Ni^{2+} + 4SO_4^{2-} + 42.5H^+ + 39.5e$

$E = 0.305 - 0.064\ pH + 0.0037 \log[Ni^{2+}] + 0.006 \log[SO_4^{2-}]$

(n_2) $Ni(OH)_2 = NiOOH + H^+ + e$

$E = 1.033 - 0.0591\ pH$

(o_2) $Ni + 2H_2O = Ni(OH)_2 + 2H^+ + 2e$

$E = 0.110 - 0.0591\ pH$

(p_2) $NiOOH + 2H_2O = NiO_2.2H_2O + H^+ + e$

$E = 1.434 - 0.0591\ pH$

(q_2) $(Fe,Ni)_9S_8 = 2FeNi_2S_4 + 2.5Fe^{2+} + 0.5Ni^{2+} + 6e$

$E = -0.273 + 0.0246\ \log[Fe^{2+}] + 0.0049\ \log[Ni^{2+}]$

(r_2) $(Fe,Ni)_9S_8 = 2FeNi_2S_4 + 2.5Fe^{3+} + 0.5Ni^{2+} + 8.5e$

$E = 0.034 + 0.017\ \log[Fe^{3+}] + 0.0035\ \log[Ni^{2+}]$

(s_2) $(Fe,Ni)_9S_8 + 7.5H_2O = 2FeNi_2S_4 + 2.5Fe(OH)_3 + 0.5Ni^{2+} + 7.5H^+ + 8.5e$

$E = 0.118 - 0.052\ pH + 0.0035\ \log[Ni^{2+}]$

(t_2) $(Fe,Ni)_9S_8 + 13.5H_2O = 4.5NiS + 4.5Fe(OH)_3 + 3.5S + 13.5H^+ + 13.5e$

$E = 0.334 - 0.0591\ pH$

(u_2) $(Fe,Ni)_9S_8 + 27.5H_2O = 4.5NiS + 4.5Fe(OH)_3 + 3.5SO_4^{2-} + 41.5H^+ + 27.5e$

$E = 0.436 - 0.089\ pH + 0.0075\ \log[SO_4^{2-}]$

(v_2) $(Fe,Ni)_9S_8 + 13.5H_2O + 3.5Ni^{2+} = 8NiS + 4.5Fe(OH)_3 + 13.5H^+ + 6.5e$

$E = 0.519 - 0.123\ pH - 0.032\ \log[Ni^{2+}]$

(w_2) $(Fe,Ni)_9S_8 + 3H_2O = 2NiS + 2S + Fe(OH)_3 + 3H^+ + 3e$

$E = 0.649 - 0.0591\ pH$

(x_2) $FeNi_2S_4 + 11H_2O = 2NiS + 2SO_4^{2-} + Fe(OH)_3 + 19H^+ + 15e$

$E = 0.415 - 0.0749\ pH + 0.0079\ \log[SO_4^{2-}]$

(y_2) $NiS = Ni^{2+} + S + 2e$

$E = 0.133 + 0.0295\ \log[Ni^{2+}]$

(z_2) $NiS + 4H_2O = Ni^{2+} + SO_4^{2-} + 8H^+ + 8e$

$E = 0.308 - 0.0591\ pH + 0.0074\ \log[Ni^{2+}] + 0.0074\ \log[SO_4^{2-}]$

(a_3) $Ni^{2+} + 2H_2O = Ni(OH)_2 + 2H^+$

$\log\ [Ni^{2+}] = 12.18 - 2\ pH$

(b_3) $NiS + 2H_2O = Ni(OH)_2 + S + 2H^+ + 2e$

$E = 0.494 - 0.0591\ pH$

(c_3) $NiS + 6H_2O = Ni(OH)_2 + SO_4^{2-} + 10H^+ = 8e$

$E = 0.391 - 0.073\ pH + 0.0074\ \log[SO_4^{2-}]$

(d_3) $Fe^{2+} + 2Ni^{2+} + 4H_2S = FeNi_2S_4 + 8H^+ + 2e$

$E = -0.341 - 0.237\ pH - 0.1183\ \log[H_2S] - 0.0592\ \log[Ni^{2+}]$
$- 0.0296\ \log[Fe^{2+}]$

(e_3) $Fe + 2Ni + 4H_2S = FeNi_2S_4 + 8H^+ + 8e$

$E = -0.271 - 0.0591\ pH - 0.0295\ \log[H_2S]$

(f_3) $Fe + 2Ni + 4HS^- = FeNi_2S_4 + 4H^+ + 8e$

$E = -0.478 - 0.0295\ pH - 0.0295\ \log[HS^-]$

(g_3) $Ni + H_2S = NiS + 2H^+ + 2e$

$E = -0.242 - 0.0591\ pH - 0.0295\ \log[H_2S]$

(h_3) $Ni + HS^- = NiS + H^+ + 2e$

$E = -0.449 - 0.0295\ pH - 0.0295\ \log[HS^-]$

(i_3) $(Fe,Ni)_9S_8 + 16H^+ = 4.5Ni^{2+} + 4.5Fe^{2+} + 8H_2S + 2e$

$E = -0.529 + 0.4733\ pH + 0.133\ \log[Ni^{2+}] + 0.133\ \log[Fe^{2+}]$
$+ 0.236\ \log[H_2S]$

(j_3) $4.5Fe + 4.5Ni + 8H_2S = (Fe,Ni)_9S_8 + 16H^+ + 16e$

$E = -0.322 - 0.059\ pH - 0.0295\ \log[H_2S]$

(k_3) $4.5Fe + 4.5Ni + 8HS^- = (Fe,Ni)_9S_8 + 8H^+ + 16e$

$E = -0.529 - 0.0295\ pH - 0.0295\ \log[HS^-]$

(l_3) $NiS + 2H^+ = H_2S + Ni^{2+}$

$$\log[Ni^{2+}] = 0.2712 - 2\ pH - \log[H_2S]$$

(m_3) $FeNi_2S_4 + 3H_2O = Fe(OH)_3 + 2Ni^{2+} + 4S + 3H^+ + 7e$

$$E = 0.354 - 0.0253\ pH + 0.0169\ \log[Ni^{2+}]$$

(n_3) $FeNi_2S_4 + 19H_2O = Fe(OH)_3 + 2Ni^{2+} + 4SO_4^{2-} + 35H^+ + 31e$

$$E = 0.357 - 0.067\ pH + 0.0038\ \log[Ni^{2+}] + 0.0076\ \log[SO_4^{2-}]$$

(o_3) $FeNi_2S_4 + 7H_2O = Fe(OH)_3 + 2Ni(OH)_2 + 4S + 7H^+ + 7e$

$$E = 0.560 - 0.0591\ pH$$

(p_3) $FeNi_2S_4 + 23H_2O = Fe(OH)_3 + 2Ni(OH)_2 + 4SO_4^{2-} + 39H^+ + 31e$

$$E = 0.403 - 0.0744\ pH + 0.0076\ \log[SO_4^{2-}]$$

(q_3) $FeNi_2S_4 = Fe^{3+} + 2Ni^{2+} + 4S + 7e$

$$E = 0.314 + 0.0084\ \log[Fe^{3+}]\ 0.017\ \log[Ni^{2+}]$$

(r_3) $FeNi_2S_4 + 16H_2O = Fe^{3+} + 2Ni^{2+} + 4SO_4^{2-} + 32H^+ + 31e$

$$E = 0.347 - 0.061\ pH + 0.0019\ \log[Fe^{3+}] + 0.0038\ \log[Ni^{2+}] + 0.0076\ \log[SO_4^{2-}]$$

3. <u>Chalcopyrite ($CuFeS_2$), Bornite (Cu_5FeS_4), Chalcocite (Cu_2S) and Covellite (CuS)</u>

(a_4) $CuFeS_2 = CuS + Fe^{2+} + S + 2e$

$$E = 0.232 + 0.0295\ \log[Fe^{2+}]$$

(b_4) $CuFeS_2 = CuS + Fe^{3+} + S + 3e$

$$E = 0.412 + 0.0197\ \log[Fe^{3+}]$$

(c_4) $CuFeS_2 = Cu^{2+} + Fe^{2+} + 2S + 4e$

$$E = 0.411 + 0.0148\ \log[Cu^{2+}]$$

(d_4) $CuFeS_2 = Cu^{2+} + Fe^{3+} + 2S + 5e$

$$E = 0.483 + 0.0118\ \log[Cu^{2+}] + 0.0118\ \log[Fe^{3+}]$$

(e_4) $CuFeS_2 + 8H_2O = Cu^{2+} + Fe^{2+} + 2SO_4^{2-} + 16H^+ + 16e$

$$E = 0.371 - 0.0591\ pH + 0.004\ \log[Cu^{2+}] + 0.004\ \log[Fe^{2+}] + 0.0074\ \log[SO_4^{2-}]$$

(f_4) $CuFeS_2 + 8H_2O = Cu^{2+} + Fe^{3+} + 2SO_4^{2-} + 16H^+ + 17e$

$$E = 0.394 - 0.0556\ pH + 0.0035\ \log[Cu^{2+}] + 0.0035\ \log[Fe^{3+}] + 0.007\ \log[SO_4^{2-}]$$

(g_4) $CuFeS_2 = CuFe_{0.2}S_{0.8} + 0.8Fe^{2+} + 1.2S + 1.6e$

$$E = 0.260 + 0.0295\ \log[Fe^{2+}]$$

(h_4) $CuFeS_2 = CuFe_{0.2}S_{0.8} + 0.8Fe^{3+} + 1.2S + 2.4e$

$$E = 0.403 + 0.0197\ \log[Fe^{3+}]$$

(i_4) $CuFe_{0.2}S_{0.8} = 0.5Cu_2S + 0.2Fe^{2+} + 0.3S + 0.4e$

$$E = 0.273 + 0.0295\ \log[Fe^{2+}]$$

(j_4) $CuFe_{0.2}S_{0.8} = 0.5Cu_2S + 0.2Fe^{3+} + 0.3S + 0.6e$

$$E = 0.439 + 0.020\ \log[Fe^{3+}]$$

(k_4) $0.5Cu_2S = 0.5CuS + 0.5Cu^{2+} + e$

$$E = 0.530 + 0.0295\ \log[Cu^{2+}]$$

(l_4) $CuFeS_2 + 3H_2O = Cu^{2+} + Fe(OH)_3 + 2S + 3H^+ + 5e$

$$E = 0.540 - 0.0355\ pH + 0.0118\ \log[Cu^{2+}]$$

(m_4) $CuFeS_2 + 11H_2O = Cu^{2+} + Fe(OH)_3 + 2SO_4^{2-} + 19H^+ + 17e$

$$E = 0.411 - 0.0661\ pH + 0.007\ \log\ [SO_4^{2-}] + 0.003\ \log[Cu^{2+}]$$

(n_4) $CuFeS_2 = Fe^{2+} + 0.5\ Cu^{2+} + 0.5CuS + 1.5S + 3e$

$$E = 0.437 + 0.01\ \log[Cu^{2+}] + 0.02\ \log[Fe^{2+}]$$

(o_4) $CuFeS_2 = Fe^{3+} + 0.5CuS + 0.5Cu^{2+}\ 1.5S + 4e$

$$E = 0.456 + 0.0074\ \log[Cu^{2+}] + 0.0148\ \log[Fe^{3+}]$$

(p_4) $CuFeS_2 + 3H_2O = CuS + Fe(OH)_3 + S + 3H^+ + 3e$

$$E = 0.507 - 0.059\ pH$$

(r_4) $CuS = Cu^{2+} + S + 2e$

$E = 0.590 + 0.0295 \log[Cu^{2+}]$

(s_4) $CuFeS_2 + 2.4H_2O = CuFe_{0.2}S_{0.8} + 0.8Fe(OH)_3 + 1.2S + 2.4H^+ + 2.4e$

$E = 0.525 - 0.0591\ pH$

(t_4) $CuFeS_2 + 7.2H_2O = CuFe_{0.2}S_{0.8} + 0.8Fe(OH)_3 + 1.2SO_4^{2-} + 12H^+ + 9.6e$

$E = 0.399 - 0.0739\ pH + 0.0074 \log[SO_4^{2-}]$

(u_4) $CuFe_{0.2}S_{0.8} + 0.6H_2O = 0.5Cu_2S + 0.2Fe(OH)_3 + 0.6H^+ + 0.3S + 0.6e$

$E = 0.534 - 0.0591\ pH$

(v_4) $CuFe_{0.2}S_{0.8} + 1.8H_2O = 0.5Cu_2S + 0.2Fe(OH)_3 + 0.3SO_4^{2-} + 3H^+ + 2.4e$

$E = 0.401 - 0.0739\ pH + 0.0074 \log[SO_4^{2-}]$

(w_4) $Cu_2S + 2H_2O = CuS + Cu(OH)_2 + 2H^+ + 2e$

$E = 0.802 - 0.0591\ pH$

(x_4) $CuS + 2H_2O = Cu(OH)_2 + 2H^+ + S + 2e$

$E = 0.863 - 0.0591\ pH$

(y_4) $CuS + 6H_2O = Cu(OH)_2 + SO_4^{2-} + 10H^+ + 8e$

$E = 0.484 - 0.0739\ pH + 0.0074 \log [SO_4^{2-}]$

(z_4) $Cu^{2+} + 2H_2O = Cu(OH)_2 + 2H^+$

$\log[Cu^{2+}] = 9.2 - 2\ pH$

(a_5) $CuFeS_2 + 5H_2O = Cu(OH)_2 + Fe(OH)_3 + 2S + 5H^+ + 5e$

$E = 0.649 - 0.0591\ pH$

(b_5) $CuFeS_2 + 13H_2O = Cu(OH)_2 + Fe(OH)_3 + 2SO_4^{2-} + 21H^+ + 17e$

$E = 0.443 - 0.073\ pH + 0.007 \log[SO_4^{2-}]$

(c_5) $Cu_2O + 3H_2O = 2Cu(OH)_2 + 2H^+ + 2e$

$E = 0.748 - 0.0591\ pH$

(d_5) $2CuS + 2H^+ + 2e = Cu_2S + H_2S$

$E = 0.082 - 0.0591\ pH - 0.0295\ \log[H_2S]$

(e_5) $2CuS + H^+ + 2e = Cu_2S + HS^-$

$E = -0.110 - 0.0295\ pH - 0.0295\ \log[HS^-]$

(f_5) $2Cu + H_2O = Cu_2O + 2H^+ + 2e$

$E = 0.472 - 0.059\ pH$

(g_5) $CuFeS_2 + 2.4H^+ + 0.8e = CuFe_{0.2}S_{0.8} + 0.8Fe^{2+} + 1.2H_2S$

$E = -0.29 - 0.177\ pH - 0.0591\ \log[Fe^{2+}] - 0.088\ \log[H_2S]$

(h_5) $2CuFeS_2 + 6H^+ + 2e = Cu_2S + 2Fe^{2+} + 3H_2S$

$E = -0.22 - 0.177\ pH - 0.0591\ \log[Fe^{2+}] - 0.089\ \log[H_2S]$

(i_5) $CuFeS_2 + 4H^+ + 2e = Cu + Fe^{2+} + 2H_2S$

$E = -0.260 - 0.118\ pH - 0.0591\ \log[H_2S] - 0.0295\ \log[Fe^{2+}]$

(j_5) $CuFeS_2 + 2H^+ = CuS + Fe^{2+} + H_2S$

$\log[Fe^{2+}] = 3.05 + \log[H_2S] + 2\ pH$

(k_5) $CuFeS_2 + 4H^+ + 4e = Cu + Fe + 2H_2S$

$E = -0.321 - 0.0591\ pH - 0.0295\ \log[H_2S]$

(l_5) $CuFeS_2 = (1-x)Cu^{2+} + (1-y)Fe^{2+} + Cu_xFe_yS_2 + 4(2-x-y)e$

(m_5) $Cu_xFe_yS_2 = (x+y)CuFeS_2 + (2-x-y)S \quad (x < 1,\ y < 1)$

(n_5) $2CuFeS_2 + 7H_2O = Cu_2O + 2Fe(OH)_3 + 4S + 8H^+ + 8e$

$E = 0.626 - 0.0591\ pH$

(o_5) $2CuFeS_2 + 23H_2O = Cu_2O + 2Fe(OH)_3 + 4SO_4^{2-} + 40H^+ + 32e$

$E = 0.425 - 0.0739\ pH + 0.0074\ \log[SO_4^{2-}]$

(p_5) $CuFeS_2 + (4-2z)H^+ + (2x+2y+2z)e = Cu_xFe_yS_z + (1-x)Cu^{2+} + (1-y)Fe^{2+} + (2-z)H_2S$

(q_5) $Cu^{+} = Cu^{2+} + e$

$$E = 0.153 + 0.0591 \log[Cu^{2+}] - 0.0591 \log[Cu^{+}]$$

(r_5) $Cu = Cu^{+} + e$

$$E = 0.520 + 0.0591 \log[Cu^{2+}]$$

(s_5) $Cu = Cu^{2+} + 2e$

$$E = 0.337 + 0.0295 \log[Cu^{2+}]$$

(t_5) $Cu + H_2S = Cu_2S + 2H^{+} + 2e$

$$E = -0.305 - 0.0591\ pH - 0.0295 \log[H_2S]$$

(u_5) $Cu^{2+} + 2Cl^{-} + e = CuCl_2^{-}$

$$E = 0.409 + 0.118 \log[Cl^{-}] + 0.0591 \log[Cu^{2+}] - 0.0591 \log[CuCl^{2-}]$$

(v_5) $CuCl_2^{-} + e = Cu + 2Cl^{-}$

$$E = -0.036 - 0.118 \log[Cl^{-}] + 0.0591 \log[CuCl_2^{-}]$$

(w_5) $5Cu_2S = 5Cu_{1.8}S + Cu^{2+} + 2e$

(x_5) $3Cu_{1.8}S = 4Cu_{1.1}S + Cu^{2+} + 2e$

(y_5) $10Cu_{1.1}S = 10CuS + Cu^{2+} + 2e$

(z_5) $Cu^{+}Fe^{3+}(S^{2-})_2 = Cu^{+}_{(1-x)}Cu^{+}_{x}Fe^{3+}_{(1-x)}(S^{2-})_2 + xFe^{2+}_{(aq)}$

(za_5) $Cu^{+}Fe^{3+}(S^{2-})_2 + 3xH^{+} + xe = Cu^{+}Fe^{3+}_{(1-x)}H^{+}_{3x}(S^{2-})_2 + xFe^{2+}_{(aq)}$

(zb_5) $Cu_2O = 3H_2O = 2HCuO_2^{-} + 4H^{+} + 2e$

$$E = 1.783 - 0.118\ pH + 0.0591 \log[HCuO_2^{-}]$$

(zc_5) $Cu_2S + H_2O = Cu_2O + S + 2H^{+} + 2e$

$$E = 0.917 - 0.0591\ pH$$

(zd_5) $Cu(OH)_2 = HCuO_2^{-} + H^{+}$

$$\log [HCuO_2^{-}] = -17.52 + pH$$

(ze_5) $Cu + 2H_2O = Cu(OH)_2 + 2H^+ + 2e$

$E = 0.609 - 0.591\ pH$

(zf_5) $CuFeS_2 + 3H_2O = CuS_2 + Fe(OH)_3 + CuS_2 + 3H^+ + 3e$

(zg_5) $CuFeS_2 + 3H_2O = 0.5Cu_2S + 1.5S + Fe(OH)_3 + 3H^+ + 3e$

$E = 0.527 - 0.0591\ pH$

(zh_5) $CuS_2 + 2H_2O = Cu(OH)_2 + 2S + 2H^+ + 2e$

(zi_5) $CuFeS_2 + 3Cu^{2+} + 4e = 2Cu_2S + Fe^{2+}$

$E = 0.709 + 0.044\ \log[Cu^{2+}] + 0.015\ \log[Fe^{2+}]$

(4) Platinum (Pt)

(a_6) $PtS_x + 2xH^+ + 2xe = Pt(H_2S)_x$

(b_6) $PtS_2 + 2H_2O = PtO_2 + 2S + 4H^+ + 4e$

(c_6) $PtS_2 + 8H_2O = PtO_2 + 2SO_4^{2-} + 16H^+ + 16e$

(d_6) $Pt(H_2S)_x = PtS_x + 2xH^+ + 2xe$

(e_6) $Pt + H_2S = PtS + 2H^+ + 2e$

$E = -0.3 - 0.0591\ pH - 0.0295\ \log[H_2S]$

(f_6) $PtS + H_2S = PtS_2 + 2H^+ + 2e$

$E = -0.01 - 0.0591\ pH - 0.0295\ \log[H_2S]$

(g_6) $Pt + H_2O = PtO + 2H^+ + 2e$

$E = 0.980 - 0.0591\ pH$

(h_6) $PtO + H_2O = PtO_2 + 2H^+ + 2e$

$E = 1.045 - 0.0591\ pH$

(i_6) $PtS_2 + H_2O = PtO + 2S + 2H^+ + 2e$

(j_6) $Pt\text{—}(S_2O_3)_{ads} + 5H_2O = 2SO_4^{2-} + 10H^+ + Pt + 8e$

(k_6) $2H_2O = O_2 + 4H^+ + 4e$

$E = 1.229 - 0.0591\ pH - 0.0148 \log p_{O_2}$

APPENDIX II : E_h-pH and Activity-pH Diagrams

1. $S-H_2O$ System

Table II(i) Free energies of formation data for species in the $S-H_2O$ System at 298 K (Source : ref. (355))

Species	ΔG_f°/kJ mol^{-1}	Species	ΔG_f°/kJ mol^{-1}
H_2O	-237.178	SO_2	300.708
H^+	0	H_2SO_3	-537.90
OH^-	-157.293	HSO_3^-	-527.81
$H_2S_{(g)}$	-33.56	SO_3^{2-}	-486.6
H_2S	-27.87	$S_2O_5^{2-}$	-791
HS^-	12.05	$S_2O_6^{2-}$	-966
S^{2-}	86.31	$SO_{3(g)}$	-371.08
S_2^{2-}	79.5	H_2SO_4	-744.63
S_3^{2-}	73.6	HSO_4	-756.01
S_4^{2-}	69.0	SO_4^{2-}	-744.63
S_5^{2-}	65.7	$S_2O_8^{2-}$	-1100.4
S_2O_3	-518.8	$H_2S_2O_8$	-1100.4
$S_5O_6^{2-}$	-956.0	S (orthorhombic)	0
$S_4O_6^{2-}$	-1022.2		
$S_2O_4^{2-}$	-600.4		
$HS_2O_4^-$	-614.6		
$H_2S_2O_4$	-616.7		
$S_3O_6^{2-}$	-958		
$SO_{2(g)}$	-300.194		

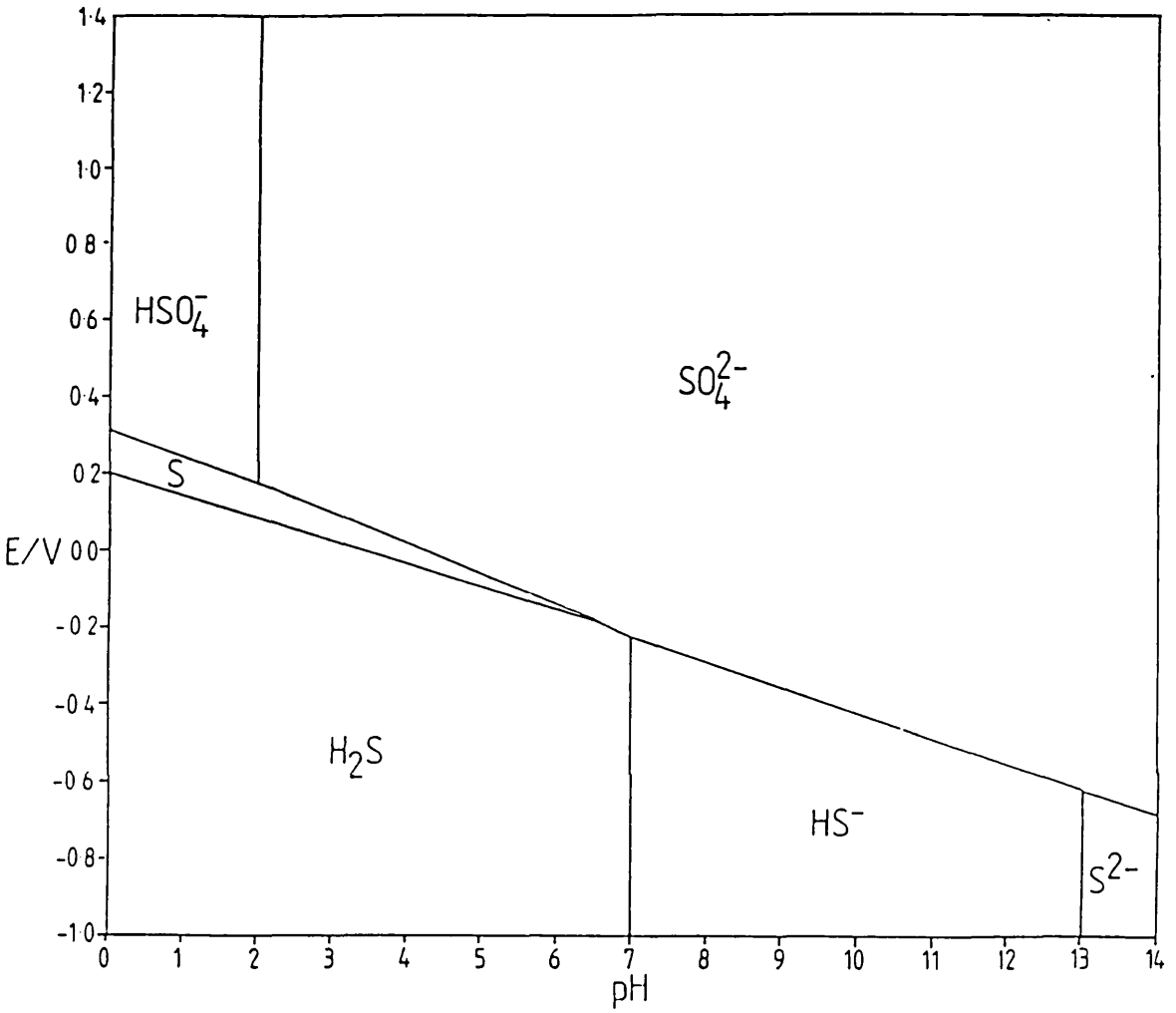


Fig II(i) Potential-pH diagram for the S-H_2O system at 298 K with a dissolved sulphur activity of 10^{-3}[361].

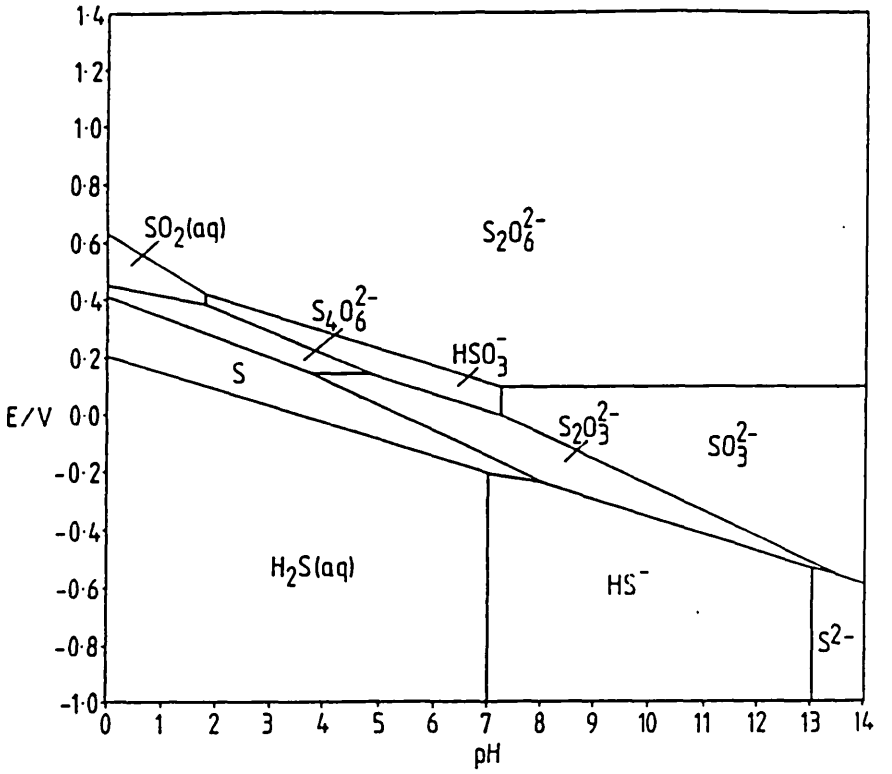


Fig II(ii) Potential-pH diagram for the S-H_2O system at 298 K with a dissolved sulphur activity of $10^{-3(361)}$. Sulphur (VI) species excluded.

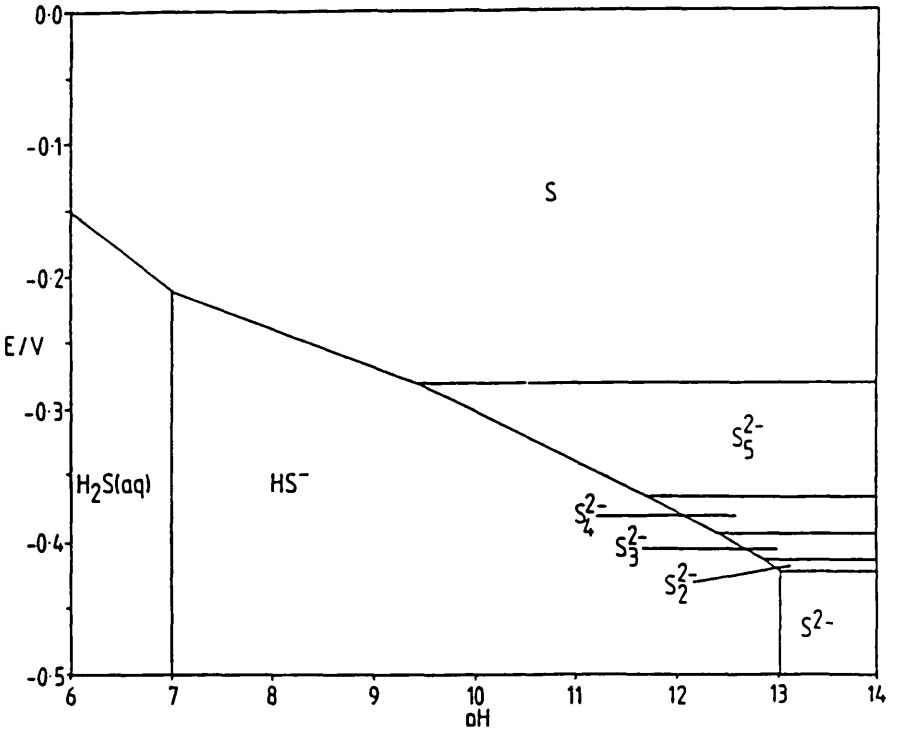


Fig II(iii) Potential-pH diagram for the S-H_2O system at 298 K with a dissolved sulphur activity of $10^{-3(361)}$. All sulphur-oxygen compounds excluded.

2. $Fe-H_2O$ and $Fe-S-H_2O$ Systems

Table II(ii) Free Energies of Formation Data for Species in the $Fe-H_2O$ and $Fe-S-H_2O$ Systems at 298 K (Source : Ref. (355)).

Species	ΔG_f°/kJ mol^{-1}	Species	ΔG_f°/kJ mol^{-1}
FeS_2 (pyrite)	-166.9	H_2O	-237.178
Fe_7S_8 (s-rich pyrrhotite)	-748.5	H^+	0
FeS (iron-rich α-pyrrhotite)	-100.4	OH^-	-157.293
Fe^{2+}	-91.5	H_2S	-27.87
Fe^{3+}	-16.7	HS^-	12.05
FeO_2^{2-}	-301	S^{2-}	86.31
$Fe_2O_{3(s)}$	-743.608	SO_4^{2-}	-744.63
$Fe_3O_{4(s)}$	-0105.359	HSO_4^-	-756.01
$FeOH^+$	-277.4	S (orthorhombic)	0
$FeOH^{2+}$	-229.41		
$Fe(OH)_2^+$	-438.1		
$FeOOH_{(s)}$	-490		
$HFeO_2^-$	-376.4		
$Fe(OH)_{2(s)}$	-486.6		
$Fe(OH)_2$	-441.0		
$Fe(OH)_{3(s)}$	-705.535		
$Fe(OH)_3$	-660		
$Fe(OH)_3^-$	-605.1		
$Fe(OH)_4^-$	-842.2		
$Fe(OH)_4^{2-}$	-769.9		
$Fe_2(OH)_2^{2+}$	-47.27		
Fe	0		

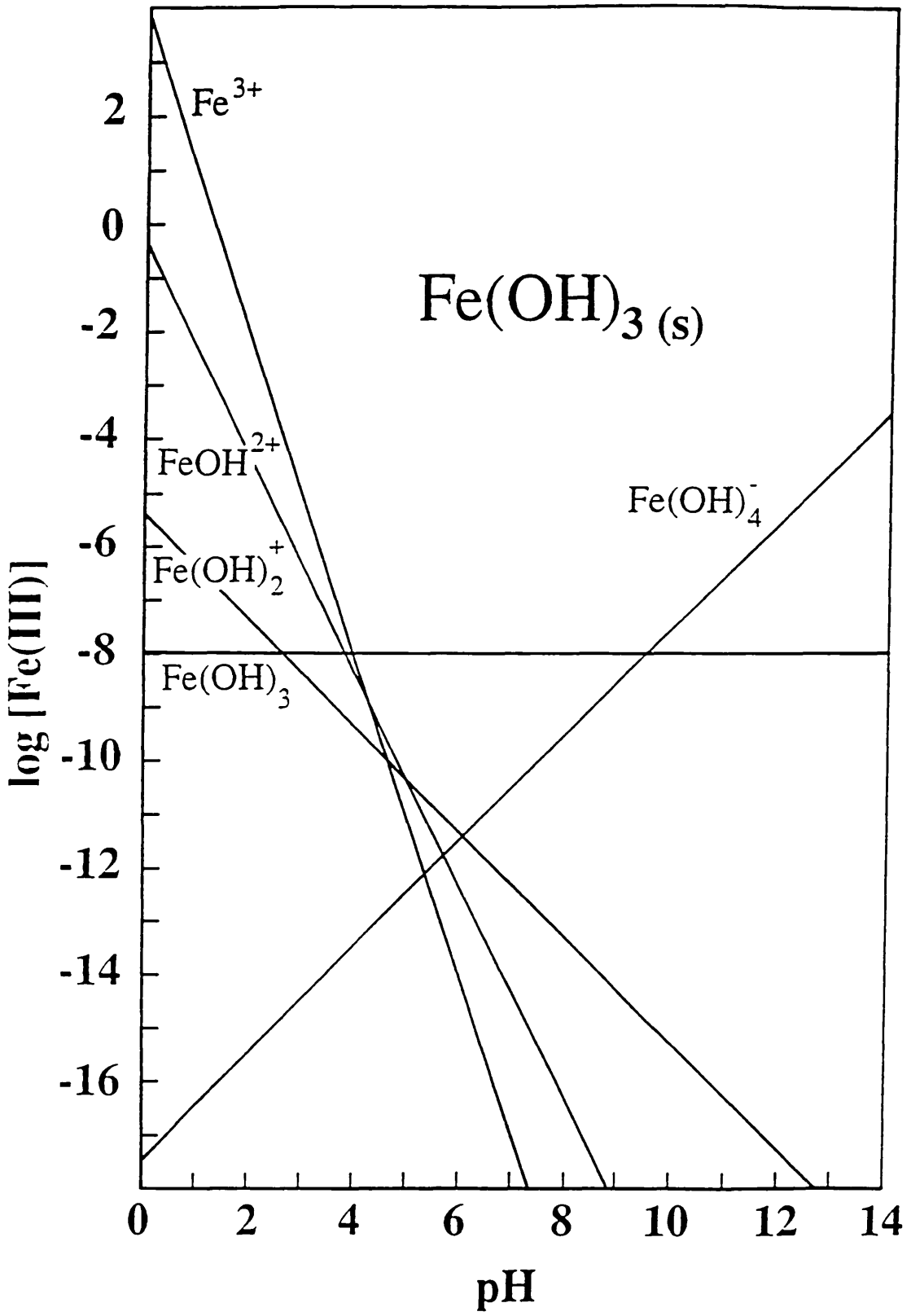


Fig II(iv) Activity-pH diagram at 298 K for Fe(III) species in equilibrium with $Fe(OH)_{3(s)}$.

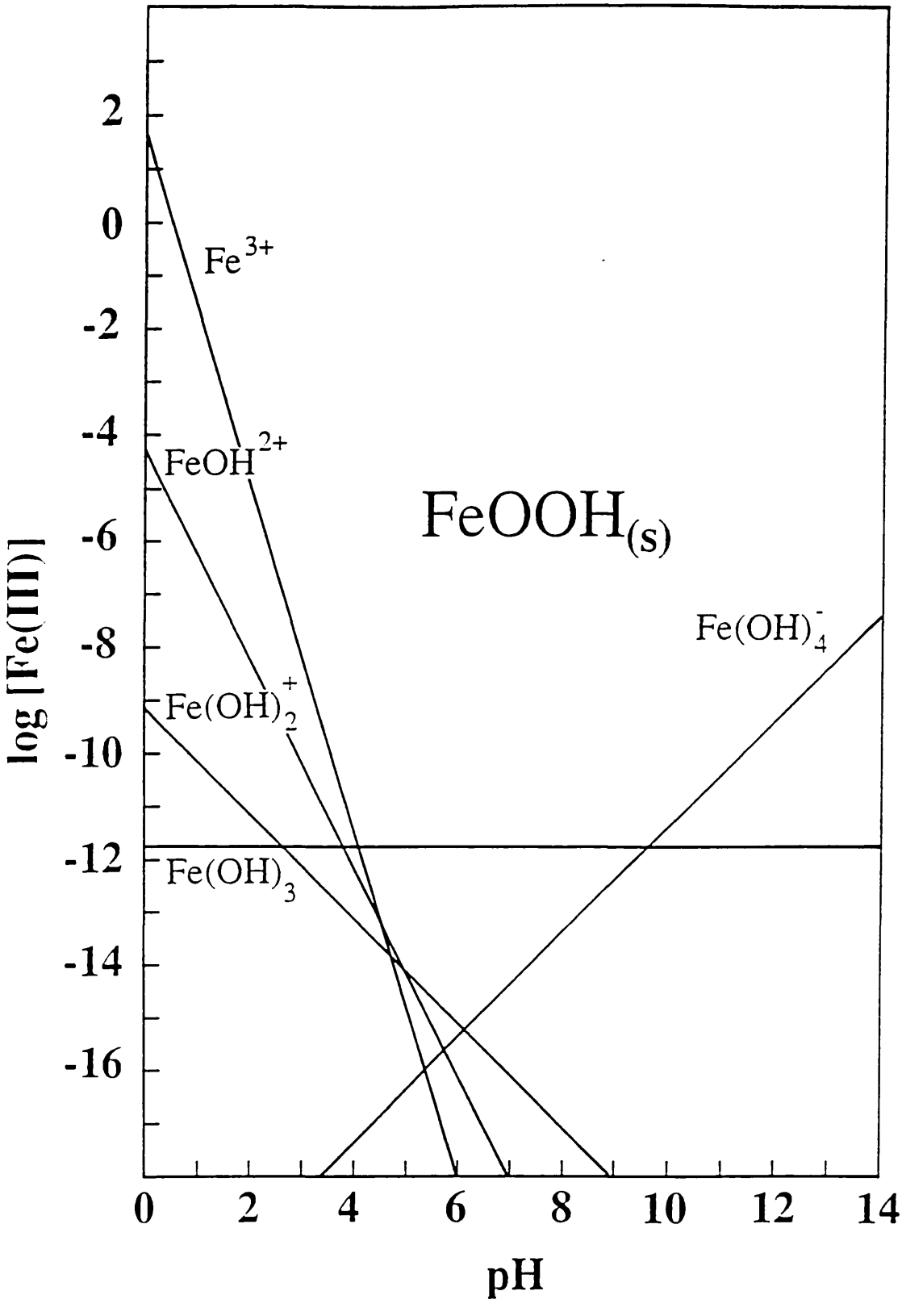


Fig II(v) Activity-pH diagram at 298 K for Fe(III) species in equilibrium with $Fe(OOH)_{(s)}$.

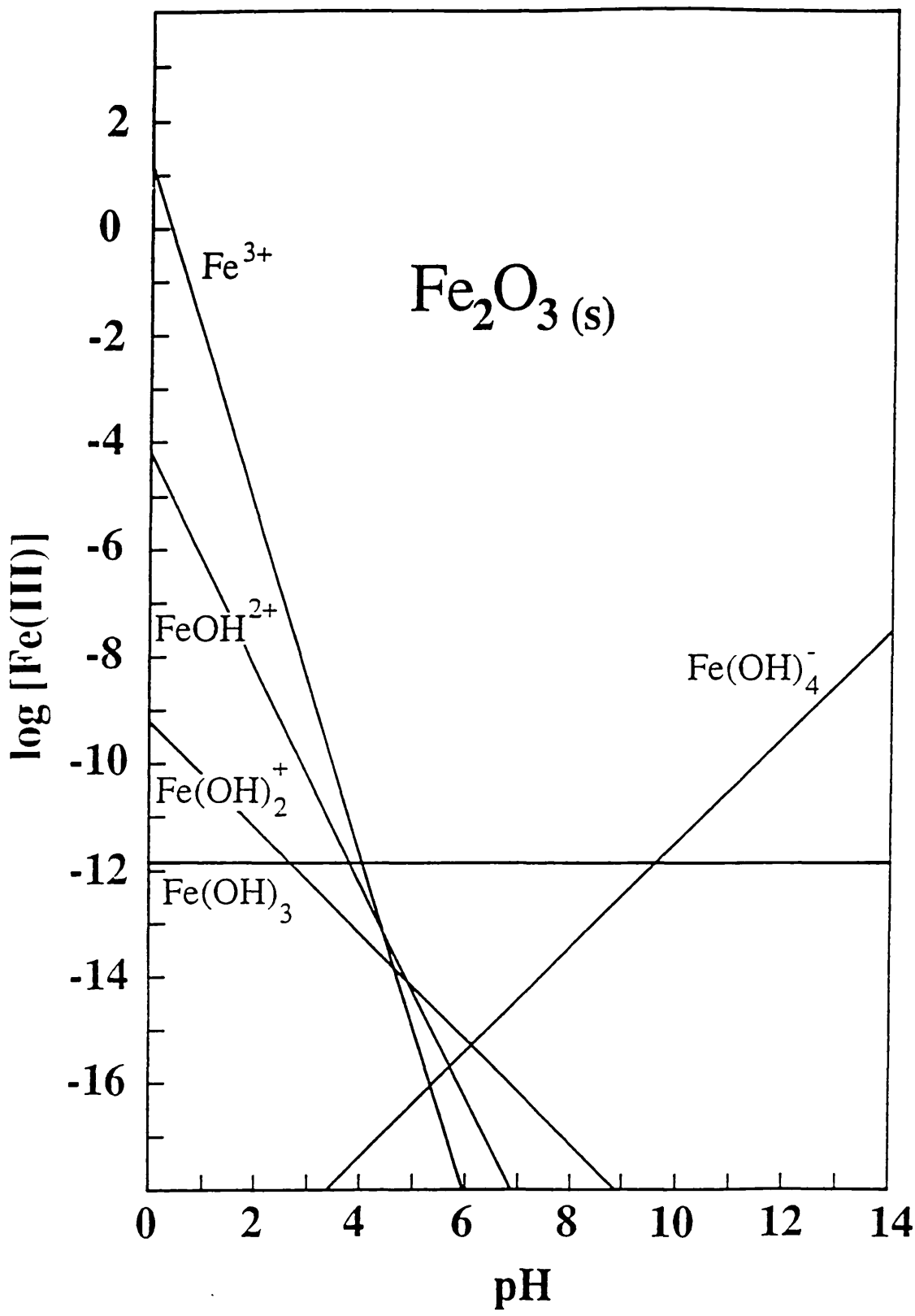


Fig II(vi) Activity-pH diagram at 298 K for Fe(III) species in equilibrium with $Fe_2O_{3(s)}$.

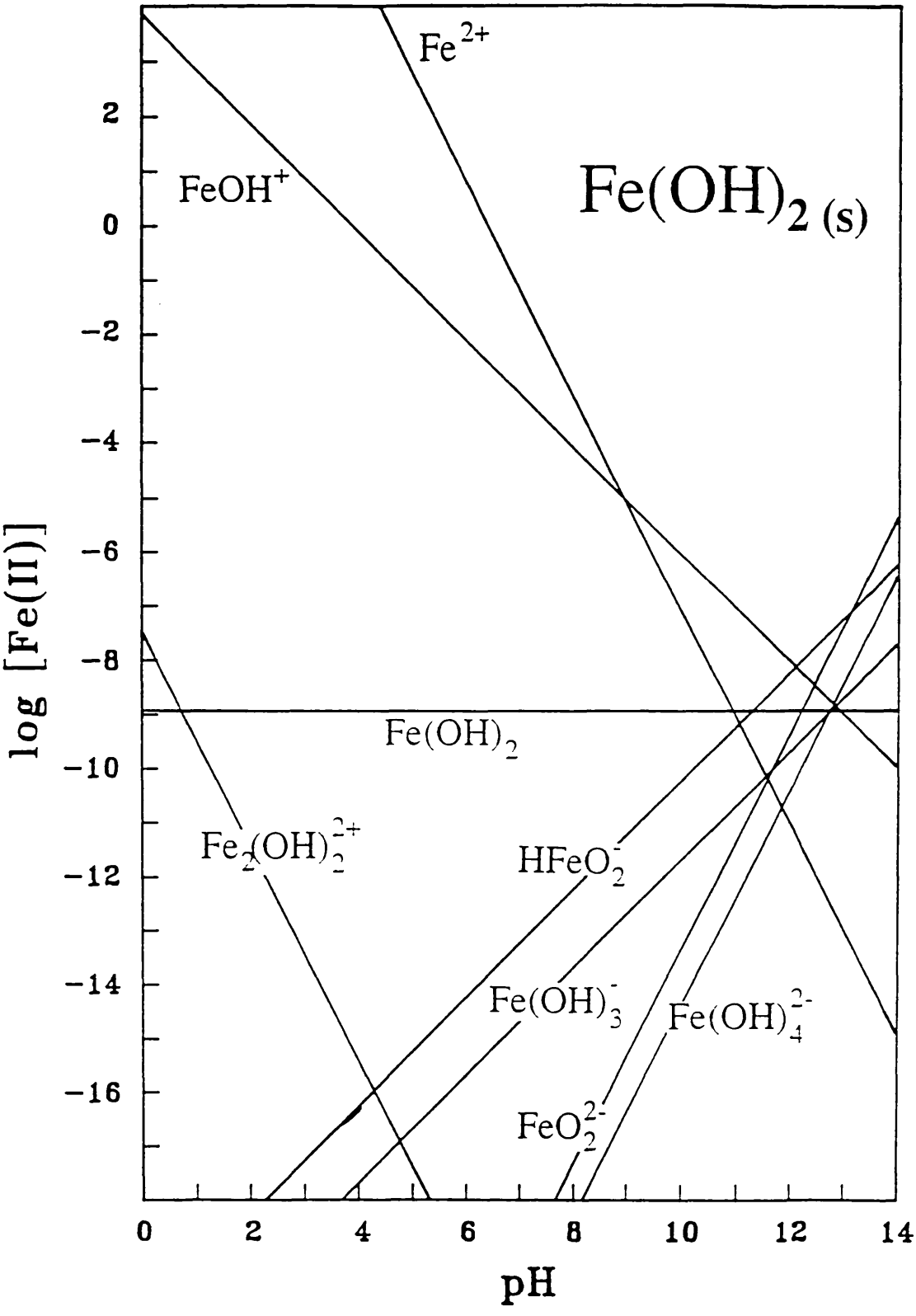


Fig II(vii) Activity-pH diagram at 298 K for Fe(II) species in equilibrium with $Fe(OH)_{2(s)}$.

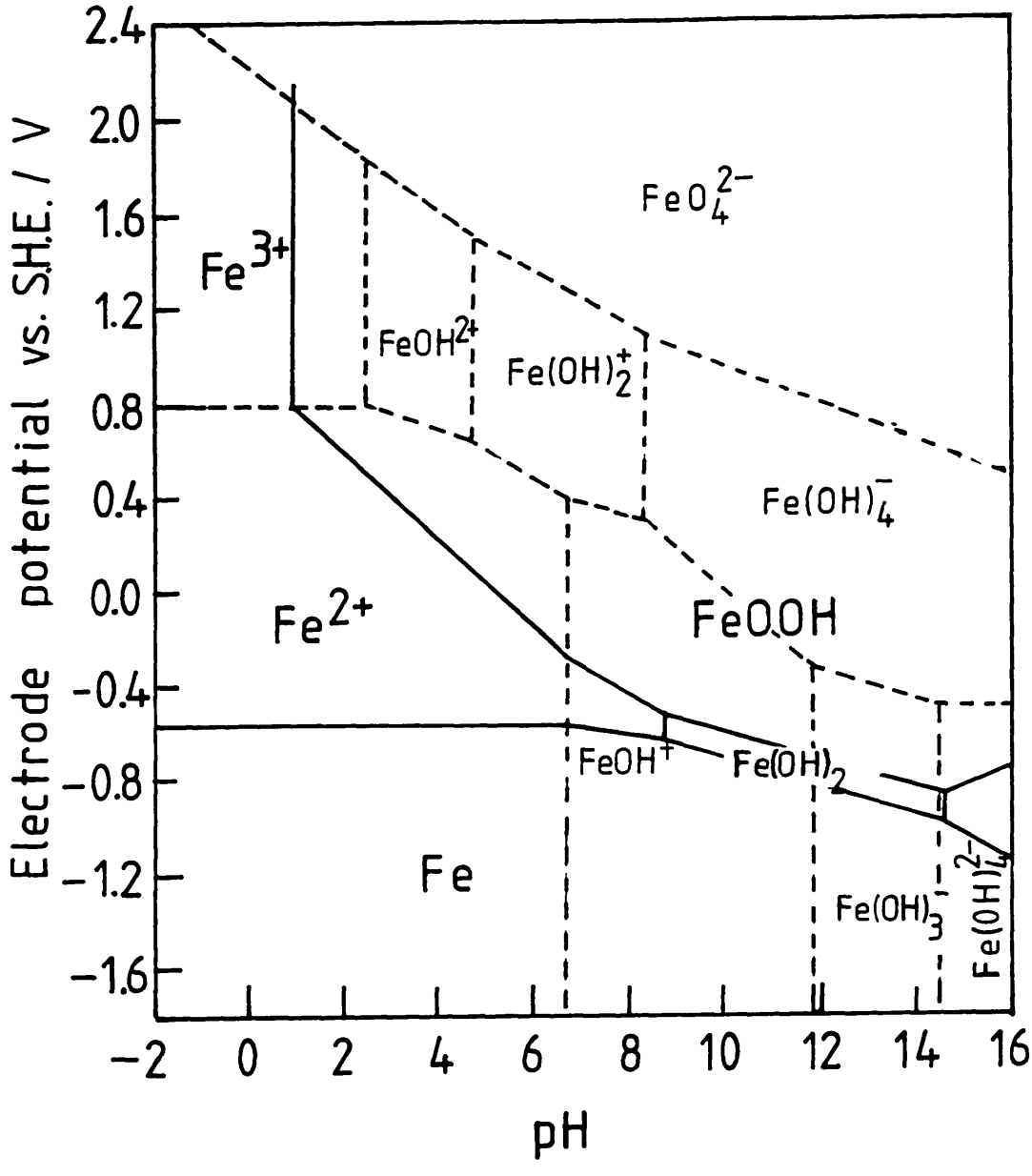


Fig II(viii) Potential-pH diagram for the Fe-H_2O system at 298 K considering Fe, $Fe(OH)_2$ and FeOOH as solid species[366].

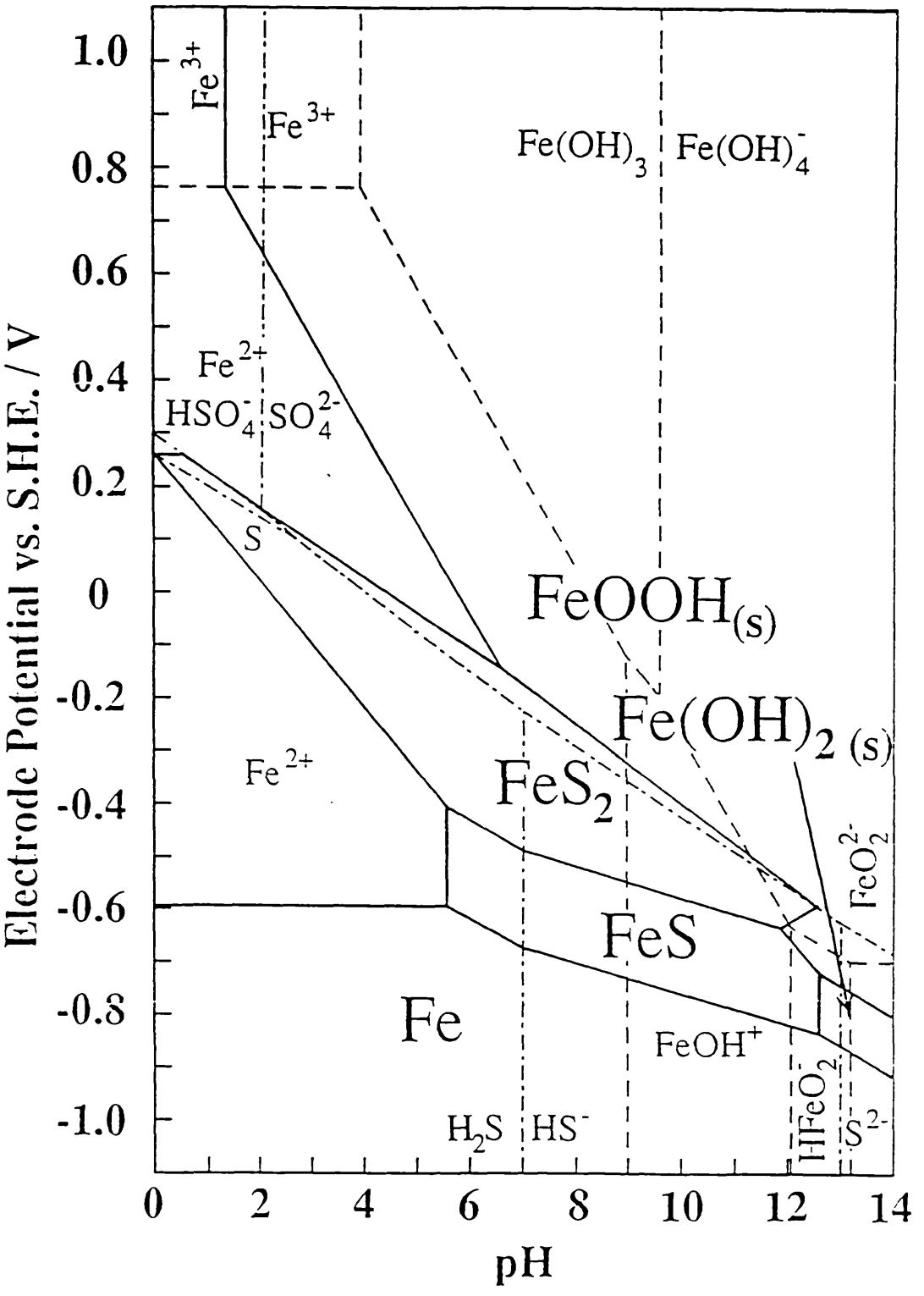


Fig II(ix) Potential-pH diagram for the Fe-S-H_2O system at 298 K for dissolved sulphur and iron activities of 10^{-4}.

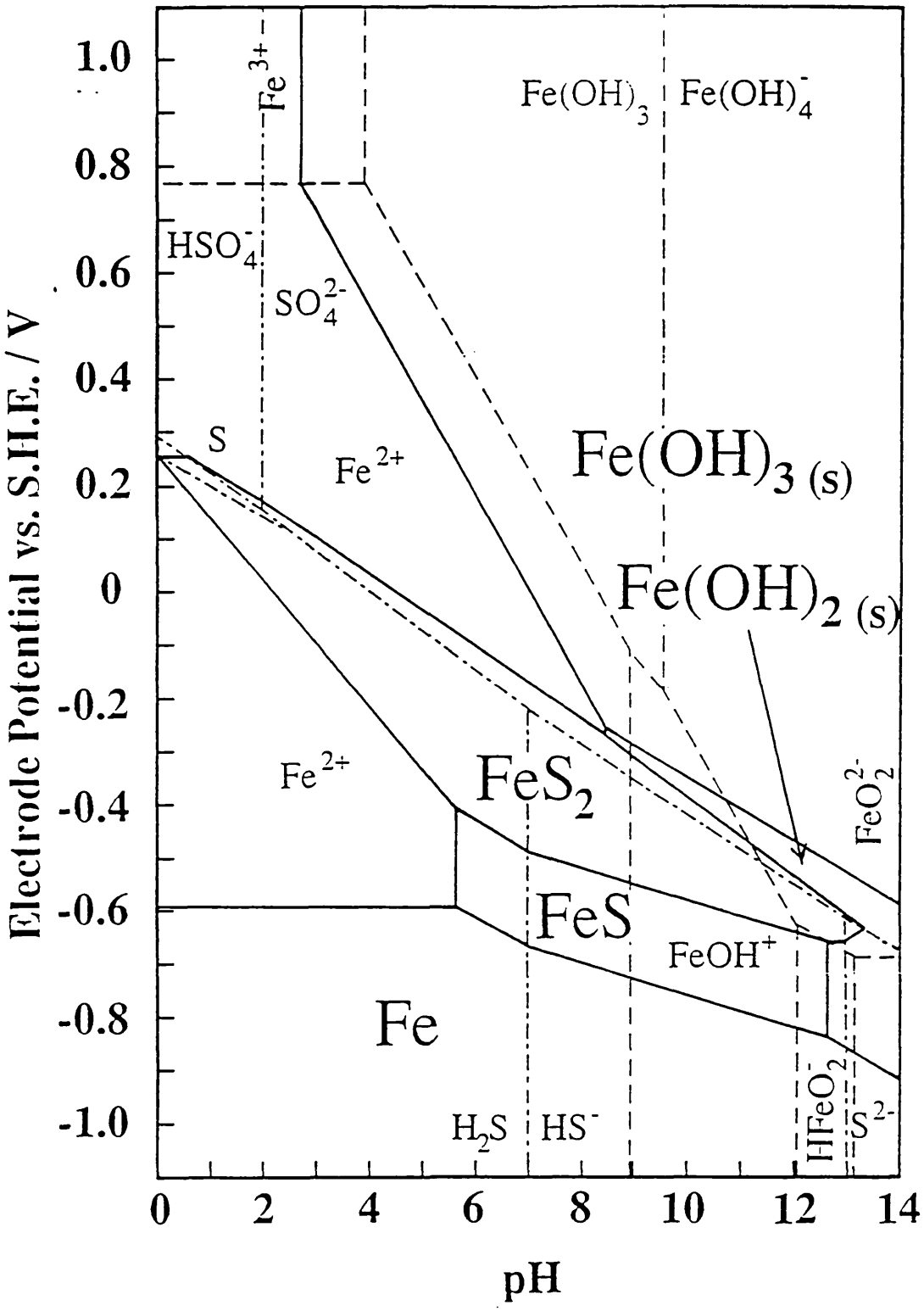


Fig II(x) Potential-pH diagram for the Fe-S-H_2O system at 298 K for dissolved sulphur and iron activities of 10^{-4}. FeOOH excluded.

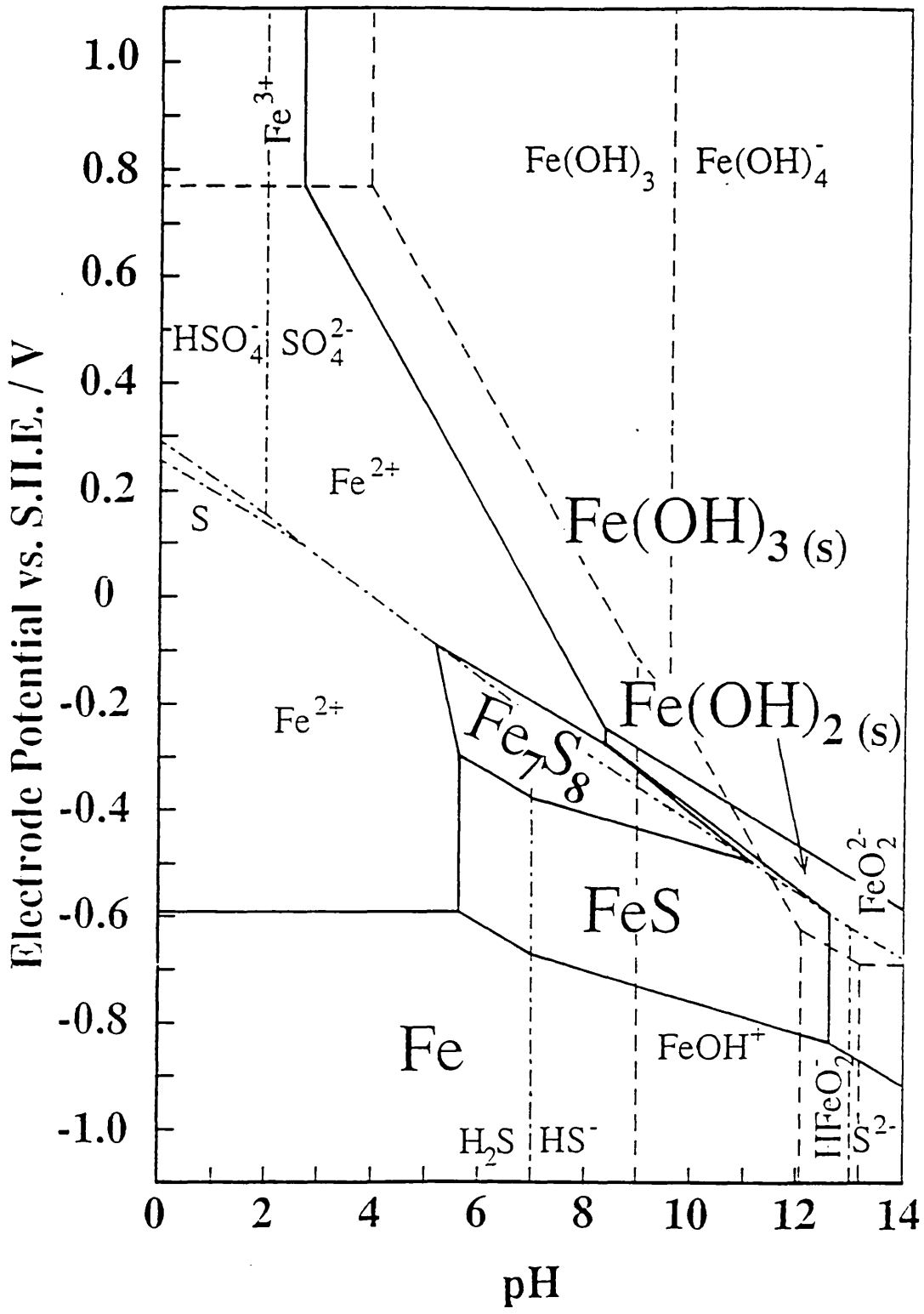


Fig II(xi) Potential-pH diagram for the Fe-S-H_2O system at 298 K for dissolved sulphur and iron activities of 10^{-4}. FeS_2 and FeOOH excluded.

3. $Ni-H_2O$ and $Fe-Ni-S-H_2O$ Systems

Table II(iii) Free Energies of Formation Data for Species in the $Ni-H_2O$ and $Fe-Ni-S-H_2O$ Systems at 298 K (Source : Ref (355), unless stated otherwise).

Species	ΔG_f°/kJ mol^{-1}	Species	ΔG_f°/kJ mol^{-1}
$(Fe,Ni)_9S_8$ (pentlandite)	-794.96[369]	$Fe(OH)_3^-$	-605.1
$FeNi_2S_4$ (violarite)	-318.82[368]	$Fe(OH)_4^-$	-842.2
NiS (millerite)	-74.06[367]	$Fe(OH)_4^{2-}$	-769.9
Ni^{2+}	-46.4	H_2O	-237.178
$Ni(OH)_{2(s)}$	-453.1	H^+	0
$Ni(OH)^+$	-232.0[69]	OH^-	157.2
$Ni(OH)_{3(s)}$	-541.8	H_2S	-27.8
Ni	0	HS^-	12.03
		S^{2-}	86.3
FeS (iron-rich α-pyrrhotite)	-100.4	SO_4^{2-}	-744.63
Fe^{2+}	-91.5	HSO_4^-	-756.01
Fe^{3+}	-16.7	S (orthorhombic)	0
$FeOH^+$	-277.4		
$FeOH^{2+}$	-229.41		
$HFeO_2^-$	-376.4		
$Fe(OH)_2$	-441.0		
$Fe(OH)_{2(s)}$	-486.6		
$Fe(OH)_2^+$	-438.1		
$Fe(OH)_{3(s)}$	-705.54		
$Fe(OH)_3$	-660		

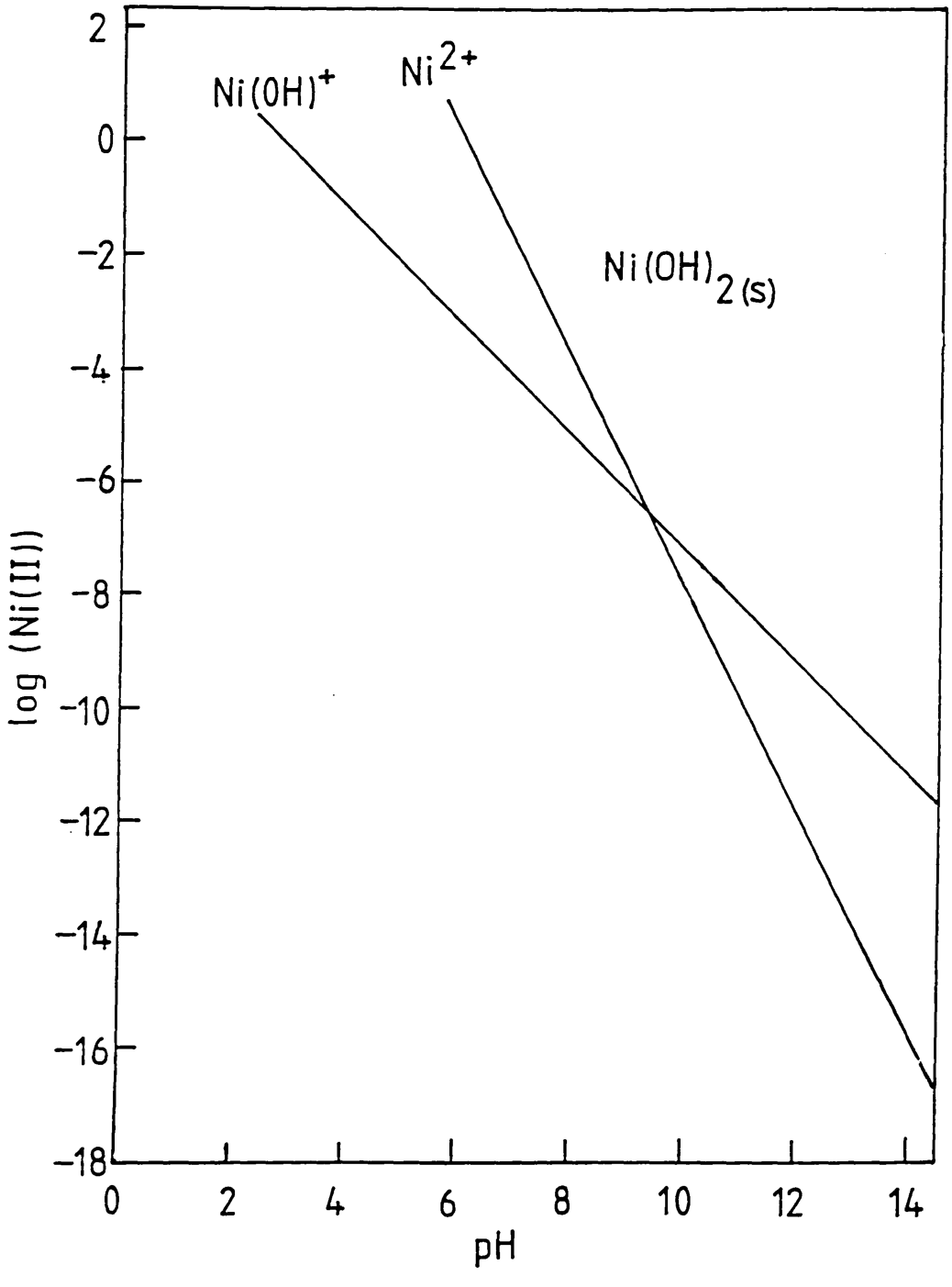


Fig II(xii) Activity-pH diagram at 298 K for Ni(II) species in equilibrium with $Ni(OH)_{2(s)}$.

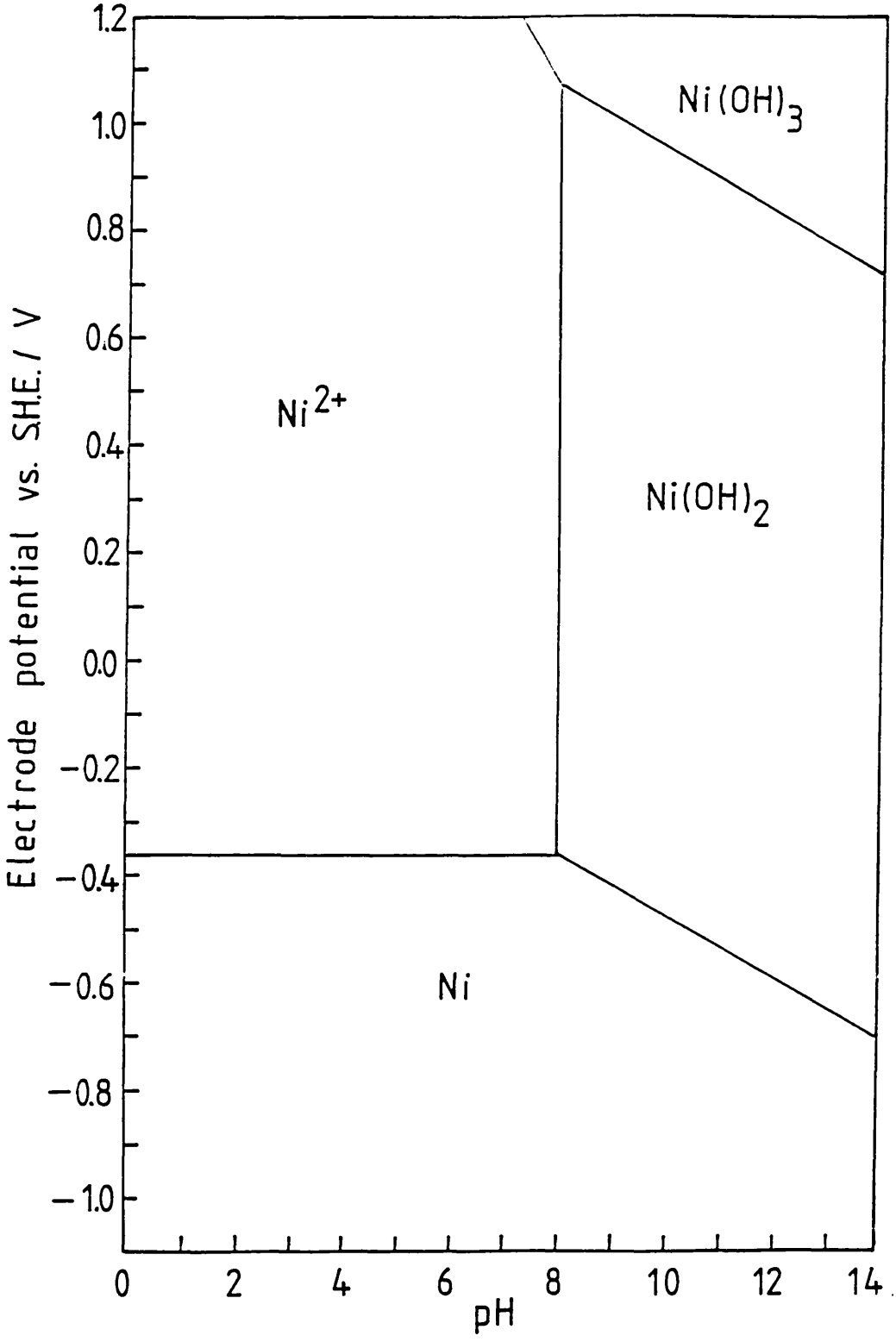


Fig II(xiii) Potential-pH diagram for the Ni-H_2O system at 298 K with a dissolved nickel activity of 10^{-4}.

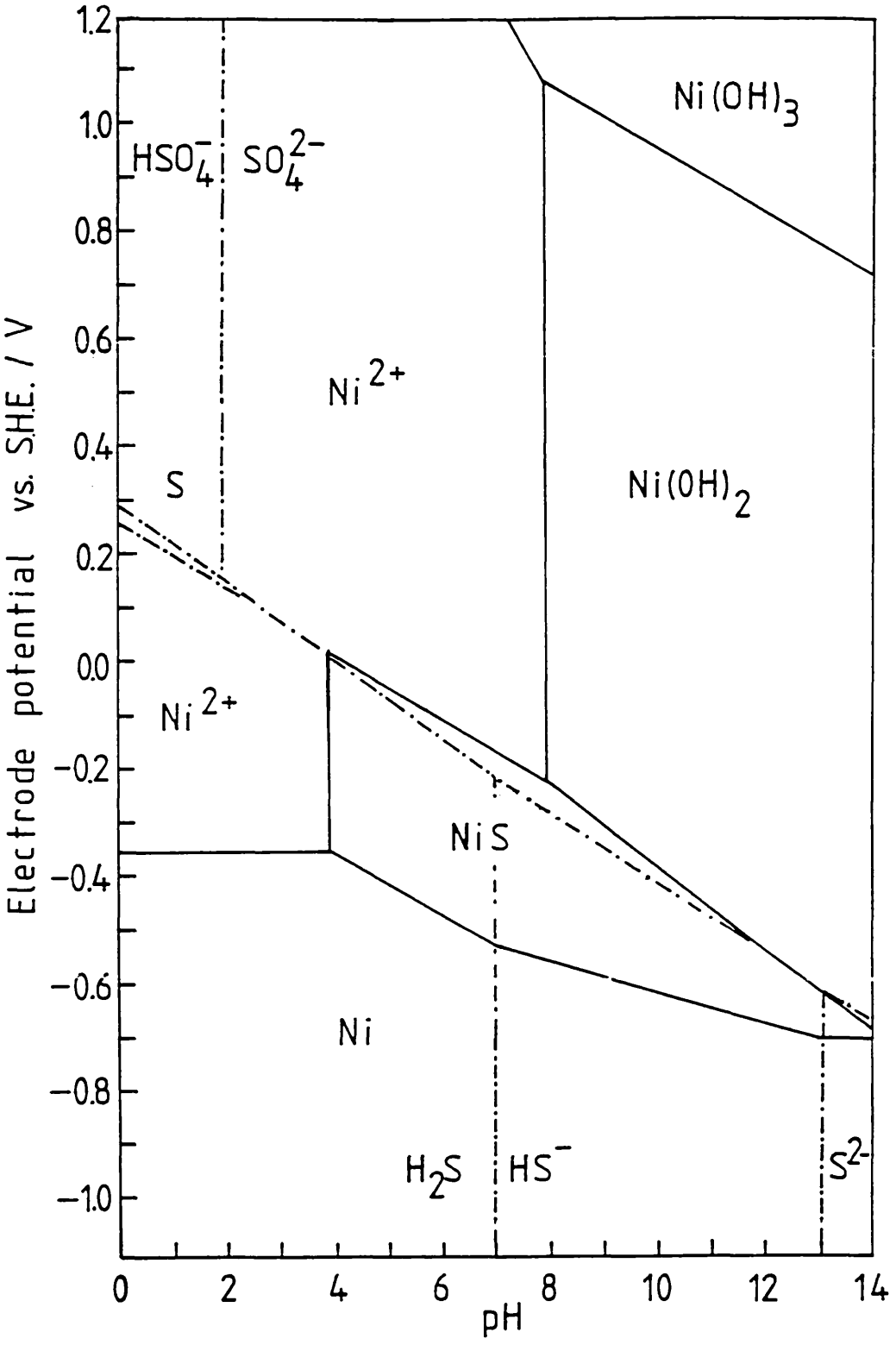


Fig II(xiv) Potential-pH diagram for the Ni-S-H_2O system at 298 K for dissolved sulphur and nickel activities of 10^{-4}.

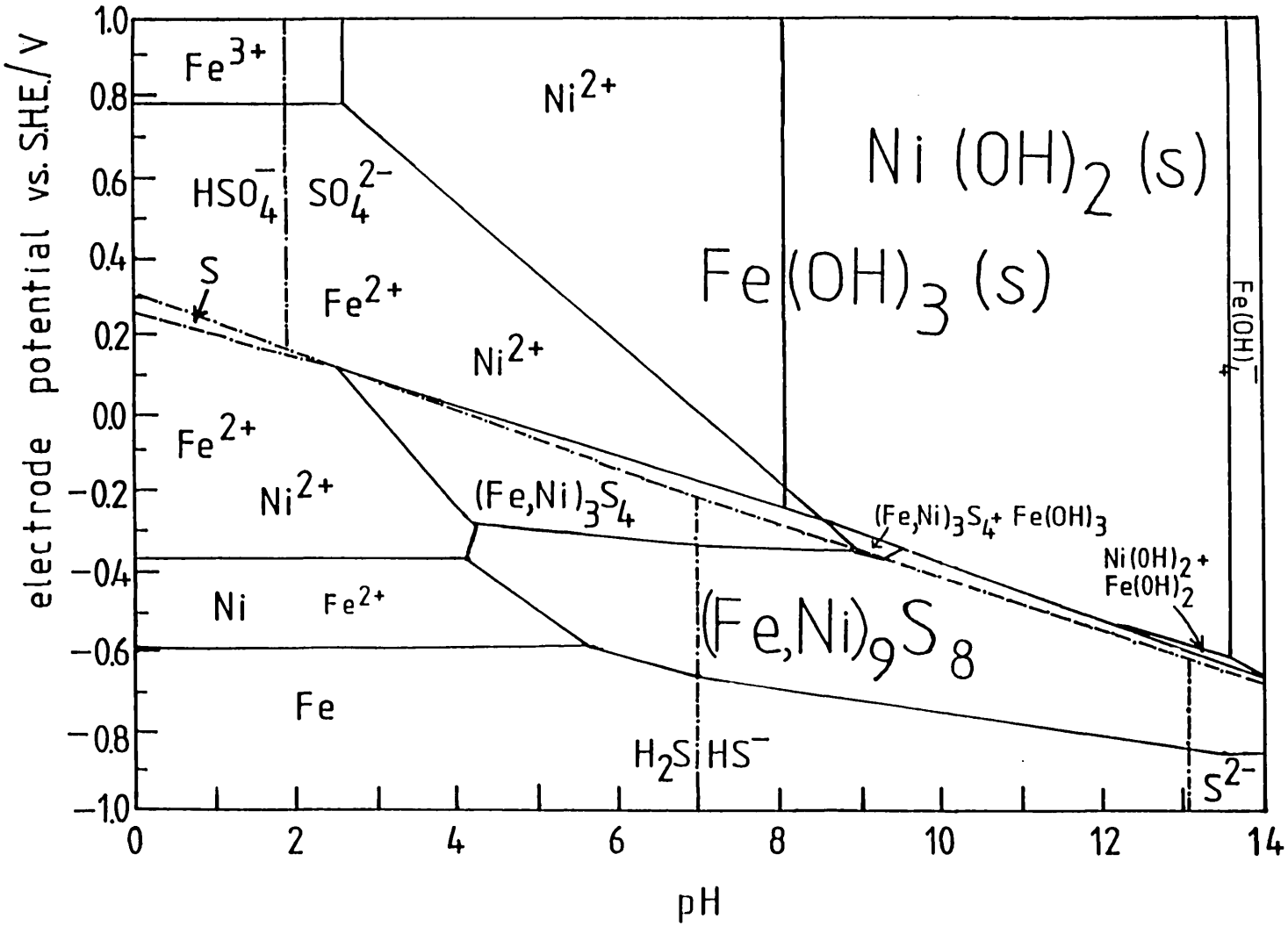


Fig II(xv) Potential-pH diagram for the Fe-Ni-S-H_2O system at 298 K for dissolved sulphur, nickel and iron activities of 10^{-4}.

4. Cu-H_2O and Cu-Fe-S-H_2O Systems

Table II(iv) Free Energies of Formation Data for Species in the Cu-H_2O and Cu-Fe-S-H_2O Systems at 298 K (Source : Ref. (355), and Ref. (69) for $CuFeS_2$ and Cu_5FeS_4).

Species	ΔG_f°/kJ mol^{-1}	Species	ΔG_f°/kJ mol^{-1}
$CuFeS_2$ (chalcopyrite)	-178.66	$Fe(OH)_2$	-441.0
Cu_5FeS_4 (bornite)	-353.13	$Fe(OH)_{3(s)}$	-705.54
Cu_2S (chalcocite)	-87.6	$Fe(OH)_3$	-660
CuS (covellite)	-53.2	$Fe(OH)_3^-$	-605.1
Cu	0.0		
Cu^+	50.3	$Fe(OH)_4^-$	-842.2
Cu^{2+}	65.7	$Fe(OH)_4^{2-}$	-769.9
$Cu_2O_{(s)}$	-148.1	H_2O	-237.178
$CuO_{(s)}$	-134.0	H^+	0
$Cu(OH)_{2(s)}$	-359.5	OH^-	-157.293
$HCuO_2^-$	-258.9	H_2S	-27.87
CuO_2^{2-}	-183.9	HS^-	12.05
$CuSO_{4(s)}$	-663.0	S^{2-}	86.31
$CuSO_4.H_2O_{(s)}$	-916.4	SO_4^{2-}	-744.63
$CuSO_4.5H_2O_{(s)}$	-1880.0	S (orthorhombic)	0.0
FeS_2 (pyrite)	-166.9		
FeS (iron-rich α-pyrrhotite)	-100.4		
Fe^{2+}	-91.5		
Fe^{3+}	-16.7		
$FeOH^+$	-277.4		
$FeOH^{2+}$	-229.41		
$HFeO_2^-$	-376.4		
$Fe(OH)_{2(s)}$	-486.6		
Fe	0.0		

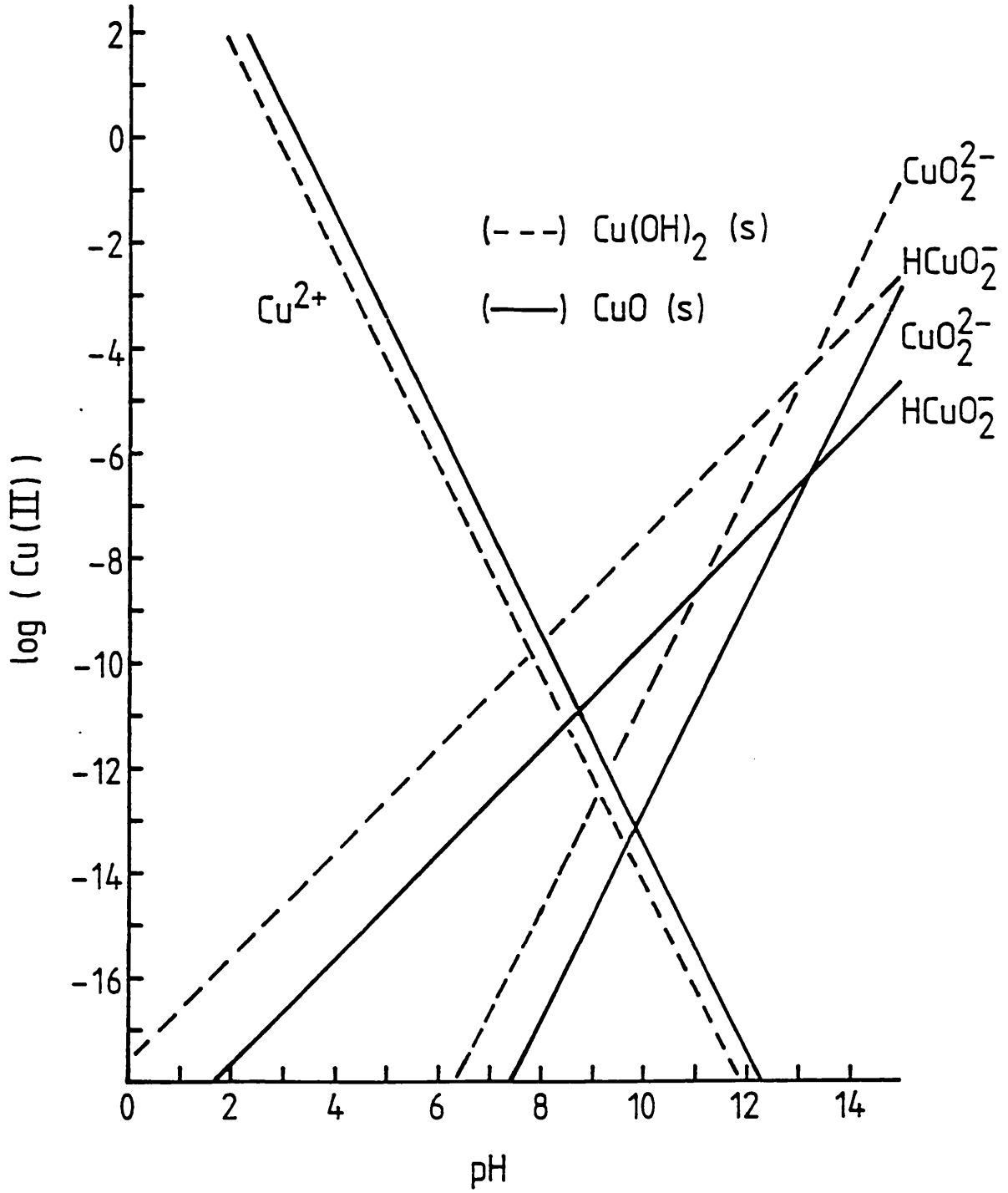


Fig II(xvi) Activity-pH diagram at 298 K for Cu(II) species in equilibrium with $Cu(OH)_{2(s)}$ (- - -) or $CuO_{(s)}$ (——)[370].

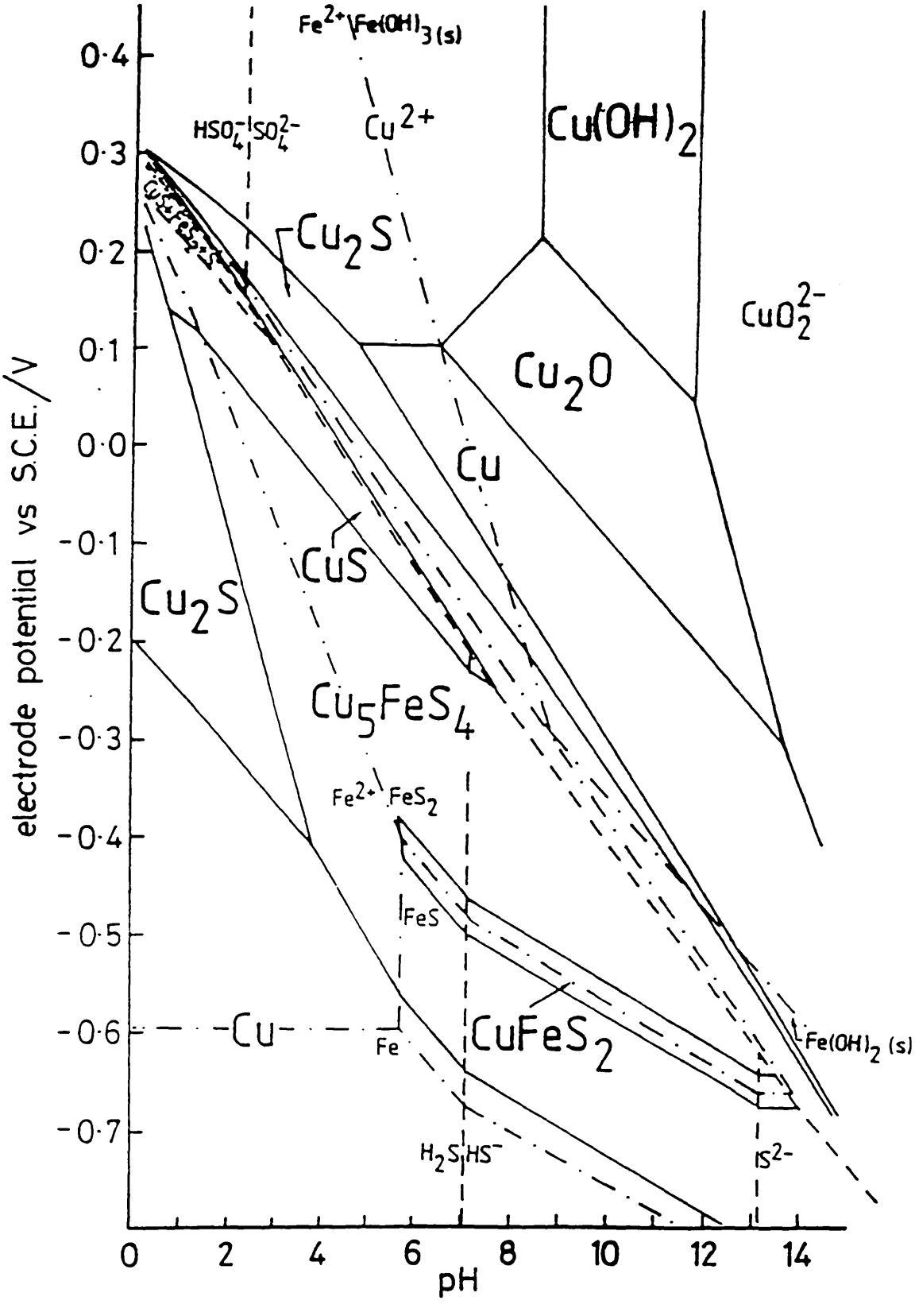


Fig II(xvii) Potential-pH diagram for the Cu-Fe-S-H_2O system at 298 K for dissolved copper, iron and sulphur activities of 10^{-6}, 10^{-4} and 10^{-4}, respectively[370].

APPENDIX III: Computer Programs

1. PCT (Program to analyse current-time transients)

```
00100 PROGRAM PCT(INPUT,OUTPUT,DATA1,DATA2,TAPE62,TAPE5=INPUT,
00110+TAPE6=OUTPUT,TAPE4=DATA1,TAPE9=DATA2)
00120 DIMENSION XARRAY(100),YARRAY(100),XTIMEM(100),IELECT(2),XT(100),C(100)
00130 DIMENSION YIR(100),YS(100),XTIMES(100),RX(24),YP(100),Q(100)
00140 CHARACTER LAB(24)*30
00150 DATA LAB(1)/'E*T]-]0].15 / SECS]-]0].15'/
00160 DATA LAB(2),LAB(8),LAB(14),LAB(20)/4*'E*T / SECS                '/
00170 DATA LAB(3),LAB(9),LAB(15),LAB(21)/4*'E*T]1].15 / SECS]1].15    '/
00180 DATA LAB(4),LAB(10),LAB(16),LAB(22)/4*'E*T]2 / SECS]2           '/
00190 DATA LAB(5),LAB(11),LAB(17),LAB(23)/4*'E*T]3 / SECS]3           '/
00200 DATA LAB(7)/'E*EXP]-]T / EXP]-]S]E]C]S '/
00210 DATA LAB(13)/'E*T]-]1 / SECS]-]1       '/
00220 DATA LAB(19)/'E*T]0].15 / SECS]0].15   '/
00230 READ(4,10) IELECT
00240 10 FORMAT(2A10)
00250 READ(4,*) RESIST,AREA,POT,PH
00260 NUM=1
00270 20 READ(4,*,END=30) XARRAY(NUM),YARRAY(NUM)
00280 YARRAY(NUM)=YARRAY(NUM)/(RESIST*AREA)
00290 NUM=NUM+1
00300 GOTO 20
00310 30 NUM=NUM-1
00320 WRITE(9,5) IELECT
00330 5 FORMAT(1H1,/,/,/,25X,'CURRENT / TIME MEASUREMENTS MADE ON A ',2A10)
00340 WRITE(9,15)
00350 15 FORMAT(25X,'-----------------------------------------------------------
00360+')
00370 WRITE(9,25)PH
00380 25 FORMAT(/,/,31X,'ELECTRODE IN PH ',F5.2,' BUFFER SOLUTION')
00390 WRITE(9,35)
00400 35 FORMAT(31X,'------------------------------------ ')
00410 WRITE(9,45) POT
00420 45 FORMAT(/,/,34X,'POTENTIAL = ',F6.3,' V VS. SHE'/,/,/)
00430 WRITE(9,55)
00440 55 FORMAT(10X,'I-------------------------------------------------------
00450+----------------------------------I')
00460 WRITE(9,56)
00470 56 FORMAT(10X,'I',39X,'I',50X,'I')
00480 WRITE(9,57)
00490 57 FORMAT(10X,'I',11X,'TIME / S',20X,'I',10X,'CURRENT DENSITY I / MA CM-**
00500+2',11X,'I')
00510 WRITE(9,56)
00520 WRITE(9,55)
00530 WRITE(9,56)
00540 DO 40 I=1,NUM
00550 WRITE(9,75) XARRAY(I),YARRAY(I)
00560 75 FORMAT(10X,'I',14X,F11.5,14X,'I',21X,F8.3,21X,'I')
00570 WRITE(9,56)
00580 40 CONTINUE
00590 WRITE(9,55)
00600 CALL START(2)
00610 L=0
00620 DO 50 NPT=1,24
00630 L=L+1
00640 IF (L.GT.24) GOTO 391
00650 GOTO(60,80,90,80,90,80,90,80,90,80,90,80,90,80,90,80,90,80,90,80,
00660+90,80,90,80),L
00670 60 CALL PLOT(0.5,1.0,-3)
00680 GOTO 70
00690 80 CALL PLOT(10.0,0.0,-3)
00700 GOTO 70
00710 90 CALL NEWPAGE
00720 CALL PLOT(0.5,1.0,-3)
00730 70 GOTO(100,130,150,160,170,290,180,130,150,160,170,290,112,130,
00740+150,160,170,290,131,130,150,160,170,290),L
00750 100 NOPTS=0
00760 R2=0.0
00770 110 NOPTS=NOPTS+1
00780 XTIMEM(NOPTS)=1.0/(SQRT(XARRAY(NOPTS)))
00790 YIR(NOPTS)=YARRAY(NOPTS)
00800 IF (NOPTS+3.EQ.NUM) GOTO 114
00810 IF (YARRAY(NOPTS+3).LE.YARRAY(NOPTS)) GOTO 110
00820 114 FT=-0.5
00830 GOTO 120
00840 112 NOPTS=0
00850 R2=0.0
00860 113 NOPTS=NOPTS+1
00870 XTIMEM(NOPTS)=1.0/XARRAY(NOPTS)
00880 YIR(NOPTS)=YARRAY(NOPTS)
00890 IF (NOPTS+3.EQ.NUM) GOTO 115
00900 IF (YARRAY(NOPTS+3).LE.YARRAY(NOPTS)) GOTO 113
00910 115 FT=-1.0
00920 GOTO 120
00930 131 NOPTS=0
00940 R2=0.0
00950 133 NOPTS=NOPTS+1
00960 XTIMEM(NOPTS)=SQRT(XARRAY(NOPTS))
00970 YIR(NOPTS)=YARRAY(NOPTS)
00980 IF (NOPTS+3.EQ.NUM) GOTO 136
00990 IF (YARRAY(NOPTS+3).LE.YARRAY(NOPTS)) GOTO 133
01000 136 FT=0.5
01010 GOTO 120
01020 130 FT=1.0
01030 GOTO 140
01040 150 FT=1.5
01050 GOTO 140
01060 160 FT=2.0
01070 GOTO 140
01080 170 FT=3.0
01090 GOTO 140
01100 180 NOPTS=0
01110 R2=0.0
01120 190 NOPTS=NOPTS+1
01130 IF (XARRAY(NOPTS).GT.100.0) XTIMEM(NOPTS)=0.0
01140 IF (XTIMEM(NOPTS).EQ.0.0) GOTO 191
01150 XTIMEM(NOPTS)=EXP(-1.0*(XARRAY(NOPTS)))
01160 191 YIR(NOPTS)=YARRAY(NOPTS)
01170 IF (NOPTS+3.EQ.NUM) GOTO 120
01180 IF (YARRAY(NOPTS+3).LE.YARRAY(NOPTS)) GOTO 190
01190 120 CALL REGRESS (XTIMEM,YIR,NOPTS,L,FT,A0,A1,R)
01200 R1=R
```

```
01200 R1=R
01210 CALL SCALE (XTIMEH,8.0,NOPTS,1)
01220 CALL SCALE (YIR,8.0,NOPTS,1)
01230 CALL AXIS (0.,0.,'                                                    ',-40,8.0,
01240+0.,XTIMEH(NOPTS+1),XTIMEH(NOPTS+2))
01250 CALL ZYMBOL (2.5,-0.8,0.21,LAB(L),0.0,26)
01260 CALL AXIS (0.,0.,'                                                    ',40,8.0,90.0,
01270+YIR(NOPTS+1),YIR(NOPTS+2))
01280 CALL ZYMBOL (-0.8,1.25,0.21,'&<C*URRENT DENSITY / M<A *CM(-)2',
01290+90.0,32)
01300 DO 200 J=1,2
01310 CALL LINE (XTIMEH,YIR,NOPTS,1,J-2,0)
01320 IF (J.EQ.2) GOTO 200
01330 A=(8.0*YIR(NOPTS+2))+YIR(NOPTS+1)
01340 DO 210 I=1,NOPTS
01350 YIR(I)=A0+(A1*XTIMEH(I))
01360 IF (YIR(I).GT.A) YIR(I)=A
01370 IF (YIR(I).LT.YIR(NOPTS+1)) YIR(I)=YIR(NOPTS+1)
01380 210 CONTINUE
01390 200 CONTINUE
01400 GOTO 220
01410 140 IRUS=NUM-NOPTS
01420 IF (IRUS.EQ.3) L=L+4
01430 IF (IRUS.EQ.3) GOTO 260
01440 DO 230 I=1,(NUM-NOPTS)
01450 J=NOPTS+I
01460 IF (L.GE.7.AND.L.LE.12) GOTO 142
01470 IF (L.GE.13.AND.L.LE.18) GOTO 146
01480 IF (L.GE.19) GOTO 152
01490 YS(I)=A0+(A1*(1.0/SQRT(XARRAY(J))))
01500 GOTO 143
01510 142 IF (XARRAY(J).GT.100.0) YS(I)=A0
01520 IF (XARRAY(J).GT.100.0) GOTO 143
01530 YS(I)=A0+(A1*EXP(-1.0*XARRAY(J)))
01540 GOTO 143
01550 146 YS(I)=A0+(A1*(1.0/XARRAY(J)))
01560 GOTO 143
01570 152 YS(I)=A0+(A1*(SQRT(XARRAY(J))))
01580 143 IF (YS(I).LT.0.0) GOTO 240
01590 YS(I)=YARRAY(J)-YS(I)
01600 GOTO 250
01610 240 YS(I)=YARRAY(J)
01620 250 XTIMES(I)=XARRAY(J)
01630 XTIMES(I)=(XTIMES(I))**FT
01640 230 CONTINUE
01650 I=I-1
01660 CALL REGRESS (XTIMES,YS,I,L,FT,B0,B1,R)
01670 IF (R.GT.R2) R2=R
01680 IF (L.EQ.6) GOTO 260
01690 IF (L.EQ.12) GOTO 260
01700 IF (L.EQ.18) GOTO 260
01710 IF (L.EQ.24) GOTO 260
01720 RX(L)=R
01730 CALL SCALE (XTIMES,8.0,I,1)
01740 CALL SCALE (YS,8.0,I,1)
01750 CALL AXIS (0.,0.,'                                                    ',-40,8.0,0.,
01760+XTIMES(I+1),XTIMES(I+2))
01770 CALL ZYMBOL (2.5,-0.8,0.21,LAB(L),0.0,26)
01780 CALL AXIS (0.,0.,'                                                    ',40,8.0,90.,
01790+YS(I+1),YS(I+2))
01800 CALL ZYMBOL (-0.8,2.5,0.21,'&*I - I!*>U&* / M<A *CM(-)2',90.0,27)
01810 DO 270 M=1,2
01820 CALL LINE (XTIMES,YS,I,1,M-2,2)
01830 IF (M.EQ.2) GOTO 270
01840 A=(8.0*YS(I+2))+YS(I+1)
01850 DO 280 MM=1,I
01860 YS(MM)=B0+(B1*(XARRAY(MM+NOPTS)**FT))
01870 IF (YS(MM).GT.A) YS(MM)=A
01880 IF (YS(MM).LT.YS(I+1)) YS(MM)=YS(I+1)
01890 280 CONTINUE
01900 270 CONTINUE
01910 GOTO 220
01920 290 RX(L) = AMAX1(RX(L-4),RX(L-3),RX(L-2),RX(L-1))
01930 IF (RX(L).EQ.RX(L-4)) GOTO 130
01940 IF (RX(L).EQ.RX(L-3)) GOTO 150
01950 IF (RX(L).EQ.RX(L-2)) GOTO 160
01960 IF (RX(L).EQ.RX(L-1)) GOTO 170
01970 260 DO 252 IX=1,NUM
01980 YP(IX)=YARRAY(IX)
01990 252 CONTINUE
02000 YP(NUM+1)=0.0
02010 XARRAY(NUM+1)=0.0
02020 CALL SCALE (XARRAY,8.0,NUM+1,1)
02030 CALL SCALE (YP,8.0,NUM+1,1)
02040 YP(NUM+1)=YP(NUM+2)
02050 YP(NUM+2)=YP(NUM+3)
02060 YP(NUM+3)=0.0
02070 XARRAY(NUM+1)=XARRAY(NUM+2)
02080 XARRAY(NUM+2)=XARRAY(NUM+3)
02090 XARRAY(NUM+3)=0.0
02100 CALL AXIS (0.,0.,'                                                    ',-40,8.0,0.,
02110+XARRAY(NUM+1),XARRAY(NUM+2))
02120 CALL ZYMBOL (2.8,-0.8,0.21,'&<T*IME / SECS',0.0,14)
02130 CALL AXIS (0.,0.,'                                                    ',40,8.0,90.,
02140+YP(NUM+1),YP(NUM+2))
02150 CALL ZYMBOL (-0.8,1.3,0.21,'&,C*URRENT DENSITY / M<A *CM(-)2',
02160+90.0,32)
02170 CALL INTENSE(20)
02180 CALL LINE (XARRAY,YP,NUM,1,1,1)
02190 CALL INTENSE(12)
02200 IF (L.EQ.12) GOTO 310
02210 IF (L.EQ.18) GOTO 315
02220 IF (L.EQ.24) GOTO 362
02230 DO 320 IX=1,NUM
02240 YP(IX)=A0+(A1*(1.0/SQRT(XARRAY(IX))))
02250 IF (YP(IX).LT.0.0) GOTO 330
```

```
02250 IF (YP(IX).LT.0.0) GOTO 330
02260 GOTO 320
02270 330 YP(IX)=0.0
02280 320 CONTINUE
02290 GOTO 340
02300 310 DO 350 IX=1,NUM
02310 IF (XARRAY(IX).GT.100.0) YP(IX)=A0
02320 IF (XARRAY(IX).GT.100.0) GOTO 311
02330 YP(IX)=A0+(A1*(EXP(-1.0*(XARRAY(IX)))))
02340 311 IF (YP(IX).LT.0.0) GOTO 360
02350 GOTO 350
02360 360 YP(IX)=0.0
02370 350 CONTINUE
02380 GOTO 340
02390 315 DO 316 IX=1,NUM
02400 YP(IX)=A0+(A1*(1.0/XARRAY(IX)))
02410 IF (YP(IX).LT.0.0) YP(IX)=0.0
02420 316 CONTINUE
02430 GOTO 340
02440 362 DO 363 IX=1,NUM
02450 YP(IX)=A0+(A1*(SQRT(XARRAY(IX))))
02460 IF (YP(IX).LT.0.0) YP(IX)=0.0
02470 363 CONTINUE
02480 340 CALL LINE(XARRAY,YP,NUM,1,0,0)
02490 IF (IRUS.EQ.3) R2=0.0
02500 IF (IRUS.EQ.3) GOTO 371
02510 A=(2.0*YP(NUM+2))+YP(NUM+1)
02520 DO 370 IX=1,NUM
02530 YP(IX)=B0+(B1*(XARRAY(IX)**FT))
02540 IF (YP(IX).LT.0.0) YP(IX)=0.0
02550 IF (YP(IX).GT.A) YP(IX)=A
02560 370 CONTINUE
02570 CALL LINE(XARRAY,YP,NUM,1,0,0)
02580 DO 372 IX=1,NUM
02590 IF (L.EQ.12) GOTO 374
02600 IF (L.EQ.18) GOTO 381
02610 IF (L.EQ.24) GOTO 387
02620 V1=A0+(A1*(1.0/SQRT(XARRAY(IX))))
02630 IF (V1.LT.0.0) V1=0.0
02640 GOTO 376
02650 374 IF (XARRAY(IX).GT.100.0) V1=A0
02660 IF (XARRAY(IX).GT.100.0) GOTO 377
02670 V1=A0+(A1*(EXP(-1.0*(XARRAY(IX)))))
02680 377 IF (V1.LT.0.0) V1=0.0
02690 GOTO 376
02700 381 V1=A0+(A1*(1.0/XARRAY(IX)))
02710 IF (V1.LT.0.0) V1=0.0
02720 GOTO 376
02730 387 V1=A0+(A1*(SQRT(XARRAY(IX))))
02740 IF (V1.LT.0.0) V1=0.0
02750 376 V2=B0+(B1*(XARRAY(IX)**FT))
02760 IF (V2.LT.0.0) V2=0.0
02770 YP(IX)=V1+V2
02780 372 CONTINUE
02790 CALL LINE(XARRAY,YP,NUM,1,0,0)
02800 371 CALL INTENSE(20)
02810 CALL PLOT(0.0,8.0,3)
02820 CALL PLOT(8.0,8.0,2)
02830 CALL PLOT(8.0,0.0,2)
02840 CALL ZYMBOL(0.5,10.5,0.28,IELECT,0.0,20)
02850 CALL ZYMBOL(0.5,10.0,0.28,'&<P*OTENTIAL <V / *VS. <SHE',0.0,27)
02860 CALL NUMBER(7.0,10.0,0.28,POT,0.0,3)
02870 CALL ZYMBOL(5.0,9.5,0.28,'&*P<H',0.0,5)
02880 CALL NUMBER(7.0,9.5,0.28,PH,0.0,1)
02890 CALL ZYMBOL(0.5,9.0,0.28,'&<R1 =',0.,6)
02900 CALL NUMBER(1.8,9.0,0.28,R1,0.0,4)
02910 CALL ZYMBOL(4.0,9.0,0.28,'&<R2 =',0.0,6)
02920 CALL NUMBER(5.3,9.0,0.28,R2,0.0,4)
02930 Q(1)=0.0
02940 XT(1)=0.0
02950 C(1)=0.0
02960 C2=0.0
02970 QMIN=0.0
02980 P3=0.000001
02990 P5=((A0*P3)+(A1*ALOG(P3)))*(-1.0)
03000 DO 550 IX=1,NUM
03010 IF (L.EQ.12) GOTO 530
03020 IF (L.EQ.18) GOTO 540
03030 IF (L.EQ.24) GOTO 545
03040 C(IX+1)=(A0*XARRAY(IX))+(2.0*A1*(SQRT(XARRAY(IX))))
03050 IF (C(IX+1).LT.C(IX)) C(IX+1)=C(IX)
03060 GOTO 535
03070 530 IF (XARRAY(IX).GT.100.0) C(IX+1)=(A0*XARRAY(IX))+A1
03080 IF (XARRAY(IX).GT.100.0) GOTO 531
03090 C(IX+1)=(A0*XARRAY(IX))+((-1.0*A1)*(EXP(-1.0*(XARRAY(IX)))))+A1
03100 531 IF (C(IX+1).LT.C(IX)) C(IX+1)=C(IX)
03110 GOTO 535
03120 540 C(IX+1)=(A0*XARRAY(IX))+(A1*(ALOG(XARRAY(IX))))+P5
03130 IF (C(IX+1).LT.C(IX)) C(IX+1)=C(IX)
03140 GOTO 535
03150 545 C(IX+1)=(A0*XARRAY(IX))+((A1*(XARRAY(IX)**1.5))/1.5)
03160 IF (C(IX+1).LT.C(IX)) C(IX+1)=C(IX)
03170 535 IF (IRUS.EQ.3) GOTO 546
03180 C2=(B0*XARRAY(IX))+((B1/(FT+1.0))*(XARRAY(IX)**(FT+1.0)))
03190 P=B0+(B1*(XARRAY(IX)**FT))
03200 IF (P.LT.0.0) C2=0.0
03210 IF (QMIN.NE.0.0) GOTO 546
03220 QMIN=ABS(C2)
03230 546 Q(IX+1)=C(IX+1)+C2+QMIN
03240 XT(IX+1)=XARRAY(IX)
03250 550 CONTINUE
03260 CALL NEWPAGE
03270 CALL PLOT(0.5,1.0,-3)
03280 CALL SCALE(XT,8.0,NUM+1,1)
03290 CALL SCALE(Q,8.0,NUM+1,1)
03300 CALL AXIS(0.,0.,'                                                    ',40,8.0,
03310+90.0,Q(NUM+2),Q(NUM+3))
03320 CALL ZYMBOL(-0.8,1.0,0.21,'&<C*UMULATIVE CHARGE <Q / *M<C*OU-12',
03330+90.0,30)
03340 CALL AXIS(0.,0.,'                                                    ',-40,8.0,
03350+0.0,XT(NUM+2),XT(NUM+3))
03360 CALL ZYMBOL(2.8,-0.8,0.21,'&<T*IME / SECS',0.0,14)
03370 CALL LINE(XT,Q,NUM+1,1,0,0)
```

```
03390 DO 600 IX=1,NUM
03400 IF (L.EQ.12) GOTO 610
03410 IF (L.EQ.18) GOTO 620
03420 IF (L.EQ.24) GOTO 625
03430 C(IX+1) = (A0*XARRAY(IX) + (2.0*A1*(SQRT(XARRAY(IX))))
03440 IF (C(IX+1).LT.C(IX)) C(IX+1)=C(IX)
03450 GOTO 630
03460 610 IF (XARRAY(IX).GT.100.0) C(IX+1) = (A0*XARRAY(IX) +A1
03470 IF (XARRAY(IX).GT.100.0) GOTO 611
03480 C(IX+1) = (A0*XARRAY(IX) + ((-1.0*A1)*(EXP(-1.0*(XARRAY(IX))))) +A1
03490 611 IF (C(IX+1).LT.C(IX)) C(IX+1)=C(IX)
03500 GOTO 630
03510 620 C(IX+1) = (A0*XARRAY(IX) + (A1*(ALOG(XARRAY(IX)))) +P5
03520 IF (C(IX+1).LT.C(IX)) C(IX+1)=C(IX)
03530 GOTO 630
03540 625 C(IX+1) = (A0*XARRAY(IX) + ((A1*(XARRAY(IX)**1.5))/1.5)
03550 IF (C(IX+1).LT.C(IX)) C(IX+1)=C(IX)
03560 630 Q(IX+1)=C(IX+1)
03570 600 CONTINUE
03580 CALL LINE (XT,Q,NUM+1,1,0,0)
03590 QMIN=0.0
03600 DO 700 IX=1,NUM
03610 C2= (B0*XARRAY(IX) + ((B1/(FT+1.0))*(XARRAY(IX)**(FT+1.0)))
03620 P=B0+ (B1*(XARRAY(IX)**FT))
03630 IF (P.LT.0.0) C2=0.0
03640 IF (QMIN.NE.0.0) GOTO 666
03650 QMIN=ABS(C2)
03660 666 Q(IX+1)=C2+QMIN
03670 700 CONTINUE
03680 CALL LINE (XT,Q,NUM+1,1,0,2)
03690 220 CALL PLOT (0.0,8.0,3)
03700 CALL PLOT (8.0,8.0,2)
03710 CALL PLOT (8.0,0.0,2)
03720 CALL ZYMBOL (0.5,10.5,0.28,IELECT,0.0,20)
03730 CALL ZYMBOL (0.5,10.0,0.28,'E<P*OTENTIAL <V / *VS. <SHE',0.0,27)
03740 CALL NUMBER (7.0,10.0,0.28,POT,0.0,3)
03750 CALL ZYMBOL (5.0,9.5,0.28,'E*P<H',0.0,5)
03760 CALL NUMBER (7.0,9.5,0.28,PH,0.0,1)
03770 IF (L.EQ.6.OR.L.EQ.12.OR.L.EQ.18.OR.L.EQ.24) GOTO 390
03780 CALL ZYMBOL (5.28,9.0,0.28,'E<R =',0.,5)
03790 CALL NUMBER (7.0,9.0,0.28,R,0.0,4)
03800 GOTO 50
03810 390 CALL ZYMBOL (0.5,9.0,0.28,'E<R1 =',0.,6)
03820 CALL NUMBER (1.8,9.0,0.28,R1,0.0,4)
03830 CALL ZYMBOL (4.0,9.0,0.28,'E<R2 =',0.0,6)
03840 CALL NUMBER (5.3,9.0,0.28,R2,0.0,4)
03850 IF (L.EQ.6.OR.L.EQ.12.OR.L.EQ.18.OR.L.EQ.24) IRUS=0
03860 50 CONTINUE
03870 391 CALL ENPLOT
03880 STOP
03890 END
03900 SUBROUTINE REGRESS(XARRAY,YARRAY,N,L,FT,A0,A1,R)
03910 DIMENSION XARRAY(0),YARRAY(0)
03920 SUMX=0.0
03930 SUMY=0.0
03940 SUMXY=0.0
03950 SUMXS=0.0
03960 SUMYS=0.0
03970 YS=0.0
03980 XY=0.0
03990 XS=0.0
04000 IF (L.EQ.6.OR.L.EQ.12.OR.L.EQ.18.OR.L.EQ.24) GOTO 60
04010 WRITE(9,5)
04020 5 FORMAT(1X,/,/,'------------------------------------------------------------
04030+-------------------------')
04040 WRITE(9,15)
04050 15 FORMAT(/,/,25X,'EQUATION OF THE LINE Y = A0 + A1 X')
04060 IF (L.EQ.1.OR.L.EQ.7.OR.L.EQ.13.OR.L.EQ.19) GOTO 10
04070 WRITE (9,25)
04080 25 FORMAT(/,/,30X,'WHERE  Y = CURRENT DENSITY I-I0 / MA CM**-2')
04090 GOTO 20
04100 10 WRITE(9,35)
04110 35 FORMAT(/,/,30X,'WHERE  Y = CURRENT DENSITY I / MA CM**-2')
04120 20 IF (L.EQ.7) GOTO 30
04130 WRITE(9,45) FT,FT
04140 45 FORMAT(/,37X,'X =T** ',F4.1,' / SECS** ',F4.1)
04150 GOTO 40
04160 30 WRITE(9,55)
04170 55 FORMAT(/,37X,'X = EXP(-T) / EXP(-SECS)')
04180 40 WRITE(9,65) N
04190 65 FORMAT(/,/,30X,'NUMBER OF DATA POINTS = ',I5,/,/)
04200 WRITE(9,75)
04210 75 FORMAT(10X,'I------------------------------------------------------------
04220+-----------------------------------------------I')
04230 WRITE(9,85)
04240 85 FORMAT(10X,'I',20X,'I',20X,'I',20X,'I',20X,'I',20X,'I')
04250 WRITE(9,95)
04260 95 FORMAT(10X,'I',10X,'X',9X,'I',10X,'Y',9X,'I',9X,'X*X',8X,'I',
04270+9X,'X*Y',8X,'I',9X,'Y*Y',8X,'I')
04280 WRITE(9,85)
04290 WRITE(9,75)
04300 WRITE(9,85)
04310 60 DO 50 I=1,N
04320 SUMX=SUMX+XARRAY(I)
04330 SUMY=SUMY+YARRAY(I)
04340 YS=(YARRAY(I))**2.0
04350 XY=XARRAY(I)*YARRAY(I)
04360 IF (XARRAY(I).EQ.0.0) XS=0.0
04370 IF (XARRAY(I).EQ.0.0) GOTO 61
04380 XS=(XARRAY(I))**2.0
04390 61 SUMXY=SUMXY+XY
04400 SUMXS=SUMXS+XS
04410 SUMYS=SUMYS+YS
04420 IF (L.EQ.6.OR.L.EQ.12.OR.L.EQ.18.OR.L.EQ.24) GOTO 50
```

```
04420 IF (L.EQ.6.OR.L.EQ.12.OR.L.EQ.18.OR.L.EQ.24) GOTO 50
04430 WRITE(9,105) XARRAY(I),YARRAY(I),XS,XY,YS
04440 105 FORMAT(10X,'I',3X,G14.5,3X,'I',3X,G14.3,3X,'I',3X,G14.6,
04450+3X,'I',3X,G14.6,3X,'I',3X,G14.6,3X,'I')
04460 WRITE(9,85)
04470 50 CONTINUE
04480 IF (L.EQ.6.OR.L.EQ.12.OR.L.EQ.18.OR.L.EQ.24) GOTO 70
04490 WRITE(9,75)
04500 WRITE(9,115) SUMX
04510 115 FORMAT(/,/,/,25X,'SUM X      = ',G14.5)
04520 WRITE(9,125) SUMY
04530 125 FORMAT(/,/,25X,'SUM Y      = ',G14.3)
04540 WRITE(9,135) SUMXS
04550 135 FORMAT(/,/,25X,'SUM (X*X)  = ',G14.6)
04560 WRITE(9,145) SUMXY
04570 145 FORMAT(/,/,25X,'SUM (X*Y)  = ',G14.6)
04580 WRITE(9,148) SUMYS
04590 148 FORMAT(/,/,25X,'SUM (Y*Y)  = ',G14.6)
04600 70 A0=((SUMY*SUMXS)-(SUMX*SUMXY))/((N*SUMXS)-(SUMX**2.0))
04610 A1=((N*SUMXY)-(SUMX*SUMY))/((N*SUMXS)-(SUMX**2.0))
04620 R=((N*SUMXY)-(SUMX*SUMY))/SQRT(((N*SUMXS)-(SUMX**2))*((N*SUMYS)-(SUMY**2.0
04630+)))
04640 IF (L.EQ.6.OR.L.EQ.12.OR.L.EQ.18.OR.L.EQ.24) GOTO 80
04650 WRITE(9,155) A0
04660 155 FORMAT(/,/,/,33X,'A0 = ',G14.6)
04670 WRITE(9,165) A1
04680 165 FORMAT(/,/,33X,'A1 = ',G14.6)
04690 IF (L.EQ.7) GOTO 177
04700 WRITE(9,175) A0,A1,FT
04710 175 FORMAT(/,/,22X,'EQUATION :  I = ',G14.6,' + ',G14.6,' T** ',F4.1)
04720 GOTO 179
04730 177 WRITE(9,178) A0,A1
04740 178 FORMAT(/,/,22X,'EQUATION :  I = ',G14.6,' + ',G14.6,'  EXP(-T) ')
04750 179 WRITE(9,185) R
04760 185 FORMAT(/,/,9X,'CORRELATION COEFFICIENT R = ',F6.4)
04770 WRITE(9,195)
04780 195 FORMAT(/,/,10X,'**********************************************************
04790+**********************************************')
04800 80 RETURN
04810 END
```

2. FRAM (Program to control the Solartron Frequency Response Analyser (FRA)).

```
1 CALL"IDENT",0,0
5 CLEAR250:GRAPH1:CALL"WRITE8",2,1,3,2
7 ?CHR$(17):REM NO PAGING
10 DIM FR(200),ZR(200),ZI(200),RR(17),CC(17),MC$(15),MC(15)
13 CF=3:REM DEFAULT CONFIG
15 PI=3.14159265
20 READ M$,SY$,FO$
25 FORI=0TO14:READMC$(I),MC(I):NEXT
26 FOR I=1TO15:READ RR(I):NEXT
28 FOR I=1TO15:READ CC(I):NEXT
29 FOR I=0TO15:CC(I)=CC(I)/1E12:NEXT
30 Y=30:GOSUB2100
35 PRINT"SWITCH ON SOLARTRON & LOAD DATA DISC TO DRIVE A . . "
40 INPUT"TO CONTINUE TYPE <CR>";R$
45 GOSUB6850:FILES0
48 GOSUB 4030:REM FILES
50 GOSUB 8000:MC(4)=MC(4)*VV:REM PARAM
51 ON BREAK GOTO100
55 GOSUB 1000:REM IDENT/RUN
60 PRINT"FRAM COMPLETE"
70 FILES3:CALL"WRITE8",2,1,3,2
80 R$=GET$(0)
82 IF R$="T" OR R$="T" THEN GOSUB7000
84 IF R$="P" OR R$="P" THEN GOSUB7500
86 IF R$="R" OR R$="R" THEN GOTO45
88 IF R$="0" THEN ERASE FO$:PRINTFO$;": ""FILE ERASED":GOTO80
90 END
100 GOSUB4100:GOTO70
800 DATA "FREQUENCY RESPONSE ANALYSIS V1.1C.          (C) CDW 1979                    CONFIGURATIONS 0(ORIG),1, 2 & 3(DEFAULT
801 DATA "FRA V1.1C"
804 DATA "LST:"
805 DATA FMAX,1E4,FMIN,1,DFLIN,100,DFLOG,1,VOUT,0.01
806 DATA BIAS,2,KBD,2,SAM,4,SWC,3,RAN,8,MODE,0,CH,3,DM,1,DLY,1,INT,1
807 DATA101,221,472,1005,2180,4810,10080,22050,47200,100300,217700,468400,988E3,2.04E6,4.545E6
808 DATA 25,25,25,25,25,25,25,25,25,25,25,25,25,25,25
1000 REM IDENT/RUN
1005 IF FO$<>"LST:" THEN INPUT"LABEL? (Y/N)";R$
1007 IF R$="N" OR R$="" THEN GOTO1025
1010 IF DT$=""THENINPUT"DATE:  ";DT$
1015 INPUT"TIME:  ";TI$:INPUT"SAMPLE ";SA$
1020 INPUT"COMPOSITION ";CO$:INPUT"ELECTRODES  ";EL$
1021 INPUT"SAMPLE LENGTH (CM)";LE$:INPUT"SAMPLE AREA (CM 2)";AR$
1022 INPUT"CELL ATMOSPHERE";AT$:INPUT"TEMPERATURE";TM$
1023 INPUT"EXCESS CAPACITANCE (PF)";CXS$:IFCXS$<>"" THEN CXS=CXS$+"E-12":INPUT "EXCESS CONDUCTANCE (MHO)";GXS$
1024 INPUT"REMARKS";RE$
1025 IFRI=0THENINPUT"MEASURING RESISTOR (OHMS)";RR(0)
1027 IF RR(0)<>0 THEN INPUT "MEASURING CAPACITOR (PF)";CC(0):CC(0)=CC(0)/1E12
1030 INPUT "CONFIGURATION (IF NOT 3)";CF$:IF CF$<>"" THEN CF=VAL(CF$)
1035 IF CF<>0 AND CF<>1 AND CF<>2 AND CF<>3 THEN GOTO1030
1040 IF CF>0 AND RR(0)=0 THEN GOTO1025
1045 IF PI(0)=0 THEN RI=1
1100 REM RUN
1102 PRINT"PROGRAMMING SOLARTRON";
1105 GOSUB5225:GOSUB5500:REM PROGRAM SOL
1106 IF RR(0)=0 AND CF=0 THEN GOSUB9000:GOSUB9500
1107 INPUT"<CR> TO CONTINUE";R$
1108 PF=8:IFRI<>0THENRI=1
1110 NR=0:GRAPH1:GOSUB 5250: REM SINGLE
1115 GOSUB5020:REM GET RESULTS
1120 REM CHECK FOR OFF
1122 EN=-1
1125 XA=2:XM=98:XD=0:GOSUB6000
1130 IF XD<>0 THEN GOSUB 5250:EN=0: REM SINGLE
1135 GOSUB 5400:REM CALC
1136 FR(NR)=FR:ZR(NR)=ZR:ZI(NR)=ZI:NR=INT(NR+1)
1137 IF NR>200 THEN EN=-1:GOSUB5225:REM OFF
1138 PRINT FR,ZR,ZI
1140 GOSUB 2000: REM GRAPHICS
1145 IF NOT EN THEN 1115
1150 GOSUB4100:REM SAVE
1160 RETURN
2000 REM GRAPHICS
2005 IFZR<00RZI>0THEN RETURN
2010 X=ZR*PF:Y=-ZI*PF:IFX>750RY>50THEN GOTO2020
2015 PLOT X+2,Y+6,2: RETURN
2020 GRAPH1:PF=PF/2:GOSUB5150:GOSUB2200
2025 FOR PO=0TONR-1:ZR=ZR(PO):ZI=ZI(PO):GOSUB2005:NEXT:RETURN
2100 REM CH PLOT
2105 FOR P=1TOLEN(M$):PLOTX,Y,ASC(MID$(M$,P,1)):X=X+2:IFX>78THENX=0:Y=Y-2
2110 NEXT:RETURN
2200 REM BORDER
2210 FOR L=0 TO 39: PLOT L*2,5,143:PLOT L*2,58,143:NEXT
2220 FOR L=2 TO 19: PLOT 0,L*3,191:PLOT 78,L*3,191:NEXT
2300 RETURN
4000 REM FILES
4005 REM CHANGE DISK
4010 FILES3:REM CLOSE OUTPUT FILE
4015 PRINT"FILE ";FO$;" CLOSED"
4020 PRINT:?"CHANGE DISK ON DRIVE B - <CR> WHEN DONE"
4025 INPUTR$:FILES0
4030 REM ENTRY TO CHANGE FILE
4035 ?:?:?:INPUT"NAME OUTPUT FILE";R$
4040 IFR$=""THEN 4055
4045 IF LEFT$(R$,1)="*"THEN FO$=MID$(R$,2):GOTO 4055
4050 FO$ = "A:"+LEFT$(R$,8)+".SOL"
4055 FILES2,FO$
4058 VV=1
4060 ?:INPUT"SOL OUTPUT DIVIDED BY 100 Y/N";VV$
4065 IF VV$="Y" OR VV$="Y" THEN VV=100
4070 RETURN
4100 REM SAVE RESULTS
4110 PRINT#,"0,",SY$
```

```
4112 IF MC(5)<>0 THEN PRINT#;"BIAS,";MC(5)
4113 PRINT#;"CFG,";STR$(CF)
4114 IF RE$<>"" THEN PRINT#;"REM,";RE$
4115 IF SA$<>"" THEN PRINT#;"IDN,";SA$
4120 IF DT$<>"" THEN PRINT#;"DTE,";DT$
4125 IF TI$<>"" THEN PRINT#;"TIM,";TI$
4126 IF RI=0 THEN PRINT#;"RST,";STR$(RR(0)):PRINT#;"CST,";STR$(CC(0))
4127 IF CXS$<>"" THEN PRINT#;"CXS,";CXS$:PRINT#;"GXS,";GXS$
4130 IF CO$<>"" THEN PRINT#;"CON,";CO$
4135 IF EL$<>"" THEN PRINT#;"ELE,";EL$
4136 IF LE$<>"" THEN PRINT#;"LEN,";LE$
4140 IF AR$<>"" THEN PRINT#;"ARE,";AR$
4141 IF TM$<>"" THEN PRINT#;"TEM,";TM$
4142 IF AT$<>"" THEN PRINT#;"ATM,";AT$
4143 IF MC(4)<>0 THENPRINT#;"VLT,";STR$(MC(4))      ELSE PRINT#;"VLT,DEF"
4144 PRINT#;"0,STX"
4145 FOR I=0 TO NR-1
4146 OP(1)=FR(I):OP(2)=ZR(I):OP(3)=ZI(I)
4148 FOR P=1TO3
4149 PO(P)=(LEFT$(STR$(OP(P)),1)="-")
4150 OP$(P)=RIGHT$(STR$(OP(P)),(LEN(STR$(OP(P)))-PO(P)-1))
4152 NEXTP
4153 PRINT#10,OP$(1);",";OP$(2);",";OP$(3)
4155 NEXTI
4160 PRINT#;"ETX,";SA$;" ";TM$
4165 RETURN
5000 REM COLLECTION/CALCULATIONS
5005 GOSUB 5250:REM SINGLE
5006 CALL"WAIT",1
5007 CALL"WAIT",1
5010 CALL"TEST",2,1,2,5,VARADR(B5):IF B5<>1 GOTO 5010:REM WAIT
5015 RETURN
5020 REM ENTRY
5025 GOSUB 5010:REM WAIT
5027 REM SAVE SWEEP STATE
5028 XA=8:XM=18:XD=0:GOSUB6000:SW=XD
5030 D=135:F=4:GOSUB6630:FR=D
5035 GOSUB 5100
5040 D= 65:F=1:GOSUB6640:AX=D=VV
5041 D= 69:F=1:GOSUB6640:BX=D=VV
5042 D=129:F=1:GOSUB6640:AY=D=VV
5043 D=133:F=1:GOSUB6640:BY=D=VV
5044 IF MC(4)<>0 THEN GOSUB5050
5045 RETURN
5050 REM TEST VX,VX
5053 VX=SQR(AX=AX+BX=BX)
5055 VR=(VX/VV)/MC(4):IF ABS(1-(VR=VV))>.1 THEN PRINT "VOLTAGE LEVEL AT X IS";(VX/VV);"VOLTS="
5060 IF VR<(0.5/VV) THEN PRINT"=CHECK CONNECTIONS="
5062 VY=SQR(AY=AY+BY=BY)
5064 IF (VY/VV)=>10 THEN PRINT SPC(6);"=VOLTAGE AT Y=";(VY/VV);"VOLTS="
5066 IF (VY/VV)>14 THEN INPUT"MEASUREMENT INVALID";R$
5075 RETURN
5100 REM TEST R
5105 D=192:F=1:GOSUB6630:REM READ R(Y/X)
5110 IF D<.095 AND RI<15 THEN GOSUB9600:GOSUB5200:GOSUB5000:GOTO5100
5116 XA=8:XM=16:XD=SW:GOSUB6000:REM RELEASE HOLD
5120 RR=RR(RI):CC=CC(RI)
5130 GOSUB5150:GOSUB2100
5140 RETURN
5150 REM LABEL RS,CS
5160 R$="RS"+STR$(RR):S$="                    ":C$="CS"+STR$(CC)
5165 M$=R$+S$+C$
5170 X=2:Y=55
5190 RETURN
5200 REM HOLD
5205 XA=8:XD=1:XM=16:GOSUB6000
5210 IFXM<0THENER=-XM:LL=5200:GOSUB9030
5215 RETURN
5225 REM OFF
5230 XA=8:XD=0:XM=16:GOSUB6000
5235 IFXM<0THENER=-XM:LL=5225:GOSUB9030
5240 RETURN
5250 REM SINGLE
5255 XA=11:XD=2:XM=16:GOSUB6000
5260 IFXM<0THENER=-XM:LL=5250:GOSUB9030
5265 RETURN
5300 REM STATS
5305 PRINT"STATS NOT YET AVAILABLE":RETURN
5400 REM CALCS
5405 REM Y/X = A + JB; Z(0) = RR + JRX
5410 REM CELL IS Y; GENERATOR IS X
5420 REM CONFIGURATION SELECT.
5422 IF CF=0 THEN AS=AX-AY:BS=BX-BY:    AU=AY : BU=BY: GOTO 5440
5424 IF CF=1 THEN AS=AY:BS=BY:          AU=AX-AY:BU=BX-BY:GOTO5440
5426 IF CF=2 THEN AS=AY-AX:BS=BY-BX:    AU=AX:BU=BX:GOTO5440
5428 IF CF=3 THEN AS=AY:BS=BY:AU=AX:  BU=BX:GOTO5440
5430 STOP
5440 AB=  AS=AS+BS=BS
5445 AA=  (AU=AS+BU=BS)/AB
5450 BB=  (AS=BU-AU=BS)/AB
5455 CM=2*PI*FR:RR=RR(RI):CC=CC(RI)
5460 GS=1/RR:OS=CM*CC:SS=GS=GS+OS=OS
5465 AZ=GS/SS:BZ=-OS/SS
5470 ZR=  AA=AZ-BB=BZ
5475 ZI=  (AZ=BB+BZ=AA)
5495 RETURN
5500 REM PROGRAM SOLARTRON
5505 REM MOS STORES
5510 XA=0:F=1:D=MC(0):GOSUB6390:?".";
5515 XA=70:F=1:D=MC(1):GOSUB6390
5520 XA=198:F=1:D=MC(2):GOSUB6390:?".";
5525 XA=199:F=2:D=MC(3):GOSUB6390
5530 XA=1:F=3:D=MC(4):GOSUB6390:?"."
5550 REM LATCH STORES
5555 REM TX MOS TO LATCH
5560 XA=0:FORXC=0TO1:XD=XC:XM=16:GOSUB6000:NEXT
5565 XA=2:XD=MC(5):XM=16:GOSUB6000
5570 FOR XA=4TO9:XM=16:XD=MC(XA):GOSUB6000:NEXT
5575 FOR XA=11TO15:XM=16:XD=MC(XA-1):GOSUB6000:NEXT
5580 RETURN
6000 REM IOBYTE
```

```
6010 REM ENTRY-XM=MODE: XA=ADDRESS
6020 REM       XD=DATA
6030 REM EXIT- ERROR IF XM -VE
6040 REM       XD=DATA
6050 REM
6060 REM CHECK ADDRESS
6070 IF XA=2 THEN6100
6080 IF XA>254 OR XA<6 THEN XM=-1:RETURN
6090 REM CHECK DATA
6100 IF XD>254 OR XD<0 THEN XM=-2:RETURN
6110 IF XM=32 THEN 6160
6120 IF XM=16 THEN XM=XM+15-XD:GOTO6160
6130 IF XM=0 THEN XM=15-XD:GOTO6160
6140 IF XM=48 THEN 6160
6150 XM=-3:RETURN
6160 XE=0
6170 CALL"WRITE8",2,1,1,XM:CALL"WRITE8",2,1,0,255-XA
6180 CALL"WRITE8",2,1,3,0:GOSUB5007:CALL"WRITE8",2,1,3,1:GOSUB5006
6190 CALL"READ8",2,1,2,VARADR OOO
6200 IF XD>127 THEN 6230
6210 XE=XE+1:IFXE>3THENXM=-4:RETURN
6220 GOTO 6170
6230 IF XM<30 THEN RETURN
6240 XD=XD/16:XD=15-(XD-INT(XD))*16:RETURN
6250 REM END OF IOBYTE
6260 REM IO  --INPUT & OUTPUT 8 DIGITS
6270 REM ENTRY XM=MODE   XA=ADDRESS
6280 REM       XD(0-7)=DATA (-1INHIBITS)
6290 REM SET XD(0-7)=0 WHEN READING!!
6300 REM EXIT  XD(0-7)=DATA
6310 REM SAVE XM
6320 XM=XM
6330 FORXI=0TO7:IFXD(XI)=-1THEN6370
6340 XD=XD(XI)
6350 GOSUB6000:IFXM<0THENER=-XM:LL=6350:GOSUB9030
6360 XD(XI)=XD:XM=XM
6370 XA=XA+8:NEXT
6380 RETURN:REM END OF IO
6390 REM OUTFORM II
6400 REM ENTRY: D=NO.TO BE OUTPUT TO SOL
6410 REM        F=FUNCTION    " "
6420 REM        XA=FUNCTION ADDRESS(MOS)
6430 REM EXIT:  D FORMATTED IN XD(0-7)
6440 REM        F=ERROR CODE
6450 ON F GOTO 6480,6530,6550
6460 REM FMAX; FMIN; DF LIN
6470 REM NORMALISE
6480 E=0
6490 IFD>=10 THEN D=D=0.1:E=E+1:GOTO6490
6500 IF D<1 THEN D=D*10: E=E-1:GOTO6500
6510 GOTO 6590
6520 REM DELTA F LOG
6530 D=D=0.1:E=-5:GOTO 6590
6540 REM VOLTS OUTPUT
6550 E=0
6560 IFD<1 AND E>-2 THEN D=D*10:E=E-1:GOTO 6560
6570 D=D=0.1:E=E-1
6580 REM FORMAT
6590 FORXI=0TO3:XT=INT(D):XD(XI)=XT
6600 D=10*(D-XT):NEXT
6610 XD(4)=0:XD(5)=0:XD(6)=-1:XD(7)=E+4
6620 XM=0:GOSUB6260:RETURN
6630 REM END OF OUTFORM
6640 REM INFORM
6650 REM ENTRY: MOS ADDRESS IN D
6660 REM        F=FORMAT
6670 REM EXIT:  DATA IN D
6680 FORXI=0TO7:XD(XI)=0:NEXT
6690 XM=32:XA=D:GOSUB6260:D=0
6700 ON F GOTO 6720,6750,6810,6830
6710 REM A;B;R;BIAS
6720 FORXI=0TO5:D=D=10+XD(XI):NEXT
6730 D=D=10*(XD(7)-9):GOTO6770
6740 REM LOGR
6750 FORXI=0TO5:D=D=10+XB(XI):NEXT:D=D=0.001
6760 REM SIGN & OVL
6770 IFXD(6)=1ORXD(6)=5THEND=-D
6780 IFXD(6)=4ORXD(6)=5THENF=-1
6790 RETURN
6800 REM THETA RADIANS
6810 FORIX=1TO7:D=D=10+XD(IX):NEXT:D=D=0.001:RETURN
6820 REM FREQUENCY
6830 FORXI=0TO3:D=D=10+XD(XI):NEXT:D=D=10*(XD(7)-7):RETURN
6840 REM END OF INFORM
6850 REM SETPORT
6860 CALL"WRITE8",2,1,4,11:RETURN
6870 REM PROGRAM SOL LATCH
6880 XJ=1:XA=2:GOSUB6920
6890 FORXA=6TO9:GOSUB6920:NEXT
6900 FORXA=11TO15:GOSUB6920:NEXT
6910 RETURN
6920 XM=16:XD=VAL(MID$(MC$,XJ,1)):XJ=XJ+1:IFXJ=3ORXJ=8THENXJ=XJ+1
6930 GOSUB6000:IFXM<0THENER=-XM:LL=6920:GOSUB9030
6940 RETURN
7000 REM TEMPSET
```

```
7000 REM TEMPSET
7005 REM
7010 PRINT
7015 INPUT"TEMPERATURE (DEG C) ";TA$
7020 TA = INT(VAL(TA$)): GOSUB 7100
7025 IF TK<0 THEN PRINT TA$ "C OUT OF RANGE . . PLEASE RETRY -": GOTO 7010
7030 IF TK<>TA THEN PRINT "CANNOT SET ";TA$;" PLEASE RETRY": GOTO 7010
7035 PRINT "CONTROLLER SET TO "; TK; "±C ---OK Y?"
7040 R$=GET$(500):IF R$="Y"ORR$="Y"THENPRINT:PRINT:PRINT"SETTING CONFIRMED AT ";TA$;"C":END
7050 GOTO 7010
7100 REM CRC TEMPSET
7101 REM ENTRY TA = TEMP REQUIRED
7102 REM EXIT  TK = TEMP SET
7103 REM ERRORS:
7104 REM       TK = -1 TEMP OUT OF RANGE
7105 REM
7110 IFTA>1000 OR TA<0 THEN TK=-1:RETURNELSE TK=0:OUT179,15
7120 IFTA=0THENGOSUB 7300:RETURN
7130 XT$=STR$(INT(TA)):XL=LEN(XT$)-1:XA=3
7140 XT$=LEFT$("0000",4-XL)+RIGHT$(XT$,XL)
7200 FORXI=1TO4:XB=8:XD=VAL(MID$(XT$,XI,1)):TK=TK*10+XD
7210 FORXJ=0TO3
7220 IFXD>=XBTHENXD=XD-XB:XK=32ELSEXK=0
7230 XB=XB/2
7240 OUT 178,XK:CALL"WRITE8",2,1,3,XK+64:CALL"WRITE8",2,1,3,XK
7250 NEXT:NEXT:CALL"WRITE8",2,1,3,128:CALL"WRITE8",2,1,3,0
7270 OUT 178,128:OUT 178,0
7280 RETURN
7300 REM CRC RESET
7310 FORXI=0TO15:CALL"WRITE8",2,1,3,64:CALL"WRITE8",2,1,3,0:NEXT:CALL"WRITE8",2,1,3,128:CALL"WRITE8",2,1,3,0:TK=0:RETURN
7320 REM END OF CRC TEMPSET
7500 PRINT
7520 PRINT"TEMPERATURE PROGRAMMING OPTION":PRINT
7540 INPUT"INITIAL TEMPERATURE";TA
7560 INPUT"  FINAL TEMPERATURE";TB
7570 IF TA>1000 OR TB>1000 THEN PRINT   "TEMPERATURES >1000 ±C NOT ALLOWED":GOTO7540
7580 INPUT"HEATING RATE ±C/MIN";HR
7587 IF HR=0 THEN GOTO7580
7590 PRINT
7600 PRINT"RUN WILL TAKE";ABS(INT((TB-TA)*(1/HR + 1/60)));"MINUTES OK Y?"
7620 R$=GET$(90)
7625 IF R$<>"Y" AND R$<>"Y" THEN GOTO7540
7630 RH=6000/HR:SR=SGN(TB-TA)
7650 FOR TA=TA TO TB STEP SR
7660 R$=GET$(90,RH)
7670 IF R$="S" OR R$="S" THEN GOTO7540
7680 GOSUB 7100
7690 PRINT CHR$(12);" T=";TA;"±C"
7700 NEXT
7800 RETURN
8000 REM SETTINGS
8002 PRINT:?:?
8005 INPUT"DEFAULT SETTINGS (Y/N) ";R$
8010 IF R$="Y" OR R$="" THEN RETURN
8015 REM ENTRY
8020 PRINT"ENTER FUNCTION, VALUE. (END WITH BLANK  LINE)"
8025 INPUTR$,V$: IF R$=""THEN RETURN
8030 FOR I=0 TO 14
8035 IF R$=MC$(I)THEN ON I+1 GOTO 8100,8100,8100,8150,8200,8230,8950,8950,8950,8950,8950,8950,8950,8250,8250
8040 NEXT:GOSUB 8800:GOTO8025
8100 REM FMAX,FMIN,DFLIN
8105 V=VAL(V$)
8110 IFV>999.9E30ORV<1E-4THEN GOSUB 8900 ELSE MC(I)=V
8115 GOTO 8025
8150 REM DFLOG
8155 V=VAL(V$)
8160 IF V>99.99ORV<0.11THEN GOSUB 8900  ELSE MC(I)=V
8165 GOTO8025
8200 REM VOLTS OUT
8205 V=VAL(V$)
8210 IF V>9.99ORV<0.001THEN GOSUB 8900:GOTO8025
8215 IF V>1THENPRINT:?"V = ";V;" VOLTS"
8225 MC(I)=V:GOTO8025
8230 REM BIAS REJECT
8235 IF VAL(V$)=0 THEN MC(I)=0 ELSE MC(I)=2
8240 GOTO8025
8250 REM INTEG/DELAY
8255 V=VAL(V$):IF V<=0 THEN MC(I)=0:GOTO 8025
8257 IF I=13 THEN V=V*10.0
8260 V=INT(LOG(V)*0.43429+0.5)
8265 IF V>3 OR V<0 THEN GOSUB 8900 ELSE MC(I)=V
8270 GOTO 8025
8800 REM ERROR RECOVERY
8805 PRINT"VALID FUNCTIONS ARE:"
8810 FORI=0TO5:PRINT MC$(I);":";:NEXT
8820 PRINTMC$(13);":";MC$(14):PRINT"PLEASE RETRY "
8825 RETURN
8900 PRINT "ERR":RETURN
8950 PRINT"OPTION NOT AVAILABLE"
8955 GOTO8025
9000 REM INCREASE RM
9010 PRINT "INCREASING RM"
9020 CALL"WRITE8",2,1,3,8:FOR L=0TO150:NEXT:CALL"WRITE8",2,1,3,0
9030 RI=RI+1
9040 RETURN
9500 REM SETTING UP
9505 PRINT
9510 PRINT"CONNECT CELL - X:CELL;Y:GEN"
9515 PRINT"NOW SETTING RM TO MIN:CHECK!"
9520 CALL"WRITE8",2,1,3,4:FORL=0TO1500:NEXT:CALL"WRITE8",2,1,3,0
9525 RETURN
9600 INPUT"INCREASE RS TYPE NEW VALUE";RI
9610 IF RI<>0 THEN RR(RI)=RI
9620 RETURN
```

3. LISTN1 (Program to plot complex plane impedance spectra using data obtained from FRA).

```
10 REM  LISTN
20 TEXT:PRINT CHR$(17):REM FASTNG
40 PRINT CHR$(12):REM CLEAR SCREEN
60 PRINT"LISTN  PLOTTING  PROGRAM  N.B.HUSSI 1981-----
80 CLEAR 1000:PI=3.14159265
100 DEF FNI(O)=INT(10^I*O+0.5)/10^I
120 DEF FNL(L)=0.43429445*LOG(L)
140 DEF FNO(O)=10^INT(FNL(O))
160 DEF FNP(P)=VAL(STR$(FNI(P/FNO(P)))+"E"+STR$(INT(FNL(P))))
180 DEF FNS(S)=SGN(S)*FNP(ABS(S))
200 DIM F(200),ZR(200),ZI(200),XX(200),YY(200),A$(20),B$(20),C$(20),X(200),Y(200)
240 GOSUB700:REM STRING READING
260 IO=0:GOSUB 500:REM FILENAME
280 GOSUB1000:REM FILEHEAD READ
300 GOSUB2000:REM FILEHEAD PRINT
320 GOSUB3000:REM INPUT CORR.FACTORS
340 GOSUB3500:REM FILEREADING DATA
360 RPL$="ZPLOT":REM FIRST PLOT Z*
380 GOTO 4060:REM QUANT/MODE SELECTION
500 REM FILENAME*********************************************
520 B$="B:":REM DEVICE
540 INPUT "WHICH FILE  ";F$:IF F$="" THEN END
560 IF LOOKUP(B$+F$+".SOL")=-1 THEN GOTO680
580 PRINT"WHICH SIDE OF DISC A,B,C,D ?"
600 B$=GET$(0)+":"
620 IF LOOKUP(B$+F$+".SOL")=-1 THEN GOTO680
640 PRINT"DIRECTORY OF SOLARTRON FILES:":DIR B$+"*.SOL":?
660 GOTO500
680 RETURN
700 REM READ DATA*************************************
720 FOR N=0 TO 17:READ A$(N),C$(N):NEXT
740 REM
760 REM
780 RETURN
800 REM DATA
820 DATA "IDN","SAMPLE          :"
830 DATA "COM","COMPOSITION     :"
840 DATA "ELE","ELECTRODES      :"
850 DATA "ATM","CELL ATMOS      :"
860 DATA "TEM","TEMPERATURE     :"
870 DATA "DTE","DATE            :"
880 DATA "TIM","TIME            :"
890 DATA "CFG","CONFIGURATION:"
900 DATA "VLT","VOLTAGE         :"
910 DATA "BIA","CELL BIAS       :"
920 DATA "LEN","SAMPLE LENGTH:"
930 DATA "ARE","SAMPLE AREA     :"
940 DATA "CST","C STANDARD      :"
950 DATA "RST","R STANDARD      :"
960 DATA "CXS","C EXCESS (PF):"
970 DATA "GXS","G EXCESS (MHO):"
980 DATA "LBL","GRAPH LABEL     :"
990 DATA "REM","REMARKS         :"
1000 REM FILEHEAD READING*****************************************
1020 BF$=B$+F$+".SOL"
1040 OPEN BF$
1060 INPUT#;A$,B$
1080 IF B$="STX"THEN GOTO1460
1100 IF A$="CFG"THEN CF=VAL(B$)
1120 FOR N=0 TO 19
1140 IF A$=A$(N) THEN B$(N)=B$
1150 NEXT:GOTO1060
1460 LB$=F$+"      "+B$(0)+"  "+B$(4)+"  "+B$(3)+"  "+B$(2)
1480 RETURN
2000 REM FILEHEAD PRINT*******************************************
2020 TEXT
2040 FOR N=0 TO 17
2060 PRINT#10,C$(N);B$(N)
2080 NEXT
2380 RETURN
3000 REM CORRECTION FACTORS***************************************
3040 IF B$(14)<>"" THEN CX=VAL(B$(14)) ELSE INPUT"EXCESS CAPACITANCE  (PF)  ";CIN:CX=CIN/1E12
3060 IF B$(15)<>"" THEN GX=VAL(B$(15)) ELSE IF CIN<>0 THEN INPUT"EXCESS CONDUCTANCE (MHO) ";GX
3080 LE=VAL(B$(10)):AR=VAL(B$(11)):I=2
3100 IF LE<>0 AND AR<>0 THEN LA=FNS(VAL(B$(10))/VAL(B$(11))):PRINT"L/A (1/CM) :";LA ELSE INPUT"GEOM. FACTO
3120 IF LA>0 THEN LA=FNS(LA) ELSE LA=1
3140 RETURN
3500 REM FILEREADING*********************************************
3520 ON EOF GOTO 3760
3540 INPUT#;A$,B$,C$
3560 A=VAL(A$):B=VAL(B$):C=VAL(C$)
3580 REM CORRECTIONS  L/A,CXS,GXS
3600 W=2*PI*A
3620 D=B*B+C*C
3640 B=(B/D-GX )*LA
3660 C=(C/D-CX*W)*LA
3680 D=B*B+C*C
3700 F(N)=A:ZR(N)=B/D:ZI(N)=C/D
3720 IF A>0 THEN M=M+1
3740 GOTO3540
3760 RETURN
4060 REM QUANTITY SELECTION***************************************
4020 LRP$=RPL$
4040 INPUT"QUANTITY TO BE PLOTTED";RPL$
4060 ON ERROR
4080 IF RPL$=""THEN RUN 40
4090 IF RPL$="+" THEN GOTO260
4100 LH$=LEFT$(RPL$,1)
4140 RH$=RIGHT$(RPL$,LEN(RPL$)-1)
4160 IF LH$="S" THEN GOSUB5000:GOTO4040
4600 REM CALCULATIONS*********************************************
4620 FOR N=0 TO M-1
4640 W=2*PI*F(N):ZR=ZR(N):ZI=ZI(N)
4660 IF LEFT$(RPL$,1)="Z"THEN XX(N)=ZR:YY(N)=-ZI:GOTO4840
4680 MI=ZR*W:MR=-ZI*W
4700 IF LEFT$(RPL$,1)="M" THEN XX(N)=MR:YY(N)=MI    :GOTO4840
4720 ZZ=ZR*ZR+ZI*ZI : YR=ZR/ZZ : YI=-ZI/ZZ
4740 IF LEFT$(RPL$,1)="Y"THEN XX(N)=YR:YY(N)=YI    :GOTO4840
```

```
4740 IF LEFT$(RPL$,1)="Y"THEN XX(N)=YR:YY(N)=YI      GOTO4940
4760 KI=-YR/W : KR=YI/W
4780 IF LEFT$(RPL$,1)="K"THEN XX(N)=KR:YY(N)=-KI:GOTO4940
4800 GOSUB9700:GOTO4000
4840 PLOT75,0,STR$(N):NEXT
4860 XQ=0:YQ=0:FOR P=0 TO M-1
4880 IF XQ<XX(P) THEN XQ=XX(P)
4900 IF YQ<YY(P) THEN YQ=YY(P)
4920 NEXTP
4940 IF XQ/75>YQ/50 THEN SP=XQ ELSE      SP=YQ*1.5
4960 SC=1:XS=0:YS=0
4980 GOSUB5000:GOTO4000
5000 REM PLOT SELECTION*********************************************
5020 IF RIGHT$(RPL$,4)="PLOT"THENGOSUB5240
5040 IF RIGHT$(RPL$,5)="PRINT"THENGOSUB7000
5060 IF RIGHT$(RPL$,4)="FLOG"THENGOSUB6500
5080 IF RIGHT$(RPL$,4)="FLIN"THENGOSUB8800
5100 IF RIGHT$(RPL$,4)="LIST"THENGOSUB8500
5120 IF RIGHT$(RPL$,4)="HIFT"THENGOSUB7300
5140 IF RIGHT$(RPL$,4)="CALE"THENGOSUB7500
5160 IF RIGHT$(RPL$,4)="DRAW"THENGOSUB9000
5180 IF RIGHT$(RPL$,4)="FILE"THENGOSUB8000
5190 IF RIGHT$(RPL$,6)="DRAWJJ"THENGOSUB12000
5200 PRINT:PRINT RPL$;SPC(2);LB$;SPC(2);B$(16):PRINT
5220 RETURN
5240 SF=SP:REM SET SF
5500 REM PLOT*******************************************
5520 GOSUB9520:GOSUB9560
5530 T=0
5540 I=1:IF SC>10 THEN I=2
5560 FOR P=0 TO M-1
5580 X=QX(P)*75/SF-3*XS)*SC:Y=(YY(P)*75/SF-3*YS)*SC
5600 IF X<0  OR X>75 THEN GOTO 5680
5620 IF Y<-6 OR Y>50 THEN GOTO 5680
5640 IF Y<0 AND Y>-3 THEN GOTO 5680
5660 PLOTX+2,Y+6,2
5665 X(T)=XX(P):Y(T)=YY(P)
5668 NP=T
5670 T=T+1
5680 NEXT P
5720 GOSUB6000:RETURN
6000 REM X AXIS LABELS*********************************************
6020 FOR P=0 TO 1
6040 QP=(P*75/SC+XS*3)*SF)/75
6060 GOSUB 6300:REM S.C.E.
6080 X=P*(80-2*LEN(QP$)):Y=5
6100 PLOT X,Y,QP$
6110 XP(P)=VAL(QP$)
6120 NEXTP
6140 FOR P=0 TO 1
6160 QP=(P*50/SC+YS*3)*SF)/75
6180 GOSUB6300:REM S.C.E.
6200 X=0:Y=7+P*50
6220 PLOT X,Y,QP$
6230 YP(P)=VAL(QP$)
6240 NEXTP
6260 RETURN
6300 REM STRING CHAR.ELIMINATION***********************************************
6320 REM ENTRY QP,EXIT QP$
6340 QS$="":REM INITIALISE
6360 IF QP>=0 THEN QP=FNS(QP)
6380 QP$=STR$(QP)
6400 FOR Q=1 TO LEN(QP$)
6420 Q$=MID$(QP$,Q,1)
6440 IF Q$=" " OR Q$="+" THEN Q$=""
6460 QS$=QS$+Q$:NEXT:QP$=QS$:QS$=""
6480 RETURN
6500 REM FLOG*******************************************
6520 GOSUB9520:GOSUB9600
6540 PLOT70,5,"LOG F"
6560 FOR P=0 TO M-1
6580 X=60-10*FNL(F(P)):Y=SC*YY(P)*50/YQ
6600 IF MID$(RPL$,2,3)="LOG" THEN IF Y>0THEN Y=50+10*(FNL(YY(P)/YQ)) ELSE GOTO6700
6620 IF X<0  OR X>79 THEN GOTO6700
6640 IF Y<-6 OR Y>50 THEN GOTO6700
6660 IF Y<0 AND Y>-3 THEN GOTO6700
6680 PLOT X,Y+6,2
6700 NEXT P
6720 IF MID$(RPL$,2,3)="LOG" THEN RETURN
6740 GOSUB6300:REM S.C.E.
6760 X=0:Y=57:PLOTX,Y,QP$
6780 RETURN
7000 REM PRINTING***************************************************
7020 PRINTER3:REM AMADEX PRINTER
7040 LNULL12,32 :REM MARGIN
7060 PRINT#2
7080 PRINT#2,"FILE          :";CHR$(14);F$;CHR$(15)
7100 PRINT#2
7120 IO=2:REM PRINTER
7140 GOSUB8500
7180 REM
7200 IO=0:REM SCREEN
7220 LPRINTCHR$(12)
7240 LNULL 0:REM NO MARGIN
7260 RETURN
7280 GRAPH1:GRAPH0:RETURN
7300 REM SHIFTING***************************************************
7320 FOR P=5TO70 STEP3:PLOTP,5,0:NEXT
7340 PRINT:INPUT"X-SHIFT <-  (MAX 25) ";XS
7350 INPUT"Y-SHIFT ^   (MAX 15) ";YS:YS=-YS
7360 RPL$=LRP$
7380 XS=INT(XS)
7400 GOTO5000
7500 REM SCALING****************************************************
```

```
7520 PRINT
7540 INPUT"SCALING FACTOR";SC
7560 RPL$=LRP$
7580 I=0:SC=FNS(SC)
7600 GOTO5000
8000 REM CREATING FILES*****************************************
8020 RESET
8040 PL$=F$+".PLT"
8060 PRINT"CREATING PLOTTING DATA FILE:";PL$
8080 INPUT"SPECIFY ALTERNATIVE NAME";RL$
8100 IF RL$<>"" THEN PL$=RL$
8120 IF LEFT$(RIGHT$(PL$,4),1)<>"." THEN PL$=PL$+".PLT"
8140 PRINTSPC(26);PL$
8160 FOR P=0 TO 2000:NEXT
8180 PRINT"SPECIFY TYPE OF PLOT FILE REQUIRED   :"
8200 PRINT"P FOR COMPLEX PLOT : R FOR REAL SPECTRUM! FOR IMAG SPECTRUM :B FOR BOTH SPECTRA"
8220 P$=GET$(P0)
8240 CREATEPL$
8260 QUOTE #10
8280 FOR P=0 TO M-1
8300 IF P$="P" OR P$="P" OR P$=" " THEN PRINT#10,XX(P),YY(P)
8320 IF P$="R" OR P$="R" OR P$="B"  OR P$="B" THEN PRINT#10,FNL(F(P)),XX(P)
8340 IF P$="I" OR P$="I" OR P$="B" OR P$="B" THEN PRINT#10,FNL(F(P)),YY(P)
8360 NEXT P
8380 CLOSE
8400 QUOTE #10,0
8420 PRINTERM,1
8480 RETURN
8500 REM LISTING DATA*******************************************
8510 TEXT:PRINT
8520 GOSUB2000
8530 FOR P=0TO3:PRINT#10:NEXT
8540 PRINT#10," FREQ.",SPC(3);LEFT$(RPL$,1);"R",SPC(2);"/";LEFT$(RPL$,1);"I/":PRINT#10
8580 FOR P=0 TO M-1:PRINT#10,F(P),XX(P),YY(P)
8600 NEXTP
8620 RETURN
9000 REM DRAWING GRAPHS*****************************************
9020 PRINTERM,1:REM HP PLOTTER
9040 LPRINT CHR$(3);"IN;IP820,800,10820,6800;SC0,10000,0,6000;"
9060 IF XQ/25>YQ/15 THEN PF=XQ ELSE PF=YQ#25/15
9080 PU=PF/FND(PF):IF PU<=2.5 THEN PP=2.5ELSEIF PU<=5 THEN PP=5 ELSE PP=12.5
9100 PO=FND(PF):PF=PP#FND(PF)
9120 SF=PF:GOSUB5500
9140 PRINT:PRINT"PLOTTER: LOWER LEFT AND UPPER RIGHT OK?"
9160 IF GET$(P0)="Y" THEN GOSUB10500:GOSUB11020
9180 RETURN
9500 REM BORDER*************************************
9520 GRAPH1:PLOT0,5,207:LINE 78,5,207:PLOT 0,58,207:LINE 78,58,207
9540 RETURN
9560 PLOT 0,6,255:LINE 0,58,255:PLOT78,58,255:LINE78,6,255
9580 RETURN
9600 FOR P=0 TO 6:PLOT 10#P,5,54-P:NEXT
9620 RETURN
9700 REM VALID FUNCTIONS****************************************
9710 PRINTCHR$(12)
9720 PRINT"VALID FUNCTIONS ARE MADE FROM A PREFIX:":?
9740 TEXT
9760 PRINT"    Y FOR ADMITTANCE"
9780 PRINT"    Z FOR IMPEDANCE"
9800 PRINT"    K FOR PERMITTANCE"
9820 PRINT"    M FOR MODULUS"
9840 PRINT
9860 PRINT"FOLLOWED BY A SUFFIX:"
9880 PRINT
9900 PRINT" PLOT FOR COMPLEX PLANE PLOT"
9920 PRINT" FLOG FOR LOGARITHMIC SPECTUM"
10020 PRINT" LIST FOR LISTING ON SCREEN"
10040 PRINT" DRAW FOR DRAWING ON PLOTTER"
10050 PRINT"DRAWJJ FOR DRAWING ON JJ PLOTTER"
10060 PRINT" FILE FOR PLOTTING FILE"
10080 PRINT"PRINT FOR PRINTING DATA"
10100 PRINT
10120 PRINT"OTHER FUNCTIONS ARE:":?
10140 PRINT"SHIFT FOR COMPLEX PLOT SHIFT"
10160 PRINT"SCALE FOR PLOT MAGNIFICATION"
10180 PRINT"+     FOR ADDING NEW FILE"
10190 PRINT
10200 RETURN
10500 REM PLOTTING DATA ON PLOTTER*******************************************
10520 LX=0:LY=0
10540 LPRINT"SM,;"
10560 FOR P=0 TO M-1
10580 X=(XX(P)/PF-XS/25)#SC#1E4:X=INT(X)
10600 Y=(YY(P)/PF-YS/25)#SC#1E4:Y=INT(Y)
10620 IF ABS(X-LX)<10 AND ABS(Y-LY)<20 THEN GOTO10740
10640 IF X<-800 OR Y<-800 OR X>10000 OR Y>6000 THEN GOTO10740
10660 LPRINT"PA";STR$(X);",";STR$(Y);";"
10680 FL=INT(20#FNL(F(P))+0.5)/20
10700 IF ABS(FL-INT(FL+.5))<.025  THEN LPRINT"CP0,0;LB"CHR$(FL;CHR$(3)
10720 LX=X:LY=Y
10740 PRINT F(P),XX(P),YY(P)
10760 NEXT
10780 LPRINT"SM;"
10800 IF XS<>0 OR YS<>0 THEN LPRINT"PA10300,800;DI0,1;LB";"SHIFT X,Y=";XS;",";YS;CHR$(13);CHR$(3);"D
10820 IF SC<>1 THEN LPRINT"PA10300,4000;DI0,1;LB";"SCALING=";SC;CHR$(13);CHR$(3);"DI;"
10840 RETURN
11000 REM LABELLING GRAPH***************************************
11020 I=2:REM DEC POINT
11040 FOR P=0TO5
11060 FOR P=0 TO 1
11080 LPRINT"PA0,0;PD;PA10000,0,10000,6000,0,6000,0,0;PU;"
11100 NEXT
11120 FOR P=0 TO 5
11140 Q=((.2#P/SC+XS/25)#PF)
11160 IF Q=0 THEN Q$="   0" ELSE Q$=STR$(FNS(Q))
11180 LPRINT"PA";STR$(2E3#P);STR$(0);";";"XT;CP-4,-1;LB";Q$;CHR$(3)
11200 NEXTP
```

```
11220 FOR P=1TO3
11240 LPRINT"PA";"10000";STR$(2E3*P);";YT;";NEXTP
11260 FOR P=1TO4
11280 LPRINT"PA";STR$((5-P)*2E3);",6000;XT;";NEXTP
11300 FOR P=0 TO 3
11320 O=((.2*(3-P)/SC*YS/25)*PF)
11340 IF O=0 THEN O$="      0" ELSE O$=STR$(FNS(O))
11360 LPRINT"PA0,";STR$((3-P)*2E3);";YT;CP-8.0;LB";O$;CHR$(3)
11380 NEXTP
11400 LPRINT"PA-800,6200;SI.3,.5;CP01,1;LB";LEFT$(RPL$,1);"   FILE:";LB$
11420 LPRINT SPC(5);B$(16);CHR$(3);"SI;"
11440 REM LPRINT"PA-800,7000;LBCFG.";CF;CHR$(3)
11460 IF CX<>0 THEN LPRINT"PA500,7000;LB";"CXS=";CX*1E12;CHR$(3)
11480 IF GX<>0 THEN LPRINT"PA3700,7000;LBGXS=";GX;CHR$(3)
11500 IF LA<>1 THEN LPRINT"PA6900,7000;LBL/A=";LA;CHR$(3)
11520 LPRINT"PA10000,7000;LBV=";B$(8);CHR$(3)
11540 RETURN
12000 CALL"IDENT",0,0
12010 CALL"XMODE",1,1
12015 TEXT
12020 PRINT "     PLOTTING PROGRAM PLOT1"
12030 PRINT
12040 PRINT "SCALE = (XMIN,YMIN) TO (XMAX,YMAX)"
12050 PRINT"FOR SAME SCALE ON X AND Y AXES"
12060 PRINT"LET XMAX = 1.25*YMAX"
12070 PRINT
12080 PRINT "SET XY RECORDER TO 5V/100MM"
12090 PRINT"CONNECT GRAPHICS BOARD WITH"
12100 PRINT"OA (XDATA) TO Y ON CHART RECORDER"
12110 PRINT"OB (YDATA) TO X ON CHART RECORDER"
12120 PRINT"PEN/Z TO PEN LIFT ON CHART RECORDER"
12130 PRINT
12140 PRINT
12150 V=.5
12160 PRINT
12170 PRINT
12180 INPUT"CHAR.SIZE 0PO";CS
12190 INPUT"ORIENTATION (1 FOR X AXIS,7 FOR Y AXIS)";OO
12200 INPUT"WORD(S)";S$
12210 IF L$="Y"GOTO12460
12214 YP(1)=YP(0)+(YP(1)-YP(0))*1.2
12215 PRINT "XMIN=",XP(0)
12216 PRINT "YMIN=",YP(0)
12217 PRINT "XMAX=",XP(1)
12218 PRINT "YMAX=",YP(1)
12219 INPUT"SCALE OK Y/N";Z$:IF Z$<"N"GOTO12230
12220 INPUT"TYPE XMIN,YMIN,XMAX,YMAX";XP(0),YP(0),XP(1),YP(1)
12230 CALL"XPLOT",1,0,0,0
12240 INPUT"IF PLOTTER IS ZEROED TYPE RETURN";E
12250 CALL"XPLOT",1,0,0,1
12260 INPUT"AXES Y/N";AX$
12270 IF AX$="N" GOTO12320
12280 CALL"XLINE",1,2047,0,3
12290 CALL"XLINE",1,2047,-1638,3
12300 CALL"XLINE",1,0,-1638,3
12310 CALL"XLINE",1,0,0,1
12320 CALL"XPLOT",1,0,0,0
12330 FOR J=0 TO NP
12340 X=INT(2047*((X(J)-XP(0))/(XP(1)-XP(0))))
12350 Y=INT(-1638*((Y(J)-YP(0))/(YP(1)-YP(0))))
12360 CX=(CS*3.333*V)
12370 CALL"XSET",1,0,CX,00
12380 CALL"XSPEED",5
12390 CALL"XPLOT",1,X,Y,0
12400 CALL"WAIT",50
12410 CALL"XCHAR",1,VARADR(S$)
12420 NEXT J
12430 INPUT"LABEL GRAPH Y/N";L$
12440 IF L$="Y"GOTO12180
12450 RETURN
12460 CALL"XPLOT",1,0,0,0
12470 INPUT"MOVE PEN TO DESIRED POSITION AND TYPE RETURN";E
12475 CX=(CS*3.333*V)
12480 CALL"XSET",1,0,CX,00
12490 CALL"XSPEED",5
12500 CALL"XPLOT",1,0,0,0
12510 CALL"WAIT",50
12520 CALL"XCHAR",1,VARADR(S$)
12530 GOTO 12430
```

APPENDIX I: Thermodynamic Equations

(1) Pyrite (FeS_2), Pyrrhotite (FeS, ($Fe_{1-x}S$)) and Sulphur

(a) $FeS_2 = Fe^{2+} + 2S = 2e$

$E = 0.423 + 0.0295 \log[Fe^{2+}]$

(b) $FeS_2 + 8H_2O = Fe^{2+} + 2SO_4^{2-} + 16H^+ + 14e$

$E = 0.367 - 0.067\ pH + 0.008 \log[SO_4^{2-}] + 0.004 \log[Fe^{2+}]$

(c) $FeS_2 + 3H_2O = Fe(OH)_3 + 2S + 3H^+ + 3e$

$E = 0.64 - 0.0591\ pH$

(d) $FeS_2 + 11H_2O = Fe(OH)_3 + 2SO_4^{2-} + 19H^+ + 15e$

$E = 0.412 - 0.0749\ pH + 0.0078 \log[SO_4^{2-}]$

(e) $FeS_2 = Fe^{3+} + 2S + 3e$

$E = 0.546 + 0.0196 \log[Fe^{3+}]$

(f) $FeS_2 + 8H_2O = Fe^{3+} + 2SO_4^{2-} + 16H^+ + 15e$

$E = 0.394 - 0.063\ pH + 0.008 \log[2SO_4^{2-}] + 0.004 \log[Fe^{3+}]$

(g) $Fe^{2+} = Fe^{3+} + e$

$E = 0.771 + 0.0591 \log[Fe^{3+}] - 0.0591 \log[Fe^{2+}]$

(h) $Fe^{2+} + H_2O = Fe(OH)^{2+} + H^+ + e$

$E = 0.914 = 0.0591\ pH + 0.0591 \log[FeOH^{2+}] - 0.0591 \log[Fe^{2+}]$

(i) $Fe^{2+} + 2H_2O = Fe(OH)_2^+ + 2H^+ + e$

$E = 1.191 - 0.1182\ pH + 0.0591 \log[Fe(OH)_2^+] - 0.0591 \log[Fe^{2+}]$

(j) $Fe^{2+} + 3H_2O = Fe(OH)_3 + 3H^+ + e$

$E = 1.056 - 0.177\ pH - 0.0591 \log[Fe^{2+}]$

(k) $Fe(OH)_2 + H_2O = Fe(OH)_3 + H^+ + e$

$E = 0.271 - 0.0591\ pH$

(l) $FeS + 3H_2O = Fe(OH)_3 + S + 3H^+ + 3e$

$E = 0.398 - 0.0591\ pH$

(m) $FeS + 2H_2O = FeOOH + S + 3H^+ + 3e$

$E = 0.290 - 0.0591\ pH$

(n) $Fe(OH)_2 + FeOOH + H^+ + e$

$E = -0.071 - 0.0591\ pH$

(o) $Fe^{2+} + 2H_2O = FeOOH + 3H^+ + e$

$E = -0.715 - 0.177\ pH - 0.0591\ \log[Fe^{2+}]$

(p) $Fe^{2+} + 2H_2S = FeS_2 + 4H^+ + 2e$

$E = -0.106 - 0.0591\ pH - 0.0295\ \log[H_2S] - 0.0295\ \log[Fe^{2+}]$

(q) $FeS + H_2S = FeS_2 + 2H^+ + 2e$

$E = -0.216 - 0.0591\ pH - 0.0295\ \log[H_2S]$

(r) $FeS + HS^- = FeS_2 + H^+ + 2e$

$E = -0.423 - 0.0295\ pH - 0.0295\ \log[HS^-]$

(s) $Fe = Fe^{2+} + 2e$

$E = -0.440 + 0.0295\ \log[Fe^{2+}]$

(t) $Fe + H_2S = FeS + 2H^+ + 2e$

$E = -0.364 - 0.0591\ pH - 0.0295\ \log[H_2S]$

(u) $Fe + HS^- = FeS + H^+ + 2e$

$E = -0.571 - 0.0295\ pH - 0.0295\ \log[HS^-]$

(v) $H_2S = S + 2H^+ + 2e$

$E = 0.141 - 0.059\ pH - 0.0295\ \log[H_2S]$

(w) $HS^- = S + H^+ + 2e$

$E = 0.065 - 0.0295\ pH - 0.0295\ \log[HS^-]$

(x) $S + H^+ + e = HS$

(y) $HS + e = HS^-$

(z) $HS^- + H^+ = H_2S$ $\qquad \log \frac{[HS^-]}{[H_2S]} = -7.00 + pH$

(a_1) $2S^{2-}_{lattice} = S_2^{2-}_{lattice} + 2e$

(b_1) $Fe + 2HS^- = FeS_2 + 2H^+ + 4e$

$E = -0.497 - 0.0295\ pH - 0.0295 \log[HS^-]$

(c_1) $Fe + 2H_2S = FeS_2 + 4H^+ + 4e$

$E = -0.290 - 0.0591\ pH - 0.0295 \log[H_2S]$

(d_1) $H_2 = 2H^+ + 2e$

$E = 0.000 - 0.0591\ pH - 0.0295 \log p_{H_2}$

(e_1) $FeS = Fe^{2+} + S + 2e$

$E = -0.078 + 0.0295 \log [Fe^{2+}]$

(f_1) $FeS + 4H_2O = Fe^{2+} + SO_4^{2-} + 8H^+ + 8e$

$E = 0.0287 - 0.0591\ pH + 0.007 \log [SO_4^{2-}] + 0.007 \log[Fe^{2+}]$

(g_1) $FeS + 7H_2O = Fe(OH)_3 + SO_4^{2-} + 11H^+ + 9e$

$E = 0.372 - 0.072\ pH + 0.007 \log[SO_4^{2-}]$

(h_1) $FeS = Fe^{3+} + S + 3e$

$E = 0.301 + 0.020 \log [Fe^{3+}]$

(i_1) $FeS + 4H_2O = Fe^{3+} + SO_4^{2-} + 8H^+ + 9e$

$E = 0.114 - 0.053\ pH + 0.007 \log [SO_4^{2-}] + 0.007 \log [Fe^{3+}]$

(j_1) $FeS + 2H^+ = Fe^{2+} + H_2S$

$\log [Fe^{2+}] = 2.582 - 2\ pH - \log [H_2S]$

(k_1) $FeS_2 + 2H^+ = Fe^{2+} + H_2S + S$

$\log [Fe^{2+}] = -9.531 - 2\ pH - \log [H_2S]$

(l_1) $FeS = (1-x)Fe^{2+} + Fe_xS + 2(1-x)e$

(m_1) $Fe_xS = xFeS + (1-x)S \quad (x < 1)$

(n_1) $Fe_xS + 2(1-x)H^+ + 2(1-x)e = xFeS + (1-x)H_2S$

(o_1) $Fe^{3+} + 3H_2O = Fe(OH)_3 + 3H^+$

$\log [Fe^{3+}] = 4.84 - 3\ pH$

(p_1) $Fe^{2+} + 2H_2O = Fe(OH)_2 + 2H^+$

$\log [Fe^{2+}] = 13.29 - 2\ pH$

(q_1) $Fe + 2H_2O = Fe(OH)_2 + 2H^+ + 2e$

$E = -0.047 - 0.0591\ pH$

(r_1) $Fe(CN)_6^{4-} = Fe(CN)_6^{3-} + e$

$E = 0.46 + 0.0591 \log[Fe(CN)_6^{3-}] - 0.0591 \log[Fe(CN)_6^{4-}]$

(s_1) $FeS_2 + 2H_2O = FeOOH + 2S + 3H^+ + 3e$

$E = 0.521 - 0.0591\ pH$

(t_1) $FeS_2 + 10H_2O = FeOOH + 2SO_4^{2-} + 19H^+ + 15e$

$E = 0.390 - 0.0749\ pH + 0.0078 \log [SO_4^{2-}]$

(u_1) $Fe^{3+} + 2H_2O - FeOOH + 3H^+$

$\log [Fe^{3+}] = -1.85 - 3\ pH$

(v_1) $FeOH^{2+} + 2H_2O = Fe(OH)_3 + 2H^+$

$\log[FeOH^{2+}] = 2.41 - 2\ pH$

(w_1) $Fe(OH)_2^+ + H_2O = Fe(OH)_3 + H^+$

$\log [Fe(OH)_2^+] = -2.28 - pH$

(x_1) $FeOH^{2+} + H_2O = FeOOH + 2H^+$

$\log [FeOH^{2+}] = -3.37 - 2\ pH$

(y_1) $Fe(OH)_2^+ = FeOOH + H^+$

$\log [Fe(OH)_2^+] = -8.06 - pH$

(z_1) $FeS + 2H_2O = FeOOH + S + 3H^+ + 3e$

$E = 0.290 - 0.591\ pH$

(ab_1) $FeS + HS^- = FeS_2 + H^+ + 2e$

$E = -0.423 - 0.0295\ pH - 0.0295 \log [HS^-]$

(ac_1) $FeS + S^{2-} + 2e$

$E = -0.837 - 0.0295 \log [S^{2-}]$

(ad_1) $Fe + HS^- = FeS + H^+ + 2e$

$E = -0.571 - 0.0295\ pH - 0.0295 \log ([HS^-]$

(ae_1) $Fe + S^{2-} = FeS + 2e$

$E = -0.985 - 0.0295 \log [S^{2-}]$

(af_1) $Fe = Fe^{2+} + 2e$

$E = -0.440 + 0.0295 \log[Fe^{2+}]$

(ag_1) $S_2^{2-}{}_{(lattice)} = 2S_{(ads)} + 2e$

(ah_1) $H_2O + 2h^+ \rightleftharpoons (O)_{ads} + 2H^+$

(ai_1) $2H_2O + 2h^+ \rightleftharpoons 2(OH)_{ads} + 2H^+$

(aj_1) $(O)_{ads} + (O)_{ads} \rightleftharpoons (O_2)_{ads}$

(ak_1) $(O)_{ads} + H_2O + h^+{}_{solid} \rightleftharpoons (O_2H)_{ads} + H^+$

(al_1) $2(OH)_{ads} + h^+{}_{solid} \rightleftharpoons (O_2H)_{ads} + H^+$

(am_1) $FeS_2 + 2H_2O \rightleftharpoons FeS_2(HO_2)_{ads} + 3H^+ + 3e$

(an_1) $FeS_2 + 3H_2O = Fe(OH)_3 + 3H^+ + 0.5S_4^{2-} + 2e$

(ao_1) $FeS_2 + 3H_2O = Fe(OH)_3 + 3H^+ + 0.4S_5^{2-} + 2.2e$

(ap_1) $xS^{2-} = S_x^{2-} + (2x-2)e$ when $2 \leq x \leq 5$

(aq_1) $S_x^{2-} = xS + 2e$ (where $2 \leq x \leq 5$)

(ar_1) $S_2^{2-} = 2S + 2e$

(as_1) $S^{2-} = S_{solid} + 2e$

(at_1) $S + 4H_2O = SO_4^{2-} + 8H^+ + 6e$

$E = 0.357 - 0.0788\ pH + 0.0098\ \log[SO_4^{2-}]$

(au_1) $(OH)_{ads} + (O)_{ads} \rightleftharpoons (O_2H)_{ads}$

(av_1) $(O_2H)_{ads} + e_{solid}^- \rightleftharpoons O_2H^-_{ads}$

(aw_1) $xHS^- = S_x^{2-} + xH^+ + (2x-2)e$

(ax_1) $2S_{(ads)} + H_2O_2 = S_2(OH)_2$

(ay_1) $xS + H^+ + 2e = HS_x^-$

(az_1) $HS_x^- + (2x-1)H^+ + 2xe = xH_2S$

(ba_1) $FeS + 6H_2O = FeOOH + SO_4^{2-} + 11H^+ + 9e$

$E = 0.341 - 0.072\ pH + 0.007\ \log[SO_4^{2-}]$

(bb_1) $SO_3^{2-} + S = S_2O_3^{2-}$

(bc_1) $4S + 6OH^- = S_2O_3^{2-} + 2S^{2-} + 3H_2O$

(bd_1) $12S + 6OH^- = S_2O_3^{2-} + 2S_5^{2-} + 3H_2O$

(be_1) $Fe_{1-x}S = (1-2x)Fe^{2+} + FeS_2 + 2(1-2x)e$

2. <u>Pentlandite ($(Fe,Ni)_9S_8$), Violarite ($FeNi_2S_4$) and Millerite (NiS)</u>

(a_2) $(Fe,Ni)_9S_8 = 4.5Ni^{2+} + 4.5Fe^{2+} + 8S + 18e$

$E = 0.067 + 0.015\ \log[Ni^{2+}] + 0.015\ \log[Fe^{2+}]$

(b_2) $(Fe,Ni)_9S_8 = 4.5Ni^{2+} + 4.5Fe^{3+} + 8S + 22.5e$

$E = 0.208 + 0.0118 \log[Ni^{2+}] + 0.118 \log [Fe^{3+}]$

(c_2) $(Fe,Ni)_9S_8 + 32H_2O = 4.5Fe^{2+} + 4.5Ni^{2+} + 8SO_4^{2-} + 64H^+ + 66e$

$E = 0.278 - 0.0573\ pH + 0.004 \log[Fe^{2+}] + 0.004 \log[Ni^{2+}] + 0.072 \log[SO_4^{2-}]$

(d_2) $(Fe,Ni)_9S_8 + 32H_2O = 4.5Ni^{2+} + 4.5Fe^{3+} + 8SO_4^{2-} + 64H^+ + 70.5e$

$E = 0.310 - 0.054\ pH + 0.0038 \log[Ni^{2+}] + 0.0038 \log[Fe^{3+}] + 0.0067 \log[SO_4^{2-}]$

(e_2) $(Fe,Ni)_9S_8 + 13.5H_2O = 4.5Ni^{2+} + 4.5Fe(OH)_3 + 8S + 13.5H^+ + 22.5e$

$E = 0.265 - 0.0355\ pH + 0.0118 \log[Ni^{2+}]$

(f_2) $(Fe,Ni)_9S_8 + 45.5H_2O = 4.5Ni^{2+} + 4.5Fe(OH)_3 + 8SO_4^{2-} + 77.5H^+ + 70.5e$

$E = 0.0328 - 0.065\ pH - 0.0038 \log[Ni^{2+}] + 0.0067 \log[SO_4^{2-}]$

(g_2) $(Fe,Ni)_9S_8 + 22.5H_2O = 4.5Ni(OH)_2 + 4.5Fe(OH)_3 + 8S + 22.5H^+ + 22.5e$

$E = 0.409 - 0.059\ pH$

(h_2) $(Fe,Ni)_9S_8 + 54.5H_2O = 4.5Ni(OH)_2 + 4.5Fe(OH)_3 + 8SO_4^{2-} + 86.5H^+ + 70.5e$

$E = 0.374 - 0.0725\ pH + 0.0067 \log[SO_4^{2-}]$

(i_2) $(Fe,Ni)_9S_8 + 22.5H_2O + 4.5NiOOH + 4.5Fe(OH)_3 + 8S + 27H^+ + 27e$

$E = 0.513 - 0.0591\ pH$

(j_2) $(Fe,Ni)_9S_8 + 54.5H_2O = 4.5NiOOH + 4.5Fe(OH)_3 + 8SO_4^{2-} + 91H^+ + 75e$

$E = 0.413 - 0.0716\ pH + 0.006 \log[SO_4^{2-}]$

(k_2) $(Fe,Ni)_9S_8 + 10.5H_2O = FeNi_2S_4 + 3.5Fe(OH)_3 + 2.5Ni^{2+} + 4S + 10.5H^+ + 15.5e$

$E = 0.225 - 0.040\ pH + 0.0095 \log[Ni^{2+}]$

(m_2) $(Fe,Ni)_9S_8 + 26.5H_2O = FeNi_2S_4 + 3.5Fe(OH)_3 + 2.5Ni^{2+} + 4SO_4^{2-} + 42.5H^+ + 39.5e$

$E = 0.305 - 0.064\ pH + 0.0037 \log[Ni^{2+}] + 0.006 \log[SO_4^{2-}]$

(n_2) $Ni(OH)_2 = NiOOH + H^+ + e$

$E = 1.033 - 0.0591\ pH$

(o_2) $Ni + 2H_2O = Ni(OH)_2 + 2H^+ + 2e$

$E = 0.110 - 0.0591\ pH$

(p_2) $NiOOH + 2H_2O = NiO_2.2H_2O + H^+ + e$

$E = 1.434 - 0.0591\ pH$

(q_2) $(Fe,Ni)_9S_8 = 2FeNi_2S_4 + 2.5Fe^{2+} + 0.5Ni^{2+} + 6e$

$E = -0.273 + 0.0246\ \log[Fe^{2+}] + 0.0049\ \log[Ni^{2+}]$

(r_2) $(Fe,Ni)_9S_8 = 2FeNi_2S_4 + 2.5Fe^{3+} + 0.5Ni^{2+} + 8.5e$

$E = 0.034 + 0.017\ \log[Fe^{3+}] + 0.0035\ \log[Ni^{2+}]$

(s_2) $(Fe,Ni)_9S_8 + 7.5H_2O = 2FeNi_2S_4 + 2.5Fe(OH)_3 + 0.5Ni^{2+} + 7.5H^+ + 8.5e$

$E = 0.118 - 0.052\ pH + 0.0035\ \log[Ni^{2+}]$

(t_2) $(Fe,Ni)_9S_8 + 13.5H_2O = 4.5NiS + 4.5Fe(OH)_3 + 3.5S + 13.5H^+ + 13.5e$

$E = 0.334 - 0.0591\ pH$

(u_2) $(Fe,Ni)_9S_8 + 27.5H_2O = 4.5NiS + 4.5Fe(OH)_3 + 3.5SO_4^{2-} + 41.5H^+ + 27.5e$

$E = 0.436 - 0.089\ pH + 0.0075\ \log[SO_4^{2-}]$

(v_2) $(Fe,Ni)_9S_8 + 13.5H_2O + 3.5Ni^{2+} = 8NiS + 4.5Fe(OH)_3 + 13.5H^+ + 6.5e$

$E = 0.519 - 0.123\ pH - 0.032\ \log[Ni^{2+}]$

(w_2) $(Fe,Ni)_9S_8 + 3H_2O = 2NiS + 2S + Fe(OH)_3 + 3H^+ + 3e$

$E = 0.649 - 0.0591\ pH$

(x_2) $FeNi_2S_4 + 11H_2O = 2NiS + 2SO_4^{2-} + Fe(OH)_3 + 19H^+ + 15e$

$E = 0.415 - 0.0749\ pH + 0.0079\ \log[SO_4^{2-}]$

(y_2) $NiS = Ni^{2+} + S + 2e$

$E = 0.133 + 0.0295\ \log[Ni^{2+}]$

(z_2) $NiS + 4H_2O = Ni^{2+} + SO_4^{2-} + 8H^+ + 8e$

$$E = 0.308 - 0.0591\ pH + 0.0074\ \log[Ni^{2+}] + 0.0074\ \log[SO_4^{2-}]$$

(a_3) $Ni^{2+} + 2H_2O = Ni(OH)_2 + 2H^+$

$$\log\ [Ni^{2+}] = 12.18 - 2\ pH$$

(b_3) $NiS + 2H_2O = Ni(OH)_2 + S + 2H^+ + 2e$

$$E = 0.494 - 0.0591\ pH$$

(c_3) $NiS + 6H_2O = Ni(OH)_2 + SO_4^{2-} + 10H^+ = 8e$

$$E = 0.391 - 0.073\ pH + 0.0074\ \log[SO_4^{2-}]$$

(d_3) $Fe^{2+} + 2Ni^{2+} + 4H_2S = FeNi_2S_4 + 8H^+ + 2e$

$$E = -0.341 - 0.237\ pH - 0.1183\ \log[H_2S] - 0.0592\ \log[Ni^{2+}] - 0.0296\ \log[Fe^{2+}]$$

(e_3) $Fe + 2Ni + 4H_2S = FeNi_2S_4 + 8H^+ + 8e$

$$E = -0.271 - 0.0591\ pH - 0.0295\ \log[H_2S]$$

(f_3) $Fe + 2Ni + 4HS^- = FeNi_2S_4 + 4H^+ + 8e$

$$E = -0.478 - 0.0295\ pH - 0.0295\ \log[HS^-]$$

(g_3) $Ni + H_2S = NiS + 2H^+ + 2e$

$$E = -0.242 - 0.0591\ pH - 0.0295\ \log[H_2S]$$

(h_3) $Ni + HS^- = NiS + H^+ + 2e$

$$E = -0.449 - 0.0295\ pH - 0.0295\ \log[HS^-]$$

(i_3) $(Fe,Ni)_9S_8 + 16H^+ = 4.5Ni^{2+} + 4.5Fe^{2+} + 8H_2S + 2e$

$$E = -0.529 + 0.4733\ pH + 0.133\ \log[Ni^{2+}] + 0.133\ \log[Fe^{2+}] + 0.236\ \log[H_2S]$$

(j_3) $4.5Fe + 4.5Ni + 8H_2S = (Fe,Ni)_9S_8 + 16H^+ + 16e$

$$E = -0.322 - 0.059\ pH - 0.0295\ \log[H_2S]$$

(k_3) $4.5Fe + 4.5Ni + 8HS^- = (Fe,Ni)_9S_8 + 8H^+ + 16e$

$$E = -0.529 - 0.0295\ pH - 0.0295\ \log[HS^-]$$

(l_3) $NiS + 2H^+ = H_2S + Ni^{2+}$

$$\log[Ni^{2+}] = 0.2712 - 2\ pH - \log[H_2S]$$

(m_3) $FeNi_2S_4 + 3H_2O = Fe(OH)_3 + 2Ni^{2+} + 4S + 3H^+ + 7e$

$$E = 0.354 - 0.0253\ pH + 0.0169\ \log[Ni^{2+}]$$

(n_3) $FeNi_2S_4 + 19H_2O = Fe(OH)_3 + 2Ni^{2+} + 4SO_4^{2-} + 35H^+ + 31e$

$$E = 0.357 - 0.067\ pH + 0.0038\ \log[Ni^{2+}] + 0.0076\ \log[SO_4^{2-}]$$

(o_3) $FeNi_2S_4 + 7H_2O = Fe(OH)_3 + 2Ni(OH)_2 + 4S + 7H^+ + 7e$

$$E = 0.560 - 0.0591\ pH$$

(p_3) $FeNi_2S_4 + 23H_2O = Fe(OH)_3 + 2Ni(OH)_2 + 4SO_4^{2-} + 39H^+ + 31e$

$$E = 0.403 - 0.0744\ pH + 0.0076\ \log[SO_4^{2-}]$$

(q_3) $FeNi_2S_4 = Fe^{3+} + 2Ni^{2+} + 4S + 7e$

$$E = 0.314 + 0.0084\ \log[Fe^{3+}]\ 0.017\ \log[Ni^{2+}]$$

(r_3) $FeNi_2S_4 + 16H_2O = Fe^{3+} + 2Ni^{2+} + 4SO_4^{2-} + 32H^+ + 31e$

$$E = 0.347 - 0.061\ pH + 0.0019\ \log[Fe^{3+}] + 0.0038\ \log[Ni^{2+}] + 0.0076\ \log[SO_4^{2-}]$$

3. Chalcopyrite ($CuFeS_2$), Bornite (Cu_5FeS_4), Chalcocite (Cu_2S) and Covellite (CuS)

(a_4) $CuFeS_2 = CuS + Fe^{2+} + S + 2e$

$$E = 0.232 + 0.0295\ \log[Fe^{2+}]$$

(b_4) $CuFeS_2 = CuS + Fe^{3+} + S + 3e$

$$E = 0.412 + 0.0197\ \log[Fe^{3+}]$$

(c_4) $CuFeS_2 = Cu^{2+} + Fe^{2+} + 2S + 4e$

$$E = 0.411 + 0.0148\ \log[Cu^{2+}]$$

(d_4) $CuFeS_2 = Cu^{2+} + Fe^{3+} + 2S + 5e$

$$E = 0.483 + 0.0118\ \log[Cu^{2+}] + 0.0118\ \log[Fe^{3+}]$$

(e_4) $CuFeS_2 + 8H_2O = Cu^{2+} + Fe^{2+} + 2SO_4^{2-} + 16H^+ + 16e$

$E = 0.371 - 0.0591\ pH + 0.004\ \log[Cu^{2+}] + 0.004\ \log[Fe^{2+}] + 0.0074\ \log[SO_4^{2-}]$

(f_4) $CuFeS_2 + 8H_2O = Cu^{2+} + Fe^{3+} + 2SO_4^{2-} + 16H^+ + 17e$

$E = 0.394 - 0.0556\ pH + 0.0035\ \log[Cu^{2+}] + 0.0035\ \log[Fe^{3+}] + 0.007\ \log[SO_4^{2-}]$

(g_4) $CuFeS_2 = CuFe_{0.2}S_{0.8} + 0.8Fe^{2+} + 1.2S + 1.6e$

$E = 0.260 + 0.0295\ \log[Fe^{2+}]$

(h_4) $CuFeS_2 = CuFe_{0.2}S_{0.8} + 0.8Fe^{3+} + 1.2S + 2.4e$

$E = 0.403 + 0.0197\ \log[Fe^{3+}]$

(i_4) $CuFe_{0.2}S_{0.8} = 0.5Cu_2S + 0.2Fe^{2+} + 0.3S + 0.4e$

$E = 0.273 + 0.0295\ \log[Fe^{2+}]$

(j_4) $CuFe_{0.2}S_{0.8} = 0.5Cu_2S + 0.2Fe^{3+} + 0.3S + 0.6e$

$E = 0.439 + 0.020\ \log[Fe^{3+}]$

(k_4) $0.5Cu_2S = 0.5CuS + 0.5Cu^{2+} + e$

$E = 0.530 + 0.0295\ \log[Cu^{2+}]$

(l_4) $CuFeS_2 + 3H_2O = Cu^{2+} + Fe(OH)_3 + 2S + 3H^+ + 5e$

$E = 0.540 - 0.0355\ pH + 0.0118\ \log[Cu^{2+}]$

(m_4) $CuFeS_2 + 11H_2O = Cu^{2+} + Fe(OH)_3 + 2SO_4^{2-} + 19H^+ + 17e$

$E = 0.411 - 0.0661\ pH + 0.007\ \log\ [SO_4^{2-}] + 0.003\ \log[Cu^{2+}]$

(n_4) $CuFeS_2 = Fe^{2+} + 0.5\ Cu^{2+} + 0.5CuS + 1.5S + 3e$

$E = 0.437 + 0.01\ \log[Cu^{2+}] + 0.02\ \log[Fe^{2+}]$

(o_4) $CuFeS_2 = Fe^{3+} + 0.5CuS + 0.5Cu^{2+}\ 1.5S + 4e$

$E = 0.456 + 0.0074\ \log[Cu^{2+}] + 0.0148\ \log[Fe^{3+}]$

(p_4) $CuFeS_2 + 3H_2O = CuS + Fe(OH)_3 + S + 3H^+ + 3e$

$E = 0.507 - 0.059\ pH$

(r_4) $CuS = Cu^{2+} + S + 2e$

$E = 0.590 + 0.0295 \log[Cu^{2+}]$

(s_4) $CuFeS_2 + 2.4H_2O = CuFe_{0.2}S_{0.8} + 0.8Fe(OH)_3 + 1.2S + 2.4H^+ + 2.4e$

$E = 0.525 - 0.0591\ pH$

(t_4) $CuFeS_2 + 7.2H_2O = CuFe_{0.2}S_{0.8} + 0.8Fe(OH)_3 + 1.2SO_4^{2-} + 12H^+ + 9.6e$

$E = 0.399 - 0.0739\ pH + 0.0074 \log[SO_4^{2-}]$

(u_4) $CuFe_{0.2}S_{0.8} + 0.6H_2O = 0.5Cu_2S + 0.2Fe(OH)_3 + 0.6H^+ + 0.3S + 0.6e$

$E = 0.534 - 0.0591\ pH$

(v_4) $CuFe_{0.2}S_{0.8} + 1.8H_2O = 0.5Cu_2S + 0.2Fe(OH)_3 + 0.3SO_4^{2-} + 3H^+ + 2.4e$

$E = 0.401 - 0.0739\ pH + 0.0074 \log[SO_4^{2-}]$

(w_4) $Cu_2S + 2H_2O = CuS + Cu(OH)_2 + 2H^+ + 2e$

$E = 0.802 - 0.0591\ pH$

(x_4) $CuS + 2H_2O = Cu(OH)_2 + 2H^+ + S + 2e$

$E = 0.863 - 0.0591\ pH$

(y_4) $CuS + 6H_2O = Cu(OH)_2 + SO_4^{2-} + 10H^+ + 8e$

$E = 0.484 - 0.0739\ pH + 0.0074 \log [SO_4^{2-}]$

(z_4) $Cu^{2+} + 2H_2O = Cu(OH)_2 + 2H^+$

$\log[Cu^{2+}] = 9.2 - 2\ pH$

(a_5) $CuFeS_2 + 5H_2O = Cu(OH)_2 + Fe(OH)_3 + 2S + 5H^+ + 5e$

$E = 0.649 - 0.0591\ pH$

(b_5) $CuFeS_2 + 13H_2O = Cu(OH)_2 + Fe(OH)_3 + 2SO_4^{2-} + 21H^+ + 17e$

$E = 0.443 - 0.073\ pH + 0.007 \log[SO_4^{2-}]$

(c_5) $Cu_2O + 3H_2O = 2Cu(OH)_2 + 2H^+ + 2e$

$E = 0.748 - 0.0591\ pH$

(d_5) $2CuS + 2H^+ + 2e = Cu_2S + H_2S$

$E = 0.082 - 0.0591\ pH - 0.0295\ \log[H_2S]$

(e_5) $2CuS + H^+ + 2e = Cu_2S + HS^-$

$E = -0.110 - 0.0295\ pH - 0.0295\ \log[HS^-]$

(f_5) $2Cu + H_2O = Cu_2O + 2H^+ + 2e$

$E = 0.472 - 0.059\ pH$

(g_5) $CuFeS_2 + 2.4H^+ + 0.8e = CuFe_{0.2}S_{0.8} + 0.8Fe^{2+} + 1.2H_2S$

$E = -0.29 - 0.177\ pH - 0.0591\ \log[Fe^{2+}] - 0.088\ \log[H_2S]$

(h_5) $2CuFeS_2 + 6H^+ + 2e = Cu_2S + 2Fe^{2+} + 3H_2S$

$E = -0.22 - 0.177\ pH - 0.0591\ \log[Fe^{2+}] - 0.089\ \log[H_2S]$

(i_5) $CuFeS_2 + 4H^+ + 2e = Cu + Fe^{2+} + 2H_2S$

$E = -0.260 - 0.118\ pH - 0.0591\ \log[H_2S] - 0.0295\ \log[Fe^{2+}]$

(j_5) $CuFeS_2 + 2H^+ = CuS + Fe^{2+} + H_2S$

$\log[Fe^{2+}] = 3.05 + \log[H_2S] + 2\ pH$

(k_5) $CuFeS_2 + 4H^+ + 4e = Cu + Fe + 2H_2S$

$E = -0.321 - 0.0591\ pH - 0.0295\ \log[H_2S]$

(l_5) $CuFeS_2 = (1-x)Cu^{2+} + (1-y)Fe^{2+} + Cu_xFe_yS_2 + 4(2-x-y)e$

(m_5) $Cu_xFe_yS_2 = (x+y)CuFeS_2 + (2-x-y)S \quad (x < 1,\ y < 1)$

(n_5) $2CuFeS_2 + 7H_2O = Cu_2O + 2Fe(OH)_3 + 4S + 8H^+ + 8e$

$E = 0.626 - 0.0591\ pH$

(o_5) $2CuFeS_2 + 23H_2O = Cu_2O + 2Fe(OH)_3 + 4SO_4^{2-} + 40H^+ + 32e$

$E = 0.425 - 0.0739\ pH + 0.0074\ \log[SO_4^{2-}]$

(p_5) $CuFeS_2 + (4-2z)H^+ + (2x+2y+2z)e = Cu_xFe_yS_z + (1-x)Cu^{2+} + (1-y)Fe^{2+} + (2-z)H_2S$

(q_5) $Cu^{+} = Cu^{2+} + e$

$$E = 0.153 + 0.0591 \log[Cu^{2+}] - 0.0591 \log[Cu^{+}]$$

(r_5) $Cu = Cu^{+} + e$

$$E = 0.520 + 0.0591 \log[Cu^{2+}]$$

(s_5) $Cu = Cu^{2+} + 2e$

$$E = 0.337 + 0.0295 \log[Cu^{2+}]$$

(t_5) $Cu + H_2S = Cu_2S + 2H^{+} + 2e$

$$E = -0.305 - 0.0591\ pH - 0.0295 \log[H_2S]$$

(u_5) $Cu^{2+} + 2Cl^{-} + e = CuCl_2^{-}$

$$E = 0.409 + 0.118 \log[Cl^{-}] + 0.0591 \log[Cu^{2+}] - 0.0591 \log[CuCl^{2-}]$$

(v_5) $CuCl_2^{-} + e = Cu + 2Cl^{-}$

$$E = -0.036 - 0.118 \log[Cl^{-}] + 0.0591 \log[CuCl_2^{-}]$$

(w_5) $5Cu_2S = 5Cu_{1.8}S + Cu^{2+} + 2e$

(x_5) $3Cu_{1.8}S = 4Cu_{1.1}S + Cu^{2+} + 2e$

(y_5) $10Cu_{1.1}S = 10CuS + Cu^{2+} + 2e$

(z_5) $Cu^{+}Fe^{3+}(S^{2-})_2 = Cu^{+}_{(1-x)}Cu^{+}_{x}Fe^{3+}_{(1-x)}(S^{2-})_2 + xFe^{2+}_{(aq)}$

(za_5) $Cu^{+}Fe^{3+}(S^{2-})_2 + 3xH^{+} + xe = Cu^{+}Fe^{3+}_{(1-x)}H^{+}_{3x}(S^{2-})_2 + xFe^{2+}_{(aq)}$

(zb_5) $Cu_2O = 3H_2O = 2HCuO_2^{-} + 4H^{+} + 2e$

$$E = 1.783 - 0.118\ pH + 0.0591 \log[HCuO_2^{-}]$$

(zc_5) $Cu_2S + H_2O = Cu_2O + S + 2H^{+} + 2e$

$$E = 0.917 - 0.0591\ pH$$

(zd_5) $Cu(OH)_2 = HCuO_2^{-} + H^{+}$

$$\log [HCuO_2^{-}] = -17.52 + pH$$

(ze_5) $Cu + 2H_2O = Cu(OH)_2 + 2H^+ + 2e$

$E = 0.609 - 0.591\ pH$

(zf_5) $CuFeS_2 + 3H_2O = CuS_2 + Fe(OH)_3 + CuS_2 + 3H^+ + 3e$

(zg_5) $CuFeS_2 + 3H_2O = 0.5Cu_2S + 1.5S + Fe(OH)_3 + 3H^+ + 3e$

$E = 0.527 - 0.0591\ pH$

(zh_5) $CuS_2 + 2H_2O = Cu(OH)_2 + 2S + 2H^+ + 2e$

(zi_5) $CuFeS_2 + 3Cu^{2+} + 4e = 2Cu_2S + Fe^{2+}$

$E = 0.709 + 0.044\ \log[Cu^{2+}] + 0.015\ \log[Fe^{2+}]$

(4) Platinum (Pt)

(a_6) $PtS_x + 2xH^+ + 2xe = Pt(H_2S)_x$

(b_6) $PtS_2 + 2H_2O = PtO_2 + 2S + 4H^+ + 4e$

(c_6) $PtS_2 + 8H_2O = PtO_2 + 2SO_4^{2-} + 16H^+ + 16e$

(d_6) $Pt(H_2S)_x = PtS_x + 2xH^+ + 2xe$

(e_6) $Pt + H_2S = PtS + 2H^+ + 2e$

$E = -0.3 - 0.0591\ pH - 0.0295\ \log[H_2S]$

(f_6) $PtS + H_2S = PtS_2 + 2H^+ + 2e$

$E = -0.01 - 0.0591\ pH - 0.0295\ \log[H_2S]$

(g_6) $Pt + H_2O = PtO + 2H^+ + 2e$

$E = 0.980 - 0.0591\ pH$

(h_6) $PtO + H_2O = PtO_2 + 2H^+ + 2e$

$E = 1.045 - 0.0591\ pH$

(i_6) $PtS_2 + H_2O = PtO + 2S + 2H^+ + 2e$

(j_6) $Pt - (S_2O_3)_{ads} + 5H_2O = 2SO_4^{2-} + 10H^+ + Pt + 8e$

(k_6) $2H_2O = O_2 + 4H^+ + 4e$

$E = 1.229 - 0.0591\ pH - 0.0148 \log p_{O_2}$